SYNTHESIS AND CHARACTERISATION OF ORGANO-METALLIC COMPLEXES FOR USE IN APPLICATIONS IN PHOTOCHEMISTRY AND MEDICINE

KINAAN MAHMOOD TAWFIQ

A thesis submitted in partial fulfilment of the requirements of the Manchester Metropolitan University for the degree of Doctor of Philosophy

Division of Chemistry and Environmental Science
School of Science and the Environment
Faculty of Science and Engineering

February 2017

ACKNOWLEDGEMENTS

First and foremost, I must thank the "Iraqi Ministry for Higher Education" for providing the funding for my PhD. I would like to thank my supervisory team Prof. Herman Potgieter and Dr Patricia A Ragazzon for their guidance and help throughout the project. I would like to thank the cell culture team at the University of Salford for the studies of the biological activities of the compounds synthesised in this thesis

I am also very thankful Dr. Claudius D'Silva, alsoI am also very thankful to Dr Mike Dempsey (Head of Faculty Research Degrees) and Dr Paul Smith. I would also like to thank all the technicians, Mr David Smith, Mr Paul Warren, Mrs Helen Bentley, Mr. Gary Miller, Mr. Bill Ellison, and Mr. Lee Harman at the Manchester Metropolitan University for their help in acquiring NMR data, the ESPRC MS Facility, Swansea University and Dr Claire Wilson of the NCS, National Crystallography Service at Southampton University.

I am also very thankful to Ms Rita Kenny, Ms Anne-Marie Walsh, MS Megan Schofield and (Research Degrees Team), Ms Clare Holdcroft (Graduate School Manager)

My heartfelt thanks are sent to my auntie I regard as my sister Mrs Bushra Tawfiq. I like to thank my cousins Mr Qusay Ahmed and Mr Shihab Ahmed for their moral and financial support throughout my studies here at MMU. I also lilke to thank my best friends Mr Faris Yousif, Dr Kareem Jumaah Al-Salihi, Dr Ali Shukur, Mr Fuad Kaseam, Mr Ziad Tariq, Dr Mostafa Al-Hsdithi, Dr Jay Dixon, Mr Matt Hulme and others for their moral support.

This this is dedicated to my beloved bother Gassan Tawfiq, since his dealth in 2008, I miss him so much and I wish he was here with me celebrate my success.

DECLARATION

I declare that this thesis is my own work and that it has not already been accepted for any other degree concurrently or any other degree of doctor of Philosophy at this or any other university.

Kinaan Mahmood Tawfiq

Signature: ……

Date: ……....

Abstract

Research on sustainable technologies has accelerated during the past two decades to find alternative energy sources and combat environmental pollution, as well as to find alternative cancer treatments. One of the most intensively researched areas to achieve this, is the development of new sources of solar energy conversion and utilisation.

The first chapter gives a summary of various solar cell technologies and photovoltaic conversion devices, and also highlights some potential medicinal applications of the prepared complexes described in this work. It states the aim and objectives of this investigation, and concludes with the hypothesis. Chapter 2 gives a summary of the Cu-catalysed [3+2] cycloaddition reaction between an aryl azide and aryl alkene, known as the "click reaction". It describes work to date on various types of addition reactions, the role of Cu(I) catalysts and the use of various solvents.

In Chapter 3 the literature review continues with a discussion of the dye solar cell compounds (DSSC) themselves, and focuses on the synthesis of a range of organic ligands (L^1-L^9). The final literature review Chapter 4 gives a summary of biological activities of bioinorganic compounds used as medicinal drugs, in particular as anticancer agents.

All the ligands and organo-transition metal complexes synthesized in this investigation, were characterised comprehensively by ^{1}H-, ^{13}C-, DEPT, ^{1}H- ^{1}H COSY, ^{1}H- ^{13}C HQMC NMR, mass spectroscopy, FT-IR measurements, melting point determinations, UV-VIS absorbance determinations, fluorescence spectroscopy, X-ray crystallography, magnetic susceptibility and conductivity measurements, with finally quantum yield calculations. The strategy was to first synthesize a series of nine ligands of the type 1,2,3-triazol-4-yl-pyridine (PYTA) (Chapter 6), and couple them to eight different transition metals (Chapter 6). These were compared to consider the effects of electron withdrawing and electron donating substituents on the various ligands on the properties, and specifically the fluorescence yields/properties, and the geometries of the final metal complexes. Finally, the chloro ligands were replaced by isothiocyanato ones and the comparison repeated for selected complexes (Chapter 8).

The investigation yielded a number of new and interesting results. In Chapter 6 a new series of PYTA ligands were readily and easily prepared through a convenient click chemistry approach. X-ray crystallography clearly indicated that the 1,2,3-triazole part had an azo-character. A novel crystal structure analysis of ligand L^4 revealed that it had a unique one-dimensional zig-zag chain structure in the solid state, which was stabilised by intermolecular hydrogen bonds and stacking π-π interactions between the phenyl rings.

In Chapter 7 the structural analysis indicated that complexes of the $[M(L^3)_2(Cl)_2]$ type were a rare example of the coexistence of two *trans*–coordinated Cl anions in the axial position. It was further demonstrated that the direct connection at the N8 position of the triazolyl ring of a 4-substituted phenyl substituent had a significant influence on the geometry of both the ligands and their corresponding M-complexes. The coplanarity of the organic framework led to slip-stacked π–π interactions between any two molecules of a complex. Additionally, it was shown that the nature of the pendant substituent (X = CH_3, OCH_3, COOH, F, Cl, CN, H, CF_3) could affect the electronic properties of the organo-metallic complexes. It was demonstrated that the pyridine and triazole rings occupied the equatorial plane, whereas the metal-Cl atoms are in the axial plane, except for Mn(II) and Cd(II) complexes where the metal-Cl atoms lay in the equatorial plane. A further new contribution was that the triazole and pyridine nitrogens from each of the ligands in the equatorial plane were *trans* to each other. Finally, it was proven that weak intermolecular interactions *via* (C–H–Cl), (C–H...N) and (C–H...O) resulted in an ordered three dimensional supramolecular structure in which the molecules adopted a head-to-tail orientation stabilised by hydrogen bonding and π…π stacking.

In Chapter 8, a structural analysis indicated that the complexes $[Zn(L^3)_2(NCS)_2]$ and $[Cd(L^3)_2(NCS)_2]$ were rare examples of the coexistence of two *trans*–coordinated NCS anions in the axial positions in the mononuclear triazole-based octahedral configuration. This is in contrast to what is found in wide band ruthenium photosensitisers (e.g. N3 and N719) that are efficient photosensitisers, where the isothiocyanato groups are *cis* to each other. It was also proven that the substitution of

the chloro ligand by an isothiocyanato group in order to enhance the fluorescence of these complexes, failed to produce the desired effect. Finally, in Chapter 9, the remarkable structural resemblance of these novel compounds to bio-inorganic molecules with anticancer properties (such as cisplatin) indicated that compounds with the linkers bound to Co and Cu showed the maximum activity against some cancer cells, with a higher preference to target and kill colon cancer cells. This is a promising new development in the fight against cancer. Chapter 9 gives a final summary of the main findings and contributions of this work.

Contributions from this research

1. K.M. Tawfiq, H. Potgieter and M.J. Al-Jeboori, Some first row transition metal complexes of 1,2,3-triazole-pyridine based ligands through click reactions: synthesis, characterisation and molecular structures, **Photoactivatable Metals: From Theory to Therapy – A Discussion Meeting, Royal Society**, London, 18 – 19 June 2012 – Poster presentation.

2. Kinaan M. Tawfiq, Gary J. Miller, Mohamad J. Al-Jeboori, Paul S. Fennell, Simon J. Coles, Graham J. Tizzard, Claire Wilson and Herman Potgieter, Comparison of the structural motifs and packing arrangements of six novel derivatives and one polymorph of 2-(1-phenyl-1H-1,2,3-triazol-4-yl)pyridine, **Acta Crystallographica**, **B**70, 379–389 (2014).

3. Kinaan M. Tawfiq, Gary J. Miller, Herman Potgieter, Mohamad J. Al-Jeboori, Graham J. Tizzard**,** and Claire Wilson, "A an unusual one-dimensional polymeric chain 2-(1-p-tolyl-1*H*-1,2,3-triazol-4-yl)-pyridine copper (II) dichloride $CuCl_2$[L] complex with an octahedral $CuCl_2[L]_2$ analogue" submitted to **Acta Crystallographica Section C: Crystal Structure Communications**.

TABLE OF CONTENTS

LIST OF ABBREVIATIONS AND SYMBOLS

AC	Alternating current
AM1.5	Air mass 1.5
BIPV	Building Integrated Photovoltaics
BPY	Bipyridine
CuAAC	Copper (I)-catalyzed alkyne-azide cycloaddition
CB	Conduction band
CDTE	Cadmium-Telluride
CIS	Copper-Indium-Selenide
CIGS	Copper-Indium-Gallium-Diselenide
C-SI	Crystalline silicon
COSY	Correlated Spectroscopy
DCM	Dichloromethane
DEPT	Distortionless enhancement by polarization transfer
DSSC	Dye Sensitised solar cell
DMSO	Dimethyl sulfoxide
ESI	Electrosprayionisation
E	Extinction coefficient
FT-IR	Fourier transform – infrared
GHG	Greenhouse gas
HMQC	Heteronuclear Multiple Quantum Coherence
HOMO	Highest Occupied Molecular Orbital
HRMS	High-resolution mass spectrometry
IC	Internal conversion
ISC	Intersystem crossing
IPCE	Incident photon to current conversion efficiency
Jsc	Short circuit current
LC	Ligand-centred
LHE	Light harvesting efficiency
LMCT	Ligand to metal charge transfer
LLCT	Ligand-to-ligand charge transfer
LUMO	Lowest unoccupied molecular orbital

MALDI-TOF	Matrix-assisted laser desorption injection time-of-flight
MLCT	Metal to ligand charge transfer
MS	Mass spectrometry
NMR	nuclear magnetic resonance
PYTA	Pyridine triazole
PV	Solar photovoltaic systems
Φf	Quantum yield
RAPS	Remote area power supplies
SC-SI	Single crystalline silicon
SPAAC	Strain-promoted azide-alkyne cycloaddition
S_0	Ground state
S_n	an excited singlet state
TMS	Trimethylsilyl
THF	Tetrahydrofuran
UV-VIS	Ultraviolet-visible
V_{OC}	Open circuit photovoltage
Au	Arbitrary units
λ max	Maximum wavelength
Λ_M	Molar conductance
B.M	Bohr magnetons
λ em	Wavelength emission
η	Solar energy to electricity conversion efficiency
Σ	Hammett constant
N	Refractive indice
Ppm	Parts per million
Δ	Chemical shift
S	Singlet
Dd	Doublet of doublet
Tdd	Triplet- doublet
μ_{eff}	effective magnetic momen
DFT	Density functional theory

LIST OF FIGURES

LIST OF TABLES

LIST OF SCHEMES

Chapter 1 : Solar Photovoltaic (PV) Technologies

1.1 Introduction

The world's fossil fuel resources are unable to sustain our current energy requirements beyond the next few decades. Therefore, the need for inexpensive alternatives has become urgent. Solar radiation is the single most abundant energy source of our planet. For many millennia, humanity relied solely on renewable forms of solar energy, making use of direct forms like lighting or heat, and indirect forms like biomass or wind. With the explosion of the world population at the beginning of the 20th century and its growing energy demand, humans started to tap non-renewable fossil forms of ancient biomass like oil, gas and coal [1]. Our dependence on the burning of fossil fuels actually is a curse, which causes geopolitical tensions, environmental damage, and puts our climate at stake [2]. One of the biggest challenges ahead of human kind is to replace the fossil fuel with renewable energy sources while keeping pace with the worldwide increasing thirst for energy because of rising demand, especially from developing countries. This challenge requires a low-cost solution, using abundantly available raw materials. The sun is an obvious source of clean and cheap energy, already used by nature to sustain almost all life on earth. even before the industrial revolution, human life quality was greatly affected by the availability of energy. The escalated consumption of conventional sources of energy is leading to forecasted energy and environmental crises. Renewable energy sources such as solar energy are considered as a feasible alternative because *"more energyfrom sunlight strikes earth in 1 hour than all of the energy consumed by humans in an entireyear"*. [3] Harvesting just a fraction of the solar energy reaching the earth may solve many problems associated with both the energy and global environment [4]. Therefore, harnessing the power of the sun with photovoltaic technologies is very attractive and potentially scalable. Indeed, solar farms are already providing electricity within many countries such as Spain, Germany, Portugal, USA, India and UAE. It is likely that solar energy will be used in conjunction with other renewable energy technologies and not on its own. Up to now, commercially available photovoltaic technologies are based on inorganic materials, which require high costs and highly energy consuming preparation methods. In addition, several of these materials, like CdTe, are toxic and have a low natural abundance. Organic photovoltaics can avoid this problem. However, the efficiencies of organic-based

photovoltaic cells are still at the moment a long way behind those obtained with purely inorganic based photovoltaic technologies. Conventional organic photovoltaic devices use donor and acceptor types of organic materials, which form a heterojunction favouring the separation of the excitation into two carriers. These carriers are then transported to the electrodes by the same organic materials that are used for the generation of the excitation. A material for classical organic photovoltaic devices should thus have both good light harvesting properties and good carrier transporting properties, which is a difficult task to achieve. On the other hand, the dye-sensitised solar cell (DSSC) technology separates the two requirements as the charge generation is done at the semiconductor-dye interface and the charge transport is done by the semiconductor and the electrolyte. Spectral properties optimisation can be done by modifying the dye alone, while carrier transport properties can be improved by optimising the semiconductor and the electrolyte composition. To obtain such compounds, organic moieties have been added on to metal cores producing bio-inorganic compounds.

Another critical problem facing modern society is medical health care, and the increasing number of the human population suffering from various cancers. Cancer has long been known to mankind, but the treatment thereof has been met with various degrees of success, and depends to a large degree on the type of cancer and the very early diagnosis thereof. In the last few decades, bio-inorganic molecules have shown diverse anticancer activities. The mechanisms of action for these molecules seem to be interaction with DNA. These agents have received much attention and generated increased interest in medicinal inorganic chemistry and have been found useful in treatment of cancers, psoriasis and various anemias [5]. Several ruthenium complexes have been developed as an alternative to *cis*-platin as potential anticancer agents, because they display lower toxicity than their platinum counterparts [6-9]. Studies on DNA-binding of any such complexes are crucial in development of nucleic acid interaction, chemotherapy and photodynamic treatment. Considerable efforts have gone into studying the binding mode, sites and affinities which could lead to opportunities to discover important information on site–specific DNA probes. Therefore, a study to modify the main ligand is quite significant for understanding the

DNA–binding and action mechanisms of selected suitable organometal complexes [10-12]. Triazoles from "click chemistry" are convenient ligands for the formation of promising organometallic complexes bearing combined triazole-amine or triazole-carboxylate moieties with different chelation modes. One triazole-amine platinum complexes that exhibited selective cytotoxicity against breast cancer cells lines was recently reported [13-15].

1.2 Photovoltaic cells

Photovoltaics (PV), also referred to as solar cells, convert sunlight directly into electricity. In 1839, Becguerel discovered the photo-voltaic effect [16]. Adams and Day found that solid selenium displays the photo-voltaic effect [17]. The first photovoltaic cell was created by Fritz in 1883, however, the efficiency was less than 1% [18]. Einstein published further information about the photovoltaic effect in 1904 but again the efficiency was less than 1% [19]. A 11% increase in efficiency was achieved by workers at the Bell Telephone Laboratories (1954) [20-22]. Currently there are three types of photovoltaic cells and are described in Scheme 1.1.

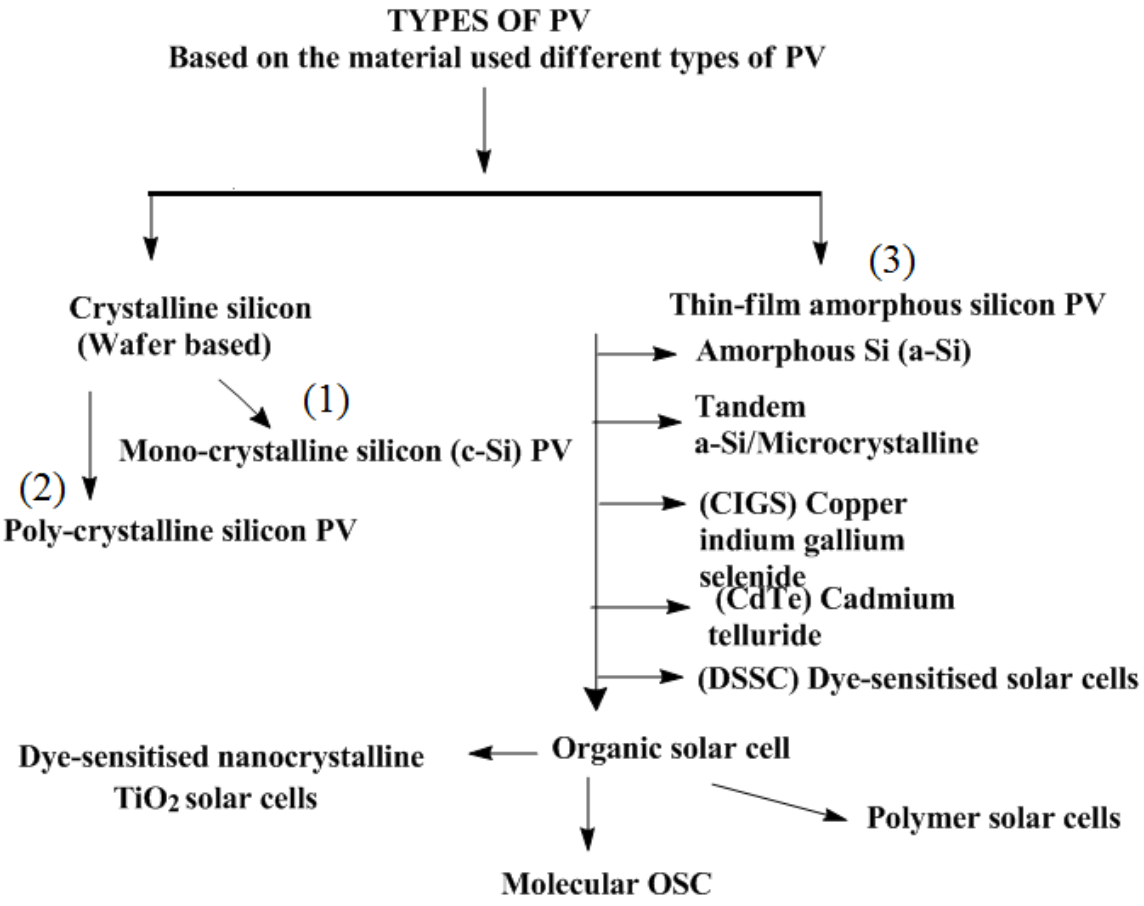

Scheme 1.1: Illustrated the three types of photovoltaic cells used in different applications [23].

The best laboratory efficiencies from various materials and a number of photovoltaic technologies over the last 35 years have been collected by the National Renewable Energy Laboratory (NREL) in the US and the data are plotted in Figure 1.1. The data show two relatively new entries; dye-sensitised solar cells (DSCs) and organic photovoltaic cells [24].

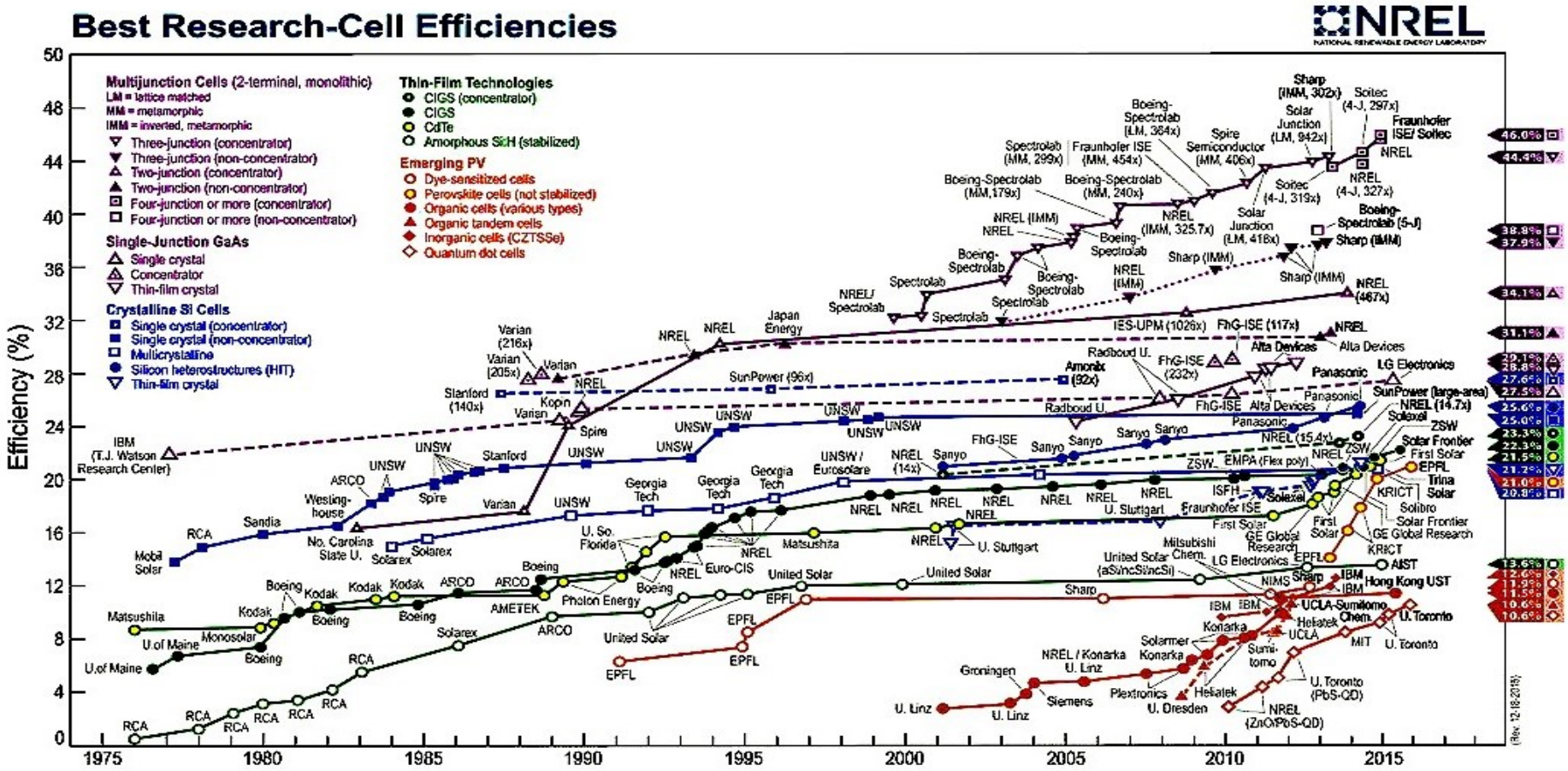

Figure 1.1: Statistics of efficiency for different kinds of solar cells [24].

PV cell technologies are divided into three generations, depending on the basic material that they contain:

• First-generation PV systems are based on the wafer-based crystalline silicon (c-Si) technology, either single crystalline (sc-Si) or multi-crystalline (mc-Si). Crystalline silicon cells are classified into three main types depending on how the Si wafers are made. They are:
• Monocrystalline (Mono c-Si) sometimes also called single crystalline (sc-Si)
• Polycrystalline (Poly c-Si), sometimes referred to as multi-crystalline (mc-Si)
• EFG ribbon silicon and silicon sheet-defined film growth (EFG ribbon-sheet c-Si) [25, 26].

The crystalline silicon solar cells have numerous advantages such as, high efficiency than that of other solar cells and easy availability which forced the producers to use them as a potential material for solar cells [27].

• Second-generation PV systems are based on thin-film technology and include three families:

1) Amorphous (a-Si) and micromorph silicon (a-Si/μc-Si).
2) Cadmium-Telluride (CdTe)3) Copper- Indium-Selenide (CIS) and Copper-Indium-Gallium-Diselenide (CIGS)
• Third-generation PV systems with concentrating PV (CPV) and organic PV cells have not yet been commercialised (e.g. multi-junction concentrating PV) and are concepts still in need of basic R&D (e.g. quantum-structured PV cells). Third-generation PV technologies can be classified into four types including; concentrating PV (CPV), dye-sensitised solar cells (DSSC) and organic solar cells [28].
• Concentrating PV (CPV).
• Dye-sensitised solar cells (DSSC).
• Organic solar cells.
• Novel and emerging solar cell concepts.

Table 1.1: illustrations an overview and comparison of major PV technologies

Table 1.1: An overview and comparison of major PV technologies [27].

		1st Generation		2nd Generation			3rd Generation		
Technology	Units	Single crystalline silicon (Si)	Poly Crystalline (sc-Si) silicon (pc-Si)	Amorphous Silicon (a-Si)	Copper Gallium Diselenide (CIS/CIGS)	Cadmium Telluride Solar cell	III-V Compound Multi junction Concentrated PV(CPV)	Dye-Sensitised (DSSC)	Organic or Polymer (OPV)
Best research solar cell efficiency at AM 1.5	%	24.7	10.4 13.2 Tandem	Single junction	20.3	16.5	43.5	11.1	11.1
Confirmed solar cell efficiency at AM 1.5	%	20-24	14-18	6-8	10-12	8-10	36-41	8.8	8.3
Commercial PV module efficiency at AM1.5	%	15-19	13-15	5-8	7-11	8-11	25-30	1-5	1
Commercial PV module efficiency at AM1.5	%	15-19	13-15	5-8	7-11	8-11	25-30	1-5	1
Confirmed maximum PV Module efficiency	%	23	16	7.1/10.0	12.1	11.2	25	-	-
Current PV module cost	USD/W	< 1.4	< 1.4	~ 0.8	~ 0.9	~ 0.9	-	-	-
Market share in 2009	%	83	3	1	13	-	-	-	-
Market share in 2010	%	87	2	2	9	-	-	-	-
Maximum PV module output	W		320	300	120	120	120	-	-
PV module size	m2	2.0	1.4-2.5	1.4	0.6-1.0	0.72	-	-	-
Area needed per KW	m2	7	8	15	10	11	-	-	-
State of commercialization	Mature with large scale production	Mature with large scale production	Early deployment phase, medium scale production	Early phase, small scale production	Early deployment phase, medium scale production	Early deployment phase, small scale production	Just commercialised, small scale production	R&D phase	R&D phase

The main advantages and disadvantages solar cell technologies are presented in Table 1.2 [26, 29].

Table 1.2: presented advantages and disadvantages of photovoltaic cells technologies

Advantages of PV Cells	Disadvantages of PV Cells
Modular "custom-made" energy, can be designed for any application from watch to a multi-megawatt power plant and not requiring large building infrastructure.	High initial costs
Renewable technology	Efficiency can be poor but improving
No use of fuels and water costs	Sunlight variability and seasonality
low operation and maintenance (O&M) costs	Requires large surface area since power density in sunlight can be low as 1,000 watts/m2
Environmentally friendly (no emissions of carbon gases and other harmful compounds	PV generates direct current: special DC appliances or inverters are needed in off-grid applications energy storage is needed, such as batteries
no noise, no moving parts, clean energy, safe, highly reliable, flexible, quiet to operate, renewable, domestically available	
PV operates even in cloudy weather conditions	PV cannot work without light
long lifetime, up to 30 years	large area needed for large scale applications
minimal maintenance requirements	cannot operate all the time

A solar PV system is powered by many crystalline or thin film PV modules. Individual PV cells are interconnected to form a PV module. This takes the form of a panel for easy installation. Figure (1.2) illustrates common PV module technologies [30].

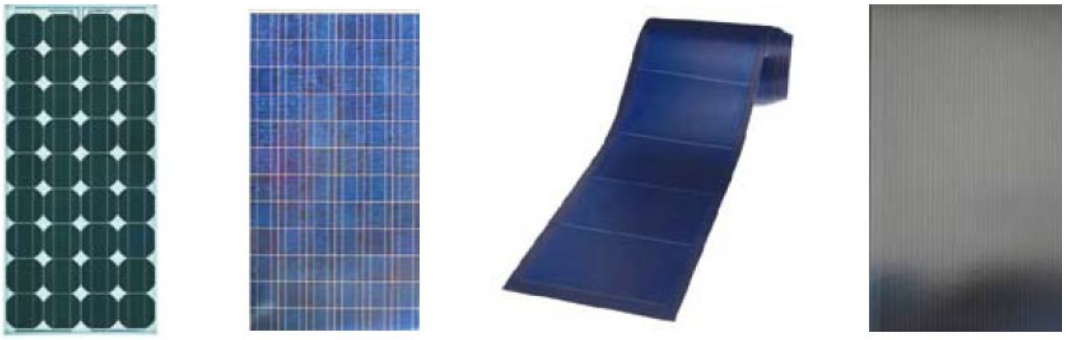

Mono-crystalline silicon | Poly-crystalline silicon | Flexible amorphous thin film | CIGS

organic solar cells thin film

Figure 1.2: Common PV module technologies

Photo-voltaics are one of the fastest growing renewable energy technologies and it is expected that it will play a major role in the global electricity generation mix.

1.2.1 Mechanism of Photovoltaic (P-N junction) cells

P-N junction photovoltaic (PV) cells are created from p-type semiconductors (having excessive electron holes (positive)) and N-type semiconductors (having excessive electron charge carriers (negative)). When solar light hits the PV cell, two types of electrons are produced, negatively and positively charged, within the semiconductors. The negatively charged electrons are attracted to the N-type semiconductor whilst the positively charged electrons are attracted to the P-type semiconductor. The potential difference across the two semiconductors allows the generation of a current if a load (e.g. light bulb) is placed between the two electrodes [31]. A pictorial representation of this mechanism is depicted in Figure 1.3.

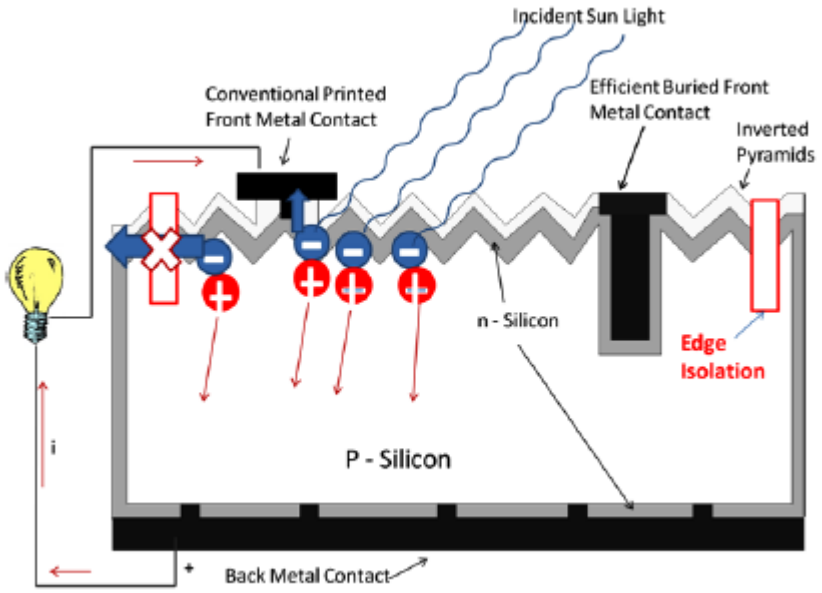

Figure 1.3: A typical structure of Si-based solar cell panel with metal contacts and anti-reflection coating [32].

1.2.2 Mechanism of Dye sensitised photovoltaic cells

Dye-sensitised solar cells (DSSC) mimic photosynthesis by utilising light absorbing pigements (in nature this is chlorophyll). In p-n junction PV cells the semiconductors provides photoelectrons, charge carrier separation and transportation, whilst in the DSSC PV cells the semiconductor is used for charge transport and the photoelectrons are created by the separate photosensitive dye. Charge separation is formed at the surface between dye, semiconductor and electrolyte (normally an organic hole transport material). The basic design of the DSSC involves semiconductor structures formed between a photo-sensitised anode and an electrolyte. The semiconductor nanocrystals antennae that harvest the sunlight (photons) and the dye molecule perform charge separation (photocurrent), mimicking natural photosynthesis [33]. DSSC was introduced by O'Regan and Grätzel in 1991 [33, 34]. These cells are low-cost materials and are simple to manufacture. They release electrons from metals covered by a light absorbing pigment. The exposure to UV light and the use of a liquid electrolyte makes the cells prone to degradation and freezing respectively over time. Broadband dyes and electrolytes have 12% efficiency [35], compared to 4% to 5% of DSSC commercial efficiencies due to the presence of few dyes that can absorb a broad

spectral range. The advantage of incorporating nanomaterials in DSSCs makes them able to accommodate thousands of organic dyes.

The mechanism of the primary steps to convert photons into current for dye sensitised solar cell (DSSC) is demonstrated in Figure 1.4.

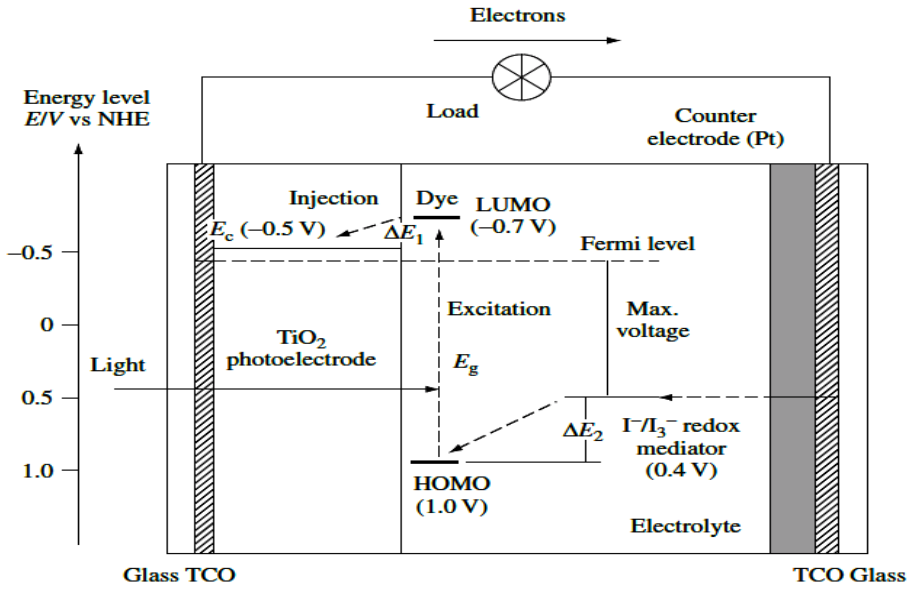

Figure 1.4: Schematic energy diagram and operating principle of DSSC [36]

The primary processes that occur in a DSSC for the solar energy–to–current conversion are given below:

1. Photosensitises (such as Ru complexes) adsorbed on a suitable substrate (TiO_2) surface absorb the incident photon flux.

2. The photosensitsers are excited from the ground state (S) to the excited state (S∗) owing to the MLCT transition. The excited electrons are injected into the conduction band of the TiO_2 electrode, resulting in the oxidation of the photosensitiser.

$$S + h\nu \rightarrow S^* \qquad (1)$$

$$S^* \rightarrow S^+ + e^- (TiO_2) \qquad (2)$$

3. Injected electrons in the conduction band of TiO_2 are transported between TiO_2 nanoparticles with diffusion toward the back contact (TCO) and consequently reach the counter electrode through the external load and wiring.

4. The oxidized photosensitiser (S^+) accepts electrons from the I^- ion redox mediator, regenerating the ground state (S), and I^- is oxidized to the oxidized state, I_3^-.

$S^+ + e^- \rightarrow S$ (3)

5. The oxidized redox mediator, I_3^-, diffuses toward the counter electrode and is re-reduced to I^- ions.

$I_3^- + 2e^- \rightarrow 3I^-$ (4)

Overall, electric power is generated without permanent chemical transformation. The performance of a DSSC is predominantly based on four energy levels of the components: the excited state (approximately LUMO) and the ground state (HOMO) of the photosensitiser, the Fermi level of the TiO_2 electrode, which is located near the conduction band level, and the redox potential of the mediator (I^-/I_3^-) in the electrolyte. The photocurrent obtained from a DSSC is determined by the energy difference between the HOMO and the LUMO of the photosensitiser, analogous to the band gap, E_g, for inorganic semiconductor materials. The smaller the HOMO–LUMO energy gap, the larger the photocurrent will be because of the utilization of the long wavelength region in the solar spectrum. The energy gap between the LUMO level and the conduction-band level of TiO_2, ΔE_1, is important, and the energy level of the LUMO must be sufficiently negative with respect to the conduction band of TiO_2 to inject electrons effectively. In addition, substantial electronic coupling between the LUMO and the conduction band of TiO_2 also leads to effective electron injection. The HOMO level of the complex must be sufficiently more positive than the redox potential of the I^-/I_3^- redox mediator to accept electrons effectively (ΔE_2). The energy gaps, ΔE_1 and ΔE_2, must be larger than approximately 200mV as driving force for each of the electron transfer reactions to take place with optimal efficiency [37]. The voltage in the DSSC is developed by the energy gap between the Fermi level of a TiO_2 electrode and the redox potential of the I^-/I_3^- in the electrolyte. The conduction band level of the TiO_2 electrode and the redox potential of I^-/I_3^- were estimated to be −0.5V versus normal hydrogen electrode (NHE) and 0.4V versus NHE, respectively, as shown in Figure 1.4. [36], (or −0.7V versus saturated calomel electrode (SCE) and 0.2V versus SCE, respectively [37, 38]). Thus, in the case of a DSSC using a TiO_2 electrode and I^-/I_3^- redox mediator, the maximum voltage is expected to be approximately 0.9V, depending on the electrolyte component because the Fermi level of the TiO_2 electrode depends on the electrolyte components and their concentrations.

In contrast to conventional p-n-type solar cells, the mechanism of a DSSC does not involve a charge-recombination process between electrons and holes because electrons are only injected from the photosensitiser into the semiconductor and a hole is not formed in the valence band of the semiconductor. In addition, charge transport takes place in the TiO_2 film, which is separated from the photon absorption site (i.e. the photosensitiser). Thus, effective charge separation is expected. This photon-to-current conversion mechanism in a DSSC is similar to the mechanism for photosynthesis in nature, in which chlorophyll functions as the photosensitiser and charge transport occurs in the membrane.

A part of this investigation will focus on a new class of organic dyes synthesised from 1,2,3-triazole compounds, synthesised using "click chemistry", in combination with various base metals to form classical organometallic complexes. These complexes will be tested as DSSC cells and thus demonstrate, as a proof of concept, their feasibility within the field.

1.4 Current Cancer incidence and trends

Cancer is a group of diseases involving uncontrolled and abnormal growth of cells, which potentially can invade or spread to other parts of the body. In 2011 in the UK more than 33 000 people were diagnosed with cancer (around 910 people every day). The is 1 in 35 for men and 1 in 20 for women risk of developing cancer up to the age of 50 years. A common approach for discovery of agents with anticancer activity start with the empiric screening for antiproliferative or cytotoxic effects in human cancer cell lines. Generally, the most commonly used anticancer chemotherapeutic drugs work by inhibiting cell division (mitosis) by different mechanisms. There are numerous methods used to treat the cancer such as surgery, chemotherapy, immunotherapy and radiotherapy. The aim of any cancer treatment is to remove cancerous cells in order to prevent them from growing and spreading. Chemotherapy treatment involves drugs, which aim to kill cancer cells. Chemotherapy drugs have been used to combat cancers. These differ in their chemical structure and their actions within the human body. The most common chemotherapy drugs used are alkylating drugs such as nitrogen mustards, alkyl sulphonates, triazines, nitrosoureas, ethylenimine derivatives and metal salts containing platinum [39]. The incorporation of metal complexes with platinum central atoms such as Cisplatin or carboplatin into

cancer drugs may improve the effectiveness of the drug. However, cancer treatment efficacy suffers from side effects and resistance phenomena to the latter drugs. These problems in e.g. platinum-based anti-cancer therapy have stimulated increased research efforts in the search for novel non-platinum containing metal species. The bio-inorganic molecules designed in this thesis have a remarkable similarity in the structures to anticancer agents therefore the latter section of this investigation will focus on the potential anti-cancer properties of the photochemical compounds synthesised and characterised in this work.

1.5 Motivation for current investigation

There is a demand for electricity due to the growing populations and expanding economies. Electricity generation depends on burning fossil fuels, which cause pollution to the environment upon their emission of greenhouse gases. Strategies have been developed to reduce greenhouse gas emissions involved in the production of electricity. Hence, renewable energy sources have been developed in order to replace fossil fuels in the production of electricity. PV systems are an attractive tool in renewable energies as it does not produce greenhouse gases and relies on clean, safe and renewable energy. PV systems such as dye-sensitised solar cell (invented in 1991) are less expensive, more efficient with the advantage of being fabricated from abundant non-toxic materials with simple manufacturing processes. This thesis intends to focus partly on the development of the dye-sensitised solar compounds by synthesising a range of potential luminescent organotransition metal complexes, and their characterisation for further use in dye solar cells. Furthermore, the potential of the various synthesised organometallic complexes will be investigated as potential anti-cancer compounds to increase the current limited arsenal of medicines that can successfully treat cancer and overcome it. In both approaches it will be attempted to increase knowledge and make a new and novel contribution to the current field of photochemical compounds and their applications.

1.6 Aim and objectives of the investigation

Inorder to accomplish the goals of this investigation, the following objectives will be pursued:

1. Synthesis of transition metal complexes
2. Characterisation of the physical properties of the complexes.
3. Characterisation of the optical, fluorescent and crystallographic properties of the complexes to predict their suitability or not for DSSC.
4. Evaluation of the complexes as potential anticancer agents.

1.7 Hypothesis

Careful ligand design and systematic variation of the metal centre can tune and optimise the optical absorption properties of a new series of chromophores and potentially useful anti-cancer drugs.

1.8 Summary

This chapter introduces the scientific areas that this research project will focus on. The next chapter elaborates on click chemistry and synthesis of organometallic complexes, particularly those involving triazoles.

1.9 References

1-Statistical B.P., Review of World Energy, (2010) B P, London (2010)

2-Solomon S., Qin D., Manning M., Chen Z., Marquis M., Averyt K B., Tignor M., Miller H L., editors. IPCC, 2007: Climate Change 2007: The Physical Science Basis. Contribution of Working Group I to the Fourth Assessment Report of the Intergovernmental Panel on Climate Change. Cambridge University Press, Cambridge, United Kingdom and New York, NY, USA (2007)

3-Lewis N S., *Science.,* 315:798(2007)

4-Nansen R., Sun Power: The Global Solution for the Coming Energy Crisis. Ocean Press, ISBN-10: 0964702118, Washington, USA. (1995)

5-Patel M N., Karia P S., Vekariya P A., Patidar A P., Synthesis of heterocyclic compounds and its applications., *Arab. J. Chem*. (2015)
doi: http://dx.doi.org/10.1016/j.arabjc.2015.06.031

6-Clarke M J., in Metal Complexes in Cancer Chemotherapy, ed. Keppler B K., VCH, Weinheim, pp.129(1993)

7-Keppler B K., Lipponer K G., Stenzel B., Kratz F., in Metal Complexes Chemotherapy, (ed), VCH, Weinheim pp.187(1993)

8-Clarke M J., Zhu F., Frasca D R., *Chem. Rev*., 99:2511(1999)

9-Sava G., Bergamo A., *Int. J. Oncol*., 17:353(2000)

10-DeRose V J., White J D., Haley M M., *Acc. Chem. Res*., 49:56(2016)

11-Urankar D., Košmrlj J., *Inorg. Chim. Acta*., 363:3817(2010)

12-Zhang J Z., Bonnitcha P., Wexselblatt E., Klein A V., Najajreh Y., Gibson D., Hambley T W., *Chem. Eur. J*., 19: 1672(2013)

13-Maisonial A., Serafin P., Traïkia M., Debiton E., Théry V., Aitken D J., Lemoine P, Viossat B., Gautier A., *Eur. J. Inorg. Chem*., 298(2008)

14-Pathak R K., McNitt C D., Popik V V., Dhar S., *Chem. Eur. J*., 20:6861(2014)

15-Ding S., Qiao X., Kucera G L., Bierbach U., *J. Med. Chem*., 55:10198(2012)

16-Becquerel A E., *Acad. Sci. Paris*, 9:561(1839)

17-The history of PV. http://www.pvpower.com/pvhistory.html; November 15, 1998

18-Fritts C. E., *J. Am. Chem. Soc*., 26:465(1883)

19-Einstein A.., *Annalen der Physik*, 17:132(1905)

20-Bell Labs Demonstrates the First Practical Silicon Solar Cell". APS News., *Am. Phys. Soc*.,18:4(2009)

21-Chapin D M., Fuller C S., Pearson G L., *J. Appl. Phys*., 25:676(1954) doi:10.1063/1.1721711.

22-Williams R., *J. Chem. Phys*., 32:1505(1960)

23-Swami R., International Journal of Scientific and Research Publications, 2:1(2012) 2 ISSN 2250-3153

24-Peter L M., *Philosophical Transactions of the Royal Society A*, 369:1840(2011)

25-Green M A., (2001) Clean Energy from Photovoltaics, World Scientific Publishing Co., Hackensack, N J

26-SCHOTT Solar (2011) Crystalline Silicon Technology, http://www.us.schott.com/photovoltaic/english/about_pv/technologies/crystalline/

27-Masson G., Latour M., Rekinger M., Theologitis I T., Papoutsi M., Global market outlook for photovoltaics 2013–2017. *European Photovoltaic Industry Association.* pp.12–32:(2013)

28-Shukla Ph N., Khare A., *International Journal of Electrical, Electronics and Computer Engineering*., 3: 91(2014)

29-Davidson J., The new solar electronic home. 20 th printing 2001

30-Handbook for Solar Photovoltaic (PV) Systems, Energy Market Authority, ISBN: 978-981-08-4462-2

31-Green M A., *Physica E*, 14:11(2002)

32-Yang C H., Nano-Crystalline Manipulation to Achieve Laser-based Crack-Free Edge Isolation for Silicon-Based Solar Cells, M.Sc. thesis, Univ. North Carolina, USA, 2012

33-Grätzel, M., O'Regan, B., *Nature*, 353:737(1991)

34-Nazeeruddin M K., De Angelis F., Fantacci S., Selloni A., Viscardi G., Liska P., Ito S., Bessho T., Graetzel M., *J. Am. Chem. Soc*., 127:16835(2005)

35-Grätzel M., *Acc.Chem. Res.*, 42:1781(2009)

36-Hagfeldt A., Grätzel M., *Acc. Chem. Res*., 33:269(2000)

37-Kalyanasundaram K., Grätzel M., *Coord. Chem. Rev*., 77:347(1998)

38-Hagfeldt A., Grätzel M., *Chem. Rev*., 95:49(1995)

39-Siddik Z H., the Cancer Handbook 1st Edition. Edited by Malcolm R. Alison John Wiley & Sons, Ltd., 1:(2002)

Chapter 2 : THE CYCLOADDITION (CUAAC) "CLICK" REACTION

2.1 Introduction

In this work, a design for a new series of chromophores using click chemistry will be proposed. This will include preparation of transition metal complexes to test as photo-sensitisers for potential use in DSSCs and medicinal drug applications. The synthesis of photosensitisers will be undertaken using the *CuAAC* (copper catalyzed azide-alkyne cycloaddition) reaction (a "click reaction") to generate a five membered triazole ring.

2.2 Click Chemistry

In 2001, K. Barry Sharpless defined the very useful and "green" concept of "click chemistry", with the aim of binding two molecular building blocks together in a facile, selective, high yielding reaction under mild water-tolerant conditions with little or no byproducts [1]. The most used "click" reaction that can fulfill these conditions is by far the Cu (I)-catalyzed azide/alkyne cycloaddition (CuAAC). Other "click" reactions are the thiol-ene, oxime, Diels-Alder, Michael addition and pyridyl sulfide reactions [1, 2].

He elaborated on the stringent criteria that the reactions must meet in order to classify the process as click chemistry. The criteria (and advantages of click chemistry) are listed below:

1. Modular

2. Wide in scope

3. High yielding

4. Stereospecific (but not necessarily enantiospecific)

5. Harmless byproducts

6. Stable

7. Show large thermodynamic driving force.

6. Simple reaction conditions

7. Readily available starting materials

9. Use of no solvent, or benign (water) or easily removed

10. Simple product isolation (non-chromatographic)

The following are reactions, which exemplify the characteristics of click chemistry:

Table 2.1. Presented the summary of typical click reactions [3].

Table 2.1: Summary of Typical Click Reactions [3]

Classifications	Mechanism	Reagent A	Reagent B	Notes on reaction
Copper catalyzed reactions	Cu-catalyzed [3+2] azide-alkyne cycloaddition (CuAAC)	azide	alkyne	2 h at 60 °C in H2O
Copper-free reactions	Strain-promoted [3+2] azide-alkyne cycloaddition (SPAAC)	azide	cyclooctyne	1 h at RT
	[3+2] Huisgen cycloaddition	azide	activated alkyne	4 h at 50 °C
	[3+2] cycloadditttion	azide	electron-deficient alkyne	12 h at RT in H_2O
	[3+2] cycloadditttion	azide	aryne	4 h at RT in THF with crown ether or 24h at RT in CH_3CN
	Diels–Alder retro-[4+2] cycloaddition	tetrazine	alkene	40 min at 25 (100% yield) N_2 is the only by-product
	1,3-dipolar cycloaddition (photoclick)	tetrazole	alkene	few mi n UV irradiation and then overnight at 4 °C
	hetero-Diels–Alder cycloaddition	dithioester	diene	10 min at RT
	[4+2] Diels–Alder reaction	anthracene	maleimide	2 days at reflux in toluene
	reaction radical addition (thio click)	thiol	alkene	30 min UV (quantitative conv.) or 24 h UV irradiation (>96%)
	Michael addition	thiol	enone	24 h at RT in CH_3CN
	Michael addition	thiol	maleimide	1 h at 40 °C in THF or 16 h at RT in dioxane
	Nucleophilic substitution	thiol	para-fluoro	overnight at RT in DMF or 60 min at 40 °C in DMF
	Nucleophilic substitution	amine	para-fluoro	20 min MW at 95 °C in NMP as solvent
	Thiol-based condensation	CBT	1,2-aminothiol	pH=7.4 in PBS

2.3 Triazoles

Triazoles are a group of compounds regarded as azoles with the molecular formula $C_2H_3N_3$ [4]. They contain a characteristic ring structure of five-membered nitrogen heterocyclic atoms in addition to one other non-carbon atom of either nitrogen, sulfur or oxygen [4]. The aromatic structures of azoles constitute two double bonds, Figure 2.1.

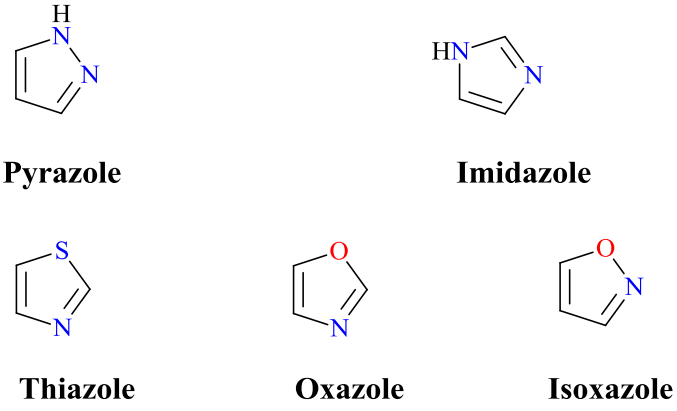

Figure 2.1: The chemical structure of azole five-membered nitrogen heterocyclic ring compounds [4].

There are two isomeric chemical compounds related to triazoles. The two isomers are given in Figure 2.2

Figure 2.2: The isomeric forms of triazole [2-5].

A 1,2,3-triazole structure contains three adjacent nitrogen atoms with three available substitution sites found at positions 1, 4 and 1, 5 Figure 2.2. The planar unsaturated ring of atoms in the 1,2,3-triazole makes it a building block for more complex compounds [5]. The development of 1,2,3-triazoles for drug discovery and industrial use has been shown to be very versatile. The uses for triazoles have been found in various areas and are continuously growing.

The synthesis of 1,2,3-triazoles is distinctive in that there are a multitude of methods by which to achieve the preferred outcome. Depending on the application of the desirable product, an acceptable procedure likely already exists. The three most common methods for the synthesis of 1,2,3-triazoles all contain elements from the Huisgen 1,3-dipolar azide- alkyne cycloaddition (AAC) [6]. Those methods include: (1)-The regiospecific, copper-calayzed azide-alkyne cycloaddition (CuAAC) [7, 8] (2)-The strain-promoted, metal free AAC of cyclooctynes [9] and (3)-The ruthenium-catalyzed azide-alkyne (RuAAC) of both terminal and internal alkynes [10]. These three methods as well as our contributions to the CuAAC will be described carefully within this chapter.

2.4 [3+2] cycloaddition reactions, Huisgen 1, 3-dipolar cycloadditions

The synthesis of complex heterocyclic compounds in a stereospecific manner is an important area of organic chemistry. The syntheses of a number of heterocyclic compounds are based upon cycloaddition reactions. Recently, asymmetric [3 + 2] cycloaddition reactions using chiral organocatalysts mediated by different metals have provided new methods for the construction of stereochemically complex heterocyclic compounds. Specifically, [3 + 2] cycloaddition is an excellent approach for the synthesis of many types of five-membered ring systems starting from a 3-atom and a 2-atom precursor.

Generally speaking, [3 + 2] cycloaddition is a broad concept that includes 1,3-dipolar cycloadditions which provide a very efficient way to synthesise complex natural products and medicinal molecules [11]. In other words, cycloaddition reactions that involve 1,3-dipoles reacting with π-bonds of dipolarophiles to give five-membered rings which are called [3 + 2] cycloaddition reactions [12]. A 1,3-dipole usually contains heteroatoms and four π-electrons which are distributed over three atoms, such as azide, diazoalkane, nitrous oxide, nitrile imine, nitrile ylide, nitrile oxide, azomethine imine, azoxy compound, azomethine ylide, as well as nitrone, carbonyl oxide and ozone [13]. A 1,3-dipolar cycloaddition reaction can also be described as involving at least one mesomeric state structure that represents a charged dipole and a dipolarophile. The dipolarophiles usually are alkene or alkyne derivatives. In 1864, Griss described organic azides as a new class of compounds [14]. Organic azides belong to the propargyl-allenyl category of dipoles as shown in Figure 2.3.

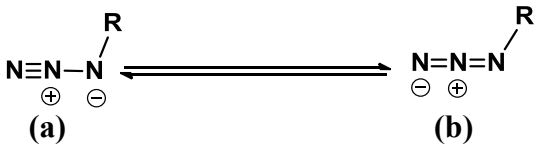

Figure 2.3: The two possible resonance forms (a) or (b) to the electronic structure of azide isomers [15].

The first reaction between azide and alkyne yielding 1,2,3-triazole (Figure 2.4) was reported at the end of the 19th century [16]: keeping an ester solution of phenyl azide (**1**) and dimethyl ether of acetylenedicarboxylic acid (**2**) in the light or heating it in a sealed ampoule (8 h at 100°C), Michael obtained the corresponding triazole (**3**).

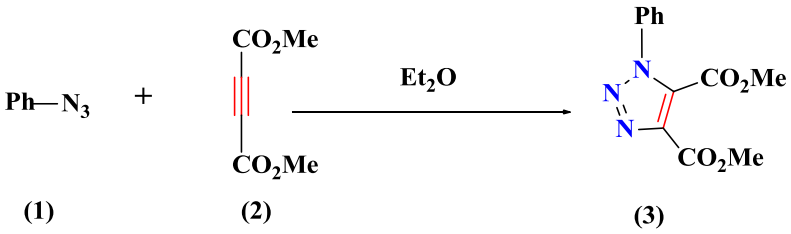

Figure 2.4: The first synthesis of 1,2,3-triazole by the cycloaddition reaction [16].

At the end of the 1950s/early 1960s, Huisgen developed the general concept of 1,3-dipolar cycloaddition [17, 18], a variant of which is the reaction between azides and alkynes.

Huisgen 1, 3-dipolar cycloadditions [19] are exergonic combining procedures that aim to integrate two unsaturated reactants to yield a wide range of five-membered heterocyclic compounds [20]. The cycloaddition of azides and alkynes to give triazoles [21] is an effective method for the latter generation. Unfortunately, the high risks involved in the development of organic azides have kept chemists from refining and studying this method in detail. Cycloaddition is a faster and more selective procedure for the production of 1,3-dipoles other than azide. This is due to its three-atom dipole structure, which makes it free of side reactions.

The reaction between azides and alkynes was actively studied. However, the fact that the interaction between asymmetric or terminal alkynes with azides (**4**) yields a mixture (frequently, hardly separable) of two triazole isomers interfered with its wide application, for example in the case of terminal alkynes (**5**), such as these 1,4- (**6**) and

1,5-disubstituted (**7**) triazoles Figure 2.5. The ratio of the products strongly depended on the type of substituents R^1 and R^2 in compounds (**4**) and (**5**) and the reaction conditions. However, it was impossible to obtain only one of the triazole isomers.

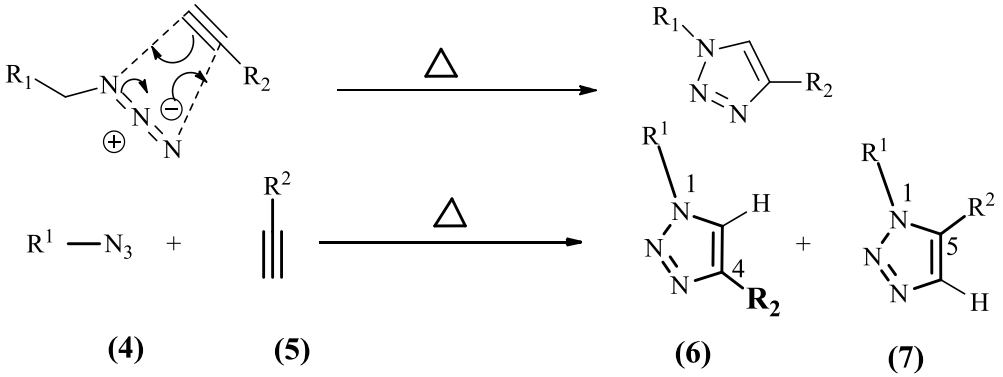

Figure 2.5: The addition of the azides to the terminal alkynes [22].

The disadvantage of this approach was that using an unsymmetric alkyne would lead to different regioisomeric products Figure 2.6. Since there was not a universal method that would guarantee regioselectivity from these reactions, the problem of how to favour the formation of the 1,4- versus the 1,5-disubstituted products became a focus of much research.

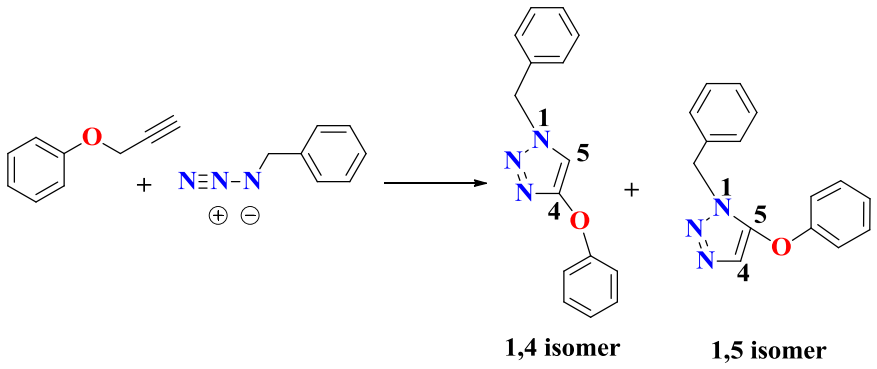

Figure 2.6: Example of regio-isomeric products when using an asymmetric alkyne [7].

A breakthrough took place in the 21st century when, in 2002, the groups of Meldal [7] and Sharpless [8]. Discovered that copper(I) compounds were able to efficiently catalyze this reaction with terminal alkynes, making the reaction itself regiospecific, i.e., the reaction yielded exclusively 1,4–disubstituted 1,2,3–triazoles (**6**) **(**see Figure 2.5).

2.5 The copper(I)-catalyzed alkyne-azide cycloaddition (CuAAC) "click" reaction

In 2002, the research groups of Fokin and Sharpless [8] and of Meldal et al. [7] independently reported the efficient Cu(I) catalysis of the azide/alkyne cycloaddition. The Huisgen reaction produces a mixture of 1,4 and 1,5-disubstitution products, whereas the CuAAC reaction of terminal alkynes is completely selective in the formation of the 1,4-disubstituted triazoles shown in Figure 2.7, with a variety of Cu(I) catalysts or precursors of Cu(I) catalysts [7, 8].

Thus, the CuAAC reaction has become very popular a "click" reaction, and more than 1000 research articles including many reviews [22-39] have been published on CuAAC since the Meldal and Fokin–Sharpless publications of 2002. The reasons for its success are that this "click" reaction is so easy to carry out and widely applicable. Indeed, it is unaffected by a variety of functional groups and can be achieved with many sources of Cu(I) catalysts and solvents, including aqueous ones. By completely changing the mechanism, the Cu(I) catalysts easily overcome the activation barrier that is high in the non-catalyzed Huisgen reaction (for instance 105kJ. mol^{-1} for the reaction between methylazide and propyne [40]).

Huisgen 1, 3-dipolar cycloaddition of azide and alkynes

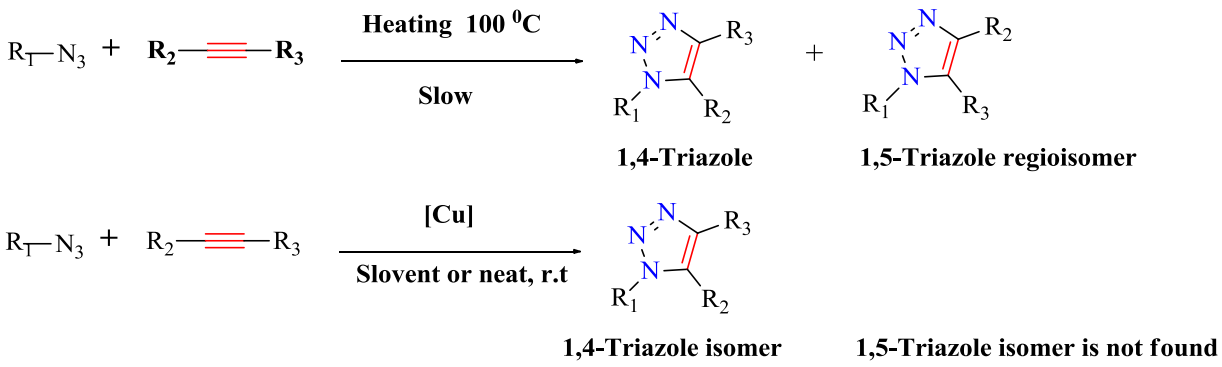

Figure 2.7: Huisgen 1, 3-dipolar cycloadditions and CuAAC reaction [8].

Comparison of the thermal reaction between benzyl azide and phenyl propargyl ether with the reaction of the same substrates but catalysed by copper shows the value of such catalysis (Figure 2.8). The thermal reaction ends in the production of two disubstituted triazole isomers. On the other hand, the reaction catalysed by copper exclusively yields the 1,4-isomer in 91% yield after 8 hours [8].

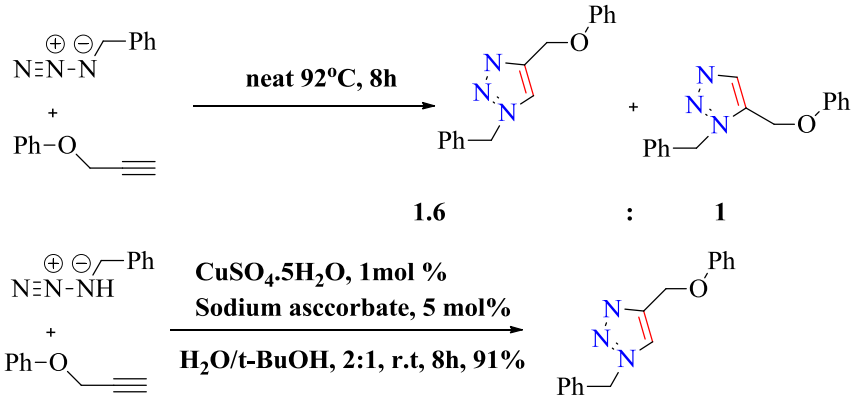

Figure 2.8: Thermal and Cu(I)-catalyzed 1,3-dipolar cycloadditions [8].

2.5.1 The Cu(I) catalysts and pre-catalysts

An extensive variety of copper catalysts can be used for the CuAAC reaction provided that some Cu(I) species is generated [7, 8]. It is essential to keep the Cu(I) concentration at its maximum in order to facilitate the reaction. The pre-catalyst can be a Cu(II) salt (usually $CuSO_4$) with a reducing agent (usually sodium ascorbate), a Cu(I) compound (preferably CuBr or CuOAc), together with a base or amine ligand and a reducing agent in order to inhibit aerobic oxidation to Cu(II), or a $Cu^{(0)}$ compound (wire, turnings, powder, or nanoparticles) [41, 42], the surface of which forms the required Cu(I) species. Some cupric salts or complexes such as $Cu(OAc)_2$ without added reductant also work as pre-catalysts, because they are strong oxidants that are reduced to catalytically active Cu(I) species by alkynes, as for instance in the well-known Glaser coupling [17, 23, 43]. The solvent is very flexible from organic to aqueous media, which is remarkable. The most common conditions are those reported by the Fokin and Sharpless group in 2002 using $CuSO_4$ and 10 equiv. sodium ascorbate in an aqueous solvent such as water + an alcohol (t-BuOH, MeOH or EtOH) in order to solubilize the substrate and retain the favourable aqueous medium (only 2

equiv. sodium ascorbate are generally used). These aqueous conditions are very useful for biochemical conjugations as well as for organic syntheses.

2.5.2. Solvents used in the CuAAC reaction

The variety of solvents used in the CuAAC reaction, is one of the most remarkable features of this reaction. The numerous solvents include non-coordinating solvents such as toluene, chloroform and dichloromethane, weakly coordinating solvents such as THF, pyridine, and dioxane, polar solvents such as acetone, MeCN, DMF, DMSO, alcohols, and aqueous solvents including mixtures of water with an alcohol, acetone, THF, MeCN, DMSO, dioxane, biphasic media mixing water with dichloromethane, and other mixtures of two or even three solvents [7]. The $CuSO_4$ + sodium ascorbate catalyst and the $Cu^{(0)}$ catalysts were used with a variety of aqueous solvents, whereas Cu(I) catalysts are used in a non-aqueous solvent most of the time. A key role of the solvent or solvent mixture is to solubilize the substrates and Cu(I) catalyst in order to ensure rapid reactions. Polar solvents favour the heterocycle bond formation step and the solubility of the substrate and catalysts, but if the solvents are coordinating, they can inhibit or slow down the required metal–substrate coordination. Therefore, DMF is an optimal solvent for the CuBr catalyst without additional ligand. In the presence of polyamine ligands, toluene gives good results, because it provides solubilisation of both catalyst and substrates without inhibiting substrate coordination.

2.5.3 Mechanism of CuAAC

Copper(I) compounds were able to efficiently catalyze this reaction with terminal alkynes, making the reaction itself regiospecific, i.e., the reaction yielded exclusively 1,4-disubstituted 1,2,3-triazoles (**6**). This is because the catalysis dramatically changes the reaction mechanism. While the thermal Huisgen 1,3-dipolar cycloaddition is a concerted process, the reaction with the involvement of monovalent copper is a stepwise one. The following mechanism for this reaction was proposed [8, 40]: alkyne (**5**) and catalyst (**8**) yield copper acetylenide (**9**) followed by the attachment of azide (**4**), thecyclization of the formed intermediate (**10**) into the structure (**11**) with the subsequent ring narrowing, the formation of the triazole copper derivative (**12**), and the final hydrolysis of the copper–carbon bond in Scheme. 2.1. In this reaction pathway, the energy of the intermediates is considerably decreased, elevating the overall transformation rate by seven to eight orders of magnitude as

compared with the concerted process. The reaction received an abbreviated name, CuAAC, i.e., Cu(I) catalyzed azide–alkyne cycloaddition. The CuAAC reaction, also referred to as the Huisgen–Meldal–Sharpless reaction, which specifically yields 1,4-disubstituted 1,2,3-triazoles (**6**) under mild conditions proceeds in a wide range of solvents, including water, appeared to be the exclusively effective method for combinatorial chemistry.

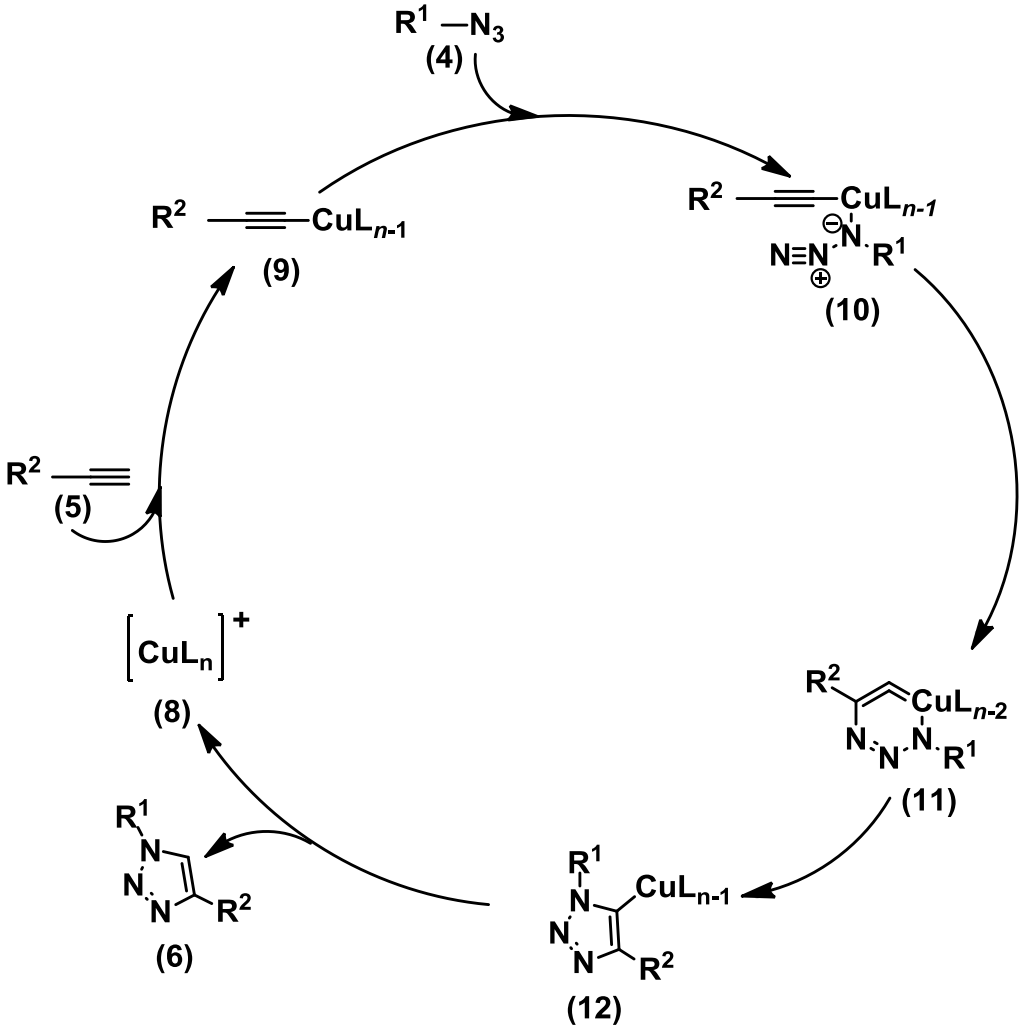

Scheme 2.1: The mechanism of Cu(I) catalyzed azide and terminal alkyne cycloaddition (CuAAC); L, monovalent ligands [8, 40].

2.5 Copper-free click chemistry

The strain-promoted 1, 3-dipolar cycloaddition of cyclooctynes and azides, also termed as the Cu-free click reaction, is a bioorthogonal reaction that enables the conjugation of two molecules in an aqueous and otherwise complex chemical environment through the formation of a stable triazole (Figure 2.9). This reaction possesses extreme selectivity and biocompatibility.

The cycloaddition of the azide with alkynes requires activation of the corresponding alkyne compound. This can be achieved either by catalysis with copper(I), usually termed click chemistry, or through ring-strain. The copper-catalysed click reaction between azides and terminal alkynes is ideal for numerous applications, but due to the cytotoxic effects of the heavy metal, the application of the copper(I)-catalysed azide alkyne cycloaddition (CuAAC) in living systems is very limited, making the strain-promoted variant the more preferable choice [44]. It was discovered by Wittig and Krebs, who observed the rapid reaction of cyclooctyne with phenyl azide providing a single product, the triazole (**13**) **(**Figure 2.9) [45].

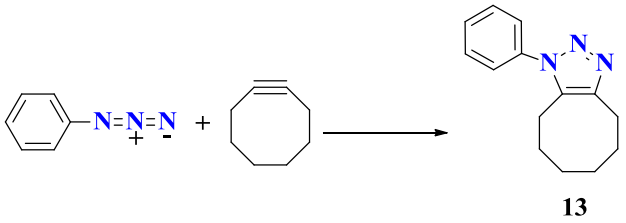

Figure 2.9: Reaction of cyclooctyne with phenyl azide to triazole 13 [45].

In 2004 Bertozzi and co-workers rediscovered this observation and since the reaction of the first substituted cyclooctyne (**14**) with azides was published, this class of reactions was named the strain-promoted azide alkyne cycloaddition (SPAAC) [9]. While the reaction rate of (**14**) Ewas only moderately increased compared to linear alkynes, many new cyclooctyne compounds with strongly improved kinetics have been produced since then, as shown in Figure 2.10.

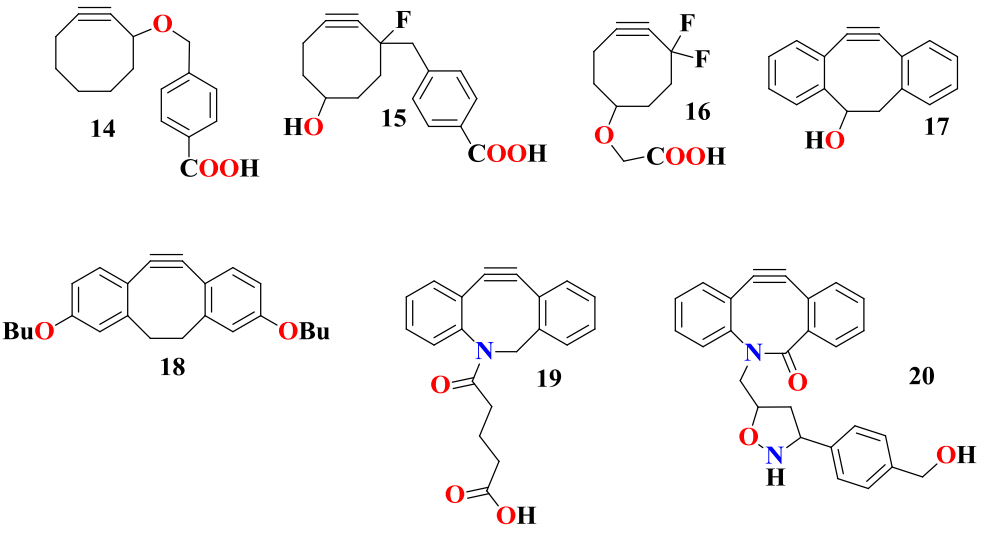

Figure 2.10: Cyclooctyne derivatives for bioorthogonal reactions [9].

The attachment of one or two electron withdrawing fluorine substituents to the cyclooctyne ring resulted in a significant increase of the reaction rates of the compounds (**15**) and (**16**) compared to (**14**) [46-47]. Boons and co-workers have reported the synthesis of the even faster dibenzocyclooctynes (**17**) and (**18**), whose reactivities are enhanced by the additional ring strain provided by the two phenyl rings [48-49]. The introduction of a nitrogen atom into the 8-ring of a dibenzocyclooctyne further elevates the ring strain due to the shorter carbon-nitrogen bond and therefore additionally improves the reaction rates of dibenzoazacyclooctyne (**19**) and dibenzoazacyclooctynone **(20**) [50-51].

2.6 The ruthenium-catalyzed azide-alkyne cycloaddition

In 2005, the group of Fokin and co-workers discovered a novel catalyst for click chemistry, and utilised various ruthenium complexes to produce either the 1,4- or the 1,5- disubstituted triazole selectively in "ideal" 100% yield, suggesting complete regiochemical control, e.g. the [pentamethylcyclopentadienyl ruthenium(II)] complexes (Cp*Ru), such as [Cp*RuCl(PPh_3)$_2$] (Scheme 2.2). Cp*Ru complexes present 1,5-substituted 1,2,3-triazoles [52] in contrast to other catalysts. Moreover, they can work on both terminal and internal alkynes alike [53]. Figure 2.11 shows an example of this reaction. Limited information is available on the role of Ru(II) complexes in click chemistry.

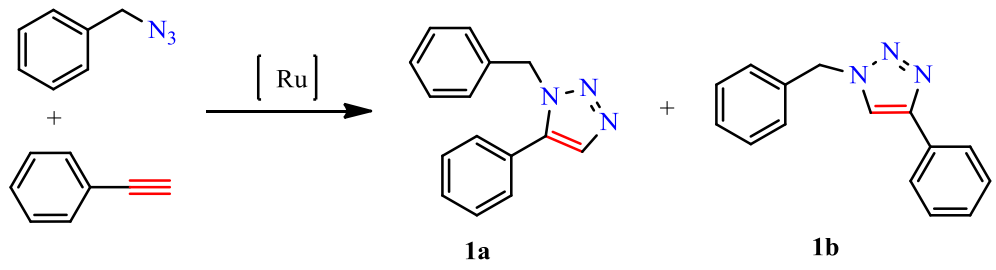

	1a	1b
$Ru(OAc)_2(PPh_3)_2$		100%
$CpRuCl(PPh_3)_2$	85%	15%
$Cp^*RuCl\|PPh_3)_2$	100%	----
$Cp^*RuCl\|NBD)$	100%	----

Figure 2.11: A (Cp*Ru) catalyst in the click reaction exclusively forms 1,5-substituted 1,2,3-triazoles.

Scheme 2.2: Ruthenium-Catalyzed Cycloaddition of Benzyl Azide to Phenylacetylene.

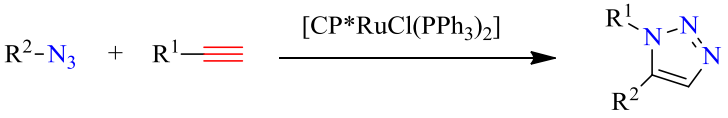

In 2008, the ruthenium catalyzed method to afford 1,5-disubstituted 1,2,3-trioazoles was reported by Fokin and co-workers [10]. A search for the catalysts revealed that pentamethylcyclopentadienyl ruthenium chloride [Cp*RuCl] complexes are capable to catalyse the cycloaddition of azides to terminal alkynes regioselectively leading to 1,5-disubstituted 1,2,3-triazoles. Furthermore, RuAAC can also be used with internal alkynes (Figure. 2.12), providing fully substituted 1,2,3-triazoles, which compares with CuAAC.

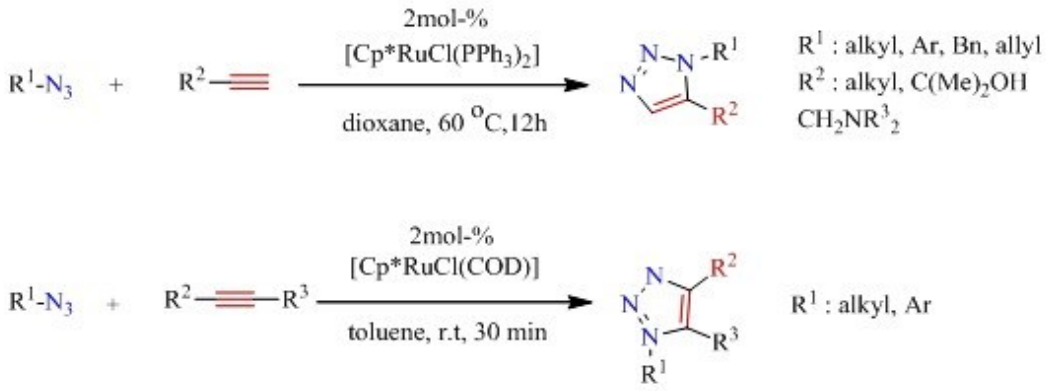

Figure 2.12: The ruthenium-catalyzed 1,3-dipolar cycloaddition [10].

In contrast to the CuAAC, terminal and internal alkynes work in the RuAAC, causing the formation of completely substituted 1,2,3-triazoles and providing key mechanistic understanding. Ruthenium - acetylide species are not formed at all or if they do form, they are not part of the catalytic cycleshown in (Scheme 2.3). The [Cp*RuCl] (pentamethylcyclopentadienyl ruthenium chloride) catalyst was found to be most reactive and its reactivity was referred to the Cp* ligands ability to stabilise the higher oxidation states of ruthenium. The orientation of the R groups in the activated complex results in the 1,5-disubstituted product. The proposed reaction mechanism was examined computationally employing DFT calculations and indicate that the [Cp*RuCl]-catalyzed reactions of azides with alkynes involve an irreversible oxidative coupling of azide and alkyne to give ruthenacycles, followed by a rate-determining reductive elimination.

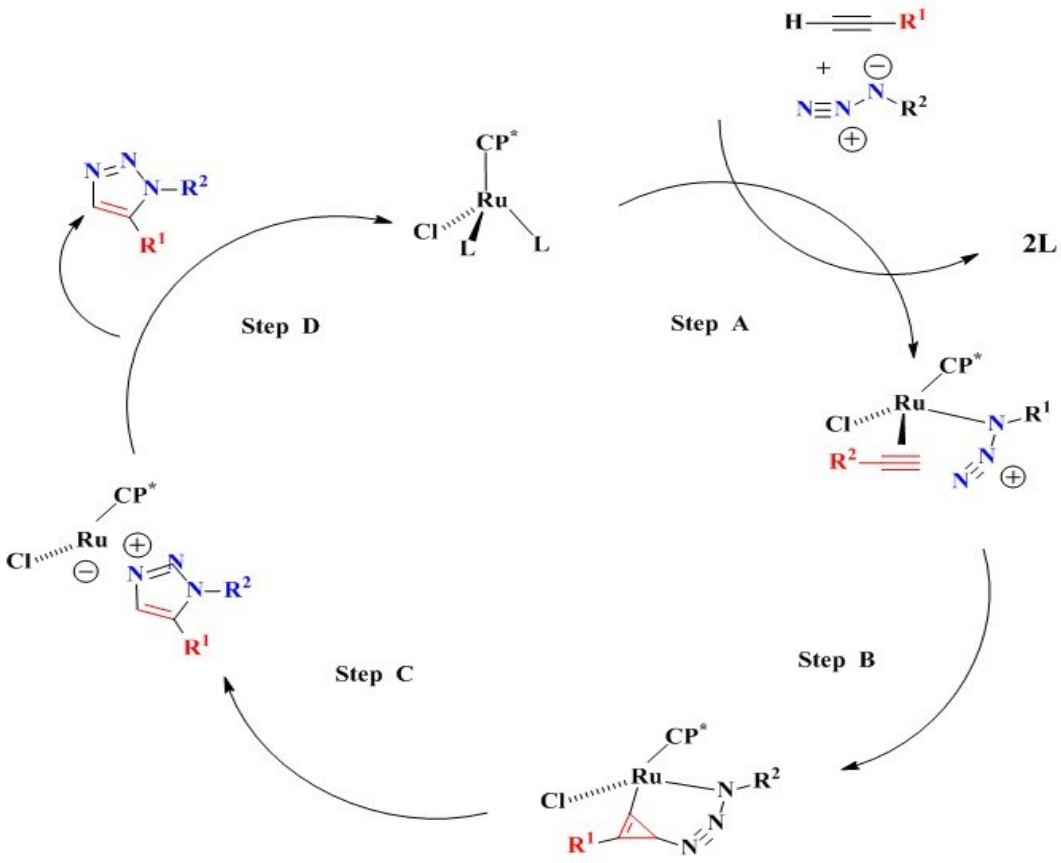

Scheme 2.3: Proposed intermediates in the catalytic cycle of the RuAAC reaction [10].

2.7 Summary

This chapter focuses on the synthetic strategies to produce metal-ligand complexes, particularly the "green" concept of "click chemistry". This concentrated the efforts on triazole modified ligands using the CuAAC reaction. Key mechanisms are discussed. The next chapter is a literature review of sensitisers for use in solar cells.

2.8 References

1-Kolb H C., Finn M G., Sharpless K B., *Angew. Chem. Int. Ed*., 40:2004(2001)

2-Iha R K., Wooley K L., Nystrom A M., Burke D.J., Kade M J., Hawker C J., *Chem. Rev*., 109:5620(2009)

3-Wang M., Yuan Y., Liang G., *Current Molecular Imaging*., 1:1(2012)

4-Eicher T., Hauptmann S., The Chemistry of Heterocycles: Structure, Reactions, Synthesis, and Applications, (June, 2003), (2nd ed.) John Wiley & Sons

5-Gilchrist T L., Heterocyclic chemistry 3rd edition, John Wiley and Sons (1992)

6-Huisgen R., *Angew. Chem., Int. Ed. Engl.,* 2:633(1963)

7-Tornoe C W., Christensen C., Meldal M., *J. Org. Chem,* 67:3057(2002)

8-Rostovtsev V V., Green L G., Fokin V V., Sharpless K B., *Angew. Chem. Int. Ed.,* 41:2596(2002)

9-Agard N J., Prescher J A., Bertozzi C R., *J. Am. Chem. Soc*,126:15046(2004)

10-Fokin V V., Boren B C., Narayan S., Rasmussen L K., Zhang L., Zhao H., Lin Z., Jia G., *J. Am. Chem. Soc.*, 130:8923(2008)

11-Corey E J., *Angew. Chem. Int. Ed.,* 48:2100(2009)

12-Smith M B., Organic Synthesis, 2nd edition, The McGraw-Hill Inc., New York, 999 (2002)

13-Smith M B., March J., March's Advanced Organic Chemistry, 5th edition, Wiley-Inter science New York, 1059 (2001)

14-Grie P, Phil Trans. R. *Soc. Lond*., 154:733(1864)

15-Huisgen R, Mbius L, Szeimies G. *Chem. Ber*., 98: 1138(1965)

16-Michael A., *J. Prakt. Chem*., 48:94(1893)

17-Huisgen R., *Angew. Chem., Int. Ed. Engl*., 2:565(1963)

18-Huisgen R., *Angew. Chem., Int. Ed. Engl*., 2:633(1963)

19-Huisgen R., 1, 3-Dipolar Cycloaddition Chemistry (Ed.: A. Padwa), Wiley, New York, (1984) pp. 1-176

20-Fan W Q., Katritzky A R., in Comprehensive Heterocyclic Chemistry II, Vol. 4 (Eds.: A. R. Katritzky, C W. Rees, E F V. Scriven), Pergamon, Oxford, (1996) pp. 101-126

21-Huisgen R., *Pure Appl. Chem*., 61:613(1989)

22-Bock V D., Hiemstra H., van Maarseveen J H., *Eur. J. Org. Chem.,* 51(2006)

23-Meldal M., Tornoe C W., *Chem. Rev.* 108:2952(2008)

24-Rodionov V O., Presolski V I., Diaz D D. , Fokin, V V. , Finn M G., *J. Am. Chem. Soc*., 129:12705(2007)

25-Hein J E., Fokin V V., *Chem. Soc. Rev*., 39:1302(2010)

26-Golas PmL., Matyjaszewski K., *Chem. Soc. Rev*., 39:1338(2010)

27-Gil M V., Arévalo M J., Lopez O., *Synthesis,* 11:1589(2007)

28-Fournier D., Hoogenboom R., Schubert U.S., *Chem. Soc. Rev.,* 36:1369(2007)

29- Sumerlin B S., Vogt A P., *Macromolecules,* 43:1(2010)

30-Droumaguet B., Velonia K,. *Macromol. Rapid Commun.,* 29:1073(2008)

31-Struthers H., Mindt T L., Schibli R., *Dalton Trans.*, 39:675(2010)

32-Binder W H., Sachsenhofer R., *Macromol.Rapid Commun*., 28:15(2007)

33-Mansfeld U., Pietsch C., Hoogenboom R., Becer C R., Schubert U S., *Polym.Chem.*, 1:1560(2010)

34-Binder W H., Zirbs R., "Click Chemistry in Macromolecular Synthesis", *Encyclopedia of Polymer Science and Technology*, Wiley, New York, 2009

35-Franc G, Kakkar A. *Chem. Commun.*, 5267(2008)

36-Lutz J F., Zarafshani Z., *Adv. Drug Deliv. Rev.,* 60:958 (2008)

37-Lutz J F., Borner H.G., *Prog. Polym. Sci.,* 33:1(2008)

38-Mullen D G., McNerny D Q. , Desai A. , Cheng X., DiMaggio S C., Kotlyar A., Zhong Y., Qin S., Kelly C V., Thomas T P., Majoros I., Orr B G., Baker J R., Holl M M., *Bioconjugate Chem.,* 22:679(2011)

39-Marsden H R., Kros A., *Macromol. Biosci.*, 9:939(2009)

40-Himo F., Lovell T., Hilgraf R., Rostovtsev V V., Noodleman L., Sharpless K B., Fokin V V., *J. Am. Chem. Soc.,*127:210(2005)

41-Molteni G., Bianchi C L., Marinoni G., Santo N., Ponti A., *New J. Chem.* 30:1137(2006)

42-Pacho L D., Van Maarseveen J H., Rothenberg G., *Adv. Synth. Catal.* 347: 811(2005)

43-Siemsen P., Livingston R.C., Diederich F., *Angew. Chem. Int. Ed.,* 39:2632(2000)
44-Debets M F., van der Doelen C W J., Rutjes F P J T., van Delft F L., *Chem. Bio. Chem*., 11:1168(2010)
45-Wittig G., Krebs A., *Chem. Ber*., 94:3260 (1961)
46-Agard N J., Baskin J M., Prescher J A., Lo A., Bertozzi C R., *ACS Chem. Biol*. 1:644(2006)
47-Baskin J M., Prescher J A., Laughlin S T., Agard N J., Chang P V., Miller I A., Lo A., Codelli J A., Bertozzi C R., Proc. Natl. Acad. Sci. USA, 104, 16793(2007)
48-Ning X., Guo J., Wolfert M A., Boons G J., *Angew. Chem*., 120:2285(2008)
49-Poloukhtine A A., Mbua N E., Wolfert M A., Boons G J., Popik V V., *J. Am. Chem. Soc*., 131:15769(2009)
50-Debets M F., van Berkel S S., Schoffelen S., Rutjes F P J T., van Hest, J C M., van Delft F L., *Chem. Commun*., 46:97(2010)
51-Jewett J C., Sletten E M., Bertozzi C R., *J. Am. Chem. Soc*., 132:3688(2010)
52-Tron G C., Pirali T., Billington R A., Canonico P L., Sorba G., Genazzani A A., *Med. Res. Rev*., 28:278(2007)
53-Ruba E., Schmid R., Kirchner K., Calhorda M J., *J. Organomet. Chem*., 682: 204(2003)

Chapter 3 : LITERATURE REVIEW: SENSITISERS FOR DSSC

3.1 Dye sensitisers

Dye sensitises serve as solar energy absorbers in DSSC makes them very efficient at harvesting light and converting photoelectric energy. The latter phenomenon depends on the capacity of the molecules to absorb incident photons, the conversion of such photons into electro-hole pairs as well as charge separation and collection [1]. An efficient photosensitiser must display three critical characteristics: first, an intense absorption in the visible region. This is followed by strong adsorption onto the semiconductor surface and the conduction band of the semiconductor must have an effective electron injection. Linearity and a rapid regeneration by the mediator layer would guarantee the recombination of electrons in the ground and excited states.

As one of the most crucial factors that influence the performance of DSSC, the sensitising dyes involve various types of molecules from synthetic metal complexes [2] to natural dyes [3]. Also, a tremendous number of new synthetic metal-free organic dyes [4, 5] have been developed and employed as sensitisers in DSSCs. Among them Ru(II)-based complex dyes remain dominant in photoelectronic conversion efficiency [6]. However, the inconvenient purification and high cost of Ru-based dyes limit their development compared to the metal-free organic dyes. Even though none of the pure organic dyes has surpassed the conversion efficiency of the Ru-based sensitisers at present [7], they still have attracted considerable attention. A large number of studies have been devoted to design novel structural dyes, to clarify the relationship between the structure and properties and to optimise the DSSC devices [5, 8].

The positions of the energy levels in the sensitiser are of great importance. A small gap between the levels leads to the possibility to harvest more low energy photons. This enables the cell to have a high photocurrent output. However, the different electron transfers in the cell need enough driving force to proceed. The excited state oxidation potential of the dye, which is referred to as the lowest unoccupied molecular orbital (LUMO) of the dye, has to be sufficiently higher (more negative) than the conduction band edge of the semiconductor for efficient electron injection. At the same time the ground state oxidation potential or the highest occupied molecular

orbital (HOMO) of the dye needs to be lower (more positive) than the redox potential of the redox couple in the electrolyte for efficient regeneration of the oxidized dye. Several reviews describing the development of sensitisers for DSSCs, including both organic and inorganic dyes, have been published during the last few years [9 - 11].

The sensitisers used in DSSC can be subdivided into organic and inorganic dyes. Inorganic dyes include metal and ruthenium complexes in addition to osmium, metal porphyrin, phthalocyanine and inorganic quantum dots, while organic dye can be natural or synthetical. Unlike organic dyes, inorganic dyes are more stable at higher temperatures.

3.2 Metal-complex sensitisers

The wide absorption and photovoltaic nature of metal complexes make them suitable for DSSC applications. Such types of complex sensitisers usually have anchoring ligands and ancillary ligands. Anchoring ligands are responsible for the complexes adsorption onto the semiconductor surface and are also chromophoric groups. Ancillary ligands are not directly attached onto the semiconductor surface and can be used for tuning the overall properties of the complexes. Polypyridinic complexes of d^6 metal ions show intense metal to ligand charge transfer (MLCT) bands in the visible region, with potential interest for promoting charge injection processes to the conduction band of wide band gap semiconductors, such as TiO_2, SnO_2 and ZnO. The energies of the (MLCT) states can be altered systematically by modifying the anchoring ligands as well as by changing the ancillary ligands or their substituents.

The wide possibilities to tune the MLCT energy resulted in the preparation of many different compounds that have been investigated for semiconductor sensitization. Among them, the best light-to-electricity conversion efficiency has been achieved by using ruthenium(II) polypyridyl complexes as TiO_2 sensitisers in dye-sensitized solar cells. In fact, a ruthenium bipyridine complex was used in the first efficient DSSC cell example reported in the breakthrough article by Grätzel and O'Regan in 1991 [11]. A metal complex consists of a central metal ion with an ancillary binding molecule bearing at least one anchoring group. The absorption of light in the discernible element of the solar spectrum is caused by a charge transfer process from

a metal to a ligand (MLCT). Thus, the central metal ion is critical for the complex in which ancillary binding molecules, typically bipyridines or terpyridines, can be used with different substituents (alkyl, aryl, heterocycle, etc.). The purpose of this is to improve the photovoltaic performance by altering the original photophysical and electrochemical properties. In order to enable the injection of the excited electron into the conduction band (CB) of the semiconductor anchoring groups can be used to attach the dye. The adjustment of energy levels of the MLCT to enhance electron injection and dye regeneration kinetics can be done on any part of the new structure.

3.2.1 Ruthenium complex dyes

Ruthenium DSCs were first reported in 1991 by O'Regan and Grätzel [11]. These first ruthenium dye DSCs achieved 7.1% conversion efficiency (Figure 3.1). However, the structure of the ruthenium dye was complicated and contained three ruthenium metal centres. In 1993, Nazeeruzzin *et al.* published DSCs with 10.3% conversion [12], using a ruthenium dye sensitiser N3 (Figure 3.1). N3 contained one ruthenium center and was thus simpler than the ruthenium dye reported in 1991. The family of complexes $[\{(4,4'\text{-}CO_2H)_2(bipy)\}_2RuX_2]$ (bipy=2,2'-bipyridyl; X=Cl, Br, I, CN, NCS) all perform well [12]. For example, the dye $[\{(4,4'\text{-}CO_2H)_2bipy\}_2Ru(NCS)_2]$ (N3) and the doubly deprotonated analogue N719 shown in Figure 3.2 give a solar-to-electrical energy conversion efficiency of over 10%. Use of a terpyridyl ligand led to the so-called "black dye" shown in Figure 3.2, which gives a very high IPCE (incident photon to current conversion efficiency) across the wavelength range 400–700 nm and a cell efficiency of over 10% [13, 14].

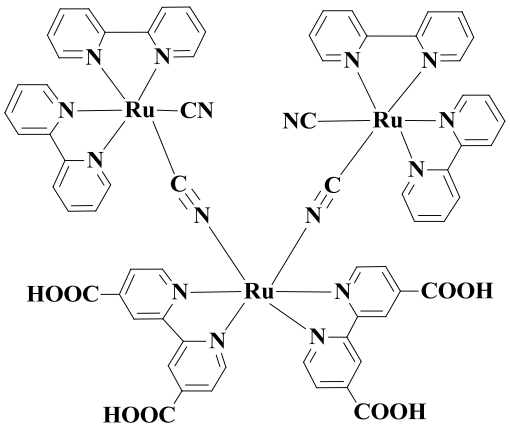

Figure 3.1: A ruthenium dye reported in *Nature* (1991) by Dr. O'Regan and Prof. Grätzel [11].

The most efficient DSSCs are based on ruthenium dyes. These were originally produced by the Grätzel group, and are known as N3, N719 and 'black' dyes [13, 14] (Figure 3.2). The metal-ligand charge transfer (MLCT) transition that mediates how the photoelectric charge is injected into TiO_2 makes these dyes more durable and superior at harvesting light. In the ruthenium complexes the charge transfer is faster and more effective. This allows electrons to merge with the oxidised dye instead of entering into the circuit to yield energy [1].

Considering that the efficiency of conversion in absorbed atoms is particularly high, most research to date has been focused on enhancing the absorption of incident light by altering the molecular structure of the dye. The main objective of this modification is to increase the extent to which photons are absorbed within a functional wavelength (as measured by the molar extinction coefficient, ε) and/or to increase the functional wavelength in itself near infrared (N-IR) [1, 12, 15].

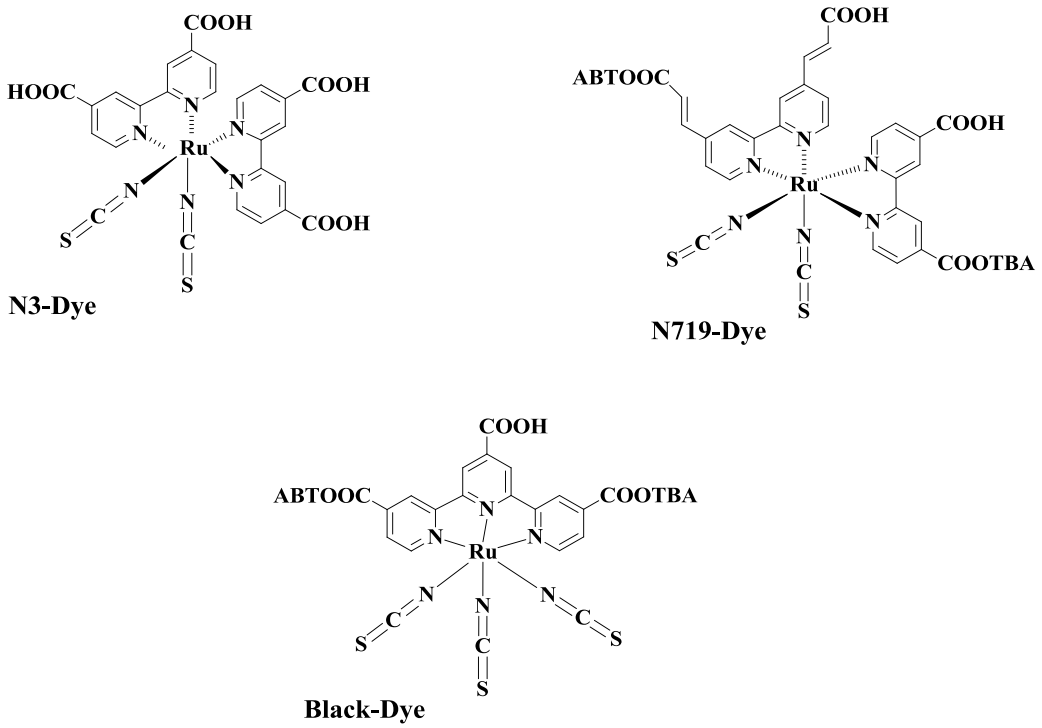

Figure 3.2: The chemical structures of the ruthenium-based dyes N3, N719 and 'black dye' developed by the Grätzel group [16, 17].

Among these complexes, polypyridyl ruthenium sensitisers have outstanding redox properties and good responses to natural visible sunlight. Using a semiconductor film electrode with either a carboxylate or a phosphonate group, sensitisers are attached to the surface allowing the injection of electrons into the band of the semiconductor. In the case of the polypyridyl ruthenium dye, the number of metal centres determines the extent of light adsorption of the sensitisers. Whereas carboxylate polypyridyl ruthenium dye and phosphonate ruthenium dye bear similar metal centres, hence the polynuclear bipyridyl ruthenium dye is clearly different. The carboxylate polypyridyl ruthenium dye shows an in level constitution and that allows quantitative electron injection into the conduction band of the semiconductor.

N3 and its tetrabutylammonium salt N719 (also known as black dye) are the most efficient amongst this type of sensitisers. N719 is considered the standard for dye sensitised solar cells, for instance. Recently, other ruthenium-based dyes such as amphiphilic ruthenium (Z907), and high-molar-extinction-coefficient ruthenium sensitisers (K19) have been the focus of extensive research for carboxylate polypyridyl ruthenium sensitisers. Both the molecular configuration and photovoltaic performance of solar cells are shown in Figure 3.3 and Table 3.1 [18 - 31].

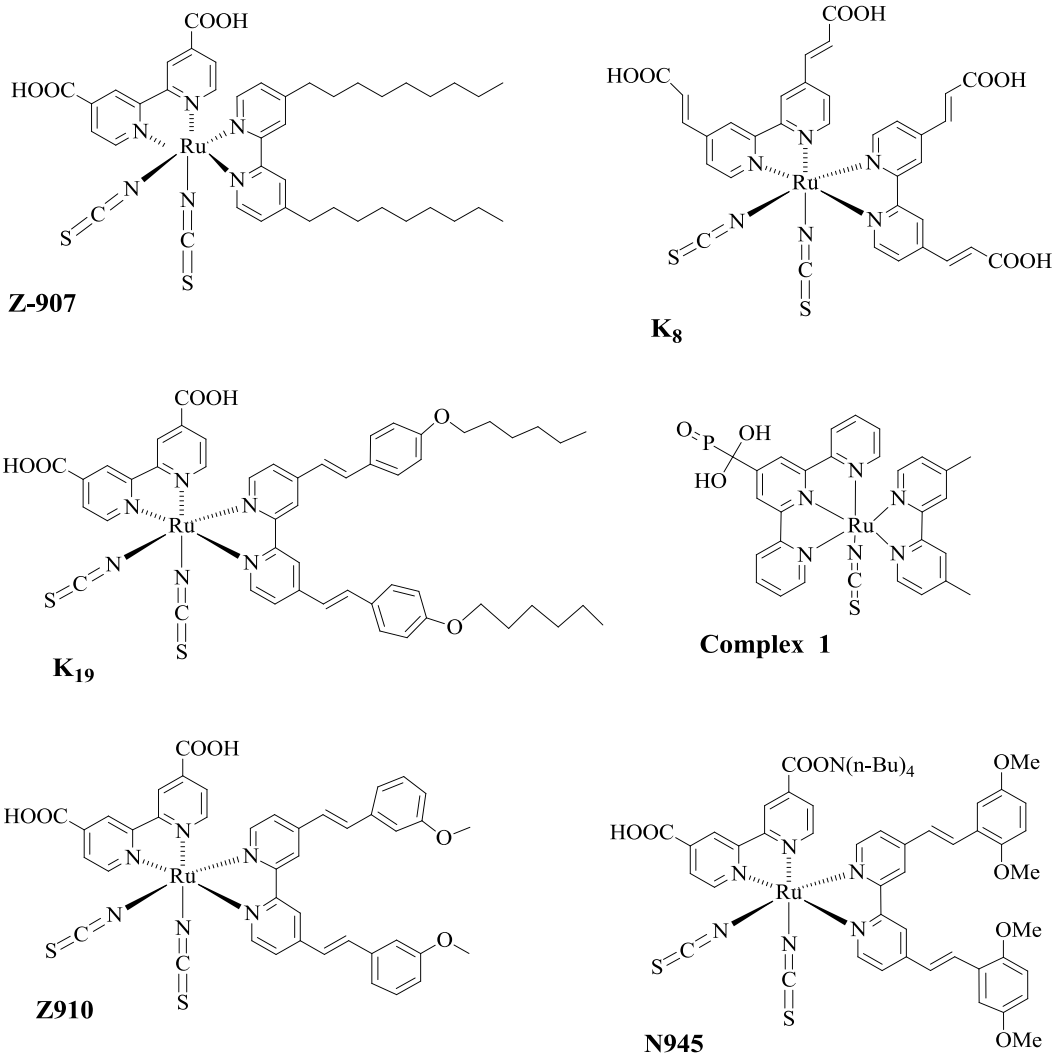

Figure 3.3: The chemical structures of the several ruthenium dye complexes [14, 18 - 31].

Table 3.1: Absorption spectra and photoelectric performance of different polybipyridyl ruthenium (II) complexes.

Dye	*Abs*/nm (ε /10^3 m^2 mol^{-1})	IPCE Incident photon-to-current efficiency	*J*sc/mA·cm^{-2} short circuit current	*V*oc/mV open circuit voltage	FF fill factor	η/% efficiency	Ref.
N3	534(1.42)	83%	18.2	720	0.73	10	[12]
N719	532(1.4)	85%	17.73	846	0.75	11.18	[18]
Black Dye	605(0.75)	80%	20.53	720	0.704	10.4	[19]
Black Dye	—	80%	20.9	736	0.722	11.1	[20,21]
Z907	526(1.22)	72%	13.6	721	0.692	6.8	[22,23]
Z907	526(1.22)	72%	14.6	722	0.693	7.3	[22]
K8	555(1.80)	77%	18	640	0.75	8.64	[24]
K19	543(1.82)	70%	14.61	711	0.671	7.0	[25]
N945	550(1.89)	80%	16.5	790	0.72	9.6	[26]
Z910	543(1.70)	80%	17.2	777	0.764	10.2	[27]
K73	545(1.80)	80%	17.22	748	0.694	9.0	[28]
K51	530(1.23)	70%	15.40	738	0.685	7.8	[29]
HRS-1	542(1.87)	80%	20	680	0.69	9.5	[30]
Z955	519(0.83)	80%	1 6.37	707	0.693	8.0	[31]

Different from carboxylate polypyridyl ruthenium sensitisers, which are easy to desorb in solutions with low pH, phosphonate polypyridyl ruthenium sensitisers are attached to the surface of the semiconductor by a phosphonate group. This makes it difficult to detach even at high pH. On the other hand, because of their non-planar conjugation, the injection of electrons is not as efficient.

The phosphonate polypyridyl ruthenium dye (complex 1) displays a 15-nanosecond lifetime in the excited state. Interestingly, it has a Langmuir adsorption coefficient of 8×10^6, which is significantly higher than other dyes including the N3 [32] and 70% photon-current conversion efficiency at a wavelength of 510 nm. On the other hand, the phosphonate polypyridyl ruthenium analogue of Z907 achieves photon-current conversion efficiency levels slightly higher than solar cells [31]. These polynuclear complexes exhibiting an antenna effect which have been employed to increase absorption coefficients due to their antenna-like properties. Nevertheless, the antenna does not occur at longer wavelengths because of the marked decrease of absorption coefficients and the IPCE spectrum (Incident photon-to-current efficiency) of ruthenium charge-transfer sensitisers' decrease strongly. In addition, these types of sensitisers are bulky and occupy more space on the TiO_2 surface while penetrating at lower rates into small cavities in relation to monocuclear compounds. Thus, the increased absorption coefficients that polynuclear compounds display are not always translated into an improved light absorption on the TiO_2 electrode because of their reduced surface frequency on the non-porous TiO_2 [33]. The binding of bipyridine and two thiocyanato (NCS) groups to N3 allows it to absorb up to800 nm in radiation. However, N3 does not show high V_{oc} (open circuit voltage) despite its high *Jsc* (short circuit current). The presence of H^+ at the two carboxyl groups in the N3 dye, different from N719 for instance, which has tetrabutylammonium (TBA^+), allows it to supply a maximum of four protons per dye turning the E_{cb} (conduction-band-edge energy level) more positive. The fill factor (FF) is essentially a measure of quality of the solar cell, and is defined as the ratio of the maximum power output per unit area to the product of Voc and Jsc. Several factors can influence the FF, such as a high inner resistance (e.g. a bad counter electrode), which will give a low fill factor and a decreased overall efficiency. Typical fill factors range from 0.5 to 0.82

Another dye with a similar adsorption performance than the N3 and N719 is the N749 dye, known as black dye. Its absorption coefficient is slightly lower at 860 nm and demands thicker TiO_2 electrodes for molecule adsorption. Thicker electrodes represent a drawback in electron transport and open circuit voltage, considering that the J_{sc} and V_{oc} values might drop. The performance of N749 is not as high as its counterpart; the N719. The hydrophobic alkyl chains attached to one of the bipyridine ligands in the Z907 allows it to keep water molecules away turning the dye more stable in the long-term, which is a considerable advantage over the dyes N3 and N719. Remarkably, the performance of the DSSCs with Z907 is stable up to 1000 h under light irradiation. This has made amphiphilic ruthenium dyes and high-molar-extinction-coefficient ruthenium sensitisers very appealing in scientific research. Table 3.1 displays the photovoltaic performance of the solar cells.

The reaction of a polypyridyl ligand with ruthenium trichloride produces ruthenium polypyridyl complexes [34]. The reaction to yield 2, 2'-bipyridine and 2, 2':6', 2"-terpyridine is given in Scheme 3.1.

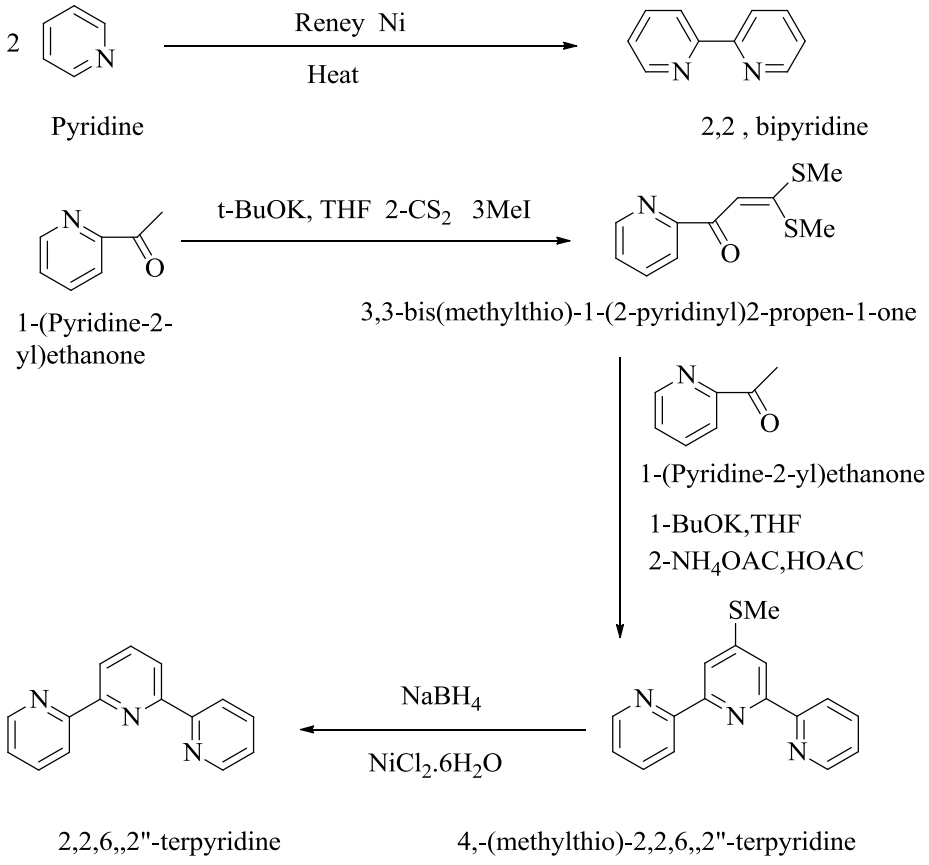

Scheme 3.1: Synthesis of polypyridyl ligands [34].

3.2.2 Other metal-complex sensitisers

Ruthenium complexes have provided the highest efficiencies to date and have therefore been widely studied. However, there are still many problems to be addressed in terms of their low molar extinction coefficient, ruthenium metal and high synthetic cost, and therefore other metal complexes have also been investigated. Considerable effort has been put into substituting Ru with other transition as Os (II), Pt (II), Re (I) Cu (I), and Fe (II). Osmium (Os (II)) complexes show promising photosensitiser properties for DSCs because of their prominent metal-to-ligand charge transfer (MLCT) absorption band in comparison with the Ru complex. Lewis *et al*. were able to develop a class of (Os) polypyridines [35 - 37] by substituting the Ru metal ion with Os. The results were the dyes $[Os(H_2L')_2(CN)_2]$ and $[Os(H_2L')_2(SCN)_2]$, Figure 3.4. These dyes show a wider light response area and similar photovoltaic performances than the DSCs. It was later proven that the slower electron transfer from iodide electrolyte to the osmium dye cation results in lower photocurrent efficiency in Os complexes [38 - 40].

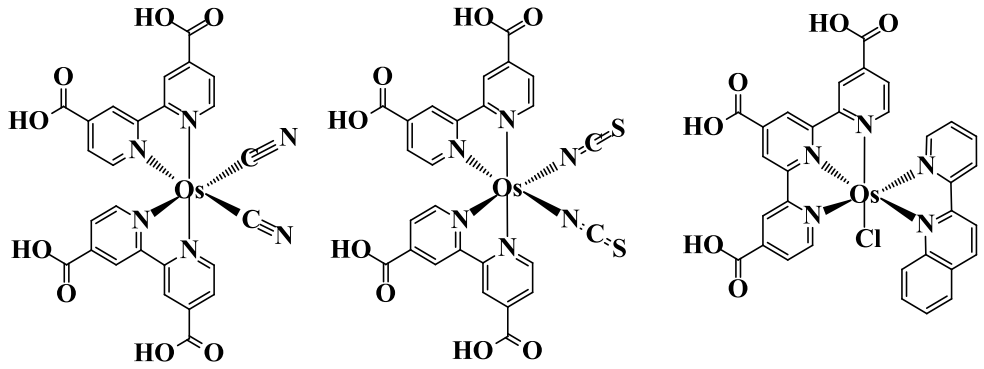

Figure 3.4: The chemical structures of the (Os) polypyridines dyes [37 - 39].

Platinum and copper have been also tested, but with poor results. Islam *et al*. synthesised square planar platinum (II) diimine dithiolate (Figure 3.5) complexes that can also efficiently sensitise nanocrystalline TiO_2 [39, 40]. They reached efficiencies up to 3%. However, recombination and aggregation problems typical of these platinum (II) complexes seem to stop these sensitisers from being more efficient.

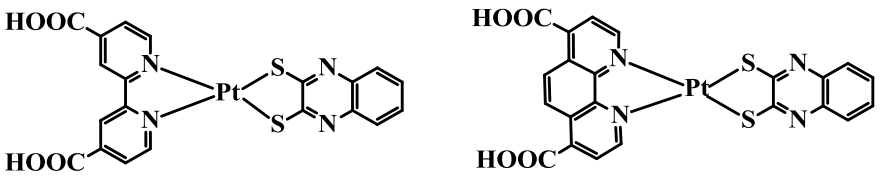

Figure 3.5: The chemical structures of the square planar platinum (II) diimine dithiolate complexes [39]

Cu (I) complexes Figure 3.6 were investigated by Sauvage and co-workers because of their similar photophysical properties to Ru complexes [43, 44]. Up to now the best efficiencies of 2.3% have been reached by Constable and co-workers [45].

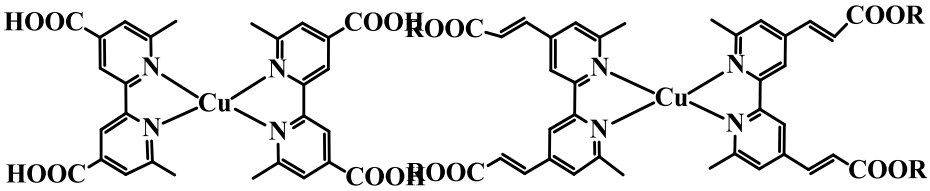

Figure 3.6: Chemical structures of the Cu(I) complexes [45].

Ferrere and co-workers engineered Fe(II) complexes for possible DSC applications, such as the [Fe(II)(2,2'-bipyridine)$_2$(CN)$_2$] these showed lower efficiency rates with IPCE values of only 10-11% in DSCs, Figure 3.7 [46 - 48].

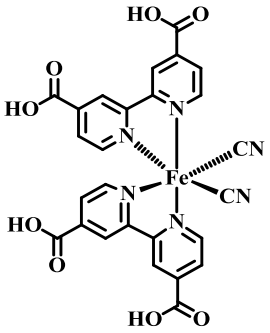

Figure 3.7: The chemical structures of the [Fe(II)(2,2'-bipyridine-4,4'-dicarboxylic acid)$_2$(CN)$_2$] complex [46 - 48].

Chlorotricarbonyl rhenium (I) complexes based on benzathiazole derivatives are shown in Figure 3.8. In relation to similar rhenium (I) 2, 2'-bipyridine compounds, these show red-shifted absorption as well as solar energy conversion efficiency rates around 1.5%

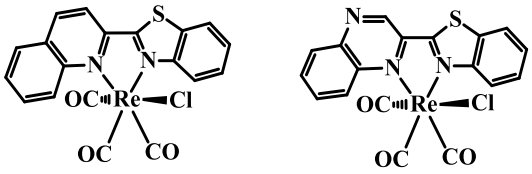

Figure 3.8: The chemical structures of the chlorotricarbonyl rhenium (I) complexes [49 - 50].

3.2.3 Porphyrin sensitisers in DSSCs

Emulation of the extraordinary chlorophyll-based photosynthetic light harvesting apparatus has inspired researchers to investigate synthetically prepared porphyrin dyes as sensitisers for dye-sensitised light harvesting applications and they remain one of the most frequently studied dyes. They are attractive for such purposes, as their synthesis is relatively straightforward and their optical and electronic properties can be tuned via chemical modification of the porphyrin core, the number of porphyrin units and the linker between the core and the inorganic oxide. Figure 3.9 shows the molecular structure of a basic phthalocyanine (special polypyridine complexes). In this figure, R means a radical like *t*-butyl, *n*-hexil, *n*-octyl, and in some cases R can be a substituted amine, and M means a metallic cation.

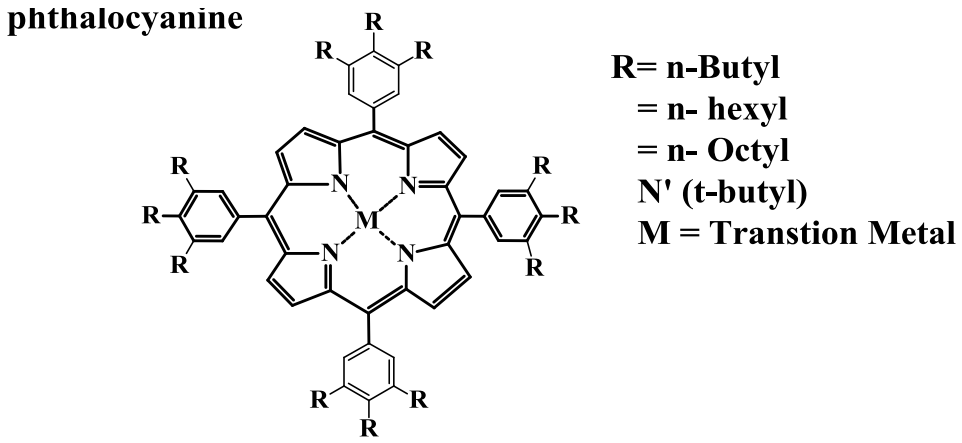

Figure 3.9: The chemical structures of tetrakis(4-carboxyphenyl)porphyrin (phthalocyanine) [51].

A further strategy for avoiding the use of expensive ruthenium in DSC dyes is to use complexes containing inexpensive metals. Large π-aromatic molecules, such as porphyrins and phthalocyanines, are attractive potential candidates for thin, low-cost, efficient DSCs, because of their photostability and high light-harvesting capability. Porphyrins show strong

absorption and emission in the visible region, as well as tunable redox potentials. These properties mean they have many potential applications, in areas such as optoelectronics, catalysis, and chemo-sensing. Self-assembled porphyrin molecular structures play a key role in solar energy research, because the photosynthetic systems of bacteria and plants contain chromophores based on porphyrins, which efficiently collect and convert solar energy into chemical energy. Various artificial photosynthetic model systems have been designed and synthesised in order to elucidate the factors that control the photoinduced electron-transfer reaction. Inspired by efficient energy transfer in naturally occurring photosynthetic reaction centres, numerous porphyrins and phthalocyanines have been synthesised and tested in DSCs.Campbell *et al.* have reported zinc porphyrin dyes (Figure 3.10) which has conversion efficiencies of 7.1% [52]. A recently reported series of zinc porphyrin dyes with donor–acceptor (D–A) substituents exhibit promising photovoltaic properties with a conversion efficiency of 6.8% (YD-2, Figure 3.11 [53]. Bessho *et al.* optimised the fabrication method for YD-2-sensitised DSCs, resulting in the achievement of an 11% solar-to-electric power conversion efficiency under standard conditions (AM 1.5G, 100 mW/cm^{-2} intensity) [54], which is the highest conversion efficiency for a DSC using a ruthenium-free dye so far.

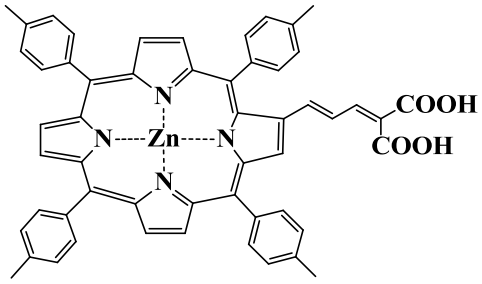

Figure 3.10: The chemical structures of the zinc porphyrin dyes [52].

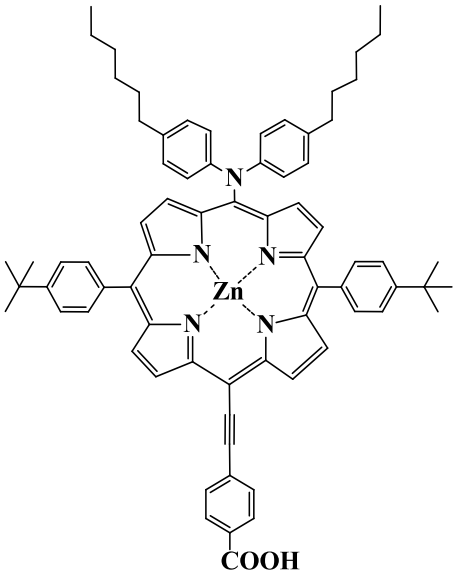

Figure 3.11: The chemical structures of the porphyrin dye YD-2 [53].

3.3 Metal-free dyes

Metal-free dyes include natural organic dyes and synthetically organic dyes.

3.3.1 Organic dyes

Ruthenium complex dyes are capable of delivering DSCs with high photo-energy conversion efficiencies. However, because ruthenium is a rare and expensive metal, ruthenium dyes are not suitable for cost-effective, environmentally friendly photovoltaic systems. This limits the range of applications for these complexes, and makes the development of DSCs that use metal-free, organic dyes essential for their practical use. As a consequence, a lot of work appeared to date in the literature aimed at the optimization of the design of metal-free dyes, and organic sensitizers with higher efficiencies. The general structural architecture of these dyes is usually composed of a push-pull system of the type donor-π bridge-acceptor (D-π-A) such as shown in Figure 3.12. This configuration permits an easy design of new structures with extended absorption spectra, adjusted HOMO and LUMO levels and ensures the necessary separation of charges within the molecule. Upon adsorption of light, there is a transfer of charge from subunit D to subunit A via the π-bridge. The electron is then injected into the conduction band through the electron acceptor group A by the excited dye.

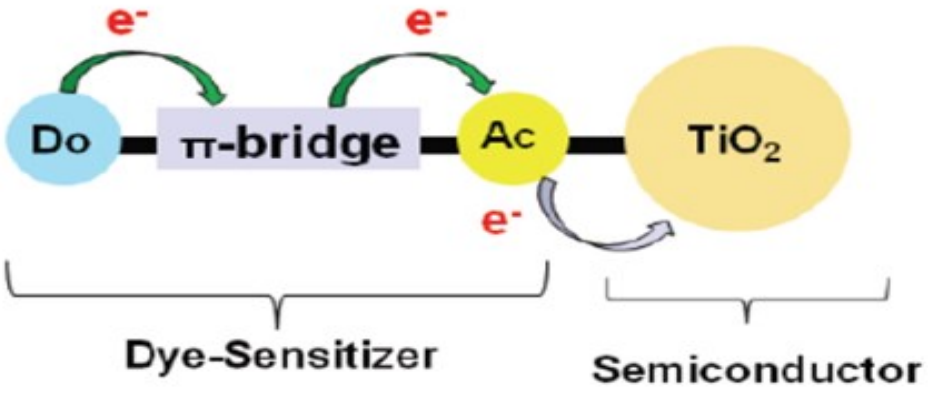

Figure 3.12: Push-pull system of the type donor-π bridge-acceptor (D-π-A) [55].

The ideal structure of the metal free dyes sensitiser is represented pictorially in the Scheme 3.2

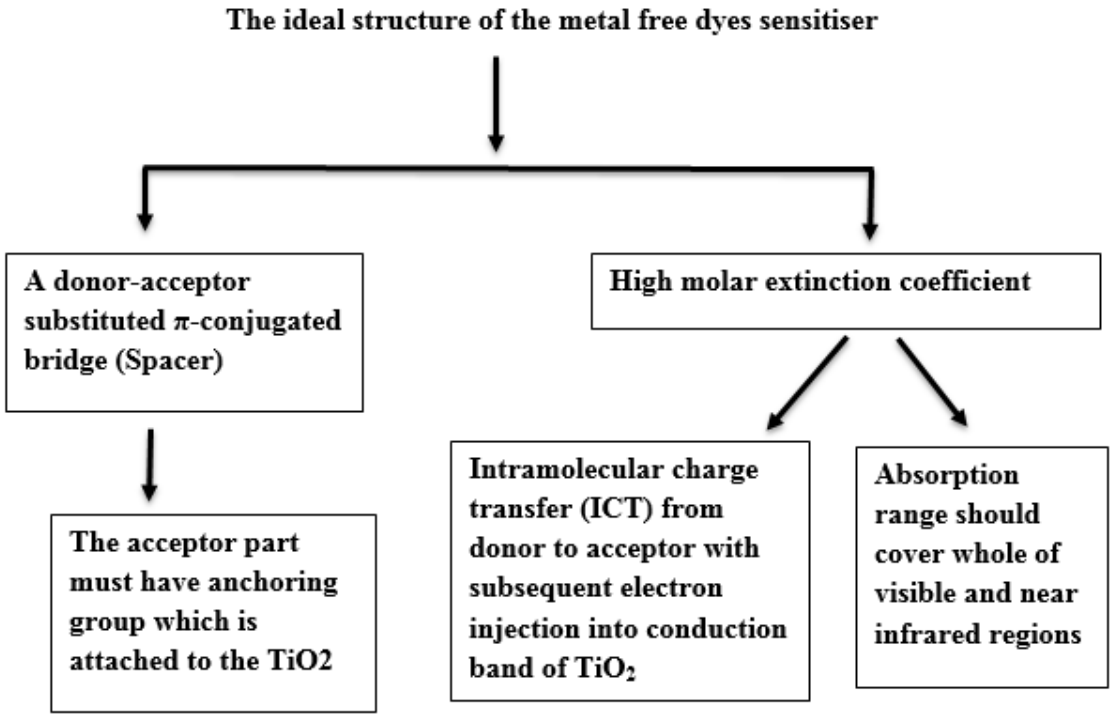

Scheme 3.2: The ideal structure of the metal free dyes sensitiser.

Significant work has been put into manipulating organic dyes in order to optimise DSC performance. Organic dyes, including coumarin, indoline, tetrahydroquinoline, triarylamine,

carbazole, squaraine, perylene, oligothiophene have been studied as sensitizers for DSCs and shown remarkable efficiency

As a donor system, triarylamines are the most studied, thanks to their great stability, electron mobility, strong donating ability and aggregation resistance due to non-planar molecular configuration. Replacement of the phenyl ring that is directly conjugated with the bridge with a heteroaromatic ring, such as a thiophene, can increase the donating strength and reduce aromatic stabilisation [56]. Concerning the spacer, in order to broaden the absorption spectra of the sensitizers in the visible and near-IR region, one strategy is to introduce more conjugate bridges between the donor and acceptor. The π-conjugated linker plays an important role, not only in tuning and modifying the optical properties of DSSC devices under the sunlight radiation, but also in controlling the intra-molecular electron-transfer and electron injection from the excited dye to the conduction band of the semiconductor. Starting from the double bond, several bridges are employed in the dyes, such as triple bonds, aromatic and heteroaromatic rings. Among these, thiophene is an appealing linker extensively used in the literature as single unit or condensed in more complex structures thanks to its electron-donor ability. However, a lot of activity in this field is still devoted to the research of an ideal bridge, which will be able to give broad red-shifted absorption spectra, but also a good electronic connection between A and D unit.

The properties of the organic sensitisers can be modified by incorporating different groups into the molecule. By choosing the right design, the sensitiser can be tuned in order to increase the long wavelength absorption, achieve a high extinction coefficient, and shift the energy levels to improve the performance of the solar cell. Organic dyes have the benefits of higher extinction coefficients, easier structural modification, and provide less environmental problems compared to many of the transition metal complexes. On the other hand, they have drawbacks such as relatively narrow absorption bands, higher tendency to aggregate, and often stability problems. Recently, numerous organic dyes for high-efficiency DSCs have been reported. New organic dyes with efficiencies over 5% (Figure 3.13) include hemicyanine dye, polyene diphenylaniline dye, thienylfluorene dye, phenothiazine dye, thienothiophene-thiophene-derived dye, phenyl conjugated polyene dye, *N*,*N*-dimethylaniline-cyanoacetic acid, oligothiophene dye, coumarin dye, indoline dye and oligo-phenylenevinylene-unit dye.

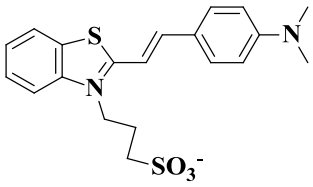

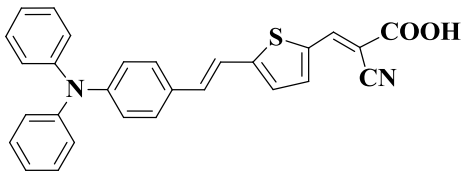

Hemicyanine dye (η = 5.1%) [57] **Polyene-diphenylaniline dye (η =5.1%) [58]**

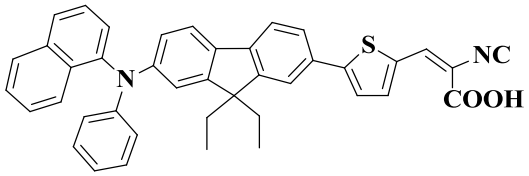

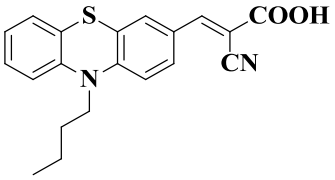

Thienylfluorene dye (η = 5.23%) [59] **Phenothiazine dye (η =5.5%) [60]**

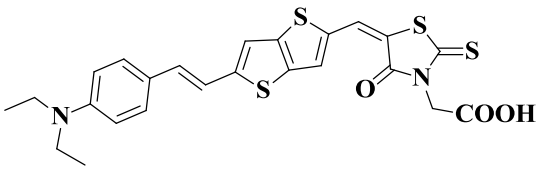

Thienothiophene-thiophene-derived dye (η = 6.23%) [61]

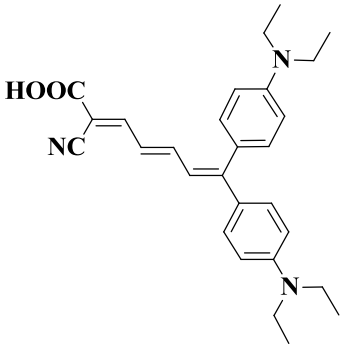

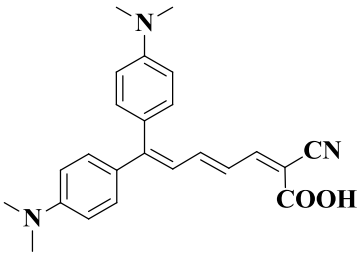

Phenyl-conjugated polyene dye (η = 6.6%) [62] ***N*,*N*-dimethylaniline-cyanoacetic acid (η = 6.8%) [63, 64].**

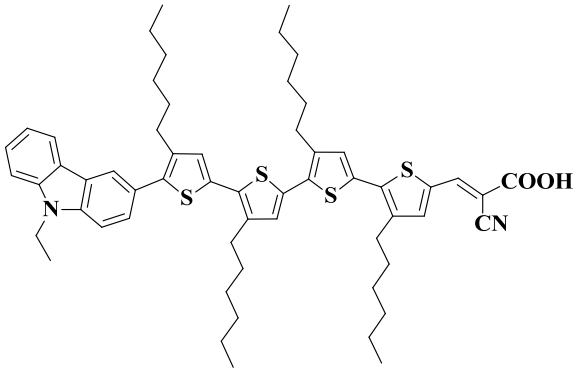

Oligothiophene dye (η = 7.7%) [65]

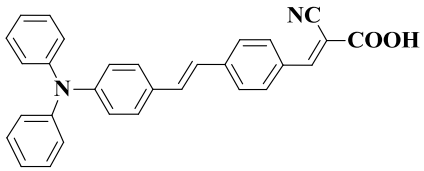

Oligo-phenylenevinylene- dye (η = 9.1%) [66]

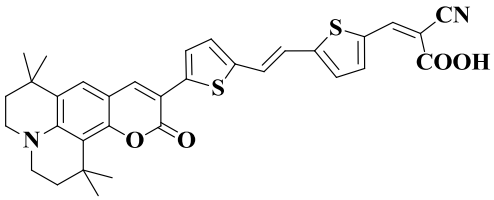

Coumarin dye (η= 8.2%) [67]

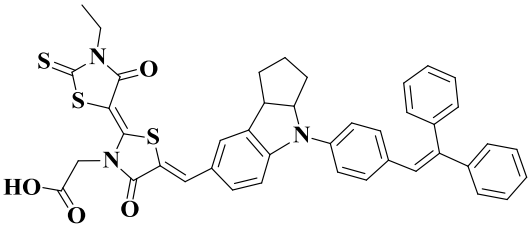

Indoline dye (D149) (η = 9.03%) [68]

Figure 3.13: Molecular structure of several organic dyes with efficiencies over 5%

3.3.2 Natural dyes

Natural dyes as sensitisers for DSSCs are promising alternatives to organic dyes, which have been found in fruits, flower petals, leaves and bark. They offer environmental friendliness, low-cost production, simple preparation techniques and widely available, easily extracted, and are biodegradable [69, 70]. In addition, as natural dyes contain many various constituents they exhibit wider absorption spectra in comparison to chemical synthesis dyes [71-73]

However, the use of natural dyes in dye-sensitised solar cells often has low conversion efficiency in comparison to ruthenium polypyridyl complex dyes [74]. Therefore, there is a need to prepare chemical synthetic dyes that encompass high efficiency along with low toxicity.

3.3.2.1 Plant pigmentation

Plant pigmentation is the result of the interaction of the pigment in the plant with sunlight. Changes in pigmentation are directed to alter the wavelength reflected by the plant. The

human visual abilities can detect wavelengths between approximately 430 and 680 nm. Pigments are determined by both the wavelength of maximum absorbance (λ_{max}) and the colour perceived by the observer. Table 3.2 illustrates the classification of plant pigments based on their type and occurrence [68].

Table 3.2: Pigments in plants.

Pigment	Common type	Occurrence
Betalains	Betacyanins	Caryophyllales and some fungi.
	Betaxanthins	
Carotenoids	Carotenes	Photosynthetic plants and bacteria.
		Retained from the diet by some birds,
	Xanthophylls	fish and Crustaceans.
Chlorophyll	Chlorophyll	All photosynthetic plants
Flavonoids	Anthocyanin	Widespread and common in plants
	Aurones	including angiosperms,
	Chalcones	
	Flavonols	Gymnosperms, ferns and
	Proanthocyanidins	bryophytes.

Table 3.3 summarises the photoelectrochemical specifications of DSSCs for a variety of natural dyes as photosensitisers amongst these dyes a highest efficiency of η = 1.70 % was obtained with an extract of Red turnip Figure 3.14 shows the molecular structure of several natural dyes used in DSSCs. Natural dyes are useful as they can be potentially efficient, cheap and biodegradable.

Table 3.3: Photo-electrochemical parameters of natural dye based DSSCs

Dye	*Jsc (mA cm^{-2})*	*V_{oc} (V)*	*FF*	*η (%)*	*Ref.*
Rosella	1.63	0.40	0.57	0.37	[75]
Blue pea	0.37	0.37	0.33	0.05	
Mixed rosella-blue pea	0.82	0.38	0.47	0.15	
Black rice	1.14	0.55	0.52	–	[76]
Capsicum	0.23	0.41	0.63	–	
Rosa xanthina	0.64	0.49	0.52	–	
Kelp	0.43	0.44	0.62	–	
Erythrina variegate	0.78	0.48	0.55	–	

Bixin	1.10	0.57	0.59	0.37	
Annatto	0.53	0.56	0.66	0.19	[77]
Norbixin	0.38	0.53	0.64	0.13	
Crocetin	2.84	0.43	0.46	0.56	
	0.45	0.58	0.60	0.16	[78]
Fruit of Calafate	6.20	0.47	0.36	–	
Syrup of Calafate	1.50	0.38	0.20	–	
Skin of Jaboticaba	7.20	0.59	0.54	–	[79]
Red Sicilian orange	3.84	0.34	0.50	–	
Purple eggplant extract	3.40	0.35	0.40	–	[80]
Dragon fruit	0.20	0.22	0.30	0.22	
Pomegranate juice	0.20	0.40	0.45	1.50	[81]
Red turnip	9.50	0.43	0.37	1.70	[82]
Wild Sicilian prickly pear	8.20	0.38	0.38	1.19	[83]
Sicilian Indian fig	2.70	0.38	0.54	0.50	
Bougainvillea	2.10	0.30	0.57	0.36	
Shisonin	3.56	0.55	0.51	1.01	
Shisonin and chlorophyll	4.80	0.53	0.51	1.31	[84]
Chlorophyll	3.52	0.43	0.39	0.59	
Hibiscus surattensis	5.45	0.39	0.54	1.14	
Sesbania grandiflora	4.40	0.41	0.57	1.02	
Hibiscus rosasinesis	4.04	0.40	0.63	1.02	[85]
Nerium olender	2.46	0.41	0.59	0.59	
Ixora macrothyrsa	1.31	0.40	0.57	0.30	
Rhododendron arboretum zeylanium	1.15	0.40	0.64	0.29	

Table (3) Continued

Dye	*Jsc (mAcm^{-2})*	*Voc (V)*	*FF*	*η (%)*	*Ref.*
Begonia	0.63	0.54	0.72	0.24	[86]
Tangerine peel	0.74	0.59	0.63	0.28	
Rhododendron	1.61	0. 59	0.61	0.57	
Fructus lyciia	0.53	0.69	0.47	0.17	
Marigold	0.51	0.54	0.83	0.23	
Perilla	1.36	0.52	0.70	0.50	
Herba artemisiae scopariae	1.03	0.48	0.68	0.34	
China loropetal	0.84	0.52	0.63	0.27	
Yellow rose	0.74	0.61	0.57	0.26	
Flowery knotweed	0.60	0.55	0.63	0.21	
Bauhinia tree	0.96	0.57	0.66	0.36	

Petunia	0.85	0.62	0.61	0.32	
Lithospermum	0.14	0.34	0.59	0.03	
Violet	1.02	0.50	0.65	0.33	
Chinese rose	0.90	0.48	0.62	0.27	
Mangosteen pericarp	2.69	0.67	0.63	1.17	
Rose	0.97	0.60	0.66	0.38	
Lily	0.51	0.50	0.67	0.17	
Coffee	0.85	0.56	0.69	0.33	
Broadleaf holly leafbase	1.19	0.61	0.65	0.47	
Red Bougainvillea glabra	2.34	0.26	0.74	0.45	[87]
Violet Bougainvillea glabra	1.86	0.23	0.71	0.31	
Red Bougainvillea spectabilis	2.29	0.28	0.76	0.48	
	1.88	0.25	0.73	0.35	
	0.47	0.55	0.51	0.13	[88]
	0.91	0.54	0.56	0.28	
Ipomoea	5.00	0.25	0.36	0.45	[89]
	6.48	0.32	0.33	0.69	
Garcinia suubelliptica	7.85	0.52	0.29	1.18	
Ficus reusa	10.9	0.50	0.27	1.49	

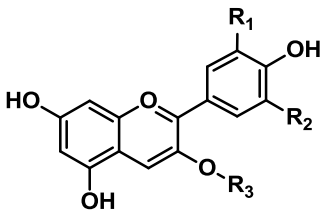

Rosella (η= 0.37) (%)

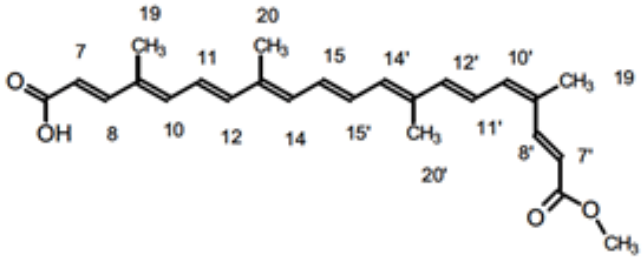

Bixin (η= 0.37) (%)

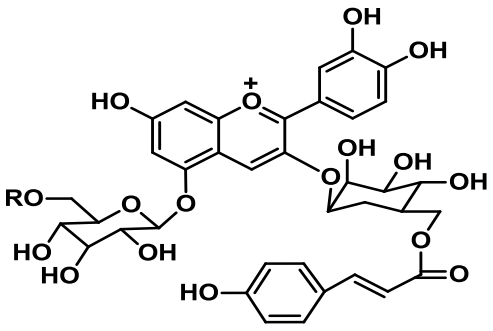

Shisonin (η= 1.01) (%)

Figure 3.14: The chemical structures of several natural dyes used in DSSCs [75, 77, 84].

3. 3.2.2 The performance of a natural dye based DSSC

The generation of natural-dye based DSSCs is inefficient (Table 3.3) due to the low interaction between the dye and TiO_2. The long R group makes the steric hindrance interfere with the binding of the oxide surface of the TiO_2. This results in inappropriate adsorption onto the TiO_2 film and poor transfer of electrons from the dye onto the conduction band of the TiO_2. The extract must have a particular intensity and light absorption since a shorter distance between the dye skeleton and the TiO_2 surface facilitates the transfer of electrons [75].

The nature of the interaction between the TiO_2 and the dye is critical for the efficiency of DSSCs. Natural dyes present low V_{oc} values due to the poor recombination pathways of electron/dye cations and the acidic dye adsorption environment [83]. Since the presence of H^+ determines the transfer of ions to TiO_2 and the level of proton adsorption results in a positive shift of the Fermi level of the TiO_2, there is a limit to the maximum photovoltage that can be conveyed by the cells. The higher the charge-transfer in the TiO_2/dye/electrolyte resistance the more significant the decrease in J_{sc} [86]. Hence, the addition of carboxyl groups and the modification of the structure of natural dyes are pivotal to achieve higher levels of efficiency from natural dyes based DSSCs. The occupying of free space between the iodine solution and TiO_2 semiconductor film surface is known as dye aggregation. This is a known problem with dyes that impedes the electron injection and low efficiency [80].

There are thus many aspects of dye structure, synthesis and application which need to be considered for successful application in any DSCC.

3.4. Summary

The literature review within this chapter covers the background and current research highlights in the development of organic and organometallic compounds for use within dye sensitised solar cells. Chapter 4 will focus on the use of organometallic complexes within cancer therapy.

3.5. References

1-Grätzel M., *Plat. Met. Rev.*, 38:151(1994)

2-Nazeeruddin M K., Klein C., Liska P., Grätzel M., *Coordin. Chem. Rev.,* 249:1460(2005)

3-Wang X F., Koyama Y., Kitao O., Wada Y., Sasaki S., Tamiaki H., *Biosens Bioelectron*., 25:1970(2010)

4-Robertson N., *Angew. Chem. Int. Ed*., 45:2338(2006)

5-Mishra A., Fischer M K R., Bäuerle P., *Angew Chem Int Ed*., 48:2474(2009)

6-Grätzel M., Chen C Y., Wang M K., Li J Y., Pootrakulchote N., Alibabaei L., Ngocle C H., Decoppet J D., Tsai J H, Gratzel C., Wu C G., Zakeeruddin S M., *ACS Nano*.,3:3103 (2009)

7-Li R Z., Liu J Y., Cai N., Zhang M., Wang P., *J. Phys. Chem. B,* 114:4461 (2010).

8-Ooyama Y., Harima Y., *Eur J Org Chem.* 18:2891(2009)

9-Hagfeldt A., Boschloo G., Sun L. C., Kloo L., Pettersson H., *Chem. Rev*.,110:6595(2010)

10-Ooyama Y., Harima Y., *Eur. J. Org. Chem*.,18:2903(2009**)**

11-O'Regan B., Grätzel M., *Nature*., 353:737(1991)

12-Nazzerruddin M K., Kay A., Podicio I., Baker R H., Müller E., Liska P., Vlachopoulos N., Grätzel M., *J. Am. Chem. Soc*., 115:6382(1993)

13-Nazeeruddin M K, Pechy P., Gratzel M., *Chem. Comm*., 1705(1997)

14-Nazeeruddin M K.., Zakeeruddin S M.., Baker R H., Jirousek M., Liska P., Vlachopoulos N., Shklover V., Fischer C H., Grätzel M., *Inorg. Chem*., 38:6298(1999)

15-Liu Y., Shen H., Deng Y., *Front.Mater. Sci. China.,* 1:293(2007)

16-Jin Z., Masuda H., Yamanaka N., Minami M., Nakamura T., Nishikitani Y., *J. Phys. Chem. C.*, 113:2618(2009)

17-Bae H., Lee C., Baek J., Yang H., Dongjin Semichem Co Ltd, 'Novel Ru-Type Sensitsers and Method of Preparing the Same', *World Appl.* 082:163(2009)

18-Nazeeruddin M K., De Angelis F., Fantacci S., *J. Am. Chem. Soc.*,127:16835(2005)

19-Nazeeruddin M K., P´echy P., Renouard T.., *J. Am. Chem. Soc.*, 123:1613(2001)

20-Han L., Chiba Y., Islam A., "High efficiency of dye Sensitised solar cells and module," in *The 16th InternationalConference of Photochemical Conversion and Solar Storage*, Uppsala, Sweden, (July 2006) W4-P-11

21-Chiba Y., Islam A., Watanabe Y., Komiya R., Koide N., Han L., *J. Appl. Phys*, 45:L638(2006)

22-Wang P., Zakeeruddin S M., Baker R H., Moser J E., Grätzel M., *Adv. Mater.*, 15:2101(2003)

23-Wang P, Zakeeruddin S M, Moser J E, Nazeeruddin M K, Sekiguchi T, Grätzel M., *Nat. Mater*., 2:402(2003)

24-Klein C, Nazeeruddin M. K, Liska P., *Inorg. Chem.,* 44:178(2005)

25-Wang P, Klein C, Humphry-Baker R, Zakeeruddin S M, Grätzel M., *J. Am. Chem. Soc.*, 127:808(2005)

26-Nazeeruddin M K, Wang Q, Cevey L., *Inorg.Chem.,* 45:787(2006)

27-Wang P., Zakeeruddin S M, Moser J E., *Adv. Mater*.,16(20):1806(2004)

28-Kuang D., Ito S., Wenger B., *J. Am. Chem. Soc*., 128:4146(2006)

29-Kuang D., Klein C., Snaith H J R., *Nano. Lett*, 6:769(2006)

30-Jiang K J., Masaki N., Xia J B., Noda S., Yanagida S., *Chem. Comm*., 23:2460(2006)

31-Wang P., Klein C., Moser J E., *J. Phys. Chem.B*.,108:17553(2004) Z955

32-P´echy P., Rotzinger F P., Nazeeruddin M K., *Chem. Comm.,* 65(1995)

33-Kohle O., Ruile S., Grätzel M., *Inorg. Chem.*, 35:4779(1996)

34-Sauve G., Cass M E., Doig S J., Lauermann I., Pomyka K L., Lewis N S., *J. Phys. Chem. B.,* 104:3488(2000)

35-Lewis N S., Kuciauskas, D., Monat, J E., Villahermosa R., Gray H B., McCusker J K., *J. Phys. Chem. B.,* 106*:* 9347(2002)

36-Lewis N S., Sauve G., Cass M E., Doig S J., Lauermann I., Pomyka K L., *J. Phys. Chem. B.,* 104:3488(2000)

37-Altobello S., Argazzi R., Caramori S., Contado C., Fre S D., Rubino P., Chone C., Larramona G., Bignozzi, C A., *J. Am. Chem. Soc*., 127:15342(2005)

38-Bignozzi, F., De Angelis., Giorgi G., Licandro E., Longhi E., *J. Phys. Chem. C*., 115:23170(2011)

39-Islam A., Sugihara H., Hara K., Singh L P, Katoh R., Yanagida M., Takahashi Y., Murata S., Arakawa H., Fujihashi G., *Inorg. Chem.*, 40:5371(2001)

40-Geary E A M., Yellowlees L J., Jack L A., Oswald I D H., Parsons S., Hirata N., Durrant J R., Robertson N., *Inorg. Chem.*, 44:242(2005)

41-Geary E A M., McCall K L., Turner A., Murray P R., McInnesE J L., Jack L A., Yellowleesa L J.; Robertson, N., *Dalton Trans.*, 3701:(2008)

42-Geary E A M., Hirata N., Clifford J., Durrant J R., Parsons S., Dawson A., Yellowlees L J., Robertson N., *Dalton Trans.*, 3757:(2003)

43-Vante N A., Nierengarten J F, Sauvage J P., *J. Chem. Soc., Dalton Trans.,* 11:1649(1994)

44-Sakaki, S., Kuroki, T., Hamada T., *J. Chem. Soc. Dalton Trans*., 840(2002)

45-Bessho T., Constable E C., Grätzel M., Redondo A H., Housecroft C E., Kylberg W., Nazeeruddin K., Neuburger M., Schaffner S., *Chem. Commum.*, 3717(2008)

46-Ferrere S., Gregg, B A., *J. Am. Chem. Soc*., 120:843(1998)

47-Ferrere S., *Chem. Mater.,* 12:1083(2000)

48-Ferrere S., *Inorg. Chim. Acta.,* 329:79(2002)

49- Hasselmann G M., Meyer G J *Z.*, *Phys. Chem. (Muenchen)*, 212:39(1999)

50- Hasselmann G M., Meyer G J *Z.*, *J. Phys. Chem. B.,* 103:767(1999)

51-Vougioukalakis G C., Philippopoulos A., Stergiopoulos T., Falaras P., *Coord. Chem. Rev.,* 255:2602(2011)

52-Campbell W M., Jolley K W., Wagner P., Wagner K., Walsh P J., Gordon C K., Schmidt M L., Nazeeruddin M d K., Wang Q., Officer D L., Grätzel M., *J. Phys. Chem. C.*, 11:11760(2007)

53-Lu H P., Tsai C Y., Yen W N., Hsieh C P., Lee C W., Yeh C Y., Diau E W G., *J. Phys. Chem*. C., 113:20990(2009)

54-Bessho T., Zakeeruddin S M., Yeh C Y., Diau E W G., Grätzel M., *Angew. Chem. Int. Ed.*, 49:6646(2010)

55-Mishra A., Fischer M K R., Bäuerle P., *Angew. Chem. Int. Ed*., 48:2474(2009)

56-Davies J A., Elangovan A., Sullivan P A., Olbricht B C., Bale D H., Ewy T R., Isborn C M., Eichinger B E., Robinson B H., Reid P J., Li X., Dalton L R., *J. Am. Chem. Soc*.,130:10565(2008)

57-Wang Z S., Li F Y., Huang C H., *J. Phys. Chem. B*., 105:9210(2001)

51-Hagberg D P., Edvinsson T., Marinado T., Boschloo G., Hagfeldt A., Sun L., *Chem.Comm.*, 2245(2006)

58-Thomas K R J., Lin J T., Hsuc Y C., Ho K C., *Chem. Comm*., 4098(2005)

59-Tian H., Yang X., Chen R., Pan Y., Li L., Hagfeldt A., Sun L., *Chem. Comm.,* 3741(2007)

60-Li S L., Jiang K J., Shao K F., Yang L M., *Chem. Comm.,* 2792(2006)

61-Kitamura T., Ikeda M., Shigaki K., Inoue T., Anderson N A., Ai X., Lian T., Yanagida S. *Chem. Mater*., 16:1806(2004)

62-Hara K., Kurashige M., Ito S, Shinpo A., Suga S., Sayama K., Arakawa H., Chem.*Comm*., 252(2003)

63-Hara K., Sato T., Katoh R., Furube A., Yoshihara T., Murai M., Kurashige M., Ito S., Shinpo A., Suga S., Arakawa H., *Adv. Funct. Mater.,* 15:246(2005)

64-Koumura N., Wang Z S., Mori S., Miyashita M., Suzuki E., Hara K., *J. Am. Chem. Soc.*,128:14256(2006)

65--Hwang S., Lee J H., Park C., Lee H., Kim C., Park C., Lee M H., Lee W., Park J., Kim K., Park N G., Kim C., *Chem. Comm.*, 4887(2007)

66-Wang Z S., Cui Y., oh Y D., Kasada C., Shinpo A., Hara K., *J. Phys. Chem. C.,*111:7224 (2007)

67-Horiuchi T., Miura H., Sumioka K., Chida S U., *J. Am. Chem. Soc*., 126:1221(2004)

68-Davies K., Plant pigments and their manipulation., Annual Review of Plant Biology 14. Blackwell Publishing Ltd, Oxford UK(2004)

69-Zhou H., Wu L., Gao Y., MaT., *J. Photochem. Photobiol*., A 219:188(2011)

70-Zhang D, Lanier S M., Downing J A., Avent J L., Lum J., McHale J L., *J. Photochem. Photobiol*., A 195.:72(2008)

71-Okoli L.U., Ekpunobi A J., Ozuomba J O., *J. Nanomat. Biostr*., 6:1929(2011)

72-Win S Y., Win T T., Maung Y., Soe K K K., Kyaw T T. Tan C K., Rajalingam S., Oo Z., *Pertanika J. Sci & Technol*., 23:119(2015)

73-Abeygunawardhana P., Palamakubura S., Thotawattage C A., Dissanayake M A K L., Senadeera G K R., (2011). Nanocrystalline TiO2 photo-sensitized with naturals dyes. Solar Asia 2011 International Cenference, pp. 229)

74- Furukawa S., Iino H., Iwamoto T., Kukita K., Yamauchi S., *Thin. Solid. Films* 518:526 (2009)

75-Wongcharee K., Meeyoo V., Chavadej S., *Sol. Energy Mater. Sol*. *Cells*., 91:566(2007)

76-Hao S., Wu J., Huang Y., Lin J., *Sol. Energy Mater. Sol. Cells*., 80:209(2006)

77-Gomez-Ortiz N M., Maldonado I A V., Espadas A R P., Rejon G J M., Barrios J A A., Oskam G., *Sol. Energy Mater. Sol. Cells*., 94:40(2009)

78-Yamazaki E., Murayama M., Nishikawa N., Hashimoto N., Shoyama M., Kurita O., *Sol. Energy Mater. Sol. Cells*., 81:512(2007)

79-Polo A S., Iha N Y M., *Sol. Energy Mater. Sol. Cells.,* 90:1936(2006)

80-Calogero G., Marco GD., *Sol. Energy Mater. Sol. Cells.,* 92:1341(2008)

81-RAM A., Nayan N., Fabrication and analysis of Dye-Sensitised solar cell using natural dye extracted from dragon fruit. *IJIE* 2:55(2010)

82-Bazargan M H., *J. Nano. Mater. Bios*., 4:723(2009)

83-Calogero G., Marco G D., Cazzanti S., Caramori S., Argazzi R., Carlo A D., Efficient dye-Sensitised solar cells using red turnip and purple wild Sicilian prickly pear fruits. *IJMS,* 11:254(2010)

84-Kumara G R A., Kaneko S., Okuya M., Ageyeman B O., Konno A., Tennakone K., *Sol. Energy. Mater. Sol. Cells*., 90:1220(2006)

85-Fernando J M R V. Senadeera G K R., *Curr. Sci*, 95:663(2008)

86-Zhou H., Wu L., Gao Y., Ma T., *Photochem. Photobiol. A,* 219:188(2011)

87-Hernández-Martinez A R., Vargas S., Estevez M., Rodriguez R., Dye-Sensitised solar cells from extracted bracts bougainvillea betalain pigments. In: 1st International Congress on Instrumentation and Applied Sciences. 1–15(2010)

88-Chang H., Wu H M., Chen T L., Huang K D., Jwo C S., Lo Y J., *J. Alloys Compd*., 495:606(2010)

89-Lai W H., Sub Y H., Teoh L G., Hona M H., *Photochem. Photobiol. A*., 195:307(2008)

Chapter 4 : Anticancer activities of bio-inorganic compounds

4.1 Introduction

Cancer comprises a group of diseases involving uncontrolled and abnormal growth of cells, which can potentially be invaded or it be spread to other parts of the body [1, 2]. Cancer starts with genetic changes in one cell or a small group of cells. The change is called mutation [3, 4]. Mutation can change the normal DNA sequence, and the most common mechanism of this process implies that one base is replaced by another during the replication process. Sometimes mutations can arise from a modification in the base, deletion of the base or addition of another base. This is quite a common process and the DNA repair mechanism generally fixes it. When this does not happen, a misfolded protein can be the result of mutations. It can happen by chance when a cell is dividing or it can be caused by the biological processes inside the cell. It can be also triggered by external factors, such as through chemicals in tobacco smoke, UV radiation and toxins. In the majority of cases, these mutations are overcome by the cell repair machinery and the damage is not occurred further [5-7]. Healthy cells produce signals by controlling cells division, and if the mutation of the erroneous signals cannot be repaired, then the cell enters into senescence (apoptosis). However, if the apoptotic signalling is not working and /or the repairing mechanism is faulty, then cells may start to multiply and grow in excess forming a lump, which is called a tumour.

The cell cycle is a series of phases that both normal cells and cancer cells go through in order to form new cells. The cell cycle has 5 phases, which are labelled below using letters and numbers.

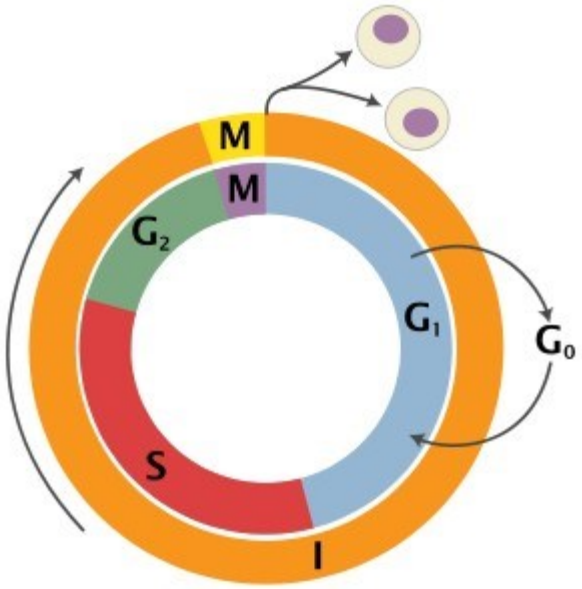

Figure 4.1: A schematic representation including the stages G0, G1, S, G2 and M of cell cycle [8].

After a cell reproduces, the 2 new cells are identical. Each of the 2 cells made from the first cell, can go through this cell cycle again when new cells are needed.

G0 phase (resting stage): The cell has not started to split. Cells spent much of their lives in this stage. Depending on the type of cell, G0 can last from a few hours to a few years. When the cell gets a signal to reproduce, it moves into the G1 phase.

G1 phase: During this phase, the cell starts making more proteins and growing larger, so the new cells will be of normal size. This phase lasts about 18 to 30 hours.

S phase: In the S phase, the chromosomes containing the genetic code (DNA) are copied so that both of the new cells formed, will have matching strands of DNA. The S phase lasts about 18 to 20 hours.

G2 phase: In the G2 phase, the cell checks the DNA and gets ready to start splitting into 2 cells. This phase lasts from 2 to 10 hours.

M phase (mitosis): In this phase, which lasts only 30 to 60 minutes, the cell essentially splits into 2 new cells. The cell cycle is important because many chemotherapy drugs work only on cells that are actively reproducing (not cells that are in the resting phase, **G0**). Some drugs actually attack cells in a particular phase of the cell cycle (the **M** or **S** phases, for example) [9].

In 2011, in the UK, more than 331,000 people were diagnosed with cancer (around 910 people every day). The risk of developing cancer up to the age of 50 years is 1 in 35 for men and 1 in 20 for women. Cancer can be developed at any age and the incidence has risen by 23% in males and by 43% in females since mid-1970s [10-12], (Cancer Research Statistics UK). The sixth most common and the third lethal cancer in the world is liver cancer with 782.000 new cases diagnosed in 2012. Development of this type of cancer is mainly linked to an unhealthy lifestyle, alcohol consumption and also Hepatitis B and C infections [13-15] (World Cancer Research Fund International). A total of 4348 people in the UK were diagnosed with liver cancer in 2011, which accounts for 1% of all cancer cases (Cancer Research, Key Statistics).

Colorectal cancer was the fourth most common cancer in the UK in 2011 and accounted for 13.6% of all new cases of cancer in that year. It is the third most common cancer in both males and females. In 2011, there were 41,581 new cases of colorectal cancer in the UK: 23,171 (56%) in men and 18,410 (44%) in women, giving a male: female ratio of 14:11. Most cases of colorectal cancer occur in older men and women. Age specific incidence rates in UK between 2009 and 2011 shows that an average 43% of new cases were diagnosed in people aged 75 years and over, and 95% were diagnosed in those aged 50 and over [16]. About 50% of patients diagnosed with colorectal cancer survive for at least 5 years after diagnosis [17]. Countries with the highest incidence rates include Australia, New Zealand, Canada, US and parts of Europe. Colorectal cancer is mainly a disease of developed countries with a Western culture [18-19]. Almost two-thirds (66%) of all bowel cancers are cancer of the colon and over one-third (34%) are cancers of the rectum (Cancer Research, Bowel Cancer statistics). Treatment modalities for colorectal cancer include surgery, radiotherapy, chemotherapy and targeted therapy [20]. Chemotherapy drugs, which are useful in treatment of colorectal cancer, include Capecitabine, Fluorouracil, Irinotecan, Oxaliplatin, Raltitrexed and UFT [21].

Hepatic cancer is now ranked as the 18th most common cancer in England. Incidence has increased by 70% among males and 60% among females since 2003. Over 80% of liver cancer cases worldwide are due to hepatitis B or C infection. Alcohol is another risk factor for hepatic cancer [22]. Studies evaluating the use of cytotoxic chemotherapy for the treatment of advanced liver cancer, have shown low response rates and no improvement in patients' survival [23]. Examples of chemotherapeutic drugs used in the treatment of liver cancer include Doxorubicin, Cisplatin and Fluorouracil [24]. Malignant tumours (cancer) have the

capability of invading tissues and cells can be spread (radiate) to distant sites in the body [25]. Treating hepatic cancer can be a difficult. There are four stages, namely A in which resection, transplant or heat can reverse it to achieve a cure of it. If it is diagnosed in stage B or C, there is no cure, but chemotherapy allows survival by stopping the cancer spreading into other organs. If the diagnosis is done at stage D, palliative care is the only option.

Cancer has an impact worldwide and there are debates in relation to the question "do we have more cancers" or "we have better diagnosis". It seems the answer lies in between the two questions. It has been postulated by the majority of researchers that current cancers are result of our lifestyle choices such as drinking alcohol, cigarette smoking, meat consumption, environmental contamination, etc. Our life expectancy, thanks to antibiotics, vaccines and sanitation, has increased dramatically. It is also important to point out that mutations in the DNA are more common with ageing, so an older population will have more chances of developing cancer later in life. Better diagnostic techniques have allowed the detection of cancers earlier on, thus giving way to improved treatment outcomes.

A common approach for discovery of agents with anticancer activity, starts with the empiric screening for antiproliferative or cytotoxic effects in human cancer cell lines [19-21, 26]. Generally, the most commonly used anticancer chemotherapeutic drugs work by inhibiting cell division (mitosis) by different mechanisms such as damaging DNA or inhibiting cellular metabolism. There are numerous methods used to treat the cancer, such as surgery, chemotherapy, immunotherapy and radiotherapy. The aim of any cancer treatment is to remove cancerous cells in order to prevent them from growing and spreading. Radiotherapy is a treatment involving the use of high-energy radiation to destroy cancer cells. It can be given externally (X-rays) or through gamma rays, at the affected area or internally (involves radioactive material placed inside of the body) [27-30].

Immunotherapy treatment uses the body's own immune system to work harder in order to attack cancer cells. It uses materials either made by the body or in a laboratory to improve, target or restore immune system functions (monoclonal antibodies, interferons, and interleukins) [31-33]. Chemotherapy treatment involves drugs, which aim to destroy cancer cells. Chemotherapy drugs can be divided into several groups, based on factors such as how they work, their chemical structure and their relationship to any another drug. There are

different methods of chemotherapy [34, 35]. Chemoembolisation delivers a chemotherapeutic agent directly to a tumour and thus minimise exposure to healthy tissue. This method reduces side effects and maximises the cancer – killing properties of the drugs. During chemoembolisation a drug is injected through a catheter directly into a tumour using image guidance. The chemotherapy drugs are mixed with particles called microspheres, which block the flow of blood to the tumour. Without blood supply, the tumour no longer has the oxygen and nutrients it needs to grow. This method is primarily used for the treatment of liver cancer. There are also other ways of receiving chemotherapy such as intravenously (IV), orally, as an injection or intraperitomeally (directly into the abdomen or peritomeal cavity) or topically [36]. Another treatment, called photodynamic therapy, involves a drug sensitive to light. Once given to the patient, light at a particular wavelength is applied, and the drug will produce reactive oxygen species that will kill the surrounding cells. It is generally applicable for cancers of the skin (not melanoma), gullet, head, neck, mouth, eyes and lungs [37-38]. The most common chemotherapy drugs used are alkylating drugs such as nitrogen mustards, alkyl sulphonates, triazines, nitrosoureas, ethylenimine derivatives and metal salts containing platinum [39, 40]. The treatment of colon cancer depends on its stage. If the cancer did not spread to distant sites, surgery is usually the primary treatment in conjunction with chemotherapy. In more advanced stages, the surgery is followed by adjuvant chemotherapy with drugs containing platinum compounds such as Folfox [41], (leucovorin and oxaliplatin) or CapeOx (capecitabine and oxaliplatin) [42, 43].

The development of metal complexes with platinum central atoms, such as cisplatin or carboplatin, had a massive impact on current cancer treatments. However, the spectrum of cancers that can be treated with platinum agents is narrow and treatment efficacy suffers from side effects and resistance phenomena. These problems in platinum-based anti-cancer therapy have stimulated increased research efforts in the search for novel non-platinum containing metal species as cytostatic agents. Preclinical and clinical trials showed promising results for complexes with iron, cobalt or gold central atoms. Compounds with titanium, ruthenium or gallium central atoms have already been evaluated in phase I and phase II trials [44]. These metals when used in photodynamic therapy, can produce reactive oxygen species that can kill the surrounding cells, though a different mechanism, therefore they have promising activities [45].

4.2 Chemotherapeutic anticancer agents

4.2.1 Platinum compounds and derivatives - based anticancer agents

Transition metal ion complexes have been widely considered, particularly because of their photophysical properties and potential biological applications and antitumor potential [45-48]. The first complex observed and investigated in this regard was cisplatin (cis-diamminedichloroplatinum(II)). This complex was synthesised for the first time in 1844 by Michele Peyrone [49]. Figure 4.2 gives a schematic representation of the compound.

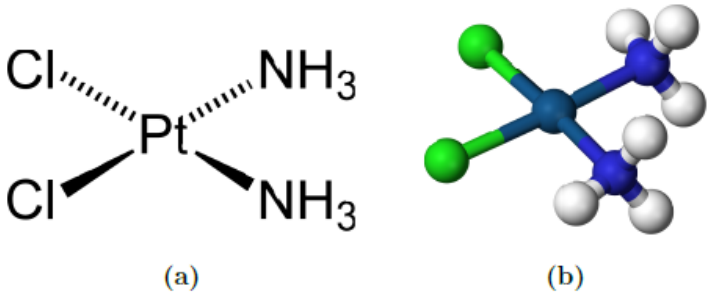

Figure 4.2: Cisplatin, cis-diamminedichloridoplatinum(II) [50-52].

The tumour-inhibiting qualities of this substance were discovered more than a century later by Rosenberg in 1969 [53]. In 1971 cisplatin entered clinical experiments shortly after its discovery and since then has become a highly active drug for treating testicular tumours, ovarian carcinomas, bladder tumours, neck and head cancer. Successful applications also occurred in cases of lung cancers, oesophageal cancer, lymphomas, breast cancer and other tumour types [54]. In spite of cisplatin's success as an anticancer drug, it also has some disadvantages. Its applicability is still restricted to a comparatively narrow scope of tumours, because some tumours have a natural resistance to cisplatin. There are also significant problems in terms of the toxicity of cisplatin and its limited solubility in aqueous solution, which restricts it, administration intravenously [55].

4.2.2. Cisplatin analogues as marketed platinum anticancer drugs

Over 3000 platinum compounds have been synthesised and screened for their biological activity [56]. Of these, less than 30 compounds have entered clinical trials [57]. Attempts to improve new anticancer platinum drugs have faced difficulties in overcoming the problems of cisplatin in actual clinical tests. At present, only four platinum drugs (anologues of cisplatin) are registered and marketed drugs (cisplatin, carboplatin, oxaliplatin and

nedaplatin) Figure 4. 3 and only one compound (oxaliplatin) has been approved by the FDA (Food and Drug Administration) for colorectal cancer [58].

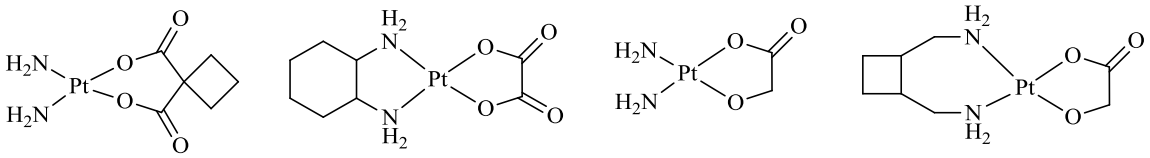

(c) Carboplatin **(d) Oxaliplatin** **(e) Nedaplatin** **(f) Laboplatin**

Figure 4.3: Molecular structure of some selected platinumdrugs: (a) Carboplatin, (b) Oxaliplatin, Nedoplatin and Labopltin [44, 59].

The platinum family of chemotherapeutics, which includes the parent compound cisplatin and its derivatives carboplatin and oxaliplatin, are among the most commonly prescribed anticancer agents, with global sales of over $670 million in 2004 [60].

Some derivatives of cisplatin complex exhibited excellent cytotoxicity, such as a platinum(II) complex with an acridinylthiourea ligand. This complex (4) was reported and exhibited excellent cytotoxicity against a leukemia cell line (Figure 4.4) [61, 62]. On the other hand, the derivatives of cis-amminedichloro(2-methylpyridine)-platinum(II) (AMD473 (5), shown in Figure 4.4, exhibited high antitumor efficacy against cisplatin-resistant mouse sarcoma 180 (S-180cisR) cell lines [63]

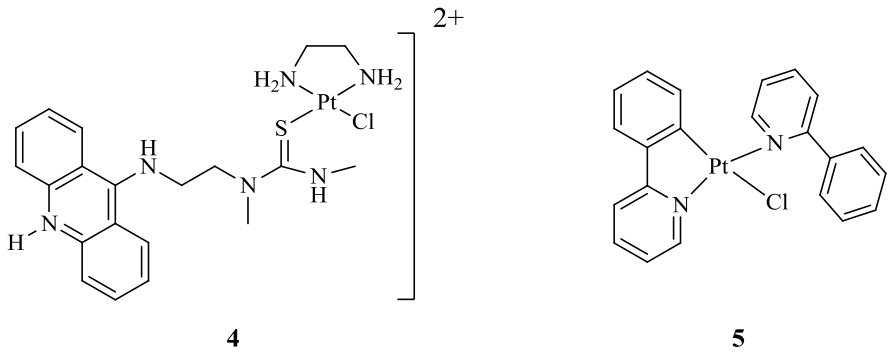

4 **5**

Figure 4.4: Structures of Pt(II) complexes (4) with acridinylthiourea ligand (5), with 2-phenylpyridine ligand.

4.2.3. Palladium anticancer chemistry

Palladium (Pd) chemistry is analogue to that of platinum (Pt). Therefore, Pd complexes (II) are expected to display antitumor activities analogous to those of Pt. Several attempts have been made to synthesise Pd (II) complexes with such activities, as Pd complexes are probable to have less kidney toxicity than Pt complexes [64]. Graham et al. (1979) and Rau et al. (1996) have synthesised several palladium complexes with promising activity against tumour cell lines. Different types of monodentate ligands were applied in the synthesis of these complexes [65-66]. Furthermore, several research groups have focused on the preparation of Pd(II) complexes bearing bidentate ligands as a approach to stabilise these compounds and to prevent any possible cis-trans isomerism [67] (see Figure 4.5).

The discovery of the cytotoxic activity of cisplatin and its analogue carboplatin has led to an extensive search for new biologically active metal drugs. Several cisplatin related platinum based drugs have been synthesised, however, high general toxicity and development of platinum-resistance to the drug have become major obstacles to its efficacy. Most of the palladium complexes are less cytotoxic compared to their platinum analogues, and the latest studies have proved that Pd metal still holds some interest as anticancer compounds with desirable properties, as depicted in Figure 4.5 [68-78].

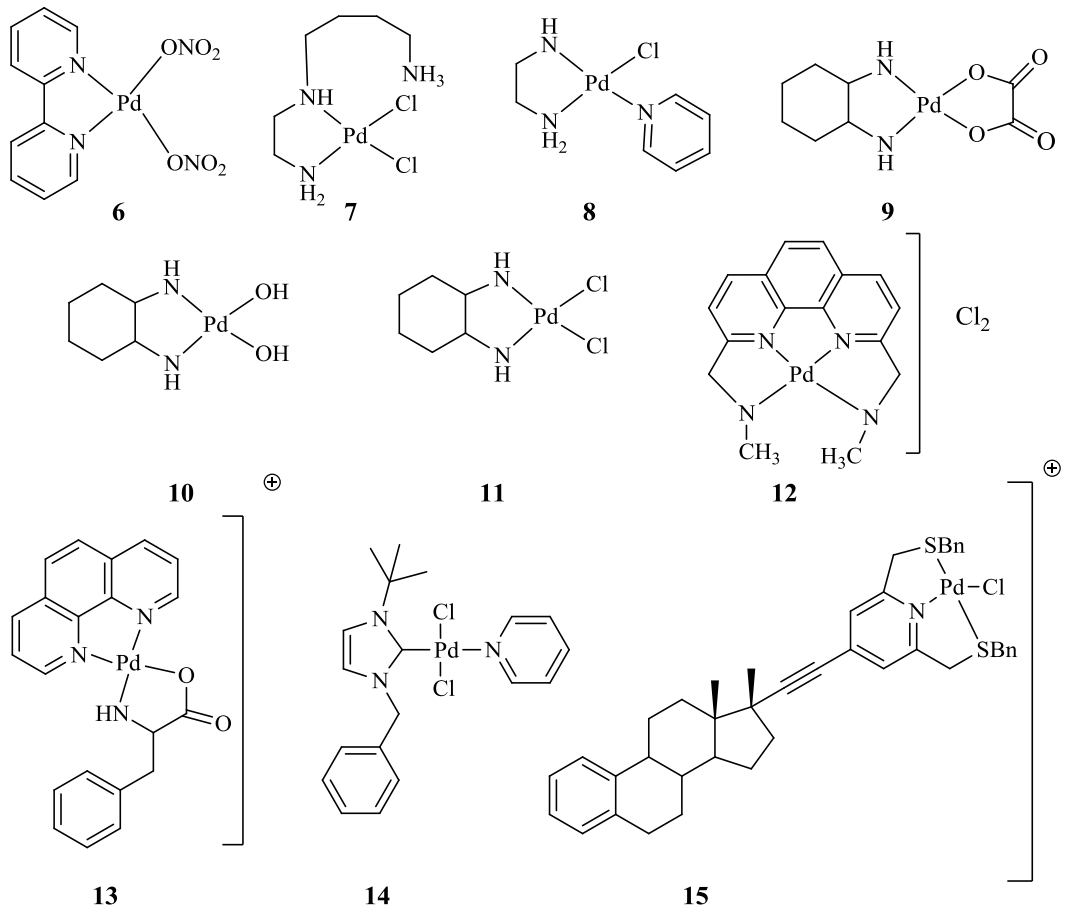

Figure 4.5: Molecular structure of selected anticancer Palladium(II) complexes containing different types of nitrogen monodentate and bidentate ligands (5-14).

In inorganic complexes, the central metal ions play a significant role in the improvement of anticancer metallodrug. The palladium complexes resulting from diamines, amine-imine, di-imines [79-83], have been found to possess excellent cytotoxicity. Metal complexes derived from click chelators are known for their cytotoxicity [84] and have displayed good versatility in the radiolabelling of biomolecules [85]. Improvement of palladium (II) metallodrugs is of importance due to the similarity in the coordination behaviour of platinum (II) and palladium (II) [86-99]. Diverse triazole functionalities, e.g. (2-pyridyl)-substituted 1,2,3-triazoles, are renowned for their metal binding properties [100-102] and can easily be added simply by the famous click reaction procedure [103].

Trivedi et al. (2012) have synthesised a number of carbohydrate containing pyridyl 1,2,3-triazole ligands by using the 'click reaction' of 2-ethynyl pyridine with the appropriate azides [104]. The pyridyl triazole containing benzyl group 2e was prepared according to a literature procedure [105]. The palladium complexes were formed by the reaction of pyridyl triazole

ligands with [Pd(COD)Cl_2] in dichloromethane. The complexes have been examined for their cytotoxic activity and demonstrated anticancer properties in various cell line, including e.g. A549 (human alveolar adenocarcinomacells), Neuro2a (mouse neuroblastoma cells), HeLa (cervical carcinoma cancer cells), MDA-MB-231(human breast adenocarcinoma cells) and MCF7 (human breast adenocarcinoma cells). The complexes exhibited significant cytotoxicity, while the ligands were non-toxic on the tested cell lines, except ligand 2b, which revealed considerably cytotoxicity with IC_{50} values ranging from 11.9-43.7 μM [106].

4.3 Other metals compounds and derivatives non-platinum anticancer agents

4.3.1 Ruthenium complexes

Other metal-based compounds have been synthesised in an effort to replace platinum compounds as anticancer agents, with much focus placed on ruthenium-based compounds because of their lower general toxicity compared to platinum anticancer compounds [107-110]. Ruthenium-DMSO complexes are believed to have great potential because of their selectivity for solid tumour metastases and low host toxicity [111]. A number of ruthenium complexes have been established which offer a significantly higher degree of selectivity towards cancerous cells than the leading commercially available platinum derived drugs. They also resulted in reduced damage to healthy tissues [112]. Currently two ruthenium complexes (NAMI, NAMI-A and KP1019), shown in Figure 4.6, are in clinical trials. The first typical of ruthenium (III) complex [HIm]-Trans-[$RuCl_4$(DMSO)(Im)] (NAMI-A) where [Cl = Chloride ion, Im = imidazole, DMSO = dimethylsulfoxide)]. This complex, improved by Sava et al. in Trieste, possesses outstanding antimetastatic properties [113]. The second, complex is [HInd] trans-[$RuCl_4(Ind)_2$], where (Ind = indazole). KP1019, another ruthenium(III) compound prepared by Keppler et al. in 1989 displayed very encouraging antitumor properties in clinical trials [114].

Various other ruthenium complexes with oxidation states of Ru(II), Ru(III) and Ru(IV), display antitumor activities, especially against metastatic cancers [115]. However, several of these compounds are very insoluble in aqueous solution, which is necessary to allow efficient administration and transport. Solubility has been increased by using dialkyl sulfoxide derivatives. Some of organometallic ruthenium complexes of the type [Ru(η6-arene)-(en)Cl]$^+$ (where arene., biphenyl or tetrahydroanthracene; en = ethylenediamine) also exhibited promising in vitro and in vivo activity, towards cisplatin-resistant cell lines (Figure 4.6) [116-118].

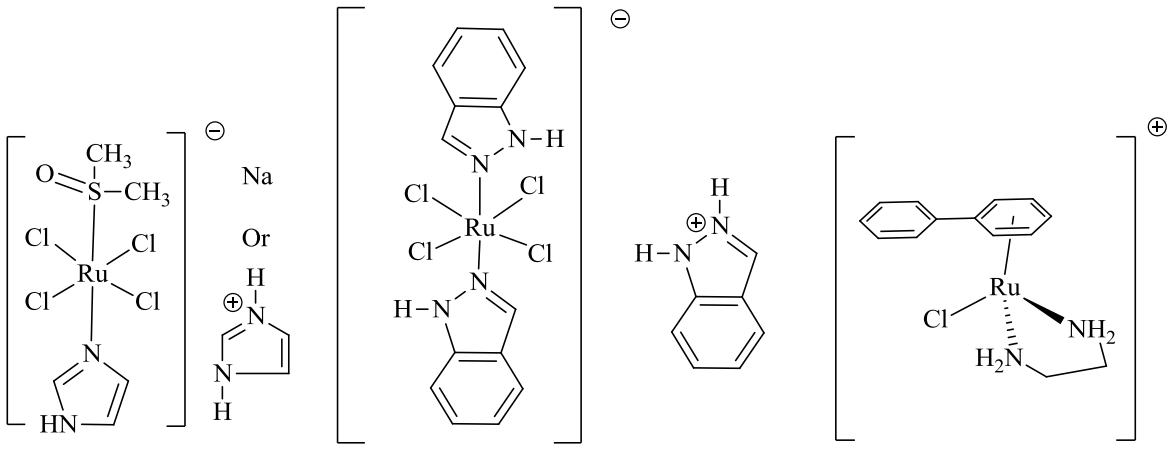

Figure 4.6: Representative structures of some ruthenium complexes with monodentate ligands tested as anticancer drugs.

4.3.2 Gold complexes as anticancer agents

A number of gold compounds, widely used as anti-infective and anti-tubercular agents [119], have been screened as anticancer agents. Serratrice et al. reported the synthesis of a series of Au(I)/Au(III) complexes with imidazolate derivatives ranging from monodentate, bidentate to tridentate nitrogen donor ligands such as 2-phenylimidazole, 2-(2′-pyridyl)imidazole, and 2,6-bis(benzimidazol-2-yl)pyridine, as well as phosphane groups, namely triphenylphosphine ligands such as 16, 17 and 18 shown in Figure 4.7 [120]. These complexes were evaluated against ovarian and breast carcinoma cell lines and the Au(I) dinuclear complexes 17 and 18 exhibited higher cytotoxicity than cisplatin.

Che and co-workers recently (2013) prepared a series of cationic Au(III) complexes with both N-heterocyclic carbine (NHC), N^N^N 2,6-bis(imidazol-2-yl)pyridine (H2IPI) and 2,6-bis(benzimidazol-2-yl)pyridine (H_2BPB) ligands to be used as both thiol ‘‘switch-on’’ anti-cancer agents and fluorescent probes, e.g the Au(III) complex 19 in Figure 4.7. Complex 20 displayed the highest in vitro cytotoxicity among the examined complexes (Figure 4.7), against human cervical epithelioid carcinoma (HeLa) xenografts [121]. Ronconi et al. have demonstrated that the Au(III)-dithiocarbamate complex 21 shown in Figure 4.7 exhibited promising anticancer properties with negligible toxic side-effects. The application of gold complexes, particularly gold(I) derivatives, in medicine has been termed “chrysotherapy” and

are also used to decrease inflammation and treat patients with rheumatoid arthritis [122]. A series of new 2-phenylpyridine Au(III) complexes of the general formula [Au(ppy)X] with various thiolate ligands has been synthesised and characterised (where X = (SCN), (NCS), tlc (thiolactate), tsc (thiosalicylate), dmp (2,3-dimercapto-1-propanol), dms (2,3-dimercaptosuccinic acid), cys (cysteine)). These complexes have been screened in vitro against human leukemia and mouse tumour cell lines, and exhibited more cytotoxicity than cisplatin [123].

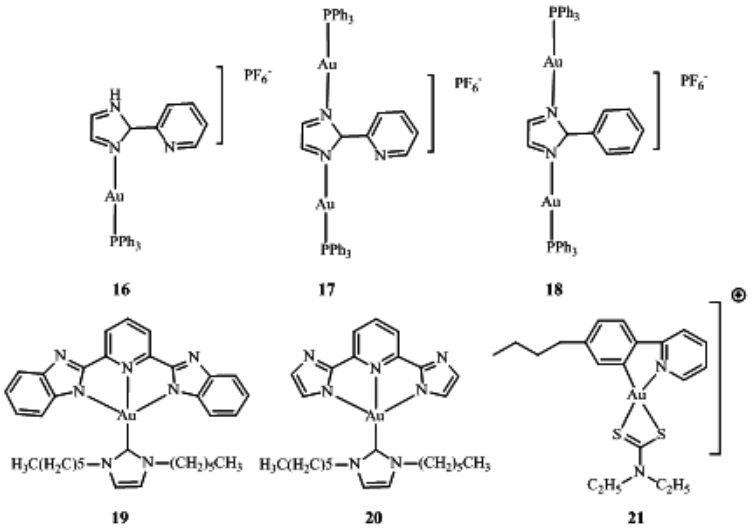

Figure 4.7: The chemical structures of Au(I) /Au(III) complexes with imidazolate derivatives (16-18). Au(III) complexes with N-heterocyclic carbene ligands (19-20) and (21) Au(III) dithiocarbamate complex.

4.3.3 Titanium complexes as anticancer

Titanocene dichloride (Cp_2TiCl_2) [124], and β-diketonato complexes of Ti such as budotitane [125] (Figure 4:8), were some of the first anticancer metal complexes used in clinical trials as anticancer drugs [126]. Both complexes bear two labile ligands and hydrolyse rapidly in water. On the other hand, the nature of their active species and the mechanism of action remained unresolved. Hence, current studies focus on water soluble but stable Ti(IV) antitumor complexes [127]

Glasner et al. (2011) reported a series of C1 symmetrical Salan titanium (IV) complexes with differently substituted aromatic rings. Usually, one ring is para-nitrated, which led to enhanced solubility in a biological environment and another is in the ortho position. Para-

halogenated rings led to increases in both the cytotoxicity and hydrolytic stability [128]. These complexes exhibited particularly high anticancer activity (Figure 4.8), ~30-fold more than that of cisplatin. Good examples are Ti(IV)-Salan complexes with of differently substituted aromatic rings such as 22 and 23 [129]. These hybrid complexes are highly stable and have much higher anticancer activity than C2 symmetrical Ti(IV)-Salan analogues (24-26) and cisplatin. A further related benefit of the hybrid complexes is their higher solubility in DMSO. The structural parameters of the ligand play an important role towards the cytotoxicity of the complexes. For example, complex 28, which consist of para substituted chlorine, were found to be much more active than complex 29, which consist of ortho substituted chlorine. This example illustrate how highly cytotoxic Ti(IV) complexes can be obtained by fine-tuning structural parameters of the ligand. The same research group has extended their study to trans-Ti(IV) complexes containing the salophen ligand (Figure 4.8) [130]. These complexes exhibited high hydrolytic stability and high cytotoxicity against different carcinoma cells.

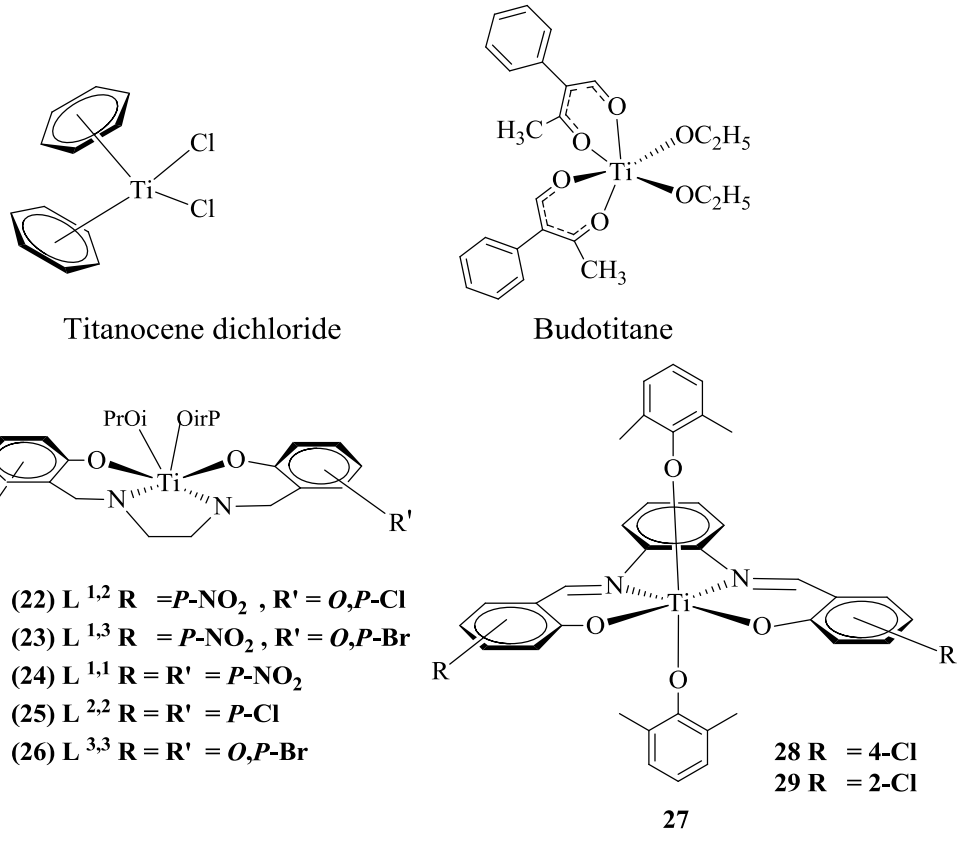

Figure 4.8: Ti anticancer drugs used in human clinical trials. (A): Titanocene dichloride, (B): budotitane. Symmetrical Ti(IV) Salan complexes (22–26). Trans-Ti(IV) complexes consisting of salophen ligand (28 and 29).

4.3.4 Copper complexes as anticancer agents

Copper is one of the most remarkable elements for many biomedical applications. Copper compounds display a wide group of biological actions, e.g containing anti-inflammatory, anti-proliferative, and others. It also displays a preference for radioisotopes, suitable for nuclear imaging and radiotherapy, rapidly progress in nanotechnology opened new possibilities for design of copper based drugs and medical materials [131]. In medicinal chemistry, copper complexes showed encouraging potential treatments [132]. Copper-based complexes as anticancer drugs have been selected on the basis that endogenous metals may be less toxic for normal cells than towards cancer cells. On the other hand, copper can also be toxic due to its redox activity. The changed metabolism of cancer cells and differential response among normal and tumour cells to copper are the basis for evolution of copper complexes with antineoplastic features. Copper is fundamentally a suitable element for most aerobic organisms, where it works as a structural and catalytic cofactor. For that reason, it can be involved in numerous biological pathways [133-135]. Considerable attention has been given to research regarding the mechanisms of absorption [136-138], distribution [139-141] metabolism, and excretion of copper in support of its role in the treatment of cancer and other diseases [142-144]. The essential features of the chemistry and biochemistry of copper, the role of this metal in medicine [145- 150], the pathology and treatment of Menkes and Wilson's disease [151-152] and the chelation therapy approach in neurodegenerative disorders by copper [153], have been extensively surveyed in recent review articles. Copper forms a rich diversity of coordination complexes with oxidation states Cu(II) and Cu(I), but very few examples of copper(III) compounds are reported [154]. The coordination chemistry of copper is controlled by Cu(II) derivatives. A number of bonding modes have been detected for thiosemicarbazones (TSCs) in their neutral or anionic forms, and depending on the substituents, they can behave as N, S bidentate, N, S, D (D = N, O) tridentate, or N_2, S, D (D = O, S) tetradentate ligands. The antitumor activity of copper-(TSCs), has been described as early as in 1960s [154-155] and new developments are still in progress [156-167].

Rosu et al. reported new Cu(II) complexes of the bidentate (κ2N,S-TSCs) ligand adducts. These Cu(II) complexes have a general formula of $[Cu(L1)Cl(H_2O)]$, $[Cu(HL1)(H_2O)_2SO_4]$, $[Cu(L1)(H_2O)_2NO_3]$, and $[Cu(L1)(H_2O)_2(OCOCH_3)]$ with 2-hydroxy-8-propyl-tricyclo-[7.3.1.0.^{2,7}] tridecane-13-one (R = n-propyl and furyl) thiosemicarbazone (HL1) derivatives as ligands (Figure 4:9).

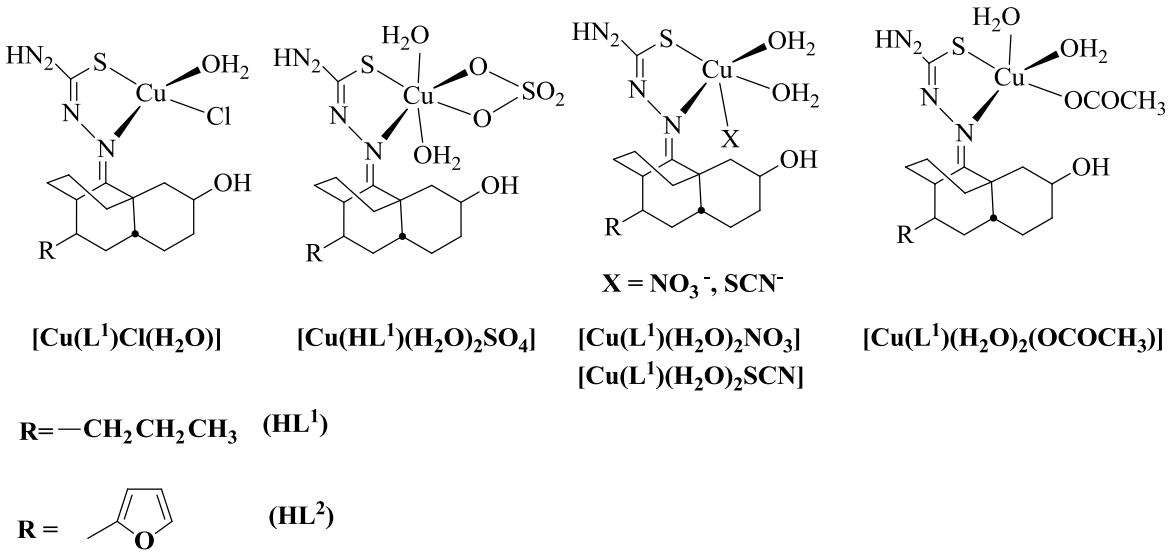

Figure 4.9: Proposed structures of copper metal complexes.

The ligands and the formed complexes were screened for them in vitro antibacterial effects against four different microorganisms and for the effects on HeLa cell proliferation. All the complexes examined showed antiproliferative activity [168]. There are also numerous copper(II) compounds with a 1,2,4-triazole moiety that demonstrated an extensive range of biological and pharmacological activities [169-170], among them the Cu(II) complex of 4-amino-1,4-dihydro-3-(2-pyridyl)-5-thioxo 1,2,4-triazole (HL) ligand $[Cu(L)Cl_2]$ which was screened for its cytotoxicity in human cancer cells [171-173].

4.4 Triazole based compounds

4.4.1 Background of 1,2,3-triazole ring used in medicinal chemistry

Medicinal chemists considered the synthesis of 1,2,3-triazole as an important category of nitrogen heterocycles in the field of medicinal and material chemistry based on heterocyclic compounds. The 1,4-disubstituted derivatives are the most common triazoles synthesized by means of 1,3-dipolar cycloaddition reactions (1,3-DCRs) and form the backbone of medicinal chemistry due to their importance and demonstrated wide range of numerous interesting biological activities. In the early part of the twentieth century researchers started working on the possibility of using 1,2,3-triazolo[4,5-d] pyrimidines (8-azapurines) for the treatment of cancer and malignant tumors [174-175]. 1,2,3-Triazoles cause peptidomimetic inhibition of tyrosinase, an enzyme which causes the browning of plant based foodstuffs and human skin diseases [176].

The click chemistry approach invented by Sharpless [177] using copper (I)-catalyzed azidealkyne cycloaddition (CuAAC) has resulted in the production of large number of 1, 4-disubstituted 1,2,3-triazoles in very high yields [178]. The copper(I)-catalyzed azidealkyne cycloaddition (CuAAC) yielded 1,2,3-triazole as one of the key structural units found in a large variety of bioactive molecules used in the different areas of the science, such as bioconjugation [179], oligonucleotide synthesis [180] construction of bolaamphiphilic structures [181], DNA labelling [182] and drug discovery [183].

The characteristics of 1,2,3-triazoles make them pharmaceutically important molecules. They are stable against reduction and oxidation, as well as against hydrolysis in acidic and basic conditions. This is an indication of high aromatic stabilisation and relative resistance to metabolic degradation [184]. Moreover, the1,2,3-triazole ring has a high dipole moment [185] and this feature enables it to participate actively in hydrogen bond formation, as well as in dipole – dipole and π - π stacking interaction with an aromatic ring such as a phenyl ring [186]. The two nitrogen atoms N(2) and N(3) can form hydrogen bonds with hydrogen bond donors or coordinate with metal ions, which could be favourable in binding easily with biological targets [187] and also improves their solubility. Moreover, the1,2,3-triazoles are very stable under physiological conditions. Among nitrogen containing compounds, 1,2,3-triazole compounds increasingly attract attention in drug discovery. The similarity of the two moieties can be seen in the size (distances between substituents are 3.8 -- 3.9 Å in amides and 5.0 - 5.1 Å in 1,2,3-triazoles), the dipolar moment (amide ~ 4 Debye, while for 1,2,3-triazole ~ 5 Debye), and the H-bond acceptor capacity (Scheme 4.1) [188]. The 1,2,3-triazole rings have sp^2-hybridized nitrogen atoms N(2) and N(3), which can act as weak hydrogen bond acceptors or donors of a lone pair of electrons. Furthermore, the strong dipole moment of 1,2,3-triazole ring polarizes the C(5) proton to such a degree that it can function as a hydrogen-bond donor similar to the amide NH. Additionally, the 1,2,3-triazole ring has a large dipole that could align with that of the other amides in a given peptide secondary structure [189]. However, unlike amides, 1,2,3-triazoles are very stable against hydrolysis. Because of the ability of 1,2,3-triazoles to function as rigid linking units that imitate the atom replacement and electronic properties of a peptide bond without the susceptibility to hydrolysis, many known 1,2,3-triazoles possess biological activity.

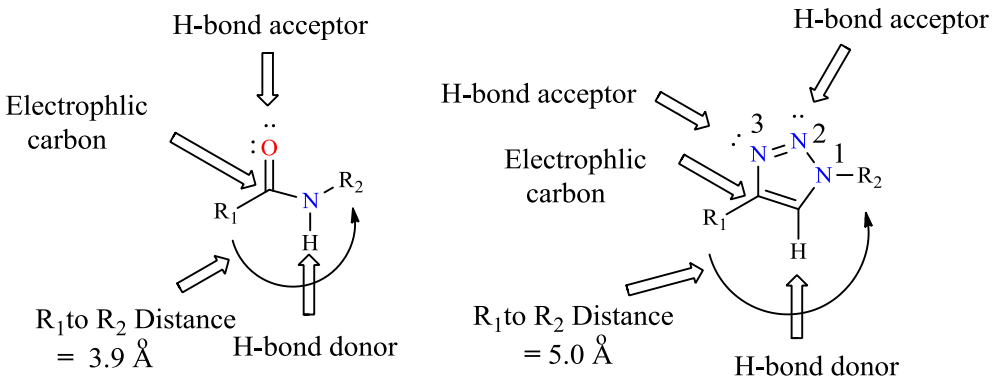

Scheme 4.1: Hypothesis on how triazoles could act as non-classic bioisosteres of amides [190]

Substances acting against the hepatitis C virus (HCV) [191] and compounds such as benzodiazepine and adenosine receptors exhibited inhibiting properties [192-193]. Some biologically active compounds are presented in Figure 4.10.

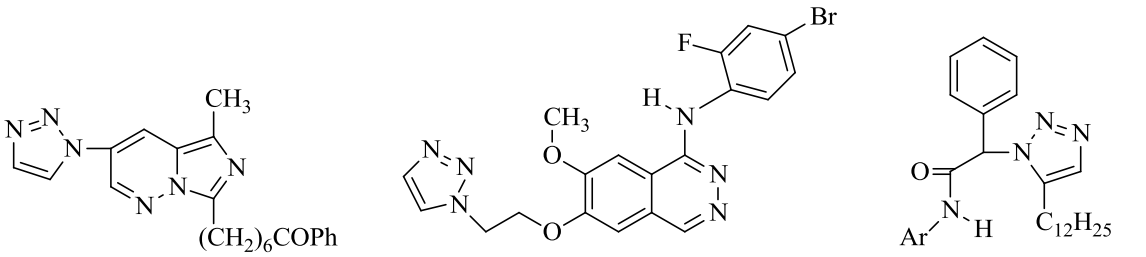

Anti-HIV activity

VEGF receptor tyrosine Kinase inhibitors

Hypocholestolemic activity

Figure 4.10: Molecules containing 1,2,3-triazole showing different applications.

When attached to a carbohydrate core, triazole derivatives have found applications as antibacterial, antihelmintic, antifungal and anticancer properties [194]; antiviral drugs [195, 196] and inhibitors of glycosidases [197-198]. Over the past few years, 1,2,3-triazole molecules have been synthesised as useful chemotherapeutic agents for various diseases [199]. A novel series of new chalcone-pyrrolo [2,1-c] [1,4]benzodiazepine (PBD) derivatives were made using alkane spacers and linked through a 1,2,3-triazole moiety. The synthesised compounds showed a promising anticancer activity with MIC ranging from <0.1-2.92 μM. The compound in Figure 4.11 was found to be the most effective with MIC-values ranging from 0.12-2.03 μM against different cancer cell lines [200].

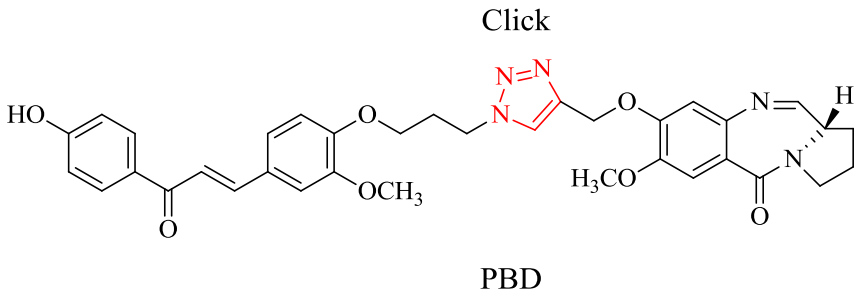

Figure 4.11: Molecule containing 1,2,3-triazole showing anticancer activates.

4.5 Compounds with a combination of metals and triazole moieties

Gautier et al. (2008) reported a series of 1,2,3-triazole ligands for platinum complexes. It is noteworthy that most of the synthesis of Pt(II) N, N or N, O complexes of biological interest are conducted in water, and proved that the click chemistry is a beneficial tool for the facile building of a series of potentially chelating triazole ligands for platinum. The structures of Pt(II) complexes chelates that coordinate through one triazole nitrogen atom and one exocyclic functionality (amine or carboxylate) are depicted in Scheme 4.2. The ligands can be divided into two categories: "regular" click ligands, in which the C4 substituent chain participates with N3 for chelation, and the isomeric counterparts, "inverse" click ligands, in which the chelation involves N2 and the substituent chain at N1. The regular and inverse ligands are expected to form five- and six-membered complexes, respectively.

(a)-regular click ligands

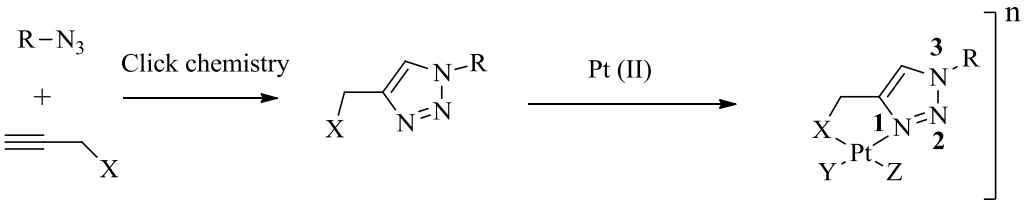

(b)-inverse click ligands

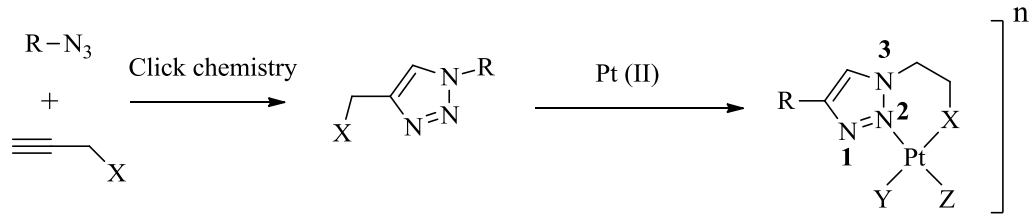

n = -1, 0, + 1 ; R = alkyl,benzyl; X= NH_2, COOH; Y, Z = Cl, DMSO

Scheme 4.2: Schematic representation of synthetic for triazoles and complexes [201].

The neutral *cis* dichloro diamino complex A, as presented in Scheme 4.3, exhibited interesting cytotoxicity against breast cancer cells, which is comparable to that of cisplatin. In contrast,

the cationic complex B in Scheme 4.3 showed no such activities, which is in accordance with the accepted structure activity relationship of platinum drugs [202, 203].

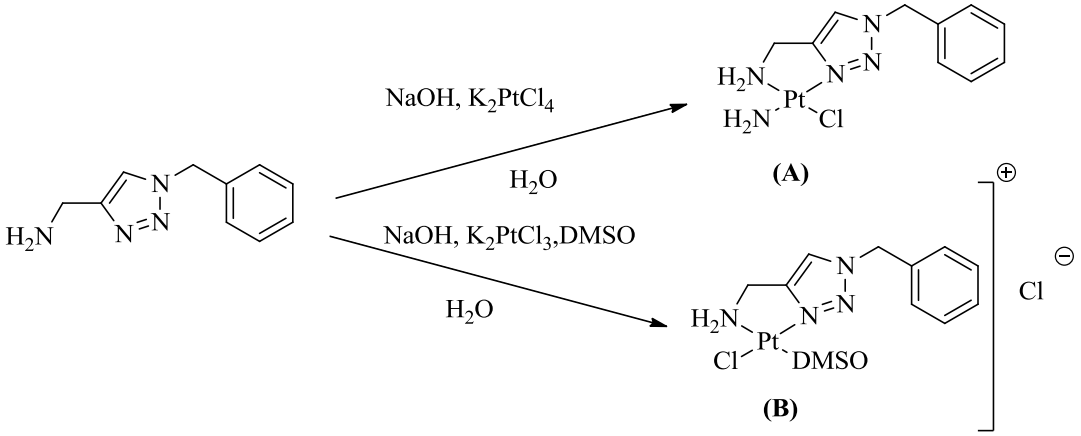

Scheme 4.3: Synthesis of regular N, N complexes.

On the other hand, the behaviour of the N, O ligand which is coordinate with Pt(II) by using a different mole ratio(stoichiometry) of the ligand as presented in Scheme 4.4, yielded the complexes C, D and E with no cytotoxicity activity.

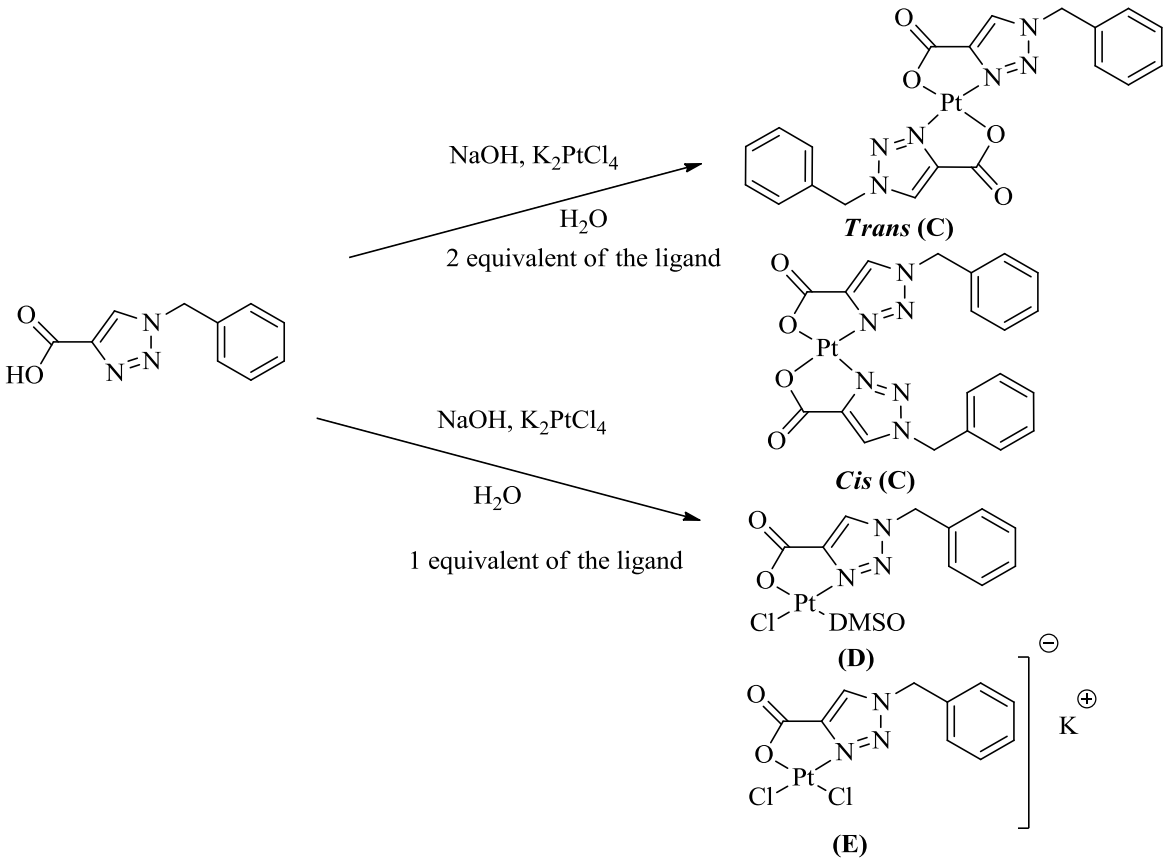

Scheme 4.4: Synthesis of regular N, O complexes [201].

4.6 Summary

From the brief overview supplied in the discussion above, it is obvious that another potential lucrative area for 1,2,3-triazole ligands is in the potential application as medicinal drugs, and in particular as anticancer agents when combined with selected metal atoms. To date a number of metal-ligand complexes with single or double N-atom bonds have been prepared and tested, some with more success than others. In the metal-1,2,3-triazole ligand category, work to date has been limited to Pt and Pd complexes. In the investigations described in this thesis, various new metal-1,2,3-triazole ligand complexes will be synthesised and evaluated for their potential anticancer applications in addition to considering them for potential dye solar cell compounds and devices. These light sensitive compounds can be used in photodynamic therpy with a light source to destroy cancer cells. Photodynamic therapy includes a drug sensitive to light. Once given to the patient, light at a particular wavelength is applied and the drug will produce reactive oxygen species that will kill the surrounding cells. It is normally relevant for cancers of the skin (not melanoma), gullet, head, neck, mouth, eyes and lungs. Chapter (6) will describe the synthesis and characterisation of just such a series 1,2,3-triazoles prepared in this investigation.

4.7 References

1-Vincent T L., Gatenby R A., *Int. J. Oncol*., 32:729(2008),

2-Vogelstein B., Kinzler the genetic basis of human cancer, 2nd Edition. (2002) New York: McGraw-Hill

3-Anand P., Kunnumakkara A B., Sundaram C., Harikumar K B., Tharakan S T., Lai O S., Sung B., Aggarwal B B., *Pharm. Res*., 25:2097(2008)

4-Hongbao M., Young M, Yan Y., *Cancer. Biol*., 4:59(2014) http://www.cancerbio.net

5-Sancar A., *Science*., 266:1954(1994)

6-Wozniak K., Blasiak J., *Acta. Biochim.Pol*., 49:583(2002)

7-Zlobinskaya O., Dollinger G D., Michalski V., Hable C., Greubel G., Multhoff Du G., Roper B., Molls M., Schmid T E., Radiat Environ Biophys., 51:23(2012)

8-N'da D D., Synthesis of methotrexate and ferrocene conjugates as potential anticancer agents, Ph D. dissertation, School of Chemistry, Wits University, (2004) p.8, 52

9-Gwyneth Morgan Senior Lecturer. University of Central England, Faculty of Health and Community Care, Centre for Palliative care and Oncology, Birmingham., Cancer Nursing Practice., 2:27(2003). http://dx.doi.org/10.7748/cnp2003.02.2.1.27.c57

10-Cancer Research UK's Statistical, Key Facts (All Cancers Combined February 2015. cruk.org/cancer stats)

11-Cancer Incidence Statistics in the UK in (2011)

12-Cancer Statistics Report January (2014)

13-Ferlay J., Soerjomataram I., Ervik M., Dikshit R., Eser S., Mathers C., Rebelo M., Parkin D M., Forman D., Bray F*., Int. J. Cancer*: 136:E359(2015)

14-Bray F, Ren J S, Masuyer E, Ferlay J., *Int. J. Cancer*., 132:1133(2013), (World Cancer Research Fund International)

15-World Cancer Research Fund International

16-Office for National Statistics, Cancer Registration Statistics, England, Statistical bulletin 2011 | 26 June 2013

17-Colon Cancer Treatment (PDQ®)". NCI. 2014-05-12. Retrieved 29 June 2014

18-Haggar F A.., Boushey R P., *Clinic. Colon. Rectal. Surg*., 22:191(2009)

19-Boyle P., Langman J S., A B C of colorectal cancer: Epidemiology. B M J., 321:805(2000)

20-Cunningham D., Atkin W., Lenz H J., Lynch H T., Minsky B., Nordlinger B., Starling N., "Colorectal cancer". Lancet 375 (9719):1030(2010)

21-Bosch F X., Ribes J, Díaz M., Cléries R., (2004). Primary liver cancer worldwide incidence and trends. Gastroenterology. 127(5 Suppl 1): S5-S16

22-Thomas M B., O'Beirne J P., Furuse J., *Ann. Surg. Oncol*., 15:1008(2008)

23-Yeo W., Mok T S., Zee B., *J. Natl. Cancer. Inst*., 97:1532(2005)

24-Weinberg R A., Hanahan D., *Cell*., 100:57(2000)

25-Devita, Hellman & Rosenberg's Cancer: Principles & Practice of Oncology, 8th Edition. p. 386(2008)

26-Malhotra V., Perry M C., Perry (2003), "Classical chemotherapy: mechanisms, toxicities and the therapeutic window".,*Cancer Biol. Ther*., 2 (4 Suppl 1): S2–4

27-Eyre H J., Lange D., Morris L B., in Informed Decisions. 2nd Edition. Atlanta, G A: *American Cancer Society*, (1996)

28-Delaney G., Jacob S., Featherstone C., Barton M., *Cancer*., 104:1129(2005)

29-Erridge S C., Featherstone C., Chalmers R., Campbelld J., Stocktond D., Blackd R., *Eur. J. Cancer*., 43:1802(2007)

30-Department of Health National Radiotherapy Advisory Group. Radiotherapy: developing a world class service for England. London: Department of Health, (2007)

31-Fox B A., Schendel D J., Butterfield L H., Aamdal S., Allison J P., Ascierto P A., Atkins M B., Bartunkova J., Bergmann L., Berinstein N., Bonorino C C., Borden E., Bramson J L., Britten C M., Cao X., Carson W E., Chang A E ., Characiejus D., Choudhury A R., Coukos G ., *J. Transl. Med*., 9:214(2011)

32-Vousden K A., Clarke D L., Lowe D C., *Inflamm & Allergy-Drug. Targets* 12:99(2013)

33-Paul M O'Byrne., Can. Respir. J., 20:23(2013)

34-Rampling R., James A., Papanastassiou V., *J. Neurol. Neurosurg. Psychiatry*., 75:24(2004)

35-Lind M J., *Medicine*, 39:711(2011)

36-Stuart K., *oncologist*., 8:425(2008)

37-Bertram J S.,*Mol.Aspects.Med*., 21:167(2000)

38-Akhavan SM., Winter W P., Abramson R K., Rucknagel D L.,*Proc. Natl. Acad. Sci*., U.S.A. 73:882(1976)

39-Mesothelioma: Categories of chemotherapy drugs. internetsources: availableat http://www.mesotheliomaweb.org/categories.htm (accessed on July, 18(2009)11., Burri R J., Lee N Y., 2009 Anticancer Therapy, Concurrent

40-Chemotherapy and Radiotherapy for head and neck cancer. Internet sources: available at

http://www.oralcancerfoundation.org/facts/chemotherapy.htm (accessed on July, 18 (2009)
41-Giacchetti S, Itzhaki M, Gruia G., *Ann. Oncol*., 10:663(1999)
42-Porschen R., Arkenau H T., Kubicka S., Greil R, Seufferlein T, Freier W, Kretzschmar A, Graeven U, Grothey A, Hinke A, Schmiegel W, Schmoll H J., *J. Clin. Oncol*., 25:4217(2007)
43-Boeck S., Hoehler T., Seipelt G., Mahlberg R., Wein A., Hochhaus A., Boeck H P., Schmid B., Kettner E., Stauch M., Lordick F., Ko Y., Geissler M., Schoppmeyer K., Kojouharoff G., Golf A., Neugebauer S., Heinemann V., *Ann. Oncol*., 19:340(2008)
44- Ott I., Gust R., *Arch. Pharm*., 340:117(2007)
45-Josefsen L B., Boyle R W., *Met-Based Drugs*., 2008:1(2008).,
http://dx.doi.org/10.1155/2008/276109
46-Maisonial P., Serafin M., Traikia E., DebitonV., Théry D., Aitken J., Lemoine P., Viossat B., Gautier A.., *Eur. J. Inorg. Chem*., 298(2008)
47-Chevry A., Teyssot M L., Maisonial A., Lemoine P., Viossat B., Traikia M., Aitken D J., Alves G., Morel L., Nauton L., Gautier A., *Eur. J. Inorg. Chem*., 3513(2010)
48-Elmes R B P., Erby M., Bright S A., Williams D C., GunnlaugssonT., *Chem. Commun*., 48:2588(2012)
49-Peyrone M., *Ann. Chemie. Pharm*., 51:1(1845)
50-Hannon M J., *Pure Appl. Chem*., 79:2243(2007)
51-http://www.pharmacopeia.cn/v29240/usp29nf24s0_m17910.ht
52-http://commons.wikimedia.org/wiki/File:Cisplatin-3D-balls.png ml
53-Rosenberg B., Van Camp L., Trosko J E., Mansour V H., *Nature*., 222:385(1969)
54-Rozencweig, M, Von Hoff, D D, Slavik, M., Muggia F M., *Ann. Intern. Med*., 86:803(1987)
55-Brabec V., DNA modications by antitumor platinum and ruthenium compounds: their recognition and repair. *Prog. Nucleic Acid Res. Mol. Biol*., 71, pp. 1-68, 2002
56-Weiss R. B., Christian M C., *A review. Drugs*., 46: 360(1993)
57-Lebwohl D., Canetta R., *Eur. J. Cancer*, 34:1522(1998)
58-Fuertes M A., Alonso C., Perez J M., *Chem. Rev*.., 103:645(2003)., Kelland L. R., Sharp S Y., O'Neill C F., Raynaud F I., Beale P J., Judson I R., *J. Inorg. Biochem*., 77:111(1999)
59-Wong E., Giandomenico C M., *Chem. Rev*., 99: 2451(1999)
60- Alderden R A., Hall M D., Hambley T W., *J. Chem. Edu*.,83:728(2006)
61-Martins ET., Baruah H., Kramarczyk J., Saluta G., Day C S., Kucera G L., Bierbach U., *J. Med. Chem*., 44:4492(2001)

62-Brow J M., Pleatman C R., Bierbach U., *Bioorg. Med. Chem. Lett*., 12:2953(2002)

63-Okada T., El-Mehasseb IM., Kodaka M., Tomohiro T., Okamato K., Okuno H., *J. Med. Chem*., 44:4661(2001)

64-Graham R D., Williams D R., *J. Inorg. Nucl.Chem*., 41:1245(1979)

65-Rau T., Alsfasser R., Zahl A., van Eldik R., *Inorg. Chem*., 37:4223(1998)

66-Rau T., Eldik R V., In Metal Ions In Biological Systems. Platinum and Other Metal Coordination Compounds in Cancer Chemotherapy Sigel H, Sigel A, Eds, Marcel Dekker: New York, 31:339-378(1996)

67-Torshizi H M., Srivastava T S., Parekh HK, Chitnis M P., *J. Inorg. Biochem*., 45:135(1992)

68-Ranninger C N., Perez J M, Zamora F., Gonzalez V M., Masaguer J R., Alono C., *J. Inorg. Biochem*., 52:37(1993)

69-Zhao G., Lin H., Yu P., Sun H., Zhu S., Su X., Chen Y., *J. Inorg. Biochem*., 73:145(1999)

70-Abu-Surrah A S, Al-Allaf TAK., Rashan L, Klinga M, Leskelä M., *Eur. J. Med. Chem*., 37:919(2002)

71-Abu–Surrah AS., Kettunen M., Lappalainen K., Piironen U., Klinga M., Leskelä M., *Polyhedron*., 21:27(2002)

72-Abu-Surrah AS., Al-Allaf TAK., Klinga M., Leskelä M., *Polyhedron*., 22:1529(2003)

73-Wimmer F Z., Wimmer S., Castan P., Cros S., Johnson N., Rodrigez E C., *Anticancer Res*., 9:791(1989)

74-Zhao G., Sun H., Lin H., Zhu S., Su X., Chen Y., *J. Inorg. Biochem*., 72:173(1998)

75-Gao E J., Liu Q T., Duan L Y., *Russ. J. Coord. Chem*., 33:120(2007)

76-Jackson A., Davis J., Pither R J., Rodger A., Hannon M J., *Inorg. Chem*., 40:3964(2001)

77-Ray S., Mohan R., Singh J K., Samantaray M K., Shaikh M M., Panda D., Ghosh P., *J. Am. Chem. Soc*., 129:15042(2007)

78-Fakih, W C., Tung D., Eierhoff C., Mock B., Krebs Z., *Anorg. Allg. Chem*., 631:1397(2005)

79- Natile G., Coluccia M., *Coord. Chem. Rev*., 383:216(2001)

80- Roberts J D., Farrell N., *Inorg. Chem*., 37:717(1998)

81- Tsubomura T., *Inorg. Chem*., 29:2622(1990)

82- Chellan P, Gouden N S, Hendricks D T., Gut J., Rosenthal P J., Lategan C., Smith P J., Chibale K., Smith G S., *Eur. J. Inorg. Chem*., 3520:(2010)

83- Conrad M L., Enman J E., Scales S J., Zhang H., Vogels C M.., Saleh M T., Decken A., Westcott S A., *Inorg.Chim. Acta*., 63:358(2005)

84- Maisonial A., Serafin P., Traïkia M., Debiton E., Théry V., Aitken D J., Lemoine P., Viossat B., Gautier A*., Eur. J. Inorg. Chem*., 298:(2008)

85-Mindt T L., Struthers H., Brans L., Angelov T., Schweinsberg C., Maes V., Tourwe D., Schibli R., *J. Am. Chem. Soc*.,128:15096(2006)

86- Dyson P J., Sava G., *Dalton. Trans*., 1929(2006)

87-Holder A A., *Annu. Rep. Prog.* Chem., Sect. A: *Inorg. Chem*., 107:359(2011)

88-Chen Y., Janczuk A., Chen X., Wang J., Ksebati M., Wang P G., Carbohy. Res., 337:1043(2002)

89-Hillard E A., Jaouen G., *Organomet*., 3020(2011)

90-Hartinger C G., Dyson P J., *Chem. Soc. Rev*., 38:391(2009)

91-Ali M A., Mirza A H., Butcher R J., Tarafder M T H., KeatT B., Ali A M., *J. Inorg. Biochem*., 92:141(2001)

92-Padhye S., Afrasiabi Z., Sinn E., Fok J., Mehta K., Rath N., *Inorg. Chem*., 44:1154(2005)

93-Al-Masoudi N A., Abdullah B H., Essa A H., Loddo R., LaColla P., *Arch. Pharm. Chem. Life Sci*., 343:222(2010)

94-Peacock A F A., Sadler P J., *Chem Asian J*., 31:1890(2008)

95-Carotti S., Marcon G., Marussich M., Mazzei T., Messori L., Mini E., Orioli P., *Chem. Biol.Interact*., 125(2000)

96-Baldini M., Ferrari M B., Bisceglie F., Pelosi G., Pinelli S., Tarasconi P., *Inorg. Chem*., 42:2049(2003)

97-Dallavalle F., Gaccioli F., FGazzola R, Lanfranchi M., Marchio L., Pellinghelli M A., Tegoni M J., *Inorg. Biochem*., 92:95(2002)

98-Perez J M., Matesanz A I., Ambite A M., Navarro P., Alonso C., Souza P J., *Inorg. Biochem*., 75: 255(1999)

99-Schweinfurth D., Pattacini R., Strobel S., Sarkar B., *Dalton Trans*., 9291:(2009)

100-Kilpin K J., Crowley J D., *Polyhedron*., 29:3111(2010)

101-Kilpin K J., Gavey E J., McAdam C J., Anderson C B., Lind S J., Keep C C., Gordon K C., Crowley J D., *Inorg. Chem*., 50:6334(2010)

102-Rostovtsev V V., Green L G., Fokin V V., SharplessK B., *Angew. Chem. Int. Ed*. 41:2596(2002)

103-Conrad M L., Enman J E., Scales S J., Zhang H., Vogels C M., Saleh M T., Decken A., Westcott S A., *Inorg. Chim. Acta*., 63:358(2005)

104-Schweinfurth D., Pattacini R., Strobel S., Sarkar B., *Dalton. Trans*., 929:(2009)

105- Trivedi R., Deepthis B., Sujitha P., Kumar C G., Sridhar B., Bhargava S K., *J. Chem. Sci*., 124:1405(2012)

106- Komeda S., Casini A., *Curr. Top. Med. Chem*., 12:219(2012)

107-Levina A., Mitra A., Lay P A., *Metallomics*., 1:458(2009)

108-YanY K., Melchart M., Habtemariam A., Sadler P J., *Chem. Commun*., 38:4764(2005)

109-Ginzinger W., Mühlgassner G., Arion V B., Jakupec M A., Roller A., Galanski M., Reithofer M., Berger W., Keppler B K., *J. Med. Chem*., 55:3398(2012)

110-Sava G., Bergamo A., *Int. J. Oncol*., 17:353(2000)

111-Jung Y., Lippard S J., *Chem. Rev*., 107:1387(2007)

112-Sava G., Alessio E., Bergamo A., Mestroni G., Top. *Biol. Inorg. Chem*., 1:143(1999)

113-Keppler B K., Henn M., Juhl U M., Berger M R., Niebl R., Wagner F E., *Prog. Clin. Biochem. Med*., 10:41(1989)

114-Clarke M J., *Coord. Chem. Rev*, 236:209(2003)

115-Bruijnincx P. C. A., Sadler P. J., *Curr. Opin. Chem. Biol*., 12:197(2008)

116-Bruijnincx P. C. A., Sadler P. J., *Adv. Inorg. Chem*., 61:1(2009)

117-LiuH K., Sadler P. J., *Acc. Chem. Res*., 44:349(2011)

118-Dyson P. J., Sava G., *Dalton. Trans*., 16:1929(2006)

119- Serratrice M., EdafeF., Mendes F., Scopelliti R., Mohammed S Z., Grätzel M., Santos I., Cinellua M A., Casini A., *Dalton. Trans*., 41:3287(2012)

120- Che C M., Zou T., Lum C T., Chui S S., *Angew. Chem. Int. Ed*., 52:2930(2013)

121- Ronconi L., Fregona D., *Dalton. Trans*., 10670(2009)

122- Fan D., Yang C T., Ranford J D., Vittal J J., Lee P F., *Dalton. Trans*., 3376(2003)

123- Kopf H., Maier K P., *Angew. Chem., Int. Ed. Engl*., 18:477(1979)

124- Keppler B K., Friesen C., Moritz H G., Vongerichten H., Vogel E., *Struct. Bonding*., (Berlin) 78:97(1991)

125- Buettner K M., Valentine A M., *Chem. Rev*., 112:1863(2012)

126- Tshuva E Y., Peri D., *Coord. Chem. Rev*., 253:2098(2009)

127- Tshuva E Y., Peri D., Meker S., Manna C M., *Inorg. Chem*., 50:1030(2011)

128- Glasner H., Tshuva E Y., *J. Am. Chem. Soc*., 133:16812(2011)

129- Tzubery A., Tshuva E Y., *Inorg. Chem*., 50:7946(2011)

130- Szymanski P., Fraczek T., Markowicz M., Olasik E M., *Biometals*., 25:1089(2012)

131- Tisato F., Marzano C., Porchia M., Pellei M., Santini C., *Med. Res. Rev*., 30:708(2010)

132- Silva F D., Kraatz H B., Metzler N N., Concepts and Models in Bioinorganic Chemistry; Wiley-VCH: Weinheim, Germany, (2006)

133-Lippard S J., Berg J M., Principles of Bioinorganic Chemistry; University Science Books: Mill Valley, CA, (1994)

134-Silva F D., Williams R J P., J J R., (The Biological Chemistry of the Elements); Clarendon: Oxford, U. K., (1991)

135- Wang T., Guo J Z., *Curr. Med. Chem*., 13:525(2006)

136- Lonnerdal Am B., *J. Clin. Nutr*., 63:821S(1996)

137- Valko M., Morris H., Cronin T D M., *Curr. Med. Chem*., 12:1161(2005)

138- Tapiero H., Townsend M D., Tew K D., *Biomed. Pharmacother*., 57: 386(2003)

139- Hellman E N., Gitlin J D., *Annu. Rev. Nutr*., 22:439(2002)

140- Linder C M., Wooten L., Cerveza P., Cotton S., Shulze R., Lomeli N *Am., J. Clin. Nutr*., 67:965S(1998)

141- Kim BE., Nevitt T., Thiele D., *J. Nat. Chem. Biol*. 4:176(2008)

142- Arredondo M., Nunez M T., *Mol. Aspects Med*., 26:313(2005)

143- Gupte A., Mumper R J., *Cancer Treat. Rev*., 35:32(2009)

144- Brewer G J., Drug Discovery Today, 10:1103(2005)

145- Goodman V L., Brewer G J., Merajver S D., *Endocr. Relat. Cancer* 11:255(2004)

146- Boal A. K., Rosenzweig A C., *Chem. Rev*., 109:4760(2009)

147- Festa R A., Thiele D J., *Curr. Biol*., 21:877(2011)

148- Iakovidis I., Delimaris I., Piperakis S M., *Mol. Biol. Int*., 10:4061(2011)

149- Biersack B., Ahmad A., Sarkar F H., Schobert R., *Curr. Med. Chem*., 19:3949(2012)

150- Crisponi G., Nurchi V M., Fanni D., Gerosa C., Nemolato S., Faa G., *Coord. Chem. Rev*., 254:876(2010)

151- Burkhead J L., Gray L W., Lutsenko S., *Bio. Metals*., 24:455(2011)

152- Khan G., Merajver S., *Expert Opin. Invest. Drugs*., 18:541(2009)

153- Melník M., Kabešová M., *J. Coord. Chem*., 50:323(2000)

154- Taylor M R., Gabe E J., Glusker J P., Minkin J A., Patterson A L., *J. Am. Chem. Soc*., 88:1845(1966)

155- Crim J A., Petering H G., *Cancer. Res*., 27:1278(1967)

156- Yu Y., Wong J., Lovejoy D B., Kalinowski D S., Richardson D R., *Clin. Cancer. Res*., 12: 6876(2006)

157- Lovejoy D B., Richardson D R., *Blood*., 100:666(2002)

158- Ming L J., *Med. Res. Rev*., 23:697(2003)

159- Wolohan P., Yoo J., Welch M J., Reichert D E., *J. Med. Chem*., 48:5561(2005)

160- Pogni R., Baratto M C., Diaz A., Basosi R J., *Inorg. Biochem*., 79:333(2000)

161- Zhang H., Thomas R., Oupicky D., Peng F J., *Biol. Inorg. Chem*., 13:47(2008)

162- Kalinowski D S., Quach P., Richardson D R., *Future. Med. Chem*., 1:1143(2009)

163- Feun L., Modiano M., Lee K., Mao J., Marini A., Savaraj N., Plezia P., Almassian B., Colacino E., Fischer J., MacDonald S., *Cancer. Chemother. Pharmacol*., 50:223(2002)

164- Ainscough E W., Brodie A M., Denny W A., Finlay G J., Ranford J D., *J. Inorg. Biochem*., 70:175(1998)

165- West D X., Liberta A E., Rajendran K G., Hall I H., *Anticancer. Drugs*., 4:241(1993)

166- Ferrari B M., Bisceglie F., Pelosi G., Tarasconi P., Albertini R., Dall'Aglio P P., Pinelli, S., Bergamo A., Sava G., *J. Inorg. Biochem*., 98:301(2004)

167-Yu Y., Kalinowski D S., Kovacevic Z., Siafakas A R.,Jansson P J.,Stefani C., Lovejoy D B., Sharpe P C., Bernhardt P V., Richardson D R., *J. Med. Chem*., 52:5271(2009)

168- Rosu T., Pahontu E., Pasculescu S., Georgescu R., Stanica N., Curaj A., Popescu A., Leabu M., *Eur. J. Med. Chem*., 45:1627(2010)

169- Baraldi P G., Pavani M G., Nunez M d C., Brigidi P., Vitali B.,Gambari R., Romagnoli R., *Bioorg. Med. Chem*., 10:449(2001)

170- Dallavalle F., Gaccioli F., Gazzola R F., Lanfranchi M., Marchio L., Pellinghelli M A., Tegoni M., *J. Inorg. BioChem*., 92:95(2002)

171- Dallavalle F., Gaccioli F., Gazzola R F., Lanfranchi M., Marchio L., Pellinghelli M A., Tegoni M., *J. Inorg. Biochem*., 92:95(2002)

172- Tardito S., Bussolati O., Maffini M., Tegoni M., Giannetto M., Asta, V D, Gazzola R F., Lanfranchi M., Pellinghelli M A., Mucchino C., Mori G., Marchio L., *J. Med. Chem*., 50:1916(2007)

173-Gaccioli F.; Gazzola R F.; Lanfranchi M., Marchio L., Metta G., Pellinghelli M A., Tardito S., Tegoni M., *J. Inorg. Biochem*., 99:1573(2005)

174-Dalvie D K., Kalgutkar A S., Khojasteh-Bakht S C., Obach R S., Donnell J P., *Chem. Res. Toxicol*., 15:269-299(2002)

175- Bock V D., Perciaccante R., Jansen T P., Hiemstra H., Van., Maarseveen J H., *Org. Lett*., 8:919(2006)

176-Bock V D, Speijer D., Hiemstra H., Van Maarseveen J H., *Org. Biomol. Chem*., 5:971(2007)

177-Sharpless K B., Kolb H C., Finn M G., *Angew. Chem. Int. Ed*., 40:2004(2001)

178-Sharpless K B., Kolb H C., Finn M G., *Angew. Chem*., 113:2056(2001)

179-Pieters R J., Rijkers D T S., Liskamp R M J., *QSAR. Comb. Sci*., 26:1181(2007)

180-Nuzzi A., Massi A., Dondoni A., *QSAR. Comb. Sci*., 26: 1191(2007)

181-Neil E J O, DiVittorio K M, Smith B D., *Org. Lett*., 9:199(2007)

182-Gierlich J., Burley G A., Gramlich P M E., Hammond D M., Carell T., *Org. Lett*., 8: 3639(2006)

183-Tron G C., Pirali T., Billington R A., Canonico P L., Sorba G., Genazzani A A., *Med. Res. Rev*., 28:278(2008)

184- Ferreira S. B., Sodero A. C., Cardoso M. F., Lima E. S., Kaiser C. R., Silva F. P., Ferreira V. F., *J. Med. Chem*., 53:2364(2010)

185-Bourne Y., Kolb H C., Radic Z., Sharpless K B., Taylor P., Marchot P., *Proc. Natl. Acad. Sci. USA*., 101:1449(2004)

186-Whiting M., Muldoon J., Lin Y C., Silverman S M., Lindstron W., Olson A J., Kolb H C., Finn M G., Sharpless K B., Elder J H., Fokin V., *Angew. Chem. Int. Ed.*, 45:1435(2006): *Angew. Chem*., 118:1463(2006)

187-Horne W S., Yadav M K., Stout C D., Ghadiri M R., *J. Am. Chem. Soc*., 126:15366(2004)

188-Tron G C., Pirali T., Billington R A., Billington R A., Canonico P L ., SorbaG., Genazzani A A., *Med. Res. Rev*., 28:278(2008)

189-Palmer M H., Findlay R H., Gaskell A J., *J. Chem. Soc. Perkin. Trans*., 2:420(1974)

190-Chow H F., Lau K N., Ke Z., Liang Y., Lo C M., *Chem. Commun*., 46:3437(2010)

191-Wang P., Du J., Rachakonda S., ChunB K., Tharnish P M., Stuyver L J., Otto M J., Schinazi R F., WatanabeK A., *J. Med. Chem*., 48:6454(2005)

192-Betti L., Biagi G., Giannaccini G., Giorgi I., Livi O., Lucacchini A., *J. Med. Chem*., 41: 668(1998)

193- Biagi G., Giogi I., Livi O., Scartoni V., Betti L., Giannaccini G., Trincavelli M L., *Eur. J. Med. Chem*., 37:565(2002)

194- KamalA., Shankaraiah N., Devaiah V., Reddy K L., Juvekar A., Sen S., Kurian N., ZingdeS., *Bioorg. Med. Chem. Lett*., 18:1468(2008)

195-Pradere U., Roy V., McBrayer T R., Schinazi R F., Agrofoglio L A., *Tetrahedron*., 64:9044(2008)

196-Montagu A., Roy V., Balzarini J., Snoeck R., Andrei G., Agrofoglio L A., *Eur. J. Med. Chem*., 46:778(2011)

197-Ferreira S B., Sodero A C R., Cardoso M F C., Lima E S., Kaiser C R., Silva J r FP., Ferreira, V F., *J. Med. Chem*., 53, 2364(2010)

198-Turks M., Rjabova J., Rjabovs V., Antonio J., Vargas M., Clavijo E M., *Cent. Eur. J. Chem.*, 10:386(2012)

199-Wang S., Wang Q., Wang Y., Liu L., Weng X., Zhang G L X., Zhou X., *Bioorg. Med. Chem. Lett*., 18:6505(2008)

200-Kamal A., Prabhakar S., Ramaiah M J., Reddy P V., Reddy C R., Mallareddy A., Shankaraiahc N., Reddyb T L N., Pushpavallib S N C V L., Bhadrab M P., *Eur. J. Med. Chem*.,46:3820(2011)

201-Gautier A., Maisonial A., Serafin P., Traïkia M., Debiton E., Théry V., Aitken D J., Lemoine P., Viossat B., *Eur. J. Inorg. Chem*., 298(2008)

202-Cleare M J., Hoeschele J D., *Bioinorg. Chem*., 2:187(1973)

203-Reedijk J., *Inorg. Chim. Acta*., 873:198(1992)

Chapter 5 : Instrumentation and Experimental Techniques

5.1 General reagents and solvents

Caution: Aryl amines should be treated as potential carcinogens and all azides considered potentially explosive and treated with care.

Precursors and solvents were purchased from Alfa Aesar, Sigma/Aldrich or Fisher Scientific and purified where appropriate or otherwise used as received. Dimethylsulphoxide (DMSO; spectrophotometer grade), hydrochloric acid, ammonium hydroxide, 4-aminobenzonitrile, 4-aminobenzoic acid, 2-ethynylpyridine, sodium azide, copper chloride, cobalt chloride, nickel chloride, cadmium chloride, phenylacetylene, iron chloride and sodium ascorbate were obtained from Sigma Aldrich. Dichloromethane, hexane, methanol, chloroform, ethyl acetate, diethyl ether, ethanol, magnesium sulphate (anhydrous) were purchased from Fisher Scientific. 4-Chloroaniline, *tert*–butanol, aniline, sodium nitrite and magnesium chloride were boughtfrom Aldrich and 4-fluoroanline, 4-methylaniline, 4-(trifluoromethyl)aniline hydrochloride from Alfa Aesar.

5.2 General Instrumentation and Characterisation Methods

^{1}H ^{13}C, COSY, ^{13}C–^{1}H correlated NMR spectra were recorded on an ECS-400 MHz, JEOL multi nuclear F.T spectrometer with Optiplex 380 Delta 5.02 software, with tetramethylsilane (TMS) as an internal standard for ^{1}H NMR analysis. Chemical shifts are reported in ppm downfield from tetramethylsilane (TMS), at 298 K with coupling constants (J) reported in Hertz (Hz). Standard abbreviations indicating multiplicity were used as follows: m = multiplet, t = triplet, d = doublet and s = singlet.

Accurate mass spectrometry data, of samples, was collected at the EPSRC (engineering and Physical Sciences Research Council) mass spectrometry service centre, University of Wales, Swansea Thermofisher LTQ Orbitrap XL; HRMS (N-NSI) or (P+NSI) Positive or Negative ion (nano-electrospray) spectrometer, while the ionisation was electrospray (ESI+ and ES-) Thermofisher LTQ Orbitrap XL was used to analyse volatile molecules in the mass range m/z 50–2000 or m/z 200–4000 Daltons. Positive Electrospray (ESI-MS) mass spectra time of flight (TOF) (MALDI-TOF), were recorded on Voyager instrument DE-STR used to analyse volatile molecules in the mass range 200 to 200000 Daltons. Facility at Swansea University

and at the Department of Chemistry at University of Sheffield using (HRMS TOF/(ESI+)). The instrument used was the 'WATERS LCT premier', the ionisation was electrospray (ESI+), the solvent was Water/Acetonitrile (1:3), (water: acetonitrile = 1:3). All strucral characteristion spectra are presented in the Appendices.

Single-crystal X-ray diffraction data and analyses were performed in the Chemical Crystallography Laboratory at the EPSRC National Crystallography Service, School of Chemistry, University of Southampton, United Kingdom. Single crystal diffraction data were collected using either a Nonius-kappa CCD area detector mounted at the window of an FR591 rotating anode generator (Mo Kα, λ=0.71073A); Rigaku Saturn 724+ area detector mounted at the window of an FR-E+ rotating anode generator (Mo Kα, λ=0.71073Å) equipped with HF Varimax optics (100μm focus).

Fourier transform infrared spectra (ATR-FTIR IR) and (FTIR) were recorded using a smart diamond ATR attachment on a Thermo-Nicolet FT-IR Spectrophotometer (AVATAR 320) over the range 4000 to 400 cm^{-1}.

Electronic spectra and UV-VIS spectra were recorded in $1cm^2$ path length quartz cell in a Perkin-Elmer Lambda 40 spectrophotometer from 245-1000 nm, by dilution of a 10^{-3}M stock solution in DMSO at 294K. Fluorescence measurements were undertaken in $1cm^2$ path length quartz cuvettes on solutions with an absorbance < 0.1 au using a Hitachi fluorescence spectrophotometer, and the data analysed using the Hitachi FL solution software. The fluorescence quantum yield was determined by (1,1':4'1"- terphenyl; PTP) dye as a reference with The ligand, complexes and the reference dye were excited at 276 nm, maintaining nearly equal absorbance (0.0954), and the emission spectra were recorded from 285 to 800 nm. All experiments were carried out at a concentration of (1×10^{-6} M).

Melting points were determined with a Stuart Scientific melting point – SMP1 (Bibby, UK) apparatus. Preparative thin layer chromatography plates Analtech (PTLC) were undertaken on 20 x 20 CM 2000 microns 12 x 12 cm silica plates, 2mm thick (ANALTECH), eluted with EtOAc/hexane (1:1) unless otherwise stated. After development the plates were examined under UV- 254nm, the individual band removed, then extracted with a suitable solvent, filtered to remove the solid silica and the filtrate evaporated under vacuum to give the pure

product. Thin layer chromatography plate Analtech, Inc. 75 Blue Hen Drive Newark, DE 19713 WWW.analtech.com 20x20 CM 2000 MICRONS.

Gas chromatography electron impact mass spectroscopy (GCEIMS) was carried out in house on a Hewlett Packard (HP), model 5890GC interfaced to a HP 5972 mass selective detector (MSD) quadropole spectrometer with mass fragmentation by electron impact (EI) ionisation. Gas chromatographic separation was undertaken on a RTX – 5MS column, (15m x 0.25mm x 0.25μm Restek; Cat no. 12620), helium gas carrier, column head pressure = 7psi, inlet temp, 275 oC and injector, 1 μl.

Conductivity measurements were carried out using aqueous DMSO solutions (1.0×10^{-3} M) at 294K using a Hanna digital conductivity meter (model EC 214) with a conductivity electrode, type H1 76300 Conductivity measurements were carried out by using 10^{-3}M concentrations of the complexes in DMSO (294 K)

Following instructions from the manufacturer. Magnetic susceptibility of complexes were recorded at room temperature (294K) using a magnetic susceptibility balance (Johnson Matthey Catalytic Systems Division Equipment).

Bioligal activity studies were carried out on two human tumour cell lines, HepG2: Hepatoma Cells (hepatic carcinoma from a 15 years old child) (Cyprotex) and HCT116: Colorectal Cancer Cell (gift from Kids Can) at the school of environmental and life sciences Salford university.

Chapter 6 : SYNTHESIS OF (1,2,3-TRIAZOL-4-YL)-PYRIDINE LIGANDS VIA A CLICK APPROACH

6.1 Introduction

The initial objective of this work, as previously stated, was to prepare novel metal complexes using bidentate ligands ((1,2,3-triazol-4-yl)-pyridine based) which were synthesised via the Cu(I)-catalysed alkyne–azide (CuAAC) ('click chemistry') reaction from a wide range of substrates. It was intended to assess the potential applications of these metal complexes in dye-based solar cells and for screening as potential anti-cancer drugs. During the course of this project a paper was published detailing the synthesis of the ligands, how the metal complexes and their X-ray structures were determined and what a novel packing pattern they displayed.

During the course of this research, many of the synthesised ligands have not been reported before, nor have they been characterised. Knowledge of their structure and characteristics is important to be able to estimate whether the coupling of these ligands to metallic ions would yield the required photochemical performance of the intended dye solar cells. The novelty of this work has been highlighted in the paper published in Acta Crystallographica Section B, 70, 379–389 (2014).

6.1.1 Synthesis of 4-(4-phenyl-1*H*-[1, 2,3]-triazol-1-yl)benzoic acid (L^1)

Before embarking on this task, the click ligand 4-(4-phenyl-1H-[1,2,3]-triazol-1-yl)benzoic acid (L^1) was targeted as a model compound to validate the conditions used to successfully effect the Cu-catalysed regioselective click reaction between 4-azidobenzoic acid and commercially available phenylacetylene (Scheme 6.1).

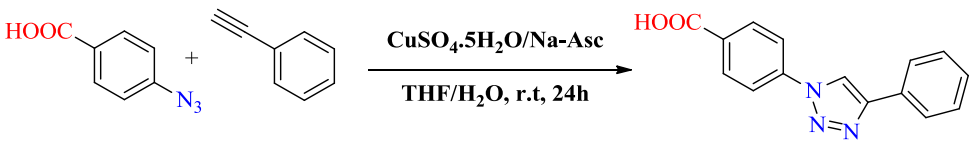

4-Azidobenzoic acid **phenylacetylene** **4-(4-phenyl-1H-[1, 2, 3]-triazol-1-yl) benzoic acid (L^1)**

Scheme 6.1: Proposed preparation route for 4-(4-phenyl-[1H-1,2,3]-triazol-1-yl)benzoic acid (L^1).

4-Azidobenzoic acid was chosen for use in this reaction in view of its easy preparation, from 4-aminobenzoic acid [1-3], as shown in the Scheme 6.2 (see below) using the Sandmeyer reaction.

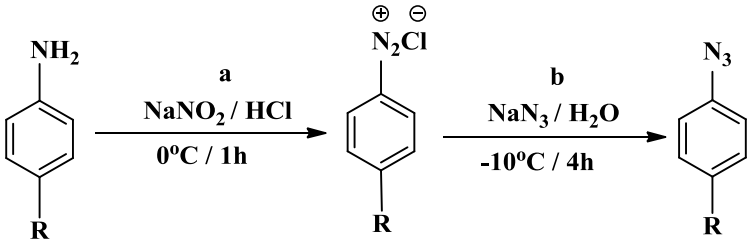

(a) Reagents and conditions: $NaNO_2$, H_2O: HCl (1:1), 0 °C
(b) NaN_3 (aq), -10°C, R.T.
R= H, CH_3, OCH_3, COOH, F, Cl, CN, CF_3

Scheme 6.2: Synthetic route for the preparation of arylazides.

The subsequent click reaction (Scheme 6.1) was undertaken as detailed in the experimental section (6.3.1.1) using THF/H_2O as a solvent. The compound, 4-(4-phenyl-1*H*-[1,2,3]-triazol-1-yl)benzoic acid (L^1), was obtained as a colourless solid in 70% yield. The structure was confirmed by NMR and HRMS spectra. After successful demonstration of the "click" reaction it was decided to prepare 2-(4-phenyl-[1,2,3]triazol-1-yl)pyridine (structure (I) in scheme 6.3), a bidentate ligand, which will form metal complexes with our desired properties.

6.1.2 Synthesis of 2-(4-phenyl-1*H*-1,2,3triazol-1-yl)pyridine ligand (I)

The synthesis of the titled bidentate ligand was attempted, as shown in Scheme 6.3, using the click reaction between 2-azidopyridine and phenylacetylene.

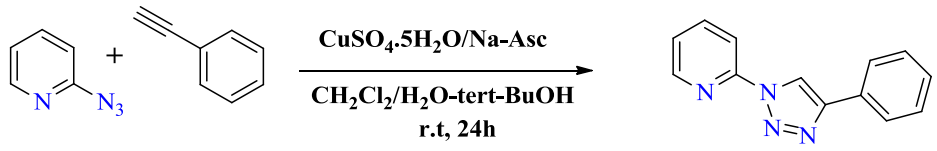

2-azidopyridine phenylacetylene 2- (4-phenyl-1*H*-1,2,3-triazol-1-yl) pyridine ligand (I)

Scheme 6.3: Proposed preparation route for 2-(4-phenyl-1*H*-1,2,3]triazol-1-yl)pyridine (I).

Whilst phenylacetylene was commercially available, 2-azidopyridine had to prepared either by the conversion of 2-fluoropyridine with NaN_3 in DMSO at 100°C [4], or by the conversion of 2-fluoropyridine to 2-hydrazine pyridine with hydrazine hydrate, followed by diazotization with $NaNO_2$/HCl and NaN_3 [5], as shown in Scheme 6.4

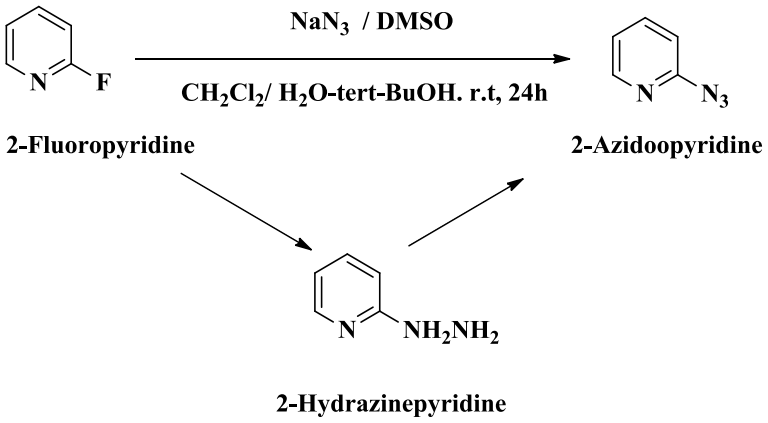

Scheme 6.4: Preparation route for 2-azidopyridine.

2-azidopyridine was successfully prepared using both these two methods and yielded crude 2-azidopyridine, as confirmed by NMR and IR, with the azide peak centered at 2130(vs) cm^{-1} and 2100(vs) cm^{-1} as reported in the literature [6]. The 2-azidopyridine was reacted with phenylacetylene (see Scheme 6.3) to produce the desired click ligand 2-(4-phenyl-[1,2,3]triazol-1-yl)pyridine(I) under similar conditions which were used to successfully prepare ligand L^1 (6.3.1.1.) Scheme 6.1. However, on organic work up of the reaction mixture, the only product identified was a remnant of the starting material with no evidence of the formation of the desired click product (I).

Heterocyclic azides such as 2-azidopyridine spontaneously cyclise as reported in the literature to the fused tetrazolo [1,5-a]pyridine, which is in equilibrium with the azide as shown in Scheme 6.5 [7]. This has been described in the literature as a tautomerism, as an azidomethine-tetrazole (imideamide-tetrazole) equilibrium, as a 1,5-dipolar cyclisation and a valence isomerisation [6-11].

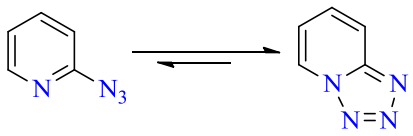

2-azidopyridine **tetrazolo[1,5-a]pyridine**

Scheme 6.5: Equilibrium tautomerism between 2-azidopyridine and its tetrazole

However, the position of the equilibrium is important with regard to the formation of the click product *via* the [3+2] cycloaddition reaction mechanism (chapter 2, Scheme 2.1), as this requires the azide structure and its dipolar character rather than a tetrazole structure to form the transition state (Scheme 2.1 (10) for product formation). The failure to form the desired click product as expected, based on Scheme 6.3, suggested that 2-azidopyridine might exist predominantly as the tetrazole in (Scheme 6.5). However, the literature in regard to the position of the azide ↔ terazole equilibrium was controversial. Spectroscopic studies on solute-solvent studies favoured the azide form exclusively and the absence of an equilibrium [7]. Computational *ab initio* calculations [12] indicated that the presence of electron withdrawing groups on the pyridine shifted the equilibrium from the tetrazole towards the azide. IR absorptions studies of the 2-azidopyridine group however, indicated that the major equilibration isomer of this compound is the tetrazolo [1,5-*a*]pyridine (Scheme 6.5) [11, 13], as reported for the solid state [14-19].

The literature indicated that the 2-azidopyridine equilibrium favoured the tetrazolo [1,5-*a*] pyridine isomer Scheme 6.5 both in solution and in the solid state, except for the publication of Rafie et al. [7], which indicated that the compound existed exclusively as the azide in solution. As the method of preparation could influence the equilibrium, it was decided to prepare 2-azidopyridine according to the method of Rafie et al. [7], i.eby diazotisation of 2-aminopyridine with (i) $NaNO_2$/HCl, and then (ii) NaN_3. However, the 2-azidopyridine when used in the click reaction with phenylacetylene again failed to give 2-(4-phenyl-[1,2,3]triazol-

1-yl)pyridine (I). After six months of research effort in trying to achieve the above research objective, it was decided to abandon the preparation of this click ligand *via* this approach.
It is noteworthy that upon completion of our research, a paper was published by Zhang *et al*. in 2012 [19], reporting the successful preparation of derivatives of this type above (6.1.2.) using a Cu(I)-acetate catalyst with 5-substituted-2-azidopyridine having electron withdrawing groups (NO_2, CN, CO_2Et) to shift the position of the tetrazole ↔ azide equilibrium to effect the azide-alkyne cycloaddition reaction. Tetrazolo [1,5-a]pyridine is formed by the conjugation of the terminal nitrogen of the azide group with the nitrogen at 1-position of the pyridine ring with subsequent electron transfer to satisfy the positive charge on the azide group (Scheme 6.5). The presence of an electron withdrawing group on the 5-position of the 2-azido pyridine causes the electron pair on the nitrogen to conjugate now with the electron withdrawing group at the 5-position to stabilise its positive character so preventing the competing reaction the formation of tetrazolo [1,5-a]pyridine.

6.1.3 Preparation of aryl azides

In order to synthesise alternative ligands a general procedure was required for the preparation of aryl azides and this is elaborated in the earlier scheme (Scheme (6.2). The synthetic route involved the use of the Sandmeyer reaction (a) where an aromatic primary amine was converted under acid conditions with $NaNO_2$ into a diazonium salt in situ, followed by nucleophilic substitution of the diazonium salt with NaN_3 to give the azido compound [20-22]. A range of 4-substituted aryl azides A1– A9 (see Table. 6.1) were synthesised with the aim of producing a series of click ligands containing electron donating (R= CH_3, OCH_3) and electron withdrawing groups (R = F, Cl, CN, CF_3, COOH) and whose Hammett substituent constants (σ_p) covered the range between -0.27 to 0.66. Experimental details are described in Appendix 1 and the yields obtained reported in Table 6.1. These compounds have been previously reported in the literature and characterised by NMR, GC-MS and IR [23-37].

Table 6.1: Chemical structure and nomenclature of aryl azide reagents (A1-A9).

Code	Compound	IUPAC nomenclature	Yield %	Literature reference
A1and A4	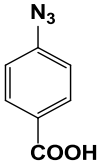	4-azidobenzoic acid	69	24-26
A2	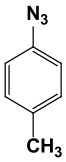	1-azido-4-methylbenzene	71	24-25
A3	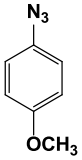	1-azido-4-methoxybenzene	79	24-26
A5	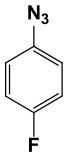	1-azido-4-fluorobenzene	90	22, 31, 37
A6	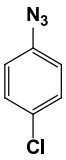	1-azido-4-chlorobenzene	83	32-34
A7	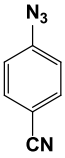	4-azidobenzonitrile	90	35-36
A8	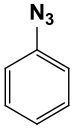	1-azidobenzene	79	23-25
A9	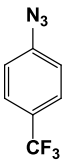	1-azido-4-(trifluoromethyl)benzene	91	24, 37

The significance of the Hammett constant is that a plot of the properties of the click ligands against the substituent constants (σ_p) would allow substituent effects on the property of the ligand or complex to be assessed in a quantitative manner under certain conditions and allow us to obtain an overview of compounds rather than examining them in isolation.

6.1.4 Synthesis of click ligands (L^2- L^9)

Due to the aforementioned problems in synthesisng 2-(4-phenyl-1*H*-1,2,3triazol-1-yl) pyridine ligand it was decided to focus on the preparation of the analogue of the desired product 2-(1-p-tolyl-1*H*-[1,2,3]-triazol-4-yl)-pyridine (L^2) using the click reaction as shown in Scheme 6.6.

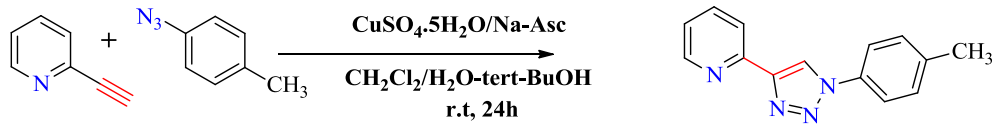

2-ethynylpyridine **1-azido-4-methylbenzene** **2-(1-p-tolyl-1*H*-[1,2,3]-triazol-4-yl)-pyridine (L^2)**

Scheme 6.6: Preparation route for 2-(1-p-tolyl-1*H*-[1,2,3]-triazol-4-yl)-pyridine (L^2).

The synthesis of 2-(1-p-tolyl-1*H*-[1,2,3]-triazol-4-yl)-pyridine (L^2) (see experimental section 6.3.1.2), required the reaction of commercially available 2-ethynylpyridine with our previously prepared 1-azido-4-methylbenzene (A2) under click conditions using $CuSO_4$/Na-ascorbate in water/tert–butyl alcohol at room temperature(RT), as shown in Scheme 6.6. The click product 2-(1-p-tolyl-1*H*-[1,2,3]-triazol-4-yl)-pyridine (L^2) was isolated after removal of insoluble copper salts using celite and organic workup to give (L^2) as a yellow solid in 74% yield. Recrystallisation from CH_2Cl_2: CH_3OH (1:1) gave the product as a colourless solid with mp 128-129^{o}C; Lit 128-129^{o}C [38]. The structure was confirmed by NMR and HRESMS [38], as well as for the first time by single crystal X-ray analysis.

Having established the methodology for the preparation of compound **L^2**, the work was extended to prepare a range of related 2-pyridyl-[1,2,3]-triazole ligands **L^{3-} L^9** as shown in Table. 6.2, by reaction of the appropriate 4-substituted aryl azides A1–A9 (Table. 6.1) with 2-ethynylpyridine under click reaction conditions as shown in Scheme 6.7.

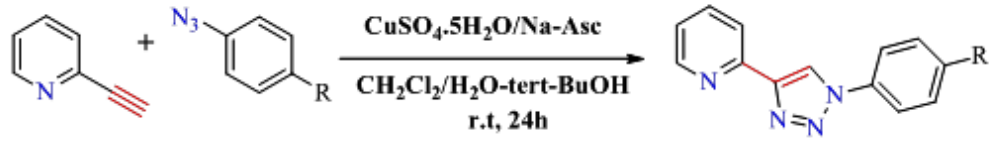

2-ethynylpyridine **1-azido-4-methylbenzene** **2-pyridyl-1,2,3-triazole ligands**

R= COOH; A1 and A4	**R= COOH; L^1 and L^4**
R= CH_3; A2	**R= CH_3; L^2**
R= OCH_3; A3	**R= OCH_3; L^3**
R= F; A5	**R= F; L^5**
R= Cl; A6	**R= Cl; L^6**
R= CN;A7	**R= CN; L^7**
R= H;A8	**R= H; L^8**
R= CF_3;A9	**R= CF_3; L^9**

Scheme 6.7: Preparation route for 2-pyridyl-[1,2,3]-triazoleligands L^1-L^9.

Table 6.2: Chemical structure and nomenclature of click 1,2,3-triazole ligands (L^1-L^9).

Code	Structure	IUPAC nomenclature	Yield (%)	Literature reference
L^1	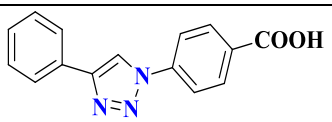	4-(4-phenyl-1*H*-[1,2,3-triazol]-1-yl)benzoic acid	71	46
L^2	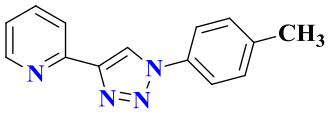	2-(1-p-tolyl-1*H*-[1,2,3]-triazol-4-yl)-pyridine	70	38
L^3	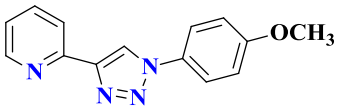	2-(1-(4-methoxyphenyl)-1*H*-[1,2,3]-triazol-4-yl)pyridine	93	39,40,41
L^4	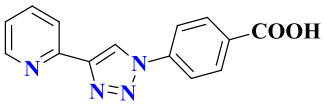	4-(4-(pyridin-2-yl)-1*H*-[1,2,3-triazol]-1-yl)benzoic acid	79	novel
L^5	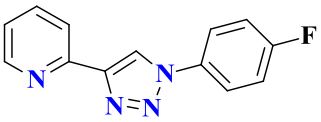	2-(1-(4-fluorophenyl)-1*H*-[1,2,3-triazol]-4-yl)pyridine	83	novel
L^6	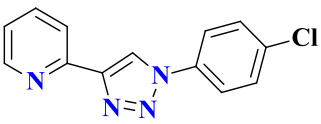	2-(1-(4-chlorophenyl)-1*H*-[1,2,3-triazol]-4-yl)pyridine	81	45
L^7	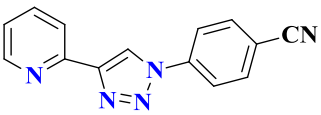	4-(4-(pyridin-2-yl)-1*H*-[1,2,3-triazol]-1-yl)benzonitrile	91	novel
L^8	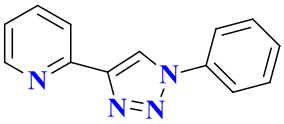	2-(1-phenyl-1*H*-[1,2,3-triazol]-4-yl)pyridine	80	42,43,44
L^9	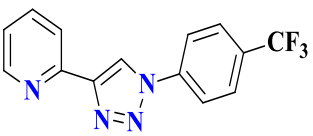	2-(1-(4(trifluoromethyl)phenyl)-1*H*-[1,2,3]-triazol-4yl)pyridine	78	novel

The click ligands L^1 and L^2- L^9 in Table 6.2 were prepared as shown in Schemes 6.1 and Schemes 6.7 using the appropriate aryl azide and obtained in good yields varying from 70-93 %. They were characterised by NMR, HRMS, IR and X-ray analysis as described in section 5.2.2. Click ligands L^2 [38], L3 [39-41], and L^8 [42-44] were previously reported in the

literature and compound L^6 [45] was prepared in 2013, in 94% yield, as a yellow solid. The click products L^1- L^9 isolated by us, were all colourless solids after recrystallisation.

6.2 Results and discussion

Comparative spectroscopic techniques have been used to study the properties of ligands L^1-L^9.

6.2.1. FTIR spectra

Infrared (ATR-FTIR-IR) spectra were recorded using a smart diamond ATR attachment on a Thermo-Nicolet FT-IR Spectrophotometer (AVATAR 320) over the range 4000 to 400 cm^{-1}. The FTIR spectral data of ligands L^1-L^9 are visually presented as an overlay of the IR spectra of L^1-L^9, as shown in Figure 6.1. These significant peaks for ligands L^1-L^9 are tabulated in Table 6.3.

Table 6.3: IR frequencies (cm^{-1}) of the ligands (L^1-L^9)

Ligand	ν(C-H)*triaz*	ν(C=N)*py*	ν(C=C)*Ar*	ν(C=C)*triaz*	ν(N-N)*triaz*	ν(N=N)*triaz*	ν(C-N)	ν(C=O)
L^1	3125	1605	1605, 1573	1557	1177,1035	1520	1229	1682
L^2	3118	1597	1592, 1566	1549	1144,1036	1517	1233	
[d]L^3	3142	1604	1592,1574	1549	1154,1022	1515	1258	
L^4	3141	1603	1588, 1573	1553	1151,1036	1517	1240	1687
L^5	3152	1589	1572, 1549	1515	1149,1035	1516	1235	
L^6	3132	1602	1589, 1570	1550	1146,1037	1501	1236	
[e]L^7	3120	1601	1572, 1549	1511	1147,1032	1511	1235	
L^8	3116	1599	1591, 1567	1544	1147,1035	1502	1237	
L^8	3122	1615	1593, 1570	1547	1105,1027	1528	1337	

[d] **ν(**C-OMe**):** 1257 cm^{-1}, ῡ =1022cm^{-1} **;** [e] **ν(**C≡N**):** 2230 cm^{-1}

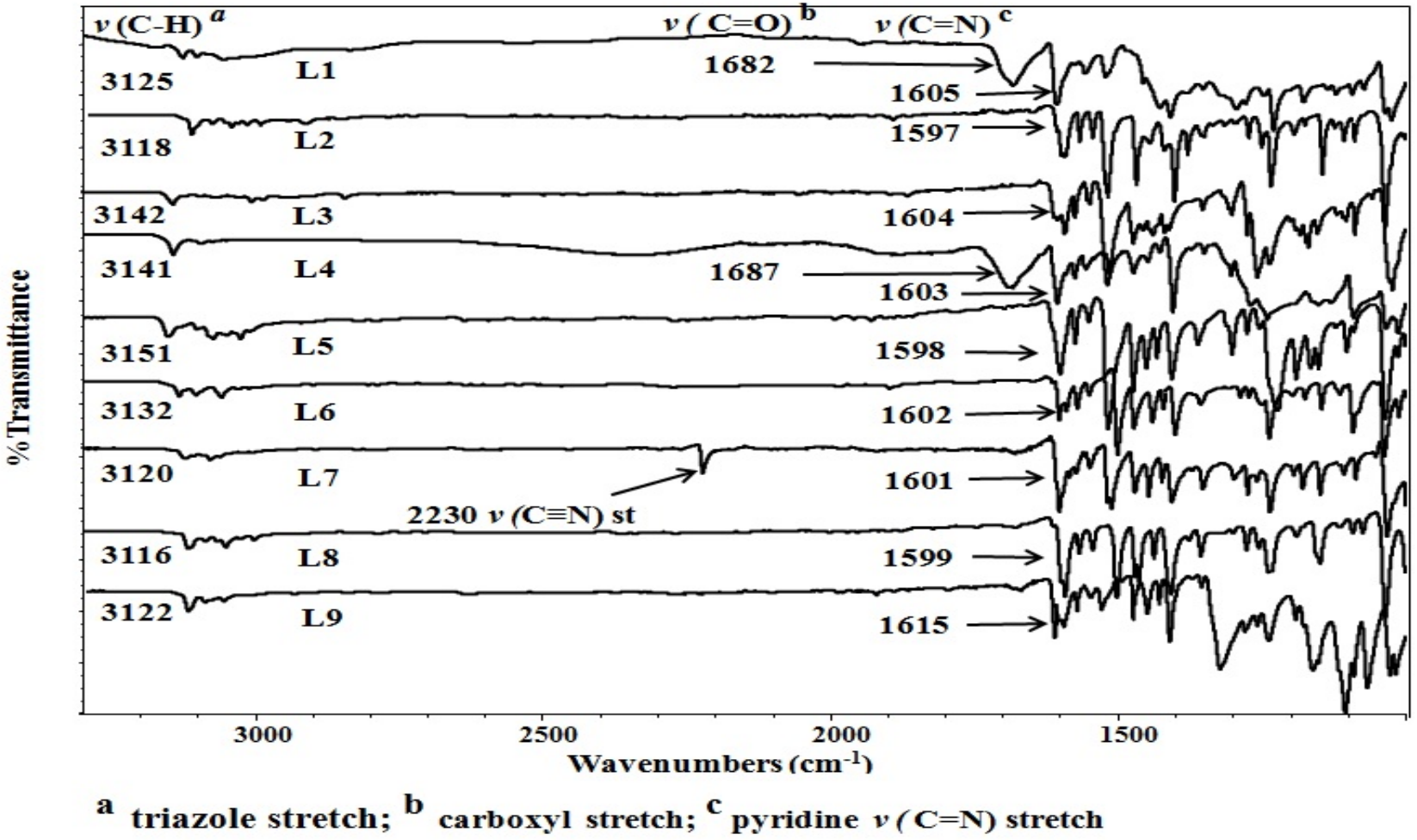

Figure 6.1: ATR-FT-IR absorption spectral data of the ligands (L^1- L^9).

Table 6.3 shows the characteristic bands common to all bond types present in click ligands L^{1}-L^{9}. The bands in the region $\bar{\upsilon}$ = 3116-3151cm^{-1} were assigned to the stretching of the ν(C-H) bond of the triazole ring [38-48] and that at $\bar{\upsilon}$ = 1615-1598 cm^{-1} to the stretching of the ν(C=N) bond of free pyridine that shifts on coordination to the metal to higher wavenumbers, indicating a new compound was obtained. The two bands at region $\bar{\upsilon}$ = 1605-1549 cm^{-1} were, attributed to the two characteristic stretching peaks of the $\nu(C=C)_{Ar}$ bond which occur as a pair of peaks in substituted benzenes. The bands observed at region 1557-1511 cm^{-1} were attributed to stretching of the $\nu(C=C)_{triaz}$ bond of the triazole ring [49, 50] and the $\bar{\upsilon}$ = 1520-1500cm^{-1} to the ν(N=N) stretching vibration [51, 52]. The band at $\bar{\upsilon}$ = 1258-1220cm^{-1} is attributed to the ν(C-N) stretching bond [53], and the bands around $\bar{\upsilon}$ = 1145cm^{-1} and $\bar{\upsilon}$ = 1036cm^{-1}were assigned to the ν(N-N) bond of the triazole ring [54]. The pair of bands in the range at $\bar{\upsilon}$ = 962-977cm^{-1} were assigned to ν(N–N=N) stretching vibration [55, 56] of the triazole ring. In addition, substituent specific bands were identified for ligands, L^{1} and L^{4} at 1682 and 1687 cm^{-1} respectively, for the ν(C=O) stretching of the COOH group and $\bar{\upsilon}$ =2230 $cm^{-1}$for the ν(C≡N) stretching of the nitrile group of L^{7}. Two bands at $\bar{\upsilon}$ = 1257 cm^{-1} and$\bar{\upsilon}$ =1022cm^{-1} were assigned for the ν(C-O) stretching of the methoxy group of L^{3} [53].

6.2.2 Hammett Plot Using UV-Vis Data

A plot of the λ_{max}vs the σ_p substituent constant for all ligands gave a concave upward deviation in the Hammett plot with a negative slope for the electron donating groups and a positive slope for electron withdrawing groups. This is a change in mechanism in which electron donating groups decrease the positive charge at the triazole ring. However, electron withdrawing groups enhance the positive charge (see Figure 6.2) at this centre. There were three substituents (H, CF_3 and COOH) which are outliers on the plot.

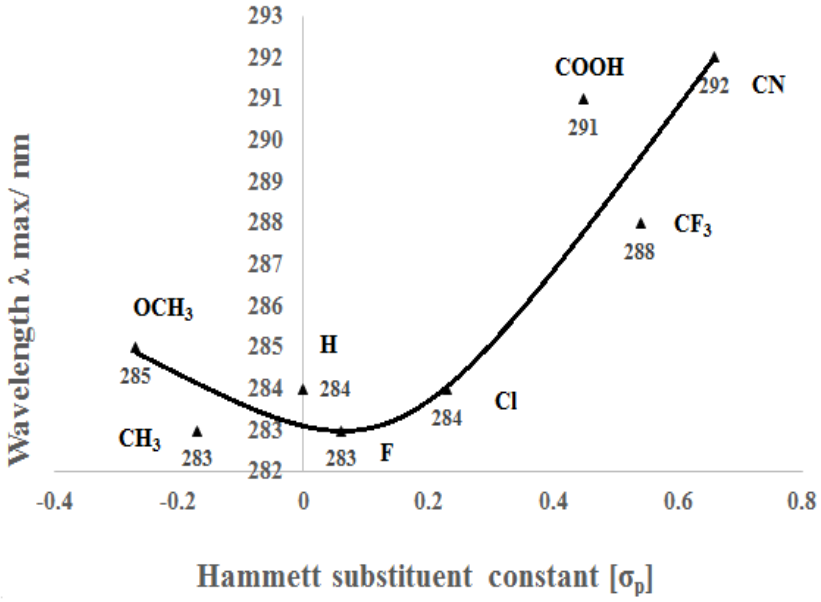

Figure 6.2: Hammett plot of correlations of the λ_{max} of L^2-L^9 ligands *vs.* σ_p values for the Hammett substituent parameters electron donor and withdrawing *para* substituents (R = H, Me, OMe, Cl, F, CN, COOH, and CN).

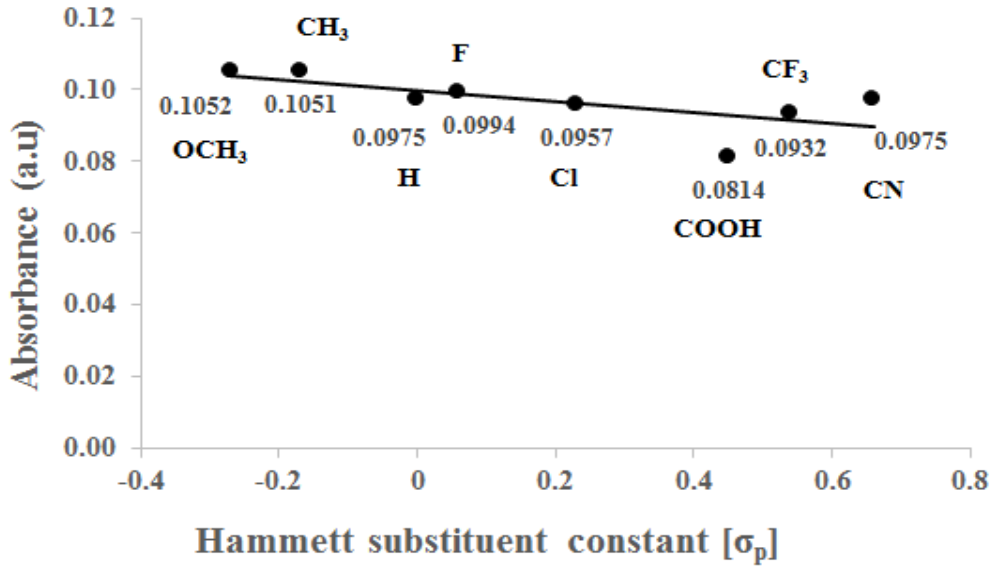

Figure 6.3: Hammett plot of absorbance maximum of L^2-L^9 ligands *vs.* σ_p values for the electron donor and withdrawing *para* substituents (R = H, Me, OMe, Cl, F, CN, COOH, and CN).

In the series L^2-L^9, the maximum absorption of both bands measured in DMSO ($1x10^{-6}$M), gives a linear correlation the between the Hammett σ_p constant for the substituent

on the *p*-position of the phenyl group (Figure 6.3). The two substituents which are outliers (COOH and CN) are not included in the plot. This suggests that compounds with these substituents act as stronger acids than one would have predicted from their values. When electron withdrawing due to mesomeric effects can be extended to the reaction centre via "***through conjugation",*** the result is an even more stabilized species. These types of correlation between the Hammett σ_ρ constant in relation to the substituent of the *p*-position and the relevant UV absorption frequencies were reported previously in literature [57-58].

Table 6.4: The absorption maxima λ_{max} vs the Hammett parameter of the σ_ρ substituent correlation in DMSO (C= 1 X10^{-6}M).

Compound	Substituent in *para* postion	σ_ρ	λ_{max}(nm)	Absorbance	$\varepsilon/10^{-6}$ M dm^3. mol^{-1}.cm^{-1}
L^2	CH_3	-0.17	283	0.1051	15100
L^3	OCH_3	-0.27	285	0.1052	15200
L^4	COOH	0.45	291	0.0814	81400
L^5	F	0.06	283	0.0994	99400
L^6	Cl	0.23	284	0.0957	95700
L^7	CN	0.66	292	0.0975	97500
L^8	H	0	284	0.0975	97500
L^9	CF_3	0.54	288	0.0932	93200

6.2.3 NMR spectra

The ^{1}H- and ^{13}C-NMR spectra for each ligand were assigned in comparison with spectra of previously reported triazoles [38-47], and supported by 2-dimensional spectra (^{1}H–^{1}HCOSY and ^{13}C–^{1}H HMQC) to confirm the proposed assignments. The chemical shift (δ) of the ^{1}H- (C-H) and ^{13}C-NMR (=CH) of the triazole moiety have been tabulated for ligands L^1-L^9 in Table 6.5. This is also shown in Figure 6.4, which indicates that the proton from the triazole ring position shifts according to the substituent in the para-position of the phenyl ring,

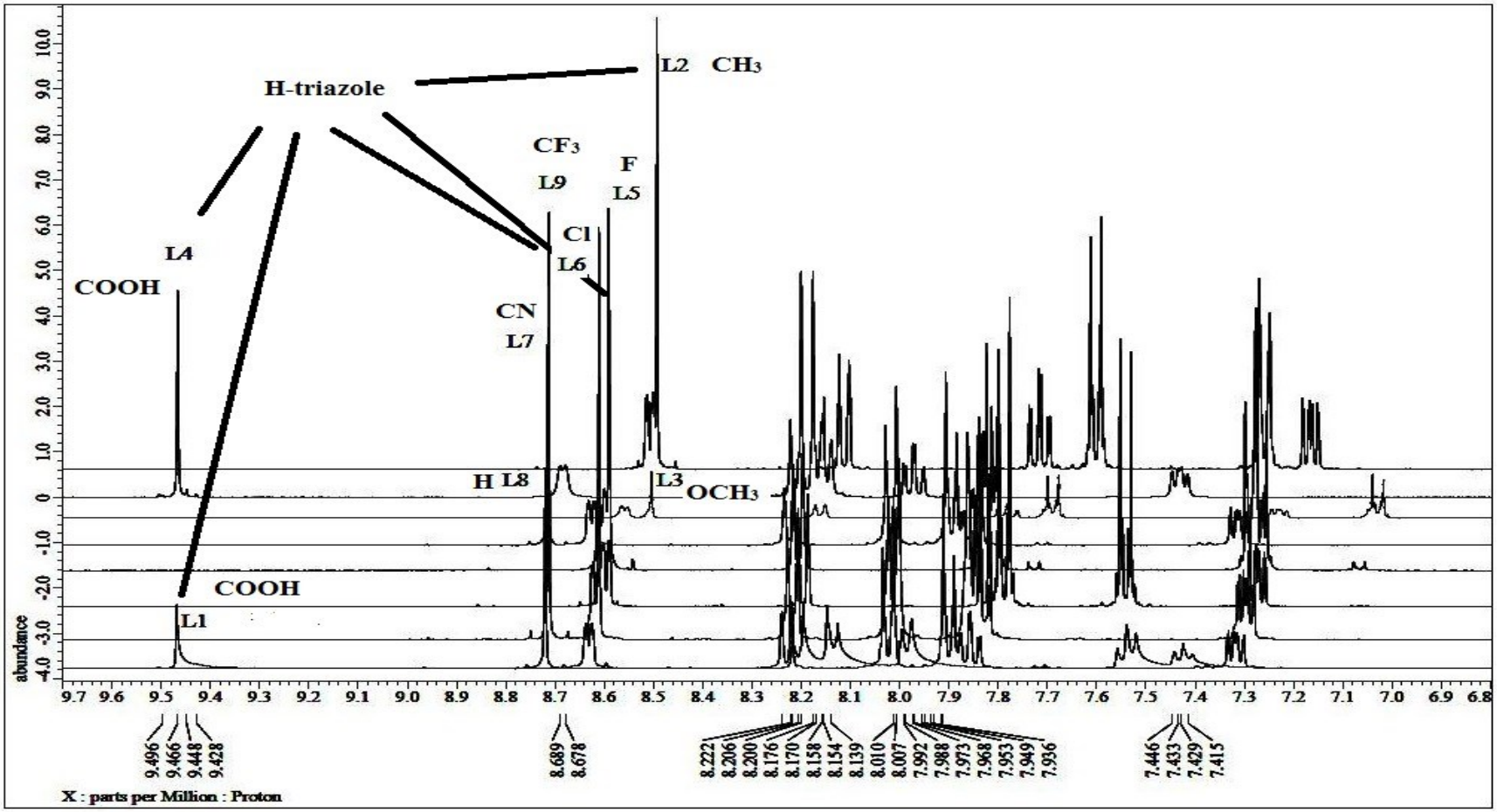

Figure 6.4: The overlayed spectra of the (C-H) triazole from the ^{1}H NMR for ligands L^{1}-L^{9} in $CDCl_2$ solutions.

The effect of the electron withdrawing substituents on the phenyl ring manifested itself in shifts of the C-H-triazole peak of the ^{1}H-1,2,3-triazole system, which was observed in the range between 8.54-9.46 ppm in the ^{1}H-NMR and 119.69-120.48 ppm in the ^{13}C-NMR spectra of ligands L^2-L^9. These values are tabulated in Table 6.5 with literature values reported for triazole ligands with a NO_2 and NH_2 substituent included [45]. To ascertain whether there was a relationship between the shifts in the C-H-triazole^{1}H-NMR peak and the substituents present on the phenyl ring, a Hammett type plot was undertaken on the data. Figure 6.5 shows the plot of the shift of δ(C-H) triazole in ppm for ligands L^2-L^9 and literature reported ligands (NH_2 andNO_2) against the Hammett σ substituent constant [59]. A linear relationship with positive slope (0.18) was observed between δ(C-H) and the σ_p substituent constant for the ligands, with R^2=0.97. L^4 (COOH) and the NO_2 substituent were outliers and were excluded from the linear regression fit. The plot Figure 6.5 suggests that COOH and NO_2 groups act as much stronger electron withdrawing groups than expected *via* the inductive effect based on their σ_p constant. They therefore cause greater deshielding of the (C-H) of the triazole ring and higher acidity.

Table 6.5: The ^{1}H- and ^{13}C-NMR spectra of the C-H-triazole ligands (L^1- L^9).

Ligand	Formula	Solvent	^{1}H-NMR δ(C-H) (triazole)	^{13}CNMR(=CH) (triazole)	σ_p constant ($-\sigma_p$) [53]
L^1	$C_{15}H_{10}N_3O_2$	DMSO- d_6	9.42 H9	119.62 (C_9)	
L^2	$C_{14}H_{12}N_4$	CD_2Cl_2	8.55 H8	120.09 (C_8)	-0.17
L^3	$C_{14}H_{12}N_4O$	CD_2Cl_2	8.54 H11	120.64 (C_{11})	-0.27
L^4	$C_{14}H_{10}N_4O_2$	DMSO- d_6	9.46 H11	121.41 (C_{11})	0.45 (0.77)
L^5	$C_{13}H_9FN_4$	CD_2Cl_2	8.58 H7	120.48 (C_7)	0.06
L^6	$C_{13}H_9ClN_4$	CD_2Cl_2	8.60 H11	120.42(C_{11})	0.23
L^6*	$C_{13}H_9ClN_4$	$CDCl_3$	8.62	119.9 [28]	0.23
L^7	$C_{14}H_9N_5$	CD_2Cl_2- d_6	8.70 H16	120.23 (C_{16})	0.66
L^8	$C_{13}H_{10}N_4$	CD_2Cl_2	8.62 H1	120.41 (C_1)	0
L^9	$C_{14}H_9F_3N_4$	CD_2Cl_2	8.70 H11	119.69(C_{11})	0.54
NO_2 [30]	$C_{14}H_9N_4$	DMSO	9.57	122.3	0.78 (1.27)
NH_2 [45]	$C_{14}H_9N_4$	DMSO- d_6	8.48	121.1	-0.66

L^6* = A value obtained from literature [43].

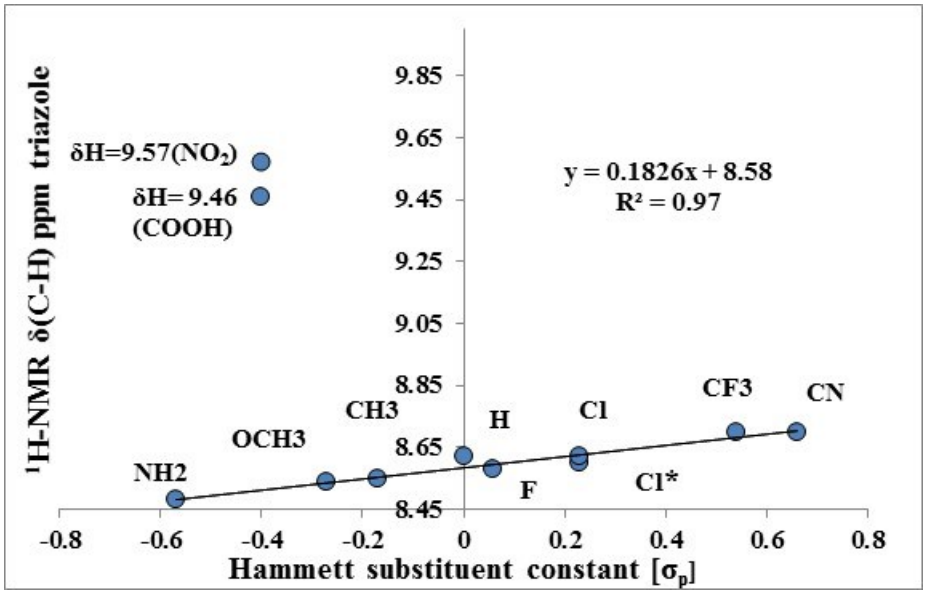

Figure 6.5: A plot of δ(C-H) ppm of triazole against the Hammett's *para* substituent constant [σ_p].

Deviation from the plot by electron withdrawing groups such as the NO_2 and COOH, can occur due to mesomeric effects, if these effects can be extended to the reaction centre *via* "through conjugation" to result in a more stabilised species.

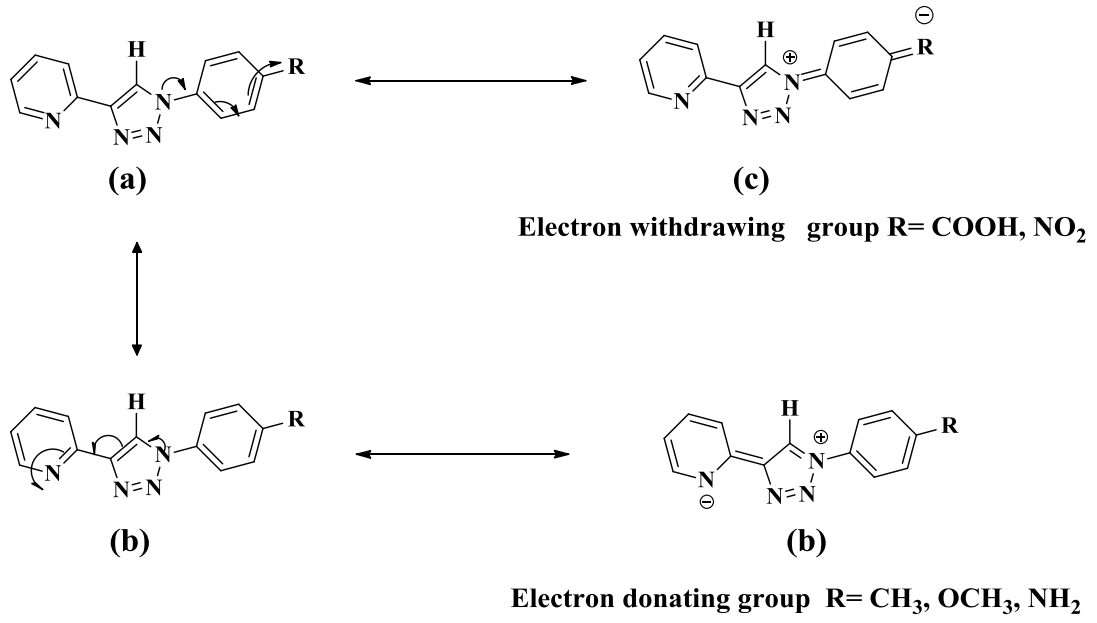

Scheme 6.8: Resonance structures proposed for 2-pyridyl-1,2,3-triazole ligands L^2- L^9.

The electron distribution of the click ligands L^2, L^3, L^5-L^9 is influenced by the resonance structure **(a)** when R is an electron withdrawing group and structures **(b)** when R: is an electron donating group (see Scheme 6.8). However, the marked deviation of the δ(C-H) and the σ_p substituent constant for ligands L^4 (COOH) and the NO_2 ligand (Figure 6.5), indicates that these electron withdrawing groups have a significant mesomeric contribution (structure **c**). The use of the modified -σ_p substituent constant for NO_2 (1.27) and COOH (0.77) that corrects for the mesomeric contribution of the substituent, failed to correct the deviation of these ligands from a linear relationship. This indicates the δ(C-H) triazole proton was significantly more acidic than expected. This may be due to structure **(c)** where conjugation resulted in the positive charge being localised on the triazole nitrogen adjacent to the triazole-H as shown in Scheme 6.8 [60].

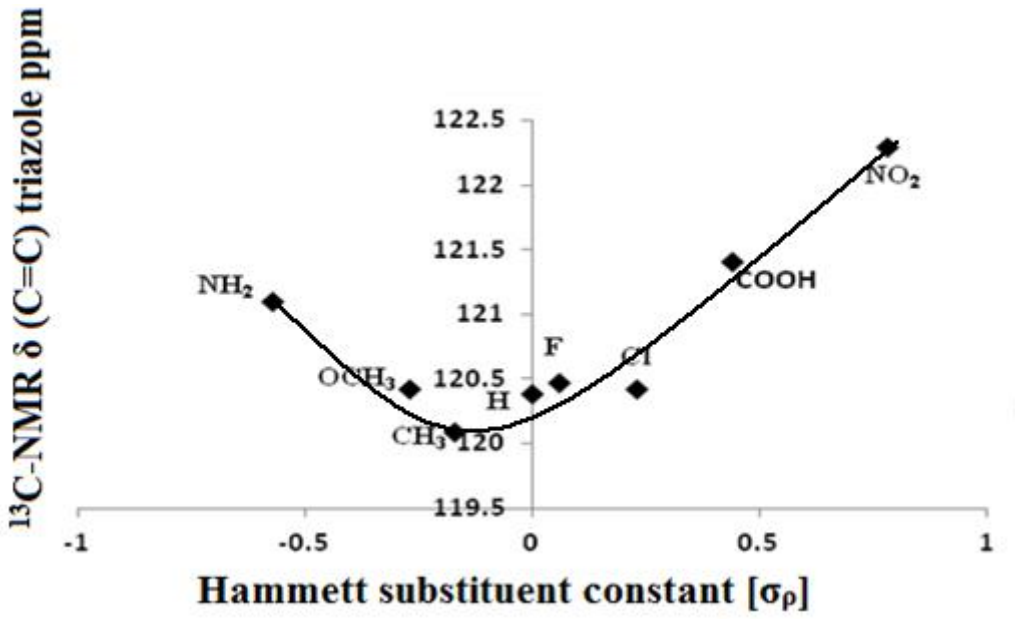

Figure 6.6: A plot of ^{13}C δ (C=C) ppm shift for the triazole carbon against the Hammett's *para* substituent constant [σ_p].

A plot of the ^{13}C δ(C=$C_{triazole}$) vs the σ_p substituent constant for all ligands gave a concave upward deviation in the Hammett plot with a negative slope for electron donating groups and positive slope for electron withdrawing groups. This indicates a change in mechanism in which donating groups decrease the positive charge on the triazole ring (**b**; Scheme 6.8), whilst electron withdrawing groups (**a** and **c**; Scheme 6.8) enhance the positive charge (see Figure 6.6) at this centre. There were two

substituents which acted as outliers (CF_3 and CN) and these are not depicted on and considered for the graph.

6.2.4 Mass spectra

The mass spectroscopic pattern presented here were experimentally observed and both positive and negative ion nano-electrospray (NSI) mass spectra were used to measure the mass of the ligands L^2-L^9 are shown in Scheme 6.9. The high resolution mass spectra obtained for compounds L^2-L^9were identical to the fragments reported in the literature for compounds L^2, L^3 and L^6, [38-47] with the formation of a metastable ion $(M+H)^+$ relative abundance (100%), Table 6.6 that subsequently fragmented by pathways A, B & C, as shown in Scheme 6.9.

$$[M\text{-}N_2]^+ \xleftarrow{A} [M+H]^+ \xrightarrow{B} [M+Na]^+ \xrightarrow{C} [2M+Na]^+$$

Scheme 6.9: Dominant fragments detected in the mass spectra pattern of ligands.

Pathway (A) involves the loss of a nitrogen molecule to give the $(M\text{-}N_2)^+$ species, seen for ligands L^2, L^3, L^5-L^9 using positive ion nano-electrospray. In the case of L^4**,** negative ion nano-electrospray was used and this species was not observed. The other species observed was the molecular ion plus sodium $(M+Na)^+$ pathway (B) and the dimeric molecular ion plus sodium $(2M+Na)^+$ pathway (C), a result of the use of sodium in the matrix solution. Table 6.6 shows the molecular weight and relative abundance of each species identified for ligands L^2-L^9.

Table 6.6: MS (P+NSI) species observed experimentally for ligands L^2, L^3, L^5-L^9 and MS (N-NSI) of L^4.

Ligand	$[M\text{-}N_2]^+$	$[M+H]^+$(100%)	$[M+Na]^+$	$[2M+Na]^+$	Ref and other fragments
L^2	209 (22%)	237	259 (7%)	495 (18%)	[39]
L^3	224 (15%)	253		527 (14%)	[41]
L^4		$265(M-H)^-$		531(9%) $(2M-H)^-$	
L^5	213 (35%)	241	263 (14%)	503 (24%)	362(5%); 391(2%)
L^6	229 (25%)	257	279 (6%)	535 (9%)	[43]
L^7	220 (55%)	248	270 (29%)	517 (33%)	
L^8	195 (37%)	223	245 (8%)	467 (13%)	[44]
L^9	263 (22%)	291		603 (9%)	391 (6%)

6.2.5 Molecular structure

The general numbering scheme shown in Figure 6.7 is used to discuss the ligand structures. This sequence is not necessarily maintained in the next chapters when the syntheses of different metal complexes are described. This is due to the X-ray crystallographic investigation and the description of atomic bonds and angles that were carried out elsewhere and not in-house. A new different numbering system will therefore be introduced in the next two chapters.

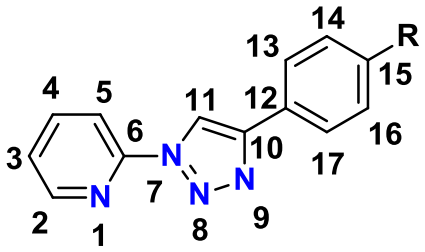

Figure 6.7: General numbering of ligands L^2-L^9.

The X-ray crystallographic structures of the ligands L^2-L^9 are depicted in Table 6.7 and the crystallographic data is presented in Table 6.8, with selected bond lengths and angles given in Table 6.9. The eight structures L^2-L^9 are similar, and the presence of substituents on the 4 position of the phenyl ring causes variation in the bond distances and angles of the triazole moiety. The effect that substituents (electron withdrawing or electron donating) on the 4-position of the phenyl arm (R = H, CH_3, OCH_3, F, Cl, CN, CF_3) have on photophysical properties, will be highlighted using experimental and theoretical studies.

Table 6.7: The molecular structures of ligands L^2- L^9.

Ligands	Formula	molecular structures	Yield
L^2	$C_{14}H_{12}N_4$	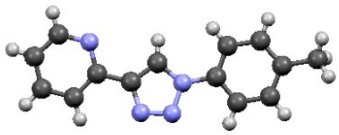	70
L^3	$C_{14}H_{12}N_4O$	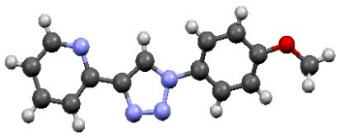	93
L^4	$C_{14}H_{10}N_4O_2$	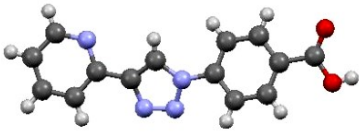	79
L^5	$C_{13}H_9FN_4$	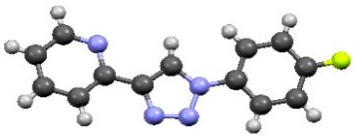	83
L^6	$C_{13}H_9ClN_4$	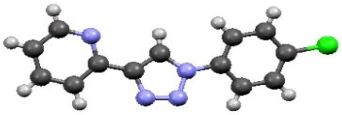	81
L^7	$C_{14}H_9N_5$	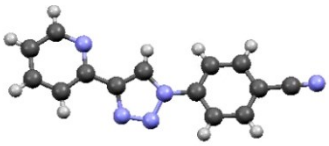	91
L^8	$C_{13}H_{10}N_4$	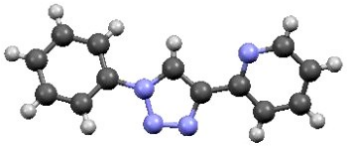	80
L^9	$C_{14}H_9F_3N_4$	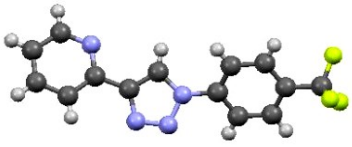	75

Table 6.8: Details of crystal structure determinations for L^2- L^9.

Ligand	L^2	L^3	L^4	L^5	L^6	L^7	L^8	L^9
Empirical formula	$C_{14}H_{12}N_4$	$C_{14}H_{12}N_4O$	$C_{14}H_{10}N_4O_2$	$C_{13}H_9FN_4$	$C_{13}H_9ClN_4$	$C_{14}H_9N_5$	$C_{13}H_{10}N_4$	$C_{14}H_9F_3N_4$
M_r	236.28	252.28	266.26	240.24	256.69	247.26	222.25	290.25
Temp/K	120(2)	100(2)	100(2)	120(2)	120(2)	100(2)	120(2)	120(2)
Cryst. syst.	Monoclinic	Triclinic	Monoclinic	Monoclinic	Monoclinic	Monoclinic	Monoclinic	Monoclinic
Space group	P21	P1	$P2_1/c$	$P2_1/c$	C2/c	C2/c	$P2_1/c$	$P2_1/c$
a/Å	5.7797(5)	3.7837(4)	10.5970(17)	12.2013(3)	16.0000(11)	16.0427(19)	22.6348(5)	5.7460(1)
b/Å	6.7414(4)	10.8502(16)	14.471(2)	7.9798(2)	5.9258(2)	5.8677(6)	5.82500(10)	7.2076(2)
c/Å	15.0259(12)	15.2200(17)	7.7343(12)	11.6329(3)	24.3829(17)	24.487(3)	17.8421(4)	15.2997(4)
α/°	90.00	109.226(11)	90.00	90.00	90.00	90.00	90.00	103.045(2)
β/°	92.359(4)	97.056(6)	90.121(6)	104.043(2)	93.109(8)	92.354(8)	113.007(1)	98.768(2)
γ/°	90.00	91.514(9)	90.00	90.00	90.00	90.00	90.00	92.290(2)
V/Å^3	584.96(8)	584.03(12)	1186.0(3)	1098.94(5)	2308.4(2)	2303.1(5)	2165.32(8)	608.25(3)
Z	2	2	4	4	8	8	8	2
R_{int}	0.0555	0.0617	0.0576	0.0314	0.0497	0.0605	0.0567	0.0351
D_{calcd}/mg /m^{-3}	1.341	1.435	1.491	1.452	1.477	1.426	1.364	1.585
Refln (all/ind)	9647/2622	6395/2617	5844/2705	13725/2510	11996/2636	9891/2638	35200/4956	14232/2785
μ/mm^{-1}	0.084	0.096	0.105	0.104	0.316	0.092	0.087	0.131
$R1/wR2$ (obsd data: $F^2 2\sigma(F^2)$)[a]	0.0482/ 0.1130	0.0534/0.1074	0.0624/0.149	0.0382/0.080	0.0450/0.1125	0.0459/0.1147	0.0456/0.1021	0.0398/0.1046
$R1/wR2$ (all data)[a]	0.0716/ 0.1244	0.0734/0.1161	0.0966/0.1606	0.0441/091	0.0765/0.1371	0.0562/0.1206	0.0545/0.1077	0.0459/1.028

[a] $1\ \Sigma(||F_o| - |F_c||)/\Sigma|F_o|$; $wR2 = [\Sigma w(|F_o| - |F_c|)^2/\Sigma w(F_o)^2]^1$

Table 6.9: Comparison of selected bond lengths (Å) and angles [°] of ligands.

	L^2	L^3	L^4	L^5	L^6	L^7	L^8	L^9
N1–N2	1.368(2)	1.355(4)	1.355(3)	1.3605(13)	1.359(2)	1.3578(17)	1.3601(18)	1.364(6)
N2–N3	1.311(3)	1.302(4)	1.299(3)	1.3107(15)	1.315(3)	1.3083(17)	1.312(2)	1.310(7)
C8-N1	1.349(3)	1.350(5)	1.346(3)	1.3527(14)	1.351(3)	1.3551(17)	1.357(2)	1.36(17)
C1–N1	1.433(3)	1.422(5)	1.425(3)	1.4310(15)	1.423(3)	1.4256(18)	1.431(2)	1.422(7)
C8-C9	1.366(3)	1.362(2)	1.378(3)	1.3733(17)	1.371(3)	1.373(2)	1.372(2)	1.366(8)
C9–C10	1.469(3)	1.463(5)	1.465(3)	1.4689(16)	1.465(3)	1.4694(19)	1.469(2)	1.459(8)
N3 - C9	1.367(3)	1.365(5)	1.366(3)	1.3660(15)	1.369(3)	1.3680(18)	1.371(2)	1.370(7)
C14–N4	1.336(3)	1.336(5)	1.340(3)	1.3381(16)	1.336(3)	1.3389(19)	1.342(2)	1.324(7)
C8–H8	0.9500	0.9500	0.9300	0.9300	0.9300	0.9500	0.9500	0.9300
N3–N2–N1	107.06(17)	107.0(3)	107.24(19)	107.35(9)	107.28(17)	107.24(11)	107.24(12)	107.8(5)
N2–N3–C9	108.89(17)	109.2(3)	109.3(2)	109.01(10)	108.87(17)	109.09(12)	108.92(13)	108.7(5)
C14–N4–C10	116.5(2)	117.0(3)	118.5(2)	117.32(11)	116.68(19)	116.85(13)	116.82(15)	117.8(5)
N4-C10-C9	116.55(18)	115.9(3)	118.6(2)	115.5(10)	115.94(19)	115.59(12)	116.28(14)	117.2 (5)
N3-C9-C10	121.09(19)	122.7(3)	120.5(2)	122.85(11)	121.89(19)	122.05(12)	121.96(14)	122.7(5)

6.2.5 X-ray crystallographic structures

Single-crystal X-ray diffraction analyses were performed in the Chemical Crystallography Laboratory at the National Crystallography Service, School of Chemistry, University of Southampton, United Kingdom. Crystals used for X-ray analysis were produced in house via the slow evaporation of ligands in a variety of solvents and different conditions, see Appendix (2). The molecular structure of L^8 where R=H is used as a model example for the discussion of all the other structures. The molecular structure of ligand L^8 was determined by single crystal X-ray diffraction (Figure. 6.8). Crystallographic data are presented in Table 6.8 and selected bond lengths with bond angles are reported in Table 6.9.

The crystallographic data for L^8 was collected at 100(2)K on a RigakuSaturn 724+ area detector mounted at the window of an FR-E+ Mo-K_α rotating anode radiation source (λ= 0.71075 Å)single crystal X-ray diffractometer. Cell determination, data collection, data reduction, cell refinement and empirical absorption correction were implemented using the *CrystalClear-SM Expert 2.0 r13* (Rigaku, 2011). The structure was solved by direct methods using SUPERFLIP [61]. The structures were refined with full-matrix least-squares techniques on F^2 using the SHELXL-97 program package [62], with the graphicsprogram OLEX2 [63]. MERCURY 3.1 was used to generate graphics [64]. All non-hydrogen atoms were refined by isotropic displacement parameters and hydrogen atoms were added at calculated positions. The crystallographic data and selected bond lengths and selected bond angles for the ligand L^8 are summarised in Table 6.9. Ligand L^8 was crystallised by slow evaporation in a hot (DMSO: CH_3CN: CH_3OH) solution under ambient conditions. Single-crystal X-ray diffraction analysis reveals that it crystallises in the monoclinic $P2_1/c$ space group and indicates four molecules per unit cell as $Z = 4$ of L^8 (See Table 6.8). In the structure of L^8 the pyridine ring adopting an almost "*anti*" conformation with respect to the triazole ring and this is also observed in similar compounds with the nitrogen atom of the pyridine ring with ligands L^2- L^9.

The angle between the least square planes of the triazole and pyridine rings is 16.7(3)°. This value is analogous to what has been previously reported for other such 1,2,3-triazole ligands [65]. The twisting of the triazole ring with respect to the phenyl ring is about 29.7(2)°, as has been previously reported [42, 65]. This value is much smaller compared to the phenyl substituted derivative for other 1,2,3-triazole ligands studied

previously. The N_2-N_3 distance of the 1,2,3-triazole unit at 1.312(2)Å is shorter than the neighbouring distance (N_3-C_9 and N_1-N_2) bonds, 1.371(2) and 1.3601(18)Å respectively, thus confirming the azo character of the triazolyl entity (see Table 6.9) [42]. The bond distance of C_8-C_9 of 1.372(2)Å is longer than the bond distance of C_8-N_1 and N_3-C_9 observed to be 1.357(2)Å and 1.371(2)Å, respectively.

For L^4, dominant intermolecular hydrogen bonding interactions between the hydrogen of the carboxylic moiety and the nitrogen atom of the pyridyl group were observed, with bond distance for the O1-H1$\cdots$N1^i of 2.626(3)A$^\circ$. The bond lengths for O-H and H-N1^i are 0.82Å and 1.82Å, respectively. The angles for the O1-H1$\cdots$N1^i is 167.2. The bond lengths and angles of these intermolecular hydrogen bonds between the donor and accepter fragments are summarised in Table 6.10. The crystal structure of L^4 exhibits intermolecular contact patterns, which result in it adopting a unique packing arrangement dominated by C-H$\cdots$O and N hydrogen bonding. This hydrogen bonding's occurred via O1-H1$\cdots$N1, C3-H3$\cdots$N9, C11-H11$\cdots$O1 and C11-H11$\cdots$O2 interactions. The hydrogen – bonded chains are linked with the chains from the other layer. The strong O-H…N hydrogen bond formed between the carboxylic acid and pyridyl groups and the C-H$\cdots$O hydrogen bond formed between the carboxylic acid and proton-pyridyl groups are dominant to the interactions. These resulted in the formation of one-dimensional zig-zag chains of molecules (see Figure 6.8). These interactions were observed between adjacent molecules. Therefore, such molecules are further assembled into infinite 1-D supramolecular chains which are governed by the O–H$\cdots$N hydrogen bonding interactions between the triazole and pyridyl units of neighboring molecules with COOH group from neighboring molecules (Figure.6.9). This in accordance with results reported previously for other triazole compounds having a carboxylic group moiety [66-68].

The closest intermolecular interactions between the different layers are weak $\pi\ldots\pi$ contacts. The overlap between phenyl and phenyl rings in adjacent molecules cause it adopt to an offset face to face-slipped – type parallel alignment where the rings are parallel displaced with respect to one another and exhibiting a centroid–centroid distance of 4.665Å. The plane–plane distance is 3.76Å. This is a higher value than accepted for the typical phenyl and phenyl rings $\pi\ldots\pi$ stacking interaction [69, 70]. The title compound L^4 is stabilised by intermolecular hydrogen bonding interactions

and intermolecular π…π stacking interactions between the phenyl rings in the solid state as shown in (Figure 6.9).

Table 6.10: Hydrogen bonding interaction parameters; D = donor and A = acceptor (Å, °) in L^4.

D-H...A/interactions	D–H (Å)	H–A (Å)	D–A (Å)	Angle (°)
O1–H1...N1	0.820	1.820(2)	3.626 (2)	167.2
C3–H3...N9	0.930	2.477(2)	3.344 (2)	155.3
C11–H11...O1	0.930	3.088(3)	3.787(8)	130.4
C11–H11...O2	0.930	2.564(2)	3.525(3)	131.4

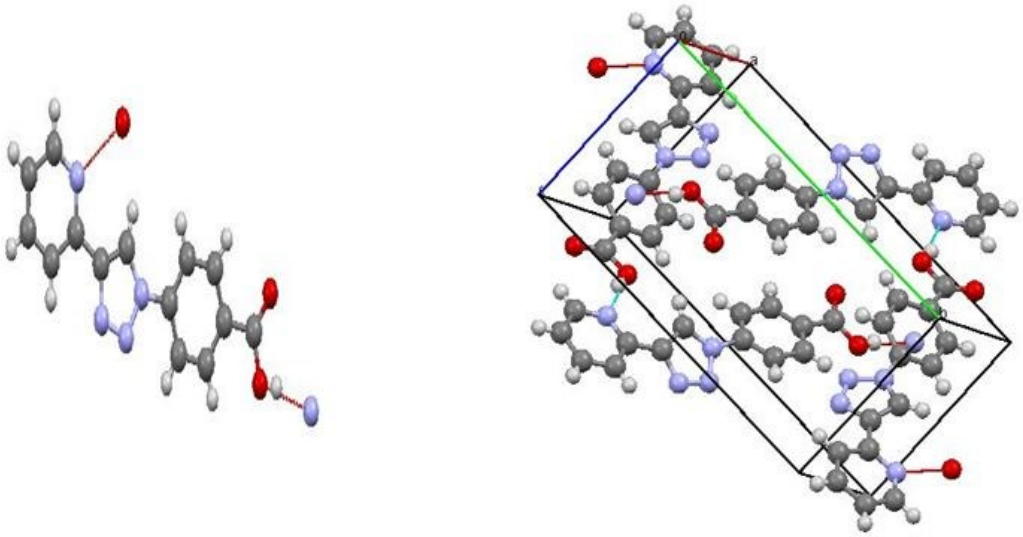

Figure 6.8: The packing arrangement adopted in crystals of the L^4 ligand, viewed along the b-axis of the main hydrogen-bonding motif of carboxylic acid - pyridyl contact, which show the formation of a one-dimensional zig-zag chain.

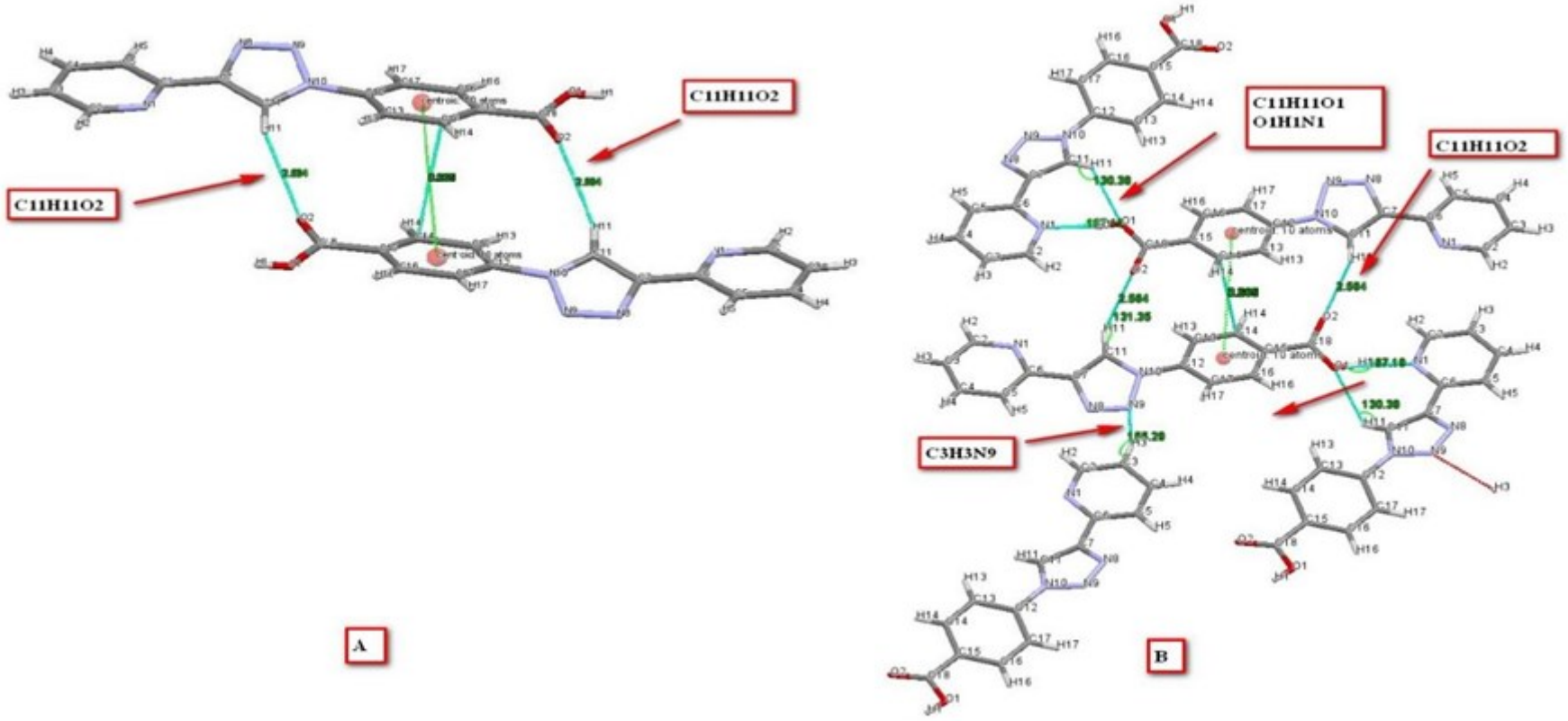

Figure 6.9: (A) A pair of L4 connected molecules arranged around a centre of symmetry, which shows the overlap between the phenyl rings with the intermolecular π…π stacking interactions shown with green dashed lines. (B) Hydrogen bonding interactions shown with blue dashed lines for C–H…O and C–H…N within an infinite 1-D zig-zag chain. The molecules are viewed along the crystallographic b-axis.

This alternation in bond length would support the increased bond length of L^4 (1.3780Å) determined from the X-ray structure when compared to the other ligands in the series L^2-L^9. This is shown by the plot of C_8-C_9 triazole bond length in A° against the Hammett's σ_ρ substituent constant (see Figure 6.10).

The plot ignoring two points (COOH, CN) shows a concave downwards deviation in the Hammett plot with a positive slope for donating groups. This indicates that increased electron density results in the C_8-C_9 triazole bond length becoming shorter and therefore enhancing the double bond character of the bond. Electron withdrawing groups result in a negative slope which reduce the double bond character of the C_8-C_9 triazole bond and cause it to become longer. A concave downwards deviation in the Hammett plot is characteristic of a change in the rate determining step (see Scheme 6.8) where the contribution of structure **b** changes over to **a** and **c** [65].

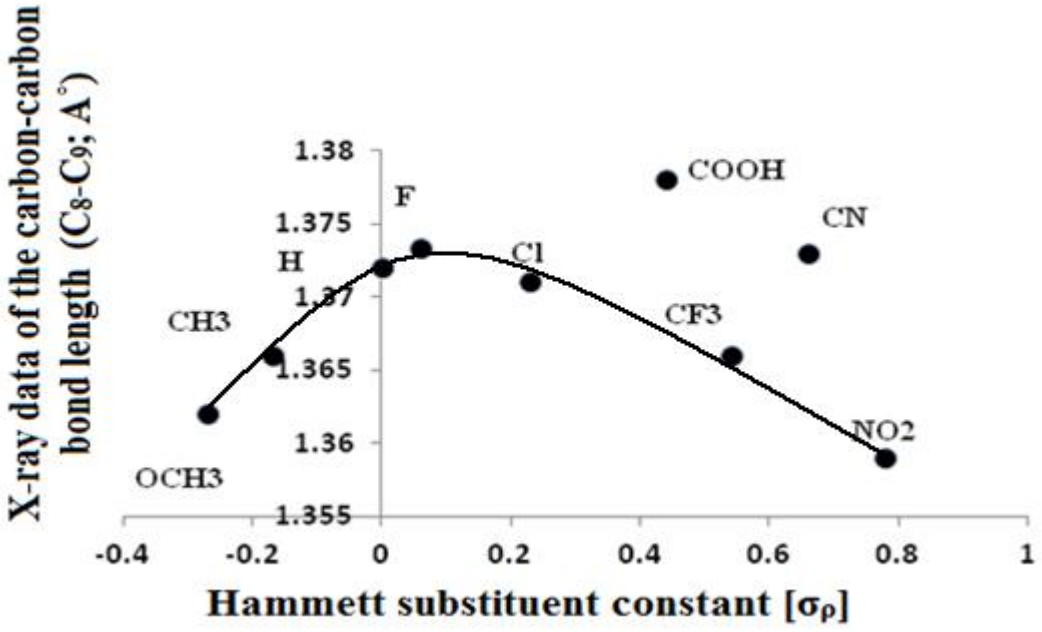

Figure 6.10: A plot of the carbon-carbon bond length C_8-C_9 (A°) of ligands L^2-L^9 against the Hammett *para* substituent constant [σ_ρ].

This is in agreement with the NMR data, in which the chemical shift of the ^{1}H NMR of the (C-H) triazole for L^4 shows more acidic character compared with that observed for other ligands, in agreement with earlier reports in literature [68].

6.3 General Experimental Procedures and Characterisationof the Ligands

6.3.1 Synthesis and characterisation of click (1,2,3-triazol-4-yl)-pyridine ligands

6.3.1.1 Synthesis and characterisation of 4-(4-phenyl-1H-[1,2,3-triazol]-1-yl) benzoic acid (L^1)

To a stirred solution of 4-azidobenzoic acid (0.65g; 3.98mmol) and phenyl acetylene 1.2eq (0.6g; 4.78mmol) dissolved in a mixture of THF (20ml) and water (10ml), was added a solution of $CuSO_4.5H_2O$ (0.184g; 7.36mmol) dissolved in water (5ml). To this was added dropwise a freshly prepared solution of Na-ascorbate (0.291g; 14.68mmol) in water (5ml) and the solution left to stir at RT for 24h. The THF was removed under vacuum and DCM (100ml) added to the residue with stirring for a further 30min, and then aqueous ammonia solution (15%) (100ml) was added. After stirring at RT for 10min, the organic phase was washed with water (2x100ml), filtered through celite, dried over $MgSO_4$ and evaporated under vacuum to give a colourless solid with yield of (0.75g; 71%), mp. 344-346°C. ATR/IR: $\bar{\upsilon}(cm^{-1})$: 3125, 1682,1605, 1557, 1520, 1427, 1408, 1293, 1229, 1177, 1092, 1024, 992, 860, 808, 753, 684. ^{1}HNMR data δ_H/ppm (400MHZ, DMSO-d_6): 13.04 (1H, bs, COOH), 9.42 (1H, s, H_9), 8.20-8.11 (4H, m, H_2, H_6, H_3, H_5), 7.97-7.95 (2H, dd, J = 7.79Hz, H_{11}, H_{15}),7.54-7.50 (2H, t,$^1J_{HH}$ = 7.79Hz, H_{12}, H_{14}), 7.42-7.39 (1H, t, J_{HH} = 7.27 Hz, H_{13}); ^{13}CNMR (100.63MHZ, D_6MSO-d_6) δ_C/ppm: 119.57(C_2, C_6), 119.62 (C_9), 125.29 (C_{11}, C_{15}), 128.32 (C_{13}), 128.96 (C_{12}, C_{14}), 129.91 (C_1), 130.70 (C_4), 131.04 (C_3, C_5), 139.35 (C_8), 147.48 (C_{10}`), 166.33 (COOH) (C_7). These assignments were confirmed using, DEPT ^{13}C (135°), ^{1}H-^{1}H COSY and ^{1}H-^{13}C HMQC two dimensional correlations. HRMS (N-NSI): $[M-H]^-$ (100%): *m/z* = 264.0778 calculated for ($C_{15}H_{10}N_3O_2$); found 264.0774 [46].

6.3.1.2 Synthesis and characterisation of 2-(1- p-tolyl)-1H-[1,2,3-triazol]-4-yl)-pyridine (L^2)

A mixture of 1-azido-4-methylbenzene (0.75g; 5.63mmol) and 2-ethynylpyridine (0.69g; 6.75mmol, 1.2eq) was dissolved in a 1:1 mixture of water/tert–butyl alcohol (100ml). After stirring for 20 min, a solution of $CuSO_4.5H_2O$ (0.41g; 1.64mmol) in water (10ml) was added dropwise followed with a freshly prepared solution of Na-ascorbate (0.37g; 1.85mmol) in water (5ml). The mixture was allowed to stir for 24h at RT, and then an aqueous ammonia solution (15%; 50ml) was added. The mixture

was stirred for a further 20min, and then extracted with dichloromethane (2x100ml). The organic phase was washed twice with water (2x100ml) and filtered through celite to remove trapped Cu(I)-salts ($[Cu(NH_3)_6]^+$). The combined organic layer was washed with brine (2x100ml), and then dried over $MgSO_4$. The organic solvent was removed under vacuum to give the crude product as a bright yellow a solid with yield of (0.98g; 74%); Recrystallisation from a mixture of CH_2Cl_2: CH_3OH (1:1) gave the product as colourless crystals (0.93g; 70%), mp. 128-129°C. ATR/IR: $\bar{\upsilon}(cm^{-1})$: 3128, 3099, 2947, 2919, 1597, 1592, 1566, 1549, 1471, 1271, 1238, 1212, 1176, 1148, 1031, 998, 813, 784 and 745. ^{1}HNMR data δ_H/ppm (400MHZ, CD_2Cl_2- d_2): 8.60-8.58 (1H, ddd, $^1J_{HH}$ = 0.92Hz , $^2J_{HH}$ = 1.83Hz, $^3J_{HH}$ = 5.04Hz, H_{14}), 8.57 (1H, s, H_8), 8.21-8.18 (1H, td, $^1J_{HH}$ = 0.92Hz , $^2J_{HH}$ = 1.37Hz, $^3J_{HH}$ = 7.79Hz , H_{11}), 7.82-7.77 (1H, dt, $^1J_{HH}$ = 1.83Hz, $^2J_{HH}$ = 7.79Hz, H_{12}), 7.70-7.67 (2H, d, J_{HH} = 8.70Hz, Ar-$H_{2,6}$), 7.35-7.33 (2H, d, J_{HH} = 8.24Hz, Ar-$H_{3,5}$), 7.26-7.23 (1H, ddd, $^1J_{HH}$ = 1.37Hz, $^2J_{HH}$ = 4.58Hz, ^3J = 7.33, H_{13}), 2.41 (3H, s, CH_3, H_7); ^{13}CNMR (100.63MHZ, CD_2Cl_2-d_2) δ_C/ppm: 21.14 (C_7), 120.34 (C_{11}), 120.37 (C_8), 120.56 (C_3,C_5), 123.26 (C_{13}), 130.56 (C_2,C_6), 135.05 (C_4), 137.13 (C_{12}), 139.40 (C_1), 149.14 (C_9), 149.89 (C_{14}), 150.48 (C_{10}). These assignments were confirmed using DEPT ^{13}C (135°), ^{1}H-^{1}H COSY and ^{1}H-^{13}C HMQC two dimensional correlations. HRMS (P+NSI): $[M+H]^+$ (100%): *m/z* = 237.1135 calculated for ($C_{14}H_{13}N_4$); found 237.1133.The fragment of the molecular ion plus H^+ $(M+H)^+$ $[(M-N_2)+H]^+$ (15%): calculated for ($C_{14}H_{13}N_2$); found *m/z* = 209.1133 [38]. Slow evaporation of a (1:1) CH_2Cl_2:CH_3OH solution of the ligand yielded crystals suitable for X-ray diffraction analysis.

6.3.1.3 Synthesis and characterisation of 2-[1-(4-methoxyphenyl)-1H-[1,2,3-triazol]-4-yl]-pyridine(L^3)

The method used was similar to that for (L^2), but with 1-azido-4-methoxy benzene (1g, 6.70mmol) instead of 1-azido-4-methylbenzene. The quantities of the other reagents were adjusted accordingly. An identical work-up procedure gave the required compound as a bright yellow solid (1.60g; 95%). The product was purified by silica gel column chromatography (95:5 CH_2Cl_2/MeOH) to give an off-white solid with yield of (1.57g; 93%); *Rf* = 0.43 (2:1 EtOAc/PE), mp. 129-130°C. ATR/IR: $\bar{\upsilon}(cm^{-1})$: 3142, 3006, 2844, 1604, 1592 1574, 1549, 1551, 1515, 1275, 1258, 1237, 1174, 1089, 1023, 996, 823 and 777. ^{1}HNMR data δ_H/ppm (400MHZ, CD_2Cl_2-d_2): 8.60-8.58 (1H, d, J_{HH} = 4.24 Hz, H_2), 8.53 (1H, s, H_{11}), 8.20 -8.18 (1H, d, J_{HH} = 7.90Hz, H_5), 7.83 - 7.79 (1H, dt, $^1J_{HH}$ = 1.72Hz, ^2J = 7.79Hz, H_4), 7.74-7.70 (2H, d, J_{HH} = 9.27Hz, $H_{13,17}$),

7.28-7.24 (1H, ddd, $^{1}J_{HH}$ = 0.92Hz, $^{2}J_{HH}$ = 4,92Hz,$^{3}J_{HH}$ = 7.44Hz, H_3), 7.08-7.06 (2H, d, J_{HH} = 9.16Hz, Ar-$H_{14,16}$), 3.88 (3H, s, CH_3, H_{19}); ^{13}CNMR (100.63MHZ, CD_2Cl_2-d_2) $\delta_{C/}$ppm: 56.06 (C_{19}), 115.17 ($C_{14,}$ C_{16} -Ar), 120.64 (C_{11}), 120.42 (C_5), 122.45 (C_{13}, C_{17} -Ar), 123.35 (C_3), 130.89 (C_{12}), 137.25 (C_4), 149.18 (C_7), 149.97 (C_2), 150.62 (C_6), 160.38 (C_{15}). These assignments were confirmed using DEPT ^{13}C (135°), ^{1}H-^{1}H COSY and ^{1}H-^{13}C HMQC two dimensional correlations. HRMS (P+NSI): $[M+H]^+$ (100%): *m/z* = 253.1084 calculated for ($C_{14}H_{13}N_4O$); found 253.1082. Slow evaporation of a 1:1 CH_2Cl_2:CH_3OH solution of the ligand yielded crystals suitable for X-ray diffraction analysis [39-41].

6.3.1.4 Synthesis and characterisation of 4-(4-(pyridin-2-yl)-[1H-1,2,3-triazol]-1-yl)benzoic acid (L^4)

The method used was analogous to that for (L^2), but with 4-azido benzoic acid (1g, 6.13mmol) instead of 1-azido-4-methylbenzene. The quantities of the other reagents were adjusted accordingly. An identical work-up procedure gave the required compound as a colourless solid (1.29g; 79%). Recrystallisation from a mixture of DMSO: CH_3OH: CH_3CN (2:8:8) gave a colourless solid with yield of (1.24g; 76%); mp. 337-339°C. ATR/IR: $\bar{\upsilon}$(cm^{-1}): 3141, 3003, 1687, 1603, 1588, 1573, 1549, 1553, 1403, 1302, 1269, 1240,1258, 1174, 1089, 1023, 991, 856, 768 and 692. ^{1}HNMR data δ_H/ppm (400MHZ, D_6MSO-d_6): 13.27 (1H, s, H_{18}), 9.46 (1H, s, H_{11}), 8.69-8.67 (1H, d, J_{HH} = 4.02Hz, H_2), 8.22-8.13 (5H, m, Ar -$H_{13,17,14,16,4}$), 7.99-7.94 (1H, dt, $^{1}J_{HH}$ = 1.93Hz, $^{2}J_{HH}$ = 7.63Hz, H_3), 7.44-7.41 (1H, dd, $^{1}J_{HH}$ = 6.48Hz, $^{2}J_{HH}$ = 7.25Hz, H_5); ^{13}CNMR (100.63MHZ, D_6MSO-d_6) $\delta_{C/}$ppm: 119.94 (C_5, C_{14}, C_{16}-Ar), 121.41 (C_{11}), 123.48 (C_3), 130.17 (C_{15}), 131.03 ($C_{13,}$ C_{17} -Ar), 137.37 (C_4), 139.46 (C_{12}), 148.43 (C_7), 149.26 (C_6), 149.72 (C_2), 166.39 (C_{18}). These assignments were confirmed using DEPT ^{13}C (135°C), ^{1}H-^{1}H COSY and ^{1}H-^{13}C HMQC two dimensional correlations. HRMS (N-NSI): $[M-H]^-$ (100%): calculated for ($C_{14}H_9N_4O_2$) *m/z* = 265.0731; found 265. 0723. Slow evaporation of a (1:4:4) DMSO: CH3OH: CH3CN solution of the ligand yielded crystals suitable for X-ray diffraction.

6.3.1.5 Synthesis and characterisation of 2-(1-(4-fluorophenyl)-1H-[1, 2, 3-triazol]-4-yl)pyridine (L^5)

The method used was analogous to that for (L^2), but with 1-azido-4-fluorobenzene (0.80g, 5.83mmol) instead of 1-azido-4-methylbenzene. The quantities of the other reagents were adjusted accordingly. An identical work-up procedure gave the required compound as a colourless solid. Recrystallisation from a mixture of CH_2CL_2: CH_3OH (1:1) gave a colourless solid with yield of (1.17g; 83%), mp 178-180°C. ATR/IR: $\bar{\upsilon}(cm^{-1})$: 3151, 3072, 3025, 1598, 1572, 1549, 1515, 1472, 1405, 1359, 1300, 1220, 1189, 1163, 1150, 1101, 1035, 994, 844, 782 and 782. ^{1}HNMR data δ_H/ppm (400MHZ, CD_2Cl_2-d_2): 8.60-8.59 (1H, dd, J_{HH} 4.58Hz, H_{13}), 8.58 (1H, s, H_7), 8.20-8.18 (1H, d, J_{HH} = 7.79 Hz, H_{10}), 7.84-7.78 (3H, m, H_{11}, Ar-$H_{2,6}$), 7.73-7.70 (td, $^1J_{HH}$ = 2.29Hz, $^2J_{HH}$ = 3.21 Hz, $^3J_{HH}$ = 9.16Hz), 7.29-7.24 (3H, m, H_{12}, Ar-$H_{3,5}$) 7.07-7.04 (td, $^2J_{H\text{-}F}$, $^1J_{HH}$ = 1.83Hz, $^2J_{HH}$ = 3.66Hz, $^3J_{HH}$ = 8.70Hz,); ^{13}CNMR (100.63MHZ, CD_2Cl_2-d_2) $\delta_{C/}$ppm: 116.98-117.20 ($^2J_{C\text{-}F}$ = 23.00Hz, C_3, C_5, Ar), 120.48 (C_7), 120.69 (C_{10}), 122.85-122.93 (d, $J^3_{C\text{-}F}$ = 8.63 Hz, C_2,C_6, Ar), 123.51 (C_{12}), 133.82 (C_1), 137.29 (C_{11}), 149.51 (C_8), 150.02 (C_{13}), 150.37 (C_9), (161.65-164.12) $J^1_{C\text{-}F}$ = 248.24Hz, (C_4). These assignments were confirmed using DEPT ^{13}C (135°), ^{1}H-^{1}H COSY and ^{1}H-^{13}C HMQC two dimensional correlations. HRMS (P+NSI): $[M+H]^+$ (100%): *m/z* = 241.0884 calculated for ($C_{13}H_{10}N_4F$); found 241.0885. The second fragment of the molecular ion plus H^+ $(M+H)^+$ calculated for ($C_{13}H_{10}N_2F$) $[(M-N_2)+H]^+$ (35%); found *m/z* = 213.0823. Slow evaporation of a (1:1) C_3H_6O:CH_3OH solution of the ligand yielded crystals suitable for X-ray diffraction analysis.

6.3.1.6 Synthesis and characterisation of 2-(1-(4-chlorophenyl)-1H-[1,2,3-triazol]-4-yl)pyridine (L^6)

The method used was similar to that for (L^2), but with 1-azido-4-chlorobenzene (0.65g, 4.23mmol) instead of 1-azido-4-methylbenzene. The quantities of the other reagents were adjusted accordingly. An identical work-up procedure gave the required compound as a colourless solid. Recrystallisation from a mixture of C_3H_6O: CH_3OH (1:1) gave a colourless solid with yield of (0.87g; 81%), mp. 203-205 °C. ATR/IR: $\bar{\upsilon}(cm^{-1})$: 3132, 3058, 1602 1589, 1570, 1570, 1550, 1473, 1440, 1421, 1399, 1355, 1236, 1174, 1145, 1114, 1091, 1037, 996, 817, 779 and 739. ^{1}HNMR data δ_H/ppm (400MHZ, CD_2Cl_2-d_2): 8.60 (1H, s, H_{11}), 8.59-8.58 (1H, ddd, $^1J_{HH}$ = 0.92Hz, $^2J_{HH}$ = 1.83 Hz, $^3J_{HH}$ = 5.04Hz, H_2), 8.20-8.18 (1H, dd, ^1J = 0.92Hz, $^2J_{HH}$ = 7.79Hz, H_5), 7.83-7.76 (3H, m, H4, Ar-$_{13,17}$), 7.56-7.52 (2H, d, J_{HH} = 9.16Hz, Ar-$H_{14,16}$), 7.28-7.25 (1H,

ddd, $^{1}J_{HH}$ = 0.92 Hz, $^{2}J_{HH}$ = 5.04Hz, $^{3}J_{HH}$ = 7.79Hz, H_3); ^{13}CNMR (100.63MHZ, CD_2Cl_2-d_2) $\delta_{C/}$ppm: 120.42(C_{11}), 120.57(C_5), 122.04 (Ar-$C_{13,17}$), 123.54 (C_3), 130.33 (Ar-$C_{14,16}$), 134.80 (C_{12}), 136.01 (C_{15}) 137.30 (C_4), 149.57 (C_7), 150.00 (C_2), 150.26 (C_6). These assignments were confirmed using DEPT ^{13}C (135°), ^{1}H-^{1}H COSY and ^{1}H-^{13}C HMQC two dimensional correlations. HRMS (P+NSI): $[M+H]^+$ (100%): *m/z* =257.0589 calculated for ($C_{13}H_9N_4Cl$); found 257.0590. The second fragment of the molecular ion plus H^+ $(M+H)^+$ $[(M+H)-(N_2)]^+$ (25%); found *m/z* = 229.0528 calculated for ($C_{13}H_9N_2Cl$). Slow evaporation of a (1:1) C_3H_6O:CH_3OH solution of the ligand yielded crystals suitable for X-ray diffraction analysis [45].

6.3.1.7 Synthesis and characterisation of 4-(4-(pyridin-2-yl)-1H-[1,2,3-triazol]-1-yl)benzonitrile (L^7)

The method used was analogous to that for (L^2), but with 4-azido-benzonitrile (1g,6.70mmol) instead of 1-azido-4-methylbenzene. The quantities of the other reagents were adjusted accordingly. An identical work-up procedure gave the required compound as a colourless solid. Recrystallisation from a mixture of CH_2Cl_2: CH_3OH (1:1) gave a colourless solid with yield of (1.57g, 91%), mp. 244-246°C. ATR/IR: $\bar{\upsilon}$(cm^{-1}): 3120, 3079, 2229, 1601, 1572, 1572, 1549, 1511, 1470, 1446, 1351, 1274, 1235, 1178, 1147, 1032, 998, 849, 782, and 742. ^{1}HNMR data δ_H/ppm (400MHZ, CD_2Cl_2-d_2): 8.70 (1H, s, H_{16}), 8.62-8.60 (1H, ddd, $^{1}J_{HH}$ = 0.92Hz, $^{2}J_{HH}$ = 1.83Hz, $^{3}J_{HH}$ = 5.04Hz, H_{14}), 8.22-8.20 (1H, d, J_{HH} = 7.79Hz, H_{15}), 8.01-7.99 (2H, d, J_{HH} = 9.16Hz, Ar-$H_{3,1}$), 7.89-7.87 (2H, d, J_{HH} = 8.70Hz, Ar-H7,10), 7.86-7.82 (1H, dt, ^{1}J = 1.83Hz, ^{2}J = 7.79Hz , H_{18}), 7.39-7.28 (1H, ddd, $^{1}J_{HH}$ = 0.92Hz, $^{2}J_{HH}$ = 4.58Hz, $^{3}J_{HH}$ = 7.79Hz, H_{19}); ^{13}CNMR (100.63MHZ, CD_2Cl_2-d_2) $\delta_{C/}$ppm: 112.77 (C_{12}), 118.21 (C_5), 120.23 (C_{16}), 120.65 (C_{15}), 120.93 ($C_{3,}$ C_{11} -Ar), 123.73 (C_{19}), 134.84 ($C_{7,}$ C_{10} -Ar), 137.39 (C_{18}), 140.21 (C_6), 149.93 (C_{17}), 150.02 (C_9), 150.12 (C_{14}). These assignments were confirmed using DEPT ^{13}C (135°C), ^{1}H-^{1}H COSY and ^{1}H-^{13}C HMQC two dimensional correlations. HRMS (P+NSI): $[M+H]^+$ (100%): *m/z* = 248.0931 calculated for ($C_{14}H_9N_5$); found 248.0933. The fragment of the molecular ion plus $H^+(M+H)^+$ $[(M-N_2)+H]^+$ (55%); found *m/z* =220.0871 calculated for $C_{14}H_9N_3$. Slow evaporation of a (1:1) CH_2Cl_2:CH_3OH solution of the ligand yielded crystals suitable for X-ray diffraction analysis.

6.3.1.8 Synthesis and characterisation of 2-(1-phenyl-1H-[1,2,3-triazol]-4-yl)pyridine (L^8)

The method used was analogous to that for (L^2), but with 1-azidobenzene (0.80g, 5.83mmol) instead of 1-azido-4-methylbenzene. The quantities of the other reagents were adjusted accordingly. An identical work-up procedure gave the required compound as a pale yellow solid with yield of (1.17g; 84%). Recrystallisation from a mixture of CH_2Cl_2:CH_3OH (1:1) gave a colourless solid with yield of (1.12g; 80 %), mp. 88-90°C (lit. 81-91°C [28]). ATR/IR: $\bar{\upsilon}$(cm^{-1}): 3116, 3051, 3001, 1599, 1591, 1567, 1544, 1502, 1471, 1405, 1354, 1237, 1189, 1147, 1091, 1035, 913, 843, 792, and 756. ^{1}HNMR data δ_H/ppm (400MHZ, CD_2Cl_2-d_2): 8.62 (1H, S, H_1), 8.61-8.59 (1H, ddd, $^1J_{HH}$ = 0.92Hz, $^2J_{HH}$ = 1.83Hz, $^3J_{HH}$ = 5.04Hz, H_7), 8.21-8.19 (1H, dt,$^1J_{HH}$ = 0.92Hz, $^2J_{HH}$ = 2.29Hz, $^3J_{HH}$ = 8.24Hz, H_4), 7.84-7.79 (3H, m, H_5, Ar-$H_{9,13}$), 7.59 - 7.55 (2H, d, J_{HH} = 7.73Hz, Ar-$H_{10,12}$), 7.50-7.45 (1H, ttt, $^1J_{HH}$ = 0.92Hz, $^2J_{HH}$ = 1.73Hz, $^3J_{HH}$ = 7.73Hz, H_{11}), 7.28-7.24 (1H, ddd, $^1J_{HH}$ = 1.73Hz, $^2J_{HH}$ = 5.04Hz, ^3J = 7.33Hz, H_6); ^{13}CNMR (100.63MHZ, CD_2Cl_2-d_2) δ_C/ppm: 120.41 (C_1), 120.41 (C_4), 120.72 (C_9, C_{13}-Ar), 123.35 (C_6), 129.12 (C_{11}), 130.11 (C_{10}, C_{12}-Ar), 137.18 (C_5), 137.39 (C_8), 149.29 (C_2), 149.92 (C_7), 150.39 (C_3). These assignments were confirmed using DEPT ^{13}C (135°C), ^{1}H-^{1}H COSY and ^{1}H-^{13}C HMQC two dimensional correlations. HRMS (P+NSI): $[M+H]^+$ (100%): *m/z* = 223.0978 calculated for ($C_{13}H_{10}N_4$); found 223.0977. The fragment of the molecular ion plus H^+ $(M+H)^+$ $[(M-N_2)+H]^+$ (35%); found *m/z* =195.0915 calculated for ($C_{13}H_{10}N_2$). Slow evaporation of a (1:1) CH_2Cl_2:CH_3OH solution of the ligand yielded crystals suitable for X-ray diffraction analysis [42-44].

6.3.1.9 Synthesis and characterisation of 2-(1-(4-(Trifluoromethyl)phenyl)-1H-[1,2,3-triazol]-4-yl)pyridine (L^9)

The method used was similar to that for (L^2), but with 1-azido-4-trifluoromethylbenzene (0.5g, 2.67mmol) instead of 1-azido-4-methylbenzene. The quantities of the other reagents were adjusted accordingly. An identical work-up procedure gave the required compound as a colourless solid with a yield of (0.613g; 78%). Recrystallisation from a mixture of CH_2Cl_2:CH_3OH (1:1) gave a colourless solid with yield of, (0.582g; 75%), mp. 168-170°C. ATR/IR: $\bar{\upsilon}$(cm^{-1}): 3122, 3060, 1615, 1593, 1570, 1547, 1528, 1472, 1409, 1322, 1279, 1237, 1191, 1161, 1104, 1066, 1027, 991, 847, 785, 746 and 694. ^{1}HNMR data δ_H/ppm (400MHZ, CD_2Cl_2-d_2): 8.70 (1H, s, H_{11}), 8.61-8.60 (1H, ddd, $^1J_{HH}$ = 0.95Hz, $^2J_{HH}$ = 1.83Hz, ^3J = 5.04Hz, H_2), 8.2-

8.19 (1H, dd, $^{1}J_{HH}$ = 0.92Hz, $^{2}J_{HH}$ = 7.79Hz, H_5), 8.01-7.99 (2H, d, J_{HH} = 8,70Hz, Ar-$H_{13,17}$), 7.85-7.78 (3H, m, $H_{4,14,16}$), 7.30-7.26 (1H, ddd, $^{1}J_{HH}$ = 1.37Hz, $^{2}J_{HH}$ = 5.04Hz, $^{3}J_{HH}$ = 7.33Hz, H_3); ^{13}CNMR (100.63MHZ, CD_2Cl_2-d_2) δ_C/ppm: 119.69 (C_{11}), 120.29 (C_{13}, C_{17}-Ar), 119.43, 122.14, 124.85, 127.27 (q, $^{1}J_{C-F}$ = 270.20Hz, C-F3 (C_{18})), 120.51 (C_5), 123.85 (C_3), 127.11, 127.14, 127.18, 127.21 (q, J^{3}_{C-F} = 3.83Hz, C_{14}, C_{16}-Ar), 130.28, 130.61, 130.94, 131.27 (q, $^{2}J_{C-F}$ = 32.59Hz, C-CF_3 (C_{15})), 137.04 (C_4), 139.31 (C_{12}), 149.39 (C_7), 149.51 (C_6), 149.55(C_2). These assignments were confirmed using DEPT ^{13}C (135°), ^{1}H-^{1}H COSY and ^{1}H-^{13}C HMQC two dimensional correlations. HRMS (P+NSI): $[M+H]^+$ (100%): *m/z* = 291.0852 calculated for ($C_{14}H_9N_4F_3$); found 291.0853.The fragment of the molecular ion plus H^+ $(M+H)^+$ $[(M-N_2)+H]^+$ (20%); found *m/z* = 263.0794 calculated for ($C_{14}H_9N_2F_3$). Slow evaporation of a (1:1) $C3H_6O$:CH_3OH solution of the ligand yielded crystals suitable for X-ray diffraction analysis.

6.4 Conclusion

In summary, a series of bi-dentate 2-pyridyl-1,2,3-triazole ligands bearing a 4-substituted phenyl arm (some of which are novel (L^4, L^7, L^5, L^9) at the time of writing this thesis), were synthesised from a variety of organic azides and alkynes via a simple cycloaddition reaction (literature method) under neat conditions and investigated. This method was also applied to generating a large number of novel complexes of bis-triazoles (49). A total of four years was spent synthesizing and characterising all the compounds reported in the thesis.

The L^2, L^3, L^8, L^6 ligands were described recently in the literature [38-47], with different functional groups (electron rich and withdrawing substituents) on the triazole heterocycle. In this work, it was demonstrated that the nature of the pendant arm (R = CH_3, OCH_3, COOH, F, Cl, CN, H, CF_3) could affect the electronic properties of the triazole moiety and the formation of metal complexes. Pyridine triazole ligands (PYTA) are readily prepared through a convenient click chemistry approach where thecopper(I)-catalyzed 1,3-dipolar cycloaddition is undertaken between 2-ethynylpyridine and an aryl azide prepared using standard procedures (see Appendix (1)) [23-26]. The reaction proceeds under mild conditions and affords the ligands regio-selectively in good yields. X-ray crystallography clearly indicates that the 1,2,3-triazole have an azo- character while the 1,2,4-triazole has an azine character.

These initial results can be considered promising, because they open up a new area for the modulation of the photophysical properties of pyridine-triazole ligands conjugated to a π-system. The exploration of the crystal structure of the ligand L^4reveals a one-dimensional zig-zag chain structure in the solid state, which is stabilised by intermolecular hydrogen bonds and π-π stacking interactions between the phenyl rings.
The success of these reactions highlights the need for future work in this area, which should include:

1-Design and synthesis of new 1,2,3-triazoles by using various other azides or using multi-azide as a starting material (i.e. bis(azide) or tris(azide)).
2-Studying the photophysical properties of the new 1,2,3-triazole ligands.
3-Computational studies for the formation of simple and complex 1,2,3-triazoles.
The yields have been reported in each specific synthesis report, and the novelty of the work has been reported in the Acta Crystallographica B paper that was published.

The next chapter focuses on the coupling of these bidentate (1,2,3-triazol-4-yl)-pyridine ligands to different transation metal to prepare a variety of organometallic complexes to be characterised and tested for dye solar cells and /or used in anticancer screening to determine their toxicity against selected cell lines.

6.5 References

1-Fotea C., D'Silva C., *Int. J. Adhes. Adhes.*25:442(2005)

2-Galardy R E., Craig L C., Jamieson J D., Printz M P., *J. Biol. Chem.*, 249:3510 (1974)

3-Edward P L., Boyd E H., Roland E B., *Biochem.*16:2581(1977)

4-Dyall L K., Wah W M., *Aust. J. Chem*. 38:1045(1985)

5-Todeschini A R., de Miranda A L P., da Silva K C M., Parrini S C., Barreiro E J., *Eur. J. Med. Chem.*, 33(3):189(1998)

6-Wender P A., Schaus. J M., White A W., *J. Am. Chem. Soc.*, 102:6159(1980)

7-Rafie H E., Mahmoud K K., *Spectrochim. Acta. Part A.*, 71:1688(2009)

8-Pizzotti M., Cenini S., Porta F., Beck W., Erbe J., *J. Chem. Soc. Dalton Trans.*, 1155:5075(1978)

9-Wentrup C., Reisinger A., Qiaob G G., Vissep P., *Pure. Appl. Chem.*, 69(4) 847(1997)

10-Sasaki T., Kanematsu K., Murata M., *Tetrahedron*., 27:5359(1971)

11-Colombano G., Travelli C., Galli U., Caldarelli A., Chini M G., Canonico P L., Sorba G., Bifulco G., Genazzani A A., *J. Med. Chem.*, 53:616(2010)

12-Kanyalkar M., Coutinho C. F., *Tetrahedron*, 56: 8775(2000)

13-Klump S P., Shechter H., *Tetrahedron Lett*. 43: 8421(2002)

14-Boga C., Vecchio E D., Forlani L., Mazzanti. A., Lario. C M., Todesco P E., Tozzi S., *J. Org. Chem.,*74:5568(2009)

15-Cmoch P., Korczak H., Stefani L., Webb G A., *J. Phys. Org. Chem.*, 12:470(1999)

16-Cmoch P., Wiench J W., Stefaniaka L., Webbb G A., *J. Mol. Struct.,* 510: 165(1999)

17-Cmoch P., Stefaniak L., Webb G A., *Magn. Reson. Chem.*, 35(13):237(1997)

18- Boyer J H., Miller E J Jr., *J. Am. Chem. Soc.*, 81: 4671(1959)

19-Zhang Q., Wang X., Cheng C., Zhu R., Liu N., Hu Y., *Org. Biomol. Chem*., 10: 2847(2012)

20-Kamalraj V K., Senthil S., Kannan P., *J. Mol.Struct.*, 892: 210(2008)

21-Nicolaides A., Enyo T., Miura D., Tomioka H., *J. Am. Chem. Soc.*,123: 2628(2001)

22-Oldo K., Hentzen J., Chabert F J D., Ducki S., Gani O A B. S. M., Sylte I., Skreden M., Florenes V A., Hansen T V., *Bioorg. Med. Chem.*, 16:4829(2008)

23-Cwiklicki A., Rehse K., *Arch, Pharm. Pharm. Med. Chem*. 337:156(2004)

24-Ciocoiu C C., Nikolic N., Nguyen H., Thoresen H G., Aasen A J., Hansen T V., *Eur. J. Med. Chem.,* 45:3047(2010).

25-Griffin R J., Calvert A H., Curtin N J., Newell D R., Golding B Th, US patent 5756510, May. 26, P.5-6, 1998 A2

26-Kurumi M., Sasaki K., Takata H., Nakayama T., *Hetrocycles*, 53:2809(2000)

27-Liu Q., Tor Y., *Org. Lett*. 5:2571(2003)

28-Galardy R E, Craig L C, Jamieson J D., Printz M P., *J. Biol Chem.*, 249:11:3510(1974)

29-Lau E P., Haley B E., Barden R E., *Biochemistry*, 16:2581(1977).

30-Fotea C., D'Sliva C., *Int. J. Adhes. Adhes*, 25:442(2005)

31-Bertolini G., Casagrande C., Santangelo F., US Patent 5081136., Jan. 14, P. 9-10(1992).

32-Ramlall p., McClelland R A, *J. Chem. Soc. Perkin Trans*., 2:225(1999)

33-Tanno M., Sueyoshi S., Kamiya S., *Chem. Pharm. Bull*., 30:3125(1982)

34-Spauschus H O., Scott J M., *J. Am. Chem. Soc*., 73, 208(1951)

35-Nicolaides A., Enyo T., Miura., Daisuke., Tomioka H., *J. Am. Chem. Soc.* 123:2628(2001)

36-Zhu Bing-Yan, Bauer., Shawn M J I A., Zhaozhong J., Probst., Gary D, Zhang., YanchenScarbprough., Robert M., E.U patent WO2006002099 A2, Jan, 5, P. 196, 2006.

37-Hu H., Anjiang Z., Ding L., Lei X., Zhang L., *Molecules,* 13:556(2008).

38-Kumar D., Reddy V B., *Synthesis*, 10:1687(2010)

39-Alonso F., Moglie Y., Radivoy G., Yus M., *Org. Biomol. Chem*., 9:6385(2011)

40-Park I S., Kwon M S., Kim Y., Lee S J., Park J., *Org. Lett.*, 10: 497(2008)

41-Park I S., Park J W., US. Patent 14. Jul:1(2011)

42-Sarkar B., Schweinfurth D., Pattacini R., S StrobelS., *Dalton Trans.*, 9291:(2009)

43-Crowley J D., Bandeen P H., Hanton, L R., *Polyhedron,* 29:70(2010)

44-McAdam C J., Crowley J D., Kilpin K J., Gavey E L., Anderson C B., Lind S J., Keep C C., Gordon K C., *Inorg. Chem*., 50: 6334(2011)

45-Wolff M., Munoz L., François A., Carrayon Ch., Seridi A., Saffon N., Picard C., Machura B., Benoist E., *Dalton Trans.*, 42:7019(2013)

46-Molina P., Ta´rraga A., RomeroT., Caballero A., *Org. Lett*., 11:3466(2009)

47-Sarkar B., Schweinfurt D., Sabine S., *Inorg. Chim. Acta*, 374: 253(2011)

48-Sun Sh., Wu P., *J. Phys. Chem. A*.114:8331(2010)

49-Policar C., Garcia L., Maisonneuve S., Xie J., Guillot R., Dorlet P., Riviere E., Desmadril M., Lambert F., *Inorg. Chem.*, 49:7282(2010)

50-Da Costa Ferreira A M., Alves W A., de Almeida Santos R H., Paduan-Filho A., Becerra C C., Borin A C., *Inorg. Chim. Acta*, 357:2269(2004)

51-Cao Z P., Dong W J., Dong H S., *Indian J. Chem. Sec. B*, 48:873(2009)

52-Naralais S., Jupally V R., Rao B A K S., *Asian*. *J. Pharm. Clin. Res.*, 5:89(2012)

53-Silverstein R M., Bassler G C., *Spectrometric Identification of Organic Compounds.,* 6th edition. New York: John Wiley and Sons (1998)

54-Bai Sh. Q., Leelasubcharoen S., Chen X., Koh L L., Zuo J L., Andy Hor T S., *Cryst. Growth Des.*, 10:1715(2010)

55-Cao Z P., Quan B., Dong H S., *J. Chin*. *Chem. Soc.*, 55:4(2008)

56-Dong H S., Dong H R., Zhang T Q., *J. Chem*.*Cryst*., 39: 32(2009)

57-Krstić V V., Uščumlić G S., Muškatirović M D., *J. Mol. Struct*.,174:247(1988)

58-Krstić V V., Uščumlić G S., Muškatirović M D., *J. Mol. Struct*.,174:251(1988)

59-Hansch C., Leo A., Taft R W., *Chem. Rev*., 97:165(1991)

60-Bunz U H F., Schweinfurth D., Hardcastle K I., *Chem. Comm*., 2203(2008)

61-Palatinus L., ChapuisG., *J. Appl. Crystallogr*., 40:786(2007)

62- Sheldrick G M., *ActaCrystallogr*., A64:112(2008)

63- Dolomanov O V., Bourhis L J., Gildea R J., Howard J A K., Puschmann H., *J. Appl. Crystallogr*., 42:339(2009)

64-MERCURY 3.1 (SUPPLIED WITH CAMBRIDGE STRUCTURAL DATABASE); CCDC: CAMBRIDGE, U.K., 2003−2004

65-Obata M., Yano S., Funabiki T., Mikata Y., Harada M., Hashimoto H., Kusumoto T., Kinoshita I., Tanaka R., Czaplewska J A., Kameyama C., Mori A., Kitamura A., *Dalton Trans.*, 3292(2008)

66-Zhao H., Wang G G., *Acta Cryst.E*, 68: o322(2012)

67-Zhao H., Lin J R., Yao J Y., *Acta Cryst.E*, 64: o1843(2008)

68-Ishak D H., Tajuddin A H A., Abdullah Z., Abd Halim S N., Tiekink E R T., *Acta. Cryst. E,* 67:o1658(2011)

69-Janiak C., *J. Chem. Soc. Dalton Trans*., 3885(2000)

70-Košmrlj J., Urankar D., Pinter B., Pevec A., De Proft F., Turel I., *Inorg. Chem.,* 49:4820(2010)

Chapter 7 : METAL COMPLEXES WITH CLICK (1,2,3-TRIAZOL-4-YL)-PYRIDINE LIGANDS

7.1 Introduction

After successfully synthesising a new series of bidentate (1,2,3-triazol-4-yl)pyridine ligands (see table 6.2), their ability to form metal-ligand complexes were investigated. The complex formation can occur with nitrogen from the pyridyl and nitrogen group of the 1,2,3-triazole unit (see Scheme 7.1). The first row transition metals were chosen due their availability and cost effectiveness and as alternatives to ruthenium metal, which is currently popular in solar cell dye research. The complexes were prepared in a 1:2 mole ratio of metal - ligand and characterised by different techniques such as: FT-IR, HRMS, NMR, UV-Vis, absorbance and fluorescence spectra, magnetic moments, conductivity measurements, melting points and X-ray molecular structure analysis. X-ray molecular structures revealed the coordination of the complexes which, in the majority of cases, had distorted octahedral geometry. In view of the large number of complexes prepared (49), the L^3 ligand complexes were selected with eight metal(II) ions see Table 7.1, based on the quality and abundance of the results obtained (X-ray quality crystals, crystallographic data and good yields) and also the Cu(II) complexes with ligands L^2-L^9 as representative examples for detailed discussion in this chapter. The characterisation data for the other complexes are presented in the Appendices (2).

7.2 Results and discussion

7.2.1 Synthesis of (1,2,3-triazol-4-yl)pyridine ligand metal complexes

The general approach for the synthesis of all the metal complexes carried out was according to a standard literature procedure, with small modifications as necessary. Appropriate metal chloride amounts (1equiv.), were reacted with all ligands (2 equiv.) under the same conditions. CH_3OH and DCM were used as solvents and the mixtures were stirred at RT for 8-10h. The solvent was removed under vacuum and the solid mass recovered and then washed with several volumes of cold methanol and diethyl ether [1]. This approach was used to prepare metal complexes between ligands L^2, L^3, L^4, L^5, L^6, L^7, L^8 and L^9 with the first row transition metal chlorides (Mn(II), Fe(II), Co(II), Ni(II), Cu(II) and Zn(II)), the second row transition metal chloride of Cd(II) and the third row transition metal chloride of Pt(II). Except in cases of the complexes of ligand L^4 where DMSO was used as a solvent, all the other reactions employed methanol and dichloro-methane. The reactions were refluxed for 24h. This is due to fact that L^4 ligand has a carboxylic group that is poorly soluble in many organic solvents. Similar observations were reported for btp 2,6-Bis(1-(4-(carboxy)benzyl)-1,2,3-triazol-4-yl)pyridine [1]. This method was very satisfactrory and good yields ranging from 74-91% (see Table 7.1 for exact yields) were obtained.

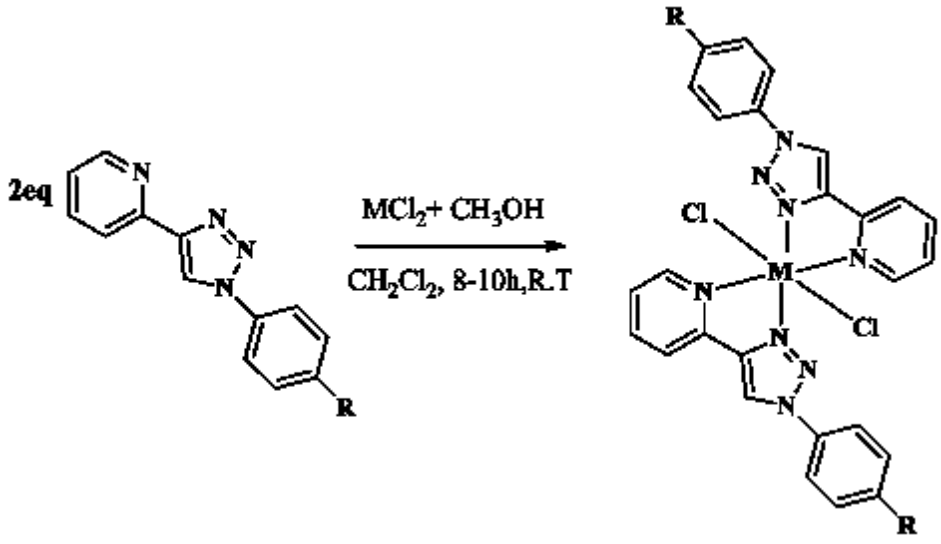

Where, R = L^2 = CH_3, L^3 = OCH_3, L^4 = COOH, L^5 = F, L^6 = Cl, L^7 = CN, L^8 = H and L^9 = CF_3

Scheme 7.1: Synthesis of the various metal complexes [2]

Table 7.1: Molecular structure, formula weight and yield of the metal-L^3 complexes.

Molecular structure	Formula weight	Sample code	Yield (%)
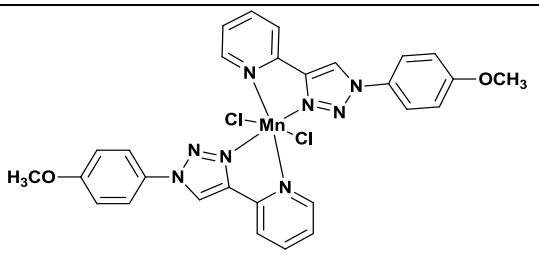	$C_{28}H_{24}Cl_2N_8O_2Mn$	$[MnL^3(1\text{-}2)]$	82
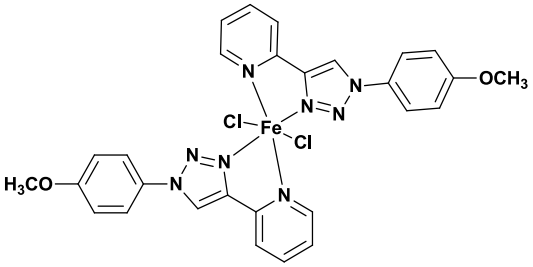	$C_{28}H_{24}Cl_2N_8O_2Fe$	$[FeL^3(1\text{-}2)]$	83
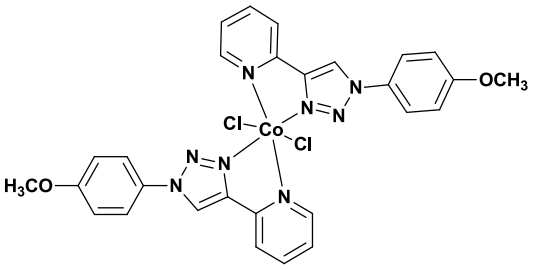	$C_{28}H_{24}Cl_2N_8O_2Co$	$[CoL^3(1\text{-}2)]$	77
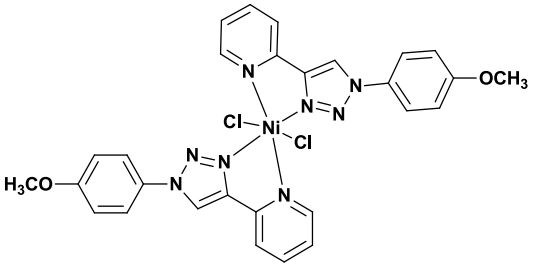	$C_{28}H_{24}Cl_2N_8O_2Ni$	$[NiL^3(1\text{-}2)]$	74
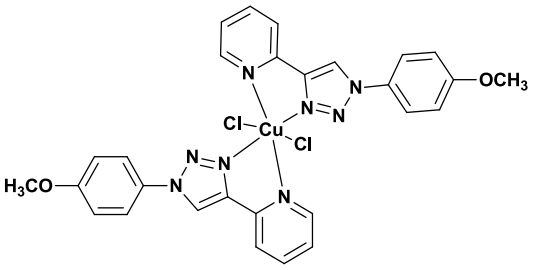	$C_{28}H_{24}Cl_2N_8O_2Cu$	$[CuL^3(1\text{-}2)]$	91

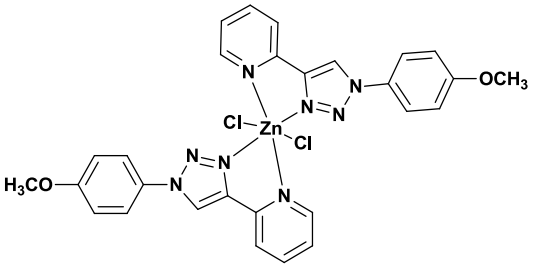	$C_{28}H_{24}Cl_2N_8O_2Zn$	$[ZnL^3(1\text{-}2)]$	77
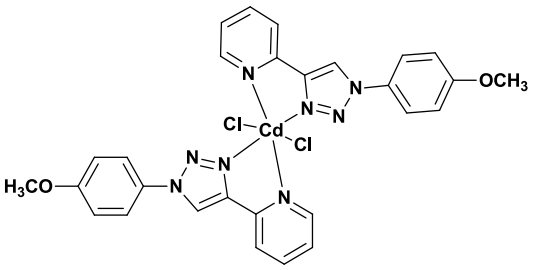	$C_{28}H_{24}Cl_2N_8O_2Cd$	$[CdL^3(1\text{-}2)]$	80
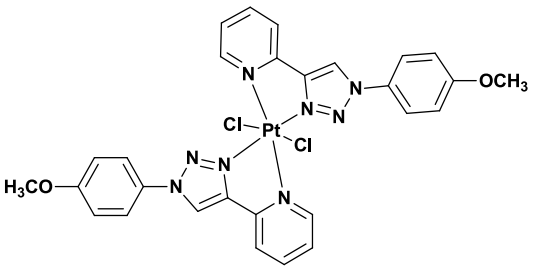	$C_{28}H_{24}Cl_2N_8O_2Pt$	$[PdL^3(1\text{-}2)]$	78

7.2.2 FTIR spectral data for L^3 complexes

An overlay of the IR spectra of L^3 and its various metal complexes is presented in Figure 6.1. The aim of these measurements is to observe any shift which may occur to the characteristic bands for the functional groups upon complex formation. The IR spectra of the metal complexes exhibited bands with appropriate shifts due to complex formation (see Table 7.2). The ν(C=N) stretching band of the pyridine moiety is observed at the value around 1604cm^{-1} for the free ligand, which is shifted to higher wavenumbers in the complexation depending on the nature of the metals ion. The bands are shifted to around 1630-1606cm^{-1} for the various complexes. It is interesting to observe that the M–$N_{(PY)}$ (pyridine nitrogen-cadmium complex) bond length is longer (as shown in the crystal structure) than the other metals. This difference is reflected in the vibrational energies in the FTIR spectrum in terms of the M–$N_{(PY)}$ bond which is shifted to higher wavenumbers compared to the other metal complexes (Figure 7.1).

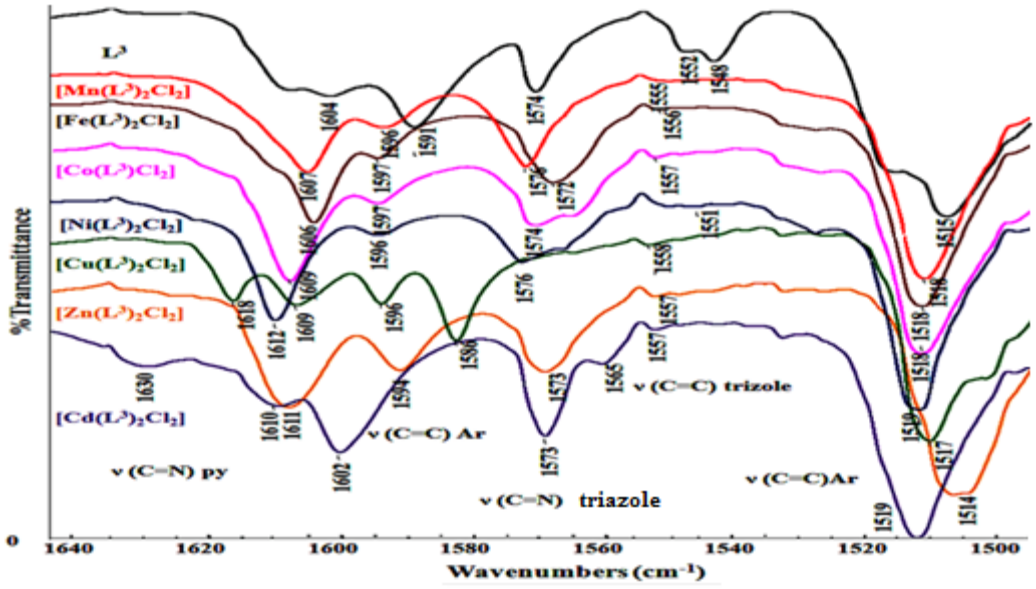

Figure 7.1: FTIR spectra of the L^3 ligand with its various metal complexes.

The IR spectra of the metal complexes exhibited bands shift due to complex formation (see Table 7.2). This indicate coordination of the nitrogen of the C=N pyridine moiety to the different metal atoms. The ν(C=C) bands of phenyl ring for the complexes, which usually appear as two absorptions are around 1602-1591cm^{-1} and 1514-1518cm^{-1}, compared with those at 1596 and 1515cm^{-1} in the free ligand [3-4]. The ν(C=N) absorption band of the triazole moiety around 1574cm^{-1} in the free ligand is detected around 1572-1586cm^{-1} in the metal complexes, while the ν(C=C) absorption band of the triazole moieties which appear at 1552cm^{-1} in the free ligand is detected around 1551-1565cm^{-1} in the metal complexes, as indicated in Table (7.2). Moreover, the ν(N=N) stretching absorption band for the triazole ring appeared around 1430-1400cm^{-1} [5-7], the ν(N=N-N) absorption band of triazole moiety is observed at 997-983cm^{-1}[8]. The important characteristics bands are presented in Table (7.2).

Table 7.2: IR frequencies in wavenumber (cm^{-1}) units of the ligands (L^3) and the metal-L^3complexes.

Compound	ν(C=N)$_{py}$, ν(C=C)$_{Ar}$, ν(C=N)$_{triaz}$ conj.	ν(C=C)$_{triaz}$	ν(N-N)$_{triaz}$	ν(C=C)$_{Ar}$	ν(C-N)
L^3	1604, 1592, 1574	1552	1154,1022	1515	1258
$[Mn(L^3)_2Cl_2]$	1607, 1596, 1576	1555	1157,1030	1518	1254
$[Fe(L^3)_2Cl_2]$	1607, 1597, 1572	1556	1147,1028	1518	1261
$[Co(L^3)_2Cl_2]$	1609, 1597, 1574	1557	1146,1028	1518	1254
$[Ni(L^3)_2Cl_2]$	1612, 1597, 1576	1551	1147,1028	1519	1263
$[Cu(L^3)_2Cl_2]$	1618, 1608, 1597,1572	1558	1149,1026	1517	1250
$[Zn(L^3)_2Cl_2]$	1610, 1594, 1573	1557	1141,1027	1514	1253
$[Cd(L^3)_2Cl_2]$	1630, 1602,1573	1565	1156,1030	1519	1268
$[Pt(L^3)_2Cl_2]$	1616, 1600,1592	1576	1169,1010	1511	1257

7.2.3 Magnetic moments, electronic absorption spectra and conductivity measurements

The introduction to magnetic susceptibility is given in Physical Appendix (Chapter11.2.6). The calculated μ_{eff} values, conductivity measurements and UV-Vis spectral data for the L^3-complexes are listed in Table (7.3).

Table 7.3: UV-Vis spectral data of L^3 complexes in DMSO solutions.

Compound	Band Position λ_{max}(nm)	Wave number (cm^{-1})	Extinction coefficient ε_{max} ($dm^3mol^{-1}cm^{-1}$)	Assignment	μ_{eff} B.M	Conductivity Λ_M ($\Omega^{-1}cm^2mol^{-1}$)
L^3	285	35087	24375, ($4x10^{-6}$M)	Intra - ligand, π→π*,n→ π*		
$[Mn(L^3)_2Cl_2]$	258, 291	38759, 34364	6210,3059, ($5x10^{-6}$M)	Intra - ligand, π→π*, n→ π*	5.32	52
	352,	28409,	32, ($1x10^{-3}$M)	CT		
	369	27100	30, ($1x10^{-3}$M)	$^6A_1g \rightarrow {}^4T_1g$		
	390	25641	21, ($1x10^{-3}$M)			
$[Fe(L^3)_2Cl_2]$	257, 291	39062, 34364	35500, 17500, ($6x10^{-6}$M)	Intra – ligand, π→π, n→π*	5.07	54
	333	30030	3810, ($8x10^{-5}$M)	CT		
	922	10845	65, ($8x10^{-5}$M)	$^5T_2g \rightarrow {}^5E_2g$		
$[Co(L^3)_2Cl_2]$	257, 292	38910, 34246	26625, 11000, ($8x10^{-6}$M)	Intra - ligand π→π*, n→ π*	3.97	42
	615	16260	38, ($1x10^{-3}$M)	$^4T_1g\,^{(F)} \rightarrow {}^4T_1g\,^{(P)}$		
	677	14771	61, ($1x10^{-3}$M)	$^4T_1g\,^{(F)} \rightarrow {}^4A_2g\,^{(F)}$		
$[Ni(L^3)_2Cl_2]$	257, 291	39682, 34364	30000, 18167 ($6x10^{-6}$M)	Intra-ligand π→π*,n→π*	2.73	54
	407	24570	61, ($1x10^{-3}$M)	$A_2g\,^{(F)} \rightarrow {}^3T_1g\,^{(p)}$		
	660	15151	43, ($1x10^{-3}$M)	$^3A_2g\,^{(F)} \rightarrow {}^3T_1g\,^{(F)}$		
$[Cu(L^3)_2Cl_2]$	257, 287	39682, 34843	39200, 19800, ($5x10^{-6}$M)	Intra - ligand π→π*, n→ π*	1.69	24
	892	11210	97, ($1x10^{-3}$M)	$^2B_1g \rightarrow {}^2B_2\,g$		
$[Zn(L^3)_2Cl_2]$	257, 291	39682, 34364	41333, 13833, ($6x10^{-6}$M)	Intra - ligand π→π*, n→ π*	diamagnetic	12
$[Cd\,(L^3)_2Cl_2]$	258, 286	38759, 34965	43332, 42308, ($2.6x10^{-6}$	Intra - ligand π→π*, n→ π*	diamagnetic	18

7.2.4 UV-Vis Spectral data for L^3 complexes

In the studies the UV-Vis spectral data were performed on the complexes, with the general formula $[M(L^n)_2Cl_2]$. The complexes were prepared in DMSO (where: M= Mn(II), Fe(II), Co(II), Ni (II), Cu(II), Zn(II) and Cd(II); n = 2 = CH_3, 3 = OCH_3, 4 = COOH, 5 = F, 6 = Cl, 7 = CN, 8= H, 9 = CF_3). These studies covered different concentrations of the complexes. Varying and increasing the concentration allows one to observe the forbidden d-d transitions. In general, the electronic spectra of the metal ion with different ligands having various substituents (R= CH_3, OCH_3, COOH, F, Cl, CN, H, CF_3) display an analogous pattern for d-d transitions, and indicate that the substituents imposed have no-effect on the splitting of the d-d orbitals. The final concentration of each complex is shown in Table 7.3. The UV-Vis spectral data for all complexes, Figures, are depicted in Physical Appendix (Chapter 11 see sections 11.2.2 to 11.2.5).

7.2.5 Conductivity measurements

Conductivity measurements were carried out by using 10^{-3}M concentrations of the complexes in DMSO (294 K) following instructions from the manufacturer. The molar conductivities of the complexes ranged from 6 -77 $\Omega^{-1}cm^2mol^{-1}$ at 294 K. The low values indicate that the chloride anions bind to the metal ions as co-ligands and do not ionize. The low conductivity values are indicative of the complexes having 1:2 metals - ligand stoichiometry of the type ML_2Cl_2, where L acts as a bidentate ligand [9]. The higher values than expected for the [M] values are usually due to the possible displacement of one chlorine atom ligand by a one molecule of the solvent DMSO in the complexes and produced intermediate behaviour $[ML_2(Cl)(DMSO)]$. Cl between those of non-electrolytes and 1:1 electrolyte. Similar behaviours were observed for several complexes, mainly measured in DMSO solvent, because this solvent is a strong donor with profitable steric properties [10, 11].

7.2.6 Magnetic moment measurements

The calculated μeff values for the L^3- complexes are listed in Table 7.3 and an introduction to the subject is detailed in Physical Appendix 11.2.6. Magnetic susceptibility measurements were conducted as per instructions from the manufacturer. Magnetic susceptibility measurements were performed using Guoy's method [76]

7.2.7 Fluorescence emission spectral data for L^3 and its complexes

The fluorescence spectra of the trizole-based ligand and its various metal M(II) complexes [M = Mn(II), Fe(II), Co(II), Ni(II), Cu(II), Zn(II) and Cd(II)], were investigated in DMSO at room temperature (294 K). See Chapter 11 Physical Appendix (11.2.7-11.2.10) for an introduction to fluorescence. Weakly fluorescence intensity with a low quantum yield was observed. The fluorescence and quantum yield was determined by using 1,1':4'1"-terphenyl (PTP) dye as a reference. This standard was chosen because its wavelength was nearest to that of the ligand and the complexes synthesised. The ligand, complexes and the reference dye were excited at 276nm, maintaining nearly equal absorbance (0.0954), and the emission spectra were recorded from 285 to 550nm. All experiments were carried out at a concentration of $1x10^{-6}$ M. The fluorescence spectrum of the free p-terphenyl when excited at 276nm showed a maxima band at 345nm and 332nm with fluorescence intensity 2720nm and a Stokes shift of $\Delta\lambda$ = 69nm and 2218nm with a Stokes shift of $\Delta\lambda$ = 56nm. The quantum yield was Φf= 1.0 at a concentration of ($1x10^{-6}$ M) [12], as shown in Figure 7.2.

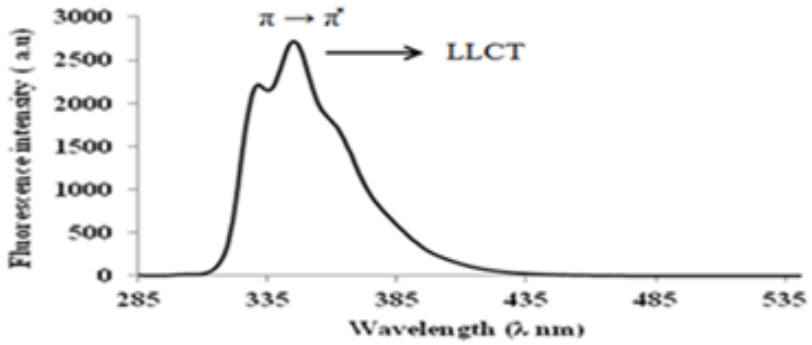

Figure 7.2: The fluorescence emission spectrum of PTP in DMSO, excited at 276 nm (C= $1X10^{-6}$M).

The free L^3 ligand emits a weak fluorescence spectrum when excited at 276nm and showed maxima bands at 345nm and 332nm with fluorescence intensity 89 and a Stokes shift of $\Delta\lambda$ = 56nm and intensity 104 with a Stokes shifts of $\Delta\lambda$ = 59nm.These can be attributed to a ($\pi\rightarrow\pi^*$) transition and LLCT transfer. The quantum yield was Φf= 0.04 at a concentration of $1x10^{-6}$ M [13-16] as shown in Figure 7.3.

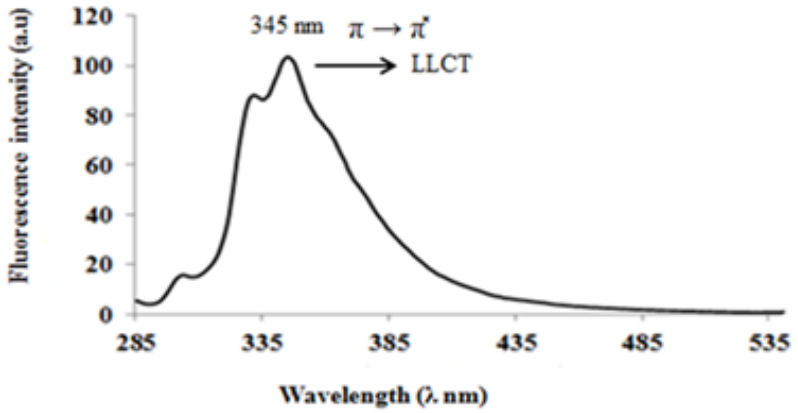

Figure 7.3: The fluorescence emission spectrum of L^3 in DMSO excited at 276 nm (C= 1X10^{-6}M).

Overall the fluorescence emission spectra of the complexes with the L^3 ligand is presented in Figure 7.4 and showed a weak fluorescence relative to the standard PTP. The Stokes shift, fluorescence intensity and quantum yield of the metal complexes having the general formula $[M(L^3)_2Cl_2]$ where [M = Mn(II), Fe(II), Co(II), Ni(II), Cu(II), Zn(II) and Cd(II)] are listed in Table 7.4. Furthermore, the emission spectra for the complexes is depicted in Figure 7.4 and were characterised by the emission band around 345-346nm. The quenching of the fluorescence is related to the complexation of the ligand by transition metal ions and is a rather common phenomenon, which is explained by processes such as magnetic perturbation, redox activity, and electronic energy transfer or by the solvent effect [17-18]. Additionally, upon complexation of the ligand, the maximum photoluminescence peak shifted to 344-346 nm with a wavelength excitation of 276nm. This emission band probably originates from a ($\pi \rightarrow \pi^*$) transition, which can be assigned to ligand-to-ligand charge transfer (LLCT).

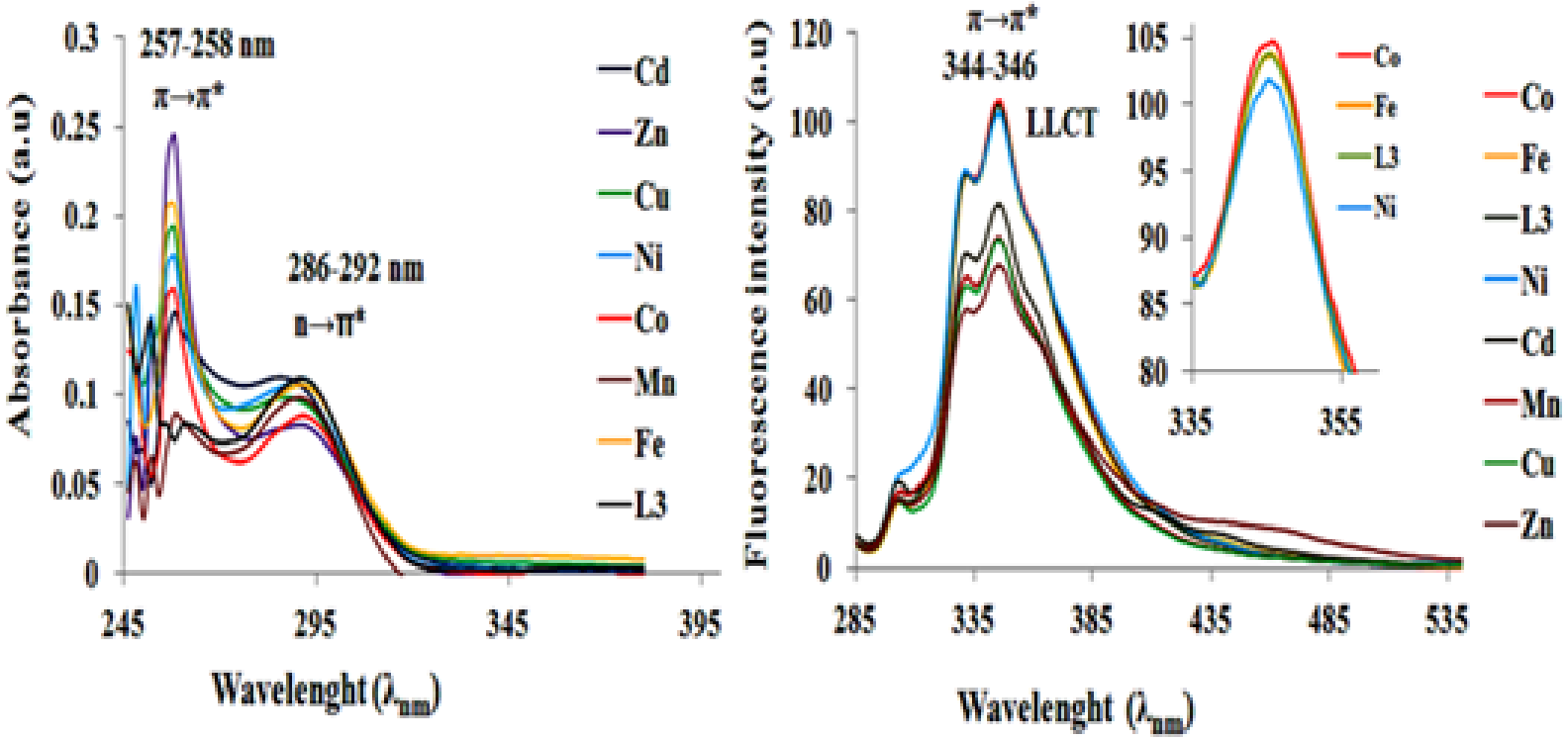

Figure 7.4: The fluorescence emission spectra of L^3 ligand and complexes in DMSO excited at 276 nm (C= $1X10^{-6}$M).

Table 7.4: Photoluminescence spectra of the ligand L^3 and its various complexes in DMSO (10^{-6} M); samples were excited at λ_{max} (ex) = 276 nm.

Compound	Intensity	Emissions ($\lambda_{em})_{nm}$, C=1X10^{-6} M	Stokes shift $(\Delta\lambda)_{nm}$	Quantum yield % ($\Phi f_)$
PTP	2720	332	56	1.0
	2218	345	69	
L^3	89	332	56	
	104	345	69	0.040
$[Mn(L^3)_2Cl_2]$	65	332	56	
	74	346	70	0.032
$[Fe(L^3)_2Cl_2]$	88	332	56	
	103	346	70	0.045
$[Co(L^3)_2Cl_2]$	89	332	56	
	104	346	70	0.050
$[Ni(L^3)_2Cl_2]$	89	331	55	
	102	345	69	0.041
$[Cu(L^3)_2Cl_2]$	63	332	56	
	74	346	67	0.034
$[Zn(L^3)_2Cl_2]$	58	332	56	
	68	345	69	0.047
$[Cd(L^1)_2Cl_2]$	70	332	41	
	82	346	55	0.037

The trend of Table 7.4 shows that the quantum yield of the complexes is low compared to the standard PTP and that the complexes have similar properties amongst them.

7.2.7.1 The fluorescence emission spectral data for Cu(II) complexes with L^2-L^9 ligands

The optical properties of the Cu(II) complexes with various ligands L^2 - L^9 were studied and investigated by using UV/Vis and fluorescence spectroscopy were recorded in DMSO solutions, and excited at wavelengths corresponding to at 276nm for (L^2 - L^9) complexes and 281nm for L^4 complexes repectively.

The fluorescence spectra of the Cu(II) complexes, depicted in Figure 7.5, showed weak fluorescence. Quantum yields, emission maxima intensity and Stokes shifts of Cu(II) complexes are summarised in Table 7.5.

The fluorescence spectrum of the $[Cu(L^4)_2Cl_2]$ complex yield maximum emission peaks at 399nm, 421nm and 443nm (under 281 nm excitation). Stokes shifts at 123,145 and 167nm respectively, occurred when the same Cu complexes have different ligands. The emission of the complex may be attributed to the ligand-centred $\pi \rightarrow \pi^*$ LLCT (ligand-to-ligand charge transfer), MLCT (metal-to-ligand charge transfer) or intraligand $\pi \rightarrow \pi^*$ transitions. These shifts may be attributed to the difference in the excited state between the ligands and Cu complex [14-16]. The triazole as dyes can be easily designed for specific sensors as needed. The electron donating/withdrawing capacity of the modified groups on the triazole can also be used to help design dyes. Using Hammett sigma plots, such as Figures 7.6 and 7.7, comparisons were made to the UV-VIS maximum absorption and wavelength. The trends in these optical properties of the complexes are influenced by the electron donating/withdrawing groups on the trizaole ligands which affect the conjugated π-electron system. These trends clearly show that substituents can enhance or decrease the optical properties performance of a dye, with potential to lead to the development of promising materials for potential DSSCs.

Table 7.5: Optical properties of the Cu Complexes with ligands (L^2-L^9) in DMSO, excited at 276-281 nm (C= 1X10^{-6} M).

Compound	Intensity	Emissions ($\lambda_{em})_{nm}$, C=1X10^{-6} M	Stokes shift $(\Delta\lambda)_{nm}$	Quantum yield % ($\Phi f_)$
PTP	2720	332	56	1.0
	2218	345	69	
$[Cu(L^2)_2Cl_2]$	14	303	17	0.010
	15	331	45	
	15	303	13	
$[Cu(L^3)_2Cl_2]$	63	332	41	0.034
	74	346	59	
$[Cu(L^4)_2Cl_2]$	11	303	27	0.054
	79	399	123	
	86	421	145	
	48	443	167	
$[Cu(L^5)_2Cl_2]$	13	302.5	16.5	0.010
	25	344.5	58.5	
$[Cu(L^6)_2Cl_2]$	12	303	15	0.0079
	12	332	44	
	12	343	57	
$[Cu(L^7)_2Cl_2]$	12	303	4	0.016
	26	345	46	
	18	374	75	
$[Cu(L^8)_2Cl_2]$	23	309	24	0.053
	99	332	47	
	110	345	60	
$[Cu(L^9)_2Cl_2]$	12	302	15	0.0095
	13	331	44	
	14	344	57	

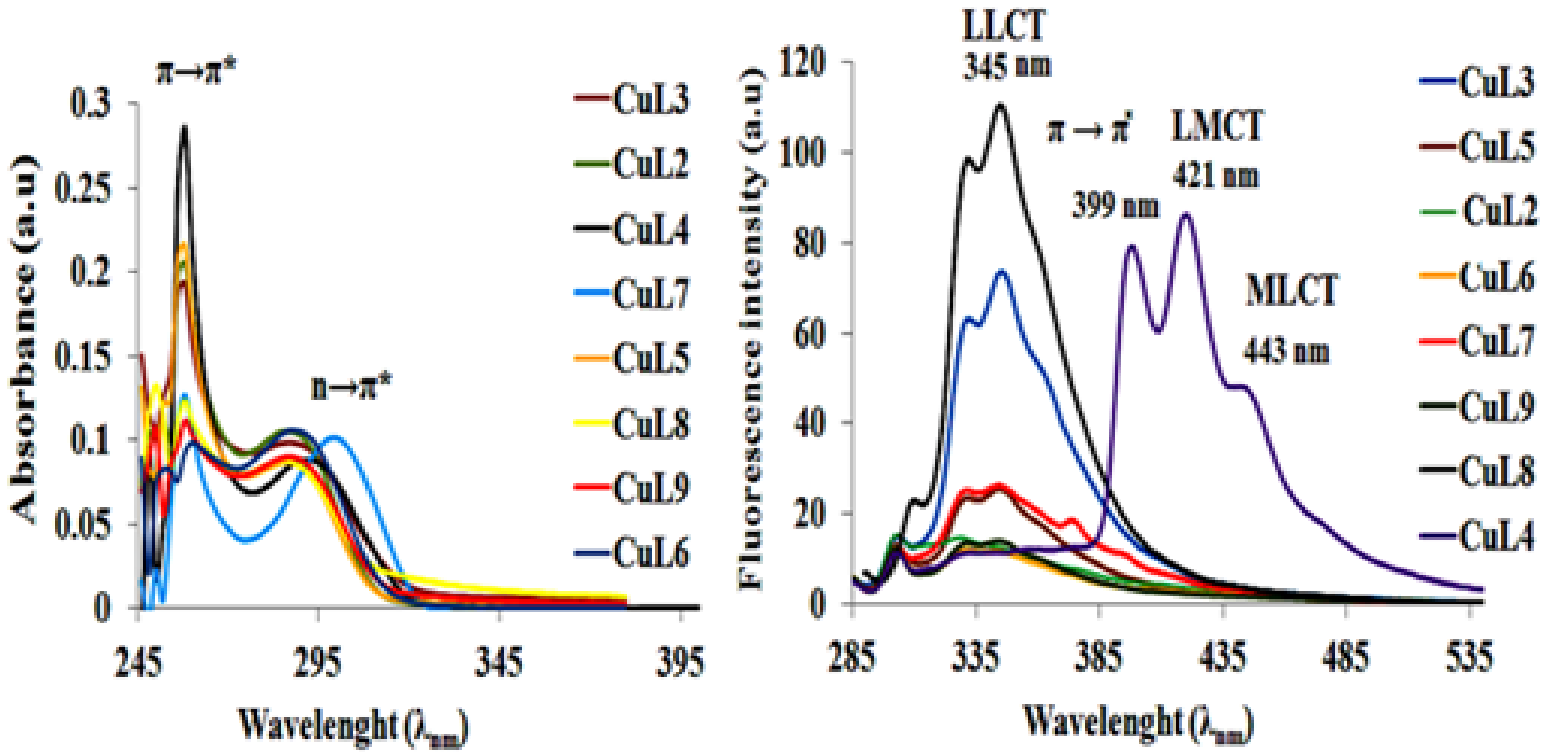

Figure 7.5: The UV-Vis and fluorescence emission spectra of Cu(II) with ligands (L^2-L^9) in DMSO excited at 276-281 nm (C= $1X10^{-6}$M).

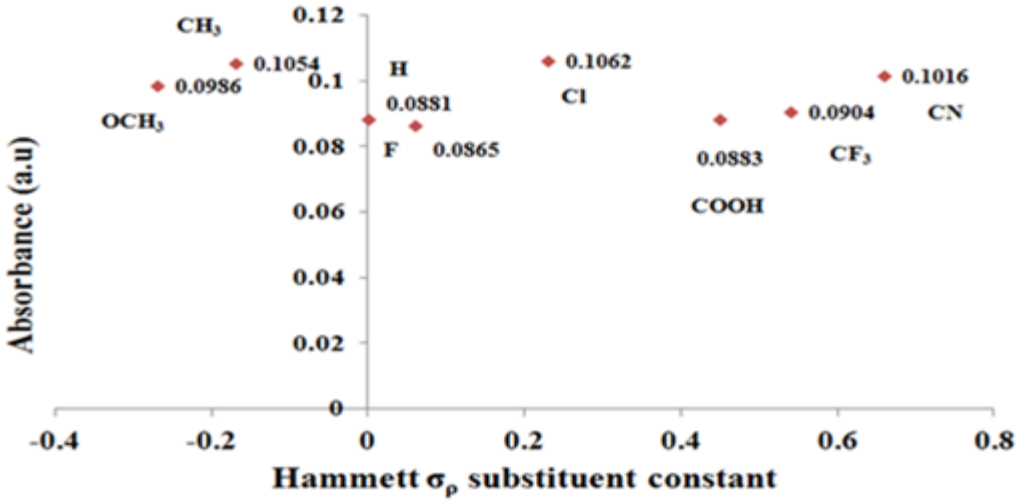

Figure 7.6: Hammett plot of absorbance maximum of Cu complexes with ligand (L^2-L^9) *vs.* σ_p values of the *para* substituent in DMSO (C= 1X10^{-6}M).

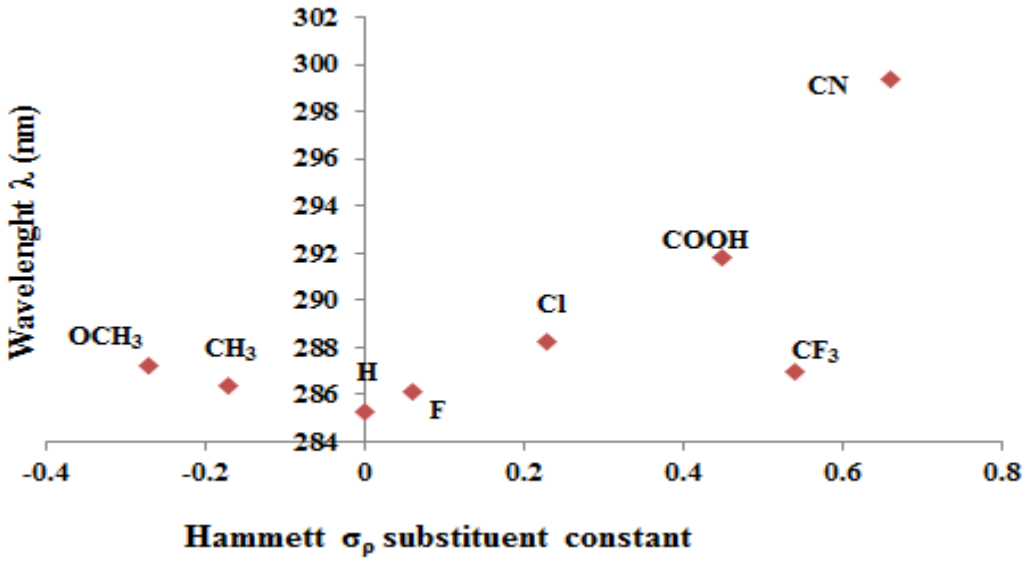

Figure 7.7: Hammett plot of wavelength of Cu complexes with ligands (L^2-L^9) *vs.* σ_p values of the *para* substituent in DMSO (C= 1X10^{-6} M).

7.2.8 Mass spectra for complexes

Of the available mass spectral techniques, positive ion TOF- electrospray (TOF MS ES+), (TOF-MOLDI-MS) and positive ion nano-electrospray (PSI) proved to be the most satisfactory techniques for the analysis and measurement of poorly soluble high MW metal complexes, such as these formed with ligands L^2-L^9. However, the molecular ion peak $[M(L^n)_2Cl_2]^+$, which corresponds to the molecular weight of the metal complexes, is not observed and the value is due to it being unstable. Only the secondary fragment ions were observed and the value is after the loss of one or more chlorine anions, ligand or metal atom using this approach. The high resolution mass spectra (HRMS) is observed and the value is were therefore undertaken on the highest MW secondary fragment ion peak $[M(L^n)_2Cl]^+$ produced after loss of a chloride anion, from the molecular ion. Therefore, the structures of these complexes have been determined on the HRMS of the secondary fragment ion $[M(L^n)_2Cl]^+$. Figure 7.8 is an example spectrum showing these different fragmentation species for the $[Cu(L^3)_2Cl_2]$ complex, while the calculated mass spectrum of complex $[Cu(L^3)_2Cl_2]$ is presented in Figure 7.9.

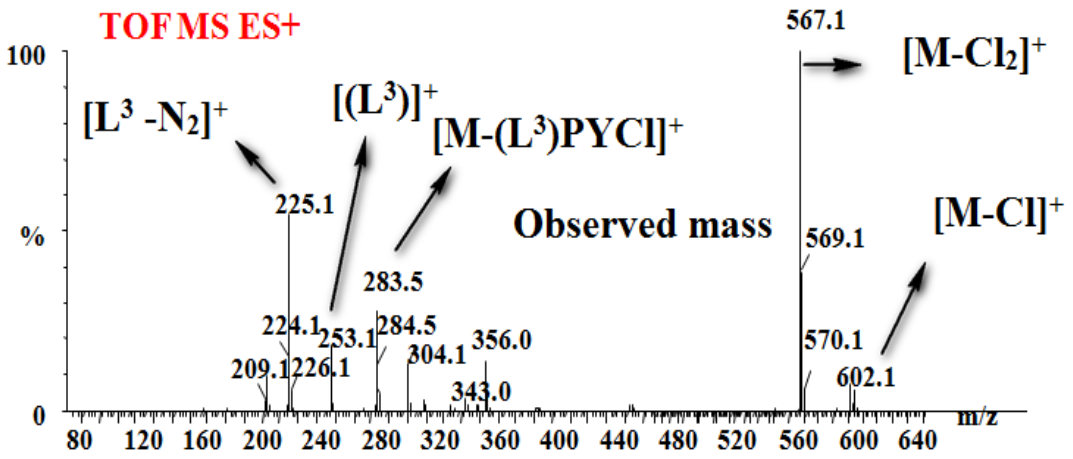

Figure 7.8: TOF MS ES (+) mass spectrum of the complex $[Cu(L^3)_2Cl_2]$.

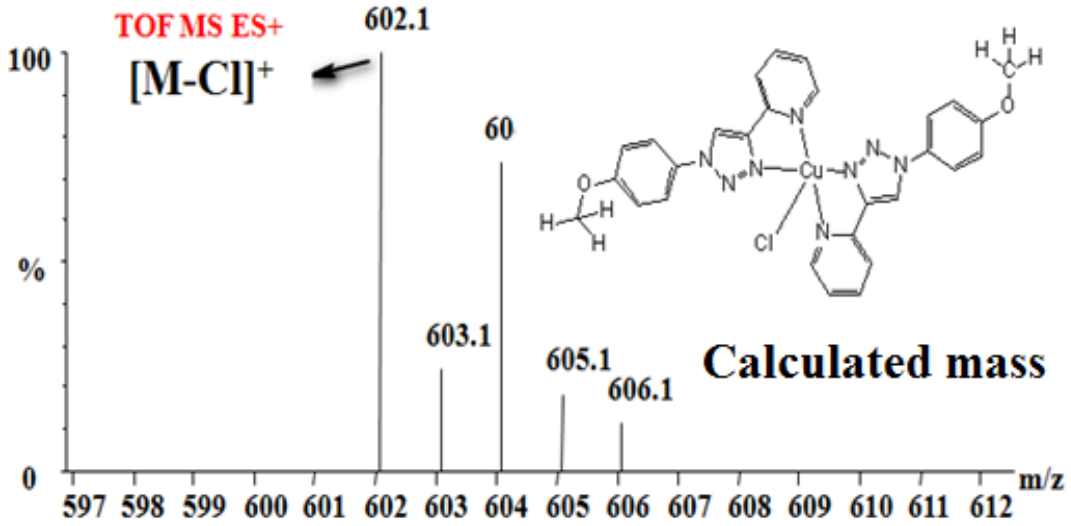

Figure 7.9: The calculated mass spectrum of the complex $[Cu(L^3)_2Cl_2]$

The mass spectroscopic pattern is observed and the value for the ratio of 1:2 (M:L) metal complexes formed with ligands L^2- L^9 by positive ion TOF- electrospray, are shown in Scheme 7.2. The molecular ion as stated was not observed, but eight secondary fragments were seen which were ascertained to have been formed by one of six different pathways, generalised and depicted in Scheme 7.2. The initial loss of either a chloride anion gives $[M(L^n)_2Cl]^+$ or two chloride ions yield $[M(L^n)_2]^+$, which was the base peak (100%) in some cases, eg. the Cu complex (see Table 7.6). Similar fragments pattern observations were reported recently for bis [1-(cyclohexyl)-4-(2-pyridyl)-1,2,3-triazole] with $NiBr_2$ [19].

Loss of a chloride anion and a ligand fragment($-Cl+C_{10}H_{11}N_3O$) gave $[M(L^n)pyCl]^+$ via pathway A, where the pyridine fragment of the ligand remained coordinated to the metal as shown in Scheme 7.2. This peak was the base peak (100%) for the Mn(II), Fe(II), Co(II) and Ni(II) complexes, see eg. Table 7.6 Loss of two chloride anions, the methoxy group from the ligand and one ligand ($-L^3 + Cl_2 + (OCH_3)$) gives the $[M(L^n)]^+$ fragment via pathway B, which was the base peak (100%), in the case of the Zn complex in Table 7.6. In some cases, such as complexes of Co(II) and Ni(II), both pathways A and B, shown in Scheme 7.2, were operative. Loss of $MLCl_2$ from the molecular ion gives the penultimate fragment $(L^n)^+$ which could undergo further loss of a nitrogen molecule to give a $(L^{n*}-N_2)^+$ fragment. Loss of the X substituent of the

ligand or part of the substituent from $(L^n)^+$ gives rise to the $(L^{n*})^+$ fragment as depicted in Scheme 7.2. In the final pathway observed, the value involved the loss of a ligand, two chlorides and a nitrogen molecule ($L+ Cl_2+ N_2$) to give the $[M(L^n)]^+$ fragment and the value is observed in the cases of Mn(II) and Ni(II).

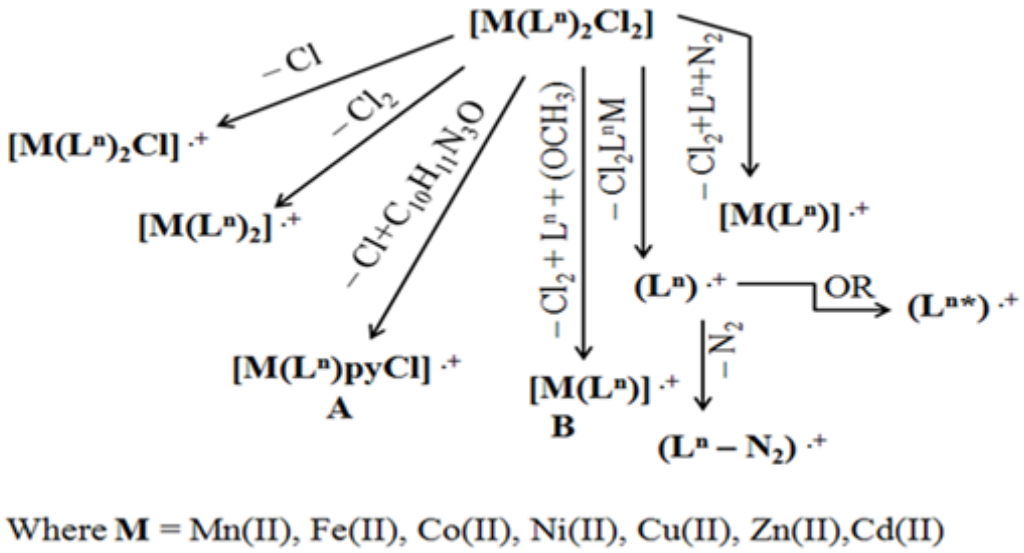

Scheme 7.2: The major fragments is observed and the values in the mass spectra for the metal complexes of general formula $[M(L^n)_2Cl_2]$.

The L^{n*} fragment identified occurs by loss of the X substituent where X = F, Cl, OCH_3, etc. or in the case of the methoxy substituent, by rearrangement through the loss of a CH_3 cation (see Scheme 7.3). In the general formula $[M(L^n)_2Cl_2]$ (M = Mn(II), Fe(II), Co(II), Ni(II), Cu(II), Zn(II), Cd(II); L^n = the ligands have various substituents such as (CH_3, OCH_3, COOH, F, Cl, CN, H, CF_3) and n = (2= CH_3, 3= OCH_3, 4= COOH, 5= F, 6= Cl,7= CN, 8= H, 9= CF_3). The generalised fragments and their relative abundances for the metal complexes $[M(L^3)_2Cl_2]$ are shown in Table 7.6. The molecular ion peak fragmentation patterns of the $[M(L^3)_2Cl]^+$ (D) are detected at *m/z* (100%) due to the fragment ion patterns $[M\text{-}Cl+C_{10}H_{11}N_3O]^+$, which could be corresponding to the rearrangement in the molecule as illustrated in Scheme 7.3. It is attributed to the loss of a part of the ligand, while the pyridine ring remains intact and is followed by the loss of a CH_3 cation group. As a result, the *para* -quinine ion is

formed. This is in accordance with fragmentation rearrangement results reported for *para*-methoxyphenyl azide and *para*-anisidine [20].

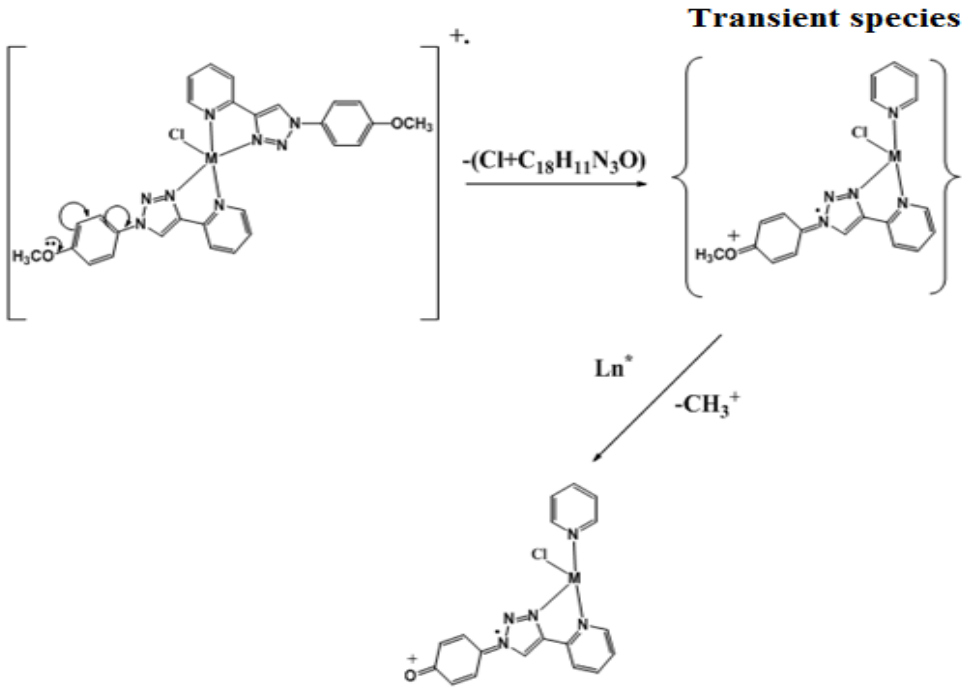

Scheme 7.3: The major fragments detected in the mass spectrum of the metal complexes of $[M(L^3)_2Cl_2]$ where: M= [Mn(II), Fe(II), Co(II) and Ni(II)].

The fragmentation results and spectra for other complexes are included in the Appendix 2 Tables and Figures. Only in the case of complexes with L^4 positive ion (TOF-MOLDI-MS) had to be used to measure the complexes.

Table 7.6: TOF MS ES+ species is observed and the value is for the complexes with L^3.

Complexes	Fragmentation (%)							
[M]+	**$[M(L)_2Cl]^{+\cdot}$**	**$[M(L)_2]^{+\cdot}$**	**$[M- Cl+C_{10}H_{11}N_3O]^+$**	**$[M- L^3+Cl_2+(OCH_3)]^+$**	**$[L^3]^{+\cdot}$**	**$[L-N_2]^{+\cdot}$**	**$[M(L)_2]^{+\cdot}$**	**Other peak**
$[Mn(L^3)_2Cl]$	594(95%)		405.5 (100%)				279.5 (40%) $[M- (L^3+Cl_2+N_2)]^+$	
$[Fe(L^3)_2Cl_2]$	595(80%)		405.8 (100%)		253(30%)	225(50%)		
$[Co(L^3)_2Cl_2]$	598(90%)		407.5 (100%)	281.5 (100%)				
$[Ni(L^3)_2Cl_2]$	597(70%)		407.0 (90%)	281.0 (100%)		224(50%)	224 (50%) $[M- (L^3+Cl_2+N_2)]^+$	
$[Cu(L^3)_2Cl_2]$	602(10%)	567.1(100 %)		284.0 (30%)	253(20%)	225(50%)		351 (5%) $[M-(L^3+Cl_2)]^+$
$[Zn(L^3)_2Cl_2]$	603(60%)	567.1 (20%)		284 (100%)	253(30%)	225(50%)		602.1 (15%) $[M- (Cl_2 + CH_3)]^+$
$[Cd(L^3)_2Cl_2]$	653(10%)			284.0 (100%)	253(50%)	225(100%)		567.1 (40%) $[M-(Cl +(C_2H_6O_2) + N_2)]^+$
$[Pt(L^3)_2Cl_2]$	725.1413 (100%)							

7.2.9 ^{1}H-^{13}C, 1H-1H COSY, HMQC two dimensional correlation spectroscopy and D.E.P.T NMR spectra for the complexes

All assignments were confirmed using DEPT-^{13}C (θ = 135 °), ^{1}H-^{1}H COSY and ^{1}H-^{13}C HMQC two dimensional correlation spectroscopy. The ^{1}H-^{13}C and DEPT NMR analysis were used to characterise the structure of ligand L^3. The samples were recorded in CD_2Cl_2 solutions (see chapter 6 section 6.3.1.3).

The ^{1}H and ^{13}C-NMR spectra for each complex were assigned in accordance with the NMR spectra of L^3 triazoles, supported by 2-dimensional spectra (^{1}H–^{1}HCOSY, ^{13}C–^{1}H HMQC) to confirm the proposed assignments. The chemical shift (δ) of the ^{1}H-(C-H) and ^{13}C-NMR (C=CH) for the triazole moiety of the Zn(II) and Cd(II) complexes are listed in Tables 7.7 and 7.8.

7.2.9.1 1H NMR spectrum for $[Zn(L^3)_2Cl_2]$

The ^{1}H NMR spectrum for $[Zn(L^3)_2Cl_2]$ in DMSO-d6 solution is shown in Figure 7.10. The spectrum displays one set of signals, thus indicating the present of one isomer in solution. The spectrum shows a chemical shift at δ = 9.05ppm (1H, S) which is attributed to $C_{11;\,11}$-H triazole proton shifted downfield relative to its position in the "free" ligand L^3, which indicates complexation to Zn(II) ions. This yield $\Delta\delta$ = 0.53ppm in comparison with the chemical shift of L^3. The downfield shift can be attributed to the reduction in the electron density of the triazole ring (the lone pair of electrons on the nitrogen triazole contributes to the metal upon complex formation).
The pyridine proton resonances are shifted in accordance with their proximity to the metal centre. The proton H2 closest to the Zn(II) centre is shifted downfield, which could also be related to the participation of the pyridine nitrogen atom in the binding to the metal. This signal is slightly shifted downfield compared to that detected in the free ligand of L^3, and yield $\Delta\delta$ = 0.04ppm. The full assignment of signals are summarised in Table 7.7. These finding are in accordance with that reported for ferrocene triazole pyridine complexes [21-23].

7.2.9.2 ^{13}C NMR and DEPT spectra for $[Zn(L^3)_2Cl_2]$

The ^{13}C NMR spectrum for $[Zn(L^3)_2Cl_2]$, Figure 7.10, shows a chemical shift at δ = 120.75ppm, which is assigned to C_{11} of the triazole. This gives a value of Δδ = 0.18ppm in comparison with the chemical shift of L^3. Signals at δ = 121.60 and 114.63ppm, are related to the *para* benzene substitution ($C_{14,16;}$ $C_{13,17}$), respectively. The chemical shift of the CH_3 group of the methoxy moiety appears as expected at δ = 55.29ppm [24-25]. The full assignment of signals are summarised in Table 7.7. DEPT-^{13}C is presented in Figure 7.12. ^1H-^{13}C HMQC correlation and ^1H-^1H COSY spectra of $[Zn(L^3)_2Cl_2]$ in DMSO-d_6 are displayed in Figure 7.13 and 7.14, respectively.

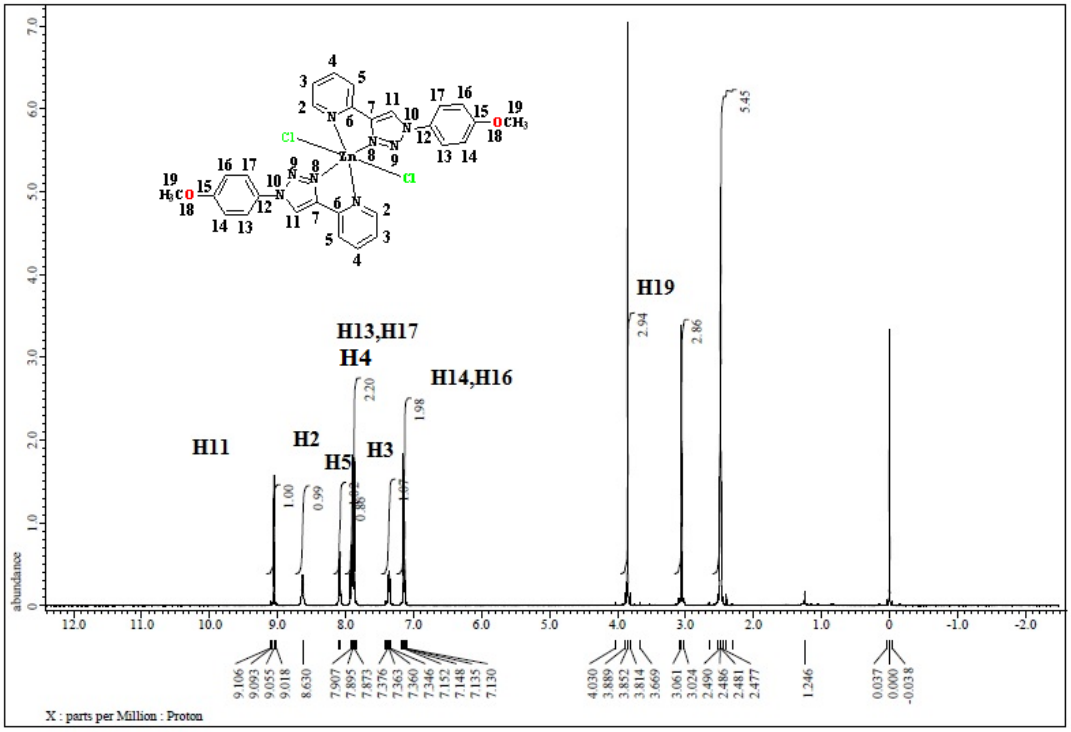

Figure 7.10: ^1H NMR spectrum of $[Zn(L^3)_2Cl_2]$ in DMSO-d_6.

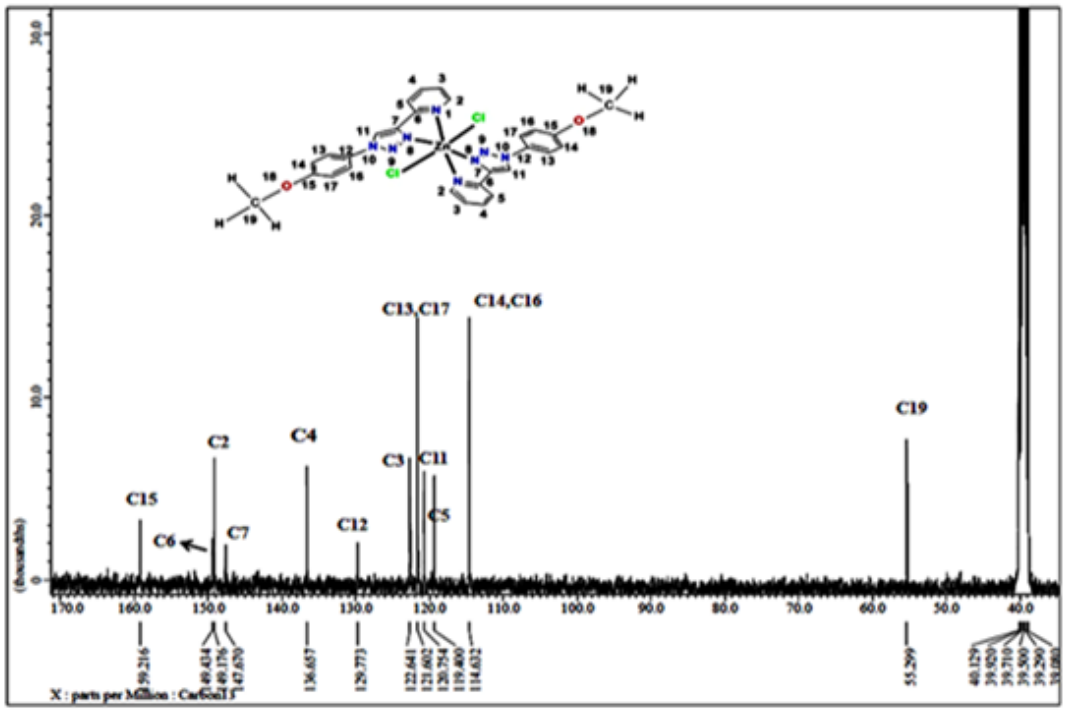

Figure 7.11: ^{13}C NMR spectrum of $[Zn(L^3)_2Cl_2]$ in DMSO-d_6.

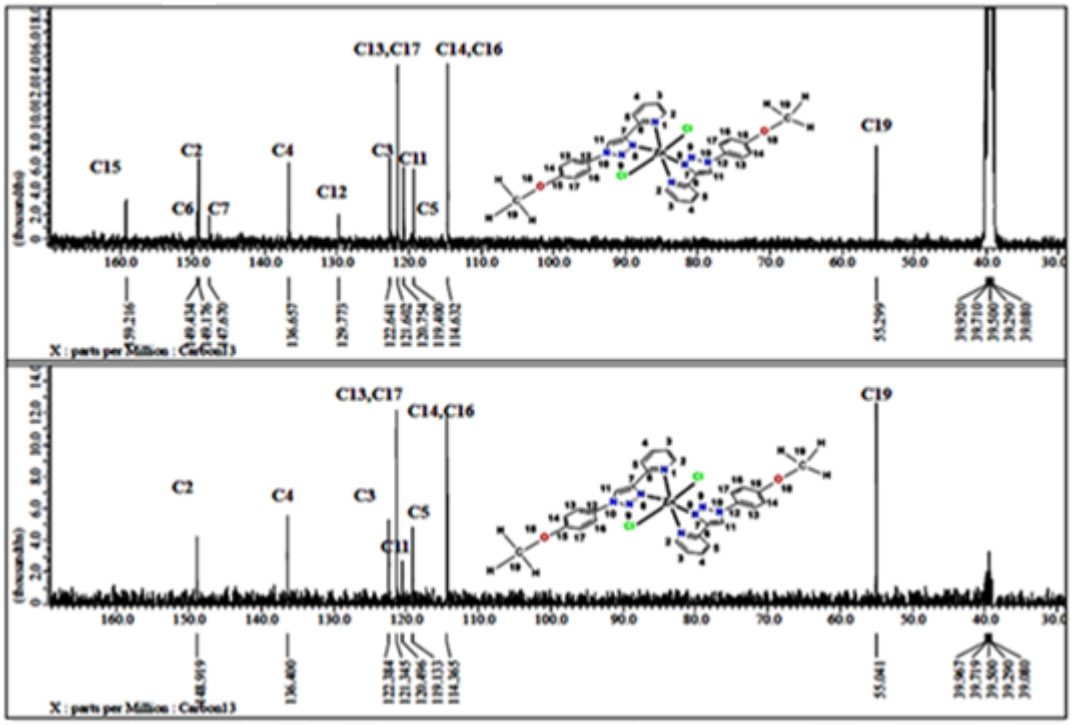

Figure 7.12: ^{13}C NMR and DEPT NMR spectrum of $[Zn(L^3)_2Cl_2]$ in DMSO-d_6.

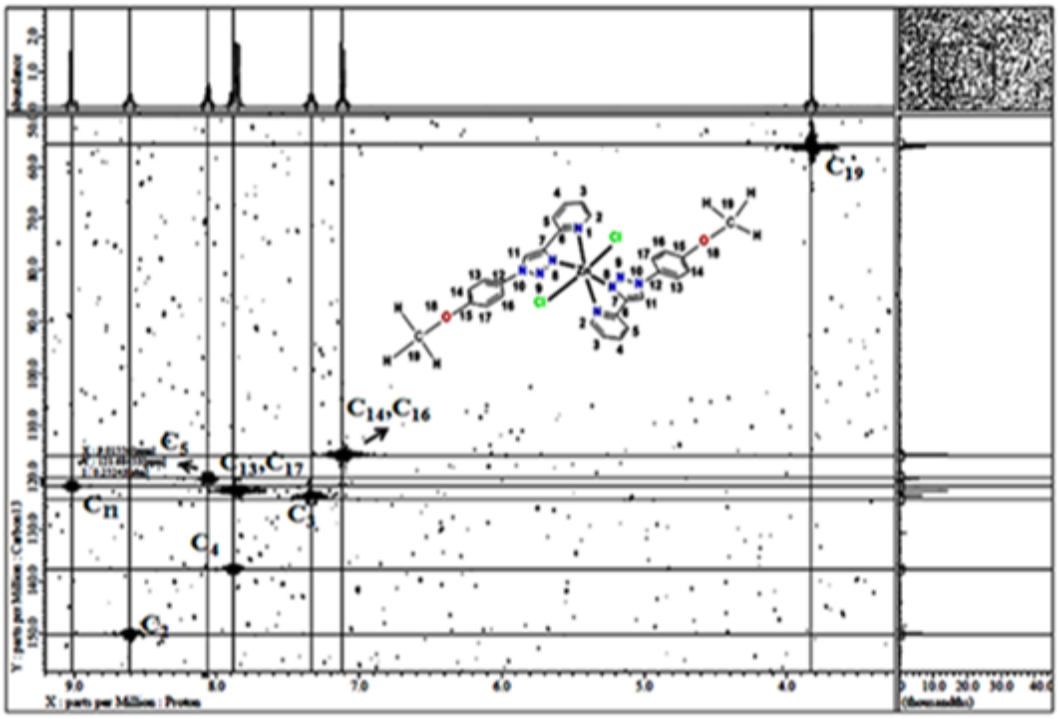

Figure 7.13: 2D ^{1}H-^{13}C HMQC correlation spectrum of $[Zn(L^{3})_2Cl_2]$ in DMSO-d_6.

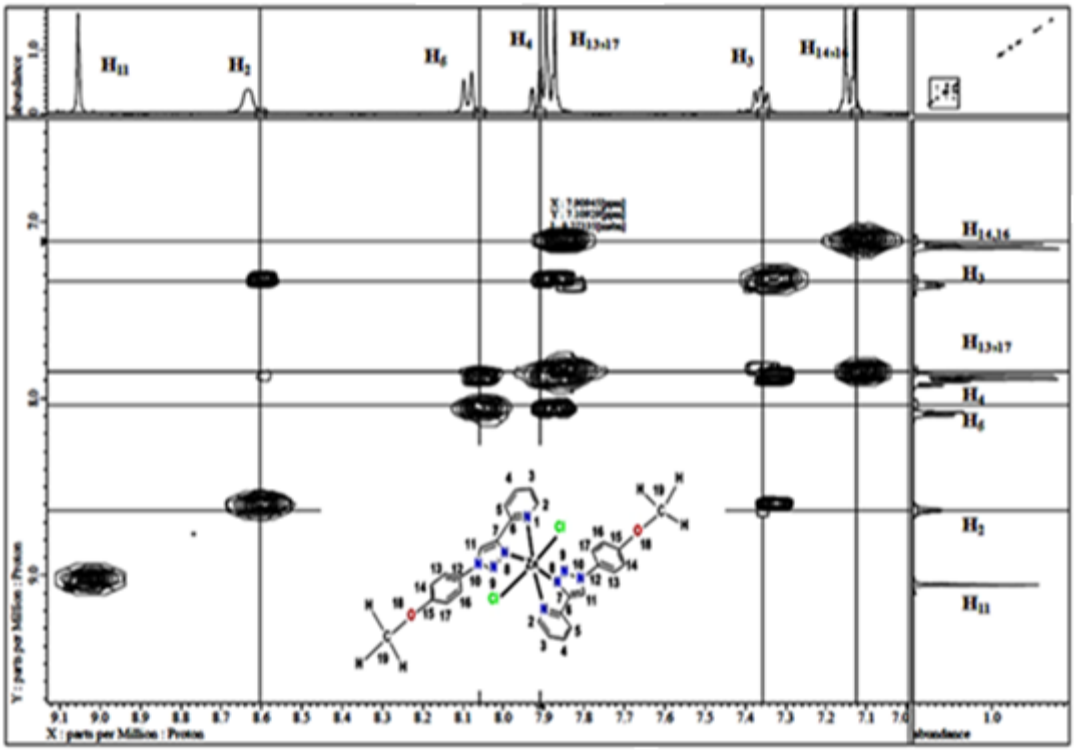

Figure 7.14: 2D ^{1}H-^{1}HCOSYcorrelation spectrum of $[Zn(L^{3})_2Cl_2]$ in DMSO-d_6.

7.2.9.3 1H NMR spectrum for [Cd(L^3)$_2$Cl$_2$]

The ^{1}H NMR spectrum for [Cd(L^3)$_2$Cl$_2$] in DMSO-d$_6$ solution is depicted in Figure 7.15. The spectrum shows a chemical shift at δ = 9.08ppm (1H, S), which is attributed to the $C_{11;\ 11}$-H of the triazole proton. This gives a value of Δδ = 0.55ppm in comparison with the free ligand L^3. The assignment of signals are summarised in Table 7.8.

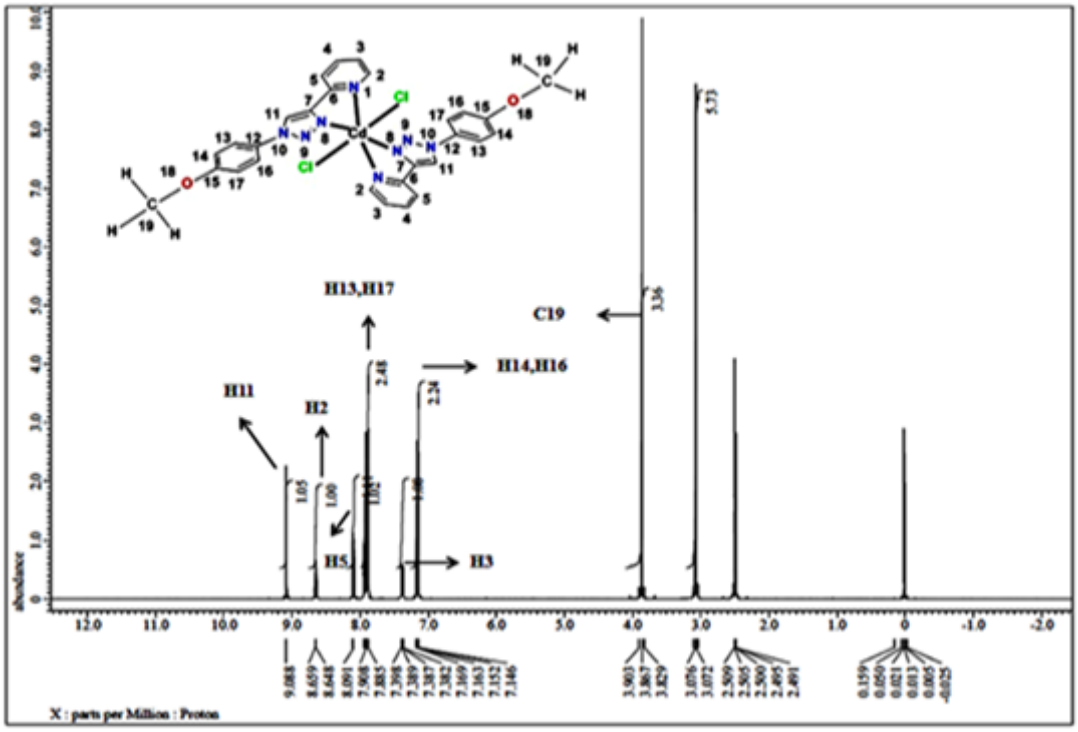

Figure 7.15: ^{1}H NMR spectrum of [Cd(L^3)$_2$Cl$_2$] in DMSO-d$_6$.

7.2.9.4 13C NMR and DEPT spectra for [Cd(L^3)$_2$Cl$_2$]

The ^{13}C-NMR spectrum for [Cd(L^3)$_2$Cl$_2$], Figure 7.16, exhibits a chemical shift at δ = 121.17ppm, which assigned to C_{11} of the triazole. This gives a value of Δδ = 0.25ppm compared with the chemical shift of L^3. Signals at δ = 121.62 and 114.64ppm are related to ($C_{14,16;}$ $C_{13,17}$), respectively. The CH_3 group of the methoxy moiety appears as expected at δ = 55.29ppm. The assignment of signals are summarised in Table 7.8. DEPT-^{13}C is presented in Figure 7.17. ^{1}H-^{13}C HMQC correlation and ^{1}H-^{1}H COSY spectra of [Cd(L^3)$_2$Cl$_2$] in DMSO-d$_6$ are shown in Figures 7.18 and 7.19, respectively.

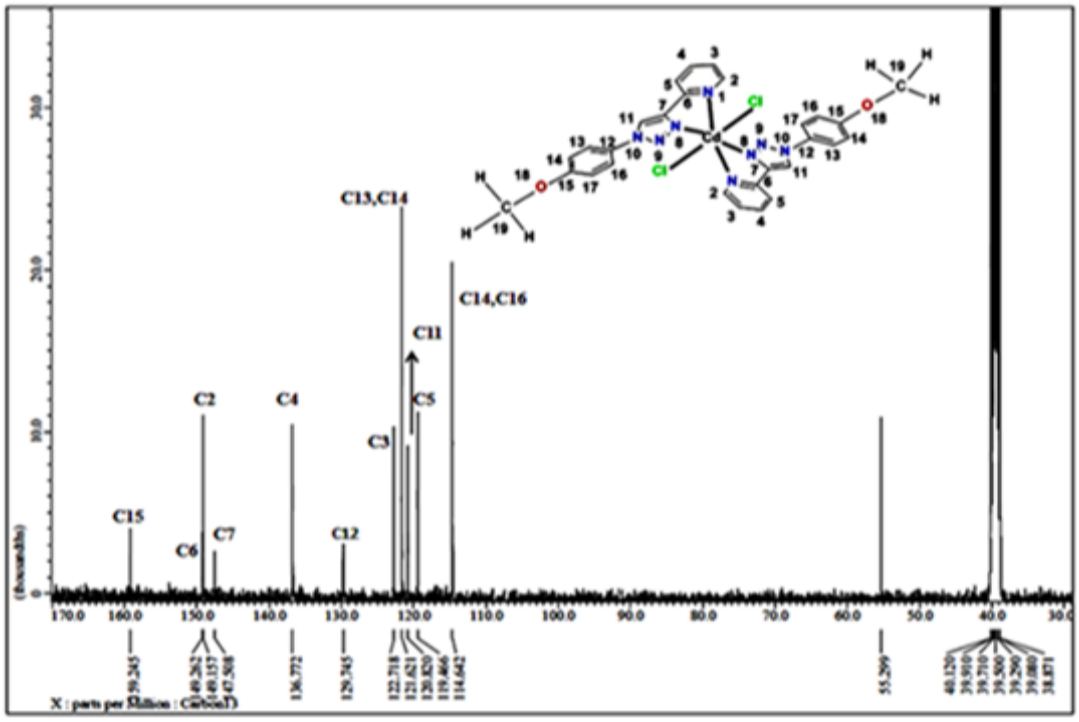

Figure 7.16: ^{13}C NMR spectrum of $[Cd(L^3)_2Cl_2]$ in DMSO-d_6.

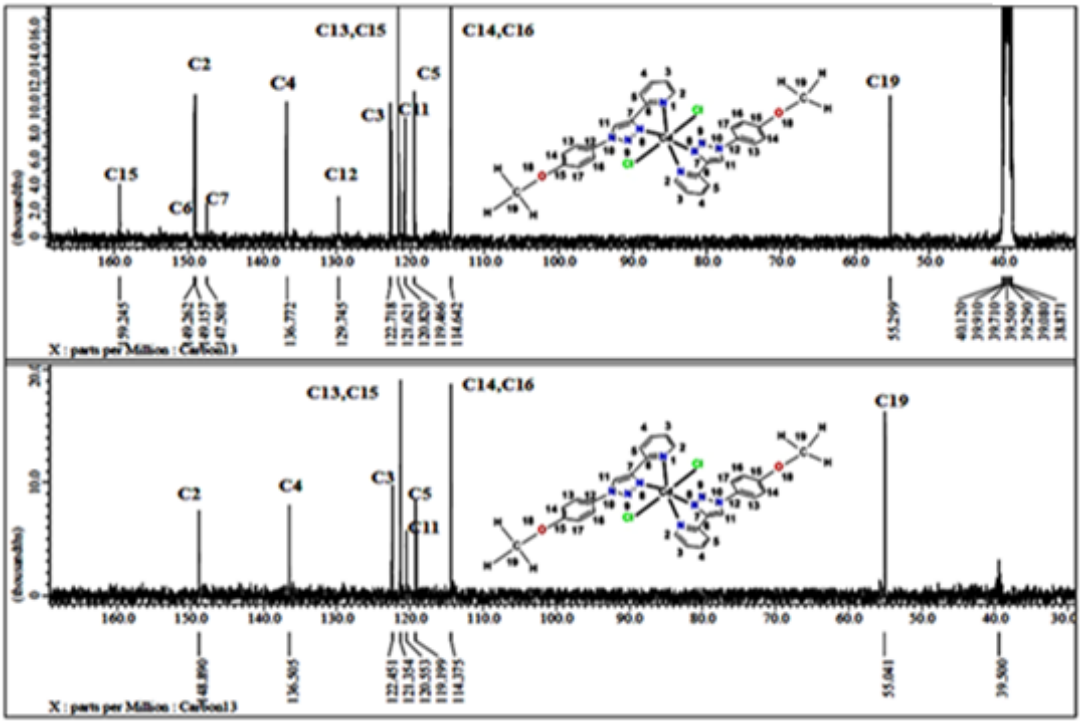

Figure 7.17: ^{13}C NMR and DEPT NMR spectrum of $[Cd(L^3)_2Cl_2]$ in DMSO-d_6.

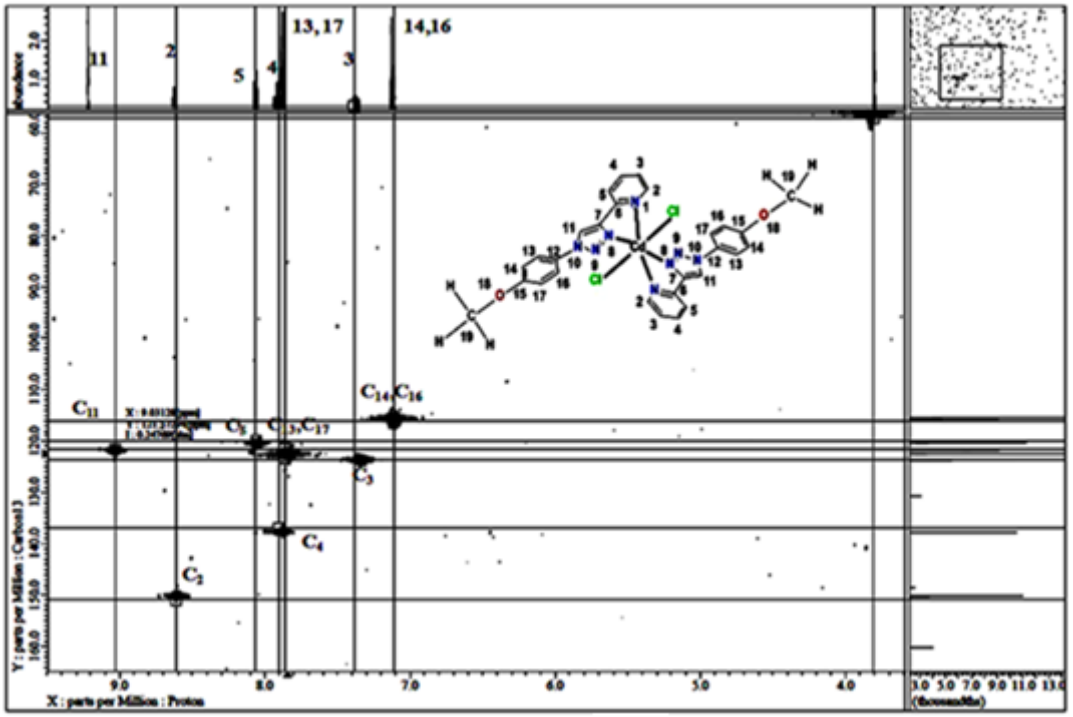

Figure 7.18: 2D ^{1}H-^{13}C HMQC correlation spectrum of $[Cd(L^3)_2Cl_2]$ in DMSO-d_6.

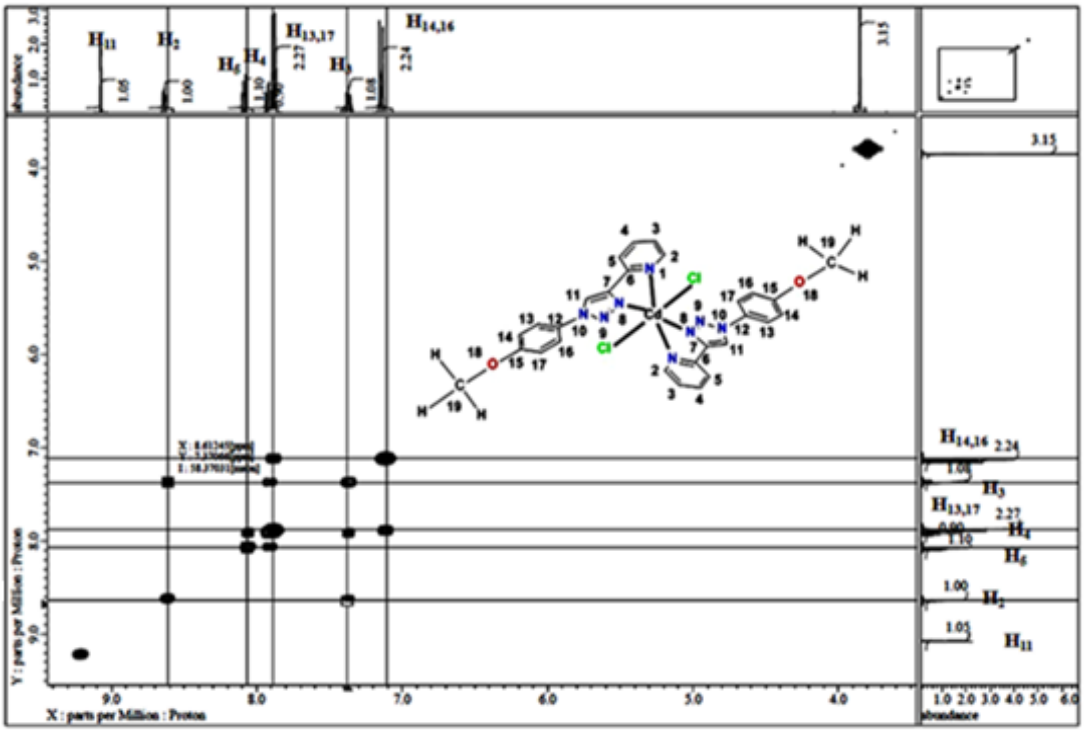

Figure 7.19: 2D ^{1}H-^{1}HCOSYcorrelation spectrum of $[Cd(L^3)_2Cl_2]$ in DMSOd_6.

7.2.9.5 The effect of metal ion on the ^{1}H and ^{13}CNMR chemical shifts of the triazole moiety for $[Zn(L^{3})_{2}Cl_{2}]$ and $[Cd(L^{3})_{2}Cl_{2}]$

The ^{1}H-, ^{13}C-NMR data for the Zn(II) and Cd(II) complexes with L^{3} are displayed as an overlay in Figures 7.20 and 7.21, respectively. Although the Zn(II) and Cd(II) ions have the same electronic configuration (d^{10}), they are lying in different transition metals series in the 3d-block and 4d-block, respectively.

The chemical shift (δ) of the ^{1}H-(C-H) and ^{13}C-NMR (C=CH) for the triazole moiety of the Zn(II) and Cd(II) complexes are listed in Tables 7.7 and 7.8. It is clear that there is a detectable shift in the ^{1}H- (C-H) and ^{13}C-NMR (C=CH) for the triazole moiety upon complexation, compared with that in the free ligand.

However, the chemical shifts between Zn(II) and Cd(II) complexes appear to be very close to each other. This may be related to the fact that the Zn(II) and Cd(II) ions in these complexes are adopting similar octahedral geometries with (2+) oxidation state.

On the other hand, Zn(II) and Cd(II) complexes with various ligands (L^{2}-L^{9}), which contain several substituents (electron donating and electron withdrawing groups) on the phenyl ring, manifested itself in shifts in the C-H-triazole peak of the ^{1}*H*-1,2,3-triazole system, which was in the range of 9.06 - 9.46ppm for the ^{1}H-NMR and in the range of 120.54-121.56ppm in the ^{13}C-NMR spectra. These values are listed in Tables 7.7 and 7.8, and display different chemical shifts in the ^{1}HNMR spectra and ^{13}C-NMR spectra due to the nature of the substituents.

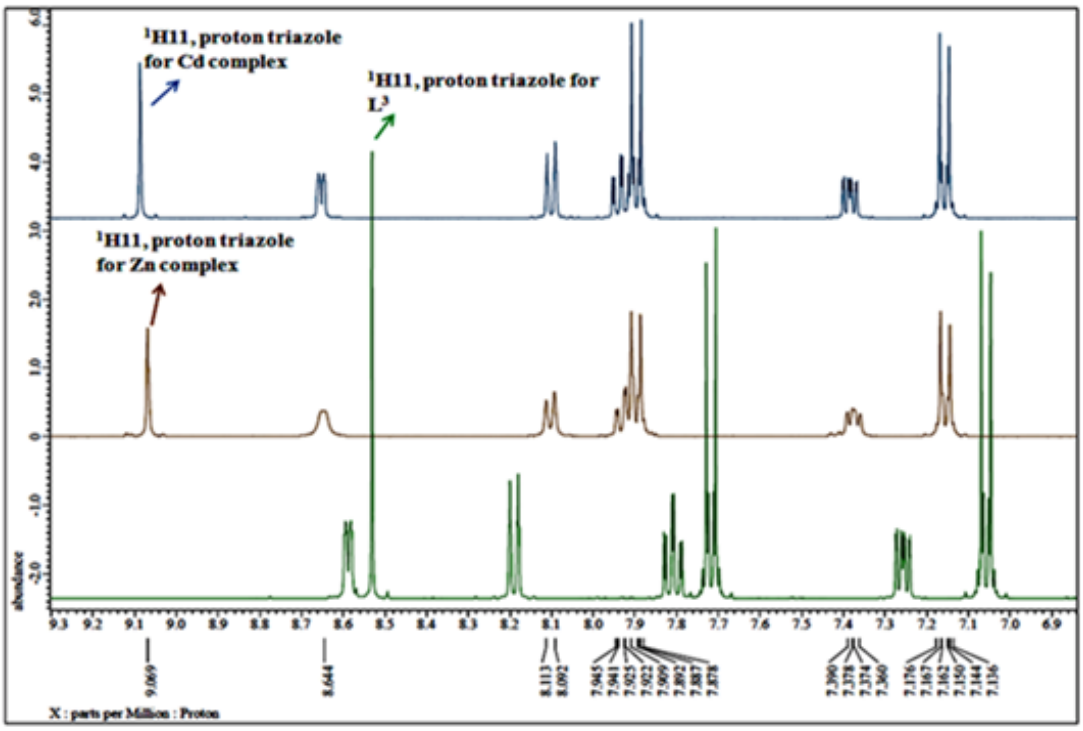

Figure 7.20: The overlay of the (C-H) triazole from the ^{1}H NMR for L^{3} in Zn(II) and Cd(II) complexes in DMSO-d_6.

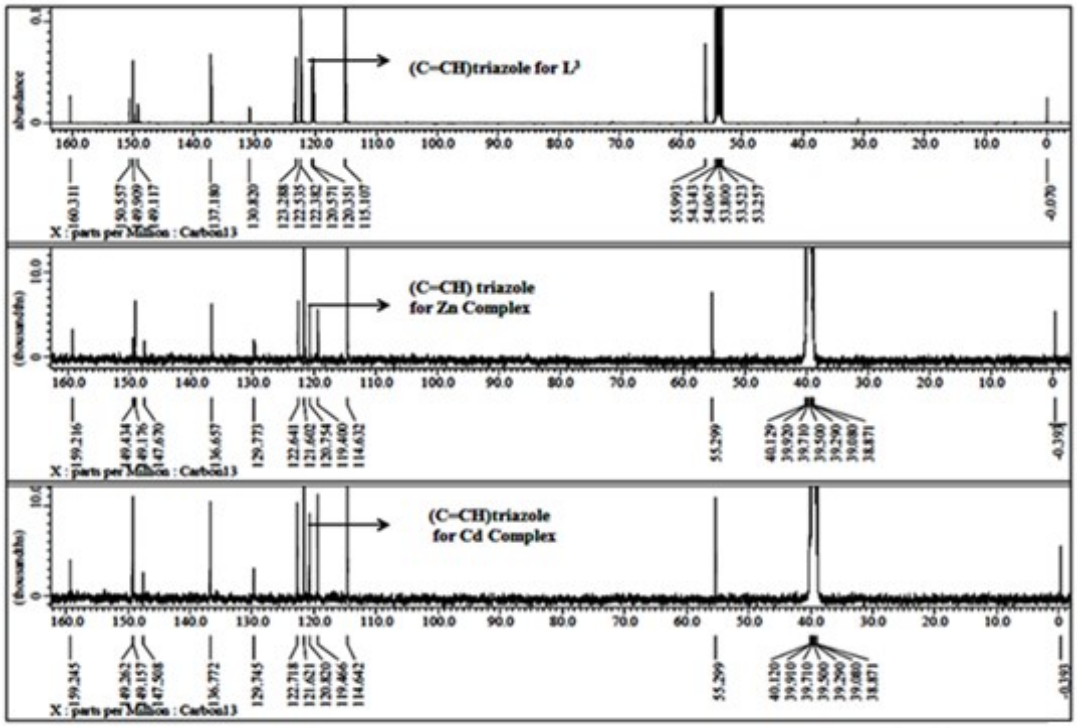

Figure 7.21: The overlay ^{13}C NMR of the (C=CH) triazole for L^{3} in $CDCl_2$ and its Zn(II) and Cd(II) complexes in DMSO-d_6.

Table 7.7: ^{1}HNMR and ^{13}CNMR chemical shifts of the Zn(II) complexes with ligands L^2–L^9 in DMSO-d_6 solutions and the corresponding Hammett substituent constants.

Complex	σ_ρ constant ($-\sigma_\rho$)	Substituent	^{1}H-NMR δ(C-H) (triazole)	^{13}CNMR(=CH) (triazole)
$[Zn(L^2)_2Cl_2]$	-0.17	*ρ*-CH_3	9.33	121.02
$[Zn\ (L^3)_2Cl_2]$	-0.27	*ρ*-OCH_3	9.06	120.75
$[Zn\ (L^4)_2Cl_2]$	0.45	*ρ*-COOH	9.38	121.21
$[Zn\ (L^5)_2Cl_2]$	0.06	*ρ*-F	9.32	121.56
$[Zn\ (L^6)_2Cl_2]$	0.23	*ρ*-Cl	9.31	121.23
$[Zn\ (L^7)_2Cl_2]$	0.66	*ρ*-CN	9.36	120.54
$[Zn\ (L^8)_2Cl_2]$	0	*ρ*-H	9.27	121.05
$[Zn\ (L^9)_2Cl_2]$	0.54	*ρ*-CF_3	9.44	121.42

Table 7.8: ^{1}HNMR and ^{13}CNMR chemical shifts of the Cd complexes with ligands L^2-L^9 in DMSO-d_6 solution and the corresponding to Hammett substituent constants.

Complex	σ_ρ constant ($-\sigma_\rho$)	Substituent	^{1}H-NMR δ(C-H) (triazole)	^{13}CNMR(=CH) (triazole)
$[Cd(L^2)_2Cl_2]$	-0.17	*ρ*-CH_3	9.36	121.16
$[Cd(L^3)_2Cl_2]$	-0.27	*ρ*-OCH_3	9.08	120.82
$[Cd(L^4)_2Cl_2]$	0.45	*ρ*-COOH	9.39	121.22
$[Cd(L^5)_2Cl_2]$	0.06	*ρ*-F	9.27	121.40
$[Cd(L^6)_2Cl_2]$	0.23	*ρ*-Cl	9.33	121.32
$[Cd(L^7)_2Cl_2]$	0.66	*ρ*-CN	9.45	121.41
$[Cd(L^8)_2Cl_2]$	0	H	9.30	121.16
$[Cd(L^9)_2Cl_2]$	0.54	*ρ*-CF_3	9.45	121.51

The ^{1}HNMR and ^{13}CNMR spectra data for the Zn(II) and Cd(II) with ligands L^2-L^9 are presented in Appendix 2.

7.2.10 X-ray crystallography diffraction data analysis of the metal complexes

During the course of this project, X-ray diffraction investigations of single crystals have been used extensively to confirm the formation of the titled complexes. These include X-ray single crystal diffraction analyses of the different metal ions and ligands complex systems. The aim of the varying ligand systems and metal ions was to investigate: (i) the effect of the ligand system on the coordination sphere of a specific ion, and (ii) the influence of varying metal ions on the coordination sphere upon binding with a specific type of ligand. Due to the large number of complexes determined using X-ray single crystals, i.e. 20 complexes, L^3 ligand were chosen as an example to show the influence of the metal ions on the coordination sphere of complexes. On the other hand, the Cu(II) ion was chosen to study the impact of varying ligand systems on the coordination sphere of the complexes. Other X-ray molecular structures are presented in the Appendix 2.

7.2.10.1 Structure determination

Single crystal X-ray diffraction measurements for $[Mn(L^3)_2Cl_2]$, $[Fe(L^3)_2Cl_2]$, $[Co(L^3)_2Cl_2]$, $[Ni(L^3)_2Cl_2]$, $[Cu(L^3)Cl_2]_n$, $[Cd(L^3)Cl_2]_n$, $[Cu(L^2)_2Cl_2]$, $[Cu(L^6)_2Cl_2]$, $[Cu(L^7)_2Cl_2]$, $[Cu(L^8)_2Cl_2]$ and $[Cu(L^9)_2Cl_2]$, were performed using a Rigaku Saturn 724+ area detector mounted at the window of an FR-E+ rotating anode generator with a (Mo Kα, λ=0.71075Å), while the data for the complex $[Cu(L^2)_2Cl_2]$ as collected using a Nonius-Kappa CCD area detector mounted at the window of an FR591 rotating anode generator (Mo Kα, λ=0.71073A). The crystals were mounted on glass fiber and the data were collected at 120K under nitrogen flow from an Oxford Cryosystems cryostream 700 device. The data for the complex $[Cu(L^9)_2Cl_2]$ as collected at 100K and with a rotating anode generator (Mo Kα, λ=0.68890Å). On the other hand, the data for the complex $[Cu(L^8)_2Cl_2]$ was collected at 293K and with a rotating anode generator (Mo Kα, λ=0.71075Å). An empirical absorption correction was carried out using SADABS and the structures were solved by direct methods using SUPERFLIP [26]. Data were processed and empirical absorption corrections were also done using Crystal Clear SM-Expert, with the unit cell parameters refined against all data [27]. The structures were solved by direct methods using SHELXS-97 with in OLEX2 [28]. All refinements on F_o^2 by full-matrix least squares refinement were solved using the SHELXL-97 program package [29]. All non-hydrogen atoms

were refined by isotropic displacement parameters and hydrogen atoms were added at calculated positions. Further refinement was done using a riding model with C-H (aromatic) 0.95Å $U_{ISO} = 1.5U_{eq}$ (C); C-H (methyl) 0.98Å $U_{ISO} = 1.5U_{eq}$ (C) [30]. The crystallographic data for the complexes are summarised in Table 7.9, while selected bond lengths, selected bond angles and selected torsion angles are presented in Tables 7.10, 7.11, 7.12 and 7.13, respectively.

7.2.10.2 X-ray crystallography diffraction data analysis of the metal complexes with ligand L^3

7.2.10.2.1 Single-crystal structure determinations of the metal complexes of [M:L-1:2]

The molecular structure of the four complexes $[Mn(L^3)_2Cl_2]$, $[Fe(L^3)_2Cl_2]$, $[Co(L^3)_2Cl_2]$ and $[Ni(L^3)_2Cl_2]$ are generally similar. The overall structures can be described as distorted octahedral. As expected, two triazole ligands are coordinated to the metal centre and lie in the equatorial plane, while the two chloro ligands are in the axial positions *trans* to each other. However, in $[Mn(L^3)_2Cl_2]$, the two chloro ligands are adopting the *cis* positions around the Mn centre.

Table 7.9: Crystallographic data for the ligand L^3 and the complexes.

Compound	L^3	$[Mn(L^3)_2Cl_2]$	$[Fe(L^3)_2Cl_2]$	$[Co(L^3)_2Cl_2]$	$[Ni(L^3)_2Cl_2]$	$[CuL^3)\ Cl_2]n$	$[Cd(L^3)_nCl_2]$
Empirical formula	$C_{14}H_{12}N_4O$	$C_{28}H_{24}Cl_2MnN_8O_2$	$C_{28}H_{24}Cl_2FeN_8O_2$	$C_{28}H_{24}Cl_2CoN_8O_2$	$C_{28}H_{24}Cl_2NiN_8O_2$	$C_{14}H_{12}Cl_2CuN_4O$	$C_{14}H_{14}CdCl_2N_4O$
M_r	252.28	630.39	631.30	634.38	634.16	386.72	451.60
Temp/K	100(2)	100 K	100(2) K	100(2) K	100(2) K	100(2) K	100(2) K
Cryst. syst.	Triclinic	Orthorhombic	Monoclinic	Monoclinic	Monoclinic	Orthorhombic	Monoclinic
Space group	P1	*Pbcn*	$P2_1/c$	$P2_1/c$	$P2_1/c$	*Pbca*	*P*121/*c*1
a/Å	3.7837(4)	13.4618(9)	10.3599(7)	10.3480(10)	10.459(15)	7.1833(5)	24.2917(18)
b/Å	10.8502(16)	9.2130(6)	13.1029(8)	12.9032(12)	12.968(17)	15.0954(11)	9.1879(7)
c/Å	15.2200(17)	22.9298(16)	10.2300(6)	10.1969(9)	10.350(15)	27.0358(19)	7.0472(5)
α/°	109.226(11)	90.00	90.00	90.00	90.00	90.00	90.00
β/°	97.056(6)	90.00	96.161(7)	95.772(7)°	95.61(3)	90.00	92.144(5)
γ/°	91.514(9)	90.00	90.00	90.00	90.00	90.00	90.00
V/Å^3	584.03(12)	2843.8(3)	1380.65(15)	1354.6(2)	1397(3)	2931.6(4)	1571.76(18)
Z	2	4	2	2	2	8	4
R_{int}	0.0617	0.1012	0.0387	0.2085	0.1445	0.084	0.094
D_{calcd}/g cm^{-3}	1.435	1.472	1.519	1.555	1.508	1.752	1.908
Refln (all/ind)	6395/ 2617	12965/ 3242	6581/ 3143	15422/ 3098	7036/ 3134	25308/ 3354	9891/ 7737
μ/mm^{-1}	0.096	1.000-0.092	0.783	0.875	0.928	1.860	1.740
*R*1/*wR*2 (obsd data: $F^2>2\sigma(F^2)$)[a]	0.0534/ 0.1074	0.0597/ 0.1345	0.0398/ 0.1021	0.0466/ 0.0762	0.0928/ 0.1629	0.0496/ 0.1127	0.1210/ 0.2914
*R*1/*wR*2 (all data)[a]	0.0734/ 0.1161	0.1127/ 0.1624	0.0458/ 0.1063	0.1516/ 0.0886	0.1772/ 0.2084	0.0731/ 0.1236	0.1668/ 0.3280

Table 7.10: Selected bond lengths in (Å) for the complexes with L^3 ligand.

Bond distance(Å)	L^3	$[Mn(L^3)_2Cl_2]$	$[Fe(L^3)_2Cl_2]$	$[Co(L^3)_2Cl_2]$	$[Ni(L^3)_2Cl_2]$	$[CuL^3)Cl_2]_n$	$[Cd(L^3)Cl_2]_n$
Empirical formula	$C_{14}H_{12}N_4O$	$C_{28}H_{24}Cl_2MnN_8O_2$	$C_{28}H_{24}Cl_2FeN_8O_2$	$C_{28}H_{24}Cl_2CoN_8O_2$	$C_{28}H_{24}Cl_2NiN_8O_2$	$C_{14}H_{12}Cl_2CuN_4O$	$C_{14}H_{14}CdCl_2N_4O$
C7–C11	1.362(6)	1.371(5)	1.375(3)	1.360(4)	1.361(9)	1.368(5)	1.39(3)
N8–N9	1.302(4)	1.305(4)	1.311(2)	1.309(4)	1.331(7)	1.323(4)	1.31(2)
N9–N10	1.355(4)	1.358(4)	1.354(2)	1.362(3)	1.368(7)	1.360(4)	1.35(2)
N8–C7	1.365(5)	1.365(4)	1.360(2)	1.360(3)	1.370(8)	1.359(4)	1.36(3)
$M–N_{(PY)}1$		2.330(3)	2.2018(15)	2.127(2)	2.1015(19)	2.066(3)	2.359(17)
$M–N_{(PY)}$ 1i		2.330(3)	2.2018(15)	2.127(2)	2.1015(19)		
$M–N_{(triazole)}1$		2.324(3)	2.1838(16)	2.105(3)	2.0739(19)	2.024(3)	2.391(18)
$M–N_{(triazole)}1^i$		2.324(3)	2.1838(16)	2.105(3)	2.0739(19)		
M–Cl1		2.4544(11)	2.4456(5)	2.4398(10)	2.4123(6)	2.6195(9)	2.563(5)
$M–Cl1^i$		2.4544(11)	2.4456(5)	2.4398(10)	2.4123(6)	2.2382(10)	2.667(6)

Table 7.11: Selected bond angles [°] for the complexes with the L^3 ligand

Bonds	$Mn(L^3)_2Cl_2]$	$[Fe(L^3)_2Cl_2]$	$[Co(L_3)_2Cl_2]$	$[Ni(L_3)_2Cl_2]$	$[Cu(L_3)Cl_2]_n$	$[Cd(L_3)Cl_2]_n$
$N_{(PY)}$ 1 –M–$N_{(PY)}$ 1^i	178.89(16)	180.0	179.999(1)	179.999(1)		
$N_{(triazole)}$ 1^i –M–$N_{(triazole)}$ 1	87.13(15)	180.0	179.999(1)	179.999(1)		
$N_{(PY)}$ 1–M–$N_{(triazole)}$ 1^i	108.95(11)	104.10(6)	102.93(10)	101.3(2)		
$N_{(PY)}$ 1 –M–$N_{(triazole)}$ 1	71.90(10)	75.90(6)	77.07(10)	78.7(2)	79.78(12)	70.0(6)
$N_{(PY)}$ 1–M– Cl 1	91.05(8)	89.80(4)	90.32(8)	90.28(15)	85.78(9)	94.5(4)
$N_{(PY)}$ 1^i –M– Cl 1	88.30(8)	90.20(4)	89.68(8)	89.72(15)		
$N_{(triazole)}$ 1^i –M– Cl 1	155.71(8)	90.20(4)	90.25(9)	89.36(18)		
$N_{(triazole)}$ 1–M– Cl 1	86.19(8)	89.80(4)	89.75(9)	90.64(18)	107.97(8)	159.3(4)
Cl 1^i –M– Cl 1	108.66(6)	180.0	179.999(1)	180.0	95.72(3)	103.30(18)
$N_{(PY)}$ 1 –M–Cl_2					174.27(9)	159.6(4)
$N_{(triazole)}$ 8 –M–Cl_2					94.50(9)	94.7(4)

Table 7.12: Selected torsion angles [°] for the complexes with the L^3 ligand.

Bonds	$[Mn(L^3)_2(Cl)_2]$	$[Fe(L^3)_2(Cl)_2]$	$[Co(L^3)_2(Cl)_2]$	$[Ni(L^3)_2(Cl)_2]$
N(*t*) 1i–M–N(*p*)1–C2	96.3(3)	0.6(3)	0.23(17)	1.7(6)
N(*t*)) 1–M–N(*p*) 1–C2	176.6(3)	–179.4(3)	–179.77(17)	–178.3(6)
Cl 1i–M–N(*p*) 1– C2	10.9(3)	–89.1(3)	90.07(15)	92.3(5)
Cl 1–M–N(*p*) 1–C2	–97.8(3)	90.9(3)	–89.93(15)	–87.7(5)
N(*t*) 1i–M–N(*t*) 1–N9	–75.5(3)	101(16)	–74(7)	21(6)
N(*p*) 1–M–N(*t*) 1–N9	173.5(4)	–179.6(4)	179.5(2)	179.7(6)
N(*p*) 1i–M–N(*t*) 1–N9	–5.8(4)	0.4(4)	–0.5(2)	–0.3
Cl 1i–M–N(*t*) 1–N9	–149.7(3)	90.8(4)	–90.40(18)	–90.4(6)
Cl 1–M–N(*t*) 1–N9	81.1(3)	–89.2(4)	89.60(18)	89.6(6)
M–N(*t*) 1–N9–N10	–160.6(3)	177.0(3)	179.13(13)	176.7(4)
N8–N9–N10–C11	–0.4(4)	–0.4(4)	–0.1(2)	–179.7(5)
N8–N9–N10–C12	–179.8(3)	179.1(3)	179.67(16)	0.7(10)

Table 7.13: Selected torsion angles [°] for the Cu and Cd complexes with the ligand L^3

Bonds	$[Cu(L^3)Cl_2]_n$	$[Cd(L^3)Cl_2]_n$
Cu1–N1–C6–C7	–4.4(4)	–1(2)
Cu1–N8–N9–N10	–174.8(2)	–166.3(15)
Cu1–N1–C6–C7	–4.4(4)	–1(2)
Cu1–N8–C7–C6	–3.5(4)	–13(2)
N8–N9–N10–C12	–179.4(3)	–179.4(18)
C7–N8–N9–N10	–0.3(4)	–1(2)
N9–N10–C12–C17	144.8(3)	169(2)
N1–C6–C7–N8	5.2(5)	10(3)
N8–N9–N10–C12	–179.4(3)	–179.4(18)
N8–N9–N10–C11	1(2)	0.5(4)

7.2.10.2.2 The X-ray Crystal structure of dichloro 2-(1-(4-methoxyphenyl)-1H-1,2,3-triazol-4-yl)pyridinenickel(II) [Ni(L^3)$_2$Cl$_2$]

The X-ray molecular structure of [Ni(L^3)$_2$Cl$_2$] is depicted in Figure 7.22. The X-ray quality crystal of the molecule [Ni(L^3)$_2$Cl$_2$] was obtained by slow evaporation in a hot mixture of DMSO: acetonitrile =1:9 solutions under ambient conditions. It crystallises in the monoclinic $P2_1/c$ space group Table 7.9 indicates two molecules per unit cell as $Z = 2$ of the [Ni(L^3)$_2$Cl$_2$] complex. Crystallographic data are presented in Table 7.9. Selected bond lengths, bond angles and torsion angles are provided in Tables 7.10, 7.11, and Table 7.12, respectively. The nickel centre in the [Ni(L^3)$_2$Cl$_2$] is in a distorted octahedral coordination arrangement, which includes two of the 2-(1-(4-methoxy-phenyl)-*1H*-1,2,3-triazol-4-yl) pyridine ligands coordinated via the $N8_{TA}$ and $N1_{PY}$ atoms from the two different ligands L^3. $N8^{eq}$–Ni–$N1^{eq}$ and $N1i^{eq}$–Ni–$N8i^{eq}$ are lying in an equatorial plane with angles 78.7(2)°. In the equatorial plane, the pyridine $N1_{PY}$ and $N8_{TA}$ donors from the two ligands are mutually *trans* to each other. The angles for $N8^{eq}$–Ni–$N8i^{eq}$ and $N1^{eq}$–Ni–$N1i^{eq}$ are 179.999(1)°.

Furthermore, the axial positions are occupied by two chloride ions $Cl1^{ax}$–Ni–$Cl1i^{ax}$, and the angle is 180.0°. The angles in the plane containing the two L^3 ligands are slightly deviated from 90° angles, because of the chelating nature of the two ligands L^3. The bond lengths of N8–N9, N9–N10 and N8–C7 of the 1,2,3-triazole ring are 1.331(7)Å, 1.368(7)Å and 1.370(8)Å, respectively. These values are slightly higher in the [Ni(L^3)$_2$Cl$_2$] (by approximately 0.028Å), compared with the free ligand, where N8–N9 1.302(4)Å, N9–N10 1.355(4)Å and N8–C7 1.365(5)Å, respectively for the free ligand, and other reported Ni(II) pyridyl-triazole complexes [19]. Both chloro moieties show bond lengths of 2.454(3) Å, confirming terminal chloro ligands. The Ni–N_{PY} bond lengths are ranging from 2.110(6)–2.111(6)Å, while the Ni–N_{TA} bond lengths are 2.091(5)Å. This is consistent with the formation of the high-spin d^8 Ni(II) metal centre. The metal-triazole bond length is slightly shorter than the metal pyridine bond length (by approximately 0.019Å). This is possibly due to π-back donation from the Ni(II) centre into the triazole ring. Such elongation of the N–N double bond has been previously observed and the value is for metal complexes containing substituted "azo" ligands [31]. Additionally, this may be because of the greater *trans* influence of the N8 of the triazole nitrogen with respect to N1 of the pyridyl nitrogen [32], and to

the better electron donating properties of the 1,2,3-triazole ring compared with the pyridine ring. Similar trends were observed and the value is in agreement with those previously reportedin metal complexes of other azole ligands containing a 2-pyridyl substituent [1, 33-35].

The twisting angles between the pyridine plane and the triazolering and the triazole plane and the substituted phenyl ring are 114.8(6)° and 119.2(5)°, respectively. As a result of conjugation, the triazole ring and the phenyl unit are essentially co-planar. The dihedral angle between the plane of the pyridyl moiety and the mean plane of the triazole ring is 2.3(8)°, while the dihedral angle between the plane of the methoxy phenyl group and the plane of the triazole moiety is tilted by 14.6(9)°. According to the literature, the values generally range from 3 to 14° [2, 36-37]. The bite angles of N1–Ni–N8 and $N1^{i}$–Ni–N8 are ranging from 78.7(2)° to 101.3(2)°, and the torsion angles between Ni1–N8–C7–C6, Ni–N1–C6–C7, Ni1-N1-C5-C6 and Ni1-N8-N9-N10 are 4.7(7)°, 1.3(7)°, 178.1(5)° and 176.7(4)°, respectively. Other torsion angles are presented in Table 7.12.

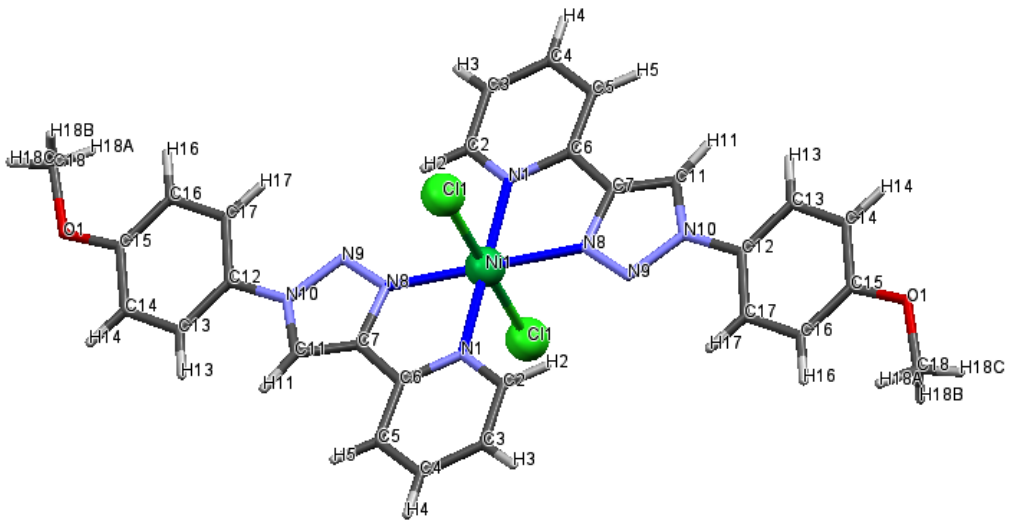

Figure 7.22: The molecular structure of $[Ni(L^3)_2Cl_2]$. The thermal ellipsoids are drawn at a 50% probability.

Moreover, there are no classic hydrogen bonds observed. The value is typical of extensive weak hydrogen bonding interactions [38, 39]. It generates a 3D supramolecular sheet in the solid state, as indicated by Table 7.14 and Figure 7. 23.

The crystal structure shows the involvement of the chloro moieties in the formation of hydrogen bonds, by acting as accepters or donors. This hydrogen bonding can be described as follows: The C4–H4 group of the pyridyl ring and C18–H18C of the methoxy group are hydrogen–bonded to the chloro ligands of the next molecule in the same layer. The second chloro ligand forms hydrogen bonds to the acidic triazole C11–H11 group on a triazole ring of the next layer. The bond length of the H11...Cl distance is 2.611Å and is well below the Van der Waals radius of H and Cl (3Å) [40]. Furthermore, in all cases the angle is located at 165° degrees out of the plane of the C–H bond. This value is closer to those values of hydrogen–bonding interactions reported for nickel complexes [1, 19, 41]. The angles between Ni–Cl...H4, Ni–Cl...H11 and Ni–Cl...H18C are 108.57(6)°, 107.09(6)° and 97.78(5)°, respectively. X-ray crystallography of $[Ni(L^3)_2Cl_2]$ established that the crystal structure is governed by short C–H...N interactions.

The atoms of involved are C–H (C–H18A) of the methoxy group as donors, and the N9 atoms of the triazole units as accepters. These hydrogen – bonded chains are linked with the chains from the other layer by [C–H and H...N-triazole], as shown in Figure 7.23. The H...N distances 2.665(7)Å are quite long and > 2.5Å. In all these C–H...N contacts the distance between the protons and the donor atomsare shorter than the sum of their van der Waals radius (2.75Å), and are comparable with published results in the literatur [39, 40]. These molecules adopt a head-to-tail orientation as shown in Figure 7.23. This head to tail arrangements are in accordance with those reported recently for Ni(II) and Pd(II) complexes with pyridyl-triazole ligands [19, 31, 32].

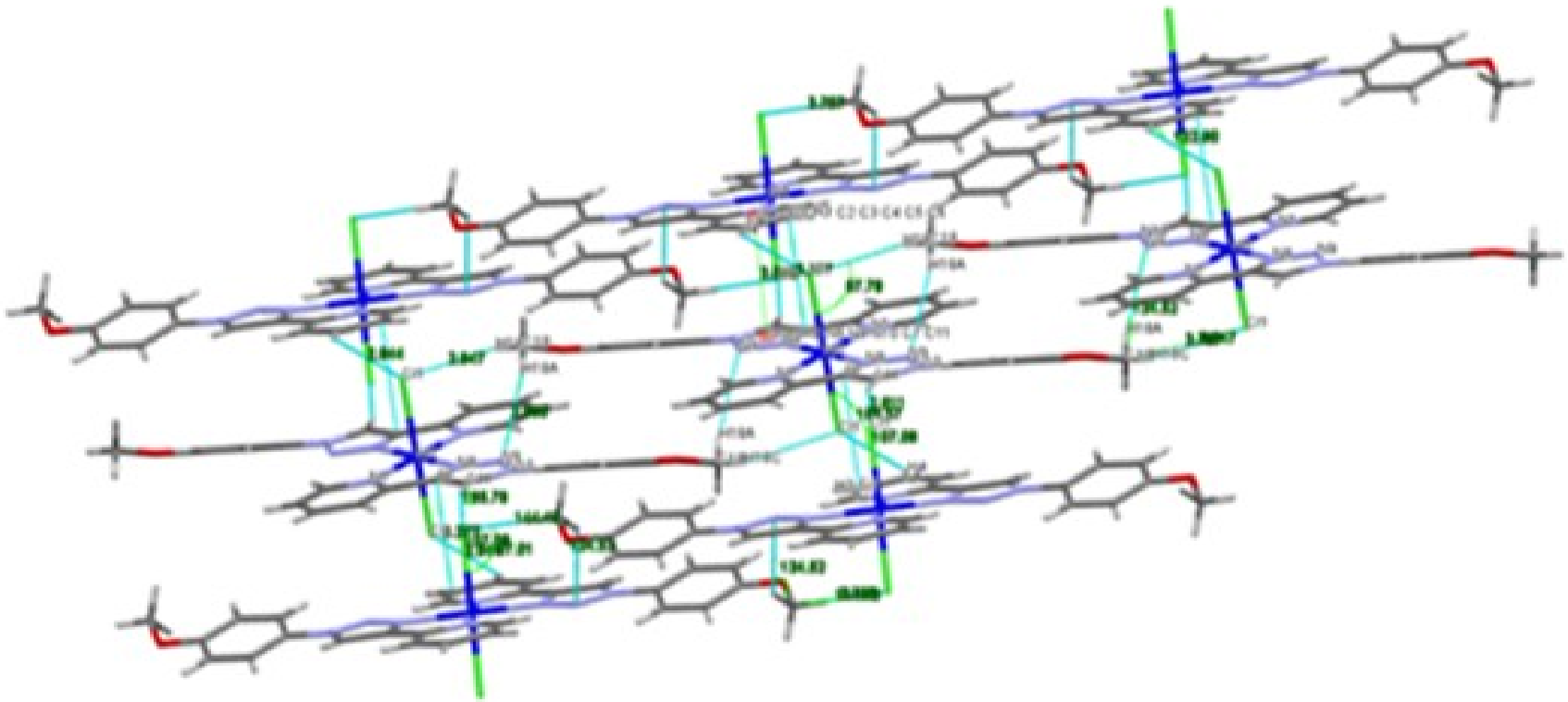

Figure 7.23: A 3D supramolecular sheet in $[Ni(L^3)_2Cl_2]$ complex showing intermolecular hydrogen bonding interactions (C–H…Cl and C–H…N).

The overlap between the triazole $N_8N_9N_{10}C_7C_{11}$ and pyridine $N_1C_2C_3C_4C_5C_6$ rings of the neighbouring molecules resulted in face–to–face and slipped-type parallel alignment. That means the rings are parallel displaced with respect to one another, exhibiting a centroid–centroid distance of 3.589Å, which is stabilised by triazole - pyridine π…π stacking and suggests the presence of some weak interactions. The adjacent pyridine ring is perfect coplanar, and the centroid - centroid distance is 3.589Å. This distance is comparable to the previously reported bond separations of a typical π…π stacking [44-47]. The centroid - plane perpendicular distance is 3.288Å and the angle between the two planes is 2.88° (see Figure 7.24).

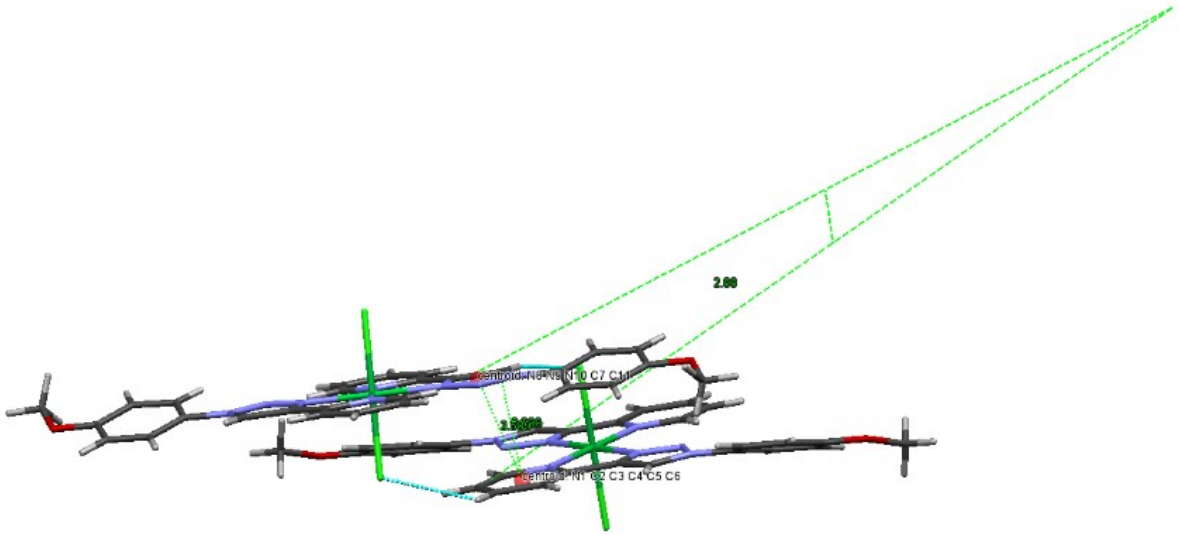

Figure 7.24: The overlap between the triazole and pyridine rings in $[Ni(L^3)_2Cl_2]$ complex showing the intermolecular π…π stacking interactions.

The complex is stabilised by hydrogen bonding interactions and intermolecular π…π stacking between the triazole and pyridyl rings. The molecules of $[Ni(L^3)_2Cl_2]$ are arranged in infinite hydrogen-bonded chains via C–H...N triazole, CH...Cl and C–H...Cl and intermolecular π…π stacking between the pyridine and the triazole rings.

Table 7.14: Weak hydrogen bonding interactions parameters; D= donor and A= acceptor (Å, °) in the complex $[Ni(L^3)_2Cl_2]$.

D-H...A/interactions	D–H (Å)	H–A (Å)	D–A (Å)	Angle (°)
C11–H11...Cl1	0.950(7)	2.611(3)	3.540 (8)	165.8(4)
C4–H4...Cl1	0.951(7)	2.944(4)	3.552 (7)	122.9(4)
C18–H18C...Cl1	0.980(1)	2.947(3)	3.787(8)	144.4(4)
C18–H18A...N9	0.980(9)	2.665(7)	3.420(1)	134.5(4)

7.2.10.2.3 X-ray Crystal structure of dichloro-2-(1-(4-methoxyphenyl)-1H-1,2,3-triazol-4-yl)pyridinemanganese(II) $[Mn(L^3)_2Cl_2]$

The molecular structure of $[Mn(L^3)_2Cl_2]$ is depicted in Figure 7.25. The complex crystallised in an orthorhombic space group *Pbcn*. Crystallographic data listed in Table 7.9 indicates four molecules per unit cell as $Z = 4$ of the $[Mn(L^3)_2Cl_2]$ complex. Selected bond lengths, bond angles and torsion angles are provided in Tables 7.10, 7.11and 7.12, respectively. The geometry about the Mn atom is essentially a distorted octahedral coordination arrangement. The octahedral basal plane is formed by the two Cl atoms Cl1 and Cl1i, which are arranged in the *cis* position to each other and two nitrogen atoms N8 and N8i. The remaining two vacant sites on the metal centre are occupied by the nitrogen atoms N1 and N1i of the pyridyl moieties adopting a *trans* position with a 178.89(16)° angle between $N1^{ax}$–Mn1–$N1i^{ax}$.

The metal-ligand angles in the Mn(II) complex deviate significantly from the ideal value of 90° or 180° (characteristic of a regular octahedron). Consequently, the ligands fold around the metal ion using *cis* conformation of the Cl^- anions and allowing the N triazoles to from an equatorial plane with the Cl^- anions (angles between $N8^{eq}$–Mn–$C1^{eq}$ and $N8i^{eq}$–Mn–$C1i^{eq}$ are 88.30(8)° and 155.71(8)°, respectively). Completing the remaining sites on the manganese atom are the N atoms of the pyridyl moieties.

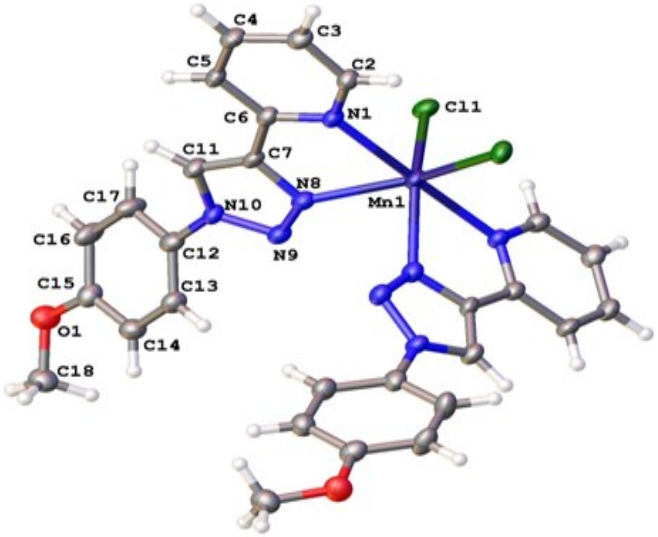

Figure 7.25: A labelled molecular structure diagram of $[Mn(L^3)_2Cl_2]$ with displacement thermal ellipsoids drawn at 50% probability.

The bite angle between N8–Mn–N1 is 71.90(10)°. Furthermore, the angle between Cl1–Mn1–Cl1 is 108.66(6)°, slightly higher thanthe angles for the Mn(II) complex having *cis* chloride atoms [48]. The bond lengths of the terminal chloro groups, Mn–Cl1 and Mn–Cl1i, are 2.4544(11)Å and 2.4543(11)Å, respectively [49]. The bond lengths of N8–N9, N9–N10 and N8–C7 of the 1,2,3-triazole segment are 1.305(4)Å, 1.358(4) and 1.365(5)Å, respectively. These distance values are similar to the distances for the free ligand. The Mn–N_{PY} and Mn–N_{TA} bond lengths of 2.330(3)Å and .324(3)Å are fairly standard [50-52]. The metal-triazole bond length is slightly shorter than the metal pyridine bond (by approximately 0.006Å), and similar reasoning to that mentioned in section 7.2.10.2.2 can be used to explain it [32, 35]. The angles between the pyridine plane and the triazole ring and between the triazole plane and the substituted phenyl ring are 115.4(3)° and 120.5(3)°, respectively. The dihedral angle between the plane of the pyridyl moiety and the mean plane of the triazole ring is 5.4(5)°. Furthermore, the dihedral angle between the plane of methoxy phenyl group and the plane of the triazole moiety is tilted by 38.6(5)°.

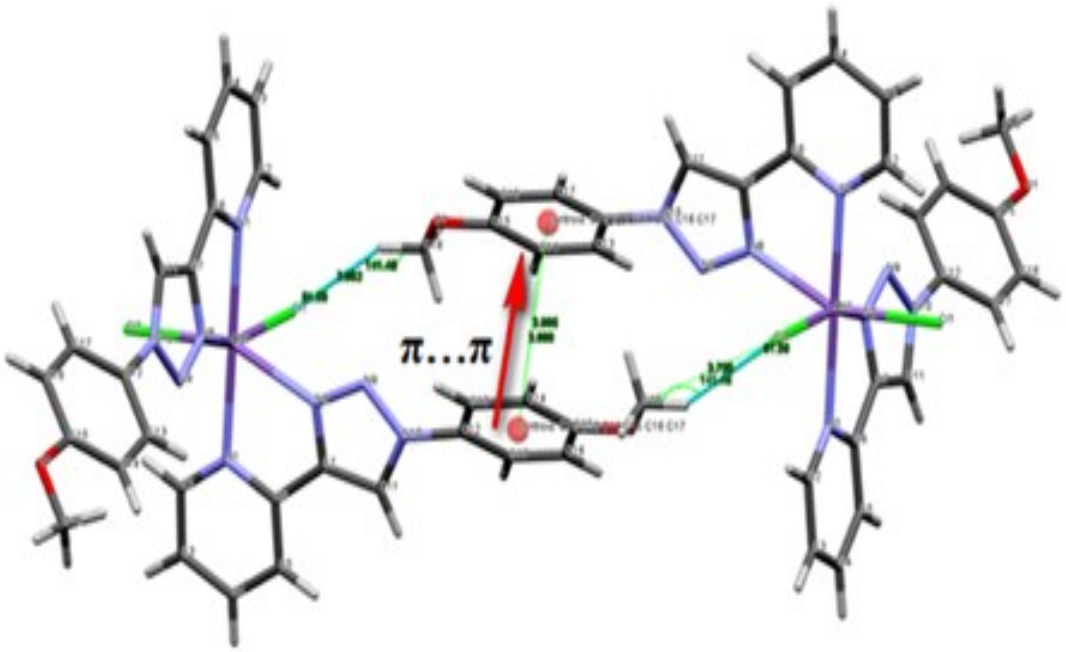

Figure 7.26: The overlap between the phenyl rings showing intermolecular π…π stacking and C–H…Cl hydrogen bonding interactions.

The overlap of the whole structure of molecules in the crystal shows weak (π…π) interactions causing stacking of the molecules, as shown in Figure 7.26. This resulted in an offest-slipped parallel alignment, which is stabilised by phenyl-phenyl π…πinteractions between the ($C_{12}C_{13}C_{14}C_{15}C_{16}C_{17}$) and the ($C_{12}C_{13}C_{14}C_{15}C_{16}C_{17}$) phenyl rings. The overlap shows the centroid – centroid distance is 3.985Å, while the centroid – plane perpendicular distance is 3.680Å. On the other hand the chelated (trizole) segment, which does not take part in the π…π interactions, is involved in a (D–H...A) interaction.

There are no classic hydrogen bonds, but there are intermolecular interactions of the type D–H...A, which include C–H...Cl, C–H...O and C–H...N hydrogen bonds (see Figure 7.27). Distances and angles are listed in Table 7.15. The C–H...Cl hydrogen bonds can be described as [CH3] C3-H3...O1, [C–H18] C18–H18A...Cl1, [C–H11] C11–H11...Cl1, [C–H4] C4–H4...N9 and [C–H5] C5–H5A...Cl1, according to Brammer *et al* [53]. Such < M–Cl…H angles prefer values ranging from 90° to 130° [53, 54]. It is observed < M–Cl…H angles listed in Table 7.15 and in all the cases of intermolecular hydrogen bonds, most of the intermolecular hydrogen bonds fit this rule.

Table 7.15: Hydrogen bonding interactions parameters; D= donor and A= acceptor (Å, °) in the complex $[Mn(L^3)_2Cl_2]$.

D–H...A	D–H	H–A	D–A	Angle
C3–H3...O1	0.950(4)	2.510(3)	3.540 (8)	159.0(2)
C18–H18A...Cl1	0.981(4)	2.882(9)	3.700(4)	141.4(2)
C5–H5...Cl1	0.950(3)	2.685(1)	3.620 (4)	168.3(2)
C4–H4... N9	0.949(4)	2.947(3)	3.787(8)	128.3(2)
C11–H11... Cl1	0.950(4)	2.599(8)	3.490(1)	156.2(4)
Mn–Cl...H5				96.75(4)
Mn–Cl...H11				115.89(4)
Mn–Cl...H18A				91.59(3)

In the crystal the molecules are arranged in infinite hydrogen-bonded 3D supramolecular chains along the b-axis direction, and within the chains are weak intermolecular π…π interactions and C–H...Cl hydrogen bonding interactions [55].

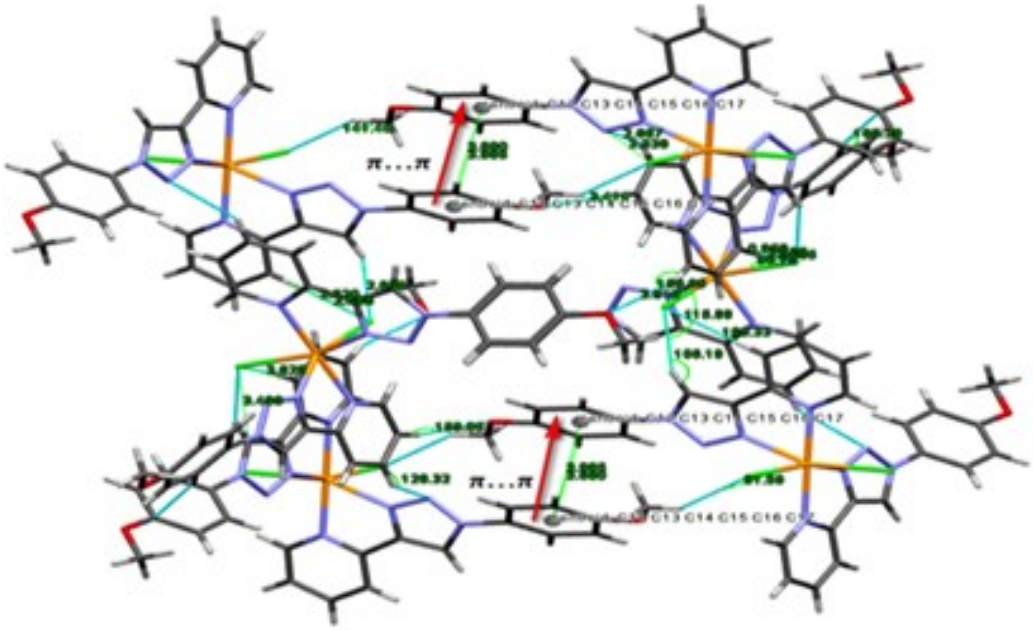

Figure 7.27: A 3D supramolecular sheet in $[Mn(L^3)_2Cl_2]$ showing intermolecular hydrogen bonding interactions C–H...Cl and (π…π) stacking interactions. The complex is viewed along the crystallographic b-axis.

7.2.10.3 Single-crystal structure determinations of the metal complexes of [M:L 1:1] obtained from [M:L 1:2] complexes

Crystals of the complexes $[Cu(L^3)Cl_2]_n$, and $[Cd(L^3)Cl_2]_n$ were obtained by slow evaporation of a hot mixture of CH_3OH: CH_3CN in a 1:1 ratio solution under ambient conditions. The $[Cu(L^3)Cl_2]_n$ crystallised in the orthorhombic *Pbcn* space group (according to Table 7.9) which indicates eight molecules per unit cell as $Z = 8$ of the $[Cu(L^3)Cl_2]_n$ complex. The $[Cu(L^3)Cl_2]_n$ complex adopted a distorted trigonal bipyramidal geometry with a coordination number of five around the metal atom. The $[Cd(L^3)Cl_2]_n$ crystallised in the monoclinic *P*b/*c*aspace group, (see table 7.9) which indicates four molecules per unit cell as $Z = 4$ of the $[Cd(L^3)Cl_2]_n$ complex. The latter adopted a distorted octahedral geometry with a coordination number of six around the metal atom. The crystal structural data are listed in Tables 7.9, 7.10, 7.11 and 7.13 and presented in Figures 7.28 and 7.31. These crystals were obtained from recrystallised complexes having a molar ratio of [M:L = 1:2]. The two complex formulas both adopted a one – dimensional infinite polymeric chain.

7.2.10.3.1 X-ray crystal structure of a one-dimensional infinite polymeric chains of (μ--chlorido)-(2-(1-(4-methoxyphenyl)-1H-1,2,3-triazol-4-yl)pyridinecupper(II) dichloride complex $C_{42}H_{36}Cl_6Cu_3N_{12}O_3$

The crystallographic data of the complex is given in Table 7.9; selected bond lengths, bond angles and torsion angles are provided in Tables 7.10, 7.11 and 7.13.

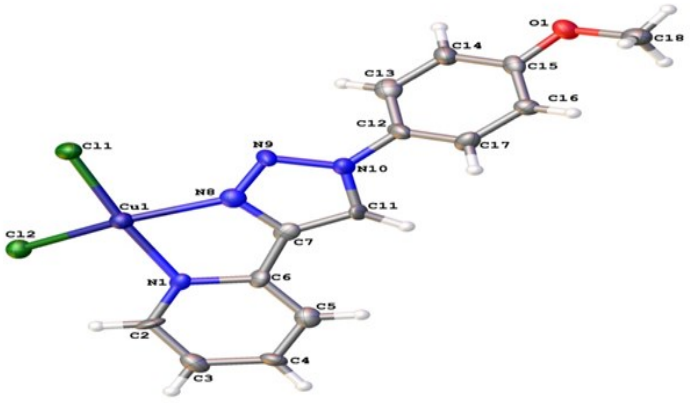

Figure 7.28: Molecular structure of the monomeric $[Cu(L^2)Cl_2]$ with displacement thermal ellipsoids drawn at 50% probability level and H atoms are shown as small spheres of arbitrary size.Solventmolecules have been omitted for clarity.

The copper centre in the complex $[Cu(L^3)Cl_2]_n$ is in a distorted trigonal bipyramidal coordination environment which includes the $N8_{TA}$ and $N1_{PY}$ atoms from one ligand L^3 in the equatorial plane Figure 7.28. The axial positions are taken up by the bridging chlorine atoms Cl2 and the terminal free chlorine atoms Cl1 appeared upward and downward from each other. The X-ray crystal structure analysis of the Cu-complex reveals the formation of an infinite 1D chain link coordination polymer. A perspective view of the title compound showing the numbering scheme is given in Figure 7.29.

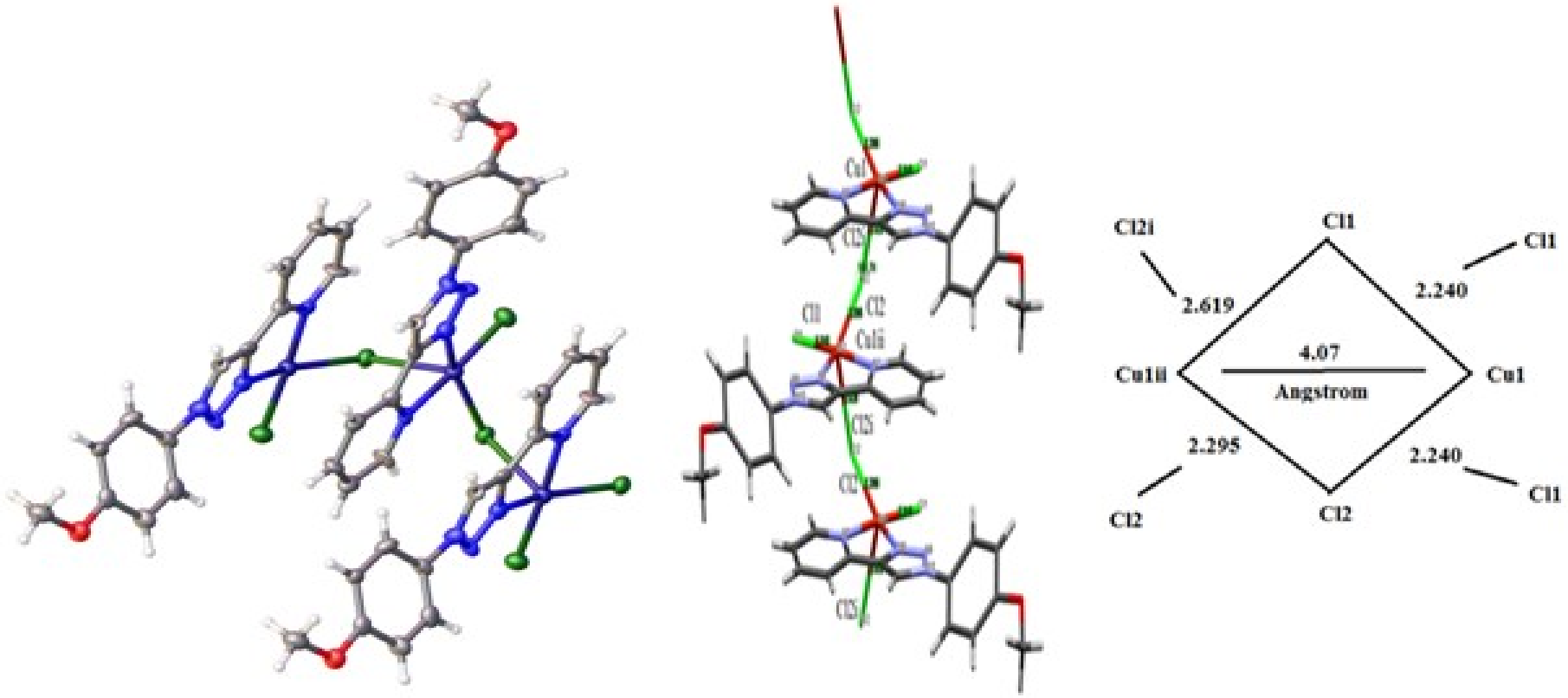

Figure 7.29: Perspective view of the one-dimensional infinite polymeric chain structure of the $[Cu(L^3)Cl_2]_n$ complex linked by Cl2. The Cu−Cu distance in the one dinuclear core is 4.070Å. The Cu(II) complex is viewed along the crystallographic b-axis.

The geometry around the copper(II) ion can be described as highly distorted square pyramidal geometry, with the basal plane formed by two nitrogen atoms (N1 and N8) of the ligand and two chloride atoms Cl1 and Cl2. The Cu–N1 distances are 2.064(8)A˚ and Cu–N8 2.046(8)A˚ respectively and the Cu–Cl distances are (Cu–Cl1) 2.240(3)A˚ and Cu–Cl2 2.295(3)A˚. The apical position is occupied by a symmetry-related image of Cl2iat a distance of Cu–Cl2i 2.629(3)A˚ from the copper ion. The N1–Cu– Cl1 angle of the base plane is 174.6(2)° with N8–Cu– Cl2 155.3(2)°. The distortion of the five-coordinate sphere can be described by the trigonality parameter τ, which is defined as: $(\varphi_1 - \varphi_2)/60$ where φ_1 and φ_2 are the two largest L-Cu-L angles of the coordination sphere. The calculated τ for the Cu(II) ion site is 0.321, which confirms the tetragonal pyramidal character [56]. The difference in the Cu-Cl bond lengths, at the apical position which is considerable, is clearly related to the Jahn–Teller distortion. The angle between the pyridine plane and the triazole ring is only 113.9(8)°. The twisting angle between the triazole plane and the substituted phenyl ring is 118.5(9)°. The phenyl ring of the triazole ligand is twisted from the neighbouring triazole ring with the dihedral angle of 38.8(13)°, while the pyridine ring twisted from the neighbouring triazole ring has a dihedral angle of 3.5(12)°. Upon complexation, the resulting zig-zag chain of Cu1 and Cl2 is the backbone of a polynuclear array running parallel to the crystallographic b-axis.

The angle between Cu1–Cl2–Cu1ii is 111.75^{o}, and the array is stabilised by π…π stacking of the triazole ring containing N8 on a symmetry-related image of the ring containing N1 (see Figure 7.30). The Cu–Cl2–Cu bridge is formed by the atoms Cu, Cl2, Cl2i and Cu^{ii}. The Cu–Cl distances in the bridging unit are 2.295(3) and 2.629(3)Å, and shows a symmetrical bridging of high degree compared to the present complex. The Cu(μ − Cl2)Cu core has each Cu(II) atom bond to a bridging chloride (μ − Cl2) (Figure 7.30). The bond length of Cu−Cl2 = 2.295(3)Å is longer than that for Cu−Cl1 (by approximately 0.055Å) at Cu−Cl1 = 2.240(3)Å. The bond length of Cu−Cl2i = 2.629(3)Å is longer thanCu−Cl2 (by approximately 0.334Å). The local arrangement for each copper indicates a tetragonal pyramidal geometry τ for the Cu(II) ion of 0.321. The equatorial plane is formed by one bidentate triazole ligand, a bridging chloride, and a terminal chloride. The Cu−Cu distance in each dinuclear Cu(II) core is 4.070(1)Å.

It was reported that a Cu(II) complex similar to this polymeric chain has a five and six coordinate environment around the Cu(II) which leads to a distorted square pyramidal symmetry [57, 58]. The packing diagram and hydrogen bonding interactions were analysed by Mercury software. The packing and hydrogen bonding interactions are viewed along b-axis and are shown in Figure 7.30 B. The crystal structure can be described as an infinite chain that develop in a zigzag pattern along the b-axis via weak hydrogen bonds of type C3–H3...O1, C–H...O1 and C–H...Cl. These chains are interconnected, through hydrogen bonds via C–H...O and C–H...Cl. The complex displayed no classic strong hydrogen bonds of a D–H...A type (Table 7.16) [38].

Table 7.16: Hydrogen bonding parameters; D= donor and A= acceptor (Å, °) in the complex $[Cu(L^3)Cl_2]_n$ chain.

D–H...A	D–H	H–A	D–A	Angle
C3–H3...O1	0.93 (1)	2.541(8)	3.27 (1)	135.4(6)
C13–H13...O1	0.96 (1)	2.554(7)	3.45 (1)	161.9(6)

The triazole ring C11–H(11)–Cl2 displayed an interaction with Cl2. The hydrogen bonding distances and angles are (D–H…A), (D–H) C11–H11= 0.929(9), (H–A) H11–Cl2= 2.880 and (D–A) C11–Cl2= 3.458Å, respectively. Table 7.17 and Figure 7.30 B show that they are very similar to the bond lengths and angles for C–H...Cl which have been published recently [1]. These types of hydrogen bonding triazole C–H...Cl^- have been reported previously in literature [53, 59-61].

Table 7.17: Hydrogen bonding parameters; D= donor and A= acceptor (Å, °) in the complex $[Cu(L^3)Cl_2]_n$ chain.

D–H...A	D–H	H–A	D–A	Angle
C11–H11...Cl2	0.929(9)	2880(2)	3.46 (1)	149.3(6)
C11–H11...Cl2i	0.929(9)	2.626(2)	3.46 (1)	149.3(6)
C2–H2...Cl2	0.93(1)	2.719(2)	3.24 (1)	116.5(6)
C6–N1...Cl2i	1.37(1)	3.110(7)	4.389(9)	154.2(6)
C6–N1...Cl2	1.37(1)	3.210(7)	4.037(8)	154.2(6)
C5–H5...Cl1	0.929(9)	2.855(3)	3.55 (1)	132.9(2)
C18–H18...Cl1	0.96(1)	2.774(3)	3.71(1)	165.9(7)
C11–H11...Cl2i	0.929(9)	2.880(2)	3.45(1)	121.2(6)

In addition to these hydrogen bond interactions, stacking molecules adopt a face-to-face parallel alignment due to (π…π) weak interactions. The value between the pyridine - triazole, centroid ($N_1C_2C_3C_4C_5C_6$) pyridine ring and the centroid of the ($N_8N_9C_7C_4N_{10}C_{11}$) triazole ring of the adjacent molecule, is 3.495 [1], and the centroid–plane perpendicular distance is 3.280Å (Table 7.18, Figure 7.30A). The angle between the two planes is 6.00°.

Table 7.18: The π…π stacking interactions in the molecular structure of the 1D $[Cu(L^3)Cl_2]_n$ chain.

Ring(triz) → Ring(py) of centroid	Distance of centroid (tri) from ring (py) (Å)	Centriods-plane perpendicular distances (Å)
Ring(PY)→ Ring(TA)	3.647	3.280
Ring(PY)→ Ring(TA)	3.900	3.280
Ring(TA)→ Ring(PY)	3.628	3.466
Ring(PY)→ Ring(TA)	3.495	3.458

The molecular structure of the complex $[Cu(L^3)Cl_2]_n$ is stabilised by non-standard weak hydrogen bonds, via C–H...Cl and C–H...O1 atoms with intermolecular hydrogen bonds and π … π stacking interactions.

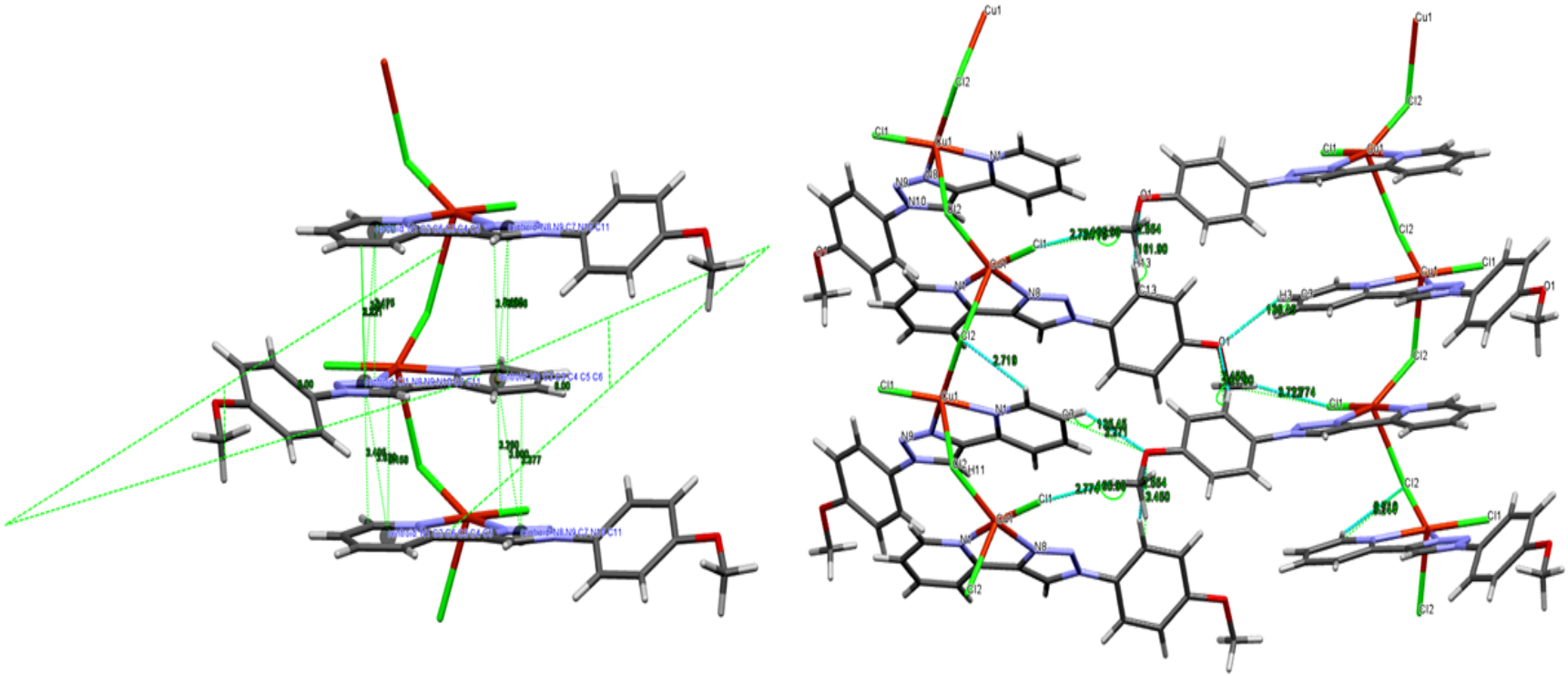

(A) **(B)**

Figure 7.30: Molecular structure of 1D chain $[Cu(L^3)Cl_2]_n$; (A)-showing the overlap layer of the complex arranged about a connected centre of symmetry. (B)- Schematic representation of the crystal structure showing the hydrogen bonding interactions (in blue line) via C–H...Cl and C–H...O1 atoms. The Cu(II) complex is viewed along the crystallographic b-axis.

7.2.10.3.2 X-ray crystal structure of a one-dimensional infinite polymeric chains of (μ--chlorido)-(2-(1-(4-methoxyphenyl)-1H-1,2,3-triazol-4-yl)pyridinecadmium(II) dichloride complex $C_{42}H_{36}Cl_6Cd_3N_{12}O_3$

Crystallographic details of the complex are given in Table 7.9. Selected bond lengths, torsion angles and bond angles are provided in Tables 7.10, 7.11 and 7.13.

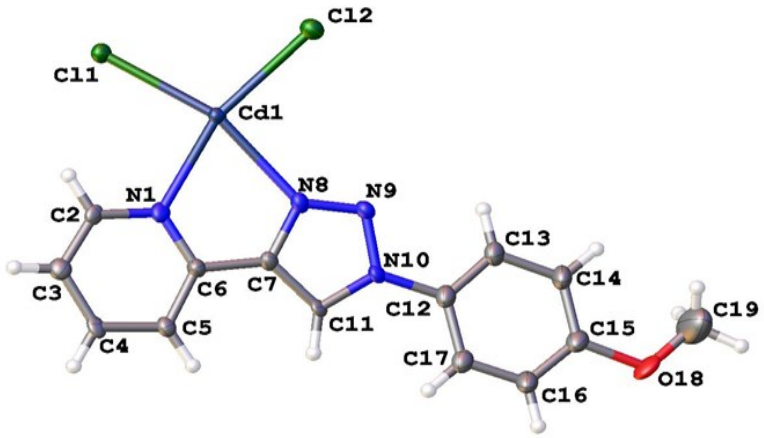

Figure 7.31: Molecular structure diagram of the monomeric $[Cd(L^2)Cl_2]$. Displacement thermal ellipsoids are drawn at 50% probability level and H atoms are shown as small spheres of arbitrary size. Solventmolecules have been omitted for clarity.

The bond length in Cd1−$N1_{PY}$ is 2.359(17)Å. However this bond length is slightly longer than those that were observed for the ligand complex bridges from mercapto-triazole ligands that have recently been published in literature and are around 2.319(4)Å [62]. The Cd–N_{PY} bond distances are similar to the literature reports for the $[Cd_3(pybta)_4I_6]_n$ complex of 2.356(4)Å [63]. The bond length of Cd1−N8(N_{TA}) is 2.391(3)Å, this is among the shortest reported yet. In a synthesis and structural study of divalent Cu, Zn, Cd and Pd complexes with 1,2,3-triazole-based chalcogen ligands, the reported bond length was 2.249(3)Å [64], and for cadmium complexes bearing 1,2,3-triazole ligands, including $[(CdCl_2)_2$(1,2-bis(benzotriazole)ethane$)_2]$ it ranged from 2.320 to2.328Å [65].The complex displays a 1D stranded chain structure consisting of tri nuclear $[Cd(PYTA)Cl_2]_3$ subunits. Within each tri nuclear subunit, three cadmium atoms are linked by one (PYTA) ligand and four chlorido ligands to form the basal plane in a zigzag conformation to complete the geometry around the metal and form an infinite 1D chain-like coordination polymer. Along the b-axis direction, each Cd(1) centre is double bridged by one pair of (PYTA) ligands and four

chlorido ligands. The (PYTA) molecule exhibits distorted conformation and the molecules are wrapped around the metal centre and are held together by Cd(1) atoms forming a one dimensional stranded chain structure as depicted Figure 7.32.

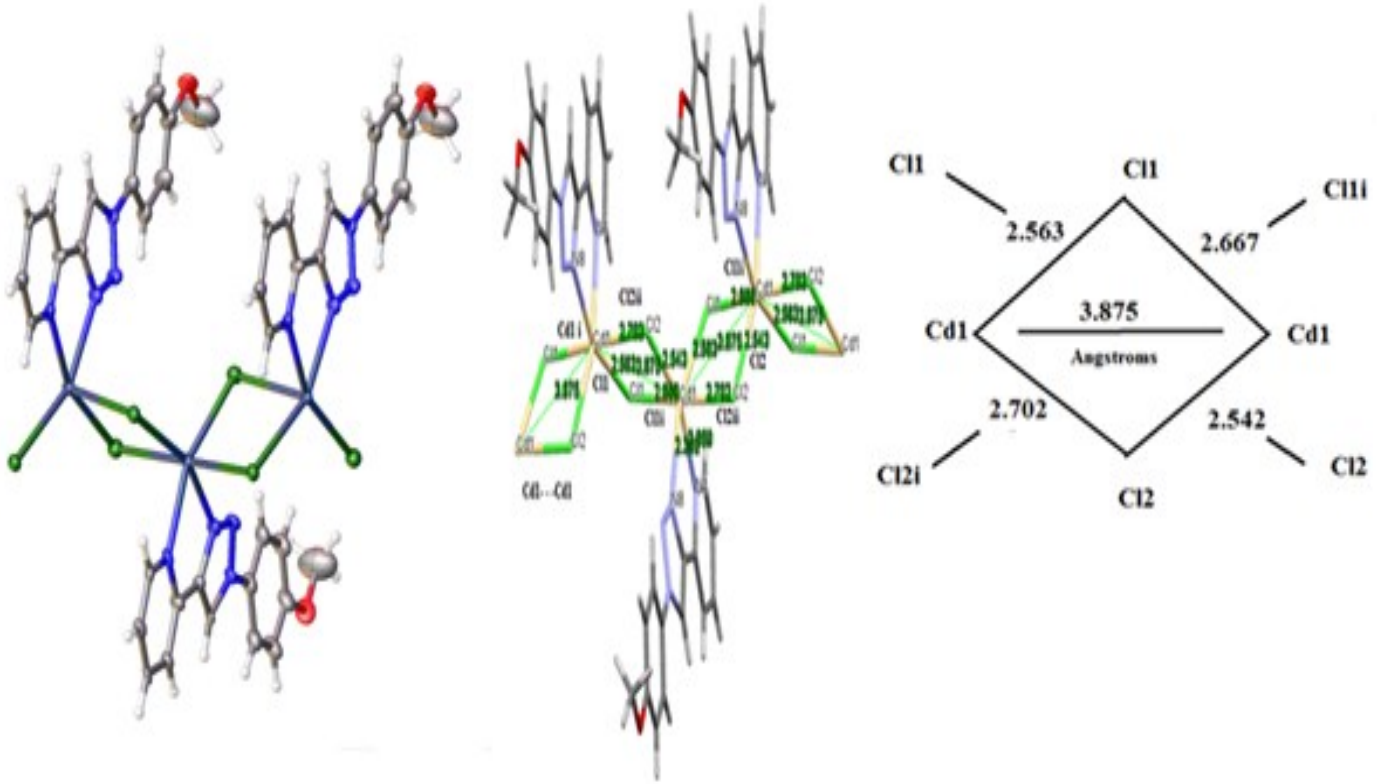

Figure 7.32: Perspective view of the one dimensional infinite polymeric chain structure of the $[Cd(L^3)Cl_2]_n$ complex linked by Cl2. The Cd−Cd distance in one dinuclear core is 3.875Å. The Cd(II) complex is viewed along the crystallographic b-axis.

The complex $[Cd(L^3)Cl_2]_n$ is in a distorted octahedral coordination environment, which includes the N8-triazole and pyridyl N1 atoms from one ligand L^3 in the equatorial plane, which participate with two chloride ions Cl1 and Cl2 in the bonding process. The angles between $N8^{eq}$–Cd1–$Cl2^{eq}$ and $N1^{eq}$–Cd1–$Cl1^{eq}$ are 94.7(4)° and 94.5(4)°, respectively. The axial positions of the Cd(II) centre are occupied by two bridging chloride atoms that are *trans* to each other [Cd1–Cl1i= 2.667(6)Å, Cd1–Cl_2^{ii} = 2.702(6)Å]. These distances are longer than that of non-bridged Cd-Cl bonds (by approximately 0.104 and 0.160Å respectively). The angle between the $Cl1i^{ex}$–Cd1–$Cl2ii^{ex}$ is 174.35(18)°, a value which is similar to one observed previously for a triazole-bridged cadmium coordination polymer [64-65]. The chloride bonds Cd−Cl1=2.563(5)Å and Cd−Cl2=2.542(6)Å are comparable to Cd-Cl bonds that was reported previously for a di- μ-dichlorido bridged cadmium(II) [67, 68] (Figure 7.33). The bond angles of $N8^{eq}$–Cd1–$Cl2^{eq}$ and $N1^{eq}$–Cd1–$Cl1^{eq}$ are 94.7(4)° and 94.5(4)°, respectively and angle between the $Cl1i^{ax}$-Cd1-$Cl1ii^{ax}$ is 174.35(18)°, suggesting a distorted octahedral geometry in the complex.

The twisted angles of two chloride groups are 103.30(18)° of Cl2-Cd1-Cl1 and 98.46(19)° of Cl2−Cd1−Cl2ii, respectively. The Cd−Cd distance in each dinuclear Cd(II) core is 3.875Å. There is an interesting change in the distance of the bond length for the C7–C11 triazole ring, and it appears that in the Cd(II) complex it is slightly longer than in the free ligand (by approximately 0.028Å). The values of C7–C11 in the triazole ring for the Cd(II) complex and the L^3 are 1.39(3) and 1.362(6)Å, respectively. These changes confirm the complexation between the metal and the ligand. In the Cd(II) complex, the metal-triazole bond length is slightly longer than the metal pyridine bond i.e. Cd–N8 = 2.391(19) and Cd–N1 = 2.359(17)Å, respectively (a change of approximately 0.032Å). These bonds are longer in the Cd(II) complex compared to others previously reported for the Cu(pyta) and the Pd(pyta) complexes [35, 38, 69-71]. From the experimental results it can be deduced that the N8 atom of the 1,2,3-triazole group is a more effective donor to coordinate with the metal than the N9 atom, due to its much higher electron density [72-73].

In the complex the length of the Cd(1)-N(1) bond is 2.359(17)Å, which is approximately is 0.032Å shorter than the Cd(1)-N(8) bond of 2.391(18)Å. This also confirms that the N8 atom has a stronger coordinating ability than the N9 atom. The

chelating N1–M–N8 bite angle is 70.0(6)° which is similar in the complex compared the same angle in the polymeric Cd(II) complex (see Table 7.11). After complexation the pyridine ring is twisted with respect to the triazole ring, and the twisting angle is equal to 114.0(19)°. The twisting angle between the triazole plane and the substituted phenyl ring is 119.4(17)°, whereas, the plane of the pyridine ring exhibits a dihedral angle of 10(3)° with the mean plane of the triazole ring.

In contrast, the dihedral angle between the triazole plane and the aromatic group plane is 11(3)°. The crystal structure of the complex shows an extensive chain that develops in a zigzag pattern along the b-axis via weak hydrogen bonds of the type D–H...A, through the C–H...O and C–H...Cl. The relevant distances and angles are summarised in Table 7.19 and Figure 7.33B. Non-classic strong hydrogen bonds of the (D–H...A) type are observed and the value in the molecular structure of $[Cd(L^3)Cl_2]_n$ for the C–H...O distances are C-H = 0.9500 Å, H...O = 2.60(2)Å and C14–O18 = 3.51(3)Å with an angle of 161(2)° for C14–H14...O18. These values are smaller than those previously reported for hydrogen bonds interactions [74, 75].

Moreover, as a result of these hydrogen bond interactions, weak interactions π…π type stacking interactions in the complex is observed. The distance between the centroid (N_1, C_2, C_3, C_4, C_5, C_6) pyridine ring and the centroid-centroid of (C_{12}, C_{13}, C_{14}, C_{15}, C_{16}, C_{17}) of the adjacent molecule is 3.666Å [22]. The centroid-plane perpendicular distance is 3.398-3.413Å (see Figure 7.33A). The angle between the two planes is 6.00°.

Table 7.19: Hydrogen bonding parameters (Å, °); D= donor and A= acceptor in the complex $[Cd(L^3)Cl_2]_n$ chain.

D–H...A	D–H	H–A	D–A	Angle
C4–H4...Cl1	0.9500(2)	2.845(5)	3.470 (2)	125.0(1)
C5–H5...Cl1	0.9500(2)	2.892(5)	3.480 (2)	121.0(1)
C11–H11...Cl2	0.9500(2)	2.677(6)	3.530 (2)	150.0(1)
C17–H17...Cl2	0.9500(3)	2.824(5)	3.760(3)	168.0(1)
Cd–H4...Cl1				135.6(2)
Cd–H5...Cl1				94.2(2)
Cd–H11...Cl2				122.5(2)
Cd–H17...Cl2				149.1(2)
CS–H1S...N9	0.9900(7)	2.590(2)	3.160(7)	117.0(4)
CS–H1S... Cl2	0.9900(7)	2.885(5)	3.400(7)	113.0(4)
C13–H13...O1S	0.9500(3)	2.560(5)	3.460(6)	158.0(2)

Where: CS, H1S and O1S are referred to the molecules of solvent CH_3OH

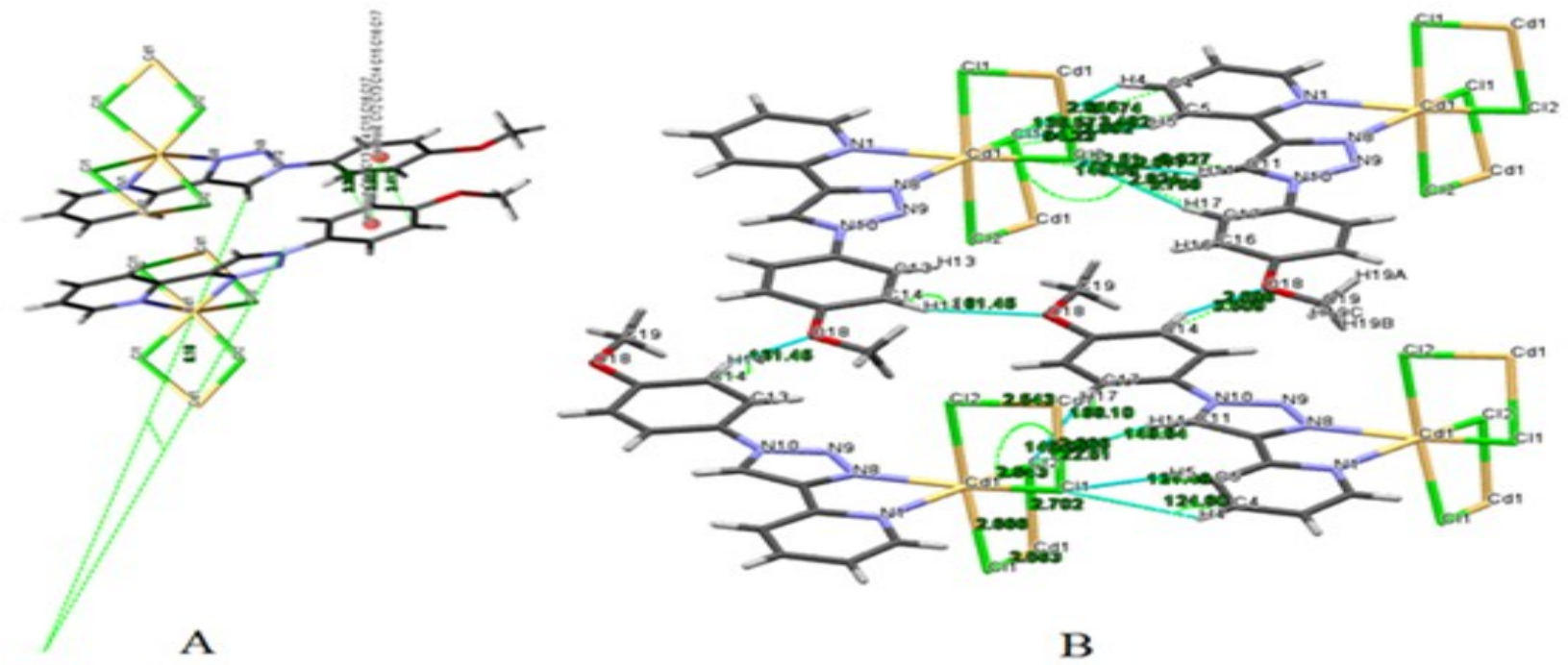

Figure 7.33: Partial view of the molecular structure of the 1D chain $[Cd(L^3)Cl_2]_n$; (A): showing the overlap between the phenyl rings as a result of intermolecular π…π stacking interaction. (B): Schematic representation of the crystal structure showing the hydrogen bonding interactions (in blue lines) via C–H...Cl and C–H...O1 atoms. The Cd(II) complex is viewed along the crystallographic b-axis.

7.2.10.4 The effect of the nature of the 1,2,3-triazole substituent ligands in the crystal structure of the various Cu(II) complexes

X-ray single-crystal diffraction analysis was used to determine the molecular structures of the complexes formed with ligands L^2, L^6, L^7, L^8 and L^9 and are depicted in Figures 7.34 and 7.37. It shows perspective views of the structure of the copper(II) complexes formed with bidentate ligands and two chloride ions as a coligands. The single crystals of the complexes $[Cu(L^2)_2Cl_2]$, $[Cu(L^6)_2Cl_2]$, $[Cu(L^7)_2Cl_2]$, $[Cu(L^8)_2Cl_2]$ and $[Cu(L^9)_2Cl_2]$, were grown by slow evaporation of methanol or methanol/acetonitrile in a ratio of 1:2 solvents. Unit cell data collection and structure refinement details are provided in Table 7.21 and selected bond lengths, angles and torsion angles are listed in Table 7.22, 7.23 and 7.24. Both the complexes $[Cu(L^2)_2Cl_2]$ and $[Cu(L^8)_2Cl_2]$ crystallised in the monoclinic space group P21/c.

The complexes $[Cu(L^6)_2Cl_2]$ and $[Cu(L^9)_2Cl_2]$ crystallised in an orthorhombic space groups of *P*ccn and Pca21, respectively. The complex $[Cu(L^7)_2Cl_2]$ crystallised in triclinic space group *P*-1. In all the Cu(II) complexes, the copper ion adopt the usual distorted octahedral coordination geometry with bond lengths and angles within the typical range found for copper complexes based on bidentate 2-pyridyl-1,2,3-triazole derivatives.

The structures are very similar to the one that was reported for the $[Cu(pyta)_2Cl_2]$ complex [2]. The copper(II) ion in the centre of complexes displays a Jahn - Teller distorted octahedral coordination, which includes two of the 2-pyridyl-1,2,3-triazole derivatives (L^2= CH_3, L^6= Cl, L^7= CN, L^8= H and L^9= CF_3ligand substituents) coordinated to the copper atom, through the N-triazole and N-pyridyl atoms from two different ligands which are lying in the equatorial plane mutually *trans* to each other. Furthermore, the axial positions are occupied by two chloride ions that are also *trans* to each other.

The angles in the plane containing the two ligands deviate from 90° because of the chelating nature of the ligands. However, the 180° angles are intact in the case of the complexes $[Cu(L^2)_2Cl_2]$, $[Cu(L^6)_2Cl_2]$ and $[Cu(L^8)_2Cl_2]$, while this angle is distorted in the $[Cu(L^7)_2Cl_2]$ and $[Cu(L^9)_2Cl_2]$ complexes. The pyridine and the chloride donor unite to adopt a square planar array around the Cu(II) ion. This angle ranges between

90.47(9)°-88.0(2)° see Table 7.23. The triazole rings and pyridine are coordinated to the copper core, leading to neutral mononuclear complexes. The most significant bond lengths of the C=C triazole and N=N inside the 1,2,3-triazole ring for each complex are changeable and depend on the electron donating or electron withdrawing nature of the substituent on the phenyl group. Interestingly, these substituents on the phenyl ring, if attached to a PYTA ligand does not affect the geometry of structures around the Cu(II) (see Figures 7.34 and 7.37). The $[Cu(L^2)_2Cl_2]$ complex is selected as an example to discuss its X-ray crystallography.

7.2.10.4.1 The X-ray crystallography of di-chloro-bis (2-(1-(p-tolyl)-1H-1,2,3-triazol-4-yl)pyridinecopper(II)

X-ray crystallography was used to determine the molecular structure of the complex. Figure 7.34 shows a perspective view of the structure of the copper(II) complex formed with bidentate ligands and two chloride ions as co-ligands. Single crystals of the complex $[Cu(L^2)_2Cl_2]$ were grown from CH_3OH.Crystallographic data are presented in Table 7.21 indicates two molecules per unit cell as $Z = 2$ of complex and selected bond lengths, angles and torsion angles are listed in Table 7.22, 7.23 and 7.24. It crystallises in a monoclinic space group P21/c. The copper ion adopt the usual distorted octahedral coordination geometry with bond lengths and angles within the typical range found for copper complexes based on bidentate 2-pyridyl-1,2,3-triazole derivatives. This structure is very similar to that reported for a related $[Cu(pyta)_2Cl_2]$ complex [2].

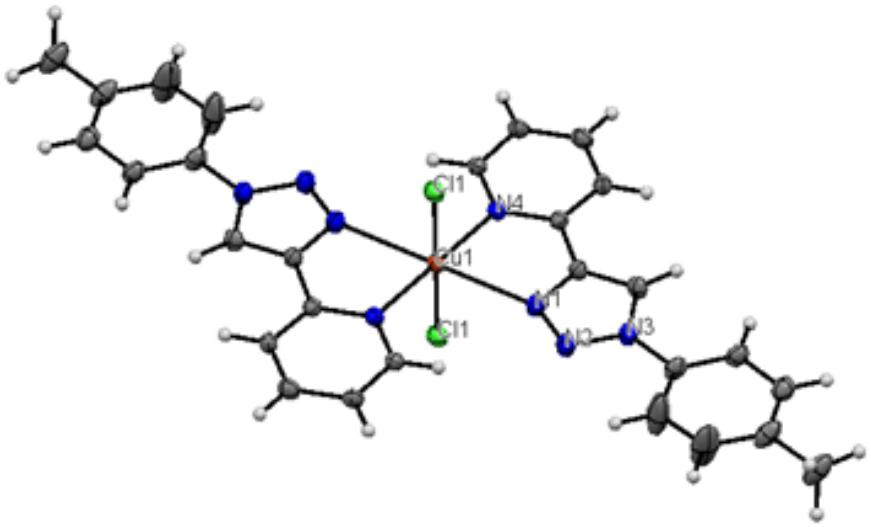

Figure 7.34: Labelled Ortep plot of the $[Cu(L^2)_2Cl_2]$. The thermal ellipsoids are drawn at 50% probability level and H atoms are shown as small arbitrary spheres.

The copper(II) ion centre in the complex displays a Jahn - Teller distorted octahedral coordination. It includes two L^2 ligands, where L^2= bis(2-(1-(p-tolyl)-*1H*-1,2,3-triazol-4-yl)pyridine, coordinated to the copper atom, through the N_{TA} and N_{PY} atoms from two different ligands which are lying in the equatorial plane and are mutually *trans* to each other. The angles for $N4^{eq}$–Cu–$N4i^{eq}$ and $N1^{eq}$–Cu–$N1i^{eq}$ are 180.0(19)° and 180.0(1)°, while the angles between $N1^{eq}$–Cu–$N4^{eq}$ and $N1i^{eq}$–Cu–$N4i^{eq}$ are similar to each other at 78.06(12)°. In addition, the axial positions are located by two chloride ions that are *trans* to each other at an angle of $Cl1^{ex}$–Cu–$Cl1i^{ex}$= 180.0°. The angles in the plane containing the two ligands deviate from 90° because of the chelating nature of the ligands. The 180° angles are intact in the case of the $[Cu(L^2)_2Cl_2]$ complex. The planar bidentate sites of the L^2 ligands constitute a square planar array around the Cu(II) ion - centred octahedron see the angles in Table 7.23. The chelating N1–Cu–N8 bite angle at 78.06(12)° is found to be lower than that reported for analogous structures around the metal centre [1, 2, 69-71].

The most significant result in the Cu(II) examples, is that the metal-triazole bond length is shorter than the metal pyridine bond: (by approximately 0.436Å) Cu-N_{TA} = 1.992(3)Å and Cu-N_{PY} = 2.428(3)Å. This is due to of the greater *trans* influence of the triazole nitrogen versus the pyridyl nitrogen [32], which is evidence for the stronger electron donating properties of the 1,2,3-triazole ring compared to the pyridine ring, as was observed previously [33-35]. The bond lengths of both monodentate chloride ions show that Cu–Cl1 is 2.3394(10)Å, similar to one that was observed and reported previously in literature [33]. The angle between Cl1–Cu1–Cl1i is 180.0°. The dihedral angle between the pyridine plane and the mean of the triazole ring is 1.3(6)°, while the 4-substituted aromatic group exhibits a dihedral angle of 0.2(7)° with the mean plane of the triazole ring [32]. The angle between the pyridine plane and the triazole ring is 116.8(3)°, while the angle between the triazole plane and the substituted phenyl ring is 121.8(3)°.

X-ray crystallography of the $[Cu(L^2)_2Cl_2]$ complex established that the crystal structures are governed by extensive hydrogen bonding C–H...Cl interactions which between the chloride ligands that are bound to the copper centres and the C–H group (see Figure 7.35). The molecules involved both of (1)- the C–H (C7–H7) atoms of the triazole ring, (2)- the C–H (C4–H4) atoms of the pyridine ring, (3)- the C–H (C9–H9), (4)- C–H (C14–H14) atoms as a donor, while the acceptors for the hydrogen bonds are the Cl^- ions and the chloride ligand bonded to C–H group of the neighbouring molecule (the next molecule in the same layer) in the crystal structure of the $[Cu(L^2)_2Cl_2]$ complex. The second chloride ligand forms hydrogen bonds to these C–H groups of the next layer. Relevant distances and angles are listed in Table 7.20. These hydrogen - bonded chains are linked with the chains from the next layer by C–H...Cl hydrogen bonds as shown in Figure 7.35.

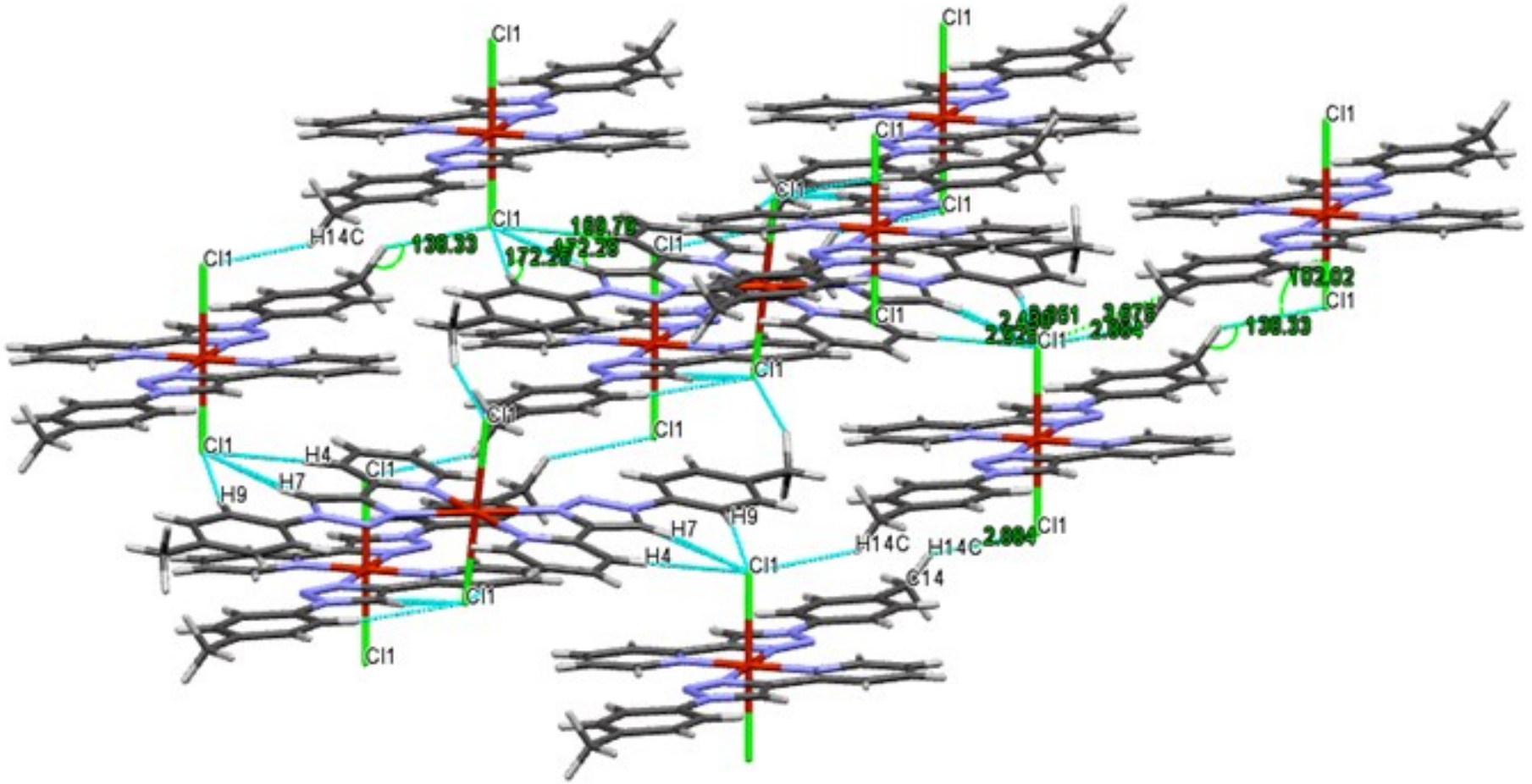

Figure 7.35: A 3D supramolecular sheet in $[Cu(L^2)_2Cl_2]$ complex showing intermolecular hydrogen bonding interactions.

In these C–H...Cl contacts the distances between the proton and the acceptor atoms are longer than the sum of their van der Waals radius (2.75Å), but the C–H...Cl linkages of the triazole rings displayed shorter distances than the sum of their van der Waals radius (2.75Å) [42-43]. The molecules of the $[Cu(L^2)_2Cl_2]$ are arranged in infinite hydrogen-bonded chains with (C–H...Cl) distances in the molecules of $[Cu(L^2)_2Cl_2]$ adopting a head-to-tail orientation as shown in Figure 7.35.

Table 7.20: Hydrogen bonding parameters; D= donor and A= acceptor (Å) in the complex $[Cu(L^2)Cl_2]$.

D–H...A	D–H	H–A	D–A	Angle(º)
C7–H7...Cl1	0.950(4)	2.430(9)	3.373(4)	172.3(2)
C4–H4...Cl1	0.950(4)	2.925(2)	3.864(4)	169.8(2)
C9–H9...Cl1	0.950(4)	2.850(9)	3.794(4)	172.2(2)
C14–H14...Cl1	0.980(5)	2.884(9)	3.675(5)	138.3(3)
Cu–Cl–H7				107.03(4)
Cu– Cl –H4				98.55(3)
Cu– Cl –H9				105.23(4)
Cu– Cl –H14				102.02(4)

This generates a 3D supramolecular sheet, which form an infinite chain in the solid state, which are governed by hydrogen bonding. The complex is stabilised by hydrogen bonding interactions and intermolecular π…π stacking between the triazole and pyridyl rings in the solid state. Similar head to tail arrangements have been reported in the literature recently for Ni(II) and Pd(II) complexes with pyridyl-triazole ligands [19, 32].

The overlap between a triazole and -phenyl of the neighbouring adjacent molecules adoptan offset-slipped parallel displacedversion. Thegeometry is stabilised by triazole-phenyl interactions, where the centroid-centroid distance is 4.105Å. This distance is comparable to the previously reported bond separation of a typical π…π stacking [44-47]. The centroid - plane perpendicular distance is 3.508Å and the angle between the two planes is 10.83º (see Figure 7.36).

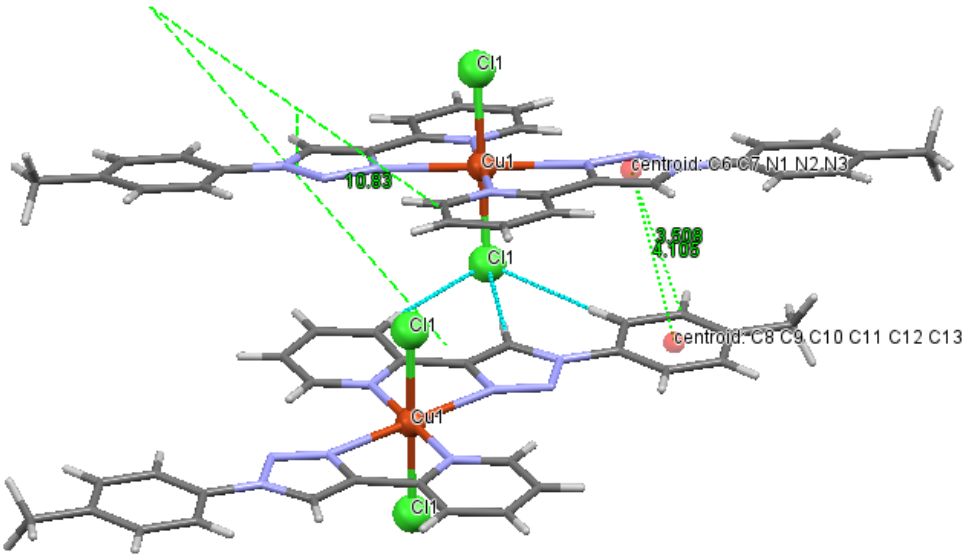

Figure 7.36: A pair of complexes arranged about a centre of symmetry. Dashed lines indicate intermolecular hydrogen bonds between C–H...Cl atoms and the π…π stacking interactions. The complex is viewed along the crystallographic b-axis of the molecules of the $[Cu(L^2)_2Cl_2]$ complex.

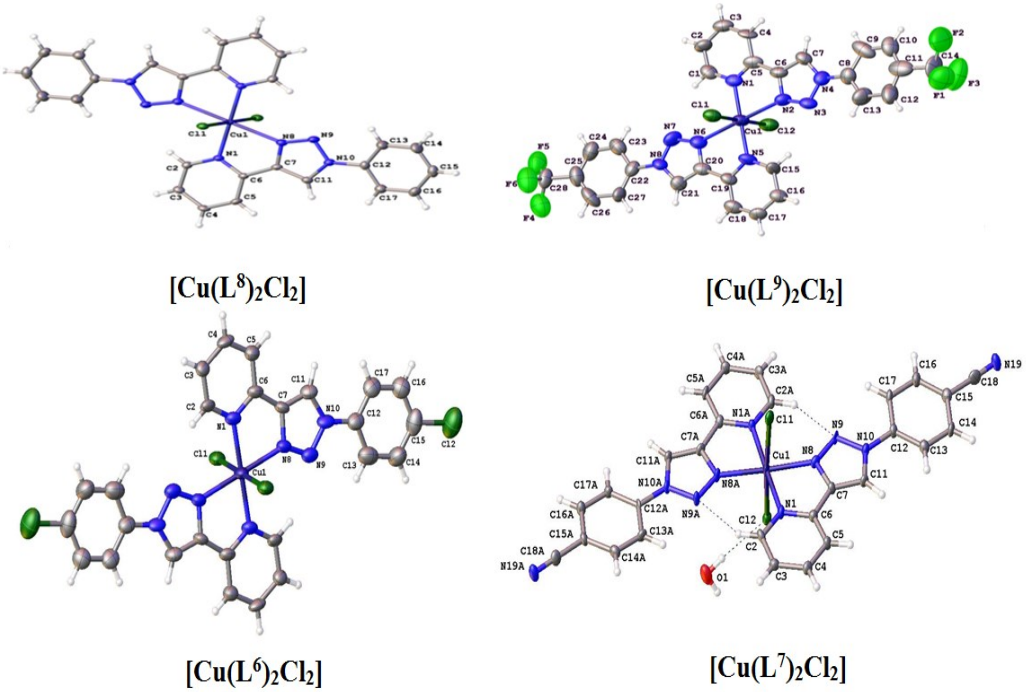

Figure 7.37: A labelled ellipsoids diagram of $[Cu(L^6)_2Cl_2]$, $[Cu(L^7)_2Cl_2]$ $[Cu(L^8)_2Cl_2]$ and $[Cu(L^9)_2Cl_2]$ complexes. The thermal ellipsoids are drawn at a 50% probability level and H atoms are shown as small spheres of arbitrary size.

Table 7.21: Crystallographic data of Cu(II) with L^2, L^6, L^7, L^8 and L^9 ligands.

Complex	$[Cu(L^2)_2Cl_2]$	$[Cu(L^6)_2Cl_2]$	$[Cu(L^7)_2Cl_2$	$[Cu(L^8)_2Cl_2]$	$[Cu(L^9)_2Cl_2]$
Formula	$C_{28}H_{24}Cl_2CuN_8$	$C_{26}H_{18}Cl_4Cu_1N_8$	$C_{28}H_{20}Cl_2CuN_{10}O$	$C_{26}H_{20}Cl_2CuN_8$	$C_{28}H_{18}Cl_2CuN_8F_6$
M_r	606.99	647.84	646.98	578.94	714.94
Temp/K	120(2)K	100 K	100(2) K	293(2) K	100(2) K
Wavelength Å	0.71073	0.71075	0.71075	0.71075	0.68890
Cryst. syst.	Monoclinic	Orthorhombic	triclinic	Monoclinic	Orthorhombic
Space group	P21/c	*Pccn*	*P*–1	P21/c	Pca21
a/Å	11.3032(7)	12.5664(12)	11.2493(8)	10.4068(7)	9.544(11)
b/Å	12.7346(8)	25.691(3)	11.5300(8)	12.7681(6)	12.724(14)
c/Å	9.8024(5)	9.7169(9)	12.0137(8)	9.4738(5)	22.54(3)
α/°	90.00	90.00	110.065(8)°	90.00	90.00
β/°	108.759(4)°	90.00	99.450(7)°	107.058(8)	90.00
γ/°	90.00	90.00	105.122(7)°	90.00	90.00
V/Å^3	1336.02(14)	3137.0(6)	1356.5(3)	1203.45(12)	2738(5)
Z	2	4	2	2	4
R_{int}	0.0586	0.0950	0.081	0.0351	0.1333
D_{calcd}/g cm^{-3}	1.509	1.372	1.584	1.598	1.735
Refln (all/ind)	12104/ 3036	7213/ 2863	16775/ 16760	6760/ 2718	17238/ 4620
μ/mm^{-1}	1.052	1.066	1.047	1.164	1.072
*R*1/*wR*2 (obsd data: $F^2>2\sigma(F^2)$)[a]	0.0637/ 0.1140	0.0879/ 0.2132	0.0778/ 0.1875	0.0378/ 0.0801	0.1135/ 0.2970
*R*1/*wR*2 (all data)[a]	0.0958/ 0.1300	0.1882/ 0.2614	0.1350/ 0.2192	0.0513/ 0.0878	0.1266/ 0.3128

Table 7.22: Selected bond lengths (Å) of Cu(II) with in L^2, L^6, L^7, L^8 and L^9 ligands

Bond distance(Å)	$[Cu(L^2)_2Cl_2]$	$[Cu(L^8)_2Cl_2]$	$[Cu(L^6)_2Cl_2]$	$[Cu(L^7)_2Cl_2$	$[Cu(L^9)_2Cl_2]$
	$C_{28}H_{24}Cl_2CuN_8$	$C_{26}H_{20}C_{l2}CuN_8$	$C_{26}H_{18}Cl_4Cu_1N_8$	$C_{28}H_{20}Cl_2CuN_{10}O$	$C_{28}H_{18}Cl_2CuN_8F_6$
C7–C11	1.367(6)	1.371(3)	1.363(10)	1.378(8)	1.393(16)
N8–N9	1.312(5)	1.308(3)	1.299(9)	1.338(7)	1.295(12)
N9–N10	1.358(5)	1.354(3)	1.361(9)	1.350(7)	1.349(13)
N8–C7	1.356(5)	1.362(3)	1.360(9)	1.357(7)	1.371(15)
N1–C6	1.344(5)	1.356(3)	1.363(10)	1.347(8)	1.286(15)
$M–N_{(PY)}1$	1.992(3)	1.997 (18)	2.010(6)	2.045(5)	1.976(10)
$M–N_{(PY)}$ 1i	1.992(3)	1.9970(18)	2.010(6)	2.051(5)	1.938(10)
$M–N_{(triazole)}1$	2.428(3)	2.3724(19)	2.130(7)	2.051(5)	2.363(9)
$M–N_{(triazole)}1^i$	2.428(3)	2.3724(19)	2.130(7)	2.047(5)	2.381(9)
M–Cl1	2.3394(10)	2.3711(6)	2.565(2)	2.8024(19)	2.563(5)
$M–Cl1^i$	2.3394 (10)	2.3710(6)	2.565(2)	2.5922(18)	2.667(6)

Table 7.23: Selected angles [°] of Cu(II) with L^2, L^6, L^7, L^8 and L^9 ligands

Bonds	$[Cu(L^2)_2Cl_2]$	$[Cu(L^6)_2\ Cl_2]$	$[Cu(L^7)_2Cl_2]$	$[Cu(L^8)_2Cl_2]$	$[Cu(L^9)_2Cl_2]$
$N_{(PY)}$ 1 –M–$N_{(PY)}$ 1^i	180.000(1)	180.0	177.8(2)	180.00(2)	179.2(5)
$N_{(triazole)}$ 1^i–M–$N_{(triazole)}$ 1	180.00(19)	180.0(2)	92.42(14)	180.00(8)	178.7(4)
$N_{(PY)}$ 1–M–$N_{(triazole)}$ 1^i	101.94(12)	99.8(3)	92.57(15)	101.89(7)	103.8(4)
$N_{(PY)}$ 1 –M–$N_{(triazole)}$ 1	78.06(12)	80.2(3)	176.80(6)	78.11(7)	77.4(3)
$N_{(PY)}$ 1–M– Cl 1	90.47(9)	89.50(19)	84.52(14)	89.01(6)	88.0(2)
$N_{(PY)}$ 1^i–M– Cl 1	89.53(9)	90.50(19)	91.77(15)	90.99(6)	92.0(3)
$N_{(triazole)}$ 1^i–M– Cl 1	88.44(10)	88.28(5)	91.77(15)	88.28(5)	89.7(3)
$N_{(triazole)}$ 1–M– Cl 1	91.56(10)	92.11(18)	86.01(15)	91.72(5)	90.1(3)
Cl 1^i–M– Cl 1	180.0	180.0	80.24(19)	179.999(10)	179.03(13)
$N_{(PY)}$ 1 –M–Cl_2	89.53(9)	90.50(19)	99.60(19)	90.99(6)	91.4(2)
$N_{(triazole)}$ 1 –M–Cl_2	88.44(10)	87.89(18)	176.1(2)	88.28(5)	90.6(3)

Table 7.24: Torsion angles [°] of the Cu and complexes with L_2, L6, L7, L_8 and L_9 ligands

Bonds	$[Cu(L^2)_2(Cl)_2]$	$[Cu(L^6)_2(Cl)_2]$	$[Cu(L^7)_2(Cl)_2]$	$[Cu(L^8)_2(Cl)_2]$	$[Cu(L^9)_2(Cl)_2]$
Cu1–N1–C6–C7	1.3(5)	2.3(9)	1.6(7)	1.3(3)	0.0(12)
Cu1–N8–N9–N10	177.5(4)	−172.8(6)	−178.0(4)	−169.6(2)	170.5(10)
Cu1–N8–C7–C6	0.6(4)	−6.2(8)	−2.6(7)	−6.4(3)	4.7(12)
N8–N9–N10–C12	−178.2(4)	−177.9(7)	177.7(5)	−179.2(2)	177.4(9)
C7–N8–N9–N10	−0.6(5)	0.0(8)	0.8(7)	−0.2(4)	2.7(12)
N9–N10–C12–C17	0.2(7)	177.8(7)	8.3(9)	−178.1(2)	173.5(10)
N1–C6–C7–N8	-1.3(6)	2.9(10)	0.7(9)	4.3(3)	-3.9(15)
N8–N9–N10–C12	−178.2(4)	−1.0(8)	177.7(5)	−179.2(2)	177.4(9)
N8–N9–N10–C11	0.5(5)	−177.9(7)	−0.1(7)	0.0(3)	2.7(12)

The plot in Figure 7.38 shows a concave downwards deviation (ignoring one point involving Cl), with a positive slope for the electron donating groups. This indicates that increased electron density results in the C_7-C_{11} triazole bond length becoming shorter and enhancing the double bond character of the bond. Electron withdrawing groups with a negative slope reduce the double bond character of the C_7-C_{11} triazole bond and causing it to become longer. A concave downwards deviation in the Hammett plot as depicted in Figure 7.38 is characteristic [25]. The plot displayed the relationship between the bond lengthsC_7-C_{11} in A˚ for the triazole carbon against the Hammett σ_ρ substituent constant of the Cu(II) complexes with L^2, L^6, L^7, L^8 and L^9 ligands. This means that the X-ray structures can be used as a sensitive probe for the electron density on the metal centre [25].

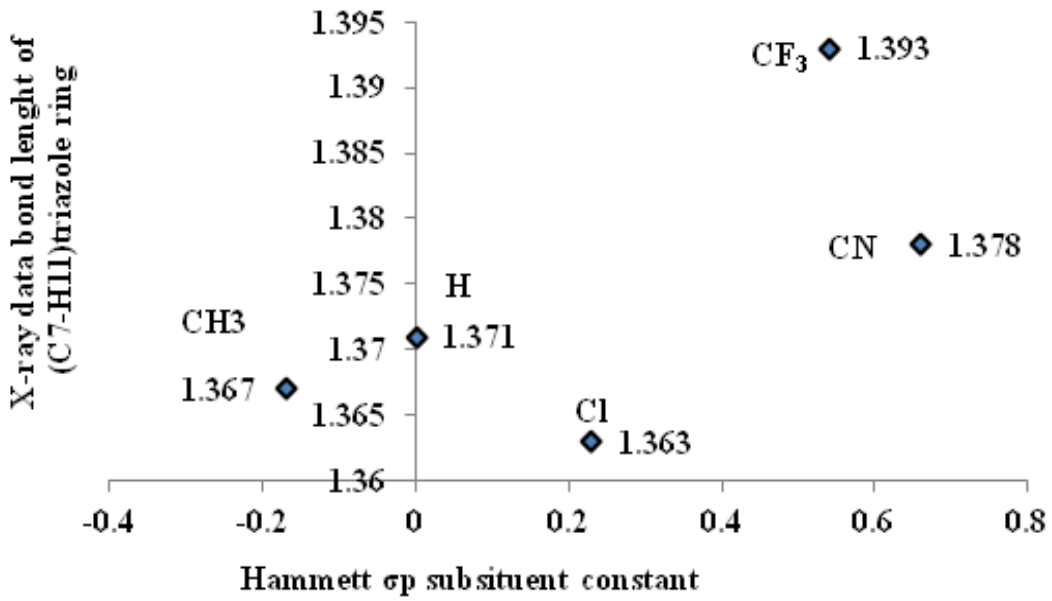

Figure 7.38: A plot of bond lengthsC_7-C_{11} in A˚ for the triazole carbon against the Hammett σ_ρ substituent constant of Cu(II) complexes with L^2, L^6, L^7, L^8 and L^9 ligands.

7.3. General Experimental Procedures and Characterisation of Dichloro bis 1*H*-1,2,3-triazol metal complexes

7.3.1 Synthesis and characterisation of the metal complexes with ligand L^2

7.3.1.1 Synthesis and characterisation of Dichloro(bis{2-[1-(4-methylphenyl)-1H-1,2,3-triazol-4-yl-kN3]pyridine-kN})manganese(II)

The $[Mn(L^2)_2Cl_2]$ complex, was prepared by stirring a solution of anhydrous $MnCl_2$ (0.041g, 0.32mmol) in CH_3OH (10ml). Asolution of the ligand L^2 (0.15g, 0.65mmol, 2eq) in CH_2Cl_2 (10ml), was added dropswise to it. A resulting pale yellow precipitate was obtained after stirring for 8-10h at RT. The solvent was then reduced in volume by a half under vacuum distillation before it was filtered and washed twice with cold methanol and then diethyl ether. A pale yellow solid, was obtained and isolated to yield a precipitate that give (0.195g, 0.32mmol, yielded 80%), mp. 324-326°C. IR: $\bar{\upsilon}(cm^{-1})$: 3068, 3055, 3022, 1606, 1595, 1575, 1521, 1473, 1446, 1253, 1253, 1062, 1044, 1011, 1000, 979, 861, 812, 784, 719. UV-Vis (DMSO) λ_{max}: The Mn(II) complex showed absorption bands at 257nm, $\varepsilon_{max} = 88450 dm^3mol^{-1}cm^{-1}$, 287nm, $\varepsilon_{max} = 40200 dm^3mol^{-1}cm^{-1}$, 682nm, $\varepsilon_{max} = 13 dm^3mol^{-1}cm^{-1}$. The complex with L^2 showed a value of μ_{eff} = 5.62 B.M. HRMS TOF (ESI+) (water: acetonitrile = 1:3) withthe highest molecular weight ion peak matching, was observed atm/z = 562.1202 (80%) and is related to $[M-Cl]^+$. The calculated value for $[C_{28}H_{24}ClMnN_8]^+$ is 562.1193. Λ_M (DMSO) = $50\Omega^{-1}cm^2mol^{-1}$.

7.3.1.2 Synthesis and characterisation of Dichloro(bis{2-[1-(4-methylphenyl)-1H-1,2,3-triazol-4-yl-kN3]pyridine-kN})iron(II)

For the preparation of $[Fe(L^2)_2Cl_2]$, the method used was analogous to that for $[Mn(L^2)_2Cl_2]$. An amount of 0.041g, 0.32mmol of anhydrous $FeCl_2$ and 0.15g, 0.65mmol of L^2 were used, and an identical work-up procedure gave the required compound as a bright yellow solid. The isolated precipitate gave (0.20g, 0.33mmol, yield 83%), mp. 310-312 °C. IR: $\bar{\upsilon}(cm^{-1})$; 3063, 3047, 3025, 1605, 1595, 1571, 1522, 1473, 1448, 1267, 1258, 1063, 1054, 1015, 1004, 886, 815, 786, 553. UV-Vis (DMSO) λ_{max}: The Fe(II) complex showed absorption bands at259nm, ε_{max} = 65500 $dm^3mol^{-1}cm^{-1}$, 287nm, $\varepsilon_{max} = 52000 dm^3mol^{-1}cm^{-1}$, 326nm, $\varepsilon_{max} = 4783 dm^3mol^{-1}cm^{-1}$, 908nm, $\varepsilon_{max} = 85 dm^3mol^{-1}cm^{-1}$. The complex with L^2 showed a value of μ_{eff} = 5.26 B.M. HRMS TOF (ESI+) (water: acetonitrile = 1:3) with the highest molecular weight ion peak matching, was observed at m/z = 563.1135 (80%) and is attributed to [M-

Cl]$^{+}$. The calculated value for [($C_{28}H_{24}N_8MnCl$)]$^{+}$ is 563.1162. Λ_M (DMSO) = 43$\Omega^{-1}cm^2\ mol^{-1}$.

7.3.1.3 Synthesis and characterisation of Dichloro(bis{2-[1-(4-methylphenyl)-1H-1,2,3-triazol-4-yl-kN3]pyridine-kN})cobalt(II)

For the preparation of [$Co(L^2)_2Cl_2$], the method used was analogous to that for [$Mn(L^2)_2Cl_2$]. An amount of 0.060g, 0.25mmol of $CoCl_2.6H_2O$ and 0.11g, 0.50mmol of L^2 were used, and an identical work-up procedure gave the required compound as a bright pink solid. The isolated precipitate gave (0.11g, 0.18mmol, yield 73%), mp. 346-348°C. IR: $\bar{\upsilon}(cm^{-1})$; 3045, 3024, 1609, 1595, 1574, 1521, 1475, 1450, 1262, 1245, 1065, 1056, 1018, 1005, 871, 814, 786, 755. UV-Vis (DMSO): The Co (II) complex showed absorption bands at 252nm, ε_{max} = 45200$dm^3mol^{-1}cm^{-1}$, 257nm, ε_{max} = 77100$dm^3mol^{-1}cm^{-1}$, 287nm, ε_{max} = 26967$dm^3mol^{-1}cm^{-1}$, 615nm, ε_{max} = 56$dm^3mol^{-1}cm^{-1}$, 678nm, ε_{max} = 89 $dm^3mol^{-1}cm^{-1}$. The complex with L^2 showed a value of μ_{eff} = 3.00 B.M. HRMS TOF (MALDI) with the highest molecular weight ion peak matching, was observed at m/z = 566.1 (100%) and is related to [M-Cl]$^{+}$. The calculated value for [($C_{28}H_{24}N_8FeCl$)]$^{+}$ is 566.1. Λ_M (DMSO) λ_{max} = 48$\Omega^{-1}cm^2mol^{-1}$.

7.3.1.4 Synthesis and characterisation of Dichloro(bis{2-[1-(4-methylphenyl)-1H-1,2,3-triazol-4-yl-kN3]pyridine-kN})nickel(II)

For the preparation of [$Ni(L^2)_2Cl_2$], the method used was as described for [$Mn(L^2)_2Cl_2$]. An amount of 0.050 g, 0.25 mmol of $NiCl_2.6H_2O$ and 0.10 g, 0.42mmol of L^2 were used, and an identical work-up procedure gave the required compound as a pale blue solid. The isolated precipitate gave (0.11g, 0.18mmol, yield 73%), mp. 340°C (decomp.). IR: $\bar{\upsilon}(cm^{-1})$; 3038, 3021, 3010, 1612, 1596, 1577, 1521, 1476, 1451, 1264, 1247, 1067, 1058, 1007, 874, 813, 786, 756, 720. UV- Vis (DMSO) λ_{max}: The Ni (II) complex showed absorption bands at 257nm, ε_{max} = 102150$dm^3mol^{-1}cm^{-1}$, 285nm, ε_{max} = 42300$dm^3mol^{-1}cm^{-1}$, 408nm, ε_{max} = 18$dm^3mol^{-1}cm^{-1}$, 668nm, ε_{max} = 9$dm^3mol^{-1}cm^{-1}$. Thecomplex with L^2 showed a value of μ_{eff} = 3.00 B.M. HRMS TOF (ESI+) (water: acetonitrile = 1:3) withthe highest molecular weight ion peak matching, was observed at m/z = 565.1167 (40%) and is related to [M-Cl]$^{+}$. The calculated value for [($C_{28}H_{24}N_8NiCl$)]$^{+}$ is 565.1166. A good single crystal for X-ray structural analysis was obtained by slow evaporation of a hot DMSO: CH_3CN = 1:9 solution of the complex. Λ_M (DMSO) = 45$\Omega^{-1}cm^2mol^{-1}$.

7.3.1.5 Synthesis and characterisation of Dichloro(bis{2-[1-(4-methylphenyl)-1H-1,2,3-triazol-4-yl-kN3]pyridine-kN})copper(II)

For the preparation of $[Cu(L^2)_2Cl_2]$, the method used was similar to that for $[Mn(L^2)_2Cl_2]$. An amount of 0.062g, 0.46mmol of anhydrous $CuCl_2$ and 0.21g, 0.92mmol of L^2 were used, and an identical work-up procedure gave the required compound as a pale green solid. The isolated precipitate gave (0.24g, 0.39mmol, yield 91%), mp. 274-276°C. IR: $\bar{\upsilon}(cm^{-1})$; 3068, 3058, 3025, 1606, 1594, 1575, 1516, 1477, 1449, 1267, 1250, 1063, 1042, 1029, 862, 817, 779, 754, 716. UV-Vis (DMSO) λ_{max}: The Cu (II) complex showed absorption bands at 257nm, ε_{max} = 52222 $dm^3mol^{-1}cm^{-1}$, 286nm, ε_{max} = 35556$dm^3mol^{-1}cm^{-1}$, 908nm, ε_{max} = 85$dm^3mol^{-1}cm^{-1}$. The complex with L^2 showed a value of μ_{eff} = 1.70 B.M. HRMS (P+NSI); $(CH_3OH)/(NH_4OAC)$ withthe highest molecular weight ion peak matching, was observed at m/z = 594.1547 (45%) and is attributed to $[(Cu(L^2)_2)^+ + (CH_3COO^-)]^+$. The calculated value for $[C_{28}H_{24}CuN_8]^+ + (CH_3COO^-)]^+$ is 594.1540.A good single crystal for X-ray structural analysis was obtained by slow evaporation of a hot CH_3OH solution of the complex. Λ_M (DMSO) = $31\Omega^{-1}cm^2mol^{-1}$.

7.3.1.6 Synthesis and characterisation of Dichloro(bis{2-[1-(4-methylphenyl)-1H-1,2,3-triazol-4-yl-kN3]pyridine-kN})zinc(II)

For the preparation of $[Zn(L^2)_2Cl_2]$, the method used was as described for that of the $[Mn(L^2)_2Cl_2]$. An amount of anhydrous $ZnCl_2$ of 0.19g, 0.80 mmol and 0.19g, 0.80mmol of L^2 were used, and an identical work-up procedure gave the required compound as a white solid. The isolated precipitate gave (0.18g, 0.39mmol, yield 78%), mp. 318-320°C. IR: $\bar{\upsilon}(cm\text{-}^{1})$; 3064, 3041, 3021, 1607, 1570, 1517, 1475, 1448, 1270, 1239, 1073, 1057, 1075, 1006, 864, 812, 774, 754, 718. UV-Vis (DMSO) λ_{max}: The Zn (II) complex showed absorption bands at 258nm, ε_{max} = 47931$dm^3mol^{-1}cm^{-1}$, 288nm, ε_{max} = 31379$dm^3mol^{-1}cm^{-1}$. ^{1}HNMR data δ_H/ppm (400MHZ, DMSO-d_6): 9.23 (1H, s, H_8), 8.66-8.65 (1H,d, J_{HH} = 4.12Hz, H_{14}), 8.11-8.09 (1H, dd, $^1J_{HH}$ = 7.79Hz, $^2J_{HH}$ = 0.92Hz, H_{11}), 7.97-7.92 (1H, dt, $^1J_{HH}$ = 7.79 Hz, $^2J_{HH}$ = 1.83Hz, H_{12}), 7.89-7.87 (2H, d, J_{HH} = 8.24Hz, Ar-$H_{2,6}$), 7.43-7.38 (3H, m, H_{13} and Ar-$H_{3,5}$), 3.22 (3H,s,CH_3,H_7); ^{13}CNMR (100.63MHZ, D_6MSO-d_6) δ_C/ppm: 20.49 (C_7), 119.83 (C_{11}), 120.09 (C_2, C_6), 121.13 (C_8), 123.25 (C_{13}), 130.14 (C_3, C_5), 134.26 (C_4), 137.31 (C_{12}), 138.49 (C_1), 148.80 (C_9), 149.33 (C_{14}), 149.54 (C_{10}). These assignments were confirmed using DEPT 13C (135°), 1H-^{1}H COSY and ^{1}H-^{13}CHMQC two dimensional correlation spectroscopy. HRMS TOF (ESI+) (water: acetonitrile = 1:3) with the

highest molecular weight ion peak matching, was at m/z = 571.1129 (80%) and is related to $[M\text{-}Cl]^+$. The calculated value for $[(C_{28}H_{24}N_8ZnCl)]^+$ is 571.1104. A good single crystal for X-ray structural analysis was obtained by slow evaporation of a hot CH_3OH solution of the complex. Λ_M (DMSO) = 8 $\Omega^{-1}cm^2mol^{-1}$.

7.3.1.7 Synthesis and characterisation of Dichloro(bis{2-[1-(4-methylphenyl)-1H-1,2,3-triazol-4-yl-kN3]pyridine-kN})cadmium(II)

For the preparation of $[Cd(L^2)_2Cl_2]$, the method used was as described for that of the $[Mn(L^2)_2Cl_2]$. An amount of anhydrous $CdCl_2$ of 0.15 g, 0.65 mmol and 0.15g, 0.65mmol of L^2 were used, and an identical work-up procedure gave the required compound as a white solid, and the isolated precipitate gave (0.18g, 0.27mmol, yield 78%), mp. 306-308°C. IR: $\bar{\upsilon}(cm^{-1})$; 3102, 1627, 1607, 1572, 1521, 1469, 1449, 1264, 1239, 1062, 1015, 1004, 815, 781, 749, 720. UV-Vis (DMSO) λ_{max}: The Cd (II) complex showed absorption bands at 256nm, ε_{max} = 33448 $dm^3mol^{-1}cm^{-1}$, 260nm, ε_{max} = 31724$dm^3mol^{-1}cm^{-1}$, 287nm, ε_{max} = 29655$dm^3mol^{-1}cm^{-1}$. ^{1}HNMR data δ_H/ppm (400MHZ, DMSO-d_6): 9.26 (1H, s, H_8), 8.66-8.67 (1H, d, J_{HH} = 4.12Hz, H_{14}), 8.11-8.10 (1H, dd, $^1J_{HH}$ = 7.73Hz, H_{11}), 7.98-7.95 (1H, dt, $^1J_{HH}$ = 7.79Hz, $^2J_{HH}$ = 1.83Hz, H_{12}), 7.89-7.87 (2H, d, J_{HH} = 8.24Hz, Ar-$H_{2,6}$), 7.43-7.41 (3H, m, H_{13} and Ar-$H_{3,5}$), 3.23 (3H, s, CH_3); ^{13}CNMR (100.63MHZ, D_6MSO-d_6) δ_C/ppm: 20.50 (C_7),119.98 (C_{11}), 120.12 (C_2, C_6), 121.27 (C_8), 123.39 (C_{13}), 130.17 (C_3, C_5), 134.23 (C_4), 137.52 (C_{12}), 138.58 (C_1), 148.47 (C_9), 148.97 (C_{14}), 149.50 (C_{10}). These assignments were confirmed using DEPT ^{13}C (135°), ^{1}H-^{1}H COSY and ^{1}H-^{13}C HMQC two dimensional correlation spectroscopy. HRMS TOF (ESI+) (water: acetonitrile = 1:3) withthe highest molecular weight ion peak matching, was observed atm/z = 621.0856 (100%) and is assigned to $[M\text{-}Cl]^+$ The calculated value for $[(C_{28}H_{24}N_8CdCl)]^+$ is 621.0846. Λ_M (DMSO) = 16 $\Omega^{-1}cm^2mol^{-1}$.

7.3.2 Synthesis and characterisation of the metals complexes with ligand L^3

7.3.2.1 Synthesis and characterisation of Dichloro(bis{2-[1-(4-methoxyphenyl)-1H-1,2,3-triazol-4-yl-kN3]pyridine-kN})Manganese(II)

For the preparation of $[Mn(L^3)_2Cl_2]$, the method used was similar to that for $[Mn(L^2)_2Cl_2]$. An amount of anhydrous $MnCl_2$ of 0.14g, 0.55mmol and 0.14g, 0.55mmol of L^3 were used, and an identical work-up procedure gave the required compound as a pale yellow solid. The isolated precipitate gave (0.14g, 0.22mmol, yield 82%), mp. 310-312°C. IR: ῡ(cm-1): 3049, 3025, 2966, 2873, 1604, 1569, 1518, 1471, 1452, 1259, 1203, 1174, 1117, 1066, 1055, 1017, 1001, 980, 864, 827, 786, 751, 718. UV-Vis (DMSO) λ_{max}: The Mn(II) complex showed absorption bands at 258nm, ε_{max} = 17780$dm^3mol^{-1}cm^{-1}$, 291nm, ε_{max} = 19480$dm^3mol^{-1}cm^{-1}$, 352nm, ε_{max} = 32 $dm^3mol^{-1}cm^{-1}$, 369nm, ε_{max} = 30$dm^3mol^{-1}cm^{-1}$, 390nm, ε_{max} = 21$dm^3mol^{-1}cm^{-1}$. The complex with L^3 showed a value of μeff = 5.32 B.M. HRMS TOF (ESI+) (water: acetonitrile = 1:3) withthe highest molecular weight ion peak matching, was observed at m/z = 594.1069 (90%) and is attributed to $[M-Cl]^+$. The calculated value for $[(C_{28}H_{24}ClMnN_8O_2)]^+$ is 594.1091. A good single crystal for X-ray structural analysis was obtained by slow evaporation of a hot methanol solution of the complex. ΛM (DMSO) = 52$\Omega^{-1}cm^2mol^{-1}$.

7.3.2.2 Synthesis and characterisation of Dichloro(bis{2-[1-(4-methoxyphenyl)-1H-1,2,3-triazol-4-yl-kN3]pyridine-kN})iron(II)

For the preparation of $[Fe(L^3)_2Cl_2]$, the method used was similar to that for $[Mn(L^2)_2Cl_2]$. An amount of anhydrous $FeCl_2$ of 0.167g, 0.63mmol and 0.040g, 0.31 mmol of L^3 were used, and an identical work-up procedure gave the required compound as a pale yellow solid. The isolated precipitate gave (0.167g, 0.46mmol, yield 83%), mp. 308-310°C; IR: ῡ(cm^{-1}); 3054, 3032, 3012, 2965, 2865, 2838, 1606, 1571, 1518, 1469, 1448, 1289, 1261, 1182, 1065, 1055, 1017, 1002, 979, 858, 825, 786, 719. UV-Vis (DMSO) λ_{max}: The Fe(II) complex showed absorption bands at 256nm, ε_{max} = 35500$dm^3mol^{-1}cm^{-1}$, 291nm, ε_{max} = 17500$dm^3mol^{-1}cm^{-1}$, 333nm, ε_{max} = 3810$dm^3mol^{-1}cm^{-1}$, 922nm, ε_{max} = 65$dm^3mol^{-1}cm^{-1}$. The complex with L^3 showed a value of μ_{eff} = 5.07 B.M. HRMS TOF (ESI+) (water: acetonitrile = 1:3) with the highest molecular weight ion peak matching, was observed at m/z = 595.1055 (88%) and is attributed to $[M-Cl]^+$. The calculated value for $[(C_{28}H_{24}ClFeN_8O_2)]^+$ is

595.1060. A good single crystal for X-ray structural analysis was obtained by slow evaporation of a hot DMSO:CH_3CN = 1:9 solution of the complex. Λ_M(DMSO) = 54$\Omega^{-1}cm^2mol^{-1}$.

7.3.2.3 Synthesis and characterisation of Dichloro(bis{2-[1-(4-methoxyphenyl)-1H-1,2,3-triazol-4-yl-kN3]pyridine-kN})cobalt(II)

For the preparation of $[Co(L^3)_2Cl_2]$, the method used was similar to that for $[Mn(L^2)_2Cl_2]$. An amount of $CoCl_2.6H_2O$ 0.045g, 0.16 mmol and 0.071g, 0.32mmol of L^3 were used, and an identical work-up procedure gave the required compound as a pale pink solid, and the isolated precipitate gave (0.091g, 0.14mmol, yield 77%), mp. 340°C (decomp.). IR: $\bar{\upsilon}(cm^{-1})$: 3068, 3052, 3030, 3014, 2966, 2839, 1609, 1597, 1574, 1518, 1471, 1453, 1320, 1261, 1204, 1175, 1067, 1058, 1019, 1003, 979, 860, 825, 786, 752, 720. UV-Vis (DMSO) λ_{max}: The Co (II) complex showed absorption bands at 257nm, ε_{max} = 26625$dm^3mol^{-1}cm^{-1}$, 292nm, ε_{max} = 11000$dm^3mol^{-1}cm^{-1}$, 615nm, ε_{max} = 38$dm^3mol^{-1}cm^{-1}$, 677nm, ε_{max} = 61$dm^3mol^{-1}cm^{-1}$. The complex with L^3 showed a value of μ_{eff} = 3.97 B.M. HRMS TOF (ESI+) (water: acetonitrile = 1:3) with the highest molecular weight ion peak matching, was observed at m/z = 598.1048 (90%) and correspond to $[M\text{-}Cl]^+$. The calculated value for $[(C_{28}H_{24}ClCoN_8O_2)]^+$ observed 598.1043. A good single crystal for X-ray structural analysis was obtained by slow evaporation of a hot DMSO: CH_3CN = 1:9 solution of the complex. Λ_M (DMSO) = 42 $\Omega^{-1}cm^2mol^{-1}$.

7.3.2.4 Synthesis and characterisation of Dichloro(bis{2-[1-(4-methoxyphenyl)-1H-1,2,3-triazol-4-yl-kN3]pyridine-kN})nickel(II)

For the preparation of $[Ni(L^3)_2Cl_2]$, the method used was similar to that for $[Mn(L^2)_2Cl_2]$. An amount of $NiCl_2.6H_2O$ of 0.037g, 0.15mmol and 0.08g, 0.31mmol of L^3 were used, and an identical work-up procedure gave the required compound as a pale blue solid, and the isolated precipitate gave (0.073g, 0.11mmol, yield 74%), mp. 345°C (decomp.). IR: $\bar{\upsilon}(cm^{-1})$; 3073, 3052, 3030, 2985, 2839, 1612, 1597, 1575, 1519, 1473, 1455, 1322, 1263, 1176, 1070, 1060, 1020, 1005, 980, 862, 825, 787, 754, 721. UV-Vis (DMSO) λ_{max}: The Ni (II) complex showed absorption bands at 257nm, $\varepsilon_{max=}$ 3602$dm^3mol^{-1}cm^{-1}$, 291nm, $\varepsilon_{max=}$ 3653$dm^3mol^{-1}cm^{-1}$, 407nm, $\varepsilon_{max=}$ 61dm^3 $mol^{-1}cm^{-1}$, 660nm, $\varepsilon_{max=}$ 43$dm^3mol^{-1}cm^{-1}$. The complex with L^3 showed a value ofμ_{eff} = 2.73 B.M. HRMS TOF (ESI+) (water: acetonitrile = 1:3) with the highest molecular weight ion peak matching, was observed at m/z = 597.1086 (80%) and is

related to $[M\text{-}Cl]^+$. The calculated value for $[(C_{28}H_{24}ClNiN_8O_2)]^+$ is 597.1064. A good single crystal for X-ray structural analysis was obtained by slow evaporation of a hot DMSO: Acetonitrile = 1:9 solution of the complex. Λ_M (DMSO) = 54 $\Omega^{-1}cm^2mol^{-1}$.

7.3.2.5 Synthesis and characterisation of Dichloro(bis{2-[1-(4-methoxyphenyl)-1H-1,2,3-triazol-4-yl-kN3]pyridine-kN})copper(II)

For the preparation of $[Cu(L^3)_2Cl_2]$, the method used was similar to that for $[Mn(L^2)_2Cl_2]$. An amount of anhydrous $CuCl_2$ of 0.042g, 0.31mmol of and 0.16g, 0.74mmol of L^3 were used, and an identical work-up procedure gave the required compound as a pale green solid. The isolated precipitate gave (0.18g, 0.28mmol, yield 91%), mp. 278-280°C. IR: $\bar{\upsilon}(cm^{-1})$; 3126, 3103, 3080, 2962, 2939, 2843, 1618, 1609, 1596, 1585, 1517, 1465, 1454, 1441, 1317, 1277, 1249, 1184, 1112, 1068, 1026, 1001, 983, 839, 819, 783, 722: UV-Vis (DMSO) λ_{max}: The Cu (II) complex showed absorption bands at 257nm, ε_{max} = 39200$dm^3mol^{-1}cm^{-1}$, 287nm, ε_{max} = 16433$dm^3mol^{-1}cm^{-1}$, 892nm, ε_{max} = 97$dm^3mol^{-1}cm^{-1}$. The complex with L^3 showed a value of μ_{eff} = 1.69 B.M. HRMS TOF (ESI+) (water: acetonitrile = 1:3) with the highest molecular weight ion peak matching, was observed at m/z = 602.1007(10%) and is related to $[M\text{-}Cl]^+$. The calculated value for $[(C_{28}H_{24}ClCuN_8O_2)]^+$ is 602.0985. Λ_M (DMSO) = 24$\Omega^{-1}cm^2mol^{-1}$.

7.3.2.6 Synthesis and characterisation of Dichloro(bis{2-[1-(4-methoxyphenyl)-1H-1,2,3-triazol-4-yl-kN3]pyridine-kN})zinc(II)

For the preparation of $[Zn(L^3)_2Cl_2]$, the method used was similar to that for $[Mn(L^2)_2Cl_2]$. An amount of anhydrous $ZnCl_2$ of 0.040g, 0.29mmol and 0.15g, 0.66mmol of L^3 were used, and an identical work-up procedure gave the required compound as a white solid, with the isolated precipitate that gave (0.14g, 0.21mmol, yield 77%), mp. 322-324°C. IR: $\bar{\upsilon}(cm^{-1})$; 3079, 3014, 2935, 2837, 1610, 1594, 1573, 1514, 1472, 1456, 1305, 1253, 1204, 1172, 1073, 1058, 1019, 1001, 983, 828, 778, 720. UV-Vis (DMSO) λ_{max}: The Zn (II) complex showed absorption bands at 258nm, ε_{max} = 64267$dm^3mol^{-1}cm^{-1}$, 285nm, ε_{max} = 32033$dm^3mol^{-1}cm^{-1}$. ^{1}HNMR data δ_H/ppm (400MHZ, DMSO-d_6): 9.05 (1H, s, H_{11}), 8.63 (1H, d, J= 2.29Hz, H_2), 8.09-8.07 (1H, d, J_{HH} = 8.24Hz, H_5), 7.92-7.90 (1H, d, $^1J_{HH}$ = 1.37Hz, $^2J_{HH}$ = 7.79 Hz, H_4), 7.89-7.86 (2H,d, J_{HH}= 8.70Hz, $H_{13,17}$), 7.37-7.34 (1H, dd, $^1J_{HH}$ = 5.04Hz, $^2J_{HH}$ = 6.64 Hz, H_3), 7.15-7.12 (2H,d, J_{HH}= 9.16Hz, $H_{14,16}$), 3.85 (3H, s, CH_3, H_{19}); ^{13}CNMR (100.63MHZ, D_6MSO-d_6) $\delta_{C/}$ppm: 55.69 (C_{19}), 115.02 (C_{14}, C_{16}-Ar), 119.79 (C_5), 121.14 (C_{11}),

121.99 (C_{13}, C_{17}), 123.03 (C_3), 130.16 (C_{12}), 137.05 (C_4), 148.06 (C_7), 149.56 (C_2), 149.82 (C_6), 159.60 (C_{15}). These assignments were confirmed using DEPT ^{13}C (135°),1H-^{1}H COSY and ^{1}H-^{13}C HMQC two dimensional correlation spectroscopy. HRMS TOF (ESI+) (water: acetonitrile = 1:3) with the highest molecular weight ion peak matching, was observed at m/z = 603.1002 (50%) and is attributed to $[M\text{-}Cl]^+$. The calculated value for $[(C_{28}H_{24}ClZnN_8O_2)]^+$ is 603.1005. A good single crystal for X-ray structural analysis was obtained by slow evaporation of a hot CH_3OH solution of the complex. ΛM (DMSO) = $12\Omega^{-1}cm^2mol^{-1}$.

7.3.2.7 Synthesis and characterisation of Dichloro(bis{2-[1-(4-methoxyphenyl)-1H-1,2,3-triazol-4-yl-kN3]pyridine-kN})cadmium(II)

For the preparation of $[Cd(L^3)_2Cl_2]$, the method used was similar to that for $[Mn(L^2)_2Cl_2]$. An amount of anhydrous of anhydrous $CdCl_2$ of 0.035g, 0.19mmol and 0.10g, 0.39mmol of L^3 were used, and an identical work-up procedure gave the required compound as a white solid. The isolated precipitate gave (0.10g, 0.14mmol, yield 80%), mp. 322-324°C. IR: ν (cm^{-1}); 3097, 1631, 1611, 1602, 1572, 1518, 1469, 1452, 1268, 1204, 1185, 1064, 1030, 1016, 1001, 981, 827, 781, 720. UV-Vis (DMSO) λmax: The Cd (II) complex showed absorption bands at 258nm, ε_{max} = $41933dm^3mol^{-1}cm^{-1}$, 286nm, ε_{max} = $29167dm^3mol^{-1}cm^{-1}$. ^{1}HNMR data δ_H/ppm (400MHZ, DMSO-d_6): 9.07 (1H, s, H_{11}), 8.64-8.61 (1H,d, J_{HH} = 4.58Hz, H_2), 8.09-8.07 (1H, d, J_{HH} = 7.79Hz, H_5), 7.94-7.91 (1H, dd, $^{1}J_{HH}$ = 7.79Hz, $^{2}J_{HH}$ = 1.83Hz, H_4), 7.90-7.84 (2H, d, J_{HH} = 9.16Hz, Ar-$H_{13,17}$), 7.38-7.35 (1H, ddd, $^{1}J_{HH}$ = 1.37Hz, $^{2}J_{HH}$ = 4.58Hz, $^{3}J_{HH}$ = 7.33Hz, H_3), 7.16-7.12 (2H, J= 9.16Hz, Ar-$H_{14,16}$), 3.85 (3H, S, CH_3, H_{19}); ^{13}CNMR (100.63MHZ, D_6MSO-d_6): δ_C/pmm; 55.69 (C_{19}), 115.03 (C_{14},C_{16} -Ar), 119.85 (C_5), 121.20 (C_{11}), 122.00 (C_{13},C_{17} -Ar), 123.10 (C_3), 130.13 (C_{12}) , 137.16 (C_4), 147.90 (C_7), 149.55 (C_2), 149.65 (C_6), 159.63 (C_{15}). These assignments were confirmed using DEPT ^{13}C (135°), ^{1}H-^{1}H COSY and ^{1}H-^{13}C two dimensional correlation spectroscopy. HRMS TOF (ESI+) (water: acetonitrile = 1:3) with the highest molecular weight ion peak matching, was observed at m/z = 653.0744 (10%) and is related to $[M\text{-}Cl]^+$. The calculated value for $[(C_{28}H_{24}ClCdN_8O_2)]^+$ is 653.0744. ΛM (DMSO) = $18\Omega^{-1}cm^2mol^{-1}$.

7.3.2.8 Synthesis and characterisation of Dichloro(bis{2-[1-(4-methoxyphenyl)-1H-1,2,3-triazol-4-yl-kN3]pyridine-kN}) platinum (II)

For the preparation of $[Pt(L^3)_2Cl_2]$. To a solution of $K_2[PtCl_4]$ (0.062g, 0.14mmol) in C_2H_5OH-H_2O 8:2 (10mL) was added dropwise to a solution of L^3 (0.085g, 0.33mmol) in CH_3CN (5mL). The resulting was stirred for 15mint at r.t and then the mixture allowed refluxing for 24h. The suspension was allowed to cool to r.t and then solvent was then reduced in volume by a half under vacuum distillation and a solid formed was filtered and washed twice with cold methanol and then diethyl ether, gave a yellow solid. The isolated precipitate gave (0.088g, 0.11mmol, yielded 78%), mp. 252-254°C. IR: $\bar{\upsilon}(cm^{-1})$; 3103,3067, 2921, 1616, 1601, 1576, 1511, 1464, 1456, 1257, 1168, 1110, 1071, 1014, 980, 835, 804,773, 748, 723. ^{1}HNMR data δ_H/ppm (400MHZ, DMSO-d_6): 9.80 (1H, s, H_{11}), 9.04-9.02 (1H,d, J_{HH} = 5.04Hz, H_2), 8.41-8.37 (1H, td, $^1J_{HH}$ = 7.79Hz, $^2J_{HH}$ = 1.73Hz, $^3J_{HH}$ = 7.79Hz, H_5), 8.20-8.18 (1H, d,J_{HH} = 7.73Hz, H_4), 7.88-7.86 (2H, d, J_{HH} = 8.70Hz, Ar-$H_{13,17}$), 7.79-7.75 (1H, td, $^1J_{HH}$ = 1.37Hz, $^2J_{HH}$ = 5.95Hz, $^3J_{HH}$ = 7.33Hz, H_3), 7.29-7.25 (2H, J= 9.16Hz, Ar-$H_{14,16}$), 3.91 (3H, S, CH_3, H_{19}); ^{13}CNMR (100.63MHZ, D_6MSO-d_6): δ_C/pmm; 56.75 (C_{19}), 116.15 (C_{14},C_{16} -Ar), 122.79 (C_5), 123.01 (C_{11}), 123.93 (C_{13},C_{17} -Ar), 125.13 (C_3), 126.75 (C_{12}) , 129.99 (C_4), 142.56 (C_7), 149.13 (C_2), 150.59 (C_6), 161.59 (C_{15}). These assignments were confirmed using DEPT ^{13}C (135°), ^{1}H-^{1}H COSY and ^{1}H-^{13}C two dimensional correlation spectroscopy. HRMS TOF (ESI+) (water: acetonitrile = 1:3) with the highest molecular weight ion peak matching, was observed atm/z = 725.1413 (100%) and is assigned to $[M\text{-}Cl]^+$ The calculated value for $[(C_{28}H_{24}N_8PtCl)]^+$ is 725.1437. Λ_M (DMSO) = 18 $\Omega^{-1}cm^2mol^{-1}$.

7.3.3 Synthesis and characterisation of the metals complexes with ligand L^4

7.3.3.1 Synthesis and characterisation of Dichloro(bis{4-[4-(pyridin-2-yl-kN)-1H-1,2,3-triazol-1-yl-kN3]benzoic acid})manganese(II)

For the prepation of $[Mn(L^4)_2Cl_2]$. An amount of $MnCl_2$ (0.028g, 0.22mmol) was stirred in a solution of anhydrous methanol (10ml). A solution of ligand L^4 (0.12g, 0.45mmol) in DMSO (10ml) was added dropwise to it and the mixture allowed to stirred for 15mint at r.t and then the mixture allowed to reflux for 24h while being stirred at rt. The solvent was reduced in volume by a half under vacuum distillation and crush ice was added to the solution. A resulting pale yellow precipitate was obtained and filtered before being washed twice with cold methanol and then diethyl ether. A pale yellow solid was isolated. The isolated precipitate gave (0.124g, 0.18mmol, yield 78%), mp. 306–308°C. IR: ῡ(cm-1); 3436, 3073, 1714, 1673, 1603, 1560, 1514, 1467, 1449, 1375, 1258, 1154, 1062, 1013, 1003, 979, 868, 783, 706. UV-Vis (DMSO) λ_{max}: The Mn(II) complex showed absorption bands at 258 nm, ε_{max} = 117800$dm^3mol^{-1}cm^{-1}$, 290nm, ε_{max} = 68467$dm^3mol^{-1}cm^{-1}$, 352nm, ε_{max} = 1113 $dm^3mol^{-1}cm^{-1}$, 370nm, ε_{max} = 1581$dm^3mol^{-1}cm^{-1}$, 390 nm, ε_{max} = 1280$dm^3mol^{-1}cm^{-1}$. The complex with L^4 showed a value of μ_{eff} = 5.62 B.M. HRMS TOF (MALDI) withthe highest molecular weight ion peak matching, was observed at m/z = 622.1 (5%) and is assigned to $[M\text{-}Cl]^+$. The calculated value for $[C_{28}H_{20}N_8MnO_4Cl]^+$ is observed and the value is 622.1. ΛM (DMSO) = 50 $\Omega^{-1}cm^2mol^{-1}$.

7.3.3.2 Synthesis and characterisation of Dichloro(bis{4-[4-(pyridin-2-yl-kN)-1H-1,2,3-triazol-1-yl-kN3]benzoic acid})iron(II)

For the preparation of $[Fe(L^4)_2Cl_2]$, the method used was similar to that for $[Mn(L^4)_2Cl_2]$. An amount of anhydrous $FeCl_2$ of 0.027g, 0.21mmol and 0.11g, 0.42mmol of L^4 were used, and an identical work-up procedure gave the required compound as a pale yellow solid. The isolated precipitate gave (0.096g, 0.14mmol, yield 73%), mp. 348-350°C. IR: ῡ(cm^{-1}); 3085, 1724, 1604, 1589, 1514, 1471, 1450, 1406, 1372, 1254, 1173, 1104, 1055, 1018, 1004, 978, 857, 774. UV-Vis (DMSO) λ_{max}: The Fe (II) complex showed absorption bands at 258nm, ε_{max} = 181600$dm^3mol^{-1}cm^{-1}$, 291nm, ε_{max} = 86500$dm^3mol^{-1}cm^{-1}$, 332nm, ε_{max} = 7053$dm^3mol^{-1}cm^{-1}$. The complex with L^4 showed a value of μ_{eff} = 5.1 B.M. HRMS TOF (MALDI) withthe highest molecular weight ion peak matching, was observed at m/z = 623.1 (100%)

and is related to $[M\text{-}Cl]^+$. The calculated value for $[C_{28}H_{20}N_8FeO_4Cl]^+$ is 623.1. Λ_M (DMSO) = $34\Omega^{-1}cm^2mol^{-1}$.

7.3.3.3 Synthesis and characterisation of Dichloro(bis{4-[4-(pyridin-2-yl-kN)-1H-1,2,3-triazol-1-yl-kN3]benzoic acid})cobalt(II)

For the preparation of $[Co(L^4)_2Cl_2]$, the method used was analogous to that for $[Mn(L^4)_2Cl_2]$. An amount of $CoCl_2.6H_2O$ of 0.028g, 0.11mmol and 0.082g, 0.30mmol of L^4 were used, and an identical work-up procedure gave the required compound as a pale pink solid. The isolated precipitate gave (0.071g, 0.10mmol, yield 71%), mp. 348°C (decomp.). IR: $\bar{\upsilon}(cm^{-1})$; 3045, 3024, 1609, 1595, 1574, 1521, 1475, 1450, 1262, 1245, 1065, 1056, 1018, 1005, 871, 814, 786, 755. UV-Vis (DMSO) λ_{max}: The Co(II) complex showed absorption bands at 258nm, ε_{max} = 95650 $dm^3mol^{-1}cm^{-1}$, 290nm, ε_{max} = 49900$dm^3mol^{-1}cm^{-1}$, 532nm, ε_{max} = 50$dm^3mol^{-1}cm^{-1}$. The complex with L^4 showed a value ofμ_{eff} = 3.68 B.M. HRMS TOF (MALDI) with the highest molecular weight ion peak matching, was observed at m/z = 626.1 (5%) and is related to $[M\text{-}Cl]^+$. The calculated value for $[C_{28}H_{20}N_8CoO_4Cl]^+$ is 626.1. Λ_M (DMSO) = $39\Omega^{-1}cm^2$ mol^{-1}.

7.3.3.4 Synthesis and characterisation of Dichloro(bis{4-[4-(pyridin-2-yl-kN)-1H-1,2,3-triazol-1-yl-kN3]benzoic acid})nickel(II)

For the preparation of $[Ni(L^4)_2Cl_2]$, the method used was similar to that for $[Mn(L^4)_2Cl_2]$. An amount of $NiCl_2.6H_2O$ of 0.030g, 0.12mmol and 0.080g, 0.30mmol of L^4 were used, and an identical work-up procedure gave the required compound as a pale blue solid, with the isolated precipitate giving (0.06g, 0.090mmol, yield 77%), mp. 350°C (decmop.). IR: $\bar{\upsilon}(cm^{-1})$; 3068, 3015, 1722, 1662, 1606, 1575, 1515, 1476, 1451, 1376, 1260, 1220, 1106, 1065, 1007, 980, 875, 784, 764, 676. UV-Vis (DMSO) λ_{max}: The Ni (II) complex showed absorption bands at 258nm, ε_{max} = 102900$dm^3mol^{-1}cm^{-1}$, 291nm, ε_{max} = 48500$dm^3mol^{-1}cm^{-1}$, 408nm, ε_{max} = 47$dm^3mol^{-1}cm^{-1}$, 662nm, ε_{max} = 20$dm^3mol^{-1}cm^{-1}$. The complex with L^4 showed a value ofμ_{eff} = 2.68 B.M. HRMS TOF (MALDI) withthe highest molecular weight ion peak matching, was observed at m/z = 625.1(55%) and is attributed to $[M\text{-}Cl]^+$.The calculated value for $[C_{28}H_{20}N_8NiO_4Cl]^+$ 625.1. A good single crystal for X-ray structural analysis was obtained by slow evaporation of hot DMSO: Acetonitrile = 1:9 solution of the complex. Λ_M (DMSO) = $47\Omega^{-1}cm^2mol^{-1}$.

7.3.3.5 Synthesis and characterisation of Dichloro(bis{4-[4-(pyridin-2-yl-kN)-1H-1,2,3-triazol-1-yl-kN3]benzoic acid})copper(II)

For the preparation of $[Cu(L^4)_2Cl_2]$, the method used was analogous to that for $[Mn(L^4)_2Cl_2]$. An amount of anhydrous$CuCl_2$ of 0.034g, 0.25mmol and 0.14g, 0.52mmol of L^4 were used, and an identical work-up procedure gave the required compound as a green solid. The isolated precipitate gave (0.168g, 0.25mmol, yield 85%), mp. 315-317°C. IR: $\bar{\upsilon}(cm^{-1})$: 3068, 3058, 3025, 1606, 1594, 1575, 1516, 1477, 1449, 1267, 1250, 1063, 1042, 1029, 862, 817, 779, 754, 716. UV-Vis (DMSO) λ_{max}: The Cu (II) complex showed absorption bands at 258nm, $\varepsilon_{max} = 119500dm^3mol^{-1}cm^{-1}$, 291nm, $\varepsilon_{max} = 44000dm^3mol^{-1}cm^{-1}$, 907nm, $\varepsilon_{max} = 88dm^3mol^{-1}cm^{-1}$. The complex with L^4 showed a value of $\mu_{eff} = 1.69$ B.M. HRMS TOF (MALDI) with the highest molecular weight ion peak matching, was observed at m/z = 630.1 (12%) and is assigned to $[M-Cl]^+$. The calculated value for $[C_{28}H_{20}CuO_4Cl]^+$ is 630.1. Λ_M (DMSO) $= 24\Omega^{-1}cm^2mol^{-1}$.

7.3.3.6 Synthesis and characterisation of Dichloro(bis{4-[4-(pyridin-2-yl-kN)-1H-1,2,3-triazol-1-yl-kN3]benzoic acid})zinc(II)

For the preparation of $[Zn(L^4)_2Cl_2]$, the method used was as described for $[Mn(L^4)_2Cl_2]$ An amount of anhydrous$ZnCl_2$of 0.075g, 0.55mmol and 0.30g, 0.11mmol check it of L^4 were used, and an identical work-up procedure gave the required compound as a white solid, the isolated precipitate gave (0.114g, 0.17mmol, yield 74%), mp. 332-334 °C. IR: $\bar{\upsilon}(cm^{-1})$; 3116, 1699, 1683, 1603, 1572, 1517, 1474, 1458, 1441, 1302, 1240, 1277, 1163, 1152, 1091, 1038, 1020, 1014, 991, 856, 804, 785, 770, 692. UV-Vis (DMSO) λ_{max}: The Zn (II) complex showed absorption bands at 258nm, $\varepsilon_{max} = 176000dm^3mol^{-1}cm^{-1}$, 292nm, $\varepsilon_{max} = 4600dm^3mol^{-1}cm^{-1}$. ^{1}HNMR data δ_H/ppm (400MHZ, DMSO-d_6): 13.12 (1H, sb, H_{18}), 9.38 (1H, s, H_{11}), 8.67-8.65 (1H, ddd, $^1J_{HH} = 0.92$Hz, $^2J_{HH} = 1.83$ Hz,$^3J_{HH} = 4.58$Hz, H_2), 8.20-8.11(5H, m, H_5, Ar-$H_{,13,17,14,16}$), 7.96-7.92 (1H, dt, $^1J_{HH} = 1.83$Hz, $^2J_{HH} = 7.63$Hz, H_4), 7.42-7.38 (1H, ddd, $^1J_{HH} = 1.22$Hz, $^2J_{HH} = 4.88$Hz, $^2J_{HH} = 7.78$Hz, H_3); ^{13}CNMR (100.63MHZ, D_6MSO-d_6): δ_C/pmm: 119.87 (C_5), 119.95 ($C_{14,}C_{16}$), 121.33 (C_{11}), 123.33 (C_3), 130.82 (C_{15}), 130.93 (C_{13}, C_{17}), 137.22 (C_4), 139.44 (C_{12}), 148.42 (C_7), 149.64 (C_2), 149.31 (C_6), 166.23 (C_{18}).These assignments were confirmed using DEPT ^{13}C (135°), ^{1}H-^{1}H COSY and ^{1}H-^{13}C HMQC two dimensional correlation spectroscopy. HRMS TOF (MALDI) with the highest molecular weight ion peak matching, was observed

at m/z = 631.1 (20%) and is assigned to $[M\text{-}Cl]^+$. The calculated value for $[C_{28}H_{20}N_8ZnO_4Cl]^+$ is 631.1. Λ_M (DMSO) = $8\Omega^{-1}cm^2mol^{-1}$.

7.3.3.7 Synthesis and characterisation of Dichloro(bis{4-[4-(pyridin-2-yl-kN)-1H-1,2,3-triazol-1-yl-kN3]benzoic acid})cadmium(II)

For the preparation of $[Cd(L^4)_2Cl_2]$, the method used was similar to that for $[Mn(L^4)_2Cl_2]$. An amount of anhydrous $CdCl_2$ of 0.035g, 0.19mmol and 0.10g, 0.38mmol of L^4 were used, and an identical work-up procedure gave the required compound as a white solid. The isolated precipitate gave (0.099g, 0.16mmol, yield 85%), mp. 340°C. IR: $\bar{\upsilon}(cm^{-1})$; 3142, 3072, 1695, 1604, 1572, 1517, 1473, 1450, 1271, 1162, 1062, 1093, 1063, 1015, 1007, 992, 857, 783, 771, 693. UV-Vis (DMSO) λ_{max}: The Cd (II) complex showed absorption bands at 258nm, ε_{max} = 166667 dm^3 $mol^{-1}cm^{-1}$, 293nm, ε_{max} = 57333 $dm^3mol^{-1}cm^{-1}$. ^{1}HNMR data δ_H/ppm (400MHZ, DMSO-d_6): 12.89 (1H, sb -H18) 9.39 (1H, s, H_{11}), 8. 66 (1H, S, H_2), 8.21-8.12 (5H, m. H_5, Ar-$H_{13,17,14,16}$), 7.97-7.93 (1H, dt, $^1J_{HH}$ = 1.46Hz, $^2J_{HH}$ = 8.05Hz, H_4), 7.42-7.39 (1H, dd, $^1J_{HH}$ = 4.39Hz, $^2J_{HH}$ = 7.32Hz, H_3); ^{13}CNMR (100.63MHZ, D_6MSO-d_6) δ_C/pmm: 120.09 (C_{14}, $C_{16,}$), 120.43(C_5), 121.83 (C_{11}), 123.86 (C_3), 131.57 (C_{13}, C_{17}), 135.77 (C_{15}), 137.80 (C_4), 138.73 (C_{12}), 148.87(C_7), 150.00 (C_2), 150.22 (C_6), 170.88 (C_{18}). These assignments were confirmed using DEPT ^{13}C (135°), ^{1}H-^{1}H COSY and ^{1}H-^{13}C two dimensional correlation spectroscopy. HRMS TOF (MALDI) with the highest molecular weight ion peak matching, was observed atm/z = 681.0 (85%) and is assigned to $[M\text{-}Cl]^+$. The calculated value for $[C_{28}H_{20}CdN_8O_4Cl]^+$ is 681.0. Λ_M (DMSO) = $14\Omega^{-1}cm^2mol^{-1}$.

7.3.4 Synthesis and characterisation of the metals complexes with ligand L^5

7.3.4.1 Synthesis and characterisation of Dichloro (bis{2-[1-(4-fluorophenyl)-1H-1,2,3-triazol-4-yl-kN3]pyridine-kN})manganese(II)

For the preparation of $[Mn(L^5)_2Cl_2]$, the method used was similar to that for $[Mn(L^2)_2Cl_2]$. An amount of anhydrous $MnCl_2$ of 0.027g, 0.21mmol and 0.10g, 0.43mmol of L^5, and an identical work-up procedure gave the required compound as a pale yellow solid. The isolated precipitate gave (0.10g, 0.158mmol, yield 78%), mp. 306-308°C. IR: $\bar{\upsilon}(cm^{-1})$; 3078, 1617, 1606, 1575, 1515, 1469, 1450, 1412, 1322, 1239, 1058, 1013, 1002, 980, 837, 781, 720. UV-Vis (DMSO) λ_{max}: The Mn(II) complex showed absorption bands at 258nm, ε_{max} = 134000$dm^3mol^{-1}cm^{-1}$, 285nm, ε_{max} =70000$dm^3mol^{-1}cm^{-1}$, 335nm, ε_{max} = 64$dm^3mol^{-1}cm^{-1}$, 353nm, ε_{max} =38$dm^3mol^{-1}cm^{-1}$, 560nm, ε_{max} = 6$dm^3mol^{-1}cm^{-1}$. The complex with L^5 showed a value of μ_{eff} = 5.82 B.M. HRMS (P+NSI) withthe highest molecular weight ion peak matching, was observed at *m/z* = 570.0686 (93%) and is attributed to $[M\text{-}Cl]^+$. The calculated value for $[C_{26}H_{18}F_2N_8MnCl]^+$ is 570.0684. Λ_M (DMSO) = 52$\Omega^{-1}cm^2mol^{-1}$.

7.3.4.2 Synthesis and characterisation of Dichloro(bis{2-[1-(4-fluorophenyl)-1H-1,2,3-triazol-4-yl-kN3]pyridine-kN})iron(II)

For the preparation of $[Fe(L^5)_2Cl_2]$, the method used was analoguouse to that for $[Mn(L^2)_2Cl_2]$. An amount of anhydrous $FeCl_2$ of 0.030g, 0.23mmol and 0.11g, 0.47mmol and of L^5 were used, and an identical work-up procedure gave the required compound as a pale yellow solid. The isolated precipitate gave (0.10g, 0.16mmol, yield 75%), mp. 258-260°C. IR: $\bar{\upsilon}(cm^{-1})$; 3065, 3041, 3026, 1605, 1578, 1515, 1472, 1453, 1412, 1333, 1239, 1258, 1159, 1061, 1015, 1005, 979, 837, 788, 718. UV-Vis (DMSO) λ_{max}: The Fe(II) complex showed absorption bands at 257nm, ε_{max} = 69630$dm^3mol^{-1}cm^{-1}$, 286nm, ε_{max} = 3111$dm^3mol^{-1}cm^{-1}$, 329nm, ε_{max} = 3380$dm^3mol^{-1}cm^{-1}$. The complex with L^5 showed a value of μ_{eff} = 4.87 B.M. HRMS TOF (MALDI)withthe highest molecular weight ion peak matching, was observed at *m/z* = 571.0635 (35%) and is assigned to $[M\text{-}Cl]^+$. The calculated value for $[C_{26}H_{18}F_2N_8MnCl]^+$ is 571.0660. Λ_M (DMSO) = 37$\Omega^{-1}cm^2mol^{-1}$.

7.3.4.3 Synthesis and characterisation of Dichloro(bis{2-[1-(4-fluorophenyl)-1H-1,2,3-triazol-4-yl-kN3]pyridine-kN})cobalt(II)

For the preparation of $[Co(L^5)_2Cl_2]$, the method used was as described for $[Mn(L^2)_2Cl_2]$. An amount of $CoCl_2.6H_2O$ of 0.035g, 0.15mmol and 0.076g, 0.30mmol of L^5 were used, and an identical work-up procedure gave the required compound as a pale pink solid. The isolated precipitate gave (0.065g, 0.10mmol, yield 73%), mp. 348-350°C. IR: $\bar{\upsilon}(cm^{-1})$: 3072, 3041, 3013, 1610, 1585, 1517, 1478, 1455, 1313, 1241, 1161, 1064, 1056, 1020, 1006, 979, 873, 838, 790, 757, 720. UV-Vis (DMSO) λ_{max}: The Co (II) complex showed absorption bands at 258nm, ε_{max} = 67000$dm^3mol^{-1}cm^{-1}$, 286nm, ε_{max} = 30000$dm^3mol^{-1}cm^{-1}$, 615nm, ε_{max} = 73$dm^3mol^{-1}cm^{-1}$, 678nm, ε_{max} = 118$dm^3mol^{-1}cm^{-1}$. The complex with L^5 showed a value of μ_{eff} = 3.92 B.M. HRMS (P+NSI) withthe highest molecular weight ion peak matching, was observed at= *m/z*598.1070 (100%) and is attributed to $[M + CH_3COO]^+$. The calculated value for $[C_{26}H_{18}F_2N_8Co + CH_3COO]^+$ is 598.1082. Λ_M (DMSO) = 54$\Omega^{-1}cm^2mol^{-1}$.

7.3.4.4 Synthesis and characterisation of Dichloro(bis{2-[1-(4-fluorophenyl)-1H-1,2,3-triazol-4-yl-kN3]pyridine-kN})nickel(II)

For the preparation of $[Ni(L^5)_2Cl_2]$, the method used was as described for $[Mn(L^2)_2Cl_2]$. An amount of $NiCl_2.6H_2O$ of 0.035g, 0.14mmol and 0.075g, 0.29 mmol of L^5 were used, and an identical work-up procedure gave the required compound as a pale blue solid. The isolated precipitate gave (0.07g, 0.11mmol, yield 75%), mp. 340°C (decomp.). IR: $\bar{\upsilon}(cm^{-1})$; 3073, 3053, 3014, 1612, 1577, 1513, 1472, 1458, 1302, 1264, 1229, 1158, 1069, 1057, 1022, 1007, 982, 835, 788, 752, 722. UV-Vis (DMSO) λ_{max}: The Ni (II) complex showed absorption bands at 258nm, ε_{max} = 52667$dm^3mol^{-1}cm^{-1}$, 283nm, ε_{max} = 31000$dm^3mol^{-1}cm^{-1}$, 409nm, ε_{max} = 14$dm^3mol^{-1}cm^{-1}$, 670nm, ε_{max} = 46$dm^3mol^{-1}cm^{-1}$, 890nm, ε_{max} = 33$dm^3mol^{-1}cm^{-1}$. The complex with L^5 were used showed a value of μ_{eff} = 2.88 B.M. HRMS (P+NSI) withthe highest molecular weight ion peak matching, was observed at *m/z*= 597.1095 (100%) and is assigned to $[M + CH_3COO]^+$. The calculated value for $[C_{26}H_{18}F_2N_8Ni + (CH_3COO)^-]^+$ is 597.1104. Λ_M (DMSO) = 58$\Omega^{-1}cm^2mol^{-1}$.

7.3.4.5 Synthesis and characterisation of Dichloro(bis{2-[1-(4-fluorophenyl)-1H-1,2,3-triazol-4-yl-kN3]pyridine-kN})copper(II)

For the preparation of $[Cu(L^5)_2Cl_2]$, the method used was similar to that for $[Mn(L^2)_2Cl_2]$. An amount of anhydrous $CuCl_2$ of 0.030g, 0.22mmol and 0.11g, 0.44mmol of L^5 were used, and an identical work-up procedure gave the required compound as a pale green solid. The isolated precipitate gave (0.13g, 0.21mmol, yield 92%), mp. 240-242°C. IR: $\bar{\upsilon}$(cm-^{1}); 3060, 3045, 3025, 1617, 1608, 1578, 1517, 1477, 1454, 1319, 1252, 1064, 1040, 1000, 982, 845, 782, 756, 693. UV-Vis (DMSO) λ_{max}: The Cu(II) complex showed absorption bands at 257nm, ε_{max} = 73333dm^{3}mol^{-1}cm^{-1}, 286nm, ε_{max} = 29000dm^{3}mol^{-1}cm^{-1}, 908nm, ε_{max} = 87 dm^{3}mol^{-1}cm^{-1}. The complex with L^5 showed a value ofμ_{eff} = 1.63 B.M. HRMS (P+NSI); with the highest molecular weight ion peak matching, was observed at *m/z*= 578.602 (100%) which is assigned to $[M\text{-}Cl]^+$. The calculated value for $[C_{26}H_{18}F_2N_8CuCl]^+$ is 578.602. Λ_M (DMSO) = 33Ω^{-1}cm^{2}mo^{-1}.

7.3.4.6 Synthesis and characterisation of Dichloro(bis{2-[1-(4-fluorophenyl)-1H-1,2,3-triazol-4-yl-kN3]pyridine-kN})zinc(II)

For the preparation of $[Zn(L^5)_2Cl_2]$, the method used was analogous to that for $[Mn(L^2)_2Cl_2]$. An amount of anhydrous $ZnCl_2$ of 0.036g, 0.26mmol and 0.14g, 0.55mmol of L^5 were used, and an identical work-up procedure gave the required compound as a white solid. The isolated precipitate gave (0.14g, 0.22mmol, yield 77%), mp. 318-320°C. IR: $\bar{\upsilon}$(cm^{-1}); 3080, 3023, 1614, 1575, 1511, 1472, 1473, 1453, 1322, 1274, 1239, 1166, 1133, 1057, 1062, 1007, 982, 839, 785, 722, 695. UV-Vis (DMSO) λ_{max}: The Zn(II) complex showed absorption bands at 257nm, ε_{max} = 60333dm^{3}mol^{-1}cm^{-1}, 287nm, ε_{max} = 28333dm^{3}mol^{-1}cm^{-1}. ^{1}HNMR data δ_H/ppm (400MHZ, DMSO-d$_6$): 9.32 (1H, s, H$_7$), 8.66-8.65 (1H, d, J_{HH} = 4.12Hz, H$_{13}$), 8.12-8.10 (1H, d, J_{HH} = 7.79Hz, H$_{10}$), 8.08-8.04 (2H,d, J_{HH} = 9.16Hz, Ar-H$_{2,6}$), 7.97-7.93 (1H, dt,$^1J_{HH}$ = 7.79Hz,$^2J_{HH}$= 1.73Hz, H$_{11}$), 7.51-7.44 (2H,d, J_{HH} = 8.70Hz, Ar-H$_{3,5}$), 7.42-7.39 (1H, dd, $^1J_{HH}$ = 6.41Hz,$^2J_{HH}$ = 5.04Hz, H$_{12}$); ^{13}CNMR (100.63MHZ, D$_6$MSO-d$_6$) δ_C/pmm: 116.53-116.77, ($^2J_{C\text{-}F}$ = 23.96Hz, C$_3$, C$_5$, Ar), 119.73 (C$_{10}$), 121.47 (C$_7$), 122.44 - 122.52 (d, $J^3_{C\text{-}F}$ = 8.63Hz, C$_2$,C$_6$), 123.32 (C$_{12}$), 133.02 (C$_1$), 137.31 (C$_{11}$), 148.06 (C$_8$), 149.27 (C$_9$), 149.56 (C$_{13}$), 162.88-160.44 ($J^1_{C\text{-}F}$ = 245.37Hz, C$_4$). These assignments were confirmed using; DEPT ^{13}C (135°), ^{1}H-^{1}H COSY and ^{1}H-^{13}C HMQC two dimensional correlation spectroscopy. HRMS (P+NSI); with the highest molecular weight ion peak matching, was observed at = *m/z*

579.0598 (43%) and is related to $[M\text{-}Cl]^+$. The calculated value for calculated value for $[C_{26}H_{18}F_2N_8ZnCl]^+$ is 579.0597. Λ_M (DMSO) = $10\Omega^{-1}cm^2mol^{-1}$.

7.3.4.7 Synthesis and characterisation of Dichloro(bis{2-[1-(4-fluorophenyl)-1H-1,2,3-triazol-4-yl-kN3]pyridine-kN})cadmium(II)

For the preparation of $[Cd(L^5)_2Cl_2]$, the method used was similar to that for $[Mn(L^2)_2Cl_2]$. An amount of anhydrous $CdCl_2$ of 0.036g, 0.17mmol and 0.088g, 0.38 mmol of L^5 were used, and an identical work-up procedure gave the required compound as a white solid. The isolated precipitate gave (0.10g, 0.15mmol, yield 83%), mp. 316-318°C. IR: $\bar{\upsilon}(cm^{-1})$; 3103, 1617, 1602, 1574, 1517, 1470, 1452, 1334, 1248, 1239, 1125, 1075, 1057, 1015, 1004, 983, 824, 780, 749, 720, 695. UV-Vis (DMSO) λ_{max}: The Cd(II) complex showed absorption bands at 258nm, ε_{max} = $35333dm^3mol^{-1}cm^{-1}$, 287nm, ε_{max} = $30667dm^3mol^{-1}cm^{-1}$. ^{1}HNMR data δ_H/ppm (400MHZ, DMSO-d_6): 9.27 (1H, s, H_7), 8.67-8.65 (1H, ddd, $^1J_{HH}$ = 0.92Hz, $^2J_{HH}$ = 1.83Hz, $^3J_{HH}$ = 5.50Hz H_{13}), 8.12-8.11 (1H, td, J_{HH} = 7.79Hz, H_{10}), 8.08-8.03 (2H,d = J_{HH} = 9.16Hz, Ar-$H_{2,6}$), 7.97-7.92 (1H, dt, $^1J_{HH}$ = 7.79Hz, $^2J_{HH}$ = 1.83Hz, H_{11}), 7.48-7.44 (2H, d, J_{HH} = 8.70Hz, Ar-$H_{3,5}$), 7.42-7.39 (1H, ddd, $^1J_{HH}$ = 0.92Hz, $^2J_{HH}$ = 4.58Hz, $^3J_{HH}$ = 7.79Hz, H_{12}); ^{13}CNMR (100.63MHZ, D_6MSO-d_6) δ_C/pmm: 116.50 - 116.74, ($^2J_{C\text{-}F}$ = 23.96Hz, C_3, C_5, Ar), 119.81 (C_{10}), 121.50 (C_7), 122.63- 122.53(d, $J^3_{C\text{-}F}$ = 9.58 Hz, C_2,C_6), 123.28 (C_{12}), 133.10 (C_1), 137.28 (C_{11}), 148.02 (C_8), 149.30 (C_{13}), 149.56 (C_9), 162.96-160.51 ($J^1_{C\text{-}F}$ = 246.33Hz, C_4). These assignments were confirmed using DEPT ^{13}C (135°), ^{1}H-^{1}H COSY and ^{1}H-^{13}C HMQC two dimensional correlation spectroscopy. HRMS (P+NSI) withthe highest molecular weight ion peak matching, was observed at *m/z* =629.0337 (55%) and is attributed to $[M\text{-}Cl]^+$. The calculated value for $[C_{26}H_{18}F_2N_8CdCl]^+$ is 629.0338. Λ_M (DMSO) = $16\Omega^{-1}cm^2mol^{-1}$.

7.3.5 Synthesis and characterisation of the metals complexes with ligand L^6

7.3.5.1 Synthesis and characterisation of Dichloro(bis{2-[1-(4-chlorophenyl)-1H-1,2,3-triazol-4-yl-kN3]pyridine-kN})manganese(II)

For the preparation of $[Mn(L^6)_2Cl_2]$, the method used was similar to that for $[Mn(L^2)_2Cl_2]$. An amount of anhydrous $MnCl_2$ of 0.030g, 0.24mmol and (0.12g, 0.47mmol of L^6 were used, and an identical work-up procedure gave the required compound as a pale yellow solid. The isolated precipitate gave 0.123g, 0.19mmol, yield 81%), mp. 312-314°C. IR: $\bar{\upsilon}(cm^{-1})$; 3090, 3055, 1607, 1574, 1518, 1472, 1452, 1409, 1286, 1259, 1158, 1141, 1062, 1053, 1024, 1007, 978, 856, 845, 825, 782, 718. UV-Vis (DMSO) λ_{max}: The Mn (II) complex showed absorption bands at 258nm, ε_{max} =46923$dm^3mol^{-1}cm^{-1}$, 289nm, ε_{max} =33846$dm^3mol^{-1}cm^{-1}$, 502nm, ε_{max} =33$dm^3mol^{-1}cm^{-1}$. The complex with L^6 showed a value of μ_{eff} = 5.98 B.M. HRMS TOF (ESI+) (water: acetonitrile = 1:3) with the highest molecular weight ion peak matching, was observed at *m/z* = 602.0092 (30%) and is related to $[M\text{-}Cl]^+$. The calculated value for $[C_{26}H_{18}N_8MnCl_3]^+$ is 602.0100. Λ_M (DMSO) = 50$\Omega^{-1}cm^2mol^{-1}$.

7.3.5.2 Synthesis and characterisation of Dichloro(bis{2-[1-(4-chlorophenyl)-1H-1,2,3-triazol-4-yl-kN3]pyridine-kN})iron(II)

For the preparation of $[Fe(L^6)_2Cl_2]$, the method used was analogous to that for $[Mn(L^2)_2Cl_2]$. An amount of anhydrous $FeCl_2$ of 0.033g, 0.26mmol and 0.13g, 0.52mmol of L^6 were used, and an identical work-up procedure gave the required compound as a pale yellow solid. The isolated precipitate gave (0.097g, 0.15mmol, yield 79%), mp. 258-260°C. IR: $\bar{\upsilon}(cm\text{-}^1)$; 3051, 3023, 3005, 1606, 1591, 1570, 1502, 1472, 1448, 1405, 1267, 1257, 1151, 1134, 1095, 1061, 1052, 1013, 1003, 977, 860, 825, 808, 789, 711. UV-Vis (DMSO) λ_{max}: The Fe(II) complex showed absorption bands at 258nm, ε_{max} = 58571$dm^3mol^{-1}cm^{-1}$, 287nm, ε_{max} = 47143$dm^3mol^{-1}cm^{-1}$, 332nm, ε_{max} = 4060$dm^3mol^{-1}cm^{-1}$, 386nm, ε_{max} = 2020$dm^3mol^{-1}cm^{-1}$. The complex with L^6 showed a value of μ_{eff} = 5.10 B.M. HRMS (ESI+) (water: acetonitrile = 1:3) with the highest molecular weight ion peak matching, was observed at *m/z* =603.0050 (75%) and is related to $[M\text{-}Cl]^+$. The calculated value for $[C_{26}H_{18}N_8MnCl_3]^+$ is603.0069. Λ_M (DMSO) = 39$\Omega^{-1}cm^2mol^{-1}$.

7.3.5.3 Synthesis and characterisation of Dichloro(bis{2-[1-(4-chlorophenyl)-1H-1,2,3-triazol-4-yl-kN3]pyridine-kN})cobalt(II)

For the preparation of $[Co(L^6)_2Cl_2]$, the method used was similar to that for $[Mn(L^2)_2Cl_2]$. An amount of anhydrous $CoCl_2.6H_2O$ of 0.040g, 0.16mmol and 0.086g, 0.33mmol of L^6 were used, and an identical work-up procedure gave the required compound as a pale pink solid. The isolated precipitate gave (0.084g, 0.13mmol, yield 78%), mp. 332-334°C. IR: $\bar{\upsilon}(cm^{-1})$; 3065, 3052, 1606, 1570, 1502, 1472, 1448, 1405, 1268, 1257, 1151, 1134, 1095, 1061, 1052, 1013, 1003, 977, 825, 789, 756, 711. UV-Vis (DMSO) λ_{max}: The Co(II) complex showed absorption bands at 257nm, ε_{max} = $3407dm^3mol^{-1}$ cm^{-1}, 287nm, $\varepsilon_{max} = 3550dm^3mol^{-1}cm^{-1}$, 615nm, $\varepsilon_{max} = 56dm^3mol^{-1}cm^{-1}$, 678nm, $\varepsilon_{max} = 93dm^3mol^{-1}cm^{-1}$. The complex with L^6 showed a value ofμ_{eff} = 4.12 B.M. HRMS (ESI+) (water: acetonitrile = 1:3) withthe highest molecular weight ion peak matching, was at *m/z* = 606.0030 (100%) and is attributed to $[M\text{-}Cl]^+$. The calculated value for $[C_{26}H_{18}N_8CoCl_3]^+$ is 606.0052. Λ_M (DMSO) = $47\Omega^{-1}cm^2mol^{-1}$.

7.3.5.4 Synthesis and characterisation of Dichloro(bis{2-[1-(4-chlorophenyl)-1H-1,2,3-triazol-4-yl-kN3]pyridine-kN})nickel(II)

For the preparation of $[Ni(L^6)_2Cl_2]$, the method used was analogous to that for $[Mn(L^2)_2Cl_2]$. An amount of $NiCl_2.6H_2O$ of 0.031g, 0.13mmol and 0.075g, 0.29mmol of L^6 were used, and an identical work-up procedure gave the required compound as a pale blue solid. The isolated precipitate gave (0.06g, 0.093mmol, yield 72%), mp. 347°C (decomp.). IR: $\bar{\upsilon}(cm^{-1})$; 3048, 3010, 1612, 1577, 1502, 1475, 1452, 1408, 1274, 1262, 1141, 1096, 1064, 1058, 1013, 1022, 1006, 978, 866, 826, 789, 758, 712. UV-Vis (DMSO) λ_{max}: The Ni(II) complex showed absorption bands at 257nm, ε_{max} = $63333dm^3mol^{-1}cm^{-1}$, 287nm, $\varepsilon_{max} = 41905dm^3mol^{-1}cm^{-1}$, 408nm, $\varepsilon_{max} = 15dm^3mol^{-1}cm^{-1}$, 670nm, $\varepsilon_{max} = 44dm^3mol^{-1}cm^{-1}$. The complex with L^6 showed a value of μ_{eff} = 2.73 B.M. HRMS (ESI+) (water: acetonitrile = 1:3) with the highest molecular weight ion peak matching, was observed at *m/z* = 605.0100 (18%) and is related to $[M\text{-}Cl]^+$. The calculated value for $[C_{26}H_{18}N_8NiCl_3]^+$ is 605.0073. Λ_M (DMSO) = $58\Omega^{-1}cm^2mol^{-1}$.

7.3.5.5 Synthesis and characterisation of Dichloro(bis{2-[1-(4-chlorophenyl)-1H-1,2,3-triazol-4-yl-kN3]pyridine-kN})copper(II)

For the preparation of $[Cu(L^6)_2Cl_2]$, the method used was as described for $[Mn(L_2)_2Cl_2]$. An amount of anhydrous $CuCl_2$ of 0.03g, 0.24mmol and 0.13g, 0.50mmol of L^6 were used, and an identical work-up procedure gave the required compound as a green solid. The isolated precipitate gave (0.135g, 0.20mmol, yield 89%), mp. 274-276°C. IR: $\bar{\upsilon}(cm^{-1})$: 3068, 3043, 3022, 1607, 1572, 1501, 1474, 1450, 1407, 1280, 1250, 1157, 1092, 1064, 1040, 1027, 1013, 998, 861, 824, 779, 781, 711. UV-Vis (DMSO) λmax: The Cu(II) complex showed absorption bands at 252nm, ε_{max} = 34583$dm^3mol^{-1}cm^{-1}$, 260nm, ε_{max} = 41250$dm^3mol^{-1}cm^{-1}$, 288nm, ε_{max} = 44167$dm^3mol^{-1}cm^{-1}$, 876nm, ε_{max} = 71$dm^3mol^{-1}cm^{-1}$. The complex with L^6 showed a value of μeff = 1.70 B.M. HRMS TOF (ESI^+) (water: acetonitrile = 1:3) with the highest molecular weight ion peak matching, was observed at m/z= 610.0009 (100%) and is corresponding to $[M\text{-}Cl]^+$. The calculated value for $[C_{26}H_{18}N_8CuCl_3]^+$ is 610.0016. A good single crystal for X-ray structural analysis was obtained by slow evaporation of hot methanol: Acetonitrile = 1:1solution of the complex. ΛM (DMSO) = $24\Omega^{-1}cm^2mol^{-1}$.

7.3.5.6 Synthesis and characterisation of Dichloro(bis{2-[1-(4-chlorophenyl)-1H-1,2,3-triazol-4-yl-kN3]pyridine-kN})zinc(II)

For the preparation of $[Zn(L^6)_2Cl_2]$, the method used was similar to that for $[Mn(L^2)_2Cl_2]$. An amount of anhydrous $ZnCl_2$ of 0.033g, 0.24mmol and 0.126g, 0.49mmol of L^6 were used, and an identical work-up procedure gave the required compound as a white solid. The isolated precipitate gave (0.122g, 0.18mmol, yield 78%), mp. 328-330°C. IR: $\bar{\upsilon}(cm\text{-}^{1})$: 3048, 3024, 3010, 1611, 1593, 1577, 1502, 1474, 1452, 1407, 1274, 1262, 1140, 1095, 1064, 1058, 1021, 1014, 1006, 978, 865, 825, 788, 757, 788, 712. UV-Vis (DMSO) λ_{max}: The Zn(II) complex showed absorption bands at 258nm, ε_{max} = 53333$dm^3mol^{-1}cm^{-1}$, 286nm, ε_{max} = 44286$dm^3mol^{-1}cm^{-1}$. ^{1}HNMR data δ_H/ppm (400MHZ, DMSO-d_6): 9.31 (1H, s, H_{11}), 8.65 (1H, ddd, $^1J_{HH}$ = 0.92Hz, $^2J_{HH}$ = 1.71Hz, $^3J_{HH}$ = 4.12Hz, H_2), 8.12-7.92 (3H, m, H_5, Ar-$H_{13,17}$), 7.97-7.92 (1H, dt, $^1J_{HH}$ = 1.83Hz, $^2J_{HH}$ = 7.79Hz, H_4), 7.70-7.67 (2H, d, J_{HH} = 9.16Hz, Ar-$H_{14,16}$), 7.41-7.38 (1H, ddd, $^1J_{HH}$ = 0.92Hz, $^2J_{HH}$ = 1.37Hz, $^3J_{HH}$ = 7.33Hz, H_3); ^{13}CNMR(100.63MHZ, D_6MSO-d_6) δ_C/pmm: 119.71 (C_5), 121.20 (C_{11}), 121.88 (C_{13},C_{17}-Ar), 123.19 (C_3), 129.64 (C_{14},C_{16}-Ar), 133.01 (C_{12}), 135.23 (C_{15}), 137.13 (C_4), 148.12 (C_7), 149.20 (C_6), 149.49 (C_2). These assignments were confirmed using;

DEPT ^{13}C (135°), ^{1}H-^{1}H COSY and ^{1}H-^{13}C HMQC two dimensional correlation spectroscopy. HRMS TOF (ESI+) (Water: acetonitrile = 1:3) with the highest molecular weight ion peak matching, was observed at m/z = 611.0039 (100%) and is related to $[M- Cl]^+$. The calculated value for $[C_{26}H_{18}N_8CdCl_3]^+$ is 611.0011. ΛM (DMSO) = 12 $\Omega^{-1}cm^2mol^{-1}$.

7.3.5.7 Synthesis and characterisation of Dichloro(bis{2-[1-(4-chlorophenyl)-1H-1,2,3-triazol-4-yl-kN3]pyridine-kN})cadmium(II)

For the preparation of $[Cd(L^6)_2Cl_2]$, the method used was analogous to that for $[Mn(L^2)_2Cl_2]$. An amount of anhydrous $CdCl_2$ of 0.035g, 0.19mmol and 0.11 g, 0.42 mmol of L^6 were used, and an identical work-up procedure gave the required compound as a white solid. The isolated precipitate gave (0.11g, 0.15mmol, yield 83%), mp. 316-318°C. IR: $\bar{\upsilon}(cm^{-1})$: 3090, 3090, 3052, 1613, 1602, 1570, 1500, 1466, 1451, 1401, 1283, 1248, 1159, 1134, 1096, 1061, 1012, 1004, 981, 828, 783, 749, 714. UV-Vis (DMSO) λ_{max}: The Cd(II) complex showed absorption bands at 256nm, ε_{max} = 57083$dm^3mol^{-1}cm^{-1}$, 287nm, ε_{max} = 36250$dm^3mol^{-1}cm^{-1}$. ^{1}HNMR data δ_H/ppm (400MHZ, DMSO-d_6): 9.33 (1H, s, H_{11}), 8.67-8.66 (1H, ddd, $^{1}J_{HH}$ = 0.92Hz, $^{2}J_{HH}$ = 1.71Hz , $^{3}J_{HH}$ = 4.12Hz, H_2), 8.12-8.10 (2H, dd, $^{1}J_{HH}$ = 0.92Hz, $^{2}J_{HH}$ = 7.79Hz, H_5), 8.08-8.01 (2H, d, J_{HH} = 8.70Hz, Ar-$H_{13,17}$), 7.98-7.93 (1H, dt, $^{1}J_{HH}$ = 1.83Hz, $^{2}J_{HH}$ = 7.79Hz, H_4), 7.70-7.67 (2H, d, J_{HH} = 9.16Hz, Ar-$H_{14,16}$), 7.43-7.40 (1H, ddd, $^{1}J_{HH}$ = 1.37Hz, $^{2}J_{HH}$ = 4.58Hz, $^{3}J_{HH}$ = 7.33Hz, H_3); ^{13}CNMR (100.63MHZ, D_6MSO-d_6) δ_C/pmm: 119.80 (C_5), 121.32 (C_{11}), 121.83 ($C_{13,}C_{17}$-Ar), 123.28 (C_3), 129.66 (C_{14},C_{16}-Ar), 133.05 (C_{12}), 135.20 (C_{15}), 137.26 (C_4), 147.91 (C_7), 149.05 (C_6), 149.48 (C_2). These assignments were confirmed using; DEPT ^{13}C (135°), ^{1}H-^{1}H COSY and ^{1}H-^{13}C HMQC two dimensional correlation spectroscopy. HRMS TOF (ESI+) (water: acetonitrile = 1:3) with the highest molecular weight ion peak matching, was observed at *m/z* = 660.9731; (70%) and is assigned to $[M-Cl]^+$. The calculated value for $[C_{26}H_{18}N_8CdCl_3]^+$ is 660.9754. Λ_M (DMSO) = 18$\Omega^{-1}cm^2mol^{-1}$.

7.3.5.8 Synthesis and characterisation of Dichloro(bis{2-[1-(4-chlorophenyl)-1H-1,2,3-triazol-4-yl-kN3]pyridine-kN})platnium(II)

For the preparation of $[Pt(L^6)_2Cl_2]$, the method used was similar to that for $[Pt(L^3)_2Cl_2]$. To solution of L^6 (0.060g, 0.23mmol) in CH_3CN (5mL) was added dropswise a solution of $K_2[PtCl_4]$ (0.075g, 0.096mmol) in C_2H_5OH-H_2O 8:2 (10mL). A yellow solid was isolatedgiving (0.10g, 0.13mmol, yielded 78%), mp. 282-284°C. IR: $\bar{\upsilon}(cm^{-1})$; 3131, 3057, 1614, 1602, 1589, 1570, 1550, 1501, 1473, 1400, 1237, 1146, 1038, 1012, 997, 990, 823, 780, 740. ^{1}HNMR data δ_H/ppm (400MHZ, DMSO-d_6): 9.41(1H, s, H_{11}), 8.70-8.69 (1H, d, $^1J_{HH}$ = 54.58Hz, H_2), 8.17-8.15 (1H, dd, $^1J_{HH}$ = 8.24Hz, H_5), 8.13-8.10 (2H, d, J_{HH} = 8.70Hz, Ar-$H_{13,17}$), 8.01-7.97 (1H, dt, $^1J_{HH}$ = 1.83Hz, $^2J_{HH}$ = 7.79Hz, H_4), 7.75-7.72 (2H, d, J_{HH} = 8.70Hz, Ar-$H_{14,16}$), 7.47-7.4340.45 (1H, ddd, $^1J_{HH}$ = 0.92Hz, $^2J_{HH}$ = 5.04Hz, $^3J_{HH}$ = 7.33Hz, H_3); ^{13}CNMR (100.63MHZ, D_6MSO-d_6) δ_C/pmm: 119.73 (C_5), 121.32 (C_{11}), 121.82 (C_{13},C_{17}-Ar), 123.33(C_3), 129.76 (C_{14},C_{16}-Ar), 133.02 (C_{12}), 135.26 (C_{15}), 137.27 (C_4), 148.21 (C_7), 149.25 (C_6), 149.59 (C_2). These assignments were confirmed using; DEPT ^{13}C (135°), ^{1}H-^{1}H COSY and ^{1}H-^{13}C HMQC two dimensional correlation spectroscopy. HRMS TOF (ESI+) (water: acetonitrile = 1:3) with the highest molecular weight ion peak matching, was observed at *m/z* = 742.0359 (30%) and is assigned to $[M\text{-}Cl]^+$. The calculated value for $[C_{26}H_{18}N_8PtCl_3]^+$ is 742.0368. Λ_M (DMSO) = $8\Omega^{-1}cm^2mol^{-1}$.

7.3.6 Synthesis and characterisation of the metals complexes with ligand L^7

7.3.6.1 Synthesis and characterisation of Dichloro (bis {4-[4-(pyridin-2-yl-kN)-1H-1,2,3-triazol-1-yl-kN3]benzonitrile})manganese(II)

For the preparation of $[Mn(L^7)_2Cl_2]$, the method used was similar to that for $[Mn(L^2)_2Cl_2]$. An amount of anhydrous $MnCl_2$ of 0.032g, 0.25mmol and 0.13g, 0.52mmol of L^7 were used, and an identical work-up procedure gave the required compound as a pale yellow solid. The isolated precipitate gave (0.125g, 0.20mmol, yield 80%), mp. 318-320°C. IR: $\bar{\upsilon}(cm^{-1})$; 3070, 3057, 3007, 2233, 1630, 1603, 1590, 1570, 1518, 1471, 1448, 1409, 1285, 1255, 1158, 1061, 1050, 1016, 1005, 978, 851, 812, 783, 717. UV-Vis (DMSO) λ_{max}: The Mn(II) complex showed absorption bands at 261nm, ε_{max} = 76000$dm^3mol^{-1}cm^{-1}$, 294nm, ε_{max} = 89000$dm^3mol^{-1}cm^{-1}$, 743nm, ε_{max} = 4$dm^3mol^{-1}cm^{-1}$. The complex with L^7 showed a value of μ_{eff} = 5.78 B.M. HRMS TOF (ESI+) (water: acetonitrile = 1:3) with the highest molecular weight ion peak matching, was observed at *m/z* = 584.0770 (100%) and is attributed to $[M\text{-}Cl]^+$. The calculated value for $[C_{28}H_{18}N_{10}ClMn]^+$ is 584.0785. Λ_M (DMSO) = $52\Omega^{-1}cm^2mol^{-1}$.

7.3.6.2 Synthesis and characterisation of Dichloro(bis{4-[4-(pyridin-2-yl-kN)-1H-1,2,3-triazol-1-yl-kN3]benzonitrile})iron(II)

For the preparation of $[Fe(L^7)_2Cl_2]$, the method used was analogous to that for $[Mn(L^2)_2\ Cl_2]$. An amount of anhydrous $FeCl_2$ of 0.028g, 0.22mmol and 0.12g, 0.48mmol of L^7 were used, and an identical work-up procedure gave the required compound as a pale yellow solid. The isolated precipitate gave (0.113g, 0.18mmol, yield 83%), mp. 308-310°C. IR: $\bar{\upsilon}(cm^{-1})$; 3071, 3057, 3025, 3012, 2233, 1604, 1591, 1572, 1514, 1471, 1451, 1410, 1287, 1258, 1259, 1140, 1061, 1052, 1016, 1006,977, 846, 787, 717. UV-Vis (DMSO) λ_{max}: The Fe(II) complex showed absorption bands at 256nm, ε_{max} = 138750$dm^3mol^{-1}cm^{-1}$, 289nm, ε_{max} = 56250$dm^3mol^{-1}cm^{-1}$, 950nm, ε_{max} = 45$dm^3mol^{-1}cm^{-1}$. The complex with L^7 showed a value of μ_{eff} = 4.26 B.M. HRMS TOF (ESI+) (water: acetonitrile = 1:3) with the highest molecular weight ion peak matching, was observed at m/z 585.0738 (70%) and is assigned to $[M\text{-}Cl]^+$. The calculated value for $[C_{28}H_{18}N_{10}ClFe]^+$ is 585.0754. ΛM (DMSO) = 39$\Omega^{-1}cm^2mol^{-1}$.

7.3.6.3 Synthesis and characterisation of Dichloro(bis{4-[4-(pyridin-2-yl-kN)-1H-1,2,3-triazol-1-yl-kN3]benzonitrile})cobalt(II)

For the preparation of $[Co(L^7)_2Cl_2]$, the method used was as described for $[Mn(L^2)_2Cl_2]$. An amount of 0.042g, 0.17mmol of $CoCl_2.6H_2O$ and 0.13g, 0.50mmol of L^7 were used, and an identical work-up procedure gave the required compound as a pale pink solid. The isolated precipitate gave (0.081g, 0.12mmol, yield 74%), mp. 350-352°C. IR: $\bar{\upsilon}(cm^{-1})$; 3077, 3059, 3041, 3013, 2232, 1630, 1603, 1591, 1575, 1518, 1472, 1451, 1410, 1286, 1261, 1245, 1144, 1061, 1053, 1018, 1006, 978, 849, 824, 794, 718. UV-Vis (DMSO) λ_{max}: The Co(II) complex showed absorption bands at 256nm, ε_{max} = 53750$dm^3mol^{-1}cm^{-1}$, 295nm, ε_{max} = 49375$dm^3mol^{-1}cm^{-1}$, 615nm, ε_{max} = 45$dm^3mol^{-1}cm^{-1}$, 677nm, ε_{max} = 97$dm^3mol^{-1}cm^{-1}$. The complex with L^7 showed a value of μ_{eff} = 3.80 B.M. HRMS TOF (ESI+) (water: acetonitrile = 1:3) with the highest molecular weight ion peak matching, was observed at *m/z* = 588.0740 (25%) and is related to [M- Cl^+. The calculated value for $[C_{28}H_{18}N_{10}ClCu]^+$ is 588.0736. Λ_M (DMSO) = 44$\Omega^{-1}cm^2mol^{-1}$.

7.3.6.4 Synthesis and characterisation of Dichloro(bis{4-[4-(pyridin-2-yl-kN)-1H-1,2,3-triazol-1-yl-kN3]benzonitrile})nickel(II)

For the preparation of $[Ni(L^7)_2Cl_2]$, the method used was similar to that for $[Mn(L^2)_2Cl_2]$. An amount of $NiCl_2.6H_2O$ of 0.033g, 0.14mmol and of 0.075g, 0.34mmol of L^7 were used, and an identical work-up procedure gave the required compound as a pale blue solid. The isolated precipitate gave (0.062g, 0.099mmol, yield 72%), mp. 346°C (decomp.). IR: $\bar{\upsilon}(cm^{-1})$; 3078, 3059, 3021, 3016, 2232, 1631, 1603, 1592, 1578, 1518, 1476, 1473, 1454, 1410, 1288, 1262, 1159, 1146, 1063, 1055, 1021, 1008, 979, 848, 824, 794, 756, 719. UV-Vis (DMSO) λ_{max}: The Ni(II) complex showed absorption bands at 256nm, ε_{max} = 55417$dm^3mol^{-1}cm^{-1}$, 292nm, ε_{max} = 37083$dm^3mol^{-1}cm^{-1}$, 408nm, ε_{max} = 14$dm^3mol^{-1}cm^{-1}$, 682nm, ε_{max} = 5$dm^3mol^{-1}cm^{-1}$. The complex with L^7 showed a value ofμ_{eff} = 2.77 B.M. HRMS (ESI+) (water: acetonitrile = 1:3) with the highest molecular weight ion peak matching, was observed at *m/z* 587.0751 (5%) and is related to $[M\text{-}Cl]^+$. The calculated value for $[C_{28}H_{18}N_{10}ClNi]^+$ is 587.0758. Λ_M (DMSO) = 50$\Omega^{-1}cm^2mol^{-1}$.

7.3.6.5 Synthesis and characterisation of Dichloro(bis{4-[4-(pyridin-2-yl-kN)-1H-1,2,3-triazol-1-yl-kN3]benzonitrile})] copper(II)

For the preparation of $[Cu(L^7)_2Cl_2]$, the method used was similar to that for $[Mn(L^2)_2Cl_2]$. An amount of anhydrous $CuCl_2$ of 0.036 g, 0.26 mmol of and 0.13g, 0.53mmol of L^7 were used, and an identical work-up procedure gave the required compound as a green solid. The isolated precipitate gave (0.136g, 0.21mmol, yield 90%), mp. 292-294°C. IR: $\bar{\upsilon}(cm^{-1})$; 3077, 3038, 3004, 2232, 1634, 1616, 1601, 1594, 1579, 1516, 1475, 1449, 1456, 1411, 1371, 1288, 1279, 1161, 1149, 1061, 1010, 978, 858, 826, 797, 720. UV-Vis (DMSO) λ_{max}: The Cu(II) complex showed absorption bands at 258nm, ε_{max} = 57278$dm^3mol^{-1}cm^{-1}$, 299nm, ε_{max} = 48636$dm^3mol^{-1}cm^{-1}$, 922nm, ε_{max} = 121$dm^3mol^{-1}cm^{-1}$. The complex with L^7 showed a value of μ_{eff} = 1.64 B.M. HRMS TOF (ESI+) (water: acetonitrile = 1:3) with the highest molecular weight ion peak matching, was observed at *m/z* = 592.0712 (75%) and is related to $[M\text{-}Cl]^+$. The calculated value for $[C_{28}H_{18}N_{10}ClCu]^+$ is 592.0700. A good single crystal for X-ray structural analysis was obtained by slow evaporation of a hot (methanol: acetonitrile =1:1) solution of the complex. Λ_M (DMSO) = 26$\Omega^{-1}cm^2mol^{-1}$.

7.3.6.6 Synthesis and characterisation of Dichloro(bis{4-[4-(pyridin-2-yl-kN)-1H-1,2,3-triazol-1-yl-kN3]benzonitrile})zinc(II)

For the preparation of $[Zn(L^7)_2Cl_2]$, the method used was similar to that for $[Mn(L^2)_2Cl_2]$. An amount of anhydrous $ZnCl_2$ of 0.025g, 0.18mmol and 0.10g, 0.40mmol of L^7 were used, and an identical work-up procedure gave the required compound as a white solid. The isolated precipitate gave (0.088g, 0.14mmol, yield 77%), mp. 288-290°C. IR: $\bar{\upsilon}(cm^{-1})$; 3076, 3052, 3010, 2228, 1631, 1602, 1591, 1574, 1518, 1472, 1452, 1409, 1286, 1259, 1158, 1141, 1062, 1053, 1024, 1007, 978, 856, 845, 825, 782, 718. UV-Vis (DMSO) λ_{max}: The Zn(II) complex showed absorption bands at 256nm, ε_{max} = 17400$dm^3mol^{-1}cm^{-1}$, 300nm, ε_{max} = 17200$dm^3mol^{-1}cm^{-1}$. ^{1}HNMR data δ_H/ppm (400MHZ, DMSO-d_6): 9.31 (1H, S, H_{16}), 8.63 (1H,s, H_{14}), 8.18-8.16 (2H, d, J_{HH} = 8.25Hz, Ar-$H_{3,11}$), 8..07-7.97 (3H, m, H_{15}, Ar-$H_{7,10}$), 7.91-7.88 (1H, t, $^1J_{HH}$ = 7.15Hz, $^2J_{HH}$ = 7.15Hz, H_{18}), 7.36-7.35 (1H, d, J_{HH} = 4.67Hz, H_{19}); ^{13}CNMR (100.63MHZ, D_6MSO-d_6) δ_C/pmm: 111.37(C_{12}), 118.12 (C_5), 120.15 (C_{15}), 120.84 (C_3,C_{11}-Ar), 121.54 (C_{16}), 123.68 (C_{19}), 134.29 (C_7,C_{10}-Ar), 137.52(C_{18}), 139.52 (C_6), 148.58 (C_{17}), 149.06 (C_9), 149.79 (C_{14}).These assignments were confirmed using DEPT ^{13}C (135), ^{1}H-^{1}H COSY and ^{1}H-^{13}C HMQC two dimensional correlation spectroscopy. HRMS TOF (ESI+) (water: acetonitrile = 1:3) with the highest molecular weight ion peak matching, was observed at *m/z* = 593.0675 (80%) and is related to $[M\text{-}Cl]^+$. The calculated value for $[C_{28}H_{18}N_{10}ClZn]^+$ is 593.0696. Λ_M (DMSO) = 6$\Omega^{-1}cm^2mol^{-1}$.

7.3.6.7 Synthesis and characterisation of Dichloro(bis{4-[4-(pyridin-2-yl-kN)-1H-1,2,3-triazol-1-yl-kN3]benzonitrile})cadmium(II)

For the preparation of $[Cd(L^7)_2Cl_2]$, the method used was analogous to that for $[Mn(L^2)_2Cl_2]$. An amount of anhydrous $CdCl_2$ of 0.029g, 0.15mmol and 0.10g, 0.40mmol of L^7 were used, and an identical work-up procedure gave the required compound as a whitesolid. The isolated precipitate gave (0.089g, 0.13mmol, yield 83%), mp. 280-282°C. IR: $\bar{\upsilon}(cm^{-1})$; 3092, 3055, 2234, 1631, 1602, 1571, 1568, 1510, 1468, 1450, 1406, 1285, 1269, 1248, 1158, 1141, 1062, 1058, 1032, 1014, 1005, 981, 839, 782, 719. UV-Vis (DMSO) λ_{max}: The Cd(II) complex showed absorption bands at 258nm, ε_{max} = 16800$dm^3mol^{-1}cm^{-1}$, 300nm, ε_{max} = 20200$dm^3mol^{-1}cm^{-1}$. ^{1}HNMR data δ_H/ppm (400MHZ, DMSO-d_6): 9.45 (1H, s, H_{16}), 8.68-8.67 (1H, d, J_{HH} = 4.12Hz, H_{14}), 8.28-8.26 (2H, d, J_{HH} = 6.60Hz, Ar-$H_{3,11}$), 8.12-8.09 (3H, m, H_{15}, Ar-$H_{7,10}$), 7.98-7.94 (1H, t, $^1J_{HH}$ = 7.42Hz, $^2J_{HH}$ = 7.70Hz, H_{18}), 7.42-7.40 (1H, t, $^1J_{HH}$ = 6.32Hz,

$^{2}J_{HH}$ = 4.95Hz, H_{19}); ^{13}CNMR (100.63MHZ, D_6MSO-d_6) δ_C/pmm: 111.12 (C_{12}), 117.84 (C_5), 119.81 (C_{15}), 120.55 (C_3,C_{11}-Ar), 121.41 (C_{16}), 123.34 (C_{19}), 134.04 (C_7,C_{10}-Ar), 137.20 (C_{18}), 139.34 (C_6), 148.35 (C_{17}), 148.94 (C_9), 150.23 (C_{14}). These assignments were confirmed using DEPT ^{13}C (135°), ^{1}H-^{1}H COSY and ^{1}H-^{13}C HMQC two dimensional correlation spectroscopy. HRMS TOF (ESI+) (water: acetonitrile = 1:3) with the highest molecular weight ion peak matching, was observed at *m/z* = 643.0438 (90%) and is attributed to $[M\text{-}Cl]^+$. The calculated value for $[C_{28}H_{18}N_{10}ClCd]^+$ is 643.0422. Λ_M (DMSO) = 13$\Omega^{-1}cm^2mol^{-1}$.

7.3.7 Synthesis and characterisation of the metals complexes with ligand L8

7.3.7.1 Synthesis and characterisation of Dichloro{bis[2-(1-phenyl-1H-1,2,3-triazol-4-yl-kN3)pyridine-kN]}manganese(II)

For the preparation of $[Mn(L^8)_2Cl_2]$, the method used was similar to that for $[Mn(L^2)_2Cl_2]$. An amount of 0.040g, 0.31mmol of anhydrous $MnCl_2$ and 0.14g, 0.62mmol of L^8 were used, and an identical work-up procedure gave the required compound as a pale yellow solid. The isolated precipitate gave (0.15g, 0.26mmol, yield 82%), mp. 318-320°C. IR: $\bar{\upsilon}$(cm^{-1}); 3068, 3011, 2970, 1607, 1596, 1577, 1504, 1471, 1444, 1285, 1255, 1063, 1046, 1010, 1001, 978, 911, 857, 790, 757, 725, 683. UV-Vis (DMSO) λ_{max}: The Mn(II) complex showed absorption bands at 257nm, ε_{max} = 72500 $dm^3mol^{-1}cm^{-1}$, 286nm, ε_{max} = 33214$dm^3mol^{-1}cm^{-1}$, 773nm, ε_{max} = 278$dm^3mol^{-1}cm^{-1}$, 910nm, ε_{max} = 143$dm^3mol^{-1}cm^{-1}$. The complex with L^8 showed a value of μ_{eff} = 5.52 B.M. HRMS TOF (ESI+) (water: acetonitrile = 1:3) with the highest molecular weight ion peak matching, was observed at *m/z* = 534.0861 (80%) and is attributed to $[M\text{-}Cl]^+$. The calculated value for $[C_{26}H_{20}N_8ClMn]^+$ is 534.0861. X-Ray quality bright yellow crystals were obtained by slow evaporation of a hot (CH_3OH:CH_3CN: 1:1) solution of the complex. Λ_M (DMSO) = 52$\Omega^{-1}cm^2mol^{-1}$.

7.3.7.2 Synthesis and characterisation of Dichloro{bis[2-(1-phenyl-1H-1,2,3-triazol-4-yl-kN3)pyridine-kN]}iron(II)

For the preparation of $[Fe(L^8)_2Cl_2]$, the method used was analogous to that for $[Mn(L^2)_2Cl_2]$. An amount of anhydrous of anhydrous $FeCl_2$ of 0.030g, 0.23mmol and 0.10g, 0.40mmol of L^8 were used, and an identical work-up procedure gave the required compound as a pale yellow solid. The isolated precipitate gave (0.11g, 0.19mmol, yield 81%), mp. 336-338°C. IR: $\bar{\upsilon}(cm^{-1})$: 3064, 3053, 3026, 3009, 1606, 1594, 1575, 1504, 1471, 1444, 1267, 1259, 1063, 1054, 1016, 1004, 977, 913, 861, 815, 785, 756, 725, 686. UV-Vis (DMSO) λ_{max}: The Fe(II) complex showed absorption bands at 258nm, $\varepsilon_{max=}$ $62593dm^3mol^{-1}cm^{-1}$, 286nm, $\varepsilon_{max=}$ $32963dm^3mol^{-1}cm^{-1}$, 333nm, $\varepsilon_{max=}$ $52917dm^3mol^{-1}cm^{-1}$, 522nm, $\varepsilon_{max=}$ $190dm^3mol^{-1}cm^{-1}$, 756nm, $\varepsilon_{max=}$ $885dm^3mol^{-1}cm^{-1}$. The complex with L^8 showed a value of μ_{eff} = 4.66 B.M. HRMS TOF (ESI+) (water: acetonitrile = 1:3) with the highest molecular weight ion peak matching, was observed at *m/z* = 535.0835 (60%) and is related to $[M\text{-}Cl]^+$. The calculated value for $[C_{26}H_{20}N_8ClFe]^+$ is 535.0849. Λ_M (DMSO) = $46\Omega^{-1}cm^2mol^{-1}$.

7.3.7.3 Synthesis and characterisation of Dichloro{bis[2-(1-phenyl-1H-1,2,3-triazol-4-yl-kN3)pyridine-kN]}cobalt(II)

For the preparation of $[Co(L^8)_2Cl_2]$, the method used was similar to that for $[Mn(L^2)_2Cl_2]$. An amount of anhydrous $CoCl_2.6H_2O$ of 0.050g, 0.21mmol and 0.094g, 0.21mmol of L^8 where used, yielding a pale pink solid. The isolated precipitate gave (0.09g, 0.15mmol, yield 75%), mp 350-352°C. IR: $\bar{\upsilon}(cm^{-1})$; 3050, 3027, 3013, 1610, 1594, 1579, 1505, 1474, 1447, 1271, 1263, 1065, 1057, 1019, 1006, 978, 914, 885, 785, 755, 685 UV-Vis (DMSO) λ_{max}: The Co(II) complex showed absorption bands at 258nm, $\varepsilon_{max=}$ $60690dm^3mol^{-1}cm^{-1}$, 286nm, $\varepsilon_{max=}$ $28966dm^3mol^{-1}cm^{-1}$, 615nm, $\varepsilon_{max=}$ $44dm^3mol^{-1}cm^{-1}$, 678nm, $\varepsilon_{max=}$$72dm^3mol^{-1}cm^{-1}$. The complex with L^8 showed a value ofμ_{eff} = 3.49 B.M. HRMS TOF (ESI+) with the highest molecular weight ion peak matching, was observed at *m/z*= 538.0851 (70%) is related to $[M\text{-}Cl]^+$. The calculated value for $[C_{26}H_{20}N_8ClCo]^+$ is 538.0831. Λ_M (DMSO) = $44\Omega^{-1}cm^2mol^{-1}$.

7.3.7.4 Synthesis and characterisation of Dichloro{bis[2-(1-phenyl-1H-1,2,3-triazol-4-yl-kN3)pyridine-kN]}nickel(II)

For the preparation of $[Ni(L^8)_2Cl_2]$, the method used was as described for $[Mn(L^2)_2Cl_2]$. An amount of $NiCl_2.6H_2O$ of 0.040g, 0.16mmol and 0.075g, 0.33mmol of L^8 where used, and an identical work-up procedure gave the required compound as a pale blue solid. The isolated precipitate gave (0.075g, 0.13mmol, yield 78%), mp. 340°C (decomp.). IR: $\bar{\upsilon}(cm^{-1})$: 3041, 3026, 3015, 1613, 1595, 1582, 1505, 1475, 1448, 1273, 1264, 1140, 1066, 1059, 1007, 978, 914, 888, 785, 756, 727, 685. UV-Vis (DMSO) λ_{max}: The Ni(II) complex showed absorption bands at 258nm, $\varepsilon_{max=}$ $80000dm^3mol^{-1}cm^{-1}$, 286nm, $\varepsilon_{max=}$ $46818dm^3mol^{-1}cm^{-1}$, 400nm, $\varepsilon_{max=}$ $20dm^3mol^{-1}cm^{-1}$, 668nm, $\varepsilon_{max=}$ $8dm^3mol^{-1}cm^{-1}$. The complex with L^8 showed a value ofμ_{eff} = 3.00 B.M. HRMS TOF (ESI+) (water: acetonitrile = 1:3) with the highest molecular weight ion peak matching, was observed at *m/z* = 537.0834 (40%) and is attributed to$[M-Cl]^+$. The calculated value for $[C_{26}H_{20}N_8ClNi]^+$ is 537.0853. Λ_M (DMSO) = $50\Omega^{-1}cm^2mol^{-1}$.

7.3.7.5 Synthesis and characterisation of Dichloro{bis[2-(1-phenyl-1H-1,2,3-triazol-4-yl-kN3)pyridine-kN]}copper(II)

For the preparation of $[Cu(L^8)_2Cl_2]$, the method used was analogous to that for $[Mn(L^2)_2Cl_2]$. An amount of anhydrous $CuCl_2$ of 0.055g, 0.40mmol and 0.18g, 0.81mmol of L^8 where used, and an identical work-up procedure gave the required compound as a green solid. The isolated precipitate gave (0.22g, 0.38mmol, yield 93%), mp. 282-284°C. IR: $\bar{\upsilon}(cm^{-1})$; 3059, 3028, 3014, 1608, 1595, 1574, 1505, 1475, 1467, 1448, 1269, 1254, 1065, 1047, 1028, 1002, 973, 912, 858,783, 757, 733, 685. UV-Vis (DMSO) λ_{max}: The Cu(II) complex showed absorption bands at 258nm, ε_{max} $_=$ $44286dm^3mol^{-1}cm^{-1}$, 285nm, $\varepsilon_{max=}$ $31429dm^3mol^{-1}cm^{-1}$, 908nm, ε_{max} = $13dm^3mol^{-1}cm^{-1}$. The complex with L^8 showed a value ofμ_{eff} = 1.71 B.M. HRMS TOF (ESI+) (water: acetonitrile = 1:3) with the highest molecular weight ion peak matching, was observed at *m/z* 542.0817 (20%) and is related to $[M-Cl]^+$. The calculated value for $[C_{26}H_{20}N_8ClCu]^+$ is 542.0795. A good single crystal for X-ray structural analysis was obtained by slow evaporation of hot (CH_3OH) solution of the complex. Λ_M (DMSO) = $26\Omega^{-1}cm^2mol^{-1}$.

7.3.7.6 Synthesis and characterisation of Dichloro{bis[2-(1-phenyl-1H-1,2,3-triazol-4-yl-kN3)pyridine-kN]}zinc(II)

For the preparation of $[Zn(L^8)_2Cl_2]$, the method used was similar to that for $[Mn(L^2)_2Cl_2]$. An amount of anhydrous $ZnCl_2$ of 0.035g, 0.25mmol and 0.11g, 0.51mmol of L^8 where used, and an identical work-up procedure gave the required compound as a white solid. The isolated precipitate gave (0.12g, 0.20mmol, yield 81%), mp. 246-248°C. IR: $\bar{\upsilon}$ (cm^{-1}); 3039, 3024, 3011, 1608, 1594, 1577, 1574, 1505, 1474, 1467, 1446, 1271, 1261, 1097, 1064, 1058, 1048, 1020, 1010, 1006, 978, 913, 869, 786, 756, 726, 686. UV-Vis (DMSO) λ_{max}: The Zn(II) complex showed absorption bands at 257nm, $\varepsilon_{max=}$ 142222$dm^3mol^{-1}cm^{-1}$, 287nm, $\varepsilon_{max=}$ 58333$dm^3mol^{-1}cm^{-1}$. ^{1}HNMR data δ_H/ppm (400MHZ, DMSO-d_6): 9.27 (1H, s, H_1), 8.66-8.65 (1H, d,$^1J_{HH}$ = 2.75Hz, H_7), 8.13-8.11 (1H, d,$^1J_{HH}$ = 7.79Hz, H_4), 8.03-8.00 (2H, d, J_{HH} = 7.33Hz, Ar-$H_{9,13}$), 7.96-7.92 (1H, dt, $^1J_{HH}$ = 1.83Hz, $^2J_{HH}$ = 7.79Hz, H_5), 7.65-7.60 (2H, d, J_{HH} = 7.33Hz, Ar-$H_{10,12}$), 7.54-7.50 (1H, td, $^1J_{HH}$ = 0.92Hz, $^2J_{HH}$ = 1.37Hz, $^3J_{HH}$ = 1.83Hz, H_{11}), 7.41-7.39 (1H, ddd, $^1J_{HH}$ = 0.92Hz, $^2J_{HH}$ = 5.04Hz, $^3J_{HH}$ = 7.79Hz, H_6); 13CNMR (100.63MHZ, D_6MSO-d_6) δ_C/pmm: 119.89 (C_4), 120.22 (C_9,C_{13}-Ar), 120.22 (C_1), 123.32 (C_6), 128.81 (C_{11}), 129.81 (C_{10},C_{12}-Ar), 136.52 (C_5), 137.36 (C_8), 147.87 (C_2), 149.22 (C_3), 149.50 (C_7). These assignments were confirmed using DEPT ^{13}C (135°), ^{1}H-^{1}H COSY and ^{1}H-^{13}C HMQC two dimensional correlation spectroscopy. HRMS (ESI+) (water: acetonitrile = 1:3) with the highest molecular weight ion peak matching, was observed at *m/z* 543.0780 (60%) and is related to $[M-Cl]^+$. The calculated value for $[C_{26}H_{20}N_8ClZn]^+$ is 543.0791. Λ_M (DMSO) = 8$\Omega^{-1}cm^2mol^{-1}$.

7.3.7.7 Synthesis and characterisation of Dichloro{bis[2-(1-phenyl-1H-1,2,3-triazol-4-yl-kN3)pyridine-kN]}cadmium(II)

For the preparation of $[Cd(L^8)_2Cl_2]$, the method used was analogous to that for $[Mn(L^2)_2Cl_2]$. An amount of anhydrous $CdCl_2$ of 0.037g, 0.20mmol and 0.10g, 0.45mmol of L^8 where used and an identical work-up procedure gave the required compound as a white solid. The isolated precipitate give (0.12g, 0.19mmol, yield 81%), mp. 294-296°C. IR: $\bar{\upsilon}$(cm^{-1}); 3102, 3066, 3011, 1624, 1604, 1597, 1574, 1504, 1486, 1447, 1267, 1250, 1064, 1016, 1010, 1002, 913, 859, 781, 753, 724, 718, 685. UV-Vis (DMSO) λ_{max}: The Cd(II) complex showed absorption bands at 257nm, $\varepsilon_{max=}$ 58095$dm^3mol^{-1}cm^{-1}$, 287nm, $\varepsilon_{max=}$ 25000$dm^3mol^{-1}cm^{-1}$. ^{1}HNMR data δ_H/ppm (400MHZ, DMSO-d_6): 9.30 (1H, s, H_1), 8.67-8.66 (1H, ddd, $^1J_{HH}$ = 0.92Hz, $^2J_{HH}$ =

1.83Hz, $^{3}J_{HH}$ = 5.04Hz, H_7), 8.13-8.11(1H, td, $^{1}J_{HH}$ = 0.92Hz, $^{2}J_{HH}$ = 1.37Hz, $^{3}J_{HH}$ = 8.24Hz, H_4), 8.03-8.00 (2H, d = 7.73Hz, Ar-$H_{9,13}$),7.98-7.94(1H, td, $^{1}J_{HH}$ = 1.83Hz, $^{2}J_{HH}$ = 7.79Hz, H_5), 7.65-7.60 (2H, d, J_{HH} = 7.78Hz, Ar-$H_{10,12}$), 7.54-7.50 (1H, dt, $^{1}J_{HH}$ = 0.92Hz, $^{2}J_{HH}$ = 1.37Hz, $^{3}J_{HH}$ = 1.83Hz, H_{11}), 7.43-7.40 (1H, ddd, $^{1}J_{HH}$ = 0.92Hz, $^{2}J_{HH}$ = 5.04Hz, $^{3}J_{HH}$ = 7.79Hz, H_6); ^{13}CNMR (100.63MHZ, D_6MSO-d_6) δ_C/pmm: 119.89 (C_4), 120.22(C_9,C_{13}-Ar), 121.28 (C_1), 123.32 (C_6), 128.81 (C_{11}), 129.81 (C_{10},C_{12}-Ar), 136.52 (C_5), 137.36 (C_8), 147.87 (C_2), 149.22 (C_3), 149.55 (C_7). These assignments were confirmed using DEPT ^{13}C (135°), ^{1}H-^{1}H COSY and ^{1}H-^{13}C HMQC two dimensional correlation spectroscopy. HRMS TOF (ESI+) (water: acetonitrile = 1:3) with the highest molecular weight ion peak matching, was observed at *m/z* = 593.0507 (10%) and is attributed to $[M\text{-}Cl]^+$. The calculated value for $[C_{26}H_{20}N_8ClCd]^+$ is 593.0533. Λ_M (DMSO) = 16$\Omega^{-1}cm^2mol^{-1}$.

7.3.7.8 Synthesis and characterisation of Dichloro{bis[2-(1-phenyl-1H-1,2,3-triazol-4-yl-kN3)pyridine-kN]}platinum(II)

For the preparation of $[Pt(L^8)_2Cl_2]$, the method used was similar to that for $[Pt(L^3)_2Cl_2]$. To a solution of L^8 (0.085g, 0.38mmol) in CH_3CN (5mL) was added dropswise a solution of $K_2[PtCl_4]$ (0.070g, 0.16mmol) in C_2H_5OH-H_2O 8:2 (10mL). A yellow solid, was isolated giving (0.094g, 0.13mmol, yielded 80%), mp. 246-248°C. IR: $\bar{\upsilon}$(cm^{-1}); 3186, 3051, 1600, 1592, 1578, 1540, 1520, 1502, 1470, 1464, 1447, 1280, 1237, 1146, 1091, 1035, 999, 840, 841, 791, 757, 722. ^{1}HNMR data δ_H/ppm (400MHZ, DMSO-d_6): 9.38 (1H, s, H_1), 8.71-8.69 (1H, ddd, $^{1}J_{HH}$ = 0.92Hz, $^{2}J_{HH}$ = 1.83Hz, $^{3}J_{HH}$ = 5.04Hz, H_7), 8.18-8.15(1H, td, $^{1}J_{HH}$ = 0.92Hz, $^{2}J_{HH}$ = 1.37Hz, $^{3}J_{HH}$ = 7.79Hz, H_4), 8.09-8.06 (2H, d = 8.24Hz, Ar-$H_{9,13}$), 8.01-7.97(1H, dt, $^{1}J_{HH}$ = 1.83Hz, $^{2}J_{HH}$ = 7.79Hz, H_5), 7.69-7.64 (2H, d, J_{HH} = 8.24Hz, Ar-$H_{10,12}$), 7.58-7.54 (1H, tt, $^{1}J_{HH}$ = 0.92Hz, $^{2}J_{HH}$ = 1.37Hz, $^{3}J_{HH}$ = 7.79Hz, H_{11}), 7.47-7.43 (1H, ddd, $^{1}J_{HH}$ = 0.92Hz, $^{2}J_{HH}$ = 4.58Hz, $^{3}J_{HH}$ = 7.79Hz, H_6); ^{13}CNMR (100.63MHZ, D_6MSO-d_6) δ_C/pmm: 120.34 (C_4), 120.71(C_9,C_{13}-Ar), 121.78 (C_1), 123.90 (C_6), 129.38 (C_{11}), 130.44 (C_{10},C_{12}-Ar), 137.09 (C_5), 137.90 (C_8), 148.74 (C_2), 150.02 (C_3), 150.21 (C_7). These assignments were confirmed using DEPT ^{13}C (135°), ^{1}H-^{1}H COSY and ^{1}H-^{13}C HMQC two dimensional correlation spectroscopy. HRMS TOF(ESI+) (MALDI) with the highest molecular weight ion peak matching, was observed at *m/z* = 675.1 (25%) and is attributed to $[M\text{-}Cl]^+$. The calculated value for $[C_{26}H_{20}N_8ClPt]^+$ is 675.1. Λ_M (DMSO) = 8$\Omega^{-1}cm^2mol^{-1}$.

7.3.8 Synthesis and characterisation of the metals complexes with ligand L^9

7.3.8.1 Synthesis and characterisation of Dichloro[bis(2-{1-[4-(trifluoromethyl)phenyl]-1H-1,2,3-triazol-4-yl-kN3}pyridine-kN)]manganese(II)

For the preparation of $[Mn(L^9)_2Cl_2]$, the method used was similar to that for $[Mn(L^2)_2Cl_2]$. An amount of anhydrous $MnCl_2$ of 0.055g, 0.43mmol and 0.25g, 0.86mmol of L^9 where used, and an identical work-up procedure gave the required compound as a pale yellow solid. The isolated precipitate gave (0.24g, 0.34mmol, yield 80%), mp. 306-308°C. IR: $\bar{\upsilon}(cm^{-1})$; 3068, 3055, 3022, 1606, 1595, 1575, 1521, 1473, 1446, 1253, 1253, 1067, 1019, 1006, 861, 812, 784, 719. UV-Vis (DMSO) λ_{max}: The Mn(II) complex showed absorption bands at 258nm, $\varepsilon_{max} = 87059 dm^3mol^{-1}cm^{-1}$, 286nm, $\varepsilon_{max} = 51765 dm^3mol^{-1}cm^{-1}$, 526nm, $\varepsilon_{max} = 570 dm^3mol^{-1}cm^{-1}$, 677nm, $\varepsilon_{max} = 135 dm^3mol^{-1}cm^{-1}$. The complex with L^9 showed a value of μ_{eff} = 5.66 B.M. HRMS TOF (ESI+) with the highest molecular weight ion peak matching, was observed at *m/z* = 670.0613 (55%) and is related to $[M-Cl]^+$. The calculated value for $[C_{28}H_{18}ClF_6N_8Mn]^+$ is 670.0622. Λ_M (DMSO) = $56 \Omega^{-1}cm^2mol^{-1}$.

7.3.8.2 Synthesis and characterisation of Dichloro[bis(2-{1-[4-(trifluoromethyl)phenyl]-1H-1,2,3-triazol-4-yl-kN3}pyridine-kN)]iron(II)

For the preparation of $[Fe(L^9)_2Cl_2]$, the method used was analogue to that for $[Mn(L^2)Cl_2]$. An amount of anhydrous $FeCl_2$ 0.050g, 0.43mmol and 0.25g, 0.86mmol of L^9, and an identical work-up procedure gave the required compound as a pale yellow solid with (0.20 g, 0.28 mmol, yielded 83%), mp. 274-276 °C. IR: $\bar{\upsilon}(cm^{-1})$;3063, 3047, 3025, 1605, 1595, 1571, 1522, 1473, 1448, 1267, 1258, 1060, 1049, 1015, 1005, 886, 815, 786. UV-Vis (DMSO) λmax: The Fe (II) complex showed absorption bands at 258nm, $\varepsilon_{max} = 58947 dm^3 mol^{-1}cm^{-1}$, 288nm, $\varepsilon_{max} = 48947 dm^3mol^{-1}cm^{-1}$, 326nm, $\varepsilon_{max} = 4511 dm^3mol^{-1}cm^{-1}$, 566 nm, $\varepsilon_{max} = 461 dm^3mol^{-1}cm^{-1}$, 590nm, $\varepsilon_{max} = 453 dm^3mol^{-1}cm^{-1}$ respectively. The complex with L^9 showed a value of μeff = 4.72 B.M. HRMS TOF (MALDI) with the highest molecular weight ion peak matching, was observed at m/z = 671.1 (100%) and is attributed to $[M-Cl]^+$. The calculated value for $[C_{28}H_{18}ClF_6N_8Fe]^+$ is 671.1. ΛM (DMSO) = $48 \Omega^{-1}cm^2mol^{-1}$.

7.3.8.3 Synthesis and characterisation of Dichloro[bis(2-{1-[4-(trifluoromethyl)phenyl]-1H-1,2,3-triazol-4-yl-kN3}pyridine-kN)]cobalt(II)

For the preparation of $[Co(L^9)_2Cl_2]$, the method used was as described for $[Mn(L^2)_2Cl_2]$. An amount of $CoCl_2.6H_2O$ of 0.040g, 0.16mmol and 0.097g, 0.33mmol of L^9 where used, and an identical work-up procedure gave the required compound as a pale pink solid. The isolated precipitate gave (0.085g, 0.12mmol, yield 70%), mp. 336-338°C. IR: $\bar{\upsilon}(cm^{-1})$; 3069, 3040, 3012, 1610, 1579, 1517, 1475, 1441, 1321, 1261, 1258, 1062, 1053, 1020, 1006, 886, 818, 818, 786, 757, 720. UV-Vis (DMSO) λmax: The Co(II) complex showed absorption bands at 258nm, $\varepsilon_{max=}$ 952944$dm^3mol^{-1}cm^{-1}$, 286nm, $\varepsilon_{max=}$ 52353$dm^3mol^{-1}cm^{-1}$, 615nm, $\varepsilon_{max=}$ 84$dm^3mol^{-1}cm^{-1}$, 679nm, $\varepsilon_{max=}$ 138$dm^3mol^{-1}cm^{-1}$. The complex with L^9 showed a value of μ_{eff} = 3.62 B.M. HRMS (P+NSI) with the highest molecular weight ion peak matching, was observed at *m/z* = 674.0565 (10%) is assigned to $[M-Cl]^+$. The calculated value for $[C_{28}H_{18}ClF_6N_8Co]^+$ is 674.0574. Λ_M (DMSO) = 46$\Omega^{-1}cm^2mol^{-1}$.

7.3.8.4 Synthesis and characterisation of Dichloro[bis(2-{1-[4-(trifluoromethyl)phenyl]-1H-1,2,3-triazol-4-yl-kN3}pyridine-kN)]nickel(II)

For the preparation of $[Ni(L^9)_2Cl_2]$, the method used was as described for $[Mn(L^2)_2Cl_2]$. An amount of $NiCl_2.6H_2O$ of 0.052g, 0.21mmol and 0.12g, 0.42mmol of L^9 where used, and an identical work-up procedure gave the required compound as a pale pink solid. The isolated precipitate gave (0.11g, 0.12mmol, yield 73%), mp. 350 °C(decomp.). IR: ν (cm^{-1}); 3075, 3051, 3012, 1613, 1588, 1580, 1518, 1477, 1456, 1313, 1260, 1243, 1066, 1057, 1022, 1008, 876, 838, 806, 759, 752, 721. UV-Vis (DMSO) λ_{max}: The Ni (II) complex have shown absorption bands at 259nm, $\varepsilon_{max=}$ 41579 $dm^3mol^{-1}cm^{-1}$, 287nm, $\varepsilon_{max=}$ 40000 $dm^3mol^{-1}cm^{-1}$, 408nm, $\varepsilon_{max=}$ 13 $dm^3mol^{-1}cm^{-1}$, 686nm, $\varepsilon_{max=}$ 4 $dm^3mol^{-1}cm^{-1}$, complex with L^9 showed a value of μ_{eff} = 3.62 B.M. HRMS TOF (MALDI); the molecular ion peak observed at*m/z* = 673.1 (100%); is related for $[M-Cl]^+$, calculated value for $[C_{28}H_{18}ClF_6N_8Ni]^+$; observed 673.1. Λ_M (DMSO) = 48 $\Omega^{-1}cm^2mol^{-1}$.

7.3.8.5 Synthesis and characterisation of Dichloro[bis(2-{1-[4-(trifluoromethyl)phenyl]-1H-1,2,3-triazol-4-yl-kN3}pyridine-kN)]copper(II)

For the preparation of $[Cu(L^9)_2Cl_2]$ the method used was similar to that for $[Mn(L^2)_2Cl_2]$. An amount of anhydrous $CuCl_2$ of 0.055g, 0.40mmol and 0.23g, 0.80mmol of L^9 where used and an identical work-up procedure gave the required compound as a pale green solid. The isolated precipitate gave (0.24g, 0.33mmol, yield 82%), mp. 248-250°C. IR: $\bar{\upsilon}(cm^{-1})$; 3060, 3044, 3026, 1617, 1608, 1577, 1526, 1518, 1478, 1453, 1332, 1274, 1251, 1065, 1038, 1028, 1015, 865, 844, 782, 757, 732. UV-Vis (DMSO) λ_{max}: The Cu(II) complex showed absorption bands at 258nm, ε_{max} = $58947dm^3mol^{-1}cm^{-1}$, 287nm, ε_{max} = $47368dm^3mol^{-1}cm^{-1}$, 496nm, ε_{max} = $62dm^3mol^{-1}cm^{-1}$, 888nm, ε_{max} = $62dm^3mol^{-1}cm^{-1}$, The complex with L^9 showed a value of μ_{eff} = 1.60 B.M. HRMS (P+NSI) with the highest molecular weight ion peak matching, was observed at *m/z* = 678.0532 (100%) and is attributed to $[M-Cl]^+$. The calculated value for $[C_{28}H_{18}ClF_6N_8Cu]^+$ is 678.0538. A good single crystal for X-ray structural analysis was obtained by slow evaporation of a hot CH_3OH solution of the complex. ΛM (DMSO) = $28\Omega^{-1}cm^2mol^{-1}$.

7.3.8.6 Synthesis and characterisation of Dichloro[bis(2-{1-[4-(trifluoromethyl)phenyl]-1H-1,2,3-triazol-4-yl-kN3}pyridine-kN)]zinc(II)

For the preparation of $[Zn(L^9)_2Cl_2]$, the method used was as described for $[Mn(L^2)_2Cl_2]$. An amount of anhydrous $ZnCl_2$ of 0.040g, 0.29mmol and 0.17g, 0.58mmol of L^9 where used, and an identical work-up procedure gave the required compound as a white solid. The isolated precipitate gave (0.20g, 0.28mmol, yield 72%), mp. 280-282°C. IR: $\bar{\upsilon}(cm^{-1})$; 3131, 3067, 3026, 1615, 1597, 1571, 1514, 1472, 1447, 1323, 1296, 1274, 1065, 1038, 1028, 1015, 1251, 825, 779, 740, 717. UV-Vis (DMSO) λ_{max}: The Zn(II) complex showed absorption bands at 256nm, $\varepsilon_{max=}$ $32880dm^3mol^{-1}cm^{-1}$, 286nm, $\varepsilon_{max=}$ $31660dm^3mol^{-1}cm^{-1}$, respectively. ^{1}HNMR data δ_H/ppm (400MHZ, DMSO-d_6): 9.44 (1H, s, H_{11}), 8.67 (1H, S, H_2), 8.34-8.24 (2H, d, J_{HH} = 8.70Hz, Ar-$H_{13,17}$), 8.14-8.09 (1H, d, $^1J_{HH}$ = 7.79Hz, H_5), 8.04-7.92 (3H, m, H_4, Ar-$H_{14,16}$), 7.43-7.40 (1H, t, $^1J_{HH}$ = 5.50Hz, $^2J_{HH}$ = 7.33Hz, H_3); ^{13}CNMR (100.63MHZ, D_6MSO-d_6) δ_C/pmm: 119.90 (C_5), 120.72 (C_{13}, C_{17}-Ar), 119.69, 122.40, 125.11, 127.82 (q, J^1_{C-F} = 270.20Hz, C-F_3 (C_{18})), 121.53 (C_{11}), 123.40 (C_3), 127.13, 127.09, 127.05, 127.09 (q, J^3_{C-F} = 3.83Hz, C_{14}, C_{16}-Ar), 128.37, 128.68, 129.01, 129.33 (q, J^2_{C-F} = 32.59Hz, C-CF_3 (C_{15})), 137.26 (C_4), 139.34 (C_{12}), 148.42 (C_7), 149.17 (C_6), 149.67 (C_2). These assignments were confirmed using DEPT ^{13}C

(135°), ^{1}H-^{1}H COSY and ^{1}H-^{13}C two dimensional correlation spectroscopy. HRMS ((P+NSI) with the highest molecular weight ion peak matching, was observed at*m/z* = 716.9202 (5%) and is assigned to $[M+H]^{+}$. The calculated value for $[C_{28}H_{18}ClF_6N_8Zn]^{+}$ is 716.0333. ΛM (DMSO) = 12$\Omega^{-1}cm^2mol^{-1}$.

7.3.8.7 Synthesis and characterisation of Dichloro[bis(2-{1-[4-(trifluoromethyl)phenyl]-1H-1,2,3-triazol-4-yl-kN3}pyridine-iN)]cadmium(II)

For the preparation of $[Cd(L^9)_2Cl_2]$, the method used was similar to that for $[Mn(L^2)_2Cl_2]$. An amount of anhydrous $CdCl_2$ of 0.045g, 0.24mmol and 0.14g, 0.49mmol of L^9, and an identical work-up procedure gave the required compound as a white solid. The isolated precipitate gave (0.13 g, 0.17 mmol, yield 68%), mp. 344-346°C. IR: $\bar{\upsilon}$(cm^{-1}); 3107, 3063, 1618, 1601, 1597, 1523, 1471, 1450, 1331, 1285, 1266, 1251, 1066, 1034, 1017, 845, 724, 704, 694. UV-Vis (DMSO) λ_{max}: The Cd(II) complex showed absorption bands at 258nm, $\varepsilon_{max=}$ 27850$dm^3mol^{-1}cm^{-1}$, 288nm, $\varepsilon_{max=}$ 26733$dm^3mol^{-1}cm^{-1}$, respectively. ^{1}HNMR data δ_H/ppm (400MHZ, DMSO-d_6): 9.52 (1H, s, H_{11}), 8.69-8.67 (1H, td, $^{1}J_{HH}$ = 0.95Hz, $^{2}J_{HH}$ = 1.83Hz, $^{3}J_{HH}$ = 4.58Hz, H_2), 8.31-8.29 (2H, d, J_{HH} = 8,70Hz, Ar-$H_{13,17}$), 8.15-8.12 (1H, dt, $^{1}J_{HH}$ = 0.95Hz, $^{2}J_{HH}$ = 1.37Hz, $^{3}J_{HH}$ = 7.79Hz, H_5), 8.02-8.00 (2H, d, J_{HH} = 8,70Hz, Ar-$H_{14,16}$), 7.99-7.95 (1H, dt,$^{1}J_{HH}$ = 1.83Hz, $^{2}J_{HH}$ = 7.79Hz, H_4), 7.45-7.41 (1H, ddd, $^{1}J_{HH}$ = 1.37Hz, $^{2}J_{HH}$ = 5.04Hz, $^{3}J_{HH}$ = 7.33Hz, H_3); ^{13}CNMR (100.63MHZ, D_6MSO-d_6) δ_C/pmm: 119.97 (C_5), 120.71 (C_{13}, C_{17}-Ar), 119.81, 122.47, 125.17, 127.88 (q, J^{1}_{C-F} = 270.20Hz, C-F_3 (C_{18})), 121.64 (C_{11}), 123.59 (C_3), 127.11, 127.14, 127.18, 127.21 (q, J^{3}_{C-F} = 3.83Hz, C_{14}, C_{16}-Ar), 129.32, 129.00, 128.66, 128.36 (q, J^{2}_{C-F} = 32.59Hz, C-CF_3 (C_{15})), 137.51 (C_4), 139.33 (C_{12}), 148.36 (C_7), 149.08 (C_6), 149.73 (C_2). These assignments were confirmed using DEPT ^{13}C (135°), ^{1}H-^{1}H COSY and ^{1}H-^{13}C HMQC two dimensional correlation spectroscopy. HRMS (P+NSI) with the highest molecular weight ion peak matching, was observed at *m/z* = 729.0279 (45%) and is attributed to $[M-Cl]^{+}$. The calculated value for $[C_{28}H_{18}ClN_8F_6Cd]^{+}$ is 729.0275. Λ_M (DMSO) = 20$\Omega^{-1}cm^2mol^{-1}$.

7.4 Conclusion

In conclusion, new metal complexes with di (*trans* or *cis*) chloro as coligands, having the general formula $[M(L^n)_2(Cl)_2]$ (where; M= Mn(II), Fe(II), Co(II), Ni(II), Cu(II), Zn(II) and CdII), and L^n = [bis-(PYTA)-1*H*-1,2,3-triazol-4-yl)pyridine] (where; L^n : n = 2 = CH_3, 3 = OCH_3, 4 = COOH, 5 = F, 6 = Cl, 7 = CN, 8= H, 9 = CF_3) have been successfully prepared and characterised by FT-IR, UV-Vis and fluorescence spectra,HRMS TOF (MALDI), NMR, magnetic moment measurements, conductivity and X-ray crystallography. The structural analysis indicates that the complexes of the type $[M(L^3)_2(Cl)_2]$ are a rare example of the coexistence of two *trans* coordinated Cl anions in the axial position or *cis* position in the mononuclear triazole-based octahedral configuration. This is an interesting finding, which deserves further investigation.

In summary, eight bidentate 2-pyridyl-1,2,3-triazole ligands bearing a 4-substituted phenyl group and their corresponding metal complexes were designed and synthesised through a convenient click chemistry strategy. In this study, it was demonstrated that the direct connection at the N8 position of the triazolyl ring of a 4-substituted phenyl group has a significant influence on the geometry of both the ligands and their corresponding M-complexes. The co-planarity of the organic framework led to slip-stacked π–π interactions between two molecules of the complex. Additionally, it was shown that the nature of the pendant group (X = CH_3, OCH_3, COOH, F, Cl, CN, H, CF_3) could affect the electronic properties of the M(II)-complexes. The methoxy- or phenyl moieties do not modify the photophysical properties of the complexes, but the presence of a cyanophenyl group (electron withdrawing groups) quenched the luminescence due to a high probability of non-radiative deactivation.

These first results were considered particularly significant, as they open up new prospects for the modulation of the photophysical properties of PYTA derivatives directly connected to a π-conjugated system. Further studies were conducted concerning the extension of the π-backbone of the PYTA core with other substituted aromatic or heteroaromatic moieties, as well as the study of the relationship between the natures of the π-conjugated arm *vs*. the electronic properties of the M-complexes. These complexes displayed weak fluorescence intensity with low quantum yield. In

this work, it has been establish that the PYTY ligand L^3 was found to bind the Fe(II), Co(II) and Ni(II) in a similar manner. The metal-Ntriazole bond was slightly shorter than metal-N pyridine bond. The pyridine and triazole rings occupied the equatorial plane, whereas the metal-Cl atoms were in the axial plane. Only in the Mn(II) and Cd(II) complexes, was it found that the metal-Cl atoms lie in the equatorial plane. All these complexes have a distorted octahedral geometry. Structural characterisation of all of the complexes showed that the bis-chelating ligands are in the equatorial plane of the octahedron, and the triazole and pyridine nitrogens from each of the ligands are *trans* to each other. Weak intermolecular interactions via C–H–Cl, C–H...N and C–H...O are observed in the solid state. This result in an ordered three-dimensional supramolecular structure in which the molecules adopted a head-to-tail orientation that are stabilised by hydrogen bonding and π…π stacking. The Cu(II) and Cd(II) complexes displayed one-dimensional infinite polymeric chain structures of the $[M(L^3)Cl_2]_n$ complexes, as well as stabilisation of these by hydrogen bonding and π…π stacking. These crystals were obtained from recrystallised complexes having an initial molar ratio of [M:L 1:2]. This metal – ligand stoichiometry gave these structures a molar ratio of [M:L 1:1] in the polymeric chains. In the case of Cu(II) with different ligands L^2, L^6 L^7, L^8 and L^9, the molecular structure of these complexes showed a distorted Jahn-Teller octahedral coordination arrangement. This can be deduced from the fact that the metal-N triazole bonds are longer in the vertical equatorial plane than the metal-N_{PY} bonds that formed in the equatorial plane. It was also observed that the coordinated Cl^- ions occupied positions in the axial plane. The most significant finding in the Cu(II) complexes was that the bond lengths of the C=C in the triazole ring and the N=N inside the 1,2,3-triazole ring for each complex are changeable depending on the presence of electron donating or electron withdrawing substituents on the phenyl group. Interestingly, such a substituent on the phenyl ring attached to a PYTY ligand does not affect the geometry of the structures around the Cu(II) metal atom, as can be seen from the data in Table 7.22. Figure 7.38 displayed a linear correlation between the bond lengthsC_7-C_{11} of the triazole carbons against the Hammett σ_p substituent constant of Cu(II) complexes with L^2, L^8 and L^9 ligands.

7.5 References

1-Byrne J. P. Kitchen J.A. Kotova O, Leigh, V, Bell A. P, Boland J.J, Albrechtb., Gunnlaugsson Th., *Dalton Trans*., 43:196(2014)

2-Crowley J D., Bandeen P H., Hanton L R., *Polyhedron*., 29:70(2010)

3-Jiang L., Wang Zh., Bai Sh Q., AndyHor T S., *Dalton Trans*., 42:9437(2013)

4-Vellas S K., Lewis J E M., Shankar M., Sagatova A., Tyndall J D A., Monk B. C., Fitchett Ch M., Hanton L R., Crowley J D., *Molecules*., 18:6383(2013)

5-Abu-Oraabi S T., Al-Hamdany R., Atfah A., Ali S A A., Abu-Shandi., *Asian. J. Chem*., 11:774(1999)

6-Pachhunga K., Bruno Th., Kollipara M R., *Inorg. Chim. Acta*., 361:3294(2008)

7-Bortoluzzi M., Scrivanti A., Reolon A., Amadio E., Bertolasi V., *Inorg. Chem. Commun.*, 33:82(2013)

8-Cao Z P., Quan B., Dong H Sh., *J. Chinese Chem. Soc*., 55:761(2008)

9-Geary W J., *Coord. Chem. Rev*., 7:81(1971)

10-Sulikowska C D., Czylkowska A., Doczekalska R., *J. Therm. Anal. Cal*., 71:395(2003)

11-Sulikowska C D., Czylkowska A., *J. Therm. Anal., Cal*., 76: 543(2004)

12-Calvert J G., Pitts J N Jr., *Photochemistry*, John Wiley and Sons, Inc (1996)

13-Bradley D D C, *Synth. Met*., 54:401(1993)

14-Zhang, J Z., Cao, W R., Pan, J X., Chen, Q W., *Inorg. Chem. Commun*., 10: 1360(2007)

15-Reguera E., Marin E., Calderon A., Hernandez R., *J. Spectrochim. Acta*. *Part A*., 68:191(2007)

16-Wang X W., Zhang Y H., *Inorg. Chem. Comm*., 11:832(2008)

17-Bagihalli G B., Avaji P G., Patil S A., Badami., P S., *Eur. J. Med. Chem*., 43:2639(2008)

18-Basak S., Soma S., Banerjee S., Samira M., Rosair G., Rodriguez M T G., *Polyhedron*., 26:5104(2007)

19-Schweinfurth D., Su C Y., Wei S C., Braunsteind P., Sarkar B., *Dalton Trans*., 41:12984(2012)

20-Abramovitch R A., Kyba E P., Scriven E F., *J. Org. Chem*., 36:3796(1971)

21-Urankar D., Romero T., Orenes R., Espinosa A., Tarraga A., Molina P., *Inorg. Chem*., 50:8214(2011)

22-Printer B., Pevec A., De Proft F D., Urankar D., Turel I., Košmrlj j G., *Inorg. Chem*., 49:4820(2011)

23-Pavia D L. Lampman G M., Kriz G S., Introduction to Spectroscopy, Third Edition, ISBN: 0-03-031961-7(2001)

24-Silverstein R M., Webster F X., D Kiemle., D J. Kiemle., Spectrometric Identification of Organic Compounds, 7th edition, Publisher: John Wiley and Sons Inc, Publication (2005)

25-Hansch. C, Leo, A., Taft, R W., *Chem. Rev*., 97:165(1991)

26-Palatinus L., Chapuis G., *J. Appl. Cryst*., 40:786(2007)

27-Rigaku Corporatiom, CrystalClear-SM Expert 2.0 r13, (2011)

28-Dolomanov O V., Bourhis L J., Gildea R J., Howard J A K., Puschmann H., *J. Appl. Cryst*., 42:339(2009)

29-Sheldrick G.M., *Acta Cryst. Sect. A*., 64:112(2008)

30-Macrae, C F., Bruno I J., Chisholm J A., Edgington P R., McCabe P., Pidcock E., Rodriguez-Monge L., Taylor R., van de Streek J., Wood P A., *J. Appl. Cryst*., 41:466(2008)

31-Dogan A., Sarkar B., Klein A., Lissner F., Schleid T., Fiedler J., Zalis S., Jain V K., Kaim W., *Inorg. Chem*., 43:5973(2004)

32-Kilpin K.J., Crowley J.D., *Polyhedron*., 29:3111(2010)

33-Obata M., Kitamura A., Mori A., Kameyama C., Czaplewska J.A., Tanaka R., Kinoshita I., Kusumoto T., Hashimoto H., Harada M., Mikata Y., Funabiki T., Yano S., *Dalton Trans*., 3292(2008).

34-Das S., Panda B K., *Polyhedron*., 25:2289(2006)

35-Schweinfurth D., Pattacini R., Strobel S., Sarkar B., *Dalton Trans*., 9291(2009)

36-Schweinfurth D., Strobel S., Sarkar B., *Inorg. Chim. Acta*, 374:253(2011)

37-Crowley J D., Bandeen P H., *Dalton Trans*., 39:612(2010)

38-Steiner. T., *Angew. Chem. Int. Ed*., 41:48(2002)

39-Jeffrey G A., *An Introduction to Hydrogen Bonding*, Oxford University Press, Oxford(1997)

40-Aakeroy C B., Evans T A., Seddon K R. Palinko I., *New J. Chem*., 23: 145(1999)

41-Flood A H., Hua Y., *Chem. Soc. Rev*.,39:1262(2010)

42-Mazik M. BlaserD., Boese R., *Tetrahedron Lett*., 41:5827(2000)

43-Mazik M. BlaserD., Boese R., *Tetrahedron.*, 57:5791(2001)

44-Yang Y., Du P., Yang J., Kan W Q., Ma J F., *Cryst. Eng. Commun*. 15: 4357(2013)

45-Janiak C., *J. Chem. Soc. Dalton Trans*., 3885(2000)

46-Košmrlj J G., Urankar D., Pevec A., Turel I., *Cryst. Growth Des*. 10:4920(2010)

47-Bratsos I., Urankar D., Zangrando E., Kalou P., Kosmrlj G., Alessio J E., Turel I., *Dalton Trans*., 40:5188(2011)

48-Dey R., Ghoshal D., *Polyhedron*., 34:24(2012)

49-Hubin T J., McCormick J M., Collinson S R., Buchalova M., Perkins C M., Alcock N W., Kahol P K. Raghunathan A., Busch D H., *J. Am. Chem. Soc*., 122:2512(2000)

50- Li Y, Zou W Q, Wu M F, Lin J.D, Zheng F K, Liu Z F, Wang S H, Guoa G C., Huanga J S., *Cryst. Eng. Comm*., 13:3868(2011)

51-Hao E, Wang Z, Jiao L., Wang S., *Dalton Trans*., 39:2660(2010)

52-Hou H., Meng X., Song Y., Fan Y., Zhu Y., Lu H., Du C., Shao W., *Inorg. Chem*., 41:4068(2002).

53-Brammer L., Bruton E.A., Sherwood P., *Cryst. Growth Des*., 1:277(2001)

54-Kovács A., Varga Z., *Coord. Chem. Rev*., 250:710(2006)

55-McCann S., McCann M., Casey R., Jackman M T M., Devereux M., McKee V., *Inorg. Chim. Acta*., 279:24(1998)

56-Addison A W., Rao T N., Reedijk J., Rijn J.V., Verschoor G C., *J. Chem. Soc. Dalton Trans*., 1349(1984).

57-Guha P.M., Phan H., Kinyon S J., Brotherton T S., Sreenath K., Simmons J T., Wang Z., Clark R J., Dalal S N., Shartruk M., Zhu L., *Inorg. Chem*., 51:3465(2012)

58-Brotherton W S., Guha P M., Phan H., Clark R J., Shatruk M., Zhu L., *Dalton Trans*., 40:3655(2011)

59-Hua Y., Flood A H., *Chem. Soc. Rev*., 39:1262(2010)

60-Li Y., Flood A.H., *J. Am. Chem. Soc*., 130:12111(2008)

61-Kathalikkattil A C., Bisht K K., Subramanian P S., Eringathodi S., *Polyhedron*, 29:1801(2010)

62-Li L., Li W., Yang S., Wei L., Wang C., Hou H., *J. Coord. Chem*., 66:2948(2013)

63-Wang J., Huang M H., Liu P., Cheng W., *J. Mol. Struct*., 875: 22(2008)

64-Medrano J P., Jancik V., Pablo E B., Otero D M., Lezama M R., Juárez T J M., *Inorg. Chim. Acta*., DOI:http://dx.doi.org/10.1016/j.ica.2013.11.039.

65-Zhai Q G., Shu N., Li X G., Jiang Y C., Hu, M C., *Cryst. Eng. Comm*., 13: 1602(2011)

66-Li H., Liu G., Liu T T., Zhang H Y., Yue F., Wang J D., *Russ. J. Coord. Chem*., 3 7:8(2011)

67-Orpen A G., Brammer L., Allen F H., Kennard O., Watson D G., Taylor R., *J. Chem. Soc. Dalton Trans*., S1–S83(1989)

68-Al-Sudani A R H., Kariuki B M., *Acta Cryst. Sect*. E69, m491– (2013)

69-Fu Y., Li H., Chen X., Qin J., *Inorg. Chem. Comm*.14:268(2011)

70-Fu Y., Liu Y., Fu X., Zou L., Li H., Li M., Chen X G., Qin J G., *J. Inorg. Chin. Chem*., 28:2226(2010)

71-Fu Y., Liu Y., Zhong C., Li H., Chen X.G., Qin, J G., *Chin. J. Inorg. Chem*., 26:1133(2010)

72- Schibli R., Struthers H., Mindt T.L., *Dalton Trans*., 39:675(2010)

73- Gautier A., Maisonial A., Serafin P., Traïkia M., Debiton E., Théry V., Aitken D.J., Lemoine P., Viossat B., *Eur. J. Inorg. Chem*., 298: (2008)

74-Corey E.J., Lee T.W., *Chem. Comm*., 1321:(2001)

75-Steiner T., *Chem. Comm*., 727:(1997)

76-Marcon P., Ostanina K., *PIERS*., 27-30, 420:2012

77-Demas J N., Grosby G A., *J. Phys. Chem*., 75:991(1971)

78-Heller C A., Henry R A., McLaughlin B A., Bliss B E., *J. Chem. Eng. Data*., 19:214(1974)

79-Das D., Chand B G., Sarker K K., Dinda J., Sinha C., *Polyhedron*., 25: 2333(2006)

80-Williams A T R., Winfield S.A., Miller J N., Analyst, 108:1067(1983)

81- Handbook of Chemistry and Physics, 65th Edition. Weast R. C., Ed; CRC: Boca Raton, Florida, USA(1985)

Chapter 8 : THE SYNTHESIS AND SUBSTITUTION REACTIONS OF NOVEL ISOTHIOCYANATE COMPLEXES OF 2-[1-(4-METHOXY-PHENYL)-1*H*-1,2,3-TRIAZOL-4-YL]-PYRIDINE LIGAND

8.1 Introduction

Since ruthenium complexes containing isothiocyanate ligands such as N719 (*Cis*-bis(isothiocyanato)-bis(2,2′-bipyridyl-4,4′-dicarboxylic acid)ruthenium(II)) [1], and the black dye BD (tri(isothiocyanato)(2,2′;6′,2″-terpyridyl-4,4′,4″ tricarboxylic acid) ruthenium(II) **[2]** are the best wideband synthesised solar dyes identified to date (higher power conversion), it is reasoned that it would be interesting to synthesise some metal isothiocyanate complexes by exchange of the chloro ligand (L^3 ligand) with an isothiocyanato. These metal isothiocyanate complexes would be tested to see if there is improved photosensitiser properties. The aim was also to replace the ruthenium dyes with alternative low-cost metal complexes.

A range of novel complexes of [(bis-isothiocyanato)-bis-2-(1-(4-methoxy-phenyl)-*1H*-1,2,3-triazol-4-yl)pyridine]metal(II), were successfully prepared based on the replacement of the chloro groups of $[M(L^3)_2(Cl)_2]$ complexes which were prepared in (Chapter 7), with isothiocyanate ligands $[M(L^3)_2(NCS)_2]$. The effect of the isothiocyanate group was investigated on the photophysical properties of the complexes, in particular absorbance, the molecular geometries and fluorescence behaviour. The complexes were prepared in good yields of between 72-84 %, (see experimental section additional details section 8.3, Table 8.10), from the reaction of one equivalent of the metal complex, $[M(L^3)_2(Cl)_2]$, dissolved in DMSO, with an excess potassium isothiocyanate (KNCS) dissolved in CH_3OH, as shown in Scheme 8.1. The complexes prepared were characterised by FT-IR, magnetic moments, conductivity measurements, melting points, mass spectra, NMR spectroscopy and X-ray crystallography in addition to their spectroscopic properties.

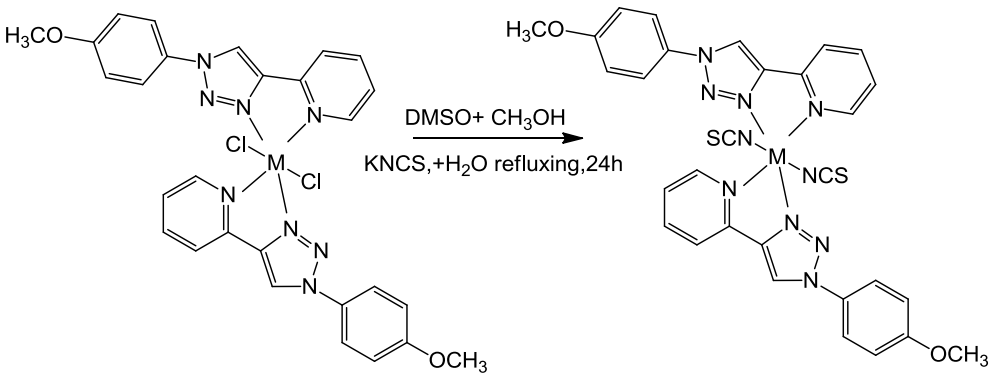

Scheme 8.1: Synthesis route of metal isothiocyanate complexes by coligand exchange in DMSO.

8.2 Results and Discussion

8.2.1 FT-IR spectral data for the complexes $[Fe(L^3)_2(NCS)_2]$, $[Co(L^3)_2(NCS)_2]$, $[Zn(L^3)_2(NCS)_2]$ and $[Cd(L^3)_2(NCS)_2]$

An overlay for the IR spectra of various L^3 metal complexes with isothiocyanate as coligands is presented in Figure 8.1. The plot aims to show differences between the spectra with regard to the shifts of functional groups on complex formation.

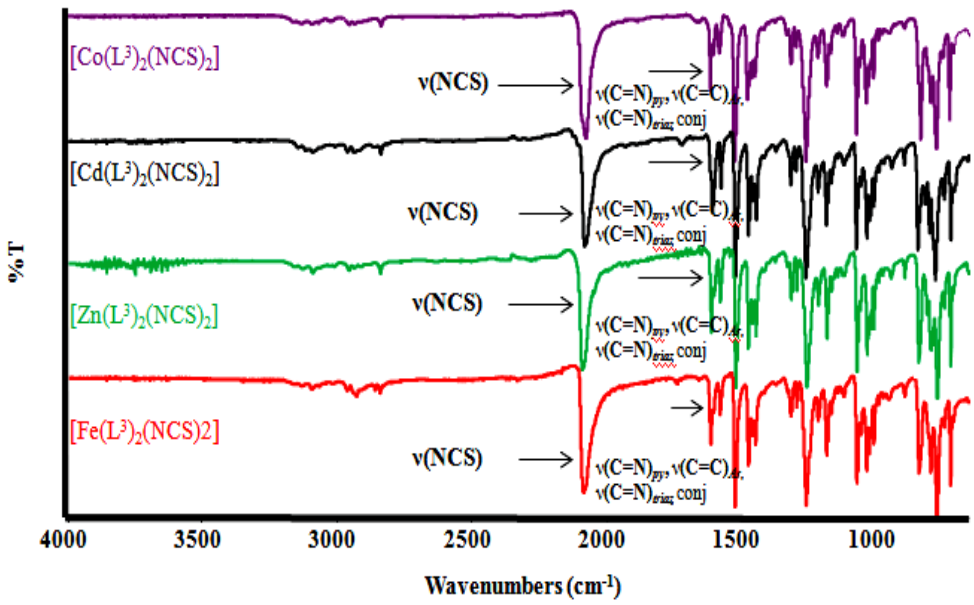

Figure 8.1: FT-IR spectra of the various metal complexes showing characteristic bands of NCS^-, $C{=}N_{py}$ and $C{=}C_{Ar}$ for $[Fe(L^3)_2(NCS)_2]$, $[Co(L^3)_2(NCS)_2]$, $[Zn(L^3)_2(NCS)_2]$ and $[Cd(L^3)_2(NCS)_2]$.

The IR spectra of the title complexes display mainly bands due to the C≡N streeting vibrations for the *trans*–coordinated NCS^-groups at ῡ2073-2087cm^{-1}. This was observed for all complexes indicating that the two *trans*-(NCS^-) anions are bound to the centre metal atom [3, 4], as shown in Scheme 8.1. The peak observed for the C≡N stretching band occurs at higher frequency than a typical C≡N stretching band, which indicates that the N atom is bound to the metal atom in the complex (near and below 2100cm^{-1}) [5, 6]. This is supported by the X-ray structure (Figure 8.27 and 8.33). The ν(C=N) stretching band of the pyridine moiety is observed around 1601-1609 cm^{-1} for the complexes, which is consistent with coordination of the nitrogen atom of the pyridine moiety with the metal atom. The ν(C=C) bands of the phenyl ring of the complexes usually appear as two absorption peaks at around 1597- 1595cm^{-1} and 1516 -1517cm^{-1}. The ν(C=N) absorption band of the triazole moiety is at around 1574 - 1571cm^{-1} in the metal complexes.

Table 8.1: IR frequencies (cm^{-1}) of the bis-isothiocyanato coligands in the (L^3) complexes.

Compound	**ν(N=C=S)**	**ν(C=N)*py*, ν(C=C)*Ar*,ν(C=N)*triaz* conj.**	**ν(N-N)*triaz***	**ν(C=C)*Ar***
[Fe(L^3)$_2$(NCS$_2$)]	2076	1606, 1597, 1574	1176,1064	1517
[Co(L^3)$_2$(NCS)$_2$]	2073	1609, 1597, 1575	1176,1065	1516
[Zn(L^3)$_2$(NCS)$_2$]	2087	1607, 1597, 1575	1179,1065	1517
[Cd(L^3)$_2$(NCS)$_2$]	2076	1601, 1571	1179,1088	1517

8.2.2 Magnetic moments, electronic spectra, and conductivity measurements for the complexes $[Fe(L^3)_2(NCS)_2]$, $[Co(L^3)_2(NCS)_2]$, $[Zn(L^3)_2(NCS)_2]$ and $[Cd(L^3)_2(NCS)_2]$

8.2.2.1 UV-Vis Spectral data for bis-isothiocyanato of L^3 metals complexes

The UV-Vis spectral data of the $[M(L^n)_2(NCS)_2]$ complexes (M= Fe(II), Co(II), Zn(II) and Cd(II)) were recorded over a wide range of concentrations of 10^{-3} M to 10^{-6} M in DMSO at room temperature (294K) using wavelength scan of 245nm to 950nm to facilitate the observation of low intensity forbidden d-d transitions. The UV-Vis spectra of the complexes are depicted in Figures 11.14 -11.17. (See Physical Appendix Chapter 11) and the data summarised in Table 8.2.

8.2.2.2 Magnetic moments and the conductivity measurements

The magnetic moments and the conductivity measurements for these metal complexes have shown similar behaviour to the complexes of the chlorido ions that are described in chapter 7 (see chapter 7 Table 7.3 and sections 7.2.5 and 7.2.6). The data is summarised in Table 8.2.

Table 8.2: UV-Vis spectral data of L^3 complexes in DMSO solutions.

Compound	Band Position λ_{max} (nm)	Band Position λ_{max} (cm^{-1})	Extinction coefficient ε_{max} ($dm^3mol^{-1}\ cm^{-1}$)	Assignment	$\mu_{effB.M}$	Conductivity Λ_M ($\Omega^{-1}\ cm^2mol^{-1}$)
$[Fe(L^3)_2(NCS)_2]$	258, 286	38760, 34965	63333, 78666 ($1.5x10^{-6}$M)	Intra – ligand, $\pi\rightarrow\pi^*$, $n\rightarrow\pi^*$	5.36	48
	351	30030	664 ($1x10^{-4}$M)	CT		
$[Co(L^3)_2(NCS)_2]$	258, 288	38760, 34246	61250, 40000 ($2.4x10^{-6}$M)	Intra – ligand, $\pi\rightarrow\pi^*$, $n\rightarrow\pi^*$	4.56	37
	538	18587	14 ($1x10^{-4}$M)	$^4T_1g\ ^{(F)} \rightarrow {}^4T_1g\ ^{(P)}$		
$[Zn(L^3)_2(NCS)_2]$	257, 288	38910,34722	57500, 38750 ($2.4x10^{-6}$M)	Intra – ligand, $\pi\rightarrow\pi^*$, $n\rightarrow\pi^*$	diamagnetic	12
$[Cd\ (L^3)_2(NCS)_2]$	257, 288	38910, 34722	48519, 36296 ($2.7x10^{-6}$M)	Intra – ligand, $\pi\rightarrow\pi^*$, $n\rightarrow\pi^*$	diamagnetic	18

8.2.3 Fluorescence emission spectral data for the complexes [Fe(L^3)2($NCS)_2$], [Co(L^3)$_2$($NCS)_2$], [Zn(L^3)$_2$($NCS)_2$] and [Cd(L^3)$_2$($NCS)_2$]

The fluorescence spectra of the triazole-based ligands and its various metal M(II) complexes with isothiocyanate NCS^- coligands, with [M = Fe(II), Co(II), Zn(II), Cd(II)], were investigated in DMSO at room temperature (294K), The fluorescence and quantum yield were determined by comparison with 1,1':4'1"-p-terphenyl; (PTP) dye as a reference. The complexes and the reference dye were both excited at 276nm, whilst maintaining a nearly equal absorbance (0.095). The emission spectra were recorded from 285 to 550nm. All experiments were carried out at absorbance values below (0.1).

The fluorescence emission spectra of the complexes with the general formula [M(L^3)$_2$($NCS)_2$], where M = Fe(II), Co(II), Zn(II) and, Cd(II), are depicted in Figure 8.2. The complexes showed weak fluorescence and low quantum yields relative to the standard PTP and the corresponding chloride complexes. The emission spectra of the complexes were characterised by their photoluminescence spectra, which were found to be red shifted from 345-346nm to 379-435nm in the isothiocyanate complexes. This indicates that the emission spectra may possibly originate from ligand-to-metal charge transfer (LMCT) [7, 8], which is distinctly different from those of the chloride complexes **[**M(L^3)$_2$$Cl_2$], as can be seen in Figures 8.2 and 8.3. The intensity, emission peaks, Stokes shifts and quantum yields for the various complexes are summarised in Table 8.3. These peaks originate from LLCT (ligand-to-ligand charge transfer) and LMCT (ligand-to-metal charge transfer) [9-11].

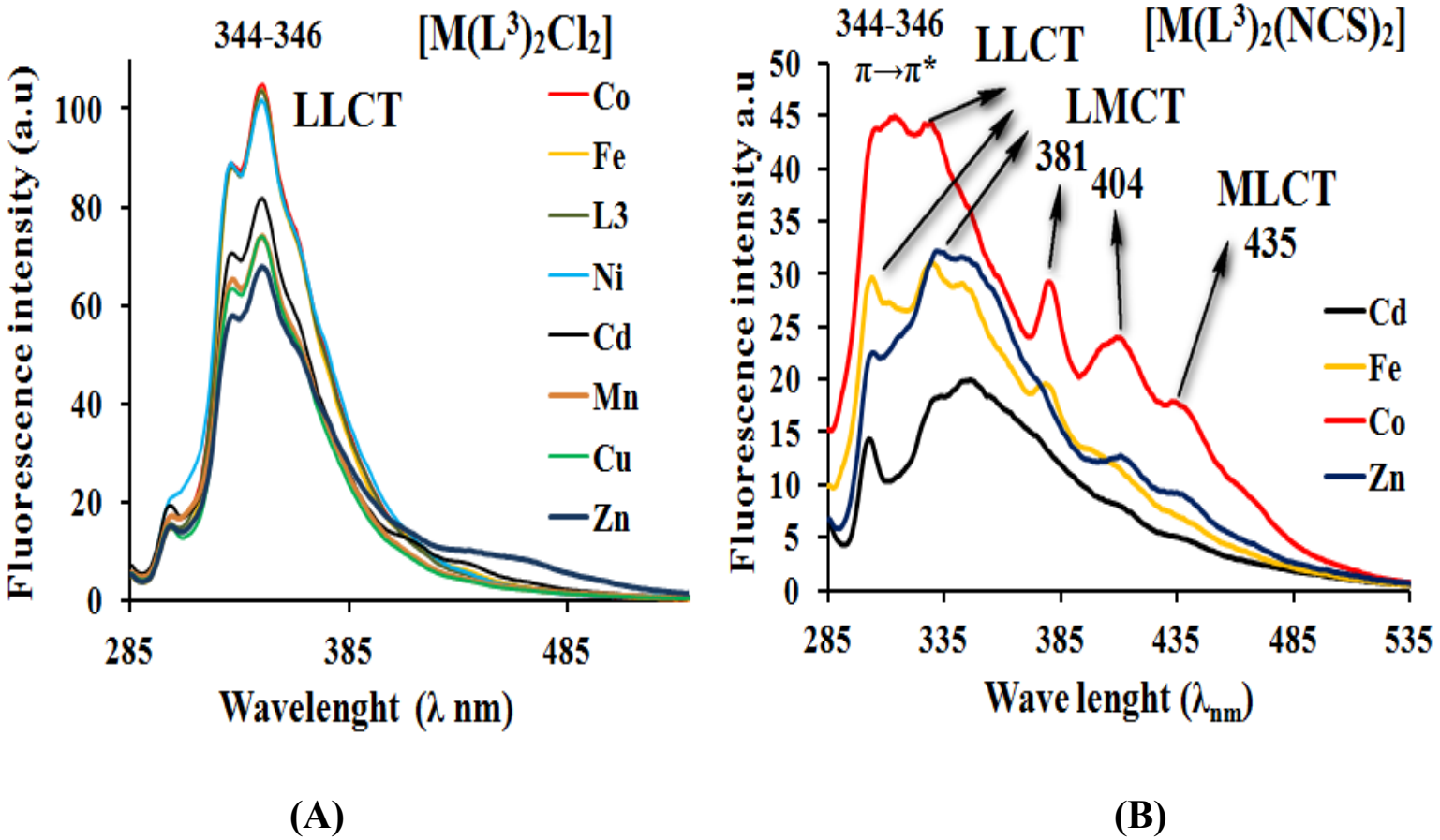

Figure 8.2: Fluorescence spectra of chloro metal complexes (A): $[M(L^3)_2Cl_2]$ and the corresponding isothiocyanate complexes (B): $[M(L^3)_2(NCS)_2]$.

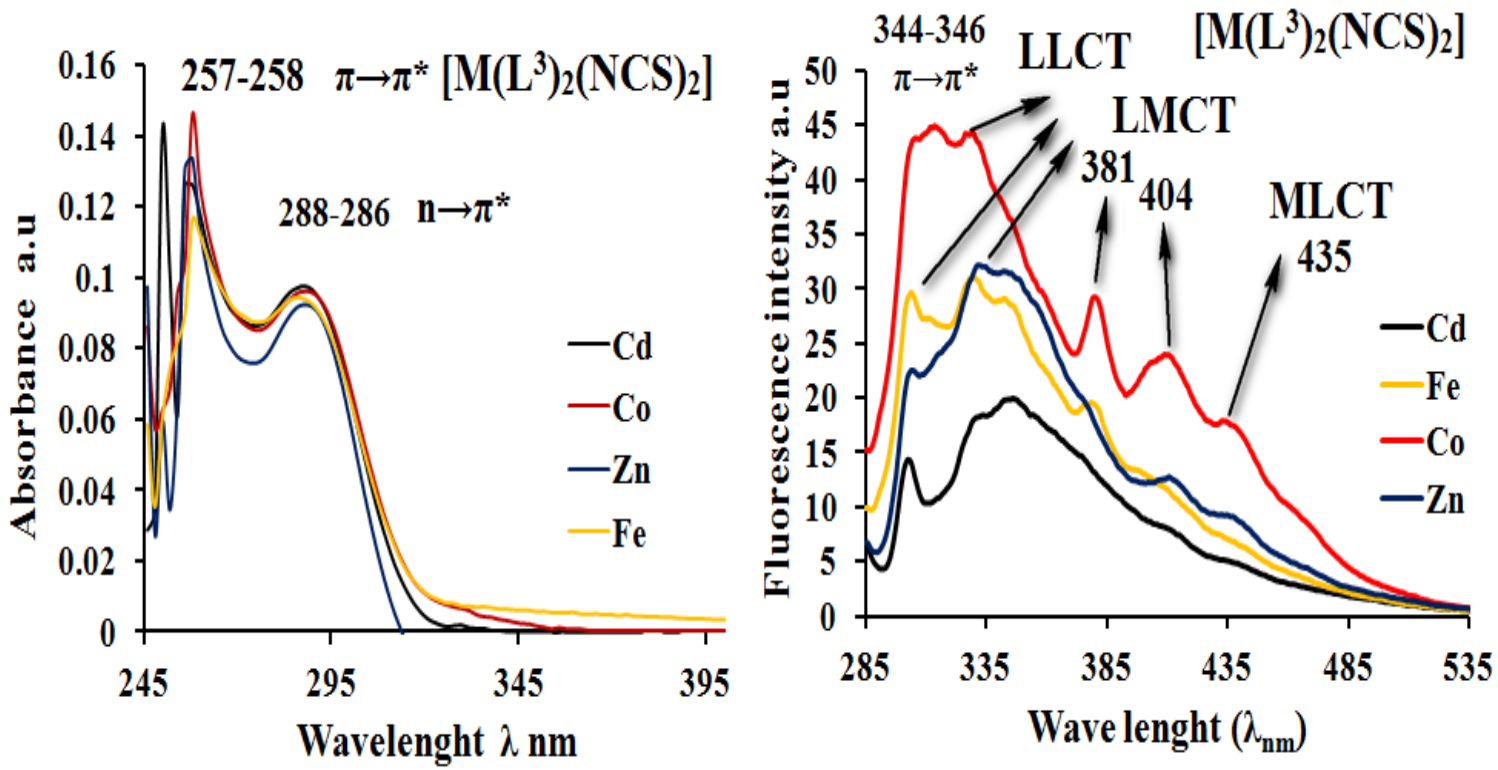

Figure 8.3: UV-Vis and Fluorescence intensity, for various metal complexes samples with isothiocyanate ($^{-}$NCS) coligands.

The introduction of the isothiocyanate group into the chlorido complex had little effect on the UV spectra but red shifted and broadened the fluorescence spectra (see Figure 8.2). In Figure 8.2B showing the fluorescence spectra of the isothiocyanate complexes, the scale was expanded (2.4 x) compared to that used for Figure 8.2A in order to illustrate the reduced fluorescence and quantum yield (Φf) of these complexes (see Table 8.3). The reduced fluorescence of the isothiocyanate complexes suggests inefficient ligand-to-metal charge transfer (LMCT) which may be a result of the structure of the complex.

Table 8.3: Photoluminescence spectra of the various complexes in DMSO (10^{-6} M); samples were excited at λ_{max} (ex) = 276 nm.

Compound	Intensity	Emissions (λ_{em}) nm, c=1 x 10^{-6} M	Stokes shift ($\Delta\lambda$)nm	Quantum yield (Φf)
PTP	2720	332	56	1.0
	2218	345	69	
$[Co(L^3)_2(NCS)_2]$	46	329	55	
	32	381	105	
	24	404	128	
	16	435	154	0.04
$[Fe(L^3)_2(NCS)_2]$	30	304	28	
	31	330	54	
	29	343	67	
	20	379	103	
	13	398	122	
	7	439	163	0.026
$[Zn(L^3)_2(NCS)_2]$	32	332	56	
	33	345	69	
	13	412	136	
	9	436	160	0.027
$[Cd(L^3)_2(NCS)_2]$	20	347	71	
	8	410	134	
	5	435	159	0.016

Quantum yields were calculated using the same method described in chapter (6):

$\Phi_{(Co)} = \Phi_{(PTP)}$ x (Area $_{(Co)}$ / (Area $_{(PTP)}$) x (ABS $_{(PTP)}$) / (ABS $_{(Co)}$) x ($\eta^2_{(DMSO)}$ / $\eta^2_{(DMSO)}$)

$$(\Phi f)Co = 1.0 \times \frac{5039.609}{121143.058} \times \frac{0.0954}{0.0960} \times \frac{1.4770}{1.4770}$$

(Φf)Co= 0.0416 x 0.994 = 0.04 %

8.2.4 Mass spectra for the complexes $[Fe(L^3)_2(NCS)_2]$, $[Co(L^3)_2(NCS)_2]$, $[Zn(L^3)_2(NCS)_2]$ and $[Cd(L^3)_2(NCS)_2]$

Positive ion TOF-MOLDI-MS was the most satisfactory technique used for the analysis and measurement of these poorly soluble, high MW metal complexes. However, the molecular ion peak $[M(L^3)_2(NCS)_2]^+$, corresponding to the molecular weight of the metal complexes, was not observed due to the poor stability of the complex. Only a secondary fragment ion was observed after the loss of one or more of the NCS^-anions, the ligand or the metal atom when using this technique (Figure 8.4). The high resolution mass spectra (HRMS) therefore was undertaken on the highest MW secondary fragment ion peak $[M(L^3)_2NCS]^+$, as can be seen in Figure 8.5 produced after the loss of anisothiocyanate NCS^- anion from the molecular ion via pathway (A) (see Scheme 8.2), as reported in literature [3, 12]. The second significant fragment ion peak $[M(L^3)_2]^+$ was formed with the loss of a $(NCS^-)_2$group from the molecular ion via pathway (B) in Scheme 8.2. Table 8.4 show the molecular weight and relative abundances of each species identified for the four metal complexes.

$$[M(L^3)_2(NCS)]^+ \xleftarrow[A]{(^-NCS)-} [M(L^3)_2(NCS)_2]^+ \xrightarrow[B]{-(^-NCS)_2} [M(L^3)_2]^+$$

Scheme 8.2: The major fragments observed in mass spectra for metal complexes of general formula $[M(L^3)_2(NCS)_2]$.

Table 8.4: MS (TOF-MOLDI-MS) species observed for complexes.

Compound	$[M-(NCS)]^+$	$[M-(NCS)_2]^+$	Other fragments
$[Fe(L^3)_2(NCS)_2]$	618.1 (100) %	560.1(3%)	
$[Co(L^3)_2(NCS)_2]$	621.0 (100) %	563.1(15%)	
$[Zn(L^3)_2(NCS)_2]$	626.0 (100) %		
$[Cd(L^3)_2(NCS)_2]$	676.1 (100) %	618.1(40%) 501.2(30%) 422(15%)	$[M(L^3)_2Py(NCS)]^+$ $[M(L^3)(NCS)]^+$

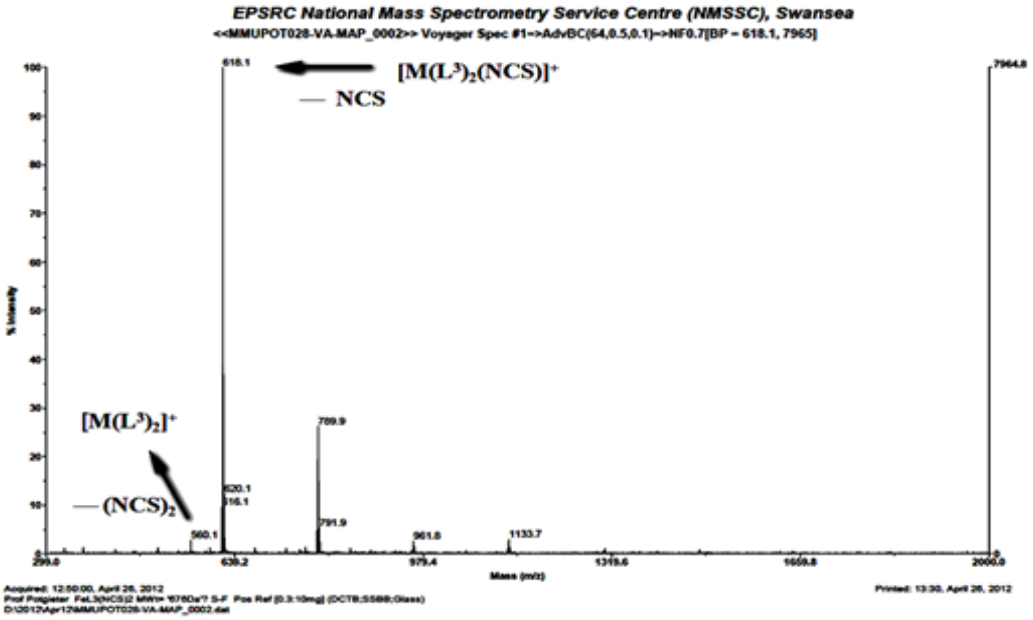

Figure 8.4: TOF-MS-ES (+) mass spectrum of the complex $[Fe(L^3)_2(NCS)_2]$.

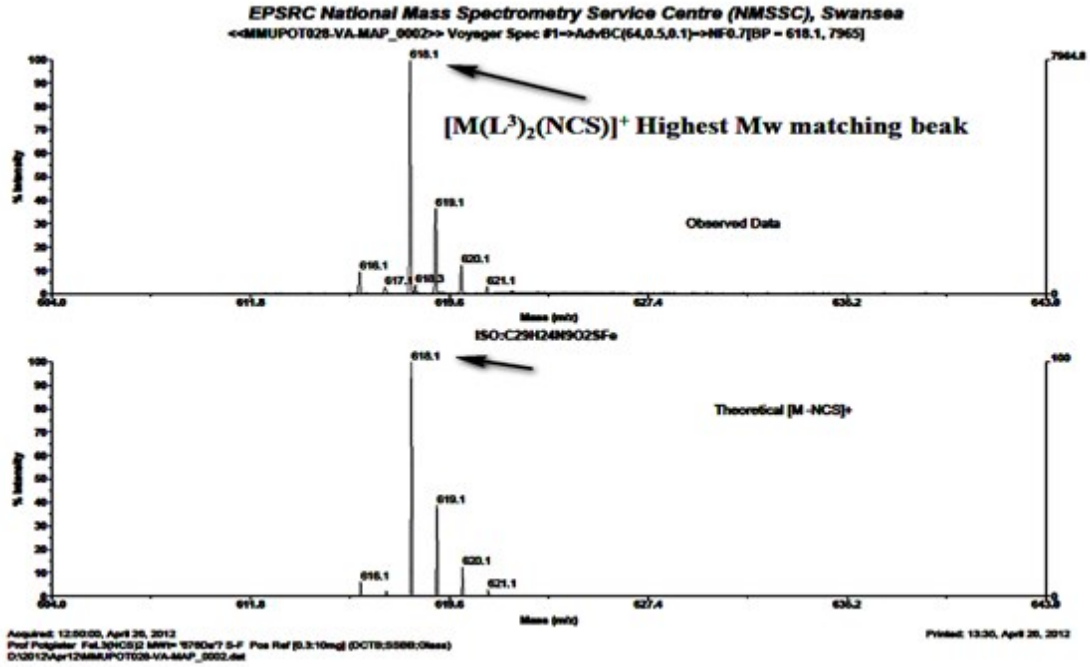

Figure 8.5: The calculated mass spectrum of complex $[Fe(L^3)_2(NCS)_2]$.

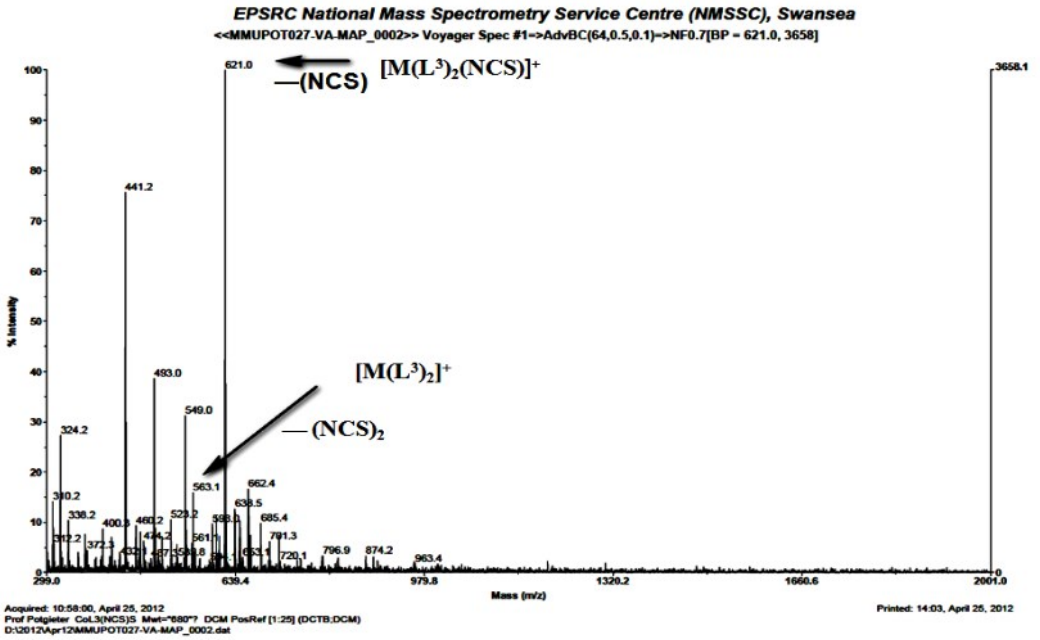

Figure 8.6: TOF-MS-ES mass spectrum of the complex $[Co(L^3)_2(NCS)_2]$.

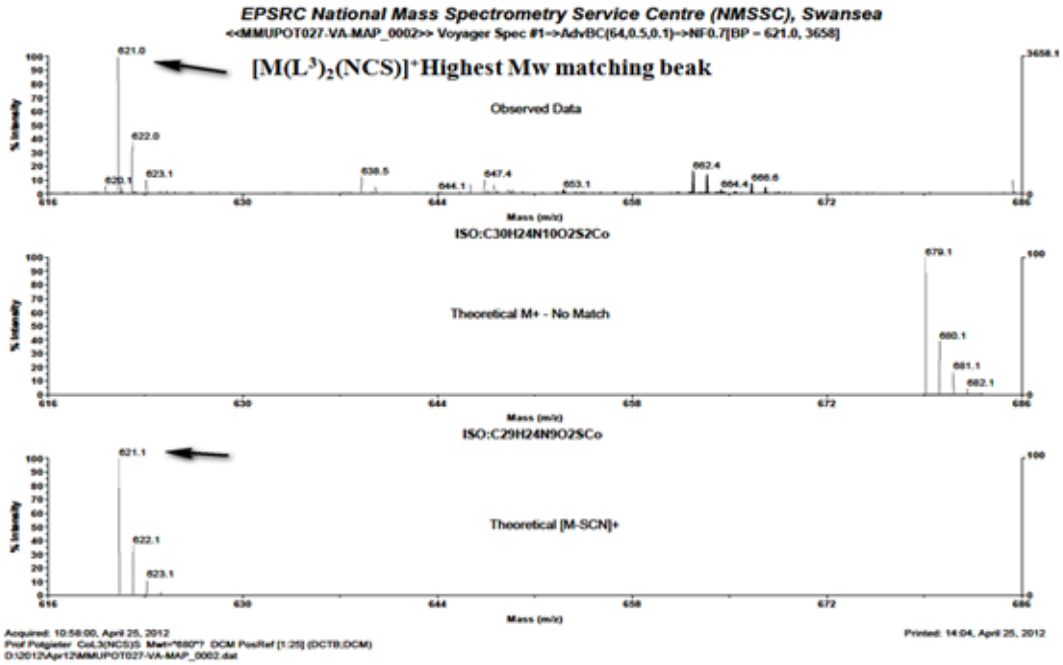

Figure 8.7: The calculated mass spectrum of the complex $[Co(L^3)_2(NCS)_2]$.

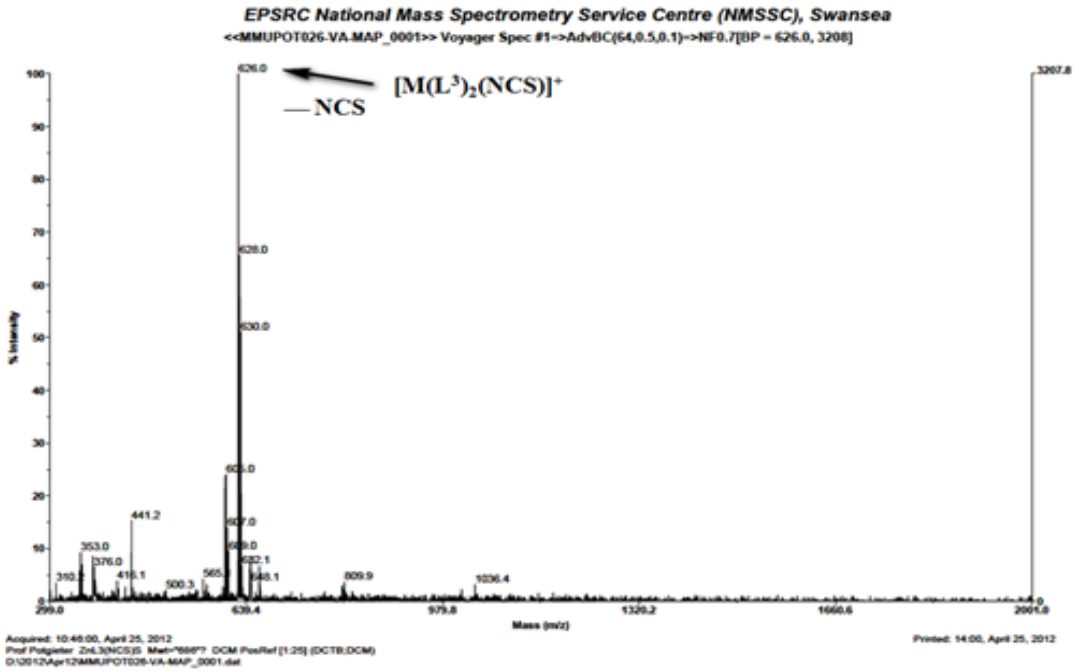

Figure 8.8: TOF-MS-ES (+) mass spectrum of complex $[Zn(L^3)_2(NCS)_2]$.

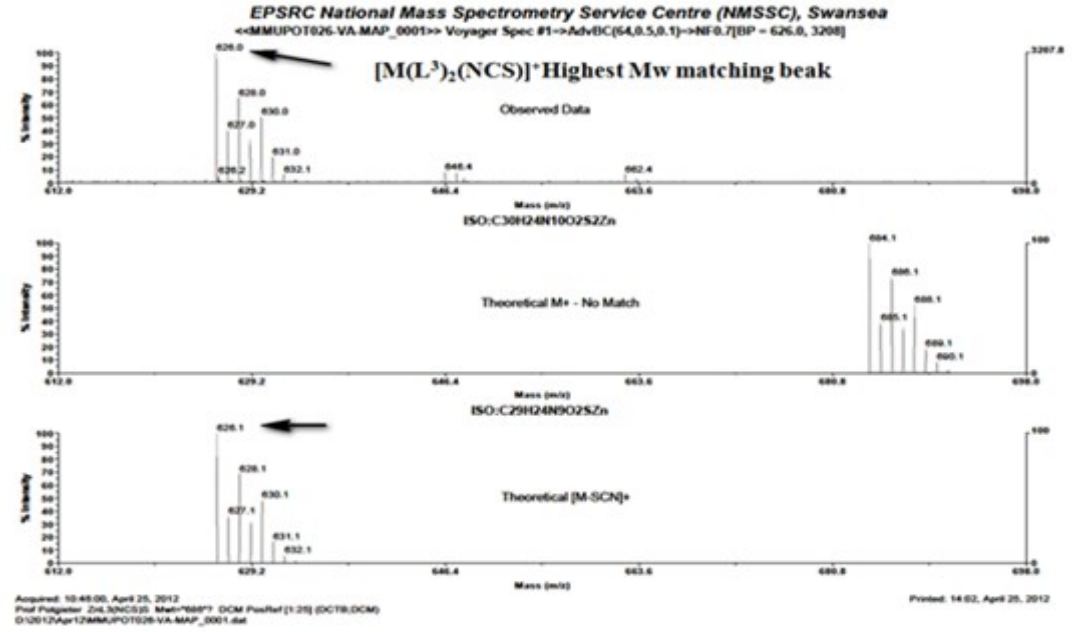

Figure 8.9: The calculated mass spectrum of complex $[Zn(L^3)_2(NCS)_2]$.

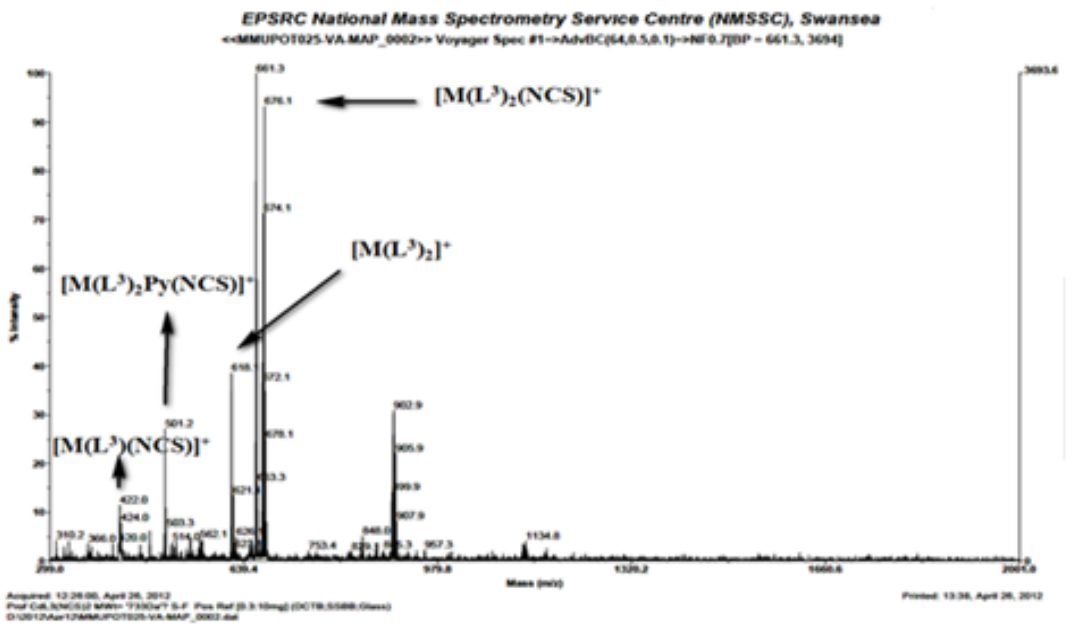

Figure 8.10: TOF-MS-ES (+) mass spectrum of complex $[Cd(L^3)_2(NCS)_2]$.

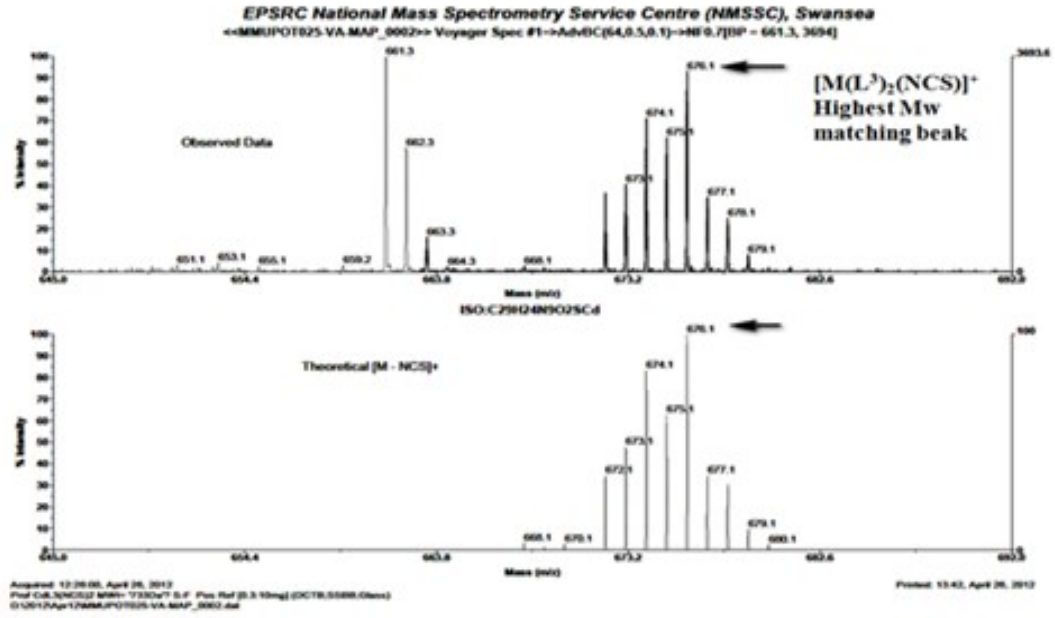

Figure 8.11: The calculated mass spectrum of complex $[Cd(L^3)_2(NCS)_2]$

8.2.5 ^{1}H, ^{13}C, HMQC two dimensional correlation spectroscopy and DEPT NMR spectra for the complexes

All assignments were confirmed using DEPT ^{13}C (135°); ^{1}H-^{1}H COSY and ^{1}H-^{13}C HMQC two dimensional correlation spectroscopy. The ^{1}H-^{13}C and DEPT NMR analysis was used to characterise the structure of the $[M(L^3)_2(NCS)_2]$ complexes.

8.2.5.1 ^{1}H and ^{13}CNMR spectra for $[Zn(L^3)_2(NCS)_2]$ and $[Cd(L^3)_2(NCS)_2]$

The ^{1}H and ^{13}C NMR data for the complexes $[Zn(L^3)_2(NCS)_2]$ and $[Cd(L^3)_2(NCS)_2]$ are displayed in Figures 8.12-8.19. The ^{1}H-NMR spectra and ^{13}C spectra for each complex were supported by 2-dimensional spectra (^{1}H–^{1}HCOSY, ^{13}C–^{1}H HMQC) to confirm the proposed assignments. The chemical shifts (δ) of the ^{1}H- (C-H) and ^{13}C-NMR (C=CH) of the complexes have been tabulated in Tables 8.5.

8.2.5.1.1 1H NMR spectra for the complex $[Zn(L^3)_2(NCS)_2]$ and $[Cd(L^3)_2(NCS)_2]$

The ^{1}H NMR spectrum for the complexes $[Zn(L^3)_2(NCS)_2]$ and $[Cd(L^3)_2(NCS)_2]$ in DMSO-d_6 solution is overlaid in Figure 8.12. The spectra display a lack of multiplicity of peaks, indicating the presence of only one isomer. The spectra in Figures 8.13 and 8.18 show a significant downfield chemical shift for the triazole proton ($C_{11;11}$-H), i.e. δ = 9.293 and δ = 9.269 ppm (1H, s) for the Zn(II) and Cd(II) isothiocyanate complexes, relative to the corresponding chlorido complexes. This shift is a consequence of the effect of the isothiocyanate group M-N^{+}≡C-S^{-} and it resonance contributors that reduce the electron density of the coordinated $[M^{2+}]$ atom via electron withdrawal. This occurs through back-bond donation from the metal d-orbital to the p-π* anti-bonding orbital of the ligand N^{+}≡C-S^{-} [13]. Another factor affecting the chemical shift is that complex formation reduces the electron density of the triazole ring (the lone electron pair on the triazole nitrogen combines with the metal). This observation is consistent with the coordination between the triazole group and metal moiety. The proton resonances of the pyridine group are shifted in accordance with its proximity to the metal centre, and the proton H2 closest to the M(II) centre is shifted downfield due the pyridine nitrogen atom binding to the metal. This signal is slightly shifted downfield compared to that detected in the free ligand and in the $[Zn(L^3)_2Cl_2]$ and $[Cd(L^3)_2Cl_2]$ complexes. Other significant signals are summarised in Table 8.5, and are similar to observations reported before in chapter 7 (see Table 7.7 and 7.8).

8.2.5.1.2 ^{13}C NMR spectra and DEPT spectra for the complexes $[Zn(L^3)_2(NCS)_2]$ and $[Cd(L^3)_2(NCS)_2]$

The ^{13}C NMR spectra for $[Zn(L^3)_2(NCS)_2]$ and $[Cd(L^3)_2(NCS)_2]$ are depicted in Figures 8.18 and 8.23. These figures shown significant chemical resonance shift in the range δ = 133.58ppm and δ = 132.28ppm in ^{13}CNMR. These shifts are attributed to the *trans* NCS carbon isothiocyanate ligands and indicates the binding of the isothiocyanate with the Zn(II) and Cd(II) ions [14,15]. The peaks at δ = 121.20 ppm and δ = 121.17ppm are assigned to the (C_{11}, triazole) for the Zn(II) and Cd(II) complexes, respectively. This gives a value of Δδ = 0.63ppm in comparison with the chemical shift of L^3. The peaks at δ = 121.73 and 114.79ppm usually are common characteristic features observed in para benzene substitutions ($C_{14,}$ $C_{16;}$ $C_{13,}$ C_{17}). These two signals are equivalent to four carbons in the same environments, and are attributed to para benzene substitution. The chemical shift of the CH_3 group of the methoxy moiety appears as expected up field in the range at δ = 55.61-55.62ppm [16, 17]. The results are summarised in Table 8.5. A sample ^{1}H-^{13}C HMQC correlation and COSY spectra of $[Zn(L^3)_2(NCS)_2]$ and $[Cd(L^3)_2(NCS)_2]$ in DMSO-d_6 are displayed in Figures 8.16-8.17 and 8.21-8.22 respectively.

Table 8.5: ^{1}H NMR data for the complexes measured in DMSO-d_6 and chemical shift in ppm (δ).

Compound	Functional group	δ (PPM)	δ (PPM) ^{13}C
L^3	$C_{(11;\,11)}$-H	8.53, s, 1H	120.57
	$C_{(2;\,2)}$- H	8.64,1H, d, J= 2.29Hz	149.99
$[Zn(L^3)_2Cl_2]$	$C_{(11;\,11)}$-H	9.06, s,1H,	120.75
	$C_{(2;\,2)}$- H	8.69-8.64,1H, d, J_{HH} = 4.58Hz	149.43
$[Cd(L^3)_2Cl_2]$	$C_{(11;\,11)}$-H	9.08, s,1H	120.82
	$C_{(2;\,2)}$- H	8.69-8.64,1H, d, J_{HH} = 4.58Hz	149.26
	C-NCS		133.58
$[Zn(L^3)_2(NCS)_2]$	$C_{(11;\,11)}$-H	9.29 H, s, 1H	121.20
	$C_{(2;\,2)}$- H	8.69-8.68,1H, d, J_{HH} = 4.12Hz	149.46
$[Cd(L^3)_2(NCS)_2]$	$C_{(11;\,11)}$-H	9.26 H, s, 1H	121.17
	$C_{(2;\,2)}$- H	8.69-8.68,1H, d, J_{HH} = 4.58Hz	149.52
	C-NCS		132.28

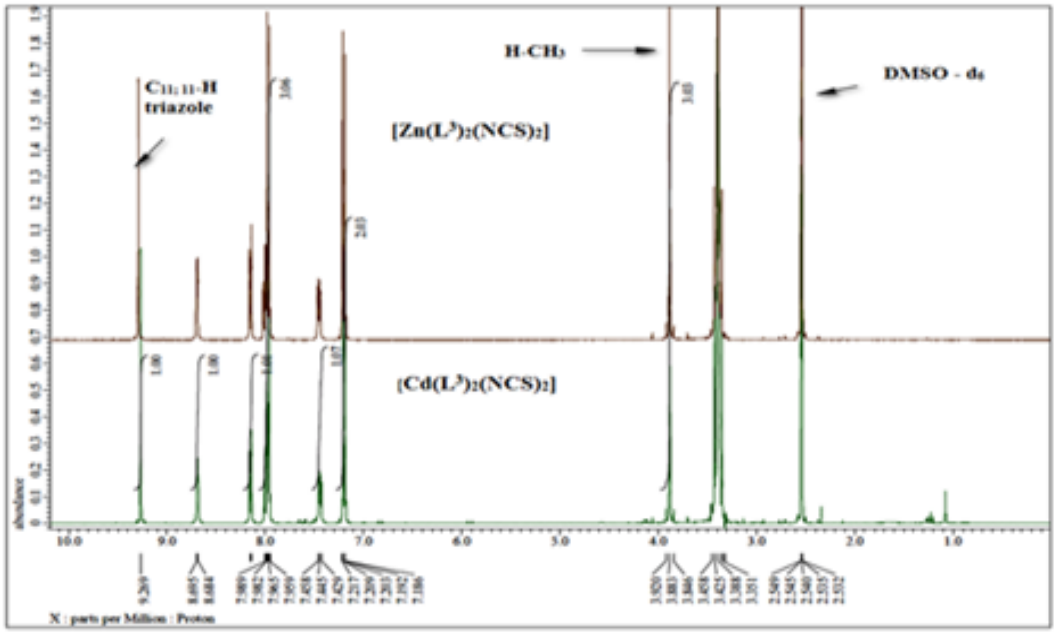

Figure 8.12: The overlay of the ^{1}H NMR for the isothiocyanato complexes of L^{3} with Zn(II) and Cd(II), highlighting in each the C-H triazole peak.

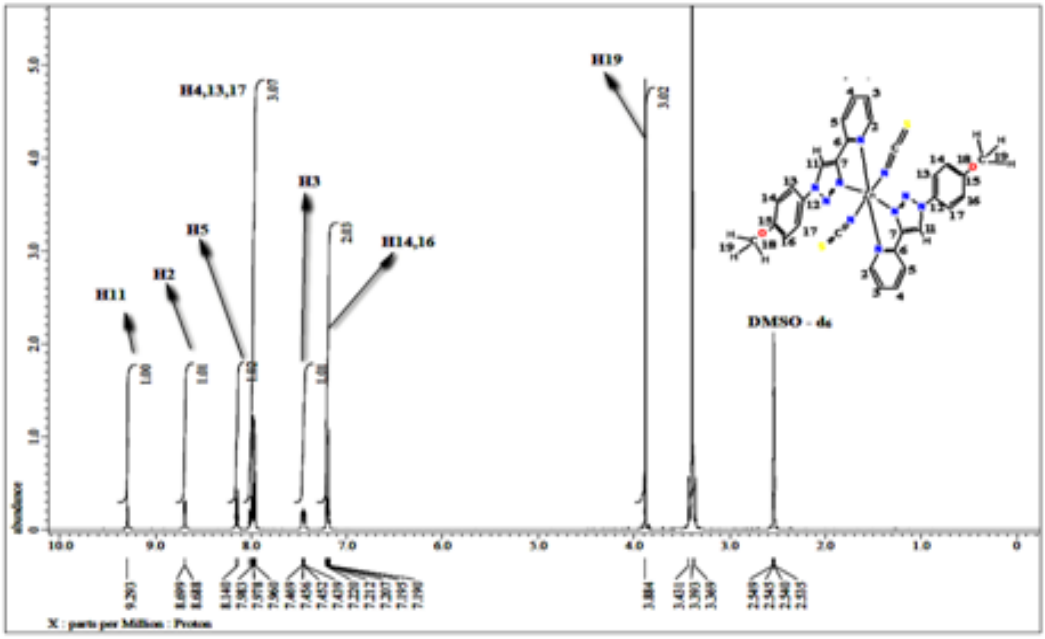

Figure 8.13: ^{1}H NMR spectrum of $[Zn(L^{3})_2(NCS)_2]$ in DMSO-d_6.

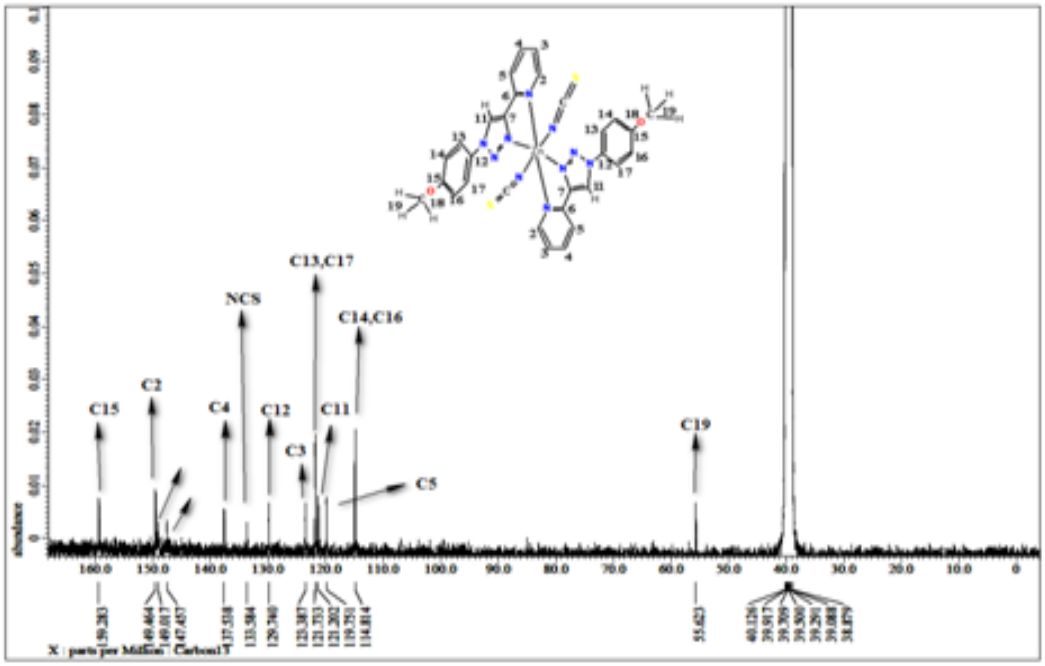

Figure 8.14: ^{13}C NMR spectrum of $[Zn(L^{3})_2(NCS)_2]$ in DMSO-d_6.

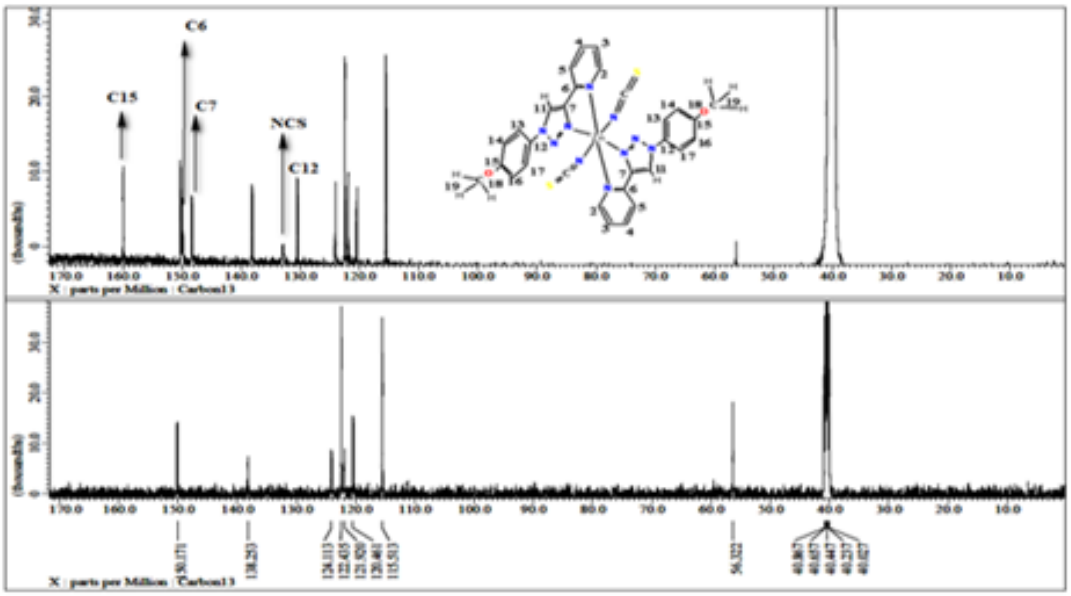

Figure 8.15: ^{13}C NMR and DEPT NMR spectrum of $[Zn(L^3)_2(NCS)_2]$ in DMSO-d_6.

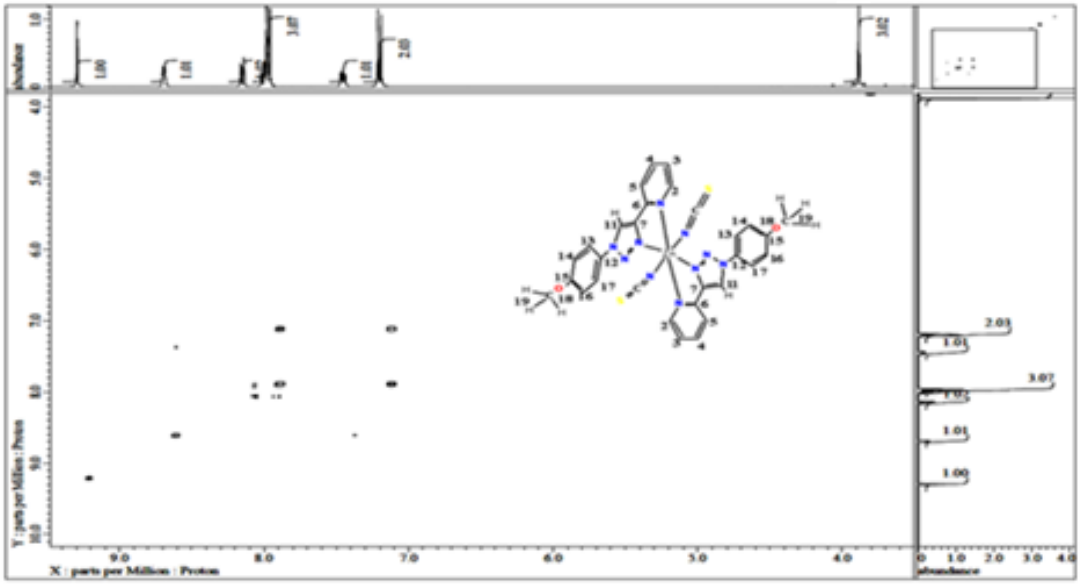

Figure 8.16: 2D ^{1}H-^{1}HCOSYcorrelation spectrum of $[Zn(L^3)_2(NCS)_2]$ in DMSO-d_6.

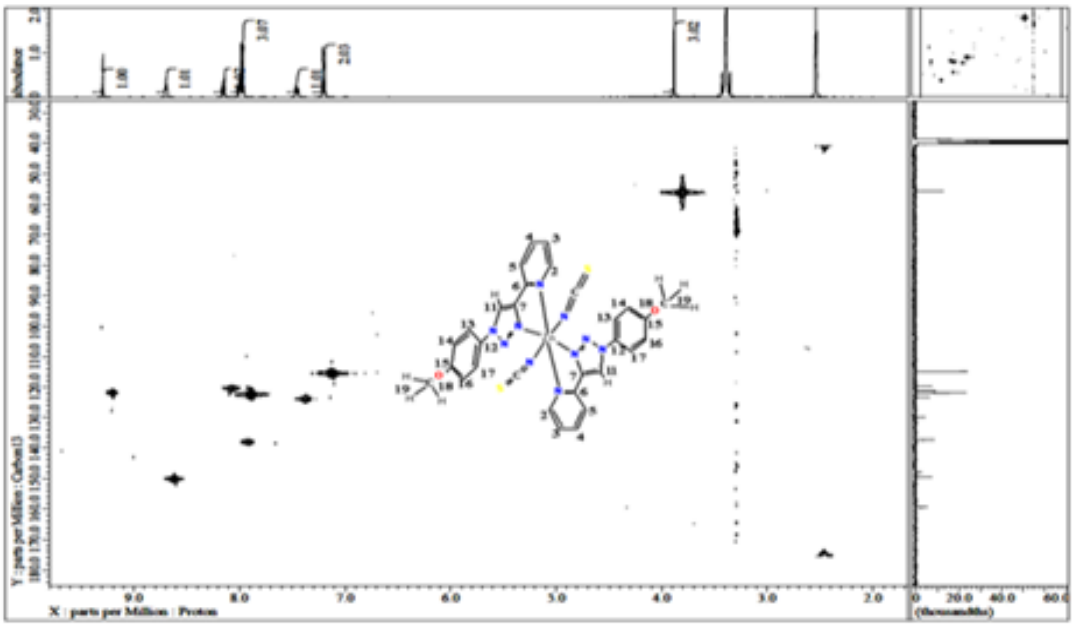

Figure 8.17: 2D ^{1}H-^{13}C HMQC correlation spectrum of $[Zn(L^{3})_2(NCS)_2]$ in DMSO-d_6.

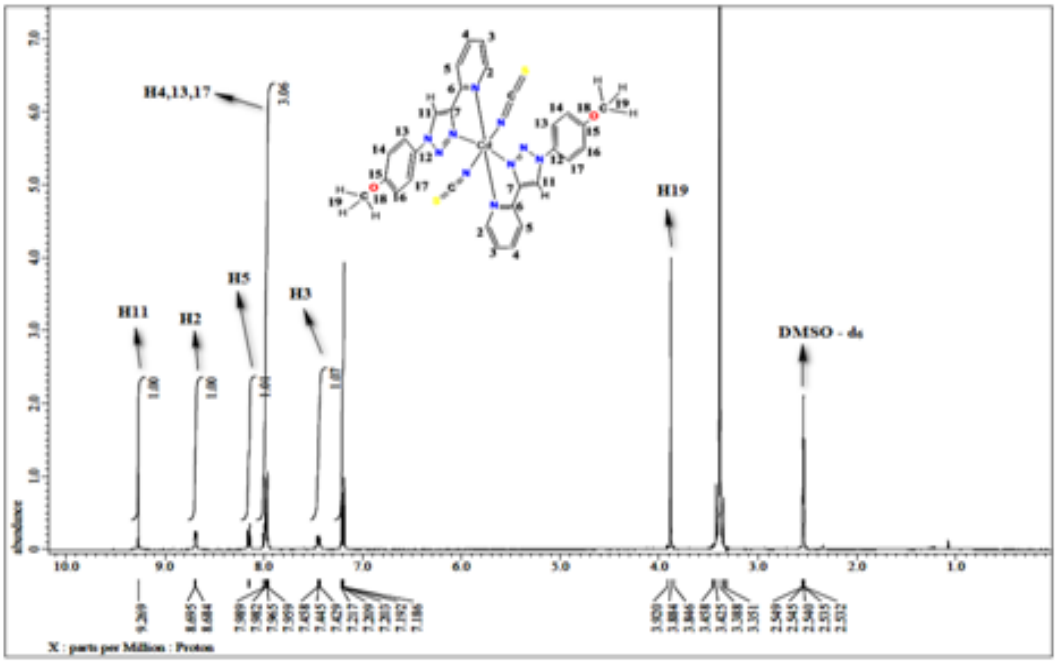

Figure 8.18: ^{1}H NMR spectrum of $[Cd(L^{3})_2(NCS)_2]$ in DMSO-d_6.

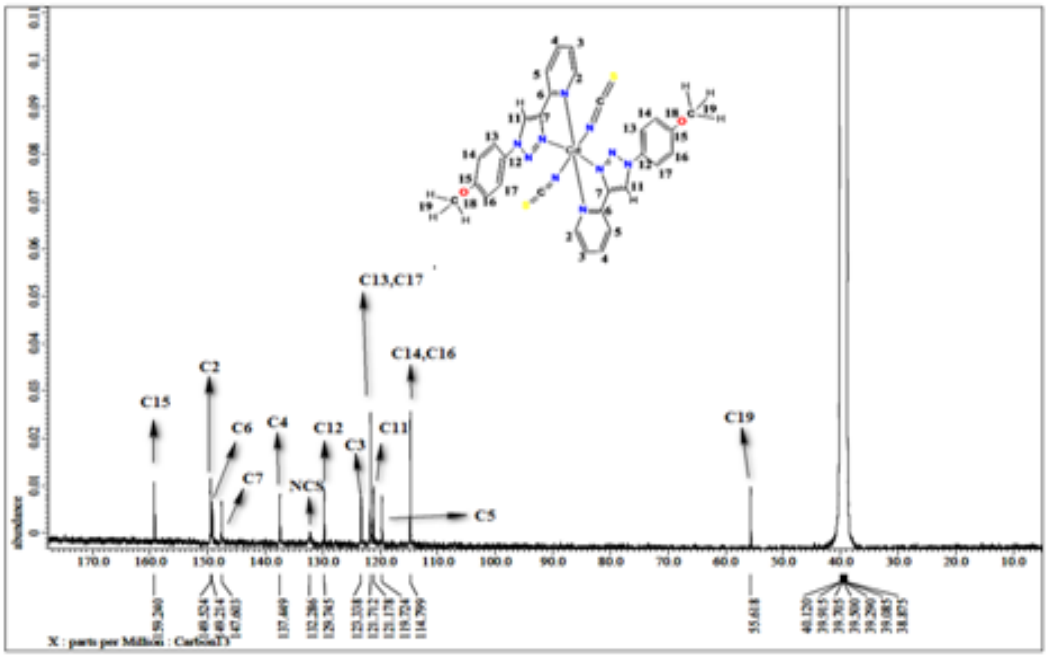

Figure 8.19: ^{13}C NMR spectrum of $[Cd(L^3)_2(NCS)_2]$ in DMSO-d_6.

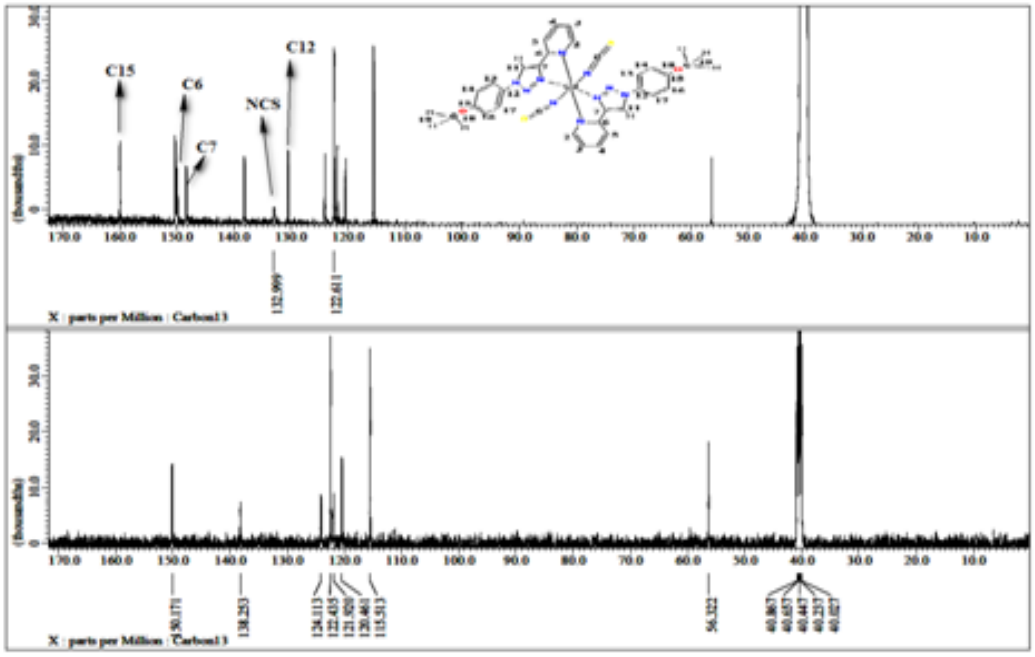

Figure 8.20: ^{13}C NMR and dept NMR spectrum of $[Cd(L^3)_2(NCS)_2]$ in DMSO-d_6.

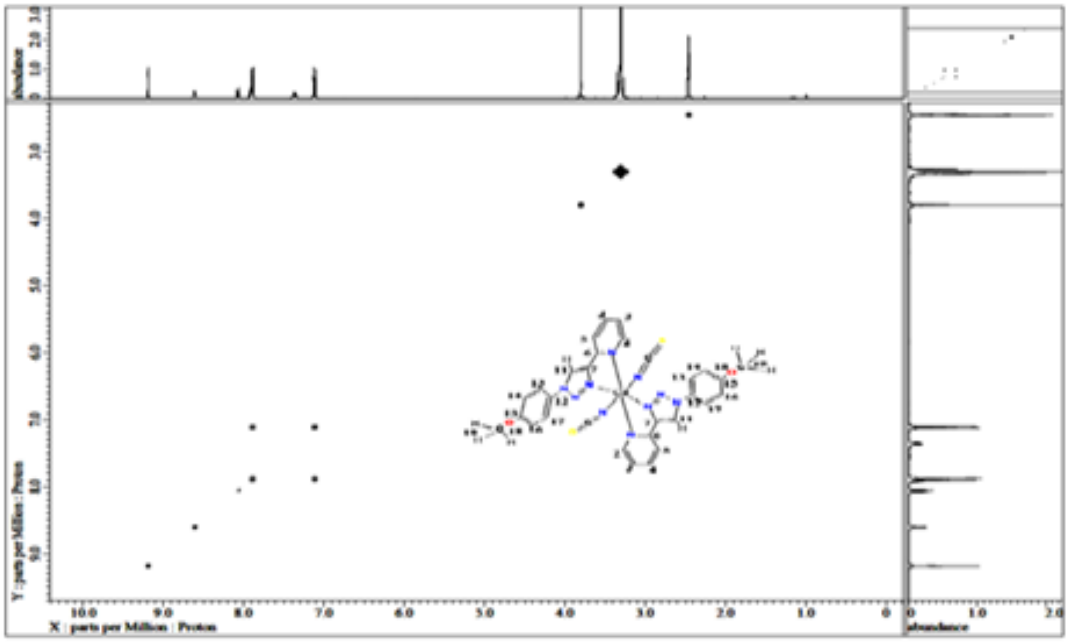

Figure 8.21: 2D ^{1}H-^{1}HCOSYcorrelation spectrum of $[Cd(L^{3})_2(NCS)_2]$ in DMSO-d_6.

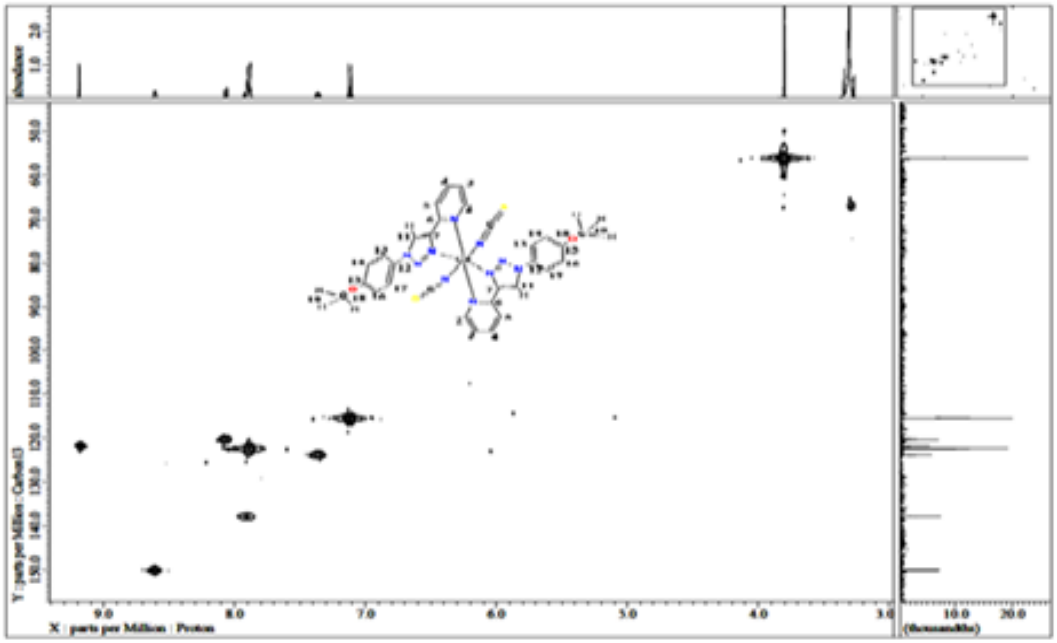

Figure 8.22: ^{13}C NMR and DEPT NMR spectrum of $[Cd(L^{3})_2(NCS)_2]$ in DMSO-d_6.

8.2.6 X-ray crystallographic diffraction of the metal various complexes

8.2.6.1 Structure determination

The single crystal X-ray diffraction measurements for $[Zn(L^3)_2(NCS)_2]$ and $[Cd(L^3)_2(NCS)_2]$ were performed using a Rigaku Saturn 724+ area detector mounted at the window of an FR-E+ rotating anode generator with Mo Kα, λ= 0.71070Å and Mo Kα, λ= 0.71075Å for $[Cd(L^3)_2(NCS)_2]$ complex at 100K. The crystals were mounted on glass fibres and the data were collected at 120K under nitrogen flow from an Oxford Cryosystems cryostream 700 device. An empirical absorption correction was carried out using SADABS and the structures were solved by direct methods using SUPERFLIP software [18]. Data were processed and empirical absorption corrections were carried out using Crystal Clear SM-Expert with the unit cell parameters refined against all data [19]. The structures were solved by direct methods using SHELXS-97 with OLEX2 [20]. All structures were refined on F_o^2 by full-matrix least squares refinement using the SHELXL-97 program package [21]. All non-hydrogen atoms were refined by isotropic displacement parameters and hydrogen atoms were added at calculated positions and refined using a riding model with C-H (aromatic) 0.950Å U_{ISO} = 1.5 U_{eq} (C); C-H (methyl) 0.980 Å U_{ISO} = 1.5 U_{eq} (C) [22]. The crystallographic data for the complexes are summarised in Table 8.6.

8.2.6.2 X-ray crystallography diffraction analysis of bis-isothiocyanato metal complexes with the L^3 ligand

8.2.6.2.1 Single-crystal structure determinations of $[Zn(L^3)_2(NCS)_2]$ and $[Cd(L^3)_2(NCS)_2]$ complexes

The molecular structure of the two complexes $[Zn(L^3)_2(NCS)_2]$ and $[Cd(L^3)_2(NCS)_2]$ were confirmed by X-ray crystallography analysis. The crystal structures of these complexes are generally similar. As expected, the two-triazole ligands are coordinated to the metal centre and lying in the same equatorial plane, while the two-isothiocyanate ligands are located in the axial positions that are *trans* to each other. These crystal structures have a six coordination number with distorted octahedron geometry typical of M(II) complexes. The X-ray diffraction data analysis of the complexes $[Zn(L^3)_2(NCS)_2]$ and $[Cd(L^3)_2(NCS)_2]$ are listed in Table 8.6, while selected bond lengths, bond angles and torsion angles are depicted in Tables 8.7 and 8.8.

Table 8.6: Crystallographic data for the complexes $[Zn(L^3)_2(NCS)_2]$ and $[Cd(L^3)_2(NCS)_2]$.

Compound	L^3	$[Zn(L^3)_2(NCS)_2]$	$[Cd(L^3)_2(NCS)_2]$
Formula	$C_{14}H_{12}N_4O$	$C_{30}H_{24}N_{10}O_2S_2Zn$	$C_{30}H_{24}N_{10}O_2S_2Cd$
M_r	252.28	686.08	451.60
Temp/K	100(2)	100(2) K	100(2) K
Cryst. syst.	Triclinic	Triclinic	Triclinic
Space group	P1	P1	P1
a/Å	3.7837(4)	6.8984(4)	6.8526(5)
Wavelenght Å	0.71075	0.71070	0.71075
b/Å	10.8502(16)	9.6078(7)	9.5938(7)
c/Å	15.2200(17)	12.2677(8)	12.6921(9)
α/°	109.226(11)	98.399(7)	101.567(13)
β/°	97.056(6)	95.666(6)	94.308(12)
γ/°	91.514(9)	110.914(5)	110.645(14)
V/Å^3	584.03(12)	741.29(8)	755.23(12)
Z	2	1	1
R_{int}	0.0617	0.0342	0.1444
D_{calcd}/g. cm^{-3}	1.435	1.537	1.612
Refln (all/ind)	6395/2617	7374/3387	6527/3384
μ/mm^{-1}	0.096	1.018	None
$R1$/$wR2$	0.0534/	0.0331/	0.0635/
(obsd data:	0.1074	0.0852	0.1366
$F^2>2\sigma(F^2)$)[a]			
$R1$/$wR2$ (all data)[a]	0.0734/	0.0431/	0.0875 /
	0.1161	0.0889	0.1483

Table 8.7: Selected bond lengths Å and angles [°] for the complexes $[Zn(L^3)_2(NCS)_2]$ and $[Cd(L^3)_2(NCS)_2]$.

Bond distance(Å)	L^3	$[Zn(L^3)_2(NCS)_2]$	$[Cd(L^3)_2(NCS)_2]$	angles (°)	$[Zn(L^3)_2(NCS)_2]$	$[Cd(L^3)_2(NCS)_2]$
Empirical formula	$C_{14}H_{12}N_4O$	$C_{30}H_{24}N_{10}O_2S_2Zn$	$C_{30}H_{24}N_{10}O_2S_2Cd$		$C_{30}H_{24}N_{10}O_2S_2Zn$	$C_{30}H_{24}N_{10}O_2S_2Cd$
C7–C11	1.362(6)	1.364(2)	1.370(6)	$N_{(PY)}$ 1 –M–$N_{(PY)}$ 1^i	180.0(6)	180.0
N8–N9	1.302(4)	1.312(2)	1.308(6)	$N_{(tz)}$ 1^i –M–$N_{(tz)}$ 1	180.0(4)	180.0
N9–N10	1.355(4)	1.345(2)	1.345(5)	$N_{(PY)}$ 1–M–$N_{(tz)}$ 1^i	102.25(5)	107.31(14)
N8–C7	1.365(5)	1.353(2)	1.352(6)	$N_{(PY)}$ 1 –M–$N_{(tz)}$ 1	77.75(5)	72.62(14)
M–$N_{(PY)}$ 1		2.1745(15)	2.348(4)	$N_{(PY)}$ 1–M– N1CS	88.80(6)	88.39(16)
M–$N_{(PY)}$ 1^i		2.1745(15)	2.348(4)	$N_{(PY)}$ 1^i–M– N1CS^i	91.20(6)	91.61(16)
M–$N_{(triazole)}$1		2.1556(14)	2.309(4)	$N_{(tz)}$ 8^i –M– N1CS^i	89.94(6)	88.39(16)
M–$N_{(triazole)}1^i$		2.1556(14)	2.309(4)	$N_{(tz)}$ 8–M– N1CS	90.06(6)	91.61(16)
M–N1S		2.1298(17)	2.307(5)	N1S–M–N1S^i	180.0	180.0
M–N1S^i		2.1298(17)	2.307(5)	N1S–C1S–S1S	179.24(17)	179.0(5)
N1S–C1S		1.154(3)	1.149(7)	C1S– N1S–M	174.71(15)	167.3(4)
S1S–C1S		1.639(2)	1.634(6)			

Table 8.8: Selected torsion angles [°] for the complexes $[Zn(L^3)_2(NCS)_2]$ and $[Cd(L^3)_2(NCS)_2]$.

Angles	$[Zn(L^3)_2(NCS)_2]$	$[Cd(L^3)_2(NCS)_2]$
N(*t*) 1^i–M–N(*p*)1–C2	−15.8(16)	−1.7(4)
N(*t*)) 1–M–N(*p*) 1–C2	178.42(16)	−175.1(3)
N1S^i–M–N(*p*) 1– C2	88.74(15)	90.6(4)
N1S–M–N(*p*) 1–C2	−91.26(15)	−90.6(4)
N(*p*) 1–M–N(*t*) 1–N9	0.47(19)	1.6(5)
N(*p*) 1^i–M–N(*t*) 1–N9	−179.53(19)	−1.6(5)
N1S^i–M–N(*t*) 1–N9	−88.29(18)	−90.2(5)
N1S–M–N(*t*) 1–N9	91.71(18)	90.2(5)
M–N(*t*) 1–N9–N10	−176.81(13)	174.8(3)
N8–N9–N10–C11	0.4(2)	−1.5(5)
N8–N9–N10–C12	174.98(15)	−177.0(4)

8.2.6.2.2 The X-ray crystal structure of bis-(isothiocyanato-N)(bis{2-[1-(4-methoxyphenyl)-1H-1,2,3-triazol-4-yl-kN3]pyridine-kN})]zinc(II) [Zn(L^3)$_2$(NCS)$_2$]

The molecular structure of the complex [Zn(L^3)$_2$(NCS)$_2$] as confirmed by single-crystal X-ray diffraction is depicted in Figure 8.23. The crystals of the molecule [Zn(L^3)$_2$(NCS)$_2$] were obtained by slow evaporation in a hot mixture of CH_3OH:CH_3CN= 1:2 under ambient conditions. It crystallises in the triclinic P-1 space group, which indicates one molecule per unit cell as Z=1of [Zn(L^3)$_2$(NCS)$_2$] complex (see Figure 8.28). The zinc centre in the [Zn(L^3)$_2$(NCS)$_2$] complex is in a distorted octahedral coordination arrangement, which includes two of the 2-(1-(4-methoxy-phenyl)-1H-1,2,3-triazol-4-yl)pyridine L^3 ligands coordinated to the zinc atom, via the N8trz and N1py atoms from the two different ligands. The $N8_{eq}$–Zn–$N1_{eq}$ and $N1^{i}_{eq}$–Ni–$N8i_{eq}$ atomic bands are lying in the equatorial plane with angles of 77.75(5)°. In the equatorial plane the pyridine $N1_{py}$ and $N8_{trz}$ donor atoms from the two ligands are mutually *trans* to each other, and the angles for $N8_{eq}$–Zn–$N8^{i}_{eq}$ and $N1_{eq}$–Zn–$N1^{i}_{eq}$ are 180.00(4)° and 180.00(6)°, respectively. Furthermore, the axial positions are occupied by two isothiocyanate ions that are *trans* to each other, with the $N1S_{ex}$ –Zn–$N1S_{ex}$ at an angle of 180.0°.

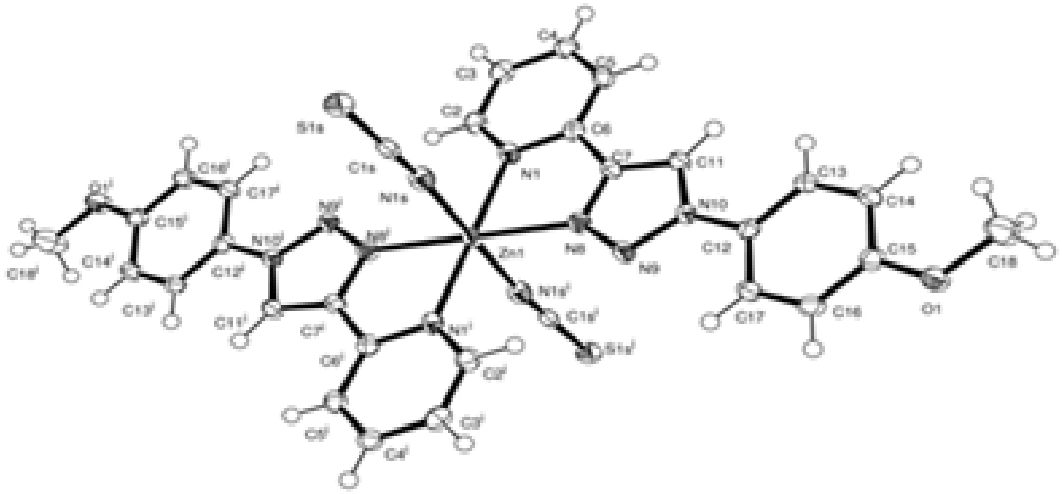

Figure 8.23: The molecular structure of [Zn(L^3)$_2$(NCS)$_2$]. The thermal ORTEP diagram is drawn at a 50% probability level and the H atoms are shown as small spheres of arbitrary size.

The angles in the plane between these two L^3 ligands slightly deviated from 90°. The angle is distorted because of the chelating nature of the ligands L^3, but the 180° angles are intact. The N8–N9 bond length inside the 1,2,3-triazole ring is 1.302(4) Å, while the N9–N10 and N8–C7 bond lengths for the free ligand are 1.355(4) and 1.365(5)Å, respectively. The distances of the bond lengths between N8–N9 1.312(2) Å, N9–N10 1.345(2)Å and N8–C7 1.353(2)Å respectively, are slightly higher in the $[Zn(L^3)_2(NCS)_2]$ complex (by approximately 0.010Å) when compared with the free ligand and another M(II)pyridyl-triazole complex published recently [23]. Both the monodentate isothiocyanate ion ligands shown bond lengths for the connection M–NCS of 2.1298(17)Å.

The C–N and C–S bond length values are 1.154(3) Å and 1.639(2) Å, respectively. These bond lengths are comparable to those bond lengths of NCS^- observed previously in the literature [24, 25]. In the complex, the metal-isothiocyanate chain indicates a π-delocalization along to the Zn–N–C angles at 174.7(2), while the angle between N1S–Zn1–$N1S^i$ is 180.0°. This provides evidence that the NCS^- anion is a perfect linear group, which is in good agreement with reports found for M(II) 3d complexes having bent terminally bonded NCS ligands (141°-174°) [25, 26]. The angles around the metal centre are listed in Table 8.7. In the Zn(II) complex, the metal-triazole bond length is slightly shorter at 2.1556(14)Å than the metal pyridine bond length at 2.1745(15)Å (by approximately 0.0189Å). These distances are normal and comparable with distances in other complexes containing the PYTA type ligands, because of the greater *trans* influence of the triazole nitrogen N8 with respect to the pyridyl nitrogen N1 [26, 27].

After complexation, the twisting angle between the pyridine plane and the triazolering is only 114.50(15)°, while the twisting angle between the triazole plane and the substituted phenyl ring is 120.87(14)°. The dihedral angle between the plane of the pyridyl moiety and the mean plane of the triazole ring is 0.5(2)°, whereas the dihedral angle between the plane of the methoxy phenyl group and the plane of the triazole moiety is tilted by 9.8(2)°. From the overlay of the structure shown in Figure 8.24, extensive weak hydrogen bonding interactions were observed.

This generates a 3D supramolecular network sheet of infinite chains in the solid state. It can be deduced that there are four kinds of weak intermolecular hydrogen bonds of type (D–H…A), which include. (1)- C11–H11...S1S and C11–H11...S1S^{i} occurring via the H-triazole (H11) from a neighbouring layer with (S) from the monodentate *trans* isothiocyanate NCS ligand, and from another H-triazole (H11) on another neighbouring second layer with (S^{i}) from the second monodentate *trans* isothiocyanate NCS^{i} ligand from the same layer, (2)-C16–H16...O1, where these intermolecular hydrogen bonds occur via the H-phenyl ring (H16) from the main layer with O1 from the methoxy group linkage to the phenyl ring of the second layer (3)-C3–H3...C1S and C1S^{i}, (4)-C17–H17...C1S and C1S^{i}. These intermolecular hydrogen bonds are summarised in Table 8.9. These values of hydrogen bonds are in agreement with values reported previously in literature [28, 29]. In the complex [Zn(L^3)$_2$(NCS)$_2$], it was observed that these intermolecular hydrogen bonds play the roles of the hydrogen bond donors and acceptors.

Table 8.9: Weak hydrogen bonding interaction parameters; D= donor and A= acceptor (Å, °) in the complex [Zn(L^3)$_2$(NCS)$_2$].

D-H...A/interactions	D–H (Å)	H–A (Å)	D–A (Å)	Angle (°)
C11–H11...S1S	0.9300	2.777(5)	3.592 (2)	146.8(1)
C11–H11... S1S^{i}	0.9300	2.777(5)	3.592 (2)	146.8(1)
C16–H16...O1	0.9300	2.532(2)	3.396 (3)	154.6(1)
C3–H3...C1S	0.9300	2.762(3)	3.451(3)	131.6(1)
C3–H3...C1S^{i}	0.9300	2.763(2)	3.451(3)	131.6(1)
C17–H17...C1S	0.9300	2.821(2)	3.642(3)	147.8(1)
C17–H17...C1S^{i}	0.9300	2.821(2)	3.642(3)	147.8(1)

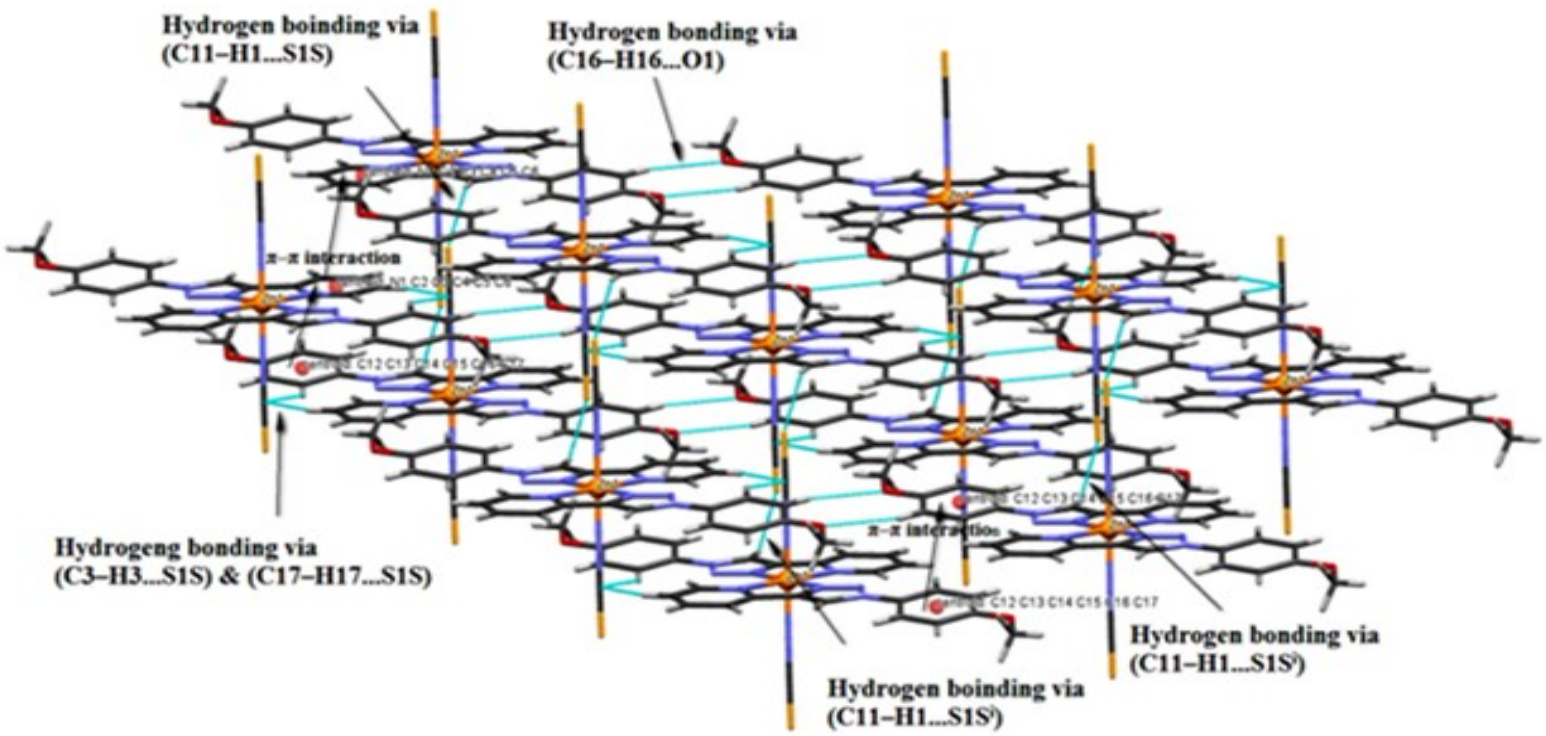

Figure 8.24: Schematic representation of a 3D supramolecular sheet, showing intermolecular hydrogen bonding interactions in an extended complex $[Zn(L^3)_2(NCS)_2]$. The molecules are linked in a layered manner viaC17–H17…S1S andC17–H17…S1S^{i}, C3–H3...S1S, C3–H3...S1S^{i} and C16–H16...O1 interactions. The complex is viewed along the crystallographic b-axis.

Notably, one offset face-to-face π…π interaction exists between two parallel coordinated pyridyl rings composed of the ($N_{12}C_2C_3C_4C_5C_6$) and ($N_{12}C_2C_3C_4C_5C_6$) molecules. The adjacent molecules adopt an offset-slipped face-to-face parallel alignment, where the adjacent pyridine ring is perfectly coplanar. The centroid – centroid distance is 3.877Å, with a plane–plane distance of 3.046Å and an angle between the planes of 2.23° (see. Figure 8.25). This distance is comparable to the previously reported bond separation of a typical π…π stacking [4]. Another π…π stacking interaction exists between two parallel phenyl rings, with a plane–plane distance of 3.534Å [43, 30] and a centroid–centroid distance of 3.345Å, as is presented in Figure 8.26. Finally, it was also observed π…π stacking interactions occurring between two parallel coordinated pyridyl rings with phenyl rings in the crystal structure of the complex $[Zn(L^3)_2(NCS)_2]$. Here the plane–plane distance is 3.325Å and the centroid–centroid distance is 3.940Å (see Figure 8.27) [31, 34]. These π…π interactions are continuous throughout the $[Zn(L^3)_2(NCS)_2]$ complex and result in a 3D infinite supramolecular structure Figure.8.24.

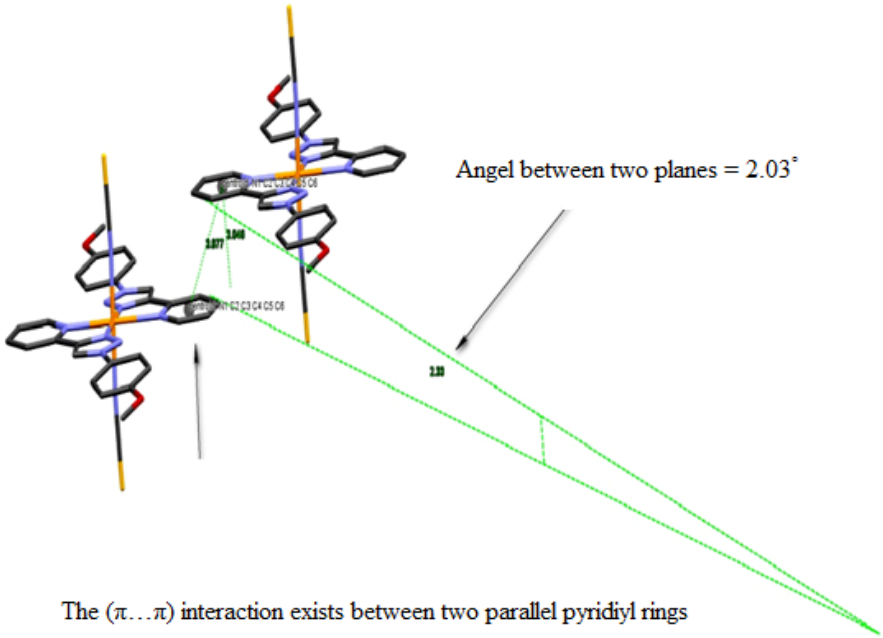

Figure 8.25: A pair of connected complexes arranged about a centre of symmetry, showing the overlap between the two pyridine rings due to intermolecular π…π interaction in molecule $[Zn(L^3)_2(NCS)_2]$. The complex is viewed along the crystallographic b-axis.

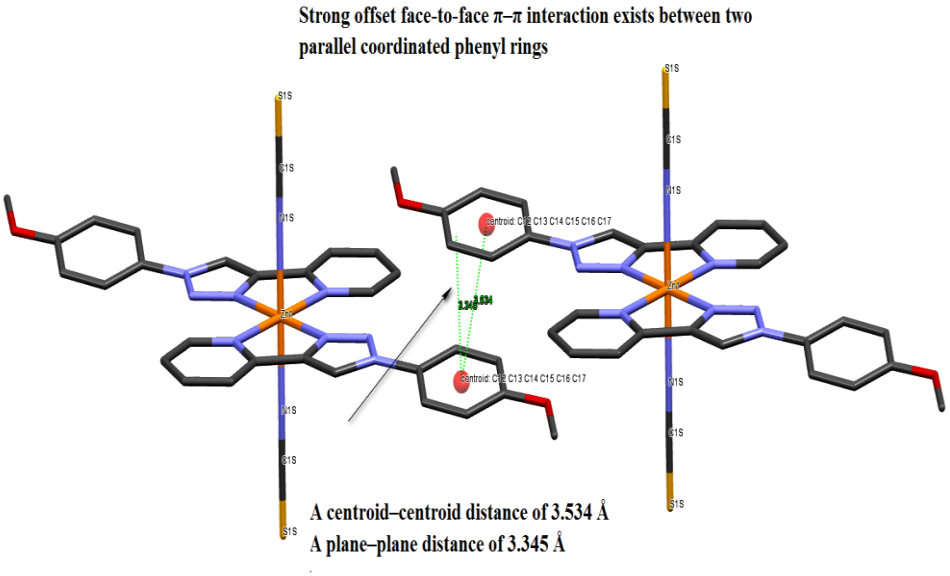

Figure 8.26: A pair of connected complexes arranged about a centre of symmetry, showing the overlap between the two phenyl rings due to intermolecular π…π interaction in the molecule $[Zn(L^3)_2(NCS)_2]$. The complex is viewed along the crystallographic b-axis.

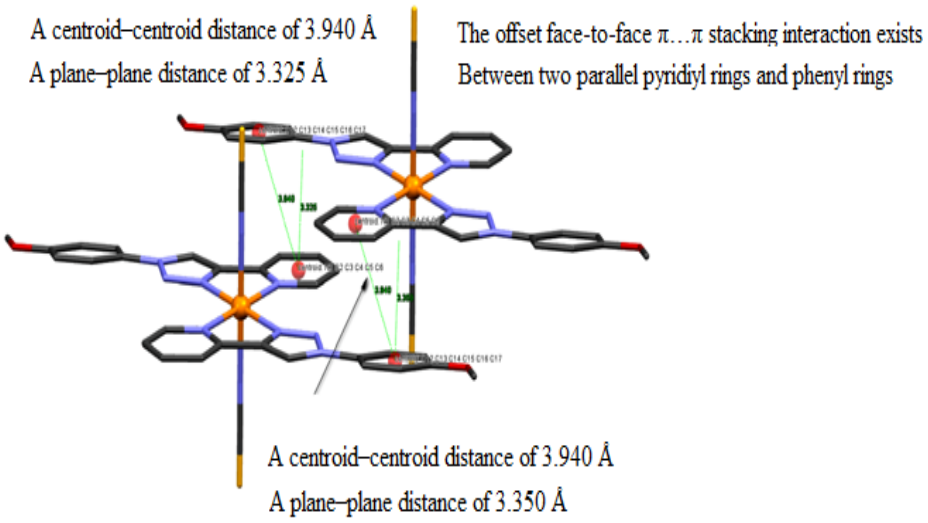

Figure 8.27: A pair of connected complexes arranged about a centre of symmetry, showing the overlap between the two parallel pyridyl rings and phenyl rings due to intermolecular π…π interactions in the molecule $[Zn(L^3)_2(NCS)_2]$. The complex is viewed along the crystallographic b-axis.

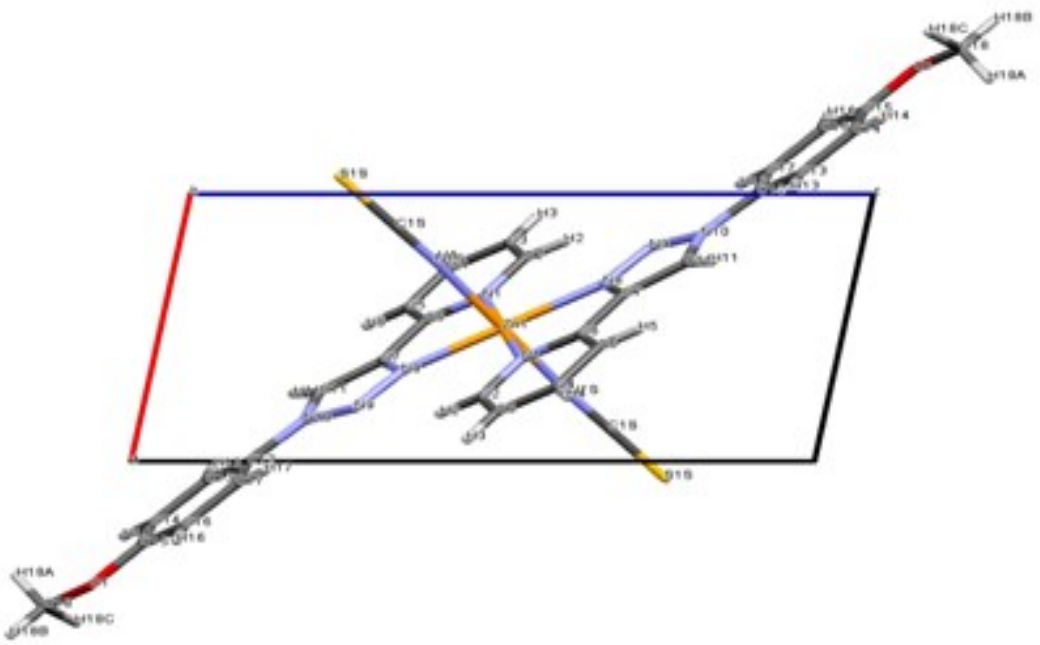

Figure 8.28: The unit cell, viewed along the crystallographic b – axis. A capped stick model of the molecular structure packing of $[Zn(L^3)_2(NCS)_2]$. H atoms are shown as small spheres of arbitrary size.

The complex $[Zn(L^3)_2(NCS)_2]$ is stabilised by four intermolecular hydrogen bonding interactions andthree intermolecular π…π interactions. The π…π stacking can be described as occurring in the solid state between (1)- the pyridyl - pyridyl rings, (2) - triazole - triazole rings and (3)- phenyl-phenyl rings. In the crystal structure, the molecules of the $[Zn(L^3)_2(NCS)_2]$ complex are arranged in infinite chains forming a 3D supramolecular network sheet. The molecules of $[Zn(L^3)_2(NCS)_2]$ adopt a head-to-tail orientation (see Figure 8.24).

8.3 General Experimental Procedures and Characterisation of Bis-Isothiocyanato bis 1*H*-1,2,3-triazol Metal Complexes

8.3.1 Synthesis and characterisation of bis-isothiocyanato of L^3 metal complexes

The general procedure referred to above and described in detail for the first complex synthesis, was used to prepare the following complexes by using the indicated amounts of each reagent.

Table 8.10: Bis-isothiocyanate Metal-L_3 complexes synthetised and characterised during the investigation.

$[M(L^3)_2(Cl)_2]$	KNCS amount	Yield (%)	MP (°C)
0.072g, 0.11mmol $[Fe(L^3)_2(NSC)_2]$	0.5g, 7.68mmol KNCS	0.056g,0.082mmol, 72%	238 - 240
0.081g, 0.12mmol $[Co(L^3)_2(NSC)_2]$	0.45g, 6.91mmol KCNS	0.076g,0.091mmol, 76%	310 - 312
0.084g, 0.13mmol $[Zn(L^3)_2(NSC)_2]$	0.60g, 9.21mmol KNCS	0.072g,0.10mmol, 80%	314 - 316
0.090g, 0.13mmol $[Cd(L_3)_2(NSC)_2]$	0.60g, 9.21mmol KNCS	0.080g,10mmol, 84%	308-310

8.3.1.1 Synthesis and characterisation of Bis(isothiocyanato-N)(bis{2-[1-(4-methoxyphenyl)-1H-1,2,3-triazol-4-yl-N3]pyridine-kN})]iron(II)

The $[Fe(L^3)_2(NCS)_2]$ complex was synthesised by dissolving (0.072g, 0.11mmol), of the complex $[Fe(L^3)_2(Cl_2)]$ in DMSO (10ml). The mixture was allowed to stir for 15 min, and then a solution of KNCS (0.5g, 7.68mmol) in a mixture of H_2O (5ml) and CH_3OH (20ml) was slowly added. The mixture was refluxed for 24h, and then allowed to stir at room temperature for 30min. The solvent was reduced under vacuum to about half its original volume, and then crushed ice was added to the solution. The resulting precipitate was filtered, washed with several volumes of cold methanol and diethyl ether to yield a pale yellow solid. The isolated product gave a yield of 72%, (0.056g, 0.082mmol), mp, 238 - 240°C. IR $\bar{\upsilon}(cm^{-1})$: 3123, 3087, 2956, 2921, 2851, 2851, 2834, 2076, 1606, 1574, 1514, 1471, 1467, 1442, 1309, 1253, 1176, 1064, 1028, 1017, 1001, 983, 836, 792, 789, 719. UV-Vis (DMSO) λ_{max}: 258nm, ε_{max} = 63333 $dm^3mol^{-1}cm^{-1}$, 286nm, ε_{max} = 78666 $dm^3mol^{-1}cm^{-1}$, 351nm, ε_{max} = 664 $dm^3mol^{-1}cm^{-1}$.

The complex showed a value of μ_{eff} = 5.36 B.M: HRMS TOF (MALDI) with the highest molecular weight peak matching, observed at m/z = 618.1 (100%) is attributed to $[M\text{-}NCS]^+$. The calculated value for $[C_{29}H_{24}N_9O_2SFe]^+$ is 618.1. The second fragment observed is at 560.1(3%) and is referred to as $[M]^+$. The calculated value for $[C_{28}H_{24}N_8O_2Fe]^+$ is observed at a value of = 560.1. Λ_M (DMSO) = $48\Omega^{-1}cm^2mol^{-1}$ [35-37].

8.3.1.2 Synthesis and characterisation of Bis(isothiocyanato-N)(bis{2-[1-(4-methoxyphenyl)-1H-1,2,3-triazol-4-yl-kN3]pyridine-kN})]cobalt(II)

IR $\bar{\upsilon}(cm^{-1})$: 3128, 3088, 2932, 2851, 2833, 2073, 1606, 1575, 1516, 1470, 1467, 1442, 1308, 1253, 1176, 1064, 1029, 1019, 1001, 983, 827, 791, 789, 720. UV-Vis (DMSO) λ_{max}: The Co(II) complex have shown absorption bands at 258nm, ε_{max} = 61250 $dm^3mol^{-1}cm^{-1}$, 288nm, ε_{max} = 40000$dm^3mol^{-1}cm^{-1}$, 538nm, ε_{max} = 14$dm^3mol^{-1}cm^{-1}$. The complex showed a value of μ_{eff} = 4.56 B.M: HRMS TOF (MALDI) with the highest molecular weight peak matching, observed at m/z = 621.0 (100%), is assigned to $[M\text{-}NCS]^+$. The calculated value for $[C_{28}H_{24}N_7O_2SCo]^+$ is 621.0. The second fragment observed at 563.1(20%) is referred to as $[M]^+$. The calculated value for $[C_{28}H_{24}N_8O_2Co]^+$ is observed at a value of 563.1. Λ_M (DMSO) = $37\Omega^{-1}cm^2mol^{-1}$[3-5].

8.3.1.3 Synthesis and characterisation of Bis(isothiocyanato-N)(bis{2-[1-(4-methoxyphenyl)-1H-1,2,3-triazol-4-yl-kN3]pyridine-kN})]zinc(II)

IR $\bar{\upsilon}(cm^{-1})$: 3122, 3088, 2955, 2934, 2834, 2081, 1608, 1575, 1517, 1470, 1455, 1442, 1309, 1253, 1177, 1065, 1028, 1017, 1002, 983, 836, 789, 769, 720. UV-Vis (DMSO) λ_{max}: The Zn(II) complex have shown absorption bands at 257nm, ε_{max} = 57500$dm^3mol^{-1}cm^{-1}$, 288nm, ε_{max} = 38750$dm^3mol^{-1}cm^{-1}$. ^{1}HNMR data δ_H/ppm (400MHZ, DMSO-d_6): 9.25 (1H, s, H_{11}), 8.65-8.64 (1H,d, J_{HH} = 4.58Hz, H_2), 8.12-8.10 (1H, d, J_{HH} = 7.79Hz, H_5), 7.98-7.89 (3H, m, H4, Ar-$H_{13,17}$), 7.42-7.39 (1 H, dd, J_{HH} = 5.04H_3), 7.17-7.13 (2H, J= 9.16Hz, Ar-$H_{14,16}$), 3.84 (3H, s, CH_3, H_{19}); ^{13}CNMR (100.63MHZ, D_6MSO-d_6) δc/ppm: 55.62 (C_{19}), 114.81 ($C_{14,}C_{16}$ -Ar), 119.76 (C_5), 121.20 (C_{11}), 121.73 ($C_{13,}C_{17}$ -Ar) 123.38 (C_3), 129.74 (C_{12}) , 133.58 (NCS), 137.53 (C_4), 147.45 (C_7), 149.01 (C_2), 149.46 (C_6), 159.28 (C_{15}): These assignments were confirmed using DEPT ^{13}C (135°), ^{1}H-^{1}H COSY and ^{1}H-^{13}C HMQC two dimensional correlation spectroscopy. HRMS TOF (MALDI) with the highest molecular weight peak matching, observed at m/z = 626.0 (100%), is assigned to $[M\text{-}NCS]^+$. The calculated value for $[C_{29}H_{24}N_9O_2SZn]^+$ is 626.1. The crystals of the molecule

$[Zn(L^3)_2(NCS)_2]$ were obtained by slow evaporation in the hot mixture of CH_3OH: CH_3CN in a ratio of 1:2 solutions. ΛM (DMSO) = $10\Omega^{-1}cm^2mol^{-1}$ [35-37].

8.3.1.4 Synthesis and characterisation of Bis(isothiocyanato-N)(bis{2-[1-(4-methoxyphenyl)-1H-1,2,3-triazol-4-yl-kN3]pyridine-kN})]cadmium(II)

IR $\bar{\upsilon}(cm^{-1})$: 3140, 3110, 3086, 2958, 2934, 2835, 2075, 1601, 1571, 1517, 1489, 1454, 1440, 1311, 1253, 1177, 1065, 1027, 1017, 1002, 983, 838, 796, 774, 718. UV-Vis (DMSO) λ_{max}: The Cd(II) complex have shown absorption bands at 258nm, ε_{max} = $48519dm^3mol^{-1}cm^{-1}$, 288nm, ε_{max} = 36296 $dm^3mol^{-1}cm^{-1}$. NMR data (ppm), δ_H (400MHZ, D_6MSO-d_6) ^{1}HNMR data δ_H/ppm (400MHZ, DMSO-d_6): 9.22 (1H, s, H_{11}), 8.66-8.64 (1H,d, J_{HH} = 4.12Hz, H_2), 8.11-8.09 (1H, d, J_{HH} = 7.79Hz, H_5), 7.96-7.91 (4H, m, H_4, Ar-$H_{13,17}$), 7.41-7.39 (1 H, dd, J_{HH} = 5.04 H_3), 7.17-7.13 (2H, J= 9.16 Hz, Ar-$H_{14,16}$), 3.84 (3H, s, CH_3, H_{19}); ^{13}CNMR (100.63MHZ, D_6MSO-d_6) δc/ppm: 55.61 (C_{19}), 114.79 ($C_{14,}C_{16}$ -Ar), 119.72 (C_5), 121.17 (C_{11}), 121.71 ($C_{13,}C_{17}$ -Ar) 123.33 (C_3), 129.74 (C_{12}), 132.23 (NCS), 137.44 (C_4), 147.66 (C_7), 149.21 (C_2), 149.52 (C_6), 159.24 C_{18}): These assignments were confirmed using DEPT ^{13}C (135°), ^{1}H-^{1}H COSY and ^{1}H-^{13}C HMQC two dimensional correlation spectroscopy. 100%. X-ray quality white crystals were obtained by slow evaporation of hot (CH_3OH). HRMS TOF (MALDI) with the highest molecular weight peak matching, observed at m/z = 676.1 (95%), is assigned to $[M\text{-}NCS]^+$. The calculated value for $[C_{29}H_{24}N_9O_2SCd]^+$ is 676.1. The second fragment observed at 618.1(40%) is assigned to $[M]^+$. The calculated value for $[C_{28}H_{24}N_8O_2Cd]^+$ is the peak at 501.2(30%) and is attributed to$[Cd(L^3)py(NCS)]^+$. The calculated value for $[C_{20}H_{17}N_6OCdS]^+$ is observed at a value of 501.2. The peak at 422.2(15%) is attributed to $[Cd(L^3)(NCS)]^+$. The calculated value for $[C_{15}H_{12}N_9OCdS]^+$ is 422.2. Λ_M (DMSO) = 12 $\Omega^{-1}cm^2mol^{-1}$ [35-37].

8.4 Conclusion

In conclusion, new complexes with *trans*-isothiocyanato as coligands, having the general formula $[M(L^3)_2(NCS)_2]$, (where; M= Fe(II), Co(II), Zn(II) and Cd(II), and L^3 = [bis-2-(1-(4-methoxy-phenyl)-1*H*-1,2,3-triazol-4-yl)pyridine] have been successfully prepared and characterised using FT-IR, UV-Vis and fluorescence measurements, HRMS TOF (MALDI), NMR, magnetic moments, conductivity and X-ray crystallography. The structural analysis indicates that the complexes of $[Zn(L^3)_2(NCS)_2]$ and $[Cd(L^3)_2(NCS)_2]$ are rare examples of the coexistence of two *trans* – coordinated NCS^- anions in the axial position in the mononuclear triazole-based octahedral configuration. The substitution of the chlorido ligand by an isothiocyanato group in the triazole complexes in order to enhance the fluorescence of these complexes failed to produce the desired effect. This could be related to the structure of these complexes. It was noted that the above substitution had very little effect of the geometry of the complex. One major difference between the triazole structure and that found in wide band ruthenium photosensitsers such as N3 and N719 which both are efficient photosensitsers is the geometry of the isothiocyanato groups which is *trans*- in the triazole complexes studied by us and *cis*- in the ruthenium complexes investigated in the literature by Grätzel *et al* [1-2]. The ruthenium complexes have a net dipole moment with respect to the isothiocyanato groups, which is absent in the triazole complexes described here. The *cis*-geometry could result in cooperative effects in relation to the MCLT properties of the complex.

Further work to address this issue could involve the substitution of the Mn and Cd-triazole chloride complexes with ligand L^8, by an isothiocyanate group in view of the fact that the chloride complexes of these metals adopt a *cis* configuration (see Figure 8.29).

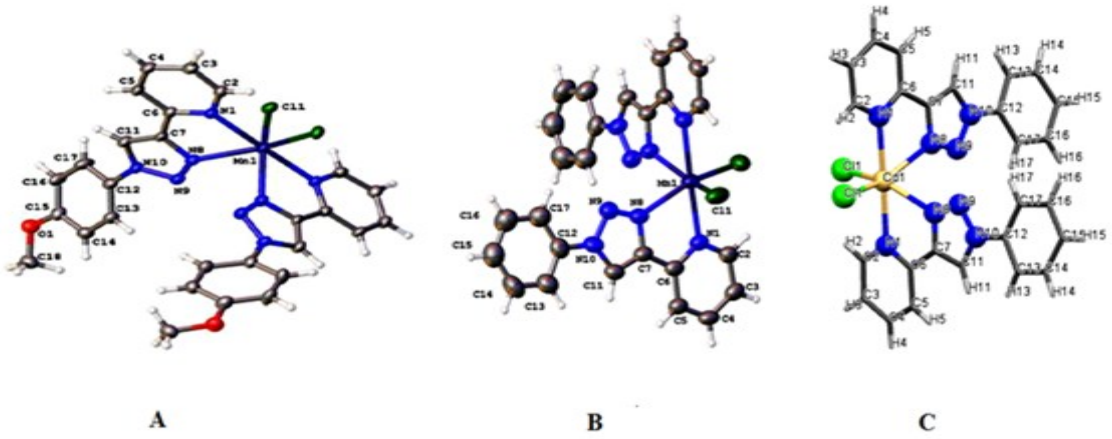

Figure 8.29: The molecular structures of cis configuration of the complexes (A) $[Mn(L^3)_2Cl_2]$, (B) $[Mn(L^8)_2Cl_2]$ and(C) $[Cd(L^8)_2Cl_2]$.

If there is a *cis* effect with respect to the properties of these complexes, then should be observe an enhancement in the fluorescence properties of these complexes with respect to their chlorido counterparts.

In summary, the click reaction has proved to be a versatile reaction for the preparation of a diverse range of *cis* and *trans* organometallic complexes as well as polymeric structures with a range of metal ions. The replacement of phenyl azide derivatives with azides prepared from known fluorescent compounds could result in the preparation of triazoles with enhanced fluorescent properties and improved solubility in organic solvents that would result in greater fluorescence, in view of the effect of solvent polarity on fluorescence and through the conjugation identified in these derivatives. The identification of triazole ligands that adopt *cis* and *trans* configurations with particular metal ions should allow us to choose appropriate transition metals and ligands to engineer photosensitsers with enhanced fluorescent properties and organic solvent solubility. The work undertaken here can contribute to the development of a new generation of low cost highly fluorescent sensitisers for investigation in dye based solar cells. The next chapter describes the evaluation of the synthesised complexes to date as potential anti-cancer agentes.

8.5 References

1-Nazeeruddin M K., De Angelis F., Fantacci S., Selloni A., Viscardi G., Liska P., Ito S., Takeru B., Grätzel M., *J. Am.Chem. Soc*., 127: 16835 (2005)

2-Nazeeruddin M K., Pe´chy P., Renouard T., Zakeeruddin S M., Baker R H., Comte P., Liska P., Cevey L, Costa E V., Shklover V., Spiccia L., Deacon G B., Bignozzi C A., Grätzel M., *J. Am. Chem. Soc.,* 123:1613(2001)

3-Zhu D R., Wang L., Jiang J J., Chen L., Shen X., Inorg. Chem. Commun. 28: 104(2013)

4-Zhu D R., Shen G P., Qi L., Xu Y., Jiang J J., Wang L., Liu X Q., You X., Dalton Trans., 42:10144(2013)

5-Nakamoto K., Infrared spectra of inorganic and coordination compounds, John Wiley-Interscience, 3rdeditionn. New York 227(1978)

6-Mukherjee A K., Guha S., Maji T K., Chaudhuri N R., *Cryst. Res. Technol*., 41:198(2006)

7-Han H., Song Y L., Hou H W., Fan Y T., Zhu Y., *J. Chem. Soc., Dalton Trans*. 1972(2006)

8-Ding B., Yi L., Wang Y., Cheng P., Liao D Z., Yan S P., Jiang Z H., Song H B., Wang H G., *J. Chem. Soc. Dalton Trans*., 665(2006)

9-Zhang J Z., Cao W R., Pan J X., Chen, Q W., *Inorg. Chem. Comm.,* 10:1360(2007)

10-Reguera E., Marin E., Calderon A., Hernandez R., *Spectrochim. Acta, Part A*.,68:191(2007)

11-Li X., Wang X W., Zhang Y H., *Inorg. Chem. Comm*.,11: 832(2008)

12-Brooker S., Hogue R W., Miller R G., White N G., Feltham H L. C., Jameson G. N L., *Chem. Commun*., 50:1435(2014)

13-Mak T C. W., Li S L., Zhang Z Z., *Inorg. Chim*. *Acta*., 268:177(1998)

14-Ahmad S., Ali S., Malik M R., Isab A A., *J. Coord. Chem*., 62:475(2009)

15-Klein C., Nazeeruddin M K., Liska P., Di Censo D., Hirata N., Palomares E., Durrant J R., Grätzel M., *Inorg. Chem*., 44:178(2005)

29-16-Pavia D. L. Lampman G. M., Kriz G. S., Introduction to spectroscopy, 3rd edition ISBN: 0-03-031961-7(2001)

17-Silverstein R M., Webster F X., Kiemle D J., Spectrometric Identification of Organic Compounds, 7th edition, Publisher: John Wiley and Sons Inc., (2005)

18-Palatinus L., Chapuis G., *J.Appl. Cryst*., 40:786(2007)

19-Rigaku Corporatiom, CrystalClear-SM Expert 2.0 r13, (2011)

20-Dolomanov O V., Bourhis L J., Gildea R J., Howard J A. K., Puschmann H., *J.Appl. Cryst*.,42:339(2009)

21-Sheldrick, G M., *Acta Cryst. Sect A*., 64:112(2008)

22-Macrae, C F., Bruno I J., Chisholm J A., Edgington P R., McCabe P., Pidcock E., Monge L R., Taylor R., van de Streek J., Wood P A., *J. Appl. Cryst*., 41:466(2008)

23-Schweinfurth D., Su C Y., Wei S C., Braunsteind P., Sarkar B., *Dalton Trans*., 41:12984(2012)

24-Kong L., Li W J., Li X L., Geng W Q., Hao F Y., Wua J Y., Zhou H P., Yang J X., Tian Y P., Jin B K., *Polyhedron*, 29:1575(2010)

25-Cundari T R., Buda C., Kazi A B., Dinescu A., *J. Chem. Inf. Model.,* 45: 965(2005)

26-Małecki J G., Machura B., Witlicka A S., *Struct. Chem*., 22:77(2011)

27-Kilpin K J., Crowley J D., *Polyhedron*, 29:3111(2010)

28-Tao J Q., GU Z G., Wang T W., Yang Q F., Zuo J L., You X Z., *Inorg. Chim. Acta*., 360:4125(2007)

29-Desiraju G. R., *Acc.Cem.Res*. 35:565(2002)

30-Meng X., Song Y., Hou H., Fan Y., Li G., Yu Zhu., *Inorg. Chem.*, 44:1306(2003)

31-Yang Y., Du P., Yang J., Kan W Q., Ma J F., *Cryst. Eng. Comm.*, 15: 4357(2013)

32-Janiak C., *J. Chem. Soc*., *Dalton Trans*., 3885(2000)

33-Urankar D., Pevec A., Turel I., Kosmrlj J., *Cryst. Growth Des.*10:4920(2010)

34-Bratsos I., Urankar D., Zangrando E., Kalou P., Kosmrlj G., Alessio J E., Turel I., *Dalton Trans.*, 40:5188(2011)

35-Geary W J., Coord. Chem. Rev., 7:81(1971).

36-Sulikowska C D., Czylkowska A., Doczekalska R., J. Therm. Anal. Cal., 71:395(2003)

37-Sulikowska C D., Czylkowska A., J. Therm. Anal., Cal., 76: 543(2004)

Chapter 9 : BIOLOGICAL AND MEDICINAL EVALUATION OF METAL-LIGAND COMPLEXES

9.1 Introduction

Since compounds similar to the ones synthesised in this investigation were reported in literature to show medicinal properties [1, 2], it was decided to conduct a preliminary assessment of the potential biological activity of selected compounds produced in the first part of this thesis. Potential anti-cancer properties could open lucrative applications of such compounds and extend their applications to areas wider than possible dye solar cell compounds. This part of the work was carried out at the University of Salford under supervision of Dr Ragazzon.

9.2 Human cell Lines

The antitumor screenings were carried out on two human tumour cell lines, HepG2: Hepatoma Cells (hepatic carcinoma from a 15 years old child) (Cyprotex) and HCT116: Colorectal Cancer Cell (gift from KidsCan).

9.3 Materials and experimental methods

RPMI sterile media, PBS (sterile phosphate buffer), FBS (foetal bovine serum) and sterile plastic ware were obtained from Fisher UK. NEAA (non-essential aminoacids), L-glutamine, trypsin, chlorpromazine and streptomycin/penicillin were obtained from Sigma-Aldrich UK. MTT was obtained from Alfa-Aesar UK. Pipettes and tips were obtained from Anachem UK.

9.3.1 Methods

9.3.2.1 MTT Assay

In 1983, Mosmann developed the MTT assay (3-(4,5-dimethylthiazol-2-yl)-2,5-diphenyl tetrazolium bromide assay) and is a method of measuring the survival of mammalian cells, in which the yellow 3-(4,5-dimethylthiazol-2-yl)-2,5-diphenyl tetrazolium bromide (MTT) is reduced to the purple formazan in living cells (Scheme 9.1) [3, 4]. In metabolically active cells, MTT is reduced by the mitochondrial enzyme succinate dehydrogenase to form insoluble formazan crystals that are subsequently solubilised, and the optical density (OD) measured spectrophotometrically. This method is commonly used to illustrate inhibition of cellular proliferation. The absorbance of this coloured solution can be quantified by measuring at a certain wavelength (usually between 500 and 600 nm) by a scanning multi-well spectrophotometer [5-8].

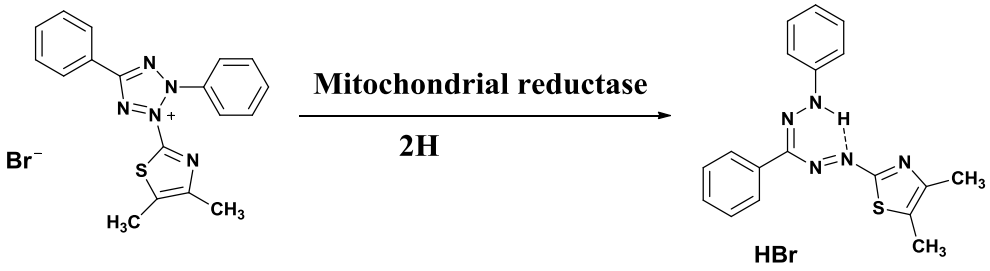

(MTT yellow) **(MTT Fromazan purple)**

Scheme 9.1: Chemical structure of MTT and its reduced formazan product

The MTT assay is a cell-based assay often used for screening collections of compounds to determine if the test molecules have effects on cell proliferation or show direct cytotoxic effects that eventually lead to cell death. The MTT (3-(4,5-dimethylthiazol-2-yl)-2,5-diphenyltetrazolium bromide) tetrazolium reduction assay was the first homogeneous cell survival assay developed for a 96-well format that was suitable for high throughput screening (HTS) [9]. The MTT substrate is prepared in a physiologically balanced solution, added to cells in culture and incubated. The quantity of formazan (presumably directly proportional to the number of viable cells) is measured by recording changes in absorbance at 570 nm using a plate reading spectrophotometer. A reference wavelength of 630 nm is sometimes used, but is not

necessary for most assay conditions. Viable cells with active metabolism convert MTT into a purple coloured formazan product with an absorbance maximum near 570 nm. When cells die, they lose the ability to convert MTT into formazan, thus colour formation serves as a useful and convenient marker of only the viable cells. The exact cellular mechanism of MTT reduction into formazan is not well understood, but likely involves reaction with NADH or similar reducing molecules that transfer electrons to MTT [10].

The formazan product of the MTT tetrazolium accumulates as an insoluble precipitate inside cells as well as being deposited near the cell surface and in the culture medium. The formazan must be solubilised prior to recording absorbance readings. The amount of signal generated is dependent on several parameters including: the concentration of MTT, the length of the incubation period, the number of viable cells and their metabolic activity. All of these parameters should be considered when optimizing the assay conditions to generate a sufficient amount of product that can be detected above background levels [9].

The conversion of MTT into formazan by cells in culture is time dependent. Longer incubation time will result in accumulation of colour and increased sensitivity up to a point. However, the incubation time is limited because of the cytotoxic nature of the detection reagents which utilize energy (reducing equivalents such as NADH) from the cell to generate a signal [9]. For cell populations in a log phase growth, the amount of formazan product is generally proportional to the number of metabolically active viable cells.

Chlorpromazine, a DNA intercalating agent with antipsychotic properties, was used as positive controls to assess the assays have worked. DMSO and media were used as negative controls [11].

9.3.2.2 Cells and cell culture conditions

For cytotoxicity determination, two different human cancer cell lines were used: HCT116 (colorectal cancer cells, gift from KidsCan) and HepG2 (hepatoma cells, gift from Cyprotex). Cell culture media and reagents were purchased from Fisher scientific, UK. Cells were grown as an adherent monolayer culture in 75cm^2 flasks in

RPMI 1640 medium supplemented with 10%, heat inactivated foetal bovine serum, 1% v/v nonessential amino acids (from 100× ready-to-use stock), 2mM L-glutamine and 115 units/mL of penicillin G, 115 μg/mL of streptomycin at 37 °C under a humidified atmosphere containing 5% CO_2 and 95% air.

9.3.2.3 IC_{50} determination:

A total of 15 compounds were chosen for IC_{50} determination based on the screening at single high dose results, and structural variation between the synthesised compounds in order to get more in depth information about the structural activity relationship. The selected compounds were tested at a range of concentrations (20, 10, 5, 2.5, 1.25, 0.625μM) on two different cancer cell lines (HepG2 and HCT116), and cell death percentage was determined by the colorimetric MTT [3-(4,5-dimethyl-2-thiazolyl)-2,5-diphenyl-2H-tetrazolium bromide] micro-culture assay. HCT and hepG2 cancer cell lines were chosen because they are the third most prevalent cancer in the UK. Cells were detached from the 75cm^2 flasks (at a confluence of 70%) by trypsinisation, seeded in 100μL aliquots into 96-well clear micro-culture plates. Cell densities of 3.0×10^3 cells/well for 72 hours of incubation, were chosen in order to ensure exponential growth of untreated controls throughout the experiment. Cells were allowed to adhere into the 96-well micro-culture plate for 24 hours prior to dosing. Stock solutions of the test compounds in DMSO were appropriately diluted in complete culture media to make up the required concentrations, and then added in 25μL aliquots into the 96-well micro-culture plate. Cells were exposed to the test compounds for 72 hours. Plates were maintained at 37°C in a humidified atmosphere containing 95% air and 5% CO_2. At the end of the incubation period 30μL/well MTT solution in phosphate-buffer (3 mg/mL) were added, and then incubated for further 3 hours. After the end of the incubation, the supernatants containing medium and MTT were removed and the formazan crystals formed by viable cells were dissolved in 100μL of DMSO per well. Optical densities at λ = 540 nm were measured with a LUMIistar Omega multi-mode plate reader. The colorimetric MTT assay was used to determine the cell death percentage at serial diluted concentration of the tested compounds (range of concentrations 20-0.625μM), and the IC_{50} (the concentration at which 50% of cell growth was inhibited as compared to the control wells which did not contain any drug) was determined from dose response curve using OriginPro 9.1 data analysis and graph software [12].

9.4 Results and discussion

9.4.1 Results of screening for anticancer activity at single high dose 100μM using the effect of the ligand nature on the (R) group substitutes in HepG2 and HCT116 cancer cell Lines

Experiments were performed in duplicates as a proof of concept and to obtain statistical errors. More number of experiments is needed to establish the results. Only the ligands and the complexes were screened. It is necessary to screen the metal chlorides too in order to complete the control experiments. The *in-vitro* of activity of 60 compounds (free ligands (L^2-L^9) and their metal complexes), were investigated against liver carcinoma (HepG2) and colon carcinoma (HCT116). In this study, a family of neutral bidentate 1,4-substituted pyridyl-1,2,3-triazole-phenyl ligands with pendent phenyl functional groups, was included, bearing different substituents on the phenyl-triazole moieties by using various (R) groups with different substituents such as electron withdrawing and electron donating (L^2-L^9) ligands, Scheme 9.2.

Where:

$L^2 = CH_3$,

$L^3 = OCH_3$,

$L^4 = COOH$,

$L^5 = F$,

$L^6 = Cl$,

$L^7 = CN$,

$L^8 = H$ and

$L^9 = CF_3$

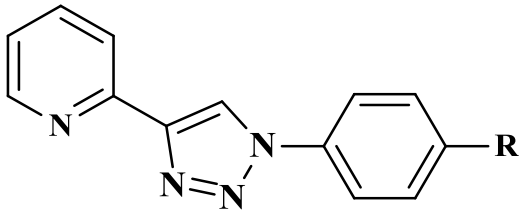

Scheme 9.2: The chemical structure of the ligands L^2-L^9.

In these complexes, Metal = Mn(II), Fe(II), Co(II), Ni(II), Cu(II), Zn(II), Cd(II) and Pt(II). The compounds were screened and evaluated for their cytotoxicity activity, after a period of time ranging from 24 and 72 hr of incubation at 100μM concentration. It was observed that all free ligands are non-toxic with an order of activity classified as: CN > COOH > H > CF3 > Cl > CH_3> OCH_3> F. The collected data is summarised in Table 9.1. It was found that the metal complexes exhibited variable cytotoxicity. The preliminary results show the significance of the presence of the metal, especially Co(II) and Cu(II), for coordination topyridyl-1,2,3-triazole. It was observed that (11) compounds displayed higher levels of cytotoxicity than the control, having cell

survival rate less than 20%. Only a few compounds exhibited cell survival rates of less than 10%. Tables and Figures are presented in the Appendix 3. When the survival is higher than 100%, it can mean:

1) The compound can stimulate growth
2) There is the possibility of contamination by bacteria in the well

As the testing was also performed at different times (data not shown), and growth was not observed it can be safely assumed there was a contamination in that particular well.

*SD: Standard deviation obtained from 2 replicates

N=2 Screening was performed as high-throughput and then active compounds taken for further assessment.

Table 9.1: *In-vitro* cytotoxicity of the ligands (L^2-L^9) against HepG2 and HCT116 human cancer cells (represented the cell survival rate after exposure to 24 and 72 hours) at 100 µM concentrations, respectively.

Compound code (100 µM)	% cell survival HepG2 24 hr	*SD	% cell survival HepG2 72 hr	*SD	% cell survival HCT116 24 hr	*SD	% cell survival HCT116 24 hr	*SD
Control	100	0.03*	100	0.07*	100	0.06*	100	0.24*
L2	64.1	0.06	173.1	0.05	69.2	0.08	118.6	0.06
L3	65.1	0.10	176.8	0.03	76.0	0.03	108.2	0.08
L4	47.7	0.00	151.5	0.04	62.8	0.03	92.3	0.05
L5	78.6	0.01	175.2	0.02	72.8	0.06	124.5	0.04
L6	61.7	0.02	195.7	0.05	67.4	0.03	94.5	0.02
L7	44.3	0.08	141.8	0.03	57.4	0.06	77.6	0.02
L8	53.4	0.09	137.2	0.04	71.9	0.00	93.6	0.14
L9	59.6	0.12	136.6	0.07	71.0	0.07	90.3	0.12

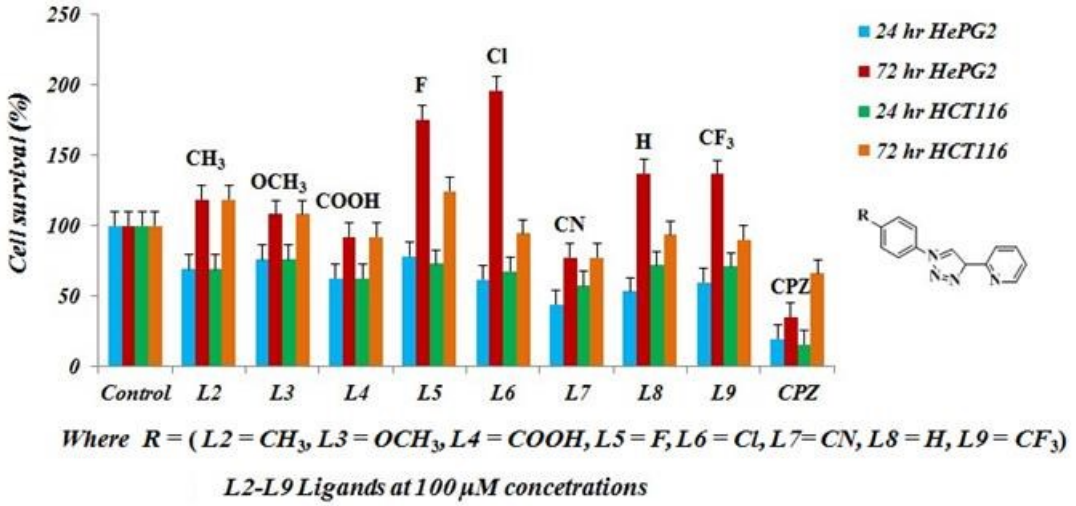

Figure 9.1: *In-vitro* cytotoxicity of the ligands (L^2-L^9) and chlorpromazine against HepG2 and HCT116 human cancer cells at various exposure time of 24 and 72 h.

9.4.2: Results of screening for anticancer activity at single high dose 100µM using colon carcinoma (HepG2) cell lines.

In general, new drugs are expected to have an IC_{50} lower than 20µM before taking them for chemical optimisation; as our initial panel included 60 compounds, it was decided a one top concentration of 100µM as cut off would give us an indication if there was any compound worth taking it forward. It is noticeable that after the complexation between the metal ions with different ligands, the compounds CoL3-2, CoL6-2, CoL7-2, CoL8-2, CuL2-2, CuL8-2 and CuL9-2 displayed cell survival rates of less than 20%, while CoL8-2, CoL9-2, CuL2-2 and CuL9-2 exhibited cell survival rates of less than 10%. The compounds with metal ions Co(II) and Cu(II) showed stronger cytotoxicity, and the improvement of anti-proliferation activity by metal complexes can be attributed to an increased in the lipophilicity. Therefore, they can infiltrate into the cells more easily [13]. Tables 9.2- 9.3 and Figures 9.2-9.3, revealed the order of cytotoxicity at 72 hours on HepG2 to be CuL9-2 > CuL2-2 > CoL6-2 > CoL3-2 > CoL8-2 > CoL7-2.

Table 9.2: *In-vitro* cytotoxicity of Co(II) complex with ligands (L^2-L^9) against HepG2 and HCT116 human cancer cells (represented the cell survival rate after exposure to 24 and 72 hours) at 100 µM concentrations, respectively.

Compound code (100 µM)	% cell survival HepG2 24 hr	*SD	% cell survival HepG2 72 hr	*SD	% cell survival HCT116 24 hr	*SD	% cell survival HCT116 24 hr	*SD
Control	100	0.03*	100	0.07*	100	0.06*	100	0.24*
CoL2-2	19.4	0.03	30.9	0.02	15.6	0.04	86.8	0.05
CoL3-2	15.0	0.01	14.1	0.02	22.6	0.10	4.7	0.02
CoL4-2	49.7	0.08	142.8	0.05	66.0	0.08	60.6	0.09
CoL5-2	18.4	0.01	65.9	0.14	11.9	0.02	18.6	0.07
CoL6-2	10.3	0.00	10.8	0.03	5.9	0.01	5.3	0.00
CoL7-2	15.4	0.00	15.5	0.01	11.6	0.01	43.2	0.03
CoL8-2	8.1	0.00	15.5	0.00	22.3	0.07	3.7	0.00
CoL9-2	9.7	0.00	133.7	0.06	46.4	0.15	20.7	0.20

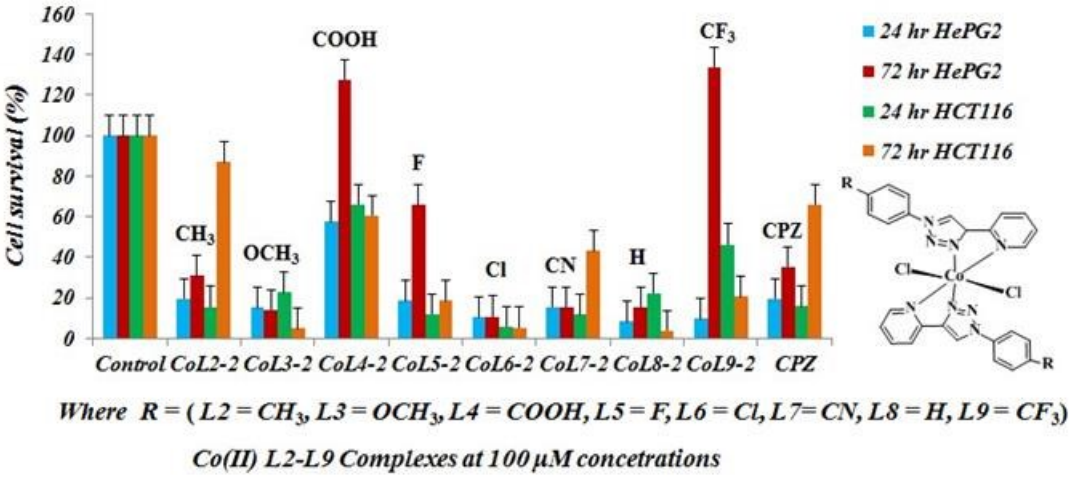

Figure 9.2: Cell survival rate of the Co(II) complex with ligands (L^2-L^9) and chlorpromazine tested on the cell lines HepG2 and HCT116 after exposed for 24 and 72 h.

Table 9.3: *In-vitro* cytotoxicity of Cu(II) complex with ligands (L^2-L^9) against HepG2 and HCT116 human cancer cells (represented the cell survival rate after exposure to 24 and 72 hours) at 100 µM concentrations, respectively.

Compound code (100 µM)	% cell survival HepG2 24 hr	*SD	% cell survival HepG2 72 hr	*SD	% cell survival HCT116 24 hr	*SD	% cell survival HCT116 24 hr	*SD
Control	100	0.03*	100	0.07*	100	0.06*	100	0.24*
CuL2-2	12.7	0.01	8.5	0.00	6.5	0.00	2.2	0.00
CuL3-2	49.5	0.06	167.7	0.04	70.4	0.01	100.2	0.05
CuL4-2	41.7	0.05	160.7	0.04	45.0	0.05	90.1	0.02
CoL5-2	18.4	0.01	65.9	0.14	5.6	0.01	3.1	0.00
CuL6-2	32.1	0.02	79.0	0.05	38.4	0.04	21.9	0.00
CuL7-2	31.9	0.03	93.1	0.14	40.3	0.03	21.8	0.05
CuL8-2	13.9	0.01	121.1	0.11	8.9	0.00	17.5	0.16
CuL9-2	9.5	0.00	7.7	0.00	4.8	0.01	1.9	0.00

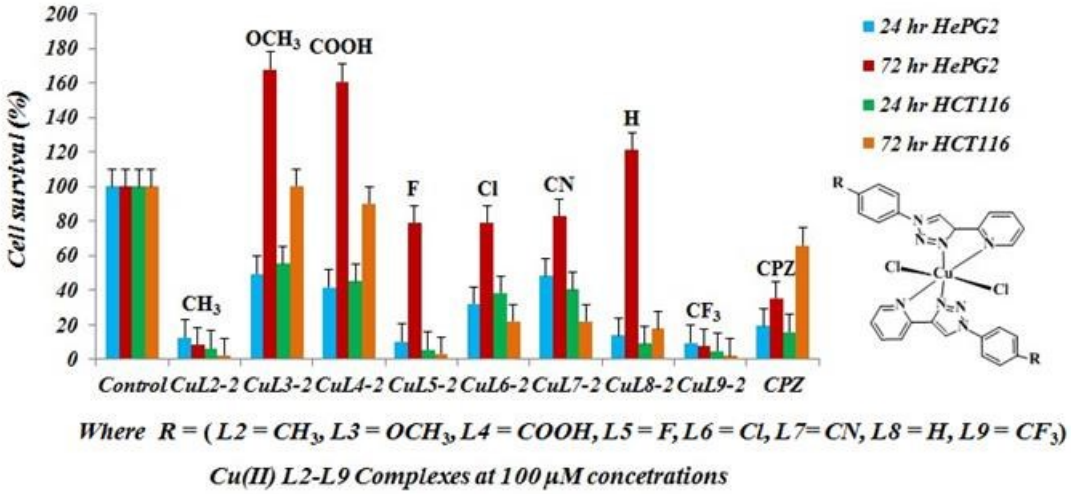

Figure 9.3: Cell survival rate of the Cu(II) complex with ligands (L^2-L^9) and chlorpromazine tested on the cell lines HepG2 and HCT116 after exposed for 24 and 72 h.

9.4.3: Results of screening for anticancer activity at single high dose 100μMusing colon carcinoma (HCT116) cell lines.

In colon carcinoma (HCT116) cell line it was observed CoL3-2, CoL5-2, CoL6-2, CoL8-2, CuL2-2, CuL5-2, CuL8-2 and CuL9-2 are more effective on HCT116. The compounds CoL5-2 and CuL8-2have cell survival rates of less than 20%. While the compounds CoL3-2, CoL6-2, CoL8-2, CuL2-2, CuL5-2 and CuL9-2 exhibited cell survival rates below 10%. CoL9-2, CuL2-2, CoL5-2 and CoL6-2 were showed to be more effective on this cell line. The copper complex of the ligand L^9 having (trifluoride carbon) group and with code CuL9-2 displays higher cytotoxicity than other the copper and cobalt analogues complexes.

9.4.4: Results of screening for anticancer activity at single high dose 100μM concentrations on the liver carcinoma (HepG2) and colon carcinoma (HCT116) cell lines.

Interesting discoveries came from the analysis, which indicate a preference for the colon cancer cell line in order of activity as follows: CuL9-2 > CuL2-2 > CuL5-2 > CoL6-2, while on hepatic cancer cell line the order for activity is: CuL9-2 > CuL2-2 > CoL6-2 > CoL8-2.

9.4.5 The influence of different metal ions on one particular ligand and how this impacts on the cell viability

In the metal 1,4-substituted pyridyl-1,2,3-triazole-phenyl complexes, besides the central metal ion, pyridyl-1,2,3-triazole-phenyl platform plays a key role in determining the biological activities. The most effective complexes on liver carcinoma (HepG2) and colon carcinoma (HCT116) are CoL6-2 and CuL9-2. These results are displayed in Figures 9.4 - 9.5 and Tables 9.4 - 9.5. The rest of the Figures and Tables for other complexes are presented in the Appendix 3.

Table 9.4: *In-vitro* cytotoxicity of ligand (L^6) and their complexes against HepG2 and HCT116 human cancer cells (represented the cell survival rate after exposure to 24 and 72 h.

Compound code (100 µM)	% cell survival HepG2 24 hr	*SD	% cell survival HepG2 72 hr	*SD	% cell survival HCT116 24 hr	*SD	% cell survival HCT116 24 hr	*SD
Control	100	0.03*	100	0.07*	100	0.06*	100	0.24*
MnL6-2	51.2	0.15	84.6	0.02	45.5	0.10	37.4	0.14
FeL6-2	64.5	0.10	138.1	0.03	55.0	0.05	37.2	0.07
CoL6-2	10.3	0.00	10.8	0.03	5.9	0.01	5.3	0.00
NiL6-2	64.3	0.12	132.5	0.02	57.5	0.02	76.8	0.21
CuL6-2	32.1	0.02	79.0	0.05	38.4	0.04	21.9	0.00
ZnL6-2	47.5	0.05	51.4	0.03	65.7	0.03	13.1	0.02
CdL6-2	46.1	0.08	98.5	0.05	38.2	0.02	42.5	0.16
PtL6-2	33.8	0.01	144.7	0.01	65.1	0.10	72.0	0.08

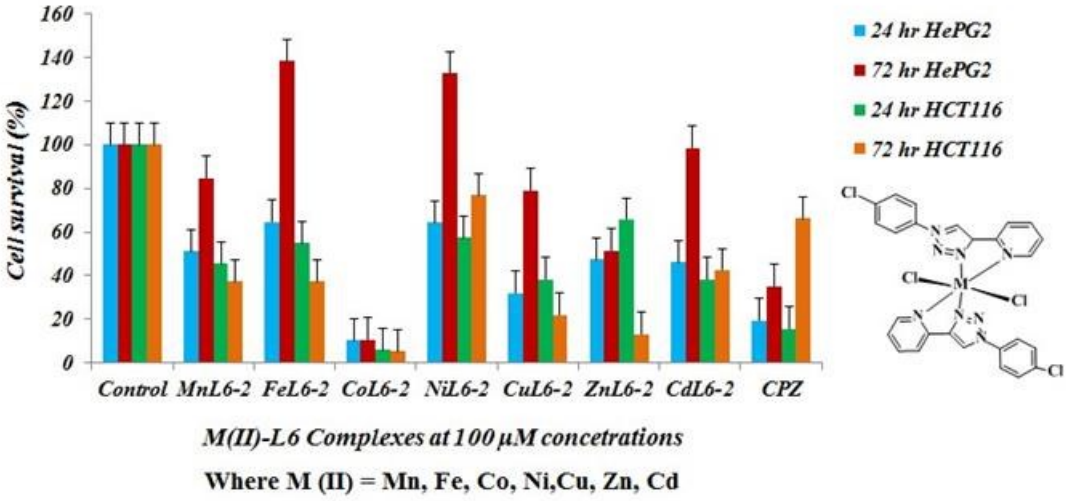

Figure 9.4: Cell survival rate of the metal(II) complexes with ligands (L^6) and chlorpromazine tested on the cell lines HepG2 and HCT116 after exposed for 24 and 72 h.

Table 9.5: *In-vitro* cytotoxicity of ligand (L^9) and their complexes against HepG2 and HCT116 human cancer cells (represented the cell survival rate after exposure to 24 and 72 h.

Compound code (100 µM)	% cell survival HepG2 24 hr	*SD	% cell survival HepG2 72 hr	*SD	% cell survival HCT116 24 hr	*SD	% cell survival HCT116 24 hr	*SD
Control	100	0.03*	100	0.07*	100	0.06*	100	0.24*
MnL9-2	60.7	0.14	50.8	0.01	69.1	0.02	55.2	0.33
FeL9-2	56.8	0.13	55.3	0.03	69.9	0.07	12.5	0.03
CoL9-2	9.7	0.00	133.7	0.06	46.4	0.15	20.7	0.20
NiL9-2	42.3	0.00	173.1	0.03	57.9	0.07	41.1	0.15
CuL9-2	9.5	0.00	7.7	0.00	4.8	0.01	1.9	0.00
ZnL9-2	40.8	0.08	147.0	0.09	50.8	0.02	59.9	0.15
CdL9-2	47.5	0.09	92.7	0.03	53.1	0.01	33.4	0.09

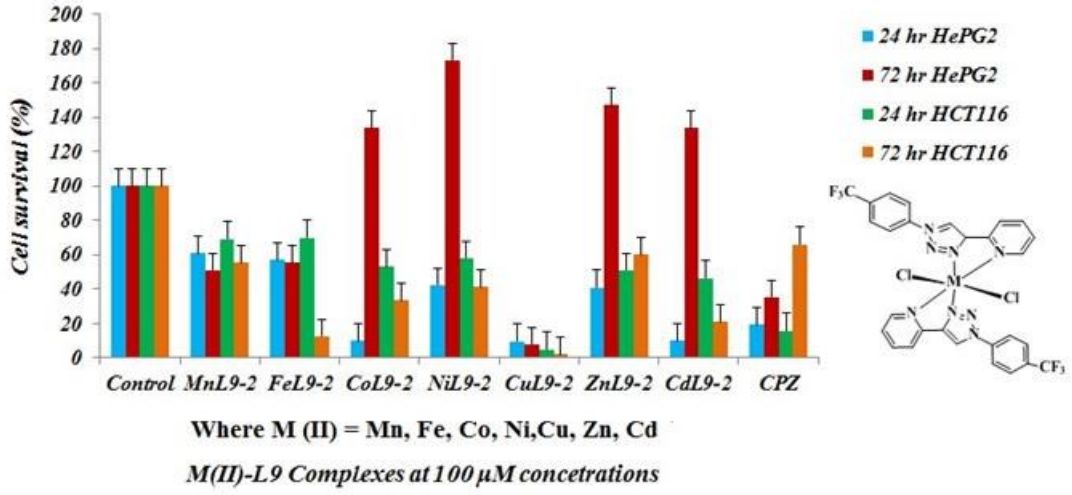

Figure 9.5: Cell survival rate of the metal(II) complex with ligands (L^9) and chlorpromazine tested on the cell lines HepG2 and HCT116 after exposed for 24 and 72 h.

9.4.6 The IC_{50} measurements of selected compounds on HepG2 cell lines at 72 hours of incubation

From the results of the first screening at 100 µM concentrations 14 compounds were selected: CoL2-2, CoL3-2, CoL5-2, CoL6-2, CoL7-2, CoL8-2, CoL9-2, $Co(L3)_2(NCS)_2$, CuL2-2, CuL3-2, CuL5-2, CuL6-2, CuL7-2, CuL9-2 and were tested for their IC_{50} levels. The IC_{50} represents the lowest concentration of a drug or chemical that is required for 50% inhibition under the experimental conditions; in other words, it is a measure of the effectiveness of a substance in inhibiting a specific biological or biochemical function [14]. The selected compounds were incubated at a range of concentration at 37ºC and 5% CO_2 for 72 hours. The data was plotted into Origin V9.1 using a dose-dependent equation to determine the IC_{50} values, Table 9.6.

Table 9.6: Cytotoxicity of pyridyl-triazole complexes on HepG2 cell lines at 72 hours of incubation.

Compounds	IC_{50} µM (*SD onHepG2)
CoL2-2	>20
CoL9-2	>20
[Co(L3)2 (NCS5)2]	>20
CoL3-2	>20
CoL5-2	>20
CoL7-2	>20
CoL6-2	2.45
CoL8-2	>20
CuL6-2	>20
CuL7-2	>20
CuL5-2	>20
CuL9-2	>20
CuL2-2	>20
CuL3-2	>20
Chlorpromazine	11.94

*SD: Standard deviation obtained from 2 replicates and obtained through Origin V9.1.

From the values in Table 9.6 it is clear that the majority of the tested compounds had an IC_{50}>20 µM after 72 hours of incubation, while a single compound (CoL6-2) having chlorine on the pendent phenyl arm connected to the triazole ring showed excellent cytotoxic activity towards HepG2 (IC_{50} = 2.45µM). The chemical structure for the complex (CoL6-2) is presented in Figure 9.6.

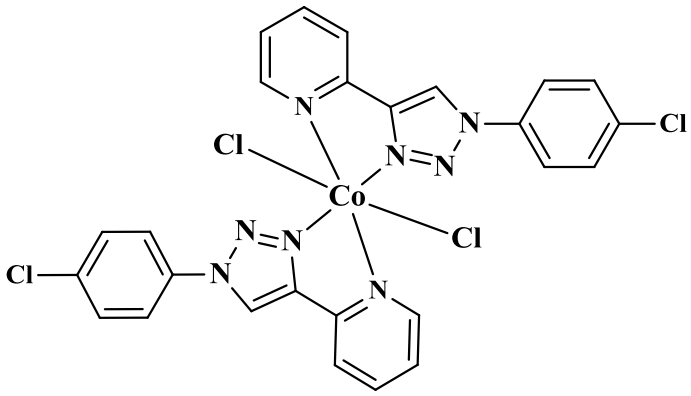

Figure 9.6: The chemical structure of the complex (CoL6-2).

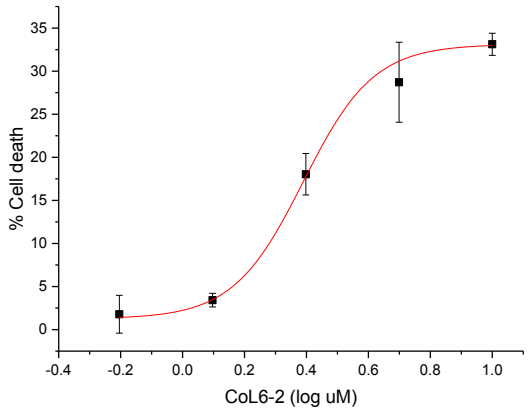

Figure 9.7: *In-vitro* cytotoxicity effects of complex CoL6-2 against human hepatic cancer cell line (HepG2) after 72 hours of incubation.

9.4.7 The IC_{50} measurements of selected compounds on HCT116 cell lines at 72 hours of incubation

CoL2-2, CoL3-2, CoL5-2, CoL6-2, CoL7-2, CoL8-2, CoL9-2, $Co(L3)_2(NCS)_2$, CuL2-2, CuL3-2, CuL5-2, CuL6-2, CuL7-2, CuL9-2) were screened for IC_{50} determination on HCT116. The results of this screening are summarised in Table 9.7. The compounds CoL2-2, $Co(L3)_2(NCS)_2$, CoL3-2, CoL5-2, CoL7-2, CuL2-2, CuL7-2 all had an IC_{50}>20 μM after 72 hours in incubation, while CoL6-2, CoL8-2, CoL9-2, CuL3-2, CuL5-2, CuL6-2, CuL9-2 demonstrated variable values of IC_{50} due to the different substituents on the phenyl-triazole moieties. The complex CuL5-2 (fluoride on the pendent phenyl arm connected to the triazole ring) displayed excellent cytotoxic activity toward HCT116 with an IC_{50} value of 0.0092 μM, CuL3-2 (methoxy) exhibited an IC_{50} value of 2.48 μM, CuL9-2 (trifluoride carbon) showed an IC_{50} value of 5.09 μM (Figure 9.9), and lastly the CuL6-2 (chloride) showed an IC_{50} value of 10.08 μM. The IC_{50} values of the cobalt complexes could be arranged in the order of: CoL6-2 (chloride) displayed IC_{50} value of 4.64 μM Figure 9.10 and CoL9-2 (trifluoride carbon) with IC_{50} value of 5.03 μM. The chemical structures of these complexes are presented in Figure 9.8.

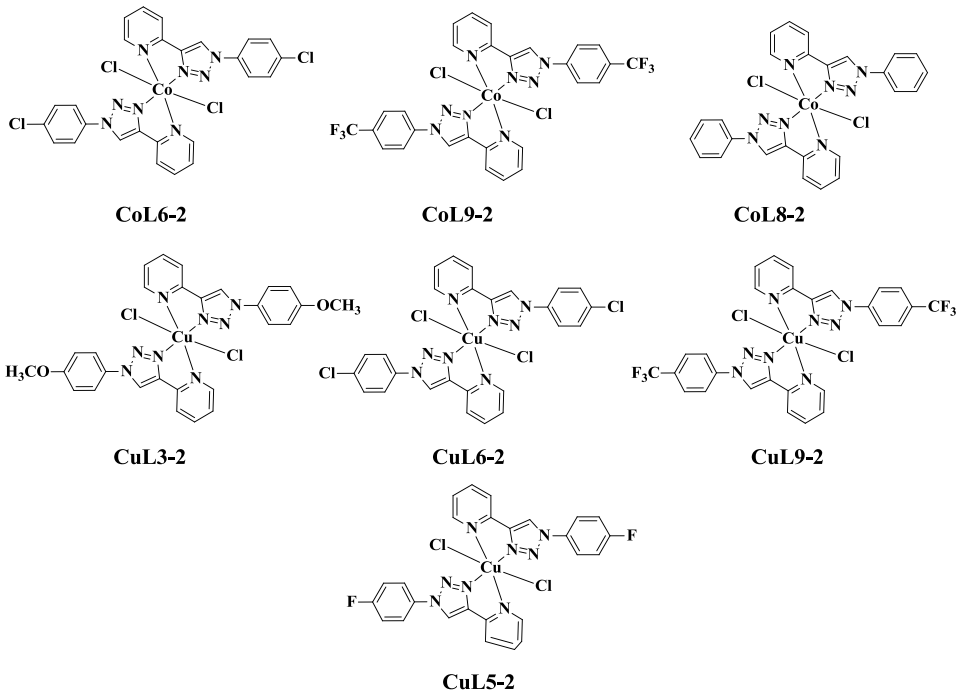

Figure 9.8: The chemical structures of the complexes (CoL6-2, CoL9-2, CoL8-2 CuL3-2, CuL5-2, CuL6-2 and CuL9-2).

Table 9.7: Cytotoxicity of pyridyl-triazole complexes on HCT116 cell lines at 72 hours of incubation.

Compounds	IC_{50} µM (*SD <5%) on HCT 116
CoL2-2	>20
CoL9-2	5.03
$[Co(L3)_2 (NCS5)_2]$	>20
CoL3-2	>20
CoL5-2	>20
CoL7-2	>20
CoL6-2	4.64
CoL8-2	3.18
CuL6-2	10.08
CuL7-2	>20
CuL5-2	0.0092
CuL9-2	5.09
CuL2-2	>20
CuL3-2	2.48
Chlorpromazine	14.31

*SD: Standard deviation obtained from 2 replicates and obtained through Origin V9.1.

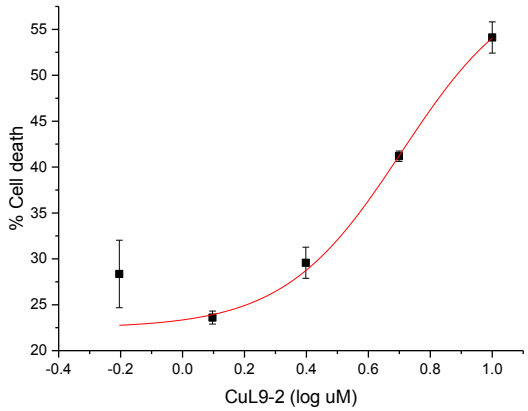

Figure 9.9: *In-vitro* cytotoxicity effects of complex CuL9-2 complex against human colon cancer cell line (HCT116) at 72 hour of incubation.

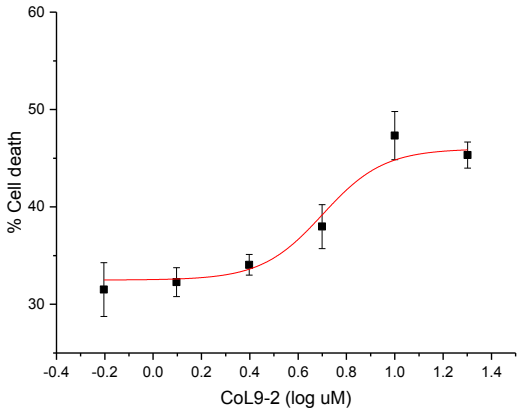

Figure 9.10: *In-vitro* cytotoxicity effects of complex CoL6-2 complex against human colon cancer cell line (HCT116) at 72 hour of incubation.

9.5 Conclusion

It was observed the free ligands are non-toxic towards the tested cell lines and the insertion of metal leads to considerable cytotoxicity. The study clearly indicates that the insertion of metal into a non-toxic pyridyl-triazole-phenyl moieties ligands functional group imparts cytotoxic activity to the compound. Among all these complexes the copper and cobalt complexes are the most effective.

Upon analysis of the activities of all compounds on both cell lines representing hepatic and colon cancers, it was found the colon carcinoma HCT116 was more sensitive, therefore it can speculate the compounds are more active on colon cancer. From the detailed analysis of IC_{50} values it was discovered the compounds CoL6-2, CoL8-2, CoL9-2, CuL3-2, CuL5-2, CuL6-2, CuL9-2, were active on both cell lines but showing a marked preference for colon carcinoma HCT116.

The compound (CoL6-2) showed a preference for HepG2, implying the compound has selectivity for hepatic cancer over colon cancer. The compounds CoL8-2, CoL9-2, CuL3-2, CuL5-2, CuL6-2 and CuL9-2 have preference for the colon carcinoma HCT116 instead of the hepatic carcinoma. This selectivity can also imply the possibility of choosing one type of cancer, this can be extrapolated to assume in the case of CoL6-2, this theoretical treatment would target hepatic cancers but would not affect the intestine epithelial with less side effects for a treatment course. Also any derivatives based on compounds CoL5-2, CoL8-2, CuL5-2 and CuL8-2 would target

the colon carcinoma but would not affect the liver, which is generally a problem with chemotherapy.

This difference could be based on compounds binding on targets that only appear on one cell line and not in both, as well as different metabolic functions in both types, in which the compounds could be activated or inactivated.

In further work, the compounds CoL8-2, CuL8-2, CoL9-2, CoL5-2, CuL3-2, CuL5-2, CoL6-2, CuL6-2 and CuL9-2should be studied for:

- Metabolism, using hepatic enzymes in first instance, to see if there is any modification to the structure.
- Toxicity in primary hepatic and colon cells.
- Target validation through cell cycle analysis and fluorescence microscopy to determine the mode of action on both tumour and primary cells.
- The compounds (CoL6-2 the lowest IC_{50} of Hepg2 and CuL5-2 the lowest IC_{50} of HCT116) could be taken as hits to explore further modifications to improve the anticancer activities.
- Synthesis and characterisation of ruthenium complexes with theses ligands for studying the biological activities on liver carcinoma (HepG2) and the colon carcinoma (HCT116).

As mentioned earlier, it is necessary to screen the metal chlorides too in order to complete the control experiments. In further work with the selected compounds from IC_{50} tests, it is recommended to assess the physico-chemical properties including pKa, lipophilicity and solubility. As the complexes can exhibit photodynamic properties when exposed to certain wavelengths, it is recommended to assess the complexes in different cell lines whilst exposed to light, to determine if the toxicity increases (IC_{50} would decrease).

The investigation into the potential anti-cancer properties of the compounds initially intended simply as dye solar cell possibilities, open a new and exciting area of application and further exploration of these synthesised complexes. It also demonstrates the well-known experience of many researchers that one often discovers different applications and uses for compounds initially intended for other purposes if

one is willing to experiment think laterally and is aware of chemical similarities between different metal complexes. This latter part of the thesis work is most satisfying in the unexpectedly positive results it yielded.

9.6 References

1-Crowley J D., Bandeen P H., Hanton L R., *Polyhedron*, 29:70(2010)

2-Byrne J P., Kitchen J A. Kotova O, Leigh, V, Bell A P., Boland J J., Albrechtb., Gunnlaugsson T h., *Dalton. Trans*., 43:196(2014)

3-Mosmann T., *J. Immunol. Meth*., 1983, 65, 55.

4-Lillie R D., H. J. Conn's Biological Stains., Willians and Wilkins, Baltimore, 1977

5-J C. Stockerta∗., A B Castro., Magdalena Canete., Horobinb R W., Villanuevaa Á., *Acta. Histochemica*., 114:785(2012)

6-Slater, T F., Sawyer B., Strauli U D., *Biochem. Biophys. Acta*., 77:383(1963)

7-Van de Loosdrecht., Beelen R H., Ossenkoppele G J., Broekhoven M G., Langenhuijsen M M A C., *J. Immunol. Meth*., 174:311(1994)

8-Alley MC., Scudiero D A., Monks A., Hursey M L., Czerwinski M J., D L. Fine, Abbott B J., Mayo J G., Shoemaker R H., Boyd M R., *Cancer. Res*., 48: 589-601, 1988.

9-Riss T L., Moravec R A., Niles A L., Benink H A., Worzella T J., Minor L., (2013). *Cell Viability Assays. Assay Guidance Manu al* [Internet]. Bethesda (MD): Eli Lilly & Company and the National Centre for Advancing Translational Sciences; 2004. Available: http://www.ncbi.nlm.nih.gov/books/NBK144065

10-Marshall N J., Goodwin, C J., Holt S J., *Growth. Reg*., 5:69(1995)

11-Y H Lee., Shin S Y., Lee K S., Y K Choi., Lim H J., Lee H G., Lim Y g., *Carcinogenesis*., 34:2089(2080)

12-Seifert, E., Origin Pro 9.1: Scientific Data Analysis and Graphing Softwar Software Review: *J. Chem. Info. Mod*., 54:1552(2014)

13-Deepthi S B., Trivedi R., Sujitha P., Kumar C G., Sridhar B., Bhargava S K., *J.Chem. Sci*., 124: 1405(2012)

14-Nalbantsoy A., Yavasoglu NU K., Sayım F., Gurhan I D., Gocmen B., Arıkan H ., Yildiz MZ.,*J. Venom. Anim. Toxins., Incl. Trop. Dis*., 18:208(2012)

Chapter 10 : Conclusions, Recommendations and Contributions

10.1 Conclusions

A series of bi-dentate 2-pyridyl-1,2,3-triazole ligands bearing a 4-substituted phenyl arm using a simple cycloaddition reaction (an example of click chemistry). were successfully synthesised. Furthermore, it has been demonstrated that different functional groups (electron rich and withdrawing substituents) on the triazole heterocycle affect the electronic properties of the triazole moiety and the formation of metal complexes. In particular, direct connection at the N8 position of the triazolyl ring of a 4-substituted phenyl group has a significant influence on the geometry of both the ligands and their corresponding M-complexes. First row transition metal complexes (Mn(II), Fe(II), Co(II), Ni(II), Cu(II), Zn(II) and Cd(II)) were synthesised due their availability and cost effectiveness as alternative solar dyes compared to the popular ruthenium metal. During the characterisation and structural studies of the complexes it was found that $[M(L^3)_2(Cl)_2]$ type complexes show a rare example of the coexistence of two *trans* coordinated Cl anions in the axial position or *cis* position in the mononuclear triazole-based octahedral configuration. The fact that the electronic properties of the ligands can be controlled via electron donating or withdrawing groups clearly will be beneficial in designing bespoke solar dyes. In an effort to increase fluorescence properties of the metal complexes it was decided to use isothiocyanates as co-ligands, alongside triazoles, with various metals (M= Fe(II), Co(II), Zn(II) and Cd(II)). Interestingly, it was found that that the complexes of $[Zn(L^3)_2(NCS)_2]$ and $[Cd(L^3)_2(NCS)_2]$ are rare examples of the coexistence of two *trans* – coordinated NCS^- anions in the axial position in the mononuclear triazole-based octahedral configuration. Unfortunately, isothiocyanate substituted metal-triazole-complexes did not produce an enhanced fluorescence possibly due to structural reasons (trans- orientation as opposed to cis-).

Since a number of interesting metal complexes were avaible, it was envisaged their use within cancer therapy. A collaboration with Dr. Ragazzon at Salford University was established to assist with this and it found that free ligands are non-toxic towards the tested cell lines and the insertion of metal leads to considerable cytotoxicity.

Using copper and cobalt complexes proved to be the most effective and cytotoxic towards the cell lines. IC_{50} values have shown that the complexes are most active in colon cancers compared to hepatic cancers and is possibly due to differences in binding mechanisms.

10.2 Further Work

Further work should involve fabrication of DSSC cells with the synthesised metal complexes and testing their solar conversion. It would be useful to address whether a cis – configuration is preferred in increasing solar efficiency compared to a trans - orientation of the ligands within these metal complexes. An exploration of the electrochemistry of the synthesised dye solar compounds should be pursued and will surely yield some interesting results and maybe even application potential.

In further work, selected complexes should also be studied for:

- Metabolism, using hepatic enzymes in first instance, to see if there is any modification to the structure.
- Toxicity in primary hepatic and colon cells.
- Target validation through cell cycle analysis and fluorescence microscopy to determine the mode of action on both tumour and primary cells
- The compounds CoL6-2 (the lowest IC_{50} of Hepg2) and CuL5-2 (the lowest IC_{50} of HCT116) could be explored and modified furthet to improve their anticancer activities.
- Synthesis and characterisation of ruthenium complexes with theses ligands for studying the biological activities on liver carcinoma (HepG2) and the colon carcinoma (HCT116).
- Establishing the mechanism of cancer cell killings by selected organometallic complexes.
- Photodynamic investigation using the synthesised organometallic complexes.

10.3 Novelty and contribution to new knowledge

The current investigation yielded several new and interesting contributions to the current field of knowledge in the area.

- New compounds have been synthesised and characterised, including several new bi-dentate 2-pyridyl-1,2,3-triazole ligands bearing a 4-substituted phrnyl arm with various electron withdrawing and electron donating groups (PYTA ligands) to produce several new novel organometallic compounds with two different types of co-ligands, namely Cl- and SCN-. There are currently one paper submitted to the arabain journal of chemistry on these molecules, with a further two papers in preparation. (See the Contributions from this research).
- Proof of a unique crystal structure packing patten of the repeating unit cells in the PYTA ligand, on which a paper has been published in crystallographica **B**70, 379–389 (2014).
- Potential new solar cell compounds that have similar structures to commercial solar cell compounds, and which can be explored more and modified further.
- Potential new anti - cancer compounds with promising and potential selective anti - cancer properties, which can be explored futher.

10.4 Achieving the aims of the investigation

The aims of the investigation, as set out in Chapter 1, were to accomplish the:

1- Synthesis of transition metal complexes.

2- Characterisation of the physical properties of the complexes.

3- Characterisation of the optical, fluorescent and crystallographic properties of the complexes to predict their suitability or not for DSSC.

4- Evolution of the complexes as potential anti - cancer agents.

All these aims were successfully achieved and described in the thesis. Furthermore, the hypotheses that careful ligand design and systemic variation of the metal centre can tune and optimise the optical absorption properties of a new series of chromophores and produce potentially useful anti – cancer drugs, have been mainly proven correctly, although further electrochemical work is required to validate the first part.

Chapter 11 : Physical Appendices

11.1 Appendix for Chapter 6

11.1.1 UV-Vis Spectral data for ligands L^2- L^9

The electronic spectra of a series of 2-pyridyl-1,2,3-triazole attached to the phenyl pendant arm are presented in (Figure 11.1) The ligands L^2-L^9 exhibit similar absorption bands spectrum of the free ligand, the absorption bands occur at 283-292nm it can be assigned to the para substituent phenyl ring, which it can be assigned to overlap of $\pi \rightarrow \pi^*$ and $n \rightarrow \pi^*$ transitions of the aromatic and other functional groups present in the ligands (see Table 11.1) [1- 2].

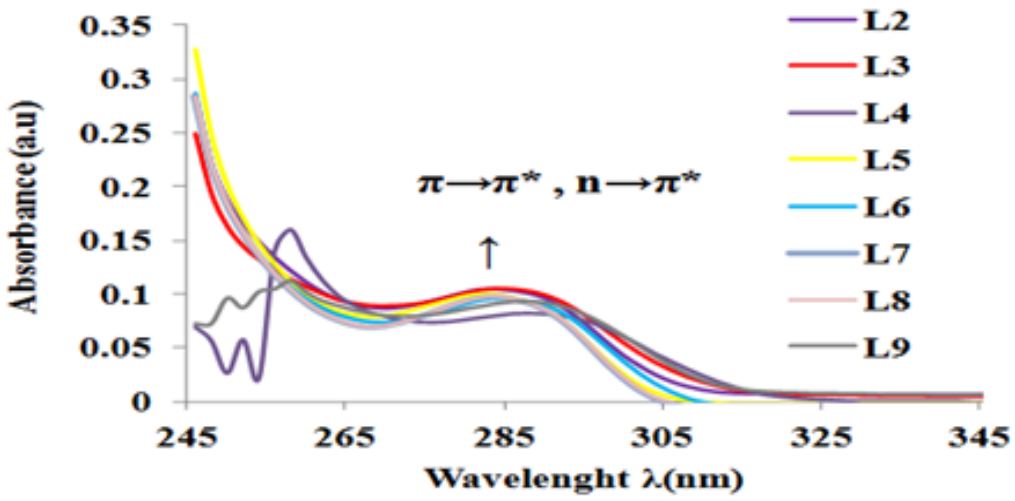

Figure 11.1: Electronic spectra of ligands L^2-L^9 in DMSO (C = 1x10^{-6}M) at 298K.

A plot of the λ_{max} vs the σ_p substituent constant for all ligands gave a concave upward deviation in the Hammett plot with a neagtive slope for the electron donating groups and a positive slope for electron withdrawing groups. This is a change in mechanism in which electron donating groups decrease the positive charge at the triazole ring. However, electron withdrawing groups enhance the positive charge (see Figure 11.2) at this centre. There were three substituents (H, CF_3 and COOH) which are outliers on the plot.

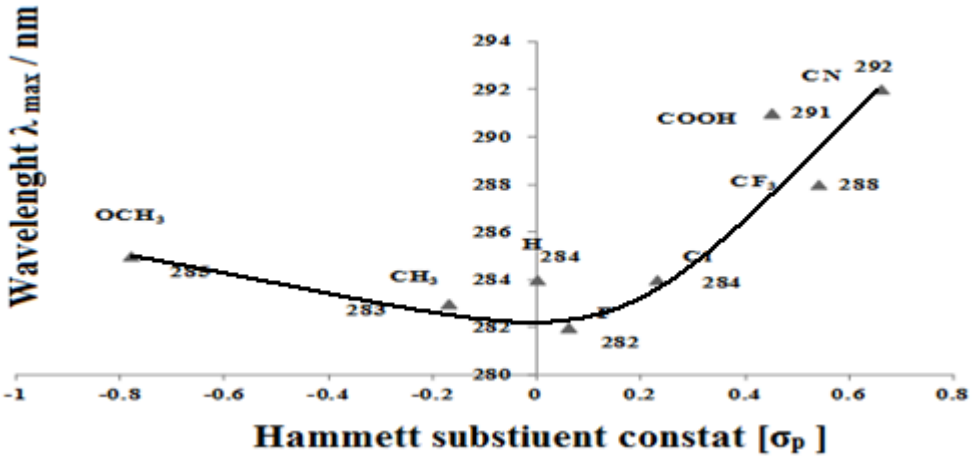

Figure 11.2: Hammett plot of correlations of the λ_{max} of L^2-L^9 ligands *vs.* σ_p values for the Hammett substituent parameters electron donor and withdrawing *para* substituents (R = H, Me, OMe, Cl, F, CN, COOH, and CN).

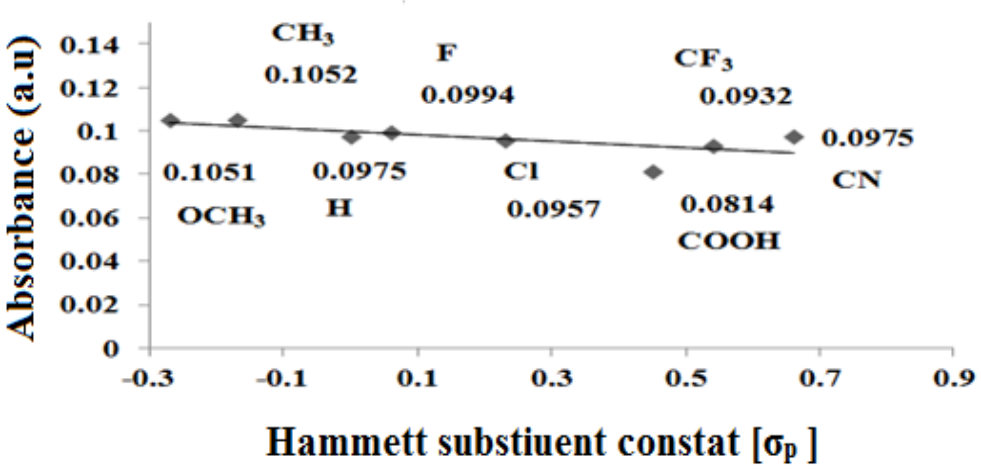

Figure 11.3: Hammett plot of absorbance maximum of L^2-L^9 ligands *vs.* σ_p values for the electron donor and withdrawing *para* substituents (R = H, Me, OMe, Cl, F, CN, COOH, and CN).

In the series L^2-L^9, the maximum absorption of both bands measured in DMSO ($1x10^{-6}$M), gives a linear correlation the between the Hammett σ_p constant for the substituent on the *p*-position of the phenyl group (Figure 11.3). The two substituents which are outliers (COOH and CN) are not included in the plot. This suggests that compounds with these substituents act as stronger acids than one would have predicted from their

values. When electron withdrawing due to mesomeric effects can be extended to the reaction centre via "***through conjugation",*** the result is an even more stabilised species. These types of correlation between the Hammett σ_ρ constant in relation to the substituent of the *p*-position and the relevant UV absorption frequencies were reported previously in literature [3, 4].

Table 11.1: The absorption maxima λ_{max} vs the Hammett parameter of the σ_ρ substituent correlation in DMSO (C= 1 X10^{-6}M).

Compound	Substituent in *para* postion	σ_ρ	λ_{max}(nm)	Absorbance	ε/10^{-6} M dm^3. mol^{-1}.cm^{-1}
L^2	CH3	-0.17	283	0.1051	15100
L^3	OCH3	-0.27	285	0.1052	15200
L^4	COOH	0.45	291	0.0814	81400
L^5	F	0.06	283	0.0994	99400
L^6	Cl	0.23	284	0.0957	95700
L^7	CN	0.66	292	0.0975	97500
L^8	H	0	284	0.0975	97500
L^9	CF3	0.54	288	0.0932	93200

11.2 Appendix for Chapter 7

11.2.1 UV-Vis Spectral data for L^3 ligand

The electronic spectrum of L^3 exhibits an intense absorption maximum at 285nm due to the overlap of $\pi \rightarrow \pi^*$ and $n \rightarrow \pi^*$ transitions, as shown in Figure 11.4. The electronic spectra of the complexes of L^3 exhibited various extents of bathochromic shift of the bands related to the intraligand $\pi \rightarrow \pi^*$ and $n \rightarrow \pi^*$ transitions. Bands in the range of 352-389nm are related to the charge transfer transitions (CT), and were observed in the spectra data for the $[M(L^n)_2Cl_2]$ complexes. Complexes of the d^5-d^9 system display several bands in the visible region due to d-d transitions. The

assignments of these bands indicate octahedral geometries around the different metal atoms (see Table 7.3 page 138 for full assignments) [1-2].

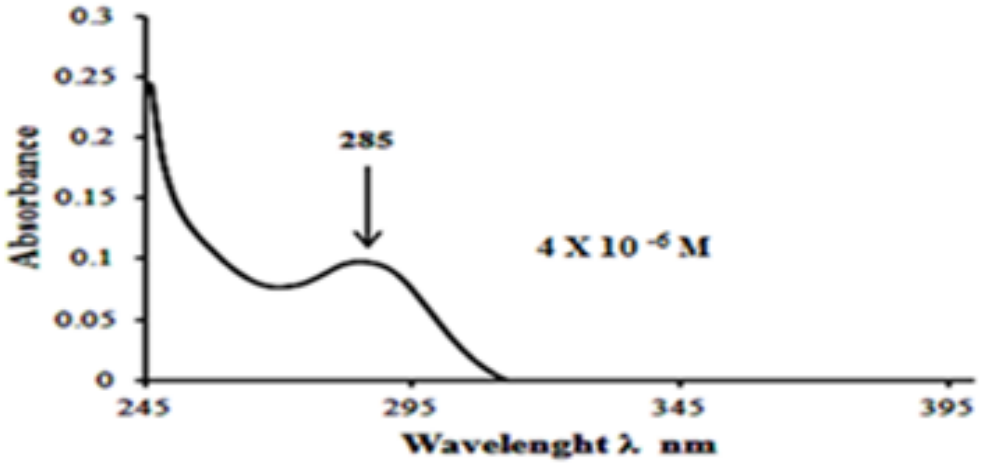

Figure 11.4: UV-Vis spectrum of L^3 at concentration of $1x10^{-6}$M.

11.2.2 UV-Vis Spectrum for $[Mn(L^3)_2Cl_2)]$

The data of the $[Mn(L^3)_2Cl_2]$ complex with different concentrations in DMSO solutions are presented in chapter 7 Table 7.3 page 138. The spectrum of the Mn(II) complex in Figure 11.5 exhibits two bands at 258 nm, and 291 nm at concentration of $5x10^{-6}$ M. These bands are related to the intraligand transitions$\pi \rightarrow \pi^*$ and $n \rightarrow \pi^*$, respectively. High spin Mn(II)-complexes are very weakly coloured compounds due to spin forbidden d-d transitions. Therefore, it is difficult to identify the d-d bands of the Mn(II) complex. At higher concentrations of the Mn(II)-complex, e.g at a concentration of $1x10^{-3}$M, the complex displays several bands. The first band at 352nm = 28409cm^{-1}; ε_{max} = 32$dm^3mol^{-1}cm^{-1}$, is assignable to a $n \rightarrow \pi^*$ transition. The metal-ligand charge transfer transition band is observed at 369nm = 27100cm^{-1}; ε_{max}= 30 dm^3 mol^{-1} cm^{-1}. Lastly the band detected at 390nm = 25641cm^{-1}; ε_{max} = 21$dm^3mol^{-1}cm^{-1}$ could be attributed to a $^4A_1g \rightarrow {}^4T_1g$ transfer. The observed room temperature magnetic moment value 5.32 B.M is typical for a high spin (d^5) configuration of Mn(II)-complexes, and confirm an octahedral geometry about Mn atom [5-7].

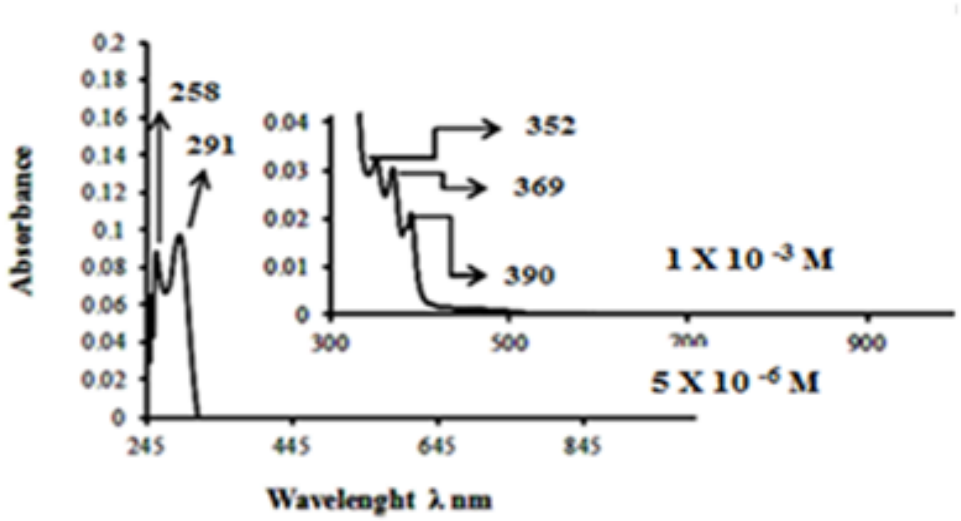

Figure 11.5: UV-Vis spectra of the $[Mn(L^3)_2Cl_2]$ complex in DMSO solutions.

11.2.3 UV-Vis Spectrum data for $[Fe(L^3)_2Cl_2)]$

The UV-Vis spectrum of the $[Fe(L^3)_2Cl_2]$ complex gave a yellow colour in DMSO solution, and is shown in Figure 11.6. The spectrum reveals two absorption peaks at 257nm and 291nm, which are assigned to the intraligand $\pi \rightarrow \pi^*$ and $n \rightarrow \pi^*$ transitions (red shift). The absorption peak at 333nm is related to the charge transfer transition. The peak detected at 922 nm is attributable to a $^5T_2g \rightarrow {}^5E_2g$ transfer. The magnetic moment of 5.07 B.M indicates a high spin octahedral geometry around the Fe atom [8-11].

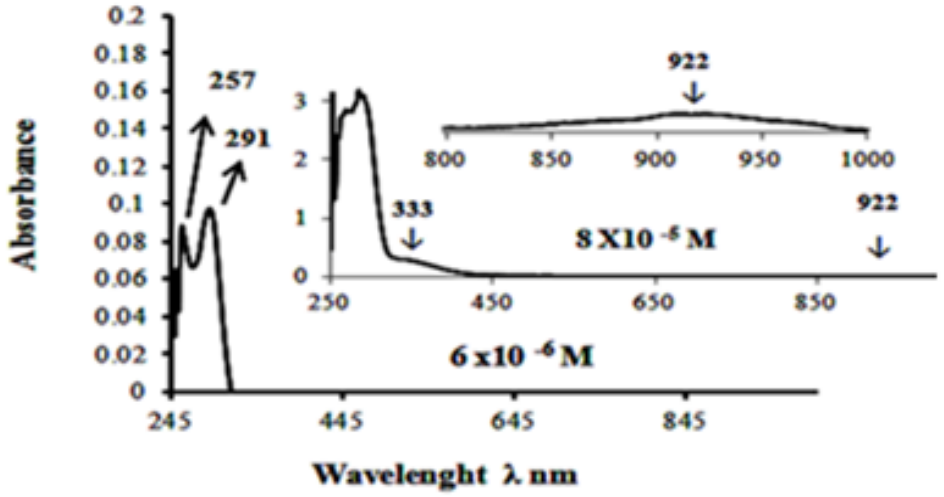

Figure 11.6: UV-Vis spectra of the $[Fe(L^3)_2Cl_2]$ complex in DMSO solutions.

11.2.4 UV-Vis Spectral data for $[Co(L^3)_2Cl_2]$, $[Ni(L^3)_2(Cl_2)]$ and $[Cu(L^3)_2(Cl_2)]$

The spectra of $[Co(L^3)_2(Cl_2)]$, $[Ni(L^3)_2(Cl_2)]$ and $[Cu(L^3)_2(Cl_2)]$ complexes depicted in Figures 11.7 to 11.9, show intraligand transitions (see Table 7.3 page 138). The Co-complex displays two additional bands in the visible region at 615 and 678nm, which are related to $^4T_1g^{(F)} \rightarrow {}^4T_2g^{(P)}$ and $^4T_1g^{(F)} \rightarrow {}^4A_2g^{(F)}$ transitions respectively. This is characteristic for the distorted octahedral geometry around the Co atom. The magnetic measurement of the Co(II) complex, with the value 3.97 B.M, corresponds to three unpaired electrons. This value is in agreement with a high spin configuration and supports an octahedral environment around the Co(II) ion [12, 13].

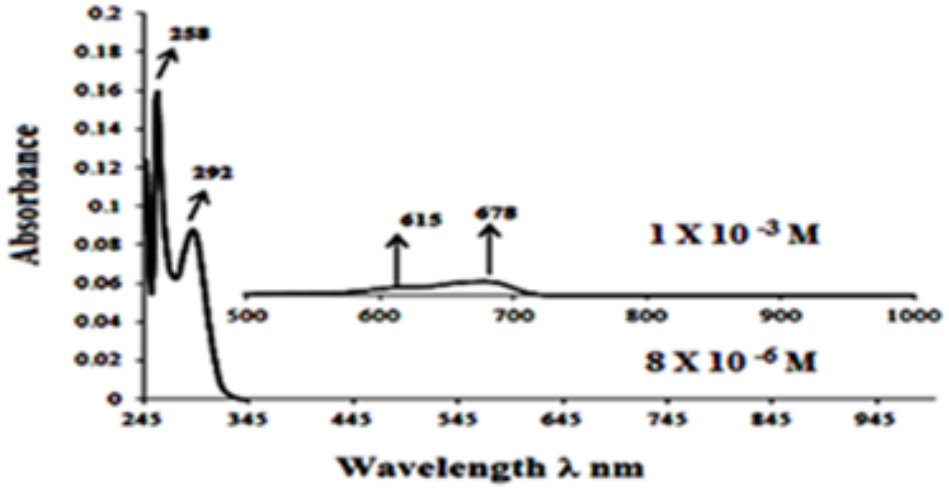

Figure 11.7: UV-Vis spectra of the $[Co(L^3)_2Cl_2]$ complex in DMSO solutions.

The spectrum of the $[Ni(L^3)_2Cl_2]$ displayed in Figure 11.8, displays peaks at 407 and 660nm attributed to $^3A_2g^{(F)} \rightarrow {}^3T_1g^{(p)}$ and $^3A_2g^{(F)} \rightarrow {}^3T_1g^{(F)}$ transitions, respectively. This is typical for a distorted octahedral geometry around the Ni atom [14]. The magnetic measurement value 2.73 B.M and corresponds to two unpaired electrons. This value is in agreement with a high spin configuration and confirmed the octahedral environment around the Ni(II) atom [15-17].

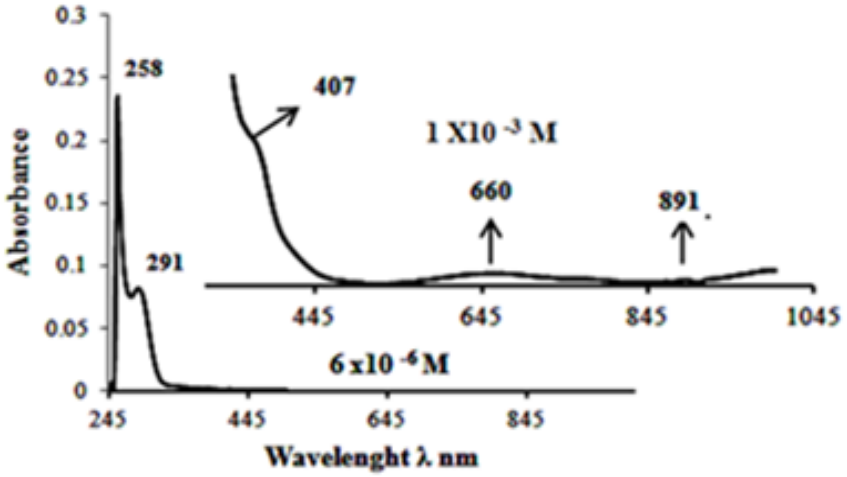

Figure 11.8: UV-Vis spectra of the $[Ni(L^3)_2Cl_2]$ complex in DMSO solutions.

The electronic spectrum of the Cu(II) complex is depicted in Figure 11.9 and consists of a broad, low intensity shoulder band centred at 892nm, which is assigned to a $^2B_1g \rightarrow {}^2B_2$ g transition, which suggests a distorted octahedral configuration. This distortion can be such as to cause the three transitions, $^2B_1g \rightarrow {}^2B_2g$, $^2B_1g \rightarrow {}^2Eg$, and $^2B_1g \rightarrow {}^2A_1g$, to remain unresolved in the spectra. It is concluded that all three transitions lie within the single broad envelope centred at the same range previously mentioned. This assignment is in agreement with the general observation that Cu(II) d-d transitions are normally close in energy. The magnetic moment measurement of the Cu(II) complex, with the value of 1.69 B.M, corresponds to one electron. This value is in agreement with a high spin configuration and of an octahedral environment around the Cu(II) atom [18, 20].

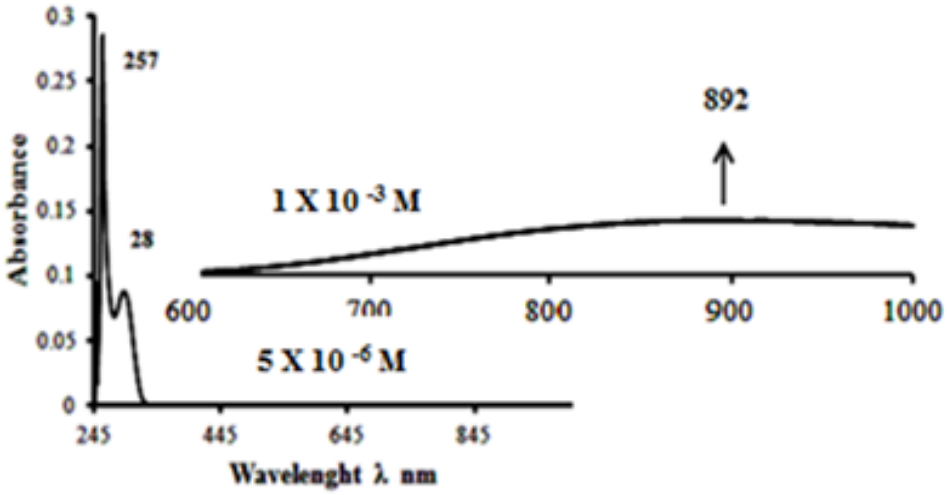

Figure 11.9: UV-Vis spectra of the $[Cu(L^3)_2Cl_2]$ complex in DMSO solutions.

Due to the Jahn-Teller (J-T) effect, the ground state ^{2}Eg is further splitted into a ^2B_1g ground state and ^{2}Ag excited state.

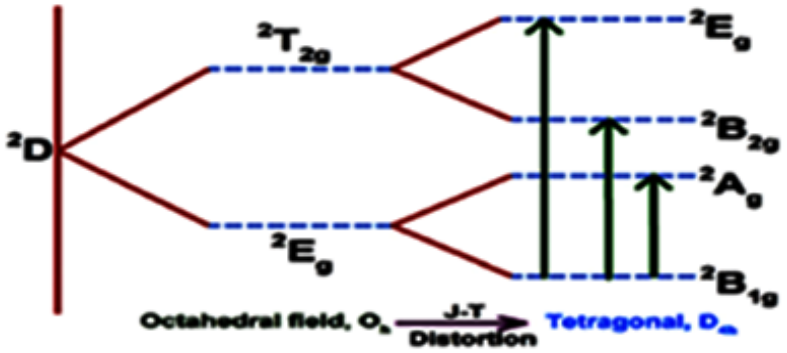

Figure 11.10: Jahn-Teller distortion of the octahedral symmetry of Cu(II) and the ^{2}Eg and ^2T_2g states of the octahedral Cu(II) ion (d^9) split under the influence of tetragonal distortion [23].

11.2.5. UV-Vis Spectral data for $[Zn(L^3)_2Cl_2]$ and $[Cd(L_3)_2(Cl_2)]$

The electronic spectra of the $[Zn(L^3)_2Cl_2]$and $[Cd(L^3)_2Cl_2]$ complexes in Figure 11.11 exhibit bands at 257nm, 291nm and 258, 286nm, respectively. These were assigned to intra-ligand transitions $\pi \rightarrow \pi^*$ and $n \rightarrow \pi^*$ (see Table 7.3 page 138), which are related to $d^{(10)}$ electron configurations of the Zn(II) and Cd(II) metals respectively [21, 22].

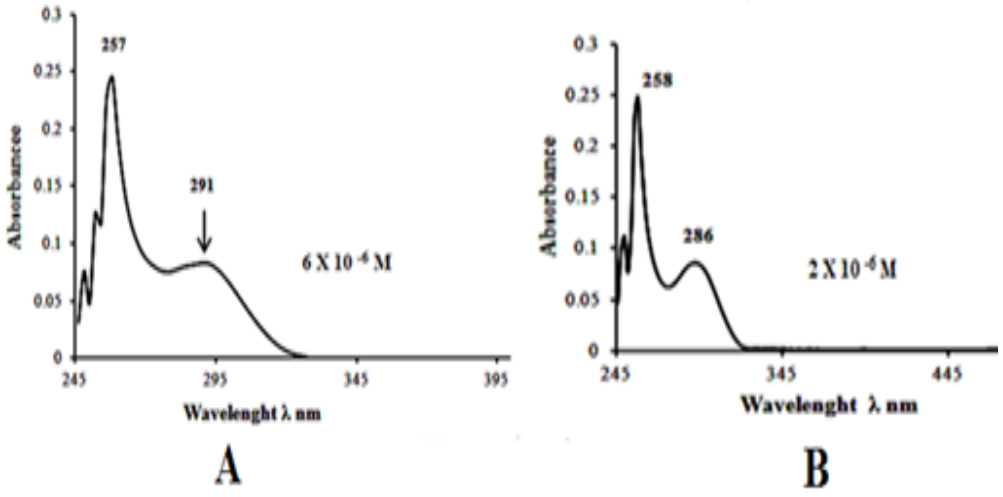

Figure 11.11: UV-Vis spectra (A) of the $[Zn(L^3)_2Cl_2]$ and (B) the $[Cd(L^3)_2Cl_2]$ complexes in DMSO solution.

11.2.6 Introduction to Magnetic Susceptibility

Magnetic susceptibility is measured using a sensitive instrument known as a magnetic susceptibility balance. The Gouy balance was used for determining the magnetic susceptibility of all the materials. The gram magnetic susceptibility for a substance can be calculated from the following equation.

$$\chi_g = (Cbal)\ (l)\ (R - R_o) / (10^9)\ (m) \qquad (11.1)$$

Where; l = height of sample in the tube in units of centimetres

m = mass of the sample in units of grams

R = reading for tube plus sample

R_o = reading for the empty tube

C_{bal} = balance calibration constant = 1.0

The molar magnetic susceptibility is then calculated from the gram magnetic susceptibility using Equation (11.2):

$$\chi_m = (\chi_g)\ (molar\ mass) \qquad (11.2)$$

The magnetic susceptibility for a particular substance is not particularly useful in itself. However, the effective magnetic moment for a particular substance can be calculated from the gram magnetic susceptibility [23] using Equation (11.3):

$$U_{eff} = 2.83\ [(X_m)\ (T)]^{1/2} \qquad (11.3)$$

In this equation T represents the Kelvin temperature (294 K).

11.2.7 Introduction to fluorescence measurements

Fluorescence is the molecular absorption of light energy at one wavelength and its nearly instantaneous re-emission at another, usually longer, wavelength. Some molecules fluoresce naturally and others can be modified to become fluorescent compounds. Fluorescent compounds have two characteristic spectra: an excitation spectrum (the wavelength and amount of light absorbed) and an emission spectrum

(the wavelength and amount of light emitted). These spectra are often referred to as a compound's fluorescence signature or fingerprint. No two compounds have the same fluorescence signature. It is this principle that makes fluorometry a highly specific analytical technique.

Fluorometry is the measurement of fluorescence. The instrument used to measure fluorescence is called a fluorometer or fluorimeter. A fluorometer generates the wavelength of light required to excite the analyte of interest. It selectively transmits the wavelength of light emitted, and then it measures the intensity of the emitted light. The emitted light is proportional to the concentration of the analyte being measured (up to a maximum concentration). Fluorometers employ monochromators (a spectrofluorometer), optical filters (a filter fluorometer), or narrow band light sources like LED's or lasers to select excitation and emission wavelengths.

Fluorometry is chosen for its extraordinary sensitivity, high specificity, simplicity, and low cost compared to other analytical techniques. Fluorometry is ordinarily 1000-fold more sensitive than absorbance measurements. It is a widely accepted and powerful technique that is used for a variety of environmental, industrial, and biotechnology applications. It is a valuable analytical tool for both quantitative and qualitative analysis [24-25].

11.2.8. Jablonski diagram (diagram of electronic transitions)

Absorption of light (photons) by a population of molecules stimulates electron transition from the singlet ground electronic level S_0 to an excited state S_n $(n > l)$. An excited molecule will return to the ground state S_0 following two consecutive steps [26]. The molecule at S_n returns to the lowest excited state S_1 by losing a part of its energy in the surrounding environment. This phenomenon is usually called internal conversion, and is shown in Figure: 11.12.

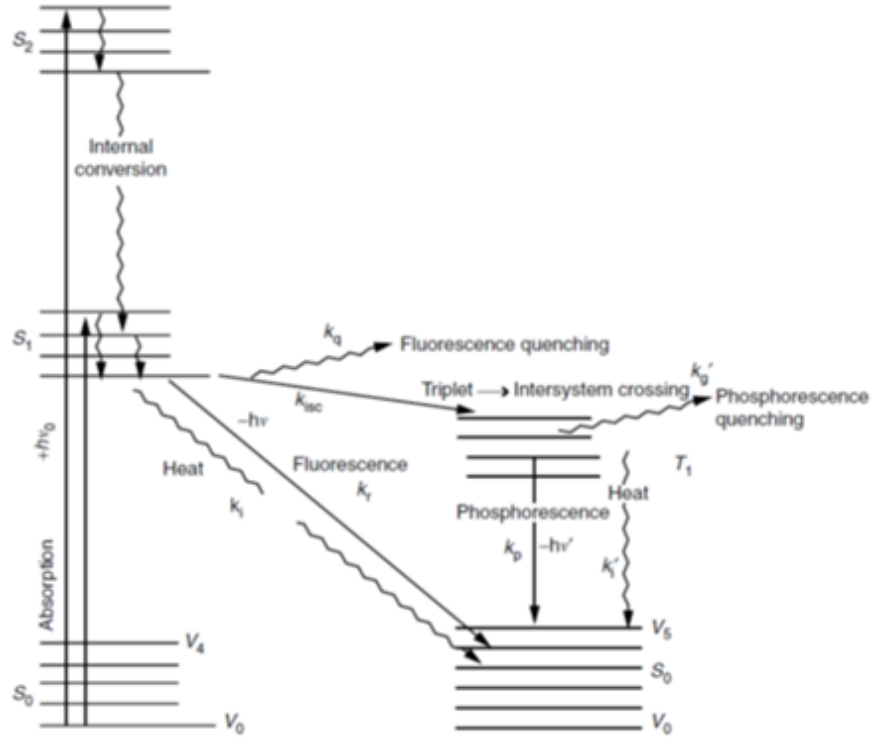

Figure 11.12: Jablonski diagram of electronic transitions. [27-28]

2- From the excited state S_1, the molecule will reach the ground state S_0 via various competitive processes:

• Emission of a photon (fluorescence) with a radiative rate constant (K_r).

• Part of the absorbed energy is dissipated in the medium as heat. This type of energy is non-radiative and happens with a rate constant (K_i).

• Excited molecules can release some of their energy to molecules located nearby. This energy transfer occurs with a rate constant K_q (collisional quenching), or with a rate constant K_t (energy transfer at distance).

• A transient passage occurs to the excited triplet state T_1 of energy lower than S_1 with a rate constant K_{isc} (inter-system crossing). For each excited state S, there is an excited state T of lower energy. The triplet state is an excited state and so is energetically unstable. Therefore, de-excitation of the molecule from the triplet state occurs via competitive processes similar to those demonstrated for the de-excitation of the excited singlet state $S1$:

- Emission of a photon with a rate constant K'_p. This phenomenon is entitled phosphorescence.

- Dissipation of non-radiative energy with a rate constant K'_i.
- Transfer of energy to another molecule at distance (rate constant K'_t) or by collision (rate constant K'_q).

Generally, the main emissions of the metal-organic hybrid complexes can be divided into three types:

1- The LLCT (Ligand - to - Ligand charge transfer)
2- LMCT (Ligand - to - metal charge trainsfer)
3- MLCT (Metal - to - Ligand charge trainsfer) [29-30]

11.2.9 Fluorescence quantum yield

Molecules in the fundamental ground state absorb light with intensity equal to I and reach an excited state S_n. Then, different competitive processes, including fluorescence, will compete with each other to de-excite the molecule. The rate constant (k) of the excited state is the sum of the kinetic constants of the competitive processes, as given in Equation (11.4):

$$k = k_r + k_{isc} + k_i \qquad (11.4)$$

The fluorescence quantum yield ϕF is the number of photons emitted by the radiative way over that absorbed by the molecule, as shown in Equation (11.5):

$$\phi F = \frac{\text{emitted photons}}{\text{absorbed photons}} = \frac{kr}{kr + kisc + ki} \qquad (11.5)$$

All the quantum yields have been referenced to the recrystalised standard p-terphenyl (λ_{max} = 276 nm). The fluorescence measurement was carried out at 294 K and at low concentrations to avoid reabsorption. The solutions were purged with helium gas to prevent oxygen quenching of the emission spectra. The unknown quantum yield $\Phi_{(x)}$ of the complex solutions relative to the quantum yield of the reference $\Phi_{(r)}$ for the standard p-terphenyl was 1.0, as calculated by Equation 11.6:

$$\Phi_{(x)} = \Phi_{(r)} \times (Area_{(x)} / (Area_{(r)}) \times (ABS_{(r)} / (ABS_{(x)}) \times (\eta^2_{(x)} / \eta^2_{(r)}) \qquad (11.6)$$

The area of the unknown and reference (Area $_{(x \text{ and } r)}$) were determined from the fluorescence spectra [31-34].

The absorbance terms in the equation are those of the unknown and reference (ABS $_{(x \text{ and } r)}$) at their appropriate excitation wavelengths, and the η^2 is the refractive index for the solvent (DMSO) = 1.4770. Usually the refractive indices can be taken from a chemistry text [35]. The area of the emission spectrum was integrated using the software available in the instrument (FL solution software). As an example, below is the quantum yield for cobalt complex calculated by Equation 11.7:

$$\Phi_{(Co)} = \Phi_{(PTP)} \times (\text{Area}_{(Co)} / (\text{Area}_{(PTP)}) \times (\text{ABS}_{(PTP)} / (\text{ABS}_{(Co)}) \times (\eta^2_{(DMSO)} / \eta^2_{(DMSO)}) \quad (11.7)$$

11.2.10 Stokes shift

Fluorescence energy is always less than the absorption energy for a given molecule. Thus, the emitted light is observed at longer wavelengths than the excitation, as shown in Figure 11.13.

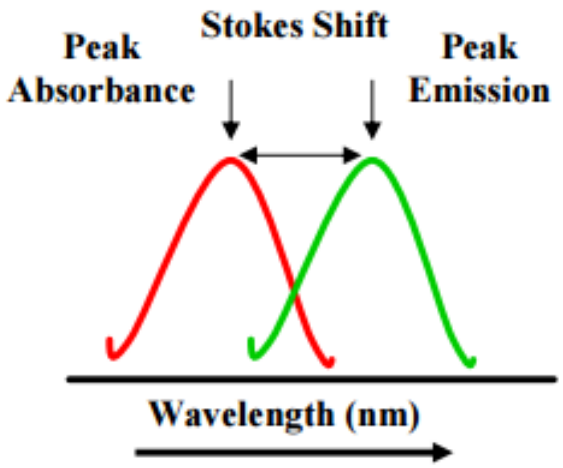

Figure 11.13: Stokes shift between the peak absorbance and peak emission [36].

1.3 Appendix for Chapter 8

11.3.1 UV-Vis Spectrum data for the $[Fe(L^3)_2(NCS)_2]$ complex

The UV-Vis spectrum of the $[Fe(L^3)_2(NCS)_2]$ complex in DMSO solution is yellow in colour (Figure 11.14). The spectrum reveals two absorption peaks at 258 and 286nm, which are assigned to intra-ligand $\pi \rightarrow \pi^*$ and $n \rightarrow \pi^*$ transitions. The absorption peak at 351nm is attributed to a charge transfer transition. The magnetic moment for the complex of 5.07 B.M, indicates via the literature an assignment of a high spin octahedral environment (see Table 8.2). [10-15].

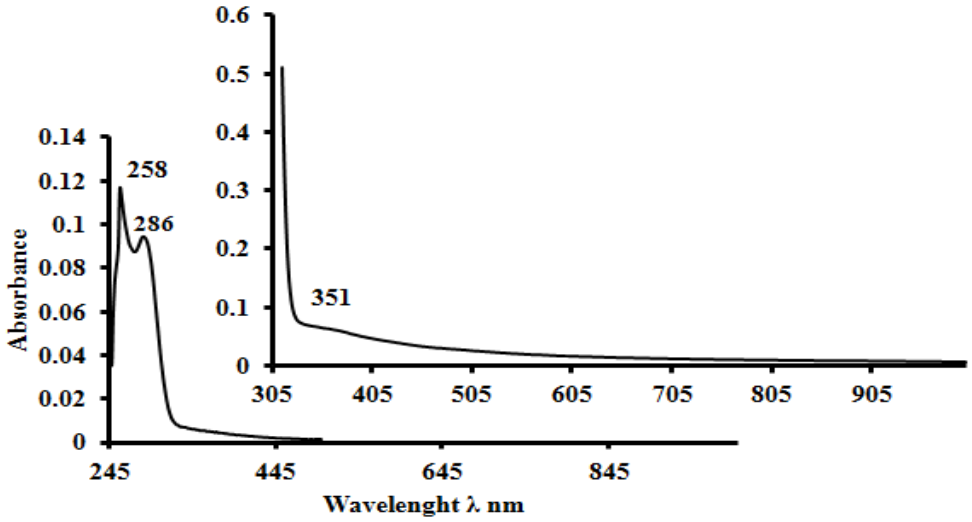

Figure 11.14: UV-Vis spectrum of $[Fe(L^3)_2(NCS)_2]$ complex in DMSO solution.

11.3.2 UV-Vis Spectral data for the $[Co(L^3)_2(NCS)_2]$ complex

The UV-Vis spectrum of the $[Co(L^3)_2(NCS)_2]$ complex is depicted in Figure 11.15. It shows intra-ligand transitions (see Table 8.2). The Co-complex displays bands in the visible region at 536nm, which are related to a $^4T_1g^{(F)} \rightarrow {}^4T_2g^{(P)}$ transfer. Other bands at 258-288nm were assigned to the intra-ligand $\pi \rightarrow \pi^*$ and $n \rightarrow \pi^*$ transitions, respectively. This is characteristic of a distorted octahedral geometry around the Co atom. The magnetic measurement of the Co(II) complex of 3.97 B.M, corresponds to three unpaired electrons and is in agreement with a high spin configuration with an octahedral environment around the Co(II) ion [5, 8-10, 20, 22].

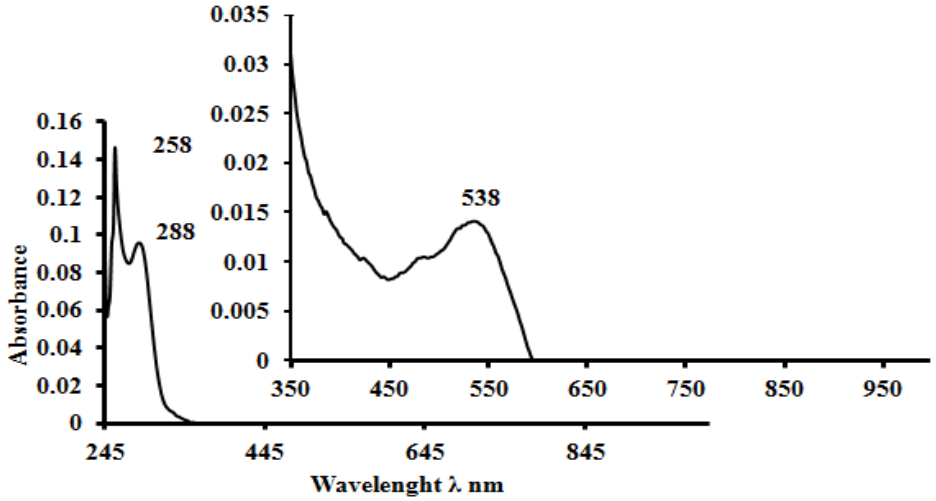

Figure 11.15: UV-Vis spectrum of $[Co(L^3)_2(NCS)_2]$ complex in DMSO solution.

11.3.3 UV-Vis Spectral data for the $[Zn(L^3)_2(NCS)_2]$ and$[Cd(L^3)_2(NCS)_2]$ complexes

The UV-Vis spectra of the $[Zn(L^3)_2(NCS)_2]$ and $[Cd(L^3)_2(NCS)_2]$ complexes in Figures 11.16 and 11.17 exhibit bands at 257 nm and 288nm, respectively. These bands were assigned to intra-ligand $\pi \rightarrow \pi^*$ and $n \rightarrow \pi^*$ transitions (see Table 8.2), and is related to the d^{10} electron configuration of the Zn(II) and Cd(II) metals, respectively [13-21].

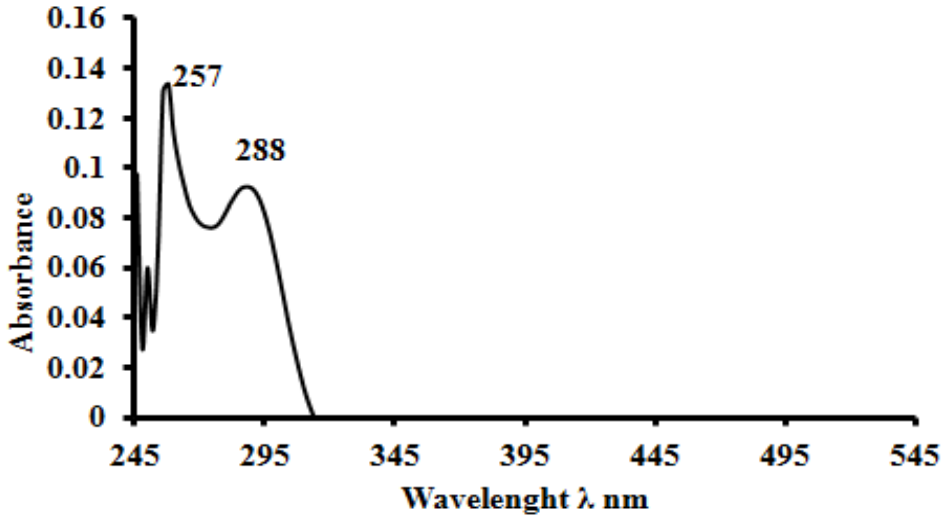

Figure 11.16: UV-Vis spectrum of $[Zn(L^3)_2(NCS)_2]$ complex in DMSO solution.

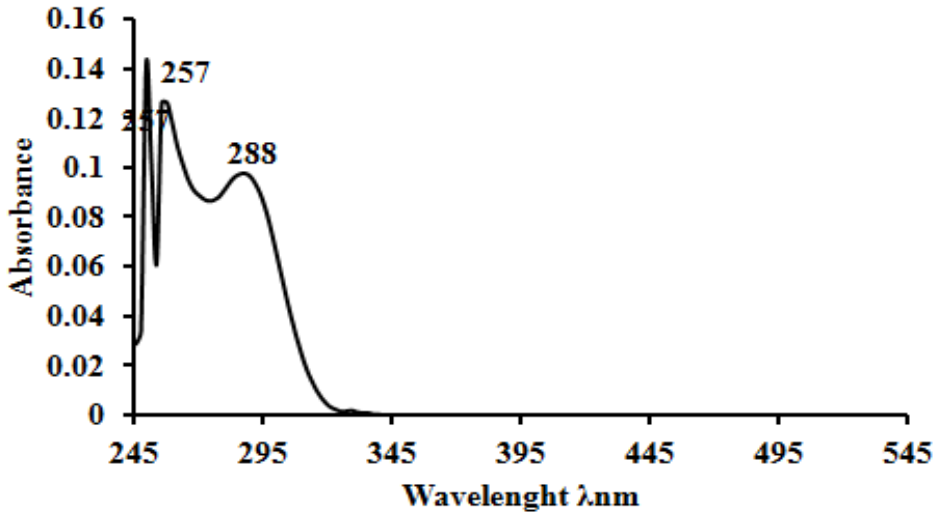

Figure 11.17: UV-Vis spectrum of $[Cd(L^3)_2(NCS)_2]$ complex in DMSO solution.

The magnetic moments and the conductivity measurements for these metal complexes have shown similar behaviour to the complexes of the chlorido ions that are described in chapter 7 (see section 7.2.5 and 7.2.6).

11.4 References

1-Wolff M., Munoz L., François A., Carrayon Ch., Seridi A., Saffon N., Picard C., Machura B., Benoist E., *Dalton Trans*., 42:7019(2013)

2-Durust Y., Yidirum., *Monatsh. Chem*., DOI 10.1007/s00706-010-035I-Z,I;(2010)

3-Krstić V V., Uščumlić G S., Muškatirović M D., *J. Mol. Struct*.,174:247(1988)

4- Krstić V V., Uščumlić G S., Muškatirović M D., *J. Mol. Struct*.,174:251(1988)

5-Lever A B P.., *Inorganic Electronic Spectroscopy*., 2nd edition., Elsevier, New York, p.249 (1986)

6-Mahmoud W H., Mohamed G G., El-Dessouky M M I., *Spectrochim. Acta*., Part A., 122:598(2014)

7-Refata M S., El-Metwaly N M., *Spectrochim. Acta*. Part A., 92:336(2012)

8-Sowjanya G., Reddy N C G., Reddy S L., Reddy B J., Frost R L., *Spectrochim. Acta* Part A., 71:751(2008)

9-Malik S., Ghosh S., Mitu L., *J. Serb. Chem. Soc*., 76:1387(2011)

10-Spinu C., Pleniceanu M., Tigae C., *J. Serb. Chem. Soc.*, 73:415(2008)

11-Modi C.K., *Spectrochim. Acta*., Part A., 71:1741(2009)

12-Raman N., Sobha S., Thamaraichelvan A., *Spectrochimi Acta.,* Part A.,78: 888(2011)

13-Revanasiddappa H D., Kumar L S., Prasad K S., Vijay B., Jayalalshmi B., *Chem. Sci. J*., CSJ-28, 1, (2011)

14-Tong Y Z., Wang Q., Si M., Qi J., Yan S., Yang G M., Cheng P., Liao D Z., *Polyhedron*., 30:3151(2011)

15-Gonzalez E., Witchel A R., Reber C., *Coord. Chem. Rev*., 251: 351(2007)

16-Chandra S., Sharma A. K., *Spectrochim. Acta., Part A*., 72:851(2009)

17-Al-Jeboori M J., Al-Dujaili., Al-Janabi A H., *Transition. Met. Chem*., 34: 109(2009)

18-Choudhury B., Dey M., Choudhury A., *Int. Nano. Lett*, 3:251(2013)

19-Refat M.S., Chandra S., Tyagi M., *J. Therm. Anal. Calorim*., 100:261(2010)

20-Cotton F.A., Wilkinson G., Murillo C. A., Bochmann M., *Advanced Inorganic Chemistry*., 6th edition.; Wiley, New York(1999)

21-Abdul-Ghani A J., Al-Jeboori M J., Al-Karawi A M., *J. Coord. Chem*., 62: 2736(2009)

22-Al-Jeboori M J., Hassan H A, Al-Saidy W A.., *Transition Met. Chem*., 34: 593(2009)

23-Bain G.A., Berry J.F., *J. Chem. Educ*., 85:532(2008)

24-Lakowicz J.R., Principles of Fluorescence Spectroscopy, Plenum Press, New York (1983)

25-Guilbault G G., Practical Fluorescence., Second Edition, Marcel Dekker, Inc, New York (1990)

26-Albani J R., Principles and Applications of Fluorescence Spectroscopy., Laboratoire de Biophysique Moléculaire Université des Sciences et Technologies de Lille France(1988)

27-Jablonski A., Zeit. fur Physik., 94:38(1935)

28-Zhang, J Z., Cao, W R., Pan, J X., Chen, Q W., *Inorg. Chem. Commun*., 10: 1360(2007)

29-Reguera E., Marin E., Calderon A., Hernandez R., *J. Spectrochim. Acta*., Part A.,68:191(2007)

30-Wang X W., Zhang Y H., *Inorg. Chem. Comm*., 11: 832(2008)

31-Demas J N., Grosby G A., *J. Phys. Chem*., 75:991(1971)

32-Heller C A., Henry R A., McLaughlin B A., Bliss B E., *J. Chem. Eng. Data*., 19:214(1974)

33-Das D., Chand B G., Sarker K K., Dinda J., Sinha C., *Polyhedron*., 25: 2333(2006)

34-Williams A T R., Winfield S.A., Miller J N., Analyst, 108:1067(1983)

35-Handbook of Chemistry and Physics, 65th Edition. Weast R. C., Ed; CRC: Boca Raton, Florida, USA(1985)

36-http://www.biosyn.com/tew/fluorescent-labeling-of-oligonucleotides.aspx